

## MHD HYBRID NANOFUIDS FLOW THROUGH POROUS STRETCHING SURFACE IN THE PRESENCE OF THERMAL RADIATION AND CHEMICAL REACTION

✉ Gladys Tharapatla<sup>a</sup>, ✉ Vijaya Lakshmi Garishe<sup>b</sup>, ✉ N. Vijaya<sup>c</sup>, ✉ Sridhar Wuriti<sup>c</sup>, ✉ G.V.R. Reddy<sup>\*c</sup>

<sup>a</sup>Department H&S, Methodist College of Engineering and Technology, Bogulkunta, Abids, Hyderabad, Telangana 500001, India

<sup>b</sup>Department of Mathematics, MGIT, Gandipet, Hyderabad, Telangana, India-500075

<sup>c</sup>Department of Mathematics, Koneru Lakshmaiah Education Foundation, Vaddeswaram, India-522302

Corresponding Author E-mail: [gvrr1976@kluniversity.in](mailto:gvrr1976@kluniversity.in)

Received June 8, 2025; revised August 2, 2025; accepted August 11, 2025

This study investigates the convective transport of heat and mass in a magnetohydrodynamic (MHD) nanofluid flow over a permeable, electrically actuated stretching surface embedded in a porous medium. The analysis incorporates key physical effects including thermal radiation, heat generation, viscosity dissipation, and chemical reactions. The governing equations are formulated to account for the influence of porosity, magnetic fields, thermal and concentration gradients, as well as chemical kinetics. Special attention is given to the control of nanoparticle volume fraction at the boundary interface. Two nanofluid models – Copper–Water (Cu–H<sub>2</sub>O) and Aluminum Oxide–Water (Al<sub>2</sub>O<sub>3</sub>–H<sub>2</sub>O)—are considered to assess thermal performance. The nonlinear boundary value problem is solved numerically using a shooting technique combined with a fourth-order Runge–Kutta method. The results show excellent agreement with previously published data, validating the accuracy and robustness of the present model. These findings have potential applications in advanced heat transfer systems, such as cooling technologies and materials processing.

**Keywords:** Hybrid nanofluids; MHD; Porous media; Thermal radiation; Skin-friction

**PACS:** 47.65.-d, 47.56.+r, 44.40.+a, 66.20.-d, 47.85.mb

### Nomenclature

Symbol	Description	Unit			
u, v	Velocity components in x- and y-directions	m/s	D <sub>B</sub>	Brownian diffusion coefficient	m <sup>2</sup> /s
ψ	Stream function	m <sup>2</sup> /s	D <sub>T</sub>	Thermophoretic diffusion coefficient	kg/(m·s)
T, T <sub>w</sub> , T <sub>∞</sub>	Temperature, wall temperature, ambient temperature	K	K <sub>0</sub>	Chemical reaction rate constant	s <sup>-1</sup>
C, C <sub>w</sub> , C <sub>∞</sub>	Concentration, wall concentration, ambient concentration	kg/m <sup>3</sup>	M	Magnetic field parameter	–
μ <sub>nf</sub> , μ <sub>f</sub>	Dynamic viscosity of nanofluid/base fluid	Pa·s	K <sub>1</sub>	Porosity parameter	–
ρ <sub>nf</sub> , ρ <sub>f</sub> , ρ <sub>s</sub>	Density of nanofluid, base fluid, solid particles	kg/m <sup>3</sup>	R	Radiation parameter	–
(ρc <sub>p</sub> ) <sub>nf</sub> , (ρc <sub>p</sub> ) <sub>f</sub> , (ρc <sub>p</sub> ) <sub>s</sub>	Heat capacity of nanofluid, base fluid, solid particles	J/(m <sup>3</sup> ·K)	Pr	Prandtl number	–
k <sub>nf</sub> , k <sub>f</sub> , k <sub>s</sub>	Thermal conductivity of nanofluid, base fluid, solid particles	W/(m·K)	Q	Heat source/sink parameter	–
α <sub>nf</sub>	Thermal diffusivity of nanofluid	m <sup>2</sup> /s	Ec	Eckert number	–
ν <sub>f</sub>	Kinematic viscosity of base fluid	m <sup>2</sup> /s	Sc	Schmidt number	–
η	Similarity variable (dimensionless)	–	K <sub>r</sub>	Chemical reaction parameter	–
f(η)	Dimensionless stream function	–	S <sub>r</sub>	Soret number	–
θ(η)	Dimensionless temperature	–	φ	Nanoparticle volume fraction	–
φ(η)	Dimensionless concentration	–	ω	Frequency parameter	s <sup>-1</sup>
σ	Electrical conductivity	S/m	a	Stretching rate constant	s <sup>-1</sup>
B <sub>0</sub>	Magnetic field strength	T	n, m	Surface concentration/temperature gradient indices	–
K	Permeability of porous medium	m <sup>2</sup>	f', f'', f'''	First, second, third derivatives of f(η)	–
Q <sub>0</sub>	Volumetric heat generation coefficient	W/m <sup>3</sup>	θ', θ''	Derivatives of θ(η)	–
q <sub>r</sub>	Radiative heat flux	W/m <sup>2</sup>	φ', φ''	Derivatives of φ(η)	–
σ*	Stefan–Boltzmann constant	W/(m <sup>2</sup> ·K <sup>4</sup> )	ω <sub>1</sub> , ω <sub>2</sub> , ω <sub>3</sub> , ω <sub>4</sub>	Non-dimensional grouped parameters	–
K*	Rosseland mean absorption coefficient	m <sup>-1</sup>			

**Cite as:** G. Tharapatla, V.L. Garishe, N. Vijaya, S. Wuriti, G.V.R. Reddy, East Eur. J. Phys. 3, 158 (2025), <https://doi.org/10.26565/2312-4334-2025-3-14>

© G. Tharapatla, V.L. Garishe, N. Vijaya, S. Wuriti, G.V.R. Reddy, 2025; CC BY 4.0 license

## 1. INTRODUCTION

The examination of nanofluids has gotten a considerable sum of consideration in modern scholastic talk. Usually due to the reality that nanofluids have made strides warm properties in differentiate to customary liquids. Nanofluids are a novel category of liquids that are characterised by the nearness of nanoparticles that are suspended inside a substrate liquid. As a result of the extraordinary warm exchange capabilities that they have, they have risen as a potential choice for a huge assortment of mechanical applications. The marvels of boundary layer stream and warm exchange over extended surfaces are basic components of an assortment of building forms. These operations incorporate the expulsion of polymer sheets, strengthening, gem arrangement forms, metal turning, and hot rolling. It was Crane [1] who played a noteworthy part within the starting stages of the examination of stream flow past a extending plate. Hence, a expansive number of analysts have examined the stream and warm exchange characteristics of a assortment of liquids over extended surfaces. The stream of a nanofluid by means of a extended sheet was examined by Khan and Pop [2], who carried out an examination into the boundary layer stream. In his consider [3], Abd El-Aziz examined the impacts of warm dissemination and dissemination thermo on the combined warm and mass exchange wonders that are related with Three-dimensional free flow of water and magnetism over a transparent, long surface, along with rays. A ponder was conducted by Hady and colleagues [4] to assess the impact that radiation has on the gooey stream of a nanofluid and the warm exchange that happens over A sheet with a nonlinear extension. The insecure boundary-layer stream and warm exchange elements with their help, Bachok et al. examined the impact of a little fluid across a penetrable stretching/ shrinkable sheet. [5]. In them consider, Rohni and colleagues [6] used Buongiorno's show to examine the stream and warm exchange characteristics that happened over an unsteady contracting sheet that was subjected to suction in a nanofluid. In arrange to clarify the convective transport forms that take put in nanofluids, Buongiorno [7] proposed a show that comprises of two components. Inside the system of a chemical response, Sandhya et al. [8] conducted inquire about to investigate Heat and mass transfer's influence on a magnetohydrodynamic stream that travelled through a porous plate that was tilted. A non-Darcy common convection administration was the subject of an examination by Murthy and Singh [9], who explored the suggestions of gooey scattering. Motsa [10] displayed an interesting ghostly unwinding method for the examination of closeness variable nonlinear boundary layer stream frameworks. This method was created for those frameworks. The components of an a non-New nanofluid flow past an inclined plate that is speeding were examined by Gladys and Reddy [11], who explored the effect of changing consistency and thermal conductivity on the stream elements. Vijaya and Reddy [12] explored the magnetohydrodynamic stream of Casson liquid across a permeability plate that is vertical, while taking into account the effects of radiation, Soret, along with chemical forms. A numerical examination into common convection was completed by Abu-Nada and Oztop [13] inside rectangular walled in areas that were in part warmed and filled with nanofluids to explore the wonder. A demonstrate in which the thickness of concentrated suspensions and arrangements is taken into thought was created by Brinkman [14]. Maxwell Garnett [15] created a conceptual system that gives a clarification for the colouration marvels that are watched in metallic oxide coatings and glasses. The application of nanofluids for the reason of upgrading warm exchange in isolated streams that are experienced in backward-facing steps was examined by Abu-Nada [16]. Beneath the impact of a attractive field, Hamad [17] was able to get an expository arrangement for the common convection stream of a nanofluid over a sheet that was amplifying in a direct method. A think about conducted by Kameswaran and colleagues [18] looked into the hydromagnetic stream of nanofluids that happened as a result of a sheet that was either extended or contracted. The analysts took into consideration the impacts of thickness dissemination and chemical intuitive. The highlights of warm exchange that are associated with a persistent extended surface that's subject to fluctuating temperature conditions were explored by Grubka and Bobba [19]. Rafique et al. [20] conducted an in-depth mathematical analysis concerning the flow behavior of A mixed nanofluid with magnetohydrodynamics (MHD) at play. This hybrid nanofluid, made up of particles and an organizing liquid, demonstrated good performance in a range of slide and gravity situations. In their study, Nisar et al. [21] examined how the process of heat transmission is affected by thermal transit in single-phase nanofluid flow across radially extended disks, showing Because using water and titanium dioxide as a foundation fluid greatly accelerates the process of heat transfer. Patil et al. [22] conducted a thorough examination of the interactions of magnetized bioconvective micropolar nanofluid as it flowed across a wedge, while also factoring in the role of oxytactic microorganisms. The investigation conducted by Rawat and others [23] focused on how non-homogeneous thermal sources and sinks react to nanoparticle aggregation to change the flow properties of a fluid with a wedge-like shape composed of titania and ethylene glycol. Umavathi [24] focused their investigation on the movement of a micropolar tiny fluids that conducts electricity via a wedge shape while accounting for the effects of ion and Hall winds and a sink or source of heat.

The primary objective of this endeavour is to delve into the flow conundrum of a hybrid nano-fluid comprising  $Al_2O_3+Cu$  paired with the base fluid  $H_2O$  through the lens of the Maxwell fluid model. Intertwined equations of momentum, energy, and mass concentration alongside the influences of Lorentz force, chemical reactions, and the impact of Soret term are considered. A porous plate that stretches linearly and is nestled within porous media is taken into account. Nanoparticles of cylindrical forms are successfully created. In the subsequent sections, the intricacies of modeling and the simulation process are elaborated upon in detail.

## 2. MATHEMATICAL FORMULATION

We consider two-dimensional steady-state boundary layer flow of an incompressible nanofluid gliding over a permeable stretching sheet, merging the phenomena of thermal and mass transport. The coordinate framework is

established such that its origin resides at the juncture where the sheet initiates its stretching, with the x-axis gracefully tracing along the stretching surface while the y-axis stands perpendicular to it. It is presumed that the externally imposed magnetic field reigns supreme over electromagnetic influences, thereby diminishing the significance of the induced magnetic field, the corresponding electric field, and the field resulting from charge separation to mere whispers. Moreover, the effects of chemical reactions, nanoparticle clustering, and sedimentation are purposefully set aside in this inquiry to home in on the fundamental transport mechanisms. The nanofluid we examine is a remarkable concoction of copper and alumina ( $Al_2O_3$ ) nanoparticles, elegantly suspended in a water-based medium, where both the fluid and the nanoparticles are believed to exist in thermal harmony—indicating a seamless connection between the phases. The governing equations of the boundary layer—encompassing continuity, momentum, energy, and concentration—are articulated in dimensional form as articulated by Gladys et al. [11], integrating influences such as Brownian motion, thermophoresis, thermal radiation, chemical reactions, and heat sources/sinks.

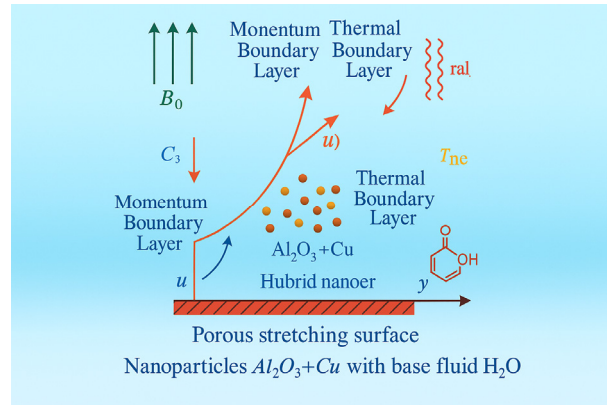


Figure 1. Physical model of the problem

The previously mentioned premises are essential for the definition of these conditions.

$$\frac{\partial u}{\partial x} + \frac{\partial v}{\partial y} = 0, \tag{1}$$

$$u \frac{\partial u}{\partial x} + v \frac{\partial u}{\partial y} = \frac{\mu_{nf}}{\rho_{nf}} \frac{\partial^2 u}{\partial y^2} - \left\{ \frac{\mu_{nf}}{\rho_{nf}} \frac{1}{K} + \frac{\sigma B_0^2}{\rho_{nf}} \right\} u, \tag{2}$$

$$u \frac{\partial T}{\partial x} + v \frac{\partial T}{\partial y} = \alpha_{nf} \frac{\partial^2 T}{\partial y^2} + \frac{Q_0}{(\rho c_p)_{nf}} (T - T_\infty) + \frac{1}{(\rho c_p)_{nf}} \frac{16\sigma^* T_\infty^3}{3K^*} \frac{\partial^2 T}{\partial y^2} + \frac{\mu_{nf}}{(\rho c_p)_{nf}} \left( \frac{\partial u}{\partial y} \right)^2 \tag{3}$$

$$u \frac{\partial C}{\partial x} + v \frac{\partial C}{\partial y} = D_B \frac{\partial^2 C}{\partial y^2} + \frac{D_T}{T_\infty} \frac{\partial^2 T}{\partial y^2} - K_0 (C - C_\infty). \tag{4}$$

The following are the requirements for the conditions governing the boundaries for equations (1) through (4):

$$\begin{cases} u = ax, v = 0, T = T_w(x) = T_\infty + m \left( \frac{x}{\omega} \right)^2, C = C_w(x) = C_\infty + n \left( \frac{x}{\omega} \right)^2 & \text{at } y = 0 \\ u \rightarrow 0, T \rightarrow T_\infty, C \rightarrow C_\infty & \text{as } y \rightarrow \infty \end{cases} \tag{5}$$

where  $\omega$  is the defining frequency and  $n, m$ , and  $a$  are all integers, and  $a > 0$ .

Here  $q_r$  is the heat flow from radiation. [12] given by

$$q_r = -\frac{4\sigma^*}{3K^*} \frac{\partial T^4}{\partial y}, \tag{6}$$

where  $K^*$  is the Rosseland average absorption factor and  $\sigma^*$  is the Stefan-Boltzmann constant. The temperature fluctuation  $T^4$  is shown using an expanded version of the Taylor series. Ignoring more complex phrases and extending  $T^4$  around  $T_\infty$  results in:

$$T^4 = 4T_\infty^3 - 3T_\infty^4. \tag{7}$$

Brinkman provided the nanofluid's efficient variable viscosity [14] as

$$\mu_{nf} = \frac{\mu_f}{(1-\phi)^{2.5}}, \tag{8}$$

where  $\phi$  and  $\mu_f$  represents the movement of the base fluid with the solid volume fraction of tiny particles, respectively. The heat impedance and warmth conductivity of nanofluids, especially those limited to spherical nanoparticles, are estimated using the Max-Garnett model (see Maxwell Garnett [15]) in equations (1) through (4).

$$\begin{aligned}
(\rho c_p)_{nf} &= (1 - \phi)(\rho c_p)_f + \phi(\rho c_p)_s, \\
\rho_{nf} &= (1 - \phi)\rho_f + \phi\rho_s, v_{nf} = \frac{\mu_{nf}}{\rho_{nf}}, \\
\alpha_{nf} &= \frac{k_{nf}}{(\rho c_p)_{nf}}, k_{nf} = k_f \left[ \frac{(k_s + k_f) - 2\phi(k_f - k_s)}{(k_s + k_f) + \phi(k_f - k_s)} \right],
\end{aligned} \tag{9}$$

where  $v_{nf}, \rho_{nf}, (\rho c_p)_{nf}, k_{nf}, k_f, k_s, \rho_s, (\rho c_p)_f, (\rho c_p)_s$ . These include the physical viscosity of nanofluids, electrical conductivity properties, particular warmth capacity of the temperature transmission of the initial fluid, the thermal conductivity of the solid individuals, the density of the particles, the heat transmission of the tiny fluids, and the solid constituents, base fluid's heat capacity, and effective heat capacity caused by tiny particles, in that order.

It introduces a function of streams  $\psi(x,y)$  to fulfil the continuity equation (1) in such a way that:

$$u = \frac{\partial \psi}{\partial y}, v = -\frac{\partial \psi}{\partial x}. \tag{10}$$

Introducing the non-dimensional variables listed below,

$$\begin{aligned}
\psi &= [av_f]^{1/2} x f(\eta), u = axf'(\eta), v = -(av_f)f(\eta), \\
\theta(\eta) &= \frac{T - T_\infty}{T_w - T_\infty}, \varphi(\eta) = \frac{C - C_\infty}{C_w - C_\infty}, \eta = \left[ \frac{a}{v_f} \right]^{1/2} y
\end{aligned} \tag{11}$$

where  $\theta(\eta)$  is the undefined temperature,  $f(\eta)$  is the dimensionless flow function, is the undetermined focus, while the similarity variables are denoted by  $\eta$ . The following two-point border value dilemma is created by combining equations (6) to (11) with the fundamental equations (2), (3), and (4) as well as the circumstances of the boundaries (5):

$$f''' + \omega_1 [ff'' - f'^2 - \frac{1}{\omega_2} Mf'] - K_1 f' = 0, \tag{12}$$

$$\left(1 + \frac{4R}{3}\right) \theta'' + \omega_3 [f\theta' - 2f'\theta + Q\theta + \frac{E_c}{\omega_4} f''^2] = 0, \tag{13}$$

$$\varphi'' + Sc(f\varphi' - 2f'\varphi + Kr\varphi) + Sr\theta'' = 0. \tag{14}$$

based on border requirements.

$$\begin{cases}
f = 0, f' = 1, \theta = 1, \varphi = 1 & \text{at } \eta = 0 \text{ and} \\
f' \rightarrow 0, \theta \rightarrow 0, \varphi \rightarrow 0 & \text{as } \eta \rightarrow \infty.
\end{cases} \tag{15}$$

Primes indicate specialization with respect to  $\eta$ , while the base fluid's thermal diffusion and velocity of motion are represented by  $\eta$ ,  $\alpha_f = \left(\frac{k_f}{\rho c_p}\right)$  and  $v_f = \frac{\mu_f}{\rho_f}$  respectively. Additional non-dimensional characteristics that show up in formulas (12) to (15) are  $M, K_1, R, Pr, Q, E_c, Sc, Kr$  and  $Sr$  indicate the parameters for heat generation, Schmidt, Eckert, scaled chemical reaction, magnetized, porous material, Soret, Prandtl, and heat radiation values. The mathematical definition of these parameters is

$$\begin{aligned}
M &= \frac{\sigma B_0^2}{a\rho_f}, K_1 = \frac{v_f}{ak}, R = \frac{4\sigma^* T_\infty^3}{k^* k_{nf}}, Sc = \frac{v_f}{D} \\
Pr &= \frac{v_f(\rho c_p)_f}{k_f}, Q = \frac{Q_0}{a(\rho c_p)_{nf}}, Kr = \frac{K_0}{a}, \\
E_c &= \frac{u_w^2}{(T_w - T_\infty)(c_p)_f}, Sr = \frac{D_1(T_w - T_\infty)}{D(C_w - C_\infty)}.
\end{aligned} \tag{16}$$

The definition of the nanoparticle volume fractions  $\phi_1$  and  $\phi_2$  is.

$$\begin{aligned}
\omega_1 &= (1 - \phi)^{2.5} \left[ 1 - \phi + \phi \left( \frac{\rho_s}{\rho_f} \right) \right], \omega_2 = 1 - \phi + \phi \left( \frac{\rho_s}{\rho_f} \right), \\
\omega_3 &= 1 - \phi + \phi \left( \frac{\rho c_p}_s}{\rho c_p}_f \right), \omega_4 = (1 - \phi)^{2.5} \left[ 1 - \phi + \phi \left( \frac{\rho c_p}_s}{\rho c_p}_f \right) \right].
\end{aligned} \tag{17}$$

### 3. SKIN FRICTION, HEAT AND MASS TRANSFER COEFFICIENTS

The mass transfer, wall heat, and surface drag ratios are described by the rate of skin friction  $C_f$ , Sherwood's regional value  $Sh_x$ , and the Nusselt code in the area  $Nu_x$ , respectively quantities of engineering relevance. The definition for the shear strain  $\tau_w$  at a structure's surface is.

$$\tau_w = -\mu_{nf} \left( \frac{\partial u}{\partial y} \right)_{y=0} = -\frac{1}{(1-\phi)^{2.5}} \rho_f \sqrt{v_f a^3} x f''(0), \tag{18}$$



where  $\mu_{nf}$  is the viscosity coefficient. The rate of skin friction is determined as.

$$C_{fx} = \frac{2\tau_w}{\rho_f U_w^2}, \tag{19}$$

and using equation (18) in (19) we obtained

$$0.5(1 - \phi)^{2.5} C_{fx} = -Re_x^{-\frac{1}{2}} f''(0). \tag{20}$$

The definition of rate of heat transfer at the level of a wall flux is.

$$q_w = -k_{nf} \left( \frac{\partial T}{\partial y} \right)_{y=0} = -k_{nf} \frac{(T_w - T_\infty)}{x} \sqrt{\frac{U_w x}{\nu_f}} \theta'(0), \tag{21}$$

where  $k_{nf}$  is the nanofluids thermal resistance. The definition of the localized Nusselt value is.

$$Nu_x = \frac{xq_w}{k_f(T_w - T_\infty)}. \tag{22}$$

Equation (21) multiplied by equation (22) yields the wall heat transfer rate without measurements.

$$\left( \frac{k_f}{k_{nf}} \right) Nu_x = -Re_x^{0.5} \theta'(0). \tag{23}$$

The definition of the borders appears, the volume of flow is

$$q_m = -D \left( \frac{\partial C}{\partial y} \right)_{y=0} = -DQ \left( \frac{x}{\omega} \right)^2 \sqrt{\frac{a}{\nu_f}} \varphi'(0), \tag{24}$$

and the local Sherwood code is obtained as.

$$Sh_x = \frac{xq_m}{D(C_w - C_\infty)}. \tag{25}$$

The rate of mass transfer across indeterminate walls from (24) and (25) is obtained as

$$Sh_x = -Re_x^{\frac{1}{2}} \varphi'(0), \tag{26}$$

where  $Re_x$ , which stands for the regional Reynolds value is explained as follows:

$$Re_x = \frac{xu_w}{\nu_f}$$

#### 4. METHOD OF SOLUTION

The mathematical expressions that are symbolized by the numbers (12) to (14) display a significant degree of non-linearity, which has the effect of making the process of deriving explicit solutions more difficult. Since this is the case, the resolutions of these mathematical constructs, in addition to the boundary conditions that were described in (15), were achieved by numerical methods that utilized combining the fourth-order Runge-Kutta process with the firing method (Figure 1).

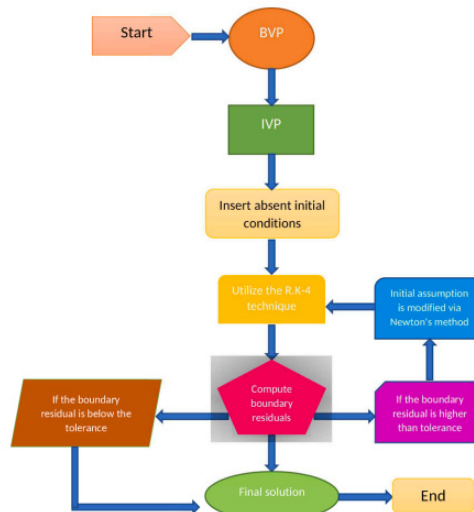


Figure 1. Model flow diagram (RK-Method).

### 5. RESULTS AND DISCUSSION

Table 1 may be an introduction of the thermophysical chattels of the nanofluids that were utilized into the numerical recreations. Broad calculations have been carried out in arrange to set up the profiles of many physical characteristics, including touching the skin, the adjacent null number, the local Forest amount, and the profiles of velocity, temperature, and concentration., counting  $\phi$ , M, K<sub>1</sub>, R, Pr, Sc, Q, Ec, Kr, and Sr.

**Table 1.** Thermal physical properties

Physical Properties	Base fluid (H <sub>2</sub> O)	Copper (Cu)	Alumina (Al <sub>2</sub> O <sub>3</sub> )
$C_p$ (J/kgK)	4179	385	765
$\rho$ (Kg/m <sup>3</sup> )	997.1	8933	3970
$k$ (W/mK)	0.613	401	40

These figures, which expand from 2 to 11, layout the impacts that physical parameters have on a combination of fluid lively characteristics. A diagram of how the alluring parameter M impacts the speed profile of the nanofluids Cu-water and Al<sub>2</sub>O<sub>3</sub>-water can be found in Figure 2. Extending the alluring parameter M comes almost in a drop inside the nanofluid speed characteristics of Cu-water and Al<sub>2</sub>O<sub>3</sub>-water. The justification for the frequent use of a transversal enticing field on a fluid that conducts control comes almost inside the arrangement of an obstructing Lorenz drive. This drive moderates down the development of the flow rate decreases when the fluid passes through the topmost layer. In any event, this results in a rise in both heat and concentrations of solutes.

The connection between the porous media parameter K<sub>1</sub> and the speed of nanofluids composed of copper water and Al<sub>2</sub>O<sub>3</sub> water is laid out in Figure 3. An increase inside the porous medium parameter K<sub>1</sub> comes almost in a drop inside the speed profiles of both of the nanofluids. The figure illustrates that the Al<sub>2</sub>O<sub>3</sub>-water nanofluids speed pattern is essentially greater than the Nanofluids of Cu-water.

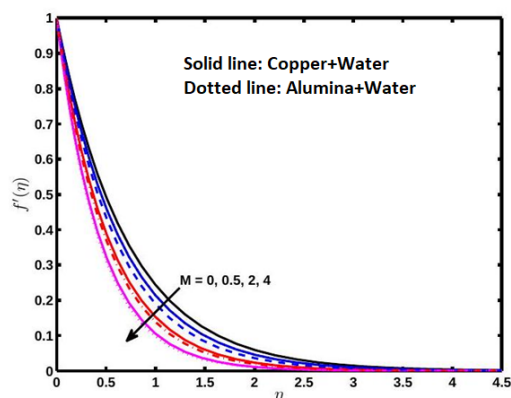


**Figure 2.** Effect of magnetic parameter  $M$  on the velocity profiles

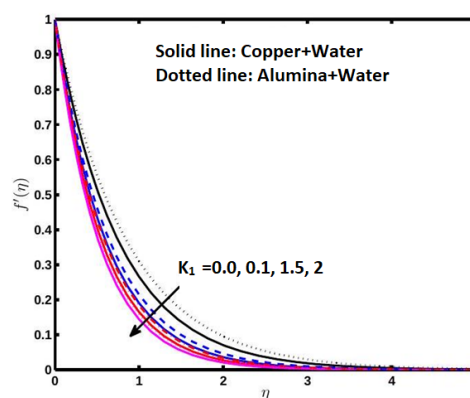


**Figure 3.** Effect of the porous medium parameter  $K_1$  on the velocity profiles

The impact of nanoparticle volume splitting on temperature, velocity, and concentrations profiles is seen in Figures 4 through 6 independently for a Cu-water tiny fluids and an Al<sub>2</sub>O<sub>3</sub>-water tiny fluids. These figures appear the impacts of the nanoparticle volume division. Extending the nanoparticle volume division comes around in a reduce inside the velocity of the Al<sub>2</sub>O<sub>3</sub>-water nanofluid is faster than that of the Cu-water tiny fluids. Figure 5 makes it generously clear that growing the increase in the heated permeability of the small fluid brought on by the particle expansion rate causes the heated boundary layer to thicken.

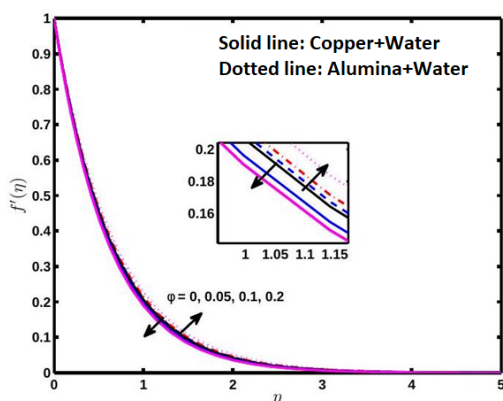


**Figure 4.** Effect of various nanoparticle values fraction  $\phi$  on velocity profiles

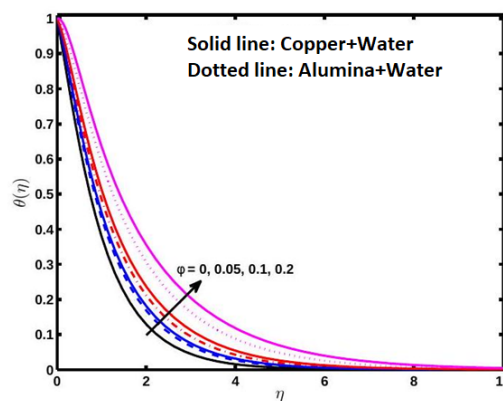


**Figure 5.** Effect of various nanoparticle values fraction  $\phi$  on temperature profiles

The temperature profile is shown to form when the nanoparticle size division values rise, as illustrated in Figure 6. Because of the reality that copper water may be a strong conductor of both warm and control, it has additionally been showed up that the temperature spread in a nanofluid composed of copper water is more noticeable than that of a nanofluid composed of aluminum oxide water. Figure 6 traces that the concentration profile of  $Al_2O_3$ -water nanofluid decreases as the total percentage of nanoparticles rises; nonetheless, it still needs Cu-water tiny fluids.

The temperature profile's response to the warm period parameter  $Q$  is portrayed in Figure 7, which portrays the circumstance including nanofluids composed of  $Al_2O_3$ -water and Cu-water. We found that as the warm producing parameter  $Q$  rose, the thermal profile for both kinds of tiny fluids increased as well. This was seen to be true. According to the findings, the Cu-water nanofluids had a greater temperature than the  $Al_2O_3$ -water nanofluids. An increase in the warm conductance of the tiny fluids and a thickening of the warm border layer result from expanding the values of the warmth era parameter  $Q$ .

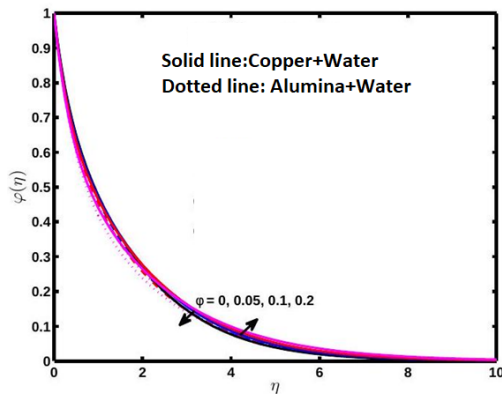


Figure 6. Effect of volume fraction  $\phi$  on the concentration profiles

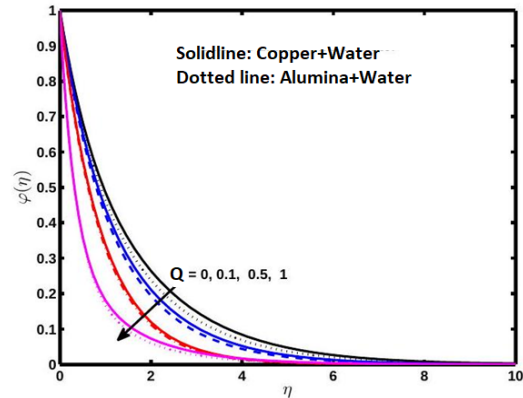


Figure 7. Effect of heat generation parameter  $Q$  on the concentration profiles

Figure 8 portrays how the gooey scattering parameter  $Ec$  influences the temperature profile for the nanofluids  $Al_2O_3$  and Cu. With an increment in  $Ec$  values, it is seen that both nanofluids' temperature profiles rise; this recommends that an increment in  $Ec$  impacts the temperature dispersion. Typically, since the liquid locale stores the vitality after it scatters due to thickness and flexible distortion. Cu-water nanofluid shows a more noteworthy temperature profile than  $Al_2O_3$ -water nanofluid, it has been watched.

Figure 9 delineates how the warm radiation parameter  $R$  influences both nanofluids' temperature distributions.  $Al_2O_3$ - and Cu-water nanofluids have higher temperature profiles when the warm radiation Parameter  $R$  is expanded. We found that Cu-water nanofluids display bigger temperature increments than  $Al_2O_3$ -water nanofluids. The warm irradiation parameter  $R$  is what leads to the thickening of the warmer border layer. Consequently, the framework is cooled and the nanofluids can release the warm vitality from the stream zone. Usually exact since a bigger Rosseland estimation causes a bigger temperature profile.

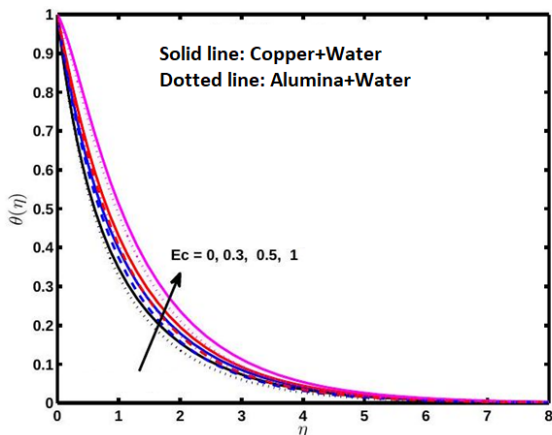


Figure 8. Effect of viscous dissipation parameter  $E_c$  on the temperature profiles

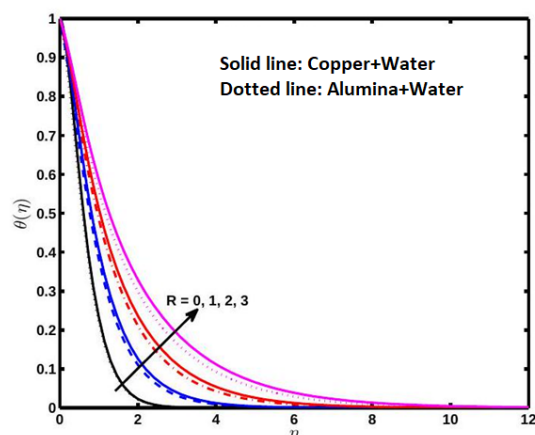


Figure 9. Effect of thermal radiation parameter  $R$  on the temperature profiles

Figure 10 appears how for Cu and  $Al_2O_3$  nanofluids, the particle size profile is affected by the Stoner number  $Sc$ . Both cases of nanofluids have a lower solutal concentration profile when  $Sc$  values are expanded. Cu water nanofluid's concentration profile is seen to extend more than  $Al_2O_3$ -water nanofluid's.

Figures 11 and 12 illustrate the effect of two parameters, to be specific the impact of the Soret number  $Sr$  and the chemical sensitive variable  $Kr$  on the level profiles of the Cu-water and  $Al_2O_3$ -water tiny fluids independently.

Distinguish how the biological reaction variable affects the pace and temperature patterns of the nanofluids in the two scenarios does not shift considerably with expanding values of the scale chemical response parameter.  $Al_2O_3$ -water nanofluid's solutal concentration profiles in Figure 11 are generally diverse from those of water and copper nanofluids. The solvent content boundary barrier's thickness in both nanofluid scenarios develops as the Soret number  $Sr$  increments, as appeared in Figure 12. We found that  $Al_2O_3$ -water nanofluid has lower solutal concentration profiles increment than Cu-water nanofluid.

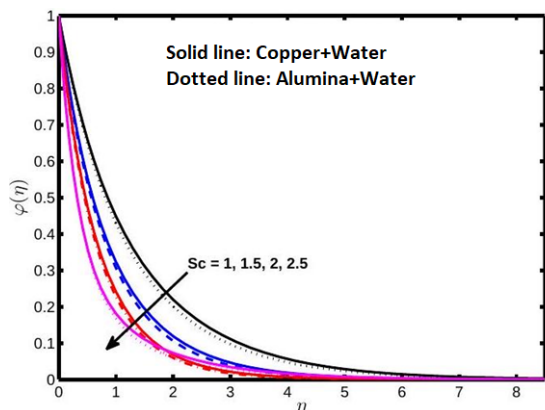


Figure 10. Effect of the Schmidt number  $Sc$  on concentration profiles

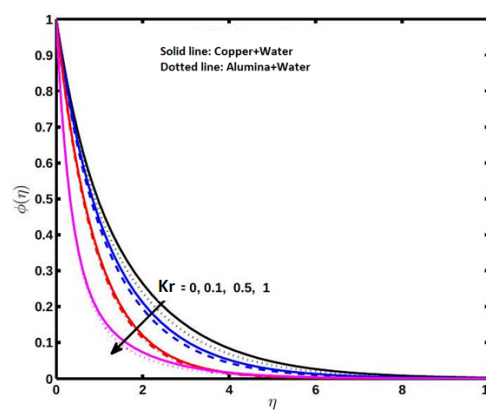


Figure 11. Effect of the chemical reaction parameter  $Kr$  on the concentration profiles

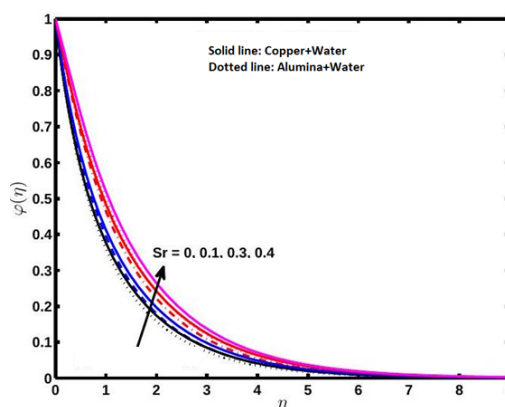


Figure 12. Effect of the Soret number  $Sr$  on concentration profiles

Table 2. SRM solutions for  $f''(0)$ ,  $-\theta'(0)$ , and  $-\phi'(0)$  are compared for various values of  $Sr, Sc, Q$  and  $Kr \cdot \phi = 0.1, E_c = 1, M = 0.5, Sc = 1, Q = 0.02, Pr = 7, K_1 = 1, Kr = 0.08, Sr = 0.2$ .

	Cu + water		$Al_2O_3$ + water			
	$\phi = 0.1, E_c = 1$		$R = 1.5, Pr = 7$	$K_1 = 1.25, M = 0.5$		
$Sr$	$f''(0)$	$-\theta'(0)$	$-\phi'(0)$	$f''(0)$	$-\theta'(0)$	$-\phi'(0)$
0.0	1.67923	0.264822	1.205443	1.543656	0.387837	1.234462
0.1	1.67923	0.264822	1.206502	1.543656	0.387837	1.226048
0.3	1.67923	0.264822	1.208618	1.543656	0.387837	1.209225
0.4	1.67923	0.264822	1.209677	1.543656	0.387837	1.200809
$Sc$						
0.6	1.67923	0.264822	1.20756	1.543656	0.387837	1.217637
0.7	1.67923	0.264822	1.578602	1.543656	0.387837	1.591183
0.8	1.67923	0.264822	1.89231	1.543656	0.387837	1.906038
0.9	1.67923	0.264822	2.168352	1.543656	0.387837	2.182708
$Kr$						
0.6	1.67923	0.264822	1.142691	1.543656	0.387837	1.158075
0.7	1.67923	0.264822	1.221807	1.543656	0.387837	1.230985
0.8	1.67923	0.264822	1.441995	1.543656	0.387837	1.442644
0.9	1.67923	0.264822	1.646539	1.543656	0.387837	1.643275

The findings from the numerical exploration shed light on how the Soret number ( $Sr$ ), the Schmidt number ( $Sc$ ), and the chemical reaction parameter ( $Kr$ ) influence the flow, thermal, and concentration boundary layers for Cu–Water and  $Al_2O_3$ –Water nanofluids, all while keeping the physical parameters uniform ( $\phi = 0.1, E_c = 1, R = 1.5, Pr = 7, K_1 = 1.25,$

$M = 0.5$ ). It becomes evident that the skin friction coefficient  $f''(0)$  and the heat transfer rate  $-\theta'(0)$  remain steadfast, showing no fluctuations with changes in  $Sr$ ,  $Sc$ , and  $Kr$  for both types of nanofluids, indicating that these factors wield a minimal influence on the momentum and thermal boundary layers in this context. Nevertheless, it is noteworthy that the mass transfer rate  $-\phi'(0)$  exhibits a dramatic surge as  $Sc$  and  $Kr$  are elevated, while  $Sr$  demonstrates a more gradual increase. This highlights the crucial significance of  $Sc$  and  $Kr$  in molding the concentration boundary layer. In a striking contrast,  $Al_2O_3$ -Water consistently showcases slightly enhanced heat and mass transfer rates compared to its counterpart,  $Cu$ -Water. This suggests that  $Al_2O_3$ -Water possesses superior capabilities for thermal and solutal transport, especially when exposed to the effects of heightened Schmidt numbers and chemical reaction rates.

## 6. CONCLUSION

This study highlights the crucial impact of thermal radiation and heat source/sink effects on the thermo-hydraulic performance of  $Al_2O_3$ /water nanofluid and  $Cu$ - $Al_2O_3$ /water hybrid nanofluids in the context of advanced energy storage systems. Utilizing the radiation heat flux model and heat source and solving the system through the Runge-Kutta numerical method, the findings reveal that increasing thermal radiation and heat generation parameters significantly enhance temperature distribution and alter fluid flow behavior. The synergistic combination of  $Cu$  and  $Al_2O_3$  nanoparticles leads to improved heat transfer efficiency while maintaining thermal and hydrodynamic stability. These outcomes provide a strong computational framework for deploying hybrid nanofluids in sustainable and efficient thermal management applications. The velocity profile decreases with increasing values of the magnetic field parameter.

- The velocity distribution also reduces as the porosity parameter increases.
- The temperature profile increases with higher values of the thermal radiation parameter and the heat source parameter, but shows a decline beyond certain values of the heat source.
- An increase in thermal radiation leads to a further rise in temperature distribution.
- The temperature profile is further enhanced as the nanoparticle volume fraction increases.
- The concentration profile decreases with increasing values of the Schmidt number and the chemical reaction parameter, but increases when the Soret number rises.

## ORCID

- Gladys Tharapatla, <https://orcid.org/0000-0003-4532-9654>; • Vijaya Lakshmi Garishe, <https://orcid.org/0000-0001-7210-5678>  
• N. Vijaya, <https://orcid.org/0000-0002-6648-1973>; • Sridhar Wuriti, <https://orcid.org/0000-0002-0978-1769>  
• G.V.R. Reddy, <https://orcid.org/0000-0002-6455-3750>

## REFERENCES

- [1] L.J. Crane, "Flow past a stretching plate," ZAMP. Angew Math. Phys, **21**, 645-647 (1970). <https://doi.org/10.1007/BF01587695>
- [2] W.A. Khan, and I. Pop, "Boundary layer flow of a nanofluid past a stretching sheet," International Journal of Heat and Mass Transfer, **53**, 2477-2483 (2010). <https://doi.org/10.1016/j.ijheatmasstransfer.2010.01.032>
- [3] M. Abd El-Aziz, "Thermal-diffusion and diffusion-thermo effects on combined heat and mass transfer by hydromagnetic three-dimensional free convection over a permeable stretching surface with radiation," Physics Letters, **372**(3), 263-272 (2007). <https://doi.org/10.1016/j.physleta.2007.07.015>
- [4] F.M. Hady, F.S. Ibrahim, S.M. Abdel-Gaied, and R.M. Eid, "Radiation effect on viscous flow of a nanofluid and heat transfer over a nonlinearly stretching sheet," Nanoscale Res. Lett. **7**, 229 (2012). <https://doi.org/10.1186/1556-276X-7-229>
- [5] N. Bachok, A. Ishak, and I. Pop, "Unsteady boundary-layer flow and heat transfer of a nanofluid over a permeable stretching/shrinking sheet," International Journal of Heat and Mass Transfer, **55**, 2102-2109 (2012). <https://doi.org/10.1016/j.ijheatmasstransfer.2011.12.013>
- [6] A.M. Rohni, A.S. Ahmad, and Md.I. Ismail, and I. Pop, "Flow and heat transfer over an unsteady shrinking sheet with suction in a nanofluid using Buongiorno's model," International Communications in Heat and Mass Transfer, **43**, 75-80 (2013). <https://doi.org/10.1016/j.icheatmasstransfer.2013.02.001>
- [7] J. Buongiorno, "Convective transport in nanofluids," ASME Journal of Heat Transfer, **128**, 240-250. <https://doi.org/10.1115/1.2150834>
- [8] A. Sandhya, G.R. Reddy, and G.V.S.R. Deekshitulu, "Heat and mass transfer effects on MHD flow past an inclined porous plate in the presence of chemical reaction," International Journal of Applied Mechanics and Engineering, **25**(3), 86-102 (2020). <https://doi.org/10.2478/ijame-2020-0036>
- [9] P.V. Murthy, and P. Singh, "Effect of viscous dissipation on a non-Darcy natural convection regime," International Journal of Heat and Mass Transfer, **40**, 1251-1260 (1997). [https://doi.org/10.1016/S0017-9310\(96\)00181-0](https://doi.org/10.1016/S0017-9310(96)00181-0)
- [10] S.S. Motsa, "A New spectral relaxation method for similarity variable nonlinear boundary layer flow systems," Chemical Engineering Communications, **16**, 23-57 (2013). <https://doi.org/10.1155/2014/341964>
- [11] T. Gladys, and G.R. Reddy, "Contributions of variable viscosity and thermal conductivity on the dynamics of non-Newtonian nanofluids flow past an accelerating vertical plate," Partial Differential Equations in Applied Mathematics, **5**, 100264 (2022). <https://doi.org/10.1016/j.padiff.2022.100264>
- [12] K. Vijaya, and G.V.R. Reddy, "Magnetohydrodynamic Casson fluid flow over a vertical porous plate in the presence of radiation, Soret and chemical reaction effects," Journal of Nanofluids, **8**(6), 1240-1248 (2019). <https://doi.org/10.1166/jon.2019.1684>
- [13] H.F. Oztop, and E. Abu-Nada, "Numerical study of natural convection in partially heated rectangular enclosures filled with nanofluids," International Journal of Heat and Fluid Flow, **29**, 1326-1336 (2008). <https://doi.org/10.1016/j.ijheatfluidflow.2008.04.009>



- [14] H.C. Brinkman, "The viscosity of concentrated suspensions and solution," *Journal of Chemical Physics*, **20**, 571-581 (1952). <https://doi.org/10.1063/1.1700493>
- [15] J.C.M. Garnett, "Colours in metal glasses and in metallic films," *Philosophical Transactions of the Royal Society of London*, **203**, 385-420 (1904). <https://doi.org/10.1098/rsta.1904.0024>
- [16] E. Abu-Nada, "Application of nanofluids for heat transfer enhancement of separated flows encountered in a backward facing step," *International Journal of Heat and Fluid Flow*, **29**, 242-249 (2008). <https://doi.org/10.1016/j.ijheatfluidflow.2007.07.001>
- [17] M.A.A. Hamad, "Analytical solution of natural convection flow of a nanofluid over a linearly stretching sheet in the presence of magnetic field," *International Communications in Heat and Mass Transfer*, **38**, 487-492 (2011). <https://doi.org/10.1016/j.icheatmasstransfer.2010.12.042>
- [18] P.K. Kameswaran, M. Narayana, P. Sibanda, and P.V. Murthy, "Hydromagnetic nanofluid flow due to a stretching or shrinking sheet with viscous dissipation and chemical reaction effects" *International Journal of Heat and Mass Transfer*, **55**, 7587-7595 (2012). <https://doi.org/10.1016/j.ijheatmasstransfer.2012.07.065>
- [19] L.G. Grubka, and K.M. Bobba, "Heat transfer characteristics of a continuous stretching surface with variable temperature," *The ASME Journal of Heat Transfer*, **107**, 248-250 (1985). <https://doi.org/10.1115/1.3247387>
- [20] K. Rafique, Z. Mahmood, and U. Khan, "Mathematical analysis of MHD hybrid nanofluid flow with variable viscosity and slip conditions over a stretching surface," *Materials Today Communications*, **36**, 106692 (2023). <https://doi.org/10.1016/j.mtcomm.2023.106692>
- [21] S. Nasir, W. Alghamdi, T. Gul, I. Ali, S. Sirisubtawee, and A. Aamir, "Comparative analysis of the hydrothermal features of TiO<sub>2</sub> water and ethylene glycol-based nanofluid transportation over a radially stretchable disk," *Numerical Heat Transfer, Part B: Fundamentals*, **83**(5), 276-291 (2023). <https://doi.org/10.1080/10407790.2023.2173343>
- [22] P.M. Patil, B. Goudar, and E. Momoniati, "Magnetized Bioconvective micropolar nanofluid flow over a wedge in the presence of oxytactic microorganisms," *Case Stud. Therm. Eng.* **49**, 103284 (2023). <https://doi.org/10.1016/j.csite.2023.103284>
- [23] S.K. Rawat, M. Yaseen, U. Khan, M. Kumar, A. Abdulrahman, S.M. Eldin, S. Elattar, *et al.*, "Insight into the significance of nanoparticle aggregation and non-uniform heat source/sink on titania-ethylene glycol nanofluid flow over a wedge," *Arab. J. Chem.* **16**, 104809 (2023). <https://doi.org/10.1016/j.ijheatmasstransfer.2012.07.065>
- [24] J.C. Umavathi, "Electrically conducting micropolar nanofluid with heat source/sink over a wedge: ion and hall currents," *J. Magn. Magn. Mater.* **559**, 169548 (2022). <https://doi.org/10.1016/j.jmmm.2022.169548>

#### ПОТІК ГІБРИДНОЇ МГД НАНОРІДИНИ ЧЕРЕЗ ПОРИСТУ ПОВЕРХНЮ З РОЗТЯГНЕННЯМ ЗА НАЯВНОСТІ ТЕПЛОВОГО ВИПРОМІНЮВАННЯ ТА ХІМІЧНОЇ РЕАКЦІЇ

Гледіс Тарапатла<sup>a</sup>, Віджая Лакшмі Гаріше<sup>b</sup>, Н. Віджая<sup>c</sup>, Шрідхар Вуріті<sup>c</sup>, Г.В.Р. Редді<sup>c</sup>

<sup>a</sup>Кафедра охорони здоров'я та безпеки, Методистський коледж інженерії та технологій, Богулкунта, Абідс, Хайдерабад, Телангана 500001, Індія

<sup>b</sup>Кафедра математики, MGIT, Гандіпет, Хайдерабад, Телангана, Індія-500075

<sup>c</sup>Кафедра математики, Освітній фонд Конеру Лакімаї, Ваддесварам, Індія-522302

Це дослідження вивчає конвективний перенос тепла та маси в магнітогідродинамічному (МГД) потоці нанорідина над проникною, електрично керованою поверхнею з розтягненням, вбудованою в пористе середовище. Аналіз враховує ключові фізичні ефекти, включаючи теплове випромінювання, тепловиділення, розсіювання в'язкості та хімічні реакції. Визначальні рівняння сформульовано з урахуванням впливу пористості, магнітних полів, градієнтів тепла та концентрації, а також хімічної кінетики. Особлива увага приділяється контролю об'ємної частки наночастинок на межі розділу. Для оцінки теплових характеристик розглядаються дві моделі нанорідин-мідь-вода (Cu-H<sub>2</sub>O) та оксид алюмінію-вода (Al<sub>2</sub>O<sub>3</sub>-H<sub>2</sub>O). Нелінійна крайова задача розв'язується чисельно за допомогою методу стрільби в поєднанні з методом Рунге-Кутти четвертого порядку. Результати демонструють чудову відповідність з раніше опублікованими даними, що підтверджує точність та надійність цієї моделі. Ці результати мають потенційне застосування в передових системах теплопередачі, таких як технології охолодження та обробка матеріалів.

**Ключові слова:** гібридні нанорідина; МГД; пористі середовища; теплове випромінювання; поверхневе тертя

## THE STAGNATION POINT FLOW OF THE MHD CASSON POLYMERIC NANOFUID FLOWS TOWARD A WAVY CIRCULAR CYLINDER SATURATED WITH A POROUS MEDIUM UNDER CONVECTIVE NIELD CONDITIONS AND THERMAL RADIATION

P. Venkata Subrahmanyam<sup>a</sup>,  Gandrakota Kathyayani<sup>a\*</sup>,  Gattu Venkata Ramudu<sup>a</sup>,  K. Venkatadri<sup>b</sup>

<sup>a</sup>Department of Applied Mathematics, Yogi Vemana University, Kadapa, A.P., India

<sup>b</sup>Department of Mathematics, Mohan Babu University (Erstwhile Sree Vidyanikethan Eng. Coll.), Tirupati A.P-517 102, India

\*Corresponding Author E-mail: [kathyagk@yvu.edu.in](mailto:kathyagk@yvu.edu.in)

Received May 3, 2025; revised June 19, 2025; accepted June 24, 2025

This study conducts a thorough numerical investigation employing the *bvp4c* technique to delve into the stagnation-point flow of a magnetohydrodynamic (MHD) Casson polymeric nanofluid around a wavy circular porous cylinder. It takes into account activation energy and thermal radiation, emphasizing the significant impact of thermal radiation on fluid flow, concentration and temperature profiles. The effects of thermal radiation within the energy equation are carefully considered, along with convective Nield boundary conditions, enabling a comprehensive analysis. By introducing dimensionless variables, the study transforms the partial differential equation into ordinary equations, facilitating the application of the shooting scheme to approximate the solution. The meticulously examined results offer detailed insights into temperature, velocity and mass concentration profiles, highlighting the profound influence of thermal radiation on these parameters. Furthermore, a comprehensive graphical presentation of each engineering parameter is provided, offering a nuanced understanding of the intricate physical phenomena involved, with particular attention to the influence of thermal radiation.

**Keywords:** Stagnation-point flow; Thermal radiation; Casson polymeric nanofluid; *bvp4c* technique; Magnetohydrodynamic (MHD)

**PACS:** 47.70.Fw, 44.20.+b, 44.25.+f, 47.10.ad, 47.15.Cb

### 1. INTRODUCTION

Casson fluids, which are non-Newtonian and possess yield stress, have emerged as valuable models for studying the flow of complex fluids in a wide range of industrial and biological systems. When magnetic fields are introduced to such systems, the effects can be quite complex due to their potential to alter the fluid dynamics and heat transfer characteristics. The present study, therefore, aims to investigate the interplay between MHD effects, Casson rheology, and nanoparticle dispersion in the context of stagnation point flow. Stagnation point flow is a critical phenomenon that occurs when a fluid is brought to rest by an external object. It has been extensively studied in the past, and it is known that the rheological properties of the fluid play a critical role in determining flow behaviour. When magnetic fields are present, the fluid dynamics can be further modified, leading to a more complex flow behaviour. Moreover, if nanoparticles are present in the fluid, their dispersion can also be affected by the magnetic field, leading to further modifications in the fluid behaviour. Thus, this study intends to examine the impact of MHD consequences, Casson rheology, and nanoparticle dispersion on stagnation point flow. The research findings will provide insights into the complex behaviour of Casson fluids under the impact of magnetic fields. They will help in designing better models for predicting the flow of complex fluids in various industrial and biological systems.

The study of Magnetohydrodynamic (MHD) Casson nanofluid flow around a cylinder that is saturated with a porous medium has gained significant attention in recent research. This phenomenon is complex and intriguing due to the interaction of MHD effects, porous medium, and nanofluid dynamics. Various numerical and analytical studies have been conducted to investigate this phenomenon. For instance, Alwawi et al. [3] delve into the characteristics of the magnetohydrodynamic (MHD) convection flow of Casson nanofluid with a shrinking sheet. The researchers used the Runge-Kutta method to perform their investigation while taking into account the effects of suction/injection on the wall. Narender et al. [5] investigated the behaviour of a fluid flow over a surface that is being stretched non-linearly. The fluid used was a type of nanofluid called the Casson nanofluid, which exhibits unique properties due to the presence of nanoparticles. The study also considered the effects of velocity and convective boundary conditions, which are important factors that can significantly influence the behaviour of the fluid. Thamaraikannan et al. [19] studied the effects of periodic body acceleration and thermal radiation on pulsating MHD Casson nanofluid flow through a porous channel. Their research sheds light on the behaviour of MHD Casson nanofluid flows under various scenarios, providing valuable insights for researchers in the field. The impact of a porous medium on the flow of MHD Casson nanofluid was examined in a recent study [12]. The study aims to examine mass and heat transfers of MHD Casson nanofluids flowing through porous media past a stretching sheet. The researchers also considered the impact of Newtonian heating and chemical reactions on the flow. By using mathematical models and simulations, the study found that the existence of a porous medium significantly affects the flow behaviour of MHD Casson nanofluid. Furthermore, the investigation carried out by Bosli et al. [4] thoroughly examined the natural convection flow and heat transfer of a Casson nanofluid flowing past a vertical plate under convective boundary conditions, while being aligned with MHD. The results of this study shed light

on the complex relationship between the dynamics of MHD Casson nanofluid and the effects of a porous medium. In recent research, there has been a focus on analyzing the behavior of Casson nanofluids in various flow scenarios. Researchers [17] looked into the numerical analysis of a three-dimensional Casson nanofluid magnetohydrodynamic (MHD) flow past an exponentially-stretching sheet.

The three-dimensional aspects of MHD Casson nanofluid flows were explored, revealing insights into the behaviour of these fluids in complex flow scenarios. On unstable MHD mixed convection flows of non-Newtonian Casson nanofluids, Gnanaprasanna & Singh [9] conducted another study on the stagnation zone of sphere-spinning impulsive fluids. This research contributed to the understanding of unsteady MHD effects on Casson nanofluid flows, particularly in the context of non-Newtonian fluids. These findings could be useful in designing more efficient and effective fluid systems in various industrial and scientific applications. The references cited in the text provide valuable information not only on MHD Casson nanofluid flows but also on related topics such as flow around cylinders and porous medium dynamics. For instance, Baig et al. [13] conducted a study that illuminates the effects of nanofluids in porous media by using thermal analysis to examine an  $\text{Al}_2\text{O}_3$ -Water nanofluid flow in a composite microchannel.

By adding nanoparticles to the base fluid, nanofluids have shown potential for enhancing heat transfer rates compared to traditional fluids. Kathyayani et al. [10] investigated nanofluid flow Stagnation-Point MHD flow Past 3-D Sinusoidal Cylinder with Brownian Motion and Thermophoresis Effects. Wang et al. [25] investigated mass transfer and natural convection heat using thermal radiation in a cavity that was partially filled with a porous material that was hygroscopic, which gives us insights into the heat and moisture transfer phenomena in porous media. One of the well-known models for modelling nanofluid hydrothermal characteristics is Buongiorno's [8] two-component nanoscale model, which includes both conservation of energy and nanoparticle diffusion (mass transfer) equations. This formulation has been very successfully applied for investigating enhanced heat transfer in nanofluids and emphasises thermophoresis and random diffusion (Brownian motion) as the dominant mechanisms. Several researchers have conducted investigations on buoyancy-driven convective flow in a closed regime filled with Buongiorno nanofluids to explore the heat transfer performance in various geometrical shapes using a wide range of computational techniques. A study by Rana et al. [20] explored the analysis of alumina and titania-water nanofluid flow using theoretical and computational methods. The study investigated the impact of velocity slip, thermal slip, and Stefan blowing at the boundary of a horizontal stretching sheet, also known as the wall. The viscosity and thermal conductivity were calculated using the Pak-Cho model in combination with the non-homogeneous Buongiorno nanofluid model. The model has been extensively utilized since its inception. Akram et al. [7], [22] and The Buongiorno model was utilised by researchers Tripathi et al. [2], [11], [15],[16] in a study of nanofluids, which yielded significant accomplishments. The use of the Buongiorno model and Cattaneo-Christov double diffusion has been quite popular among researchers [14], [18], [21],[23] over the years for studying the heat and mass transmission of fluids.

The research field of Casson nanofluid has yet to explore the evaluation of its impact on a sinusoidal cylinder using a two-phase nanofluid model. Our work is distinctive in that it examines the effects of both Neild's conditions, which are taken to be exponential and Casson nanofluid convective flow over a sinusoidal cylinder. The controlled PDEs used in our research are ODEs, which are subsequently solved computationally with MATLAB software's `bvp4c` and the shooting approach. The present method has the potential to address several environmental, pharmaceutical, and biological problems. This study has the potential to contribute to a better understanding of various fields and provide solutions to numerous challenges.

## 2. MATHEMATICAL MODEL

A steady stagnation-point flow incompressible Casson nanofluid was considered towards a wavy cylinder (Fig. 1). At each extreme radius of the cylinder's radius there were points of stagnation (points A, B, and C). The equation  $x = \delta y^{1/c}$  can be used to characterise the streamlines, where  $c$  is a fraction of the stream velocities slope and stated as  $c = b/a$  with  $0 < c < 1$  called nodal point or with  $-1 < c < 0$  called saddle point and  $c=0$  refers to plane flow,  $\delta$  is constant, provides a particular streamline. In the cylinder, points of minimum and maximum stagnation can be observed at positions B, A, and C. The velocity profiles of fluid flow particles in the  $x$ ,  $y$ , and  $z$ -directions were taken into consideration with  $u$ ,  $v$  and  $w$  respectively. In the Cartesian coordinate system  $Oxyz$ , the stagnation point is located at the system's origin, and the velocity profiles are expressed as

$$u_e = ax, \quad v_e = aby, \quad w_e = -(a+b)z. \quad (1)$$

In the stress-strain relation, the constitutive equation for a Casson fluid is as follows:

$$\tau^2 = \tau_0^2 + \mu \dot{\gamma}^2$$

$$\tau_{ij} = \begin{cases} 2\left(\mu_B + \frac{P_y}{\sqrt{2\pi}}\right)e_{ij}, & \pi > \pi_c \\ 2\left(\mu_B + \frac{P_y}{\sqrt{2\pi_c}}\right)e_{ij}, & \pi_c > \pi \end{cases} \quad (2)$$

A sinusoidal cylinder's boundary layer can be modelled by applying the following equations to represent the cylinder's boundary layer by the assumptions suggested above and using the Bernoulli equation, the pressure is removed, to model the sinusoidal cylinder's boundary layer by incorporating the Casson rheological effect term from Eq. (2) (sec [14, 18,24]).

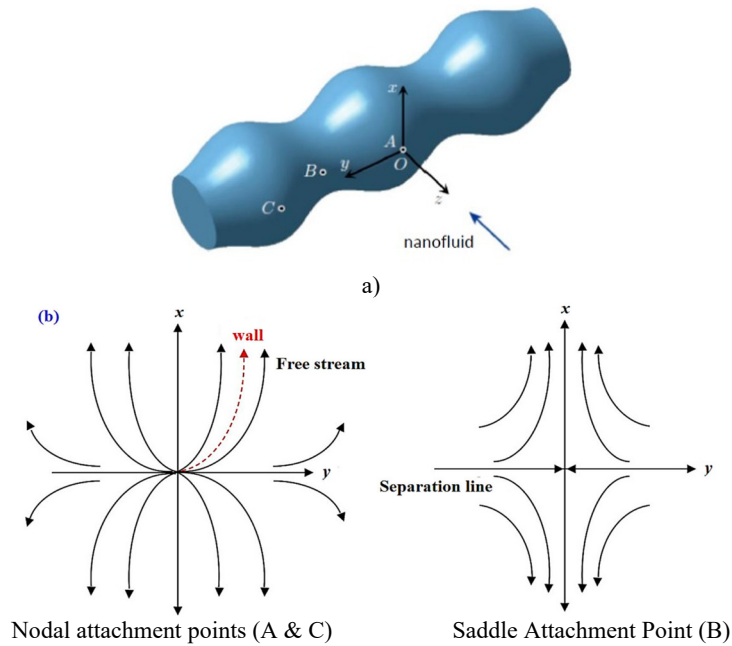


Figure 1. Schematic model and the streamlines

$$\frac{\partial u}{\partial x} + \frac{\partial v}{\partial y} + \frac{\partial w}{\partial z} = 0 \tag{3}$$

$$u \frac{\partial u}{\partial x} + v \frac{\partial u}{\partial y} + w \frac{\partial u}{\partial z} = a^2 x + v \left( 1 + \frac{1}{\beta} \right) \frac{\partial^2 u}{\partial z^2} - \frac{\sigma B_0^2}{\rho} (u - ax) - \frac{v}{\kappa} (u - ax) \tag{4}$$

$$u \frac{\partial v}{\partial x} + v \frac{\partial v}{\partial y} + w \frac{\partial v}{\partial z} = b^2 y + v \left( 1 + \frac{1}{\beta} \right) \frac{\partial^2 v}{\partial z^2} - \frac{\sigma B_0^2}{\rho} (v - by) - \frac{v}{\kappa} (v - by) \tag{5}$$

$$u \frac{\partial T}{\partial x} + v \frac{\partial T}{\partial y} + w \frac{\partial T}{\partial z} = \left( \alpha + \frac{16\sigma_s T_\infty^3}{3k^* (\rho c_p)} \right) \frac{\partial^2 T}{\partial z^2} + \tau \left[ D_B \frac{\partial T}{\partial z} \frac{\partial C}{\partial z} + \frac{D_T}{T_\infty} \left( \frac{\partial T}{\partial z} \right)^2 \right] \tag{6}$$

$$u \frac{\partial C}{\partial x} + v \frac{\partial C}{\partial y} + w \frac{\partial C}{\partial z} = D_m \frac{\partial^2 C}{\partial z^2} + \frac{D_T}{T_\infty} \frac{\partial^2 T}{\partial z^2} - K_c^2 \left( \frac{T}{T_\infty} \right)^n e^{-\frac{E_a}{K_0 T}} (C - C_\infty) \tag{7}$$

It also noticeable term in the equation (7), that the Arrhenius term is  $K_c^2 (C - C_\infty) \left( \frac{T}{T_\infty} \right)^n \exp \left( - \left( \frac{E_a}{K_0 T} \right) \right)$ .

The first-order chemical reaction rate was represented by  $K_c$ , When  $K_c$  is more than 0, a destructive reactant is produced. These boundary conditions lead to the following formula:

$$u = v = w = 0, -\kappa T_z = h_f (T_f - T), D_B C_z + \frac{D_T}{T_\infty} T_z = 0 \quad \text{at } z = 0 \tag{8}$$

$$u \rightarrow u_e, v \rightarrow v_e, T \rightarrow T_\infty, C \rightarrow C_\infty \quad \text{as } z \rightarrow \infty$$

Each of the following equations has a similarity solution

$$u = axf'(\eta), v = byg'(\eta), w = -\sqrt{av}(f(\eta) + cg(\eta)), \frac{T - T_\infty}{T_w - T_\infty} = \theta(\eta) \tag{9}$$

$$\phi(\eta) = \frac{C - C_\infty}{C_w - C_\infty}, \eta = z\sqrt{\frac{a}{v}}$$

Notably, the derivative with respect to  $\eta$  indicates primes. The differential equations (3)-(7) converted to ODEs, which are nonlinear in nature, with the help of similarity transformations (9)

$$\left(1 + \frac{1}{\beta}\right) f''' + (f + cg) f'' - (f')^2 + 1 - M(f'-1) - \lambda(f'-1) = 0 \tag{10}$$

$$\left(1 + \frac{1}{\beta}\right) g''' + (f + cg) g'' - c(g')^2 + c - M(g'-1) - \lambda(g'-1) = 0 \tag{11}$$

$$\left(1 + \frac{4}{3} Rd\right) \frac{1}{Pr} \theta'' + (f + cg) \theta' + Nb \theta' \phi' + Nt(\theta')^2 = 0 \tag{12}$$

$$\phi'' + Sc(f + g) \phi' + \frac{Nt}{Nb} \theta'' - Sc \sigma (1 + \delta\theta)^n \exp\left(\frac{-E}{1 + \delta\theta}\right) \phi = 0 \tag{13}$$

The modified boundary conditions are

$$\begin{aligned} f = 0, f' = 0, g = 0, g' = 0, \theta' = -Bi(1 - \theta), Nt\phi' + Nb\theta' = 0 & \text{ at } \eta = 0 \\ f' = 0, g' = 0, \theta = 0, \phi = 0 & \text{ at } \eta = \infty \end{aligned} \tag{14}$$

Where Thermophoresis  $Nt = \frac{D_T(T_w - T_\infty)}{\nu T_\infty}$ , Brownian motion  $Nb = \frac{D_B(T_w - T_\infty)}{\nu}$ , Prandtl number  $Pr = \frac{\nu}{\alpha}$ , Magnetic field  $M = \frac{\sigma B_0^2}{a\rho}$ , Schmidt number  $Sc = \frac{\nu}{D_m}$ . Modified Eckert number  $Ec_m = \frac{Ec_x}{Ec_y}$ . The interested quantities are friction coefficients in the x and y directions which are connected by two physical parameters  $C_{fx}$  and  $C_{fy}$ , the local Nusselt and Sherwood numbers are defined by:

$$C_{fx} = \frac{\tau_{wx}}{\rho u_e^2}, C_{fy} = \frac{\tau_{wy}}{\rho v_e^2}, Nu_x = \frac{xq_w}{k(T_w - T_\infty)}, Sh_x = \frac{xS_w}{D_B(C_w - C_\infty)} \tag{15}$$

Where  $\tau_{wx} = \mu \left(1 + \frac{1}{\beta}\right) \frac{\partial u}{\partial z} \Big|_{z=0}$  and  $\tau_{wy} = \mu \left(1 + \frac{1}{\beta}\right) \frac{\partial v}{\partial z} \Big|_{z=0}$ , the surface shear stress along the x and y directions, respectively,  $q_w = -k \frac{\partial T}{\partial z} \Big|_{z=0}$  the surface heat flux, and  $s_w = -D_B \frac{\partial C}{\partial z} \Big|_{z=0}$  is the surface mass flux.

Using Eq. (9), we obtain

$$\begin{aligned} [Re_x]^{\frac{1}{2}} C_{fx} &= \left(1 + \frac{1}{\beta}\right) f''(0), \left(\frac{x}{y}\right) C_{fy} [Re_x]^{\frac{1}{2}} = c \left(1 + \frac{1}{\beta}\right) g''(0), \\ [Re_x]^{\frac{-1}{2}} Nu_x &= -\theta'(0), [Re_x]^{\frac{-1}{2}} Sh_x = -\phi'(0), Re_x = \frac{u_e x}{\nu} \end{aligned} \tag{16}$$

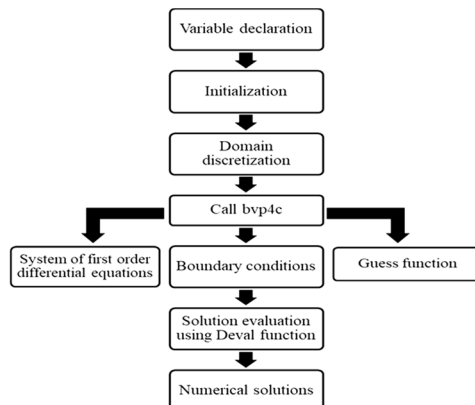


Figure 2. Numerical method Flowchart



### 3. NUMERICAL METHOD

To effectively solve the given set of nonlinear differential equations (10), (11), (12), (13) and boundary conditions (14), the linearity technique can be used to convert them into first-order ODEs. This will enable us to simplify the problem and solve it more efficiently, leading us towards a constructive solution as follows.

$$y_1 = f, y_2 = f', y_3 = f'', y_4 = g, y_5 = g', y_6 = g'', y_7 = \theta, y_8 = \theta', y_9 = \phi, y_{10} = \phi' \tag{17}$$

$$y_1' = y_2$$

$$y_2' = y_3$$

$$y_3' = \frac{-((y_1 + cy_4)y_3 - (y_2)^2 + 1 - M(y_2 - 1) - \lambda(y_2 - 1))}{1 + \frac{1}{\beta}}$$

$$y_4' = y_5$$

$$y_5' = y_6$$

$$y_6' = \frac{-((y_1 + cy_4)y_6 - c(y_5)^2 + c - M(y_5 - 1) - \lambda(y_5 - 1))}{1 + \frac{1}{\beta}}$$

$$y_7' = y_8$$

$$y_8' = \frac{-Pr((y_1 + cy_4)y_8 + Nb y_8 y_{10} + Nt(y_8)^2)}{1 + \frac{4}{3}Rd}$$

$$y_9' = y_{10}$$

$$y_{10}' = -\left( Sc(y_1 + cy_4)y_{10} + \frac{Nt}{Nb}(y_8') - Sc \sigma (1 + \delta y_7)^n e^{\left(\frac{-E}{1 + \delta y_7}\right)} y_9 \right)$$

where the initial conditions

$$\begin{aligned} y_1(0) = 0, y_2(0) = 0, y_3(0) = I_1, y_4(0) = 0, y_5(0) = 0, y_6(0) = I_2, \\ y_7(0) = I_3, y_8(0) + Bi(1 - y_7(0)) = 0, y_9(0) = I_4, Nt y_{10}(0) + Nb y_8(0) = 0 \end{aligned} \tag{18}$$

Arbitrary parameters, denoted by  $I_1, I_2, I_3, I_4$ , will be determined to solve the system of equations given in Eq. (17) along with the initial conditions listed in (18). The MATLAB program is used in combination with the shooting method and the fourthorder Runge-Kutta method to solve the system. The obtaining the results in a sequence of steps, these are well present in Fig.2. The program ensures that the error is minimized and the final conditions are met.

$$y_1(\infty) = 0, y_4(\infty) = 0, y_7(\infty) = 0, y_9(\infty) = 0.$$

In order to verify the validity of our code, we conducted a comparison of the skin friction coefficient results obtained for Reynolds number of pure water with those previously reported by Wang [24], Ishak et al. [6] and Ahmed et al. [1]. After conducting the analysis, we observed that our results were in better agreement with those reported in Table 1. This comparison was an essential step in ensuring that our code was accurately simulating the physical phenomenon being studied.

**Table 1.** Comparison of various values of skin friction, for regular fluid (water) and Pr = 0.7

Re	Wang [24]	Ishak et al. [6]	Ahmed et al. [1]	Present
2	-1.59390	-1.5941	-1.59444	-1.6061299
5	-2.41745	-2.4175	-2.41798	-2.420235
10	-3.34445	-3.3445	-3.34511	-3.345029

### 4. RESULTS AND DISCUSSION

The presented data includes the numerical outcomes of fluid velocity, thermal distribution, and nanoparticle distribution. **Worth note that the results are indicates Newtonian fluid – Dashed lines and Non-Newtonian Casson fluid – Solid line.** The graphs and tables provided an analysis of the impact of different parameters, such as the Brownian motion parameter  $Nb$ , magnetic parameter  $M$ , porous medium parameter  $\lambda$ , thermal radiation parameter  $Rd$ , Gradient of

streamline parameter  $c$ , Casson fluid parameter  $\beta$ , thermophoresis parameter  $Nt$ , chemical reaction parameter  $\sigma$ , thermal biot number  $Bi$ , activation energy parameter  $Ea$  at a constant value.

In Fig. 3-20, the impacts of different parameters on streamwise velocity profiles  $f'(\eta)$  and  $g'(\eta)$  are illustrated. Specifically, the influence of magnetic parameter  $M$ , which measures the magnetic field strength in a porous medium, is shown. Additionally, the impact of porous permeability parameter  $\lambda$ , which characterizes the ability of a porous medium to transmit fluid, is depicted. Finally, the effect of Gradient of streamline parameter  $c$ , which relates to the change in streamlines with respect to distance in the direction of flow, is also demonstrated. Overall, these parameters play a major role in determining the behavior of fluid flow.

The comparative analysis of velocity profiles for Newtonian and Casson fluid flows over sinusoidal cylinder with the influenced by magnetic parameter  $M$  have been presented in the Fig 3. As the magnetic parameter rises, the velocity profiles are increased and worth noting that the greater velocity profile is observed in Newtonian fluid induced by Lorentz force. The similar mechanism of velocity profiles is noted by the porosity parameter, which is observed from the Fig 4. The effect of  $c$  on the velocity profiles are depicted in the Fig. 5.

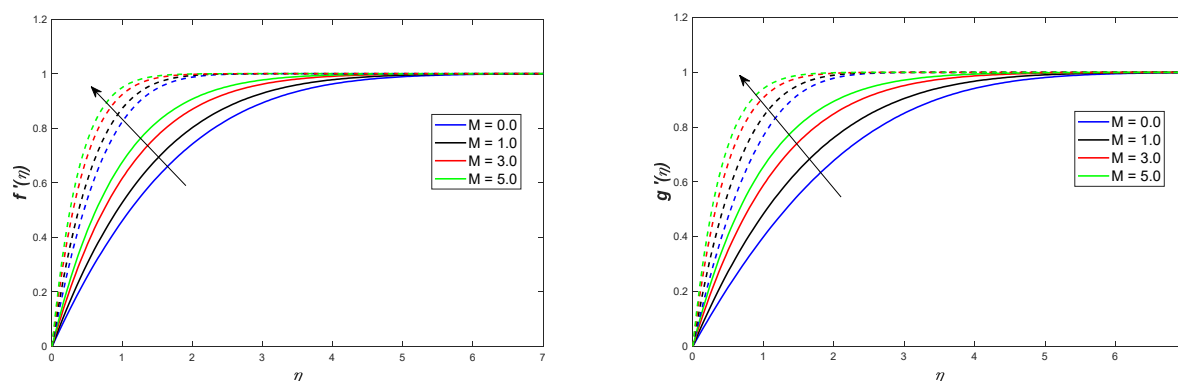


Figure 3. Variation in velocity due to  $M$

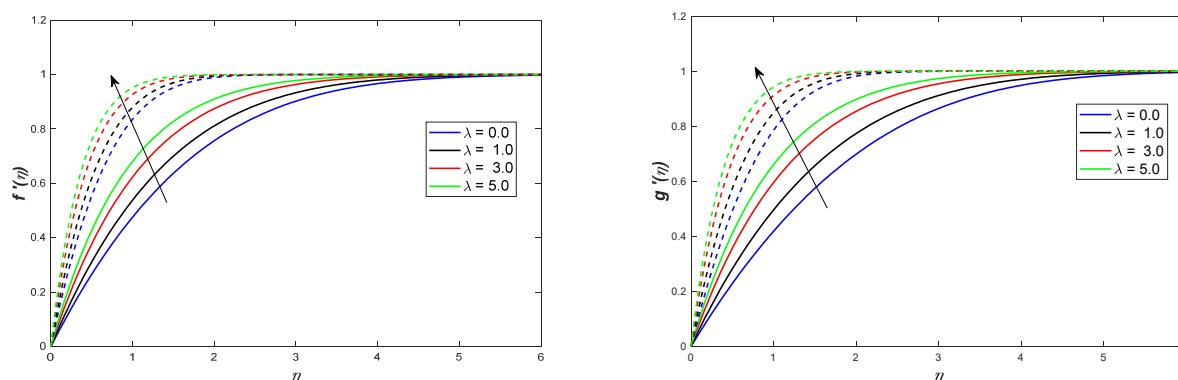


Figure 4. Variation in velocity due to  $\lambda$

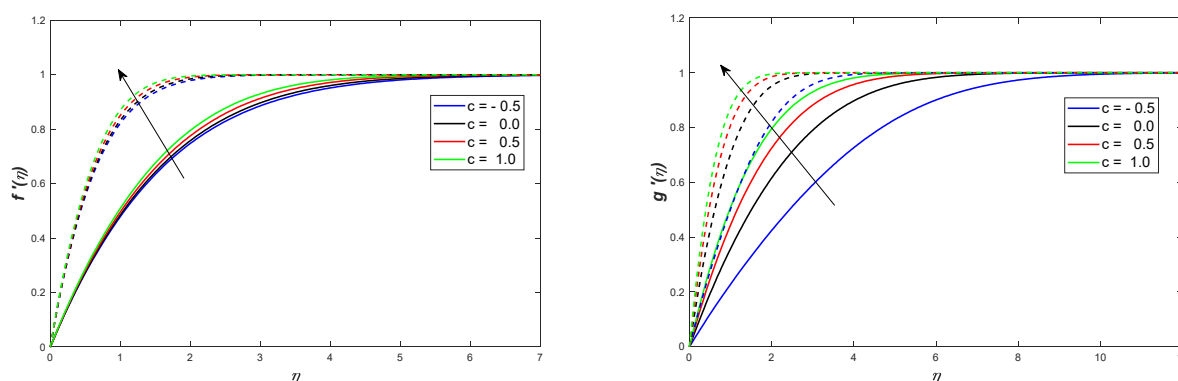


Figure 5. Variation in velocity due to  $c$

The geometry of saddle/nodal stagnation point  $c$  plays a crucial role of velocity profiles. The significant impact is observed on the fluid flow velocity profiles is observed with various values of saddle/nodal stagnation point  $c$ . majorly

we examine saddle stagnation point, nodal stagnation points and stagnation point. Maximal velocity profile is notice at nodal stagnation points; minimum velocity profile is observed at saddle stagnation point in both velocity profiles.

**Figs. 6-12** presents the effect of magnetic parameter  $M$ , porosity parameter  $\lambda$ , Nodal/Saddle point  $c$ , thermal radiation  $Rd$ , thermophoresis  $Nt$ , Brownian motion  $Nb$  and Biot number  $Bi$ , on temperature profile. **Fig. 6 and 7** displays the effect of magnetic parameter and porosity parameter on temperature profiles respectively. The temperature profile decreases in both the fluids when increasing of the magnetic field and porosity. This mechanism is happened due to Lorentz force and the Darcian body force is inversely proportional to the medium. The significant impact is observed on the temperature profiles is observed with various values of nodal/saddle stagnation point  $c$ .

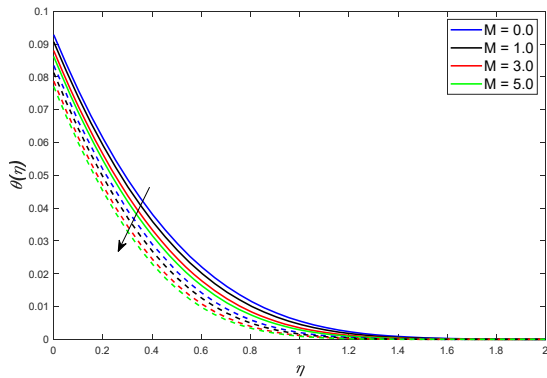


Figure 6. Variation in Temperature due to  $M$

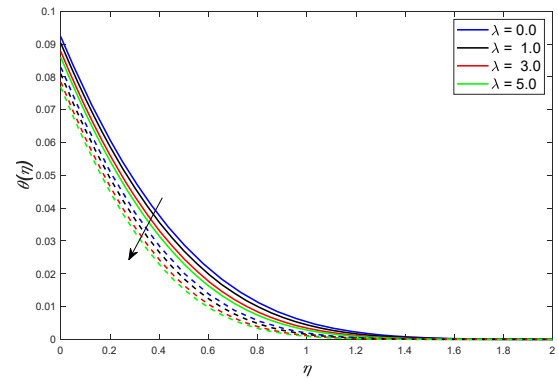


Figure 7. Variation in Temperature due to  $\lambda$

The thermal distribution reduces with the increasing of the nodal/saddle stagnation point  $c$ , is observed in the **Fig. 8**. Thermophoresis  $Nt$  and Brownian motion parameter  $Nb$  impact on temperature profile is depicted in the **Fig. 9 and 10**.

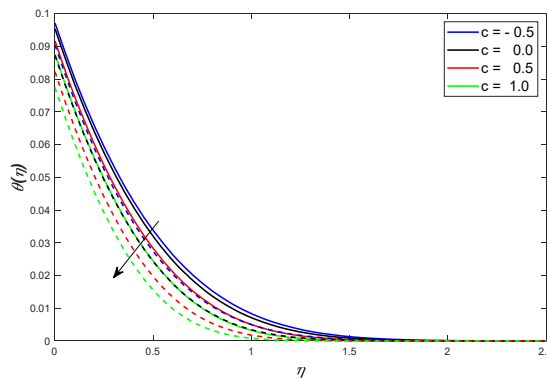


Figure 8. Variation in Temperature due to  $c$

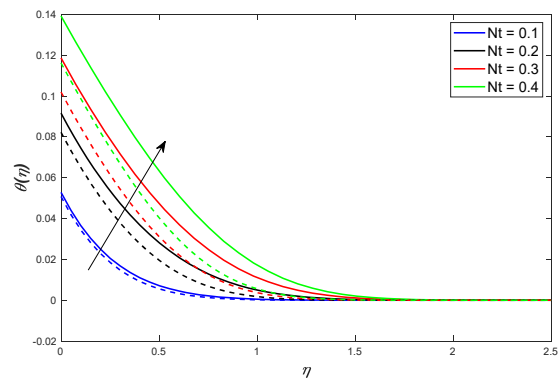


Figure 9. Variation in Temperature due to  $Nt$

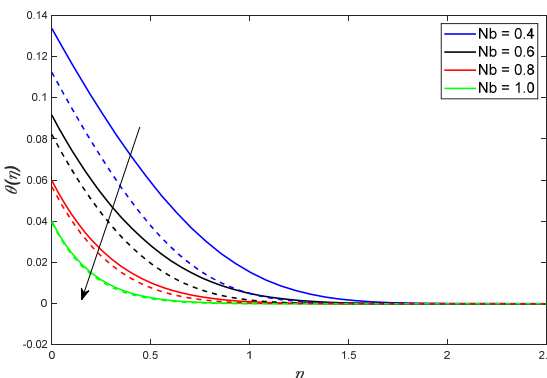


Figure 10. Variation in Temperature due to  $Nb$

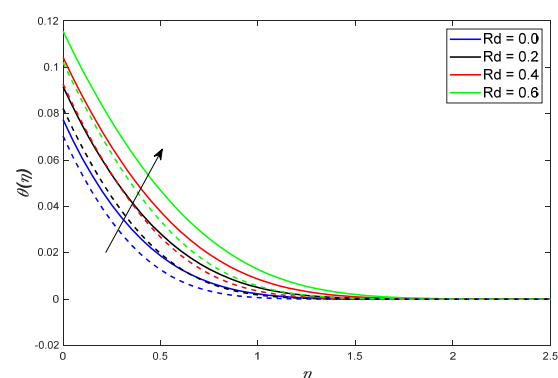


Figure 11. Variation in Temperature due to  $Rd$

Thermophoresis is a fascinating phenomenon that takes place in fluid-particle mixtures. It results from uneven temperature distribution, which leads to the displacement of nanoparticles towards the colder region. This process is driven by thermophoretic forces that cause a non-uniform distribution of particles. To put it simply, thermophoresis is like a tiny invisible hand that pushes particles towards the cold region and causes them to accumulate there. Additionally, the thermophoresis increases as the fluid's temperature increases. Brownian motion is observed in the movement of particles suspended in a fluid. This random movement is caused by the collision of fluid molecules with the particles. The speed

of Brownian motion depends on the particle's size and the fluid's temperature. Larger nanoparticles experience slower Brownian motion, while smaller ones move faster. Additionally, the nanoparticles' Brownian motion increases as the fluid's temperature decreases. The effect of thermal radiation on temperature profile is depicted in the Fig. 11.

When thermal radiation is present, it can raise the temperature profile of a fluid. This happens because the thermal radiation parameter helps improve the fluid's thermal conditions, which can lead to more fluid being present in the boundary layer. As a result, the velocity of the fluid may increase. The effect of Biot number Bi on the temperature profile is seen in Fig. 12.

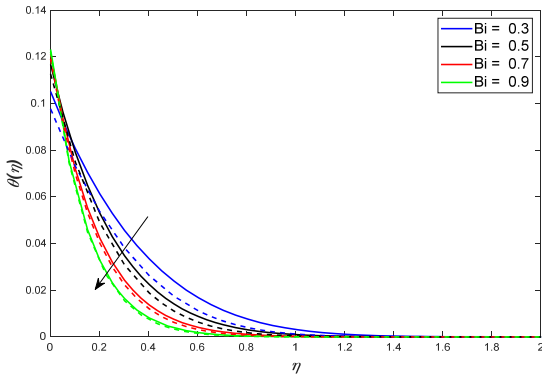


Figure 12. Variation in Temperature due to Bi

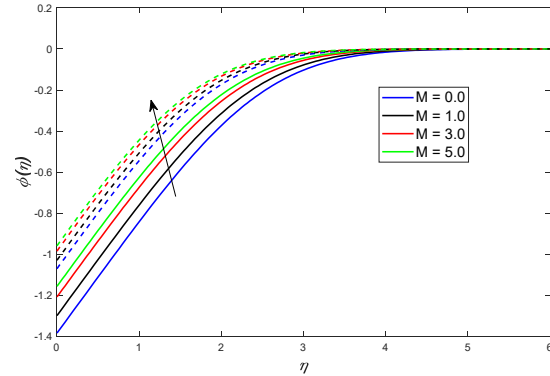


Figure 13. Variation in Temperature due to M

The Biot number is a proper dimensionless quantity when performing heat transfer calculations. It measures the relative resistance to heat transfer due to conduction inside a body versus convection at the body's surface. The temperature profiles reduce with the increasing of Biot number values is observed.

Figs. 13-20 presents the impact of magnetic parameter M, porosity parameter  $\lambda$ , Nodal/Saddle point c, Brownian motion Nb, thermophoresis Nt, Biot number Bi, chemical reaction parameter  $\sigma$  and Activation parameter E on concentration profile. The concentration profile enhancement is observed with the magnetic parameter M, porosity parameter  $\lambda$ , Nodal/Saddle point c, and thermophoresis Nt, when increasing of these parameters the significant increment is notice, which are shown in Figs. 13-16. In addition, the Casson nanofluid concentration profile is diminishes with incremental values of Nb, Bi,  $\sigma$ , the great observation from the Figs.17-19 the Brownian motion Nb, Biot number Bi, chemical reaction parameter  $\sigma$  are deaccelerates the concentration profile while the opposite mechanism is found with the Activation parameter E seen in Fig. 20.

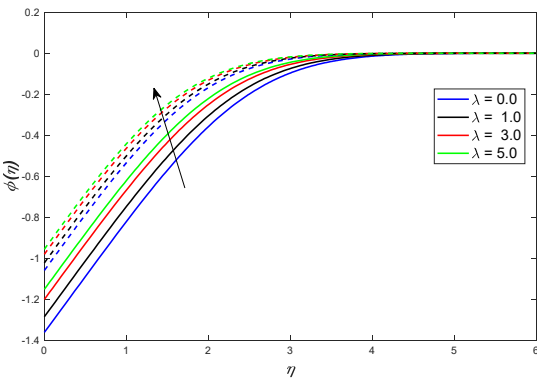


Figure 14. Variation in concentration due to  $\lambda$

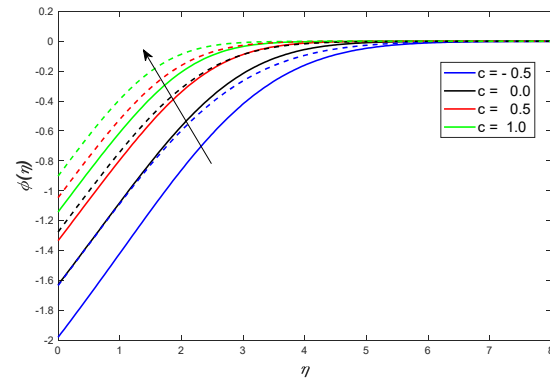


Figure 15. Variation in concentration due to c

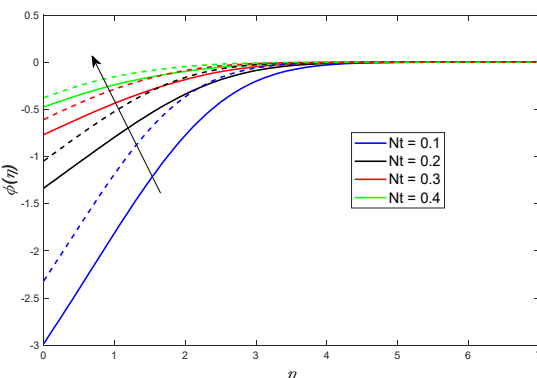


Figure 16. Variation in concentration due to Nt

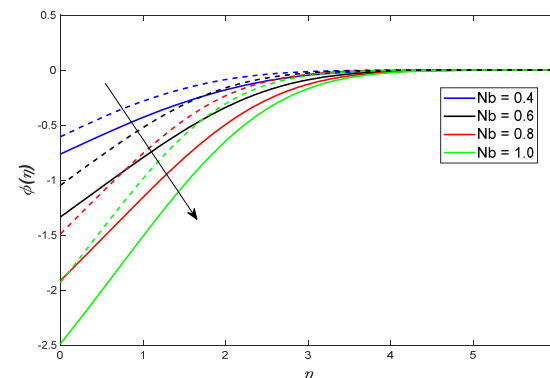


Figure 17. Variation in concentration due to Nb

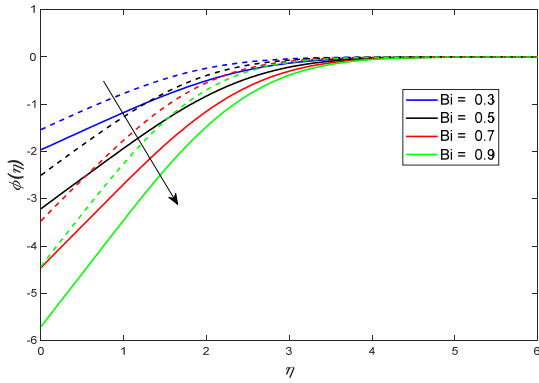


Figure 18. Variation in concentration due to Bi

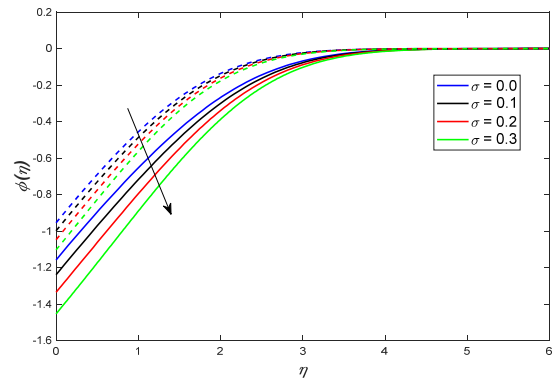


Figure 19. Variation in concentration due to τσ

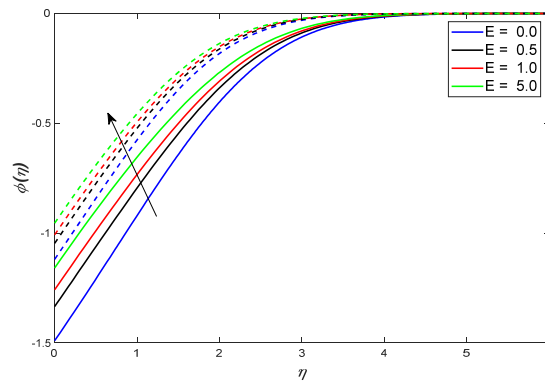


Figure 20. Variation in concentration due to E

The tables provide comprehensive insights into the dynamics of skin friction, Nusselt number and Sherwood number variations, presented in Tables 2, 3, and 4, respectively.

Table 2.  $Cf_x$  and  $Cf_y$  for various values

c	M	$\lambda$	$Cf_x$		$Cf_y$	
			$\beta = \infty$	$\beta = 0.2$	$\beta = \infty$	$\beta = 0.2$
-0.5			1.5056	0.6146	1.5056	0.6146
0.0			1.5212	0.6210	1.5212	0.6210
0.5			1.5495	0.6326	1.5495	0.6326
1.0			1.5841	0.6467	1.5841	0.6467
	0.0		1.3796	0.5632	1.3796	0.5632
	1.0		1.7027	0.6951	1.7027	0.6951
	3.0		2.2123	0.9032	2.2123	0.9032
	5.0		2.6252	1.0717	2.6252	1.0717
		0.0	1.4500	0.5919	1.4500	0.5919
		1.0	1.7602	0.7186	1.7602	0.7186
		30.	2.2570	0.9214	2.2570	0.9214
		5.0	2.6630	1.0871	2.6630	1.0871

Table 3. Nu values for different emerging parameter values

Bi	Rd	M	Nb	Nt	c	Nu	
						$\beta = \infty$	$\beta = 0.2$
0.3						0.1238	0.1332
0.5						0.1428	0.1479
0.7						0.1508	0.1534
0.9						0.1546	0.1560
	0.0					0.0703	0.0774
	0.2					0.1042	0.1161
	0.4					0.1423	0.1599
	0.6					0.1839	0.2081
		0.0				0.1057	0.1176
		1.0				0.1030	0.1149
		3.0				0.0997	0.1115
		5.0				0.0976	0.1092



Bi	Rd	M	Nb	Nt	c	Nu	
						$\beta = \infty$	$\beta = 0.2$
			0.4			0.1424	0.1694
			0.6			0.1042	0.1161
			0.8			0.0721	0.0759
			1.0			0.0498	0.0509
				0.1		0.0643	0.0670
				0.2		0.1042	0.1161
				0.3		0.1292	0.1504
				0.4		0.1472	0.1764
					-0.5	0.1146	0.1230
					0.0	0.1106	0.1208
					0.5	0.1042	0.1161
					1.0	0.0981	0.1109

**Table 4.** Sh values for different emerging parameter values

c	M	Nb	Nt	Bi	$\sigma$	E	Sh	
							$\beta = \infty$	$\beta = 0.2$
-0.5							1.6335	1.9807
0.0							1.2756	1.6293
0.5							1.0463	1.3343
1.0							0.9018	1.1418
	0.0						1.0695	1.3828
	1.0						1.0285	1.2977
	3.0						0.9838	1.2071
	5.0						0.9582	1.1556
		0.4					0.6059	0.7632
		0.6					1.0463	1.3343
		0.8					1.4884	1.9125
		1.0					1.9302	2.4872
			0.1				2.3170	2.9825
			0.2				1.0463	1.3343
			0.3				0.6081	0.7686
			0.4				0.3763	0.4732
				0.3			1.5364	1.9625
				0.5			2.5039	3.2102
				0.7			3.4685	4.4576
				0.9			2.5039	3.2102
					0.0		0.9535	1.1570
					1.0		0.9971	1.2377
					2.0		1.0463	1.3343
					3.0		1.1022	1.4523
						0.0	1.1190	1.4895
						0.5	1.0463	1.3343
						1.0	1.0074	1.2576
						5.0	0.9544	1.1588

These parameters offer crucial physical understanding of the heat and mass transfer processes within the system. Notably, as the unsteadiness parameter increases, both skin friction coefficients and local Nusselt numbers show a consistent uptrend. This indicates that higher levels of unsteadiness correspond to increased frictional forces and enhanced convective heat transfer rates from the surface to the fluid. However, an intriguing observation emerges when examining local Sherwood number. At a critical value of the unsteadiness parameter, particularly when thermophoresis effects come into play, a minimum local Sherwood number is noted. This phenomenon suggests a nuanced interplay between unsteadiness and thermophoresis, where certain conditions may optimize mass transfer rates. Moreover, the analysis underscores the significance of thermophoresis effects on heat transfer. It is evident that the highest heat transfer rates occur under conditions where thermophoresis effects are minimal. Conversely, increasing the thermophoresis parameter leads to a reduction in heat transfer rates, indicating the inhibitory role of thermophoresis on overall heat transfer efficiency. Furthermore, the behavior of the local Nusselt number unveils additional insights. With the rise in the unsteadiness parameter, the local Nusselt number escalates, reflecting the heightened convective heat transfer rates characteristic of more dynamic flow conditions. Notably, peak heat transfer rates are achieved when Brownian motion is minimal or approaches zero, emphasizing the intricate relationship between flow dynamics and particle behavior. Finally, the occurrence of negative local Nusselt numbers for certain unsteadiness parameter values is particularly intriguing. Such instances signify a reversal in the heat transfer direction, indicating heat transfer from the nanofluid to the body. This phenomenon underscores the complex interplay of various parameters in determining the directionality and efficiency of

heat transfer processes within the system, highlighting the need for a comprehensive understanding of fluid dynamics and transport phenomena.

## 5. CONCLUSIONS

In summary, our investigation delved into a transient three-dimensional boundary layer scenario surrounding the flow of magnetohydrodynamic (MHD) Casson polymeric nanofluid around a wavy circular porous cylinder. Incorporating considerations of thermal radiation and activation energy, we emphasized the nonlinear aspects of chemical reaction in the energy equation and utilized convective Nield boundary conditions for a comprehensive analysis. By transforming the boundary layer equations into a self-similar form, we enabled numerical solutions. Notably, we observed the expansion of the velocity field with a certain indicative parameter and its flattening in the presence of an external magnetic field. The impact of thermal conditions on heating and cooling processes proved significant, emphasizing the need for minimization, particularly in air conditioning systems. Furthermore, as the porous parameter increased, we noted improvements in the thermal boundary layer and weakening in the concentration boundary layer. Our findings revealed that the Nusselt number increased with advancements in the thermal radiation parameter and the Sc number within the thermal boundary layer regime. Additionally, we observed a proportional rise in the Nusselt number with increasing activation energy and a decrease in wall mass. Moreover, variations in the nodal/saddle point parameter resulted in changes in the skin-friction coefficients. Finally, we found that the Nusselt number decreased with higher  $Bi$  values but increased with rising Brownian parameters, and increasing activation energy led to a decrease in the Sherwood number. These insights offer valuable contributions to understanding the complex dynamics of boundary layer phenomena in fluid mechanics and thermal transport processes.

### Declaration of Competing Interest

The authors declare that they have no known competing financial interests or personal relationships that could have appeared to influence the work reported in this paper.

### Conflict of interest statement

The authors did not disclose any possible conflicts of interest.

### Data availability statement

There are no data related to the text.

### CRedit authorship contribution statement

P. Venkata Subrahmanyam: Writing – review & editing, Writing – original draft, Visualization, Validation, Methodology, Investigation, Conceptualization. G. Kathyayani: Supervision. G. Venkata Ramudu: Supervision.

### Funding Declaration

This research did not receive any specific grant from funding agencies in the public, commercial, or not-for-profit sectors.

## ORCID

©Gandrakota Kathyayani, <https://orcid.org/0000-0002-1019-7033>

©Gattu Venkata Ramudu, <https://orcid.org/0009-0001-0253-6613>

©K. Venkatadri, <https://orcid.org/0000-0001-9248-6180>

## REFERENCES

- [1] S.E. Ahmed, A.K. Hussein, H.A. Mohammed, and S. Sivasankaran, "Boundary layer flow and heat transfer due to permeable stretching tube in the presence of heat source/sink utilizing nanofluids," *Applied Mathematics and Computation*, **238**, 149-162 (2014). <https://doi.org/10.1016/j.amc.2014.03.106>
- [2] D. Tripathi, A. Sharma, and O.A. Beg, "Joule heating and buoyancy effects in electro-osmotic peristaltic transport of aqueous nanofluids through a microchannel with complex wave propagation," *Adv. Powder Technol.* **29**, 639–653 (2018). <https://doi.org/10.1016/j.appt.2017.12.009>
- [3] F. Alwawi, H. Alkasasbeh, A. Rashad, and R. Idris, "Heat transfer analysis of ethylene glycol-based casson nanofluid around a horizontal circular cylinder with MHD effect," *Proceedings of the Institution of Mechanical Engineers Part C Journal of Mechanical Engineering Science*, **234**(13), 2569-2580(2020). <https://doi.org/10.1177/0954406220908624>
- [4] F. Bosli, A. Suhaimi, S. Ishak, M. Ilias, A. Rahim, and A. Ahmad, "Investigation of nanoparticles shape effects on aligned MHD Casson nanofluid flow and heat transfer with convective boundary condition," *Journal of Advanced Research in Fluid Mechanics and Thermal Sciences*, **91**(1), 155-171(2022). <https://doi.org/10.37934/arfmts.91.1.155171>
- [5] G. Narendar, K. Govardhan, and G. Sarma, "Magnetohydrodynamic stagnation point on a casson nanofluid flow over a radially stretching sheet," *Beilstein Journal of Nanotechnology*, **11**, 1303-1315 (2020). <https://doi.org/10.3762/bjnano.11.114>
- [6] A. Ishak, R. Nazar, and I. Pop, "Uniform suction/blowing effect on flow and heat transfer due to a stretching cylinder," *Applied Mathematical Modelling*, **32**(10), 2059-2066 (2008). <https://doi.org/10.1016/j.apm.2007.06.036>
- [7] J. Akram, N.S. Akbar, and D. Tripathi, "Numerical simulation of electrokinetically driven peristaltic pumping of silver-water nanofluids in an asymmetric micro-channel," *Can. J. Phys.* **68**, 745–763 (2020). <https://doi.org/10.1016/j.cjph.2020.10.015>
- [8] J. Buongiorno, "Convective transport in nanofluids," *ASME J. Heat Transfer*, **128**, 240–250 (2006). <https://doi.org/10.1115/1.2150834>
- [9] K. Gnanaprasanna, and A. Singh, "A numerical approach of forced convection of casson nanofluid flow over a vertical plate with varying viscosity and thermal conductivity," *Heat Transfer*, **51**(7), 6782-6800 (2022). <https://doi.org/10.1002/htj.22623>
- [10] G. Kathyayani, and P.V. Subrahmanyam, "Numerical study of MHD Stagnation-Point Flow of Nanofluid Flow Past a 3-D Sinusoidal Cylinder with Thermophoresis and Brownian Motion Effects," in: *Disruptive Technologies in Computing and*

- Communication Systems – Conference Proceedings*, (Taylor & Francis Group, London, 2024), pp. 408-406, <https://doi.org/10.1201/9781032665535-66>
- [11] G. Kathyayani, and R.L. Devi, “Effect of induced magnetic field and Linear / non-linear vertical stretching sheet on mixed convection Jeffrey fluid near a Stagnation-Point flow through a Porous medium with suction or injection,” *J. Phys.: Conf. Ser.* **1597**, 012003 (2020). <https://doi.org/10.1088/1742-6596/1597/1/012003>
- [12] L. Panigrahi, J. Panda, K. Swain, and G. Dash, “Heat and mass transfer of mhd casson nanofluid flow through a porous medium past a stretching sheet with newtonian heating and chemical reaction,” *Karbala International Journal of Modern Science*, **6**(3), (2020). <https://doi.org/10.33640/2405-609x.1740>
- [13] M. Baig, G. Chen, and C. Tso, “The thermal performance analysis of an al<sub>2</sub>o<sub>3</sub>-water nanofluid flow in a composite microchannel,” *Nanomaterials*, **12**(21), 3821 (2022). <https://doi.org/10.3390/nano12213821>
- [14] M.K. Nayak, “MHD 3D flow and heat transfer analysis of nanofluids by shrinking surface inspired by thermal radiation and viscous dissipation,” *Int. J. Mech. Sci.* **124**, 185–193 (2017). <https://doi.org/10.1016/j.ijmecsci.2017.03.014>
- [15] M.K. Nayak, N.S. Akbar, D. Tripathi, and V.S. Pandey, “Three dimensional MHD flow of nanofluid over an exponential porous stretching sheet with convective boundary conditions,” *Therm. Sci. Eng. Prog.* **3**, 133–140 (2017). <https://doi.org/10.1016/j.tsep.2017.07.006>
- [16] M.K. Nayak, N.S. Akbar, D. Tripathi, Z.H. Khan, and V.S. Pandey, “MHD 3D free convective flow of nanofluid over an exponentially stretching sheet with chemical reaction,” *Adv. Powder Technol.* **28**, 2159–2166 (2017). <https://doi.org/10.1016/j.appt.2017.05.022>
- [17] M. Senapati, K. Swain, and S. Parida, “Numerical analysis of three-dimensional mhd flow of casson nanofluid past an exponentially stretching sheet,” *Karbala International Journal of Modern Science*, **6**(1), (2020). <https://doi.org/10.33640/2405-609x.1462>
- [18] N.A. Halim, R.U. Haq, and N.F.M. Noor, “Active and passive controls of nanoparticles in Maxwell stagnation point flow over a slipped stretched surface,” *Meccanica*, **52**, 1527–1539 (2017). <https://doi.org/10.1007/s11012-016-0517-9>
- [19] N. Thamarai Kannan, S. Karthikeyan, D. Chaudhary, and S. Kayikci, “Analytical investigation of magnetohydrodynamic non-newtonian type casson nanofluid flow past a porous channel with periodic body acceleration,” *Complexity*, **2021**, 1-17 (2021). <https://doi.org/10.1155/2021/7792422>
- [20] P. Rana, N. Shukla, O.A. Bégin, *et al.*, “Lie Group Analysis of Nanofluid Slip Flow with Stefan Blowing Effect via Modified Buongiorno’s Model: Entropy Generation Analysis,” *Differ. Equ. Dyn. Syst.* **29**, 193–210 (2021). <https://doi.org/10.1007/s12591-019-00456-0>
- [21] S. Han, L. Zheng, C. Li, and X. Zhang, “Coupled flow and heat transfer in viscoelastic fluid with Cattaneo-Christov heat flux model,” *Appl. Math. Lett.* **38**, 87–93 (2014). <https://doi.org/10.1016/j.aml.2014.07.013>
- [22] V.K. Narla, D. Tripathi, and O.A. Beg, “Electro-osmotic nanofluid flow in a curved microchannel,” *Can. J. Phys.* **67**, 544-558 (2020). <https://doi.org/10.1016/j.cjph.2020.08.010>
- [23] V. Tibullo, and V. Zampoli, “A uniqueness result for the Cattaneo-Christov heat conduction model applied to incompressible fluids,” *Mech. Res. Commun.* **38**, 77–79 (2011). <https://doi.org/10.1016/j.mechrescom.2010.10.008>
- [24] C.Y. Wang, “Fluid flow due to a stretching cylinder,” *The Physics of fluids*, **31**(3), 466-468 (1988). <https://doi.org/10.1063/1.866827>
- [25] Y. Wang, K. Yang, Z. Zhang, W. Qi, and J. Yang, “Natural convection heat and moisture transfer with thermal radiation in a cavity partially filled with hygroscopic porous medium,” *Drying Technology*, **34**(3), 275-286 (2015). <https://doi.org/10.1080/07373937.2015.1047953>

## ТОЧКА СТАГНАЦІЇ МГД-ПОТОКІВ ПОЛІМЕРНОЇ НАНОРІДИНИ КАССОНА У НАПРЯМКУ ДО ХВИЛЯСТОГО КРУГОВОГО ЦИЛІНДРУ, НАСИЧЕНОГО ПОРИСТИМ СЕРЕДОВИЩЕМ В УМОВАХ КОНВЕКТИВНОГО ПОЛЯ І ТЕПЛОВОГО ВИПРОМІНЮВАННЯ

П. Венката Субрахманьям<sup>а</sup>, Гандракота Катъяїні<sup>а</sup>, Гатту Венката Рамуду<sup>а</sup>, К. Венкатадрі<sup>б</sup>

<sup>а</sup>Кафедра прикладної математики, Університет Йогі Вемана, Кадапа, А.П., Індія

<sup>б</sup>Кафедра математики, Університет Мохана Бабу (колишній інженерний коледж Шрі Відьянікетан), Тірупаті А.Р.-517 102, Індія

У цьому дослідженні проводиться ретельне числове дослідження з використанням методу *bvp4c* для вивчення потоку магнітогідродинамічної (МГД) полімерної нанорідини Кассона навколо хвилястого круглого пористого циліндра в точці застою. У ньому враховується енергія активації та теплове випромінювання, що підкреслює значний вплив теплового випромінювання на потік рідини, концентрацію та профілі температури. Вплив теплового випромінювання в рівнянні енергії ретельно розглянуто разом з конвективними граничними умовами Нільда, що дозволяє провести комплексний аналіз. Вводячи безрозмірні змінні, дослідження перетворює диференціальне рівняння з частинними похідними на звичайні рівняння, що полегшує застосування схеми стрільби для наближення розв'язку. Ретельно досліджені результати пропонують детальне розуміння профілів температури, швидкості та масової концентрації, підкреслюючи глибокий вплив теплового випромінювання на ці параметри. Крім того, надається комплексне графічне представлення кожного інженерного параметра, що пропонує тонке розуміння складних фізичних явищ, що беруть участь, з особливою увагою до впливу теплового випромінювання.

**Ключові слова:** потік у точці застою; теплове випромінювання; полімерна нанорідина Кассона; метод *bvp4c*; магнітогідродинаміка (МГД)

## DARCY-FORCHHEIMER FLOW OF OLDROYD-B NANOFLUID OVER AN INCLINED PLATE WITH EXOTHERMIC CHEMICAL REACTIONS AND BAYESIAN NEURAL NETWORK MODELLING

 **Gadamsetty Revathi**<sup>a\*</sup>,  **M. Rekha**<sup>b</sup>,  **P. Srividya Devi**<sup>b</sup>,  **B.Ch. Nookaraju**<sup>c</sup>

<sup>a</sup>Department of Mathematics, Gokaraju Rangaraju Institute of Engineering and Technology, Bachupally, Hyderabad – 500090, India

<sup>b</sup>Department of EEE, Gokaraju Rangaraju Institute of Engineering and Technology, Bachupally, Hyderabad – 500090, India

<sup>c</sup>Department of Mechanical Engineering, Gokaraju Rangaraju Institute of Engineering and Technology, Bachupally, Hyderabad, - 500 090, India

\*Corresponding Author e-mail: [grevathi1545@grietcollege.com](mailto:grevathi1545@grietcollege.com)

Received May 3, 2025; revised June 12, 2025; accepted July 4, 2025

This study investigates the steady, laminar motion of a non-Newtonian Oldroyd-B nanofluid over an inclined plate, integrating Buongiorno's nanofluid model to account for Brownian motion and thermophoresis. The novel integration of couple stress and Forchheimer inertia in the analysis, coupled with advanced Bayesian-regularized ANN modelling, distinguishes this work. Governing equations are transformed using similarity variables and solved numerically via MATLAB's `bvp4c` solver. The effects of couple stress, relaxation time, Forchheimer number, thermal radiation, thermophoresis, Brownian motion, and activation energy on velocity, temperature, and concentration profiles are systematically analyzed. Results reveal that couple stress and relaxation time reduce velocity, while thermal radiation and thermophoresis elevate temperature. Brownian motion decreases concentration, and activation energy influences both temperature and concentration oppositely. Multiple linear regression models quantify relationships between friction factor, Nusselt, and Sherwood numbers and key parameters, while a Bayesian-regularized artificial neural network (ANN) demonstrates high predictive accuracy (R-values  $\sim 1$ ). It is noticed that increasing the couple stress parameter from 0.1 to 2.5 reduces friction factor by 59.8%, increasing the thermophoresis parameter from 0.1 to 2.5 decreases the Nusselt number by 7.8%, reflecting reduced heat transfer, and increasing the Brownian motion parameter from 0.1 to 2.5 reduces the mass transmission rate by 2.6%.

**Keywords:** *Non-Newtonian fluid; Thermophoresis; bvp4c; Brownian motion; Activation energy; Thermal radiation*

**PACS:** 47.15.-x, 47.50.-d

### Nomenclature

$u, v$ – the velocity components in the directions of x-axis and y-axis $\sigma^*$ – Stefan-Boltzman constant $Pr$ – Prandtl number $\tau$ – Heat capacity ratio $\nu$ – Kinematic viscosity $g$ – Acceleration due to gravity $\rho$ – Density $\gamma$ – Angle of inclination $\mu$ – Viscosity of the fluid $K$ – Permeability $Fr$ – Forchheimer number $k$ – Thermal conductivity $B_0$ – Magnetic strength $Mg$ – Magnetic field parameter $\sigma$ – Electrical conductivity $\lambda$ – Parameter due to Mixed convection	$\eta$ – Similarity variable $Nb$ – Brownian motion parameter $C_p$ – Specific heat capacity $\Lambda$ – Porosity parameter $Nt$ – Thermophoresis parameter $k_r$ – Chemical reaction parameter $f$ – Stream function (non-dimensional) $k_0$ – Mean Absorption coefficient $\lambda^*$ – Parameter due to buoyancy $D_T$ – Diffusion coefficient (Thermophoresis) $D_B$ – Diffusion coefficient (Brownian motion) $\alpha$ – Thermal diffusivity $\alpha_1$ – Temperature ratio parameter $m$ – The fitted rate constant $\Gamma$ – Reaction rate parameter (non-dimensional) $A$ – Activation energy parameter $Ra$ – Radiation parameter
--	---

### 1. INTRODUCTION

Newtonian as well as non-Newtonian fluids are the two main types taken into account in fluid mechanics. The viscosity and flow characteristics of these fluids under shear stress serve as the basis for differentiation. Regardless of the applied shear rate, the viscosity of Newtonian fluids remains constant. For instance, water, fuel, alcohol, and many more substances. Because of their rheological properties, non-Newtonian fluids are helpful in a huge range of industrial and technical purposes. A number of significant studies on non-Newtonian fluid models are documented due to said broader use and applications. Many modellings have been proposed to illustrate the fluid response that the Navier-Stokes model cannot explain. These models are divided into three types: differential, integral, and rate models. Oldroyd's [1] report, which was influenced by Frohlick and Sack's [2] work, established a methodical procedure for creating a viscoelastic fluid modelling that was precisely of rate type, even though it had nothing to do with thermodynamical concerns. Among

the several models he presented, the Oldroyd-B fluid modelling was analytically feasible and, more importantly, experimentally supported. It was characterised by three material constants namely, the viscosity, relaxation and retardation time. Oudina et al. [3] provided a study of heat transfer efficiency methods in various enclosures as well as nanofluidic applications. Boudjemline et al. [4] investigated Jeffery-Hamel flow extension and Oldroyd-B nanofluid in an enlarged channel. Yasir et al. [5] scrutinized the unsteady motion of an Oldroyd-B fluid that used energy transmission to form an extendable cylindrical surface. Analytic series convergence was one of their topics. Using Buongiorno's model, they also investigated the characteristics of Brownian motion brought on by nanoparticles. Sun et al. [6] reported the numerical outcomes on the Oldroyd-B motion across a triangular cylinder. This study investigates the flow motion in different orientations. Discussion of magnetic impact in the motion of Oldroyd-B fluid along a semi-vertical plate with absorbing boundary assumptions in another discussion of Liu et al. [7]. Fetecau et al. [8] presented the results for MHD motion of Oldroyd-B fluid by a circular cylinder in a saturated porous region. Munir et al. [8] studied numerically the flow behaviour of Oldroyd-B nanofluid. They also reported the entropy generation through their study. Kang et al. [9] used the characteristics of Brownian movement and thermophoresis in a radiative motion of Oldroyd-B fluid. With the help of non-Fourier heat flux, Ahmed et al. [10] presented the outcomes for chemically reactive Oldroyd-B nanofluid bidirectionally with external heat source. Yasir et al. [12] also discussed the unsteady motion of Oldroyd-B fluid via convectively heated surface.

Industrial applications depend heavily on chemical reactions that release energy as heat. However, most of these chemical reactions can become uncontrollable, which is why scientists and engineers are looking for a very efficient way to achieve this aim while maintaining safety, reaction control, and appropriate heat management. Due to this reason, a good amount of literature found on these reactions. For instance, exploration of endothermic and exothermic chemical reactions in a nanofluid motion over a permeable microchannel by Madhukesh et al. [13]. Impacts of these chemical reactions on the different fluid motions discussed by many authors. Ramesh et al. [14], Agbolade and Fatunmbi [15], Maleque [16], Alarabi et al. [17], Shanmugapriya et al. [18], Oderinu et al. [19] and Khan et al. [20] are few of the many recent studies. The reason behind these investigations is that the exothermic chemical reactions have a major impact on engineering applications such chemical separation, oil separation, and combustion processes that require heat transfer in the presence of nanofluids.

Researchers have lately become interested in the movement of fluid through a porous area and objects of various forms immersed in the porous region. Numerous fields, including applied mathematics, mechanical engineering, geothermal physics, nuclear engineering, bioengineering, and civil engineering, have used it. Some processes that include fluid flow via a porous area include the use of geothermal energy, the casting solidification, flow of blood in arteries or lungs, underground electrical wires, the dispersal of pollutants in aquifers, heat pipes (porous), and chemical catalytic connections. The flow filled in the porous region is widely interpreted using Darcy's law. The effects of high velocity and turbulence in the porous region render Darcy's law inapplicable. Practical impact of this law in a variety of mathematical modellings was discussed by many of the researchers in the past and recent literature. Hayat et al. [21] examined the Darcy-Forchheimer motion along with nonlinear mixed convection. Later Khan [22] studied the forced convective Darcy-Forchheimer motion of hybrid nanofluid through a rotating disk. Revathi et al. [23] proposed a similar modelling for the nanofluid flow via an angled plate together with activation energy and thermal radiation. A similar modelling under Darcy-Forchheimer flow together with chemical reactions has been reported by Rasheed et al. [24] recently. Few more relevant studies in recent literature are listed in [25-31] which describes the modelling of Darcy-Forchheimer motion of the nano/hybrid fluids in addition to a variety of physical constraints.

Motivation from the mentioned works a numerical examination is carried out to drag the consequences for a Darcy-Forchheimer motion of Oldroyd-B nanofluid across an inclined plate with hexothermic chemical reactions on the basis of Bayesian Neural Network modelling. No such reports on this modelling are not yet being discussed by the authors. To fill this research gap, we assumed this type of modelling and presented the numerical outcomes via plots and tables. It means the novel aspect of present investigation is hidden in its formulation. Usage of couple stress, Darcy-Forchheimer and ANN distinguishes from the similar studies. The numerical outcomes are picked out from `bvp4c` solver in MATLAB. Validation of the results also presented with Bayesian Neural Network.

## 2. FORMULATION OF THE STUDY

This research focuses on the flow characteristics of a non-Newtonian (Oldroyd B) fluid across an angled upright plate. Assumptions for this study are outlined as below:

- The flow is steady and laminar.
- The plate is inclined at an angle  $\alpha$ , with the  $x$  –axis along the flow and the  $y$  –axis normal to it.
- Buongiorno's nanofluid model is used, incorporating:
  - Brownian motion (nanoparticle diffusion).
  - Thermophoresis (nanoparticle migration due to temperature gradients).
- A uniform magnetic field  $B$  is applied vertically (along  $y$  –axis).
- The induced magnetic field is negligible (low magnetic Reynolds number).
- Joule heating and Viscous dissipation are omitted.
- No-slip condition at the plate surface.



- The Boussinesq approximation is used for buoyancy effects.
- The chemical reaction is considered to be exothermic, meaning that it releases heat ( $\beta > 0$ ).

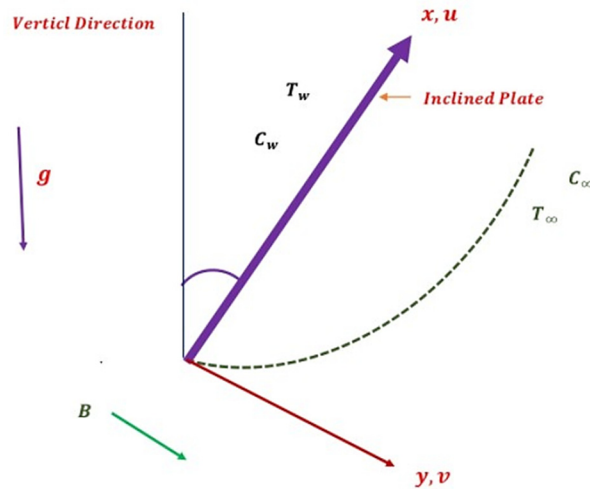


Figure 1. Graphical depiction of the current research

The following conditions and equations are essential for this investigation, based on the previously given assumptions (Singh et al. [32], Muhammad et al. [33], Reddy et al. [34]):

$$\frac{\partial v}{\partial y} + \frac{\partial u}{\partial x} = 0 \tag{1}$$

$$\begin{aligned} \frac{\partial u}{\partial y} v + \frac{\partial u}{\partial x} u &= \frac{\partial^2 u}{\partial y^2} \frac{\mu}{\rho} - \delta_1 \left( u^2 \frac{\partial^2 u}{\partial x^2} + 2uv \frac{\partial^2 u}{\partial x \partial y} + v^2 \frac{\partial^2 u}{\partial y^2} \right) \\ &+ \frac{\mu}{\rho} \delta_2 \left( u \frac{\partial^3 u}{\partial x \partial y^2} - \frac{\partial u}{\partial x} \frac{\partial^2 u}{\partial y^2} + v \frac{\partial^3 u}{\partial y^3} - \frac{\partial u}{\partial y} \frac{\partial^2 v}{\partial y^2} \right) - \frac{\mu}{\rho} \frac{1}{\kappa} u - B^2 u \frac{\sigma}{\rho} - \frac{\gamma_0}{\rho} \frac{\partial^4 u}{\partial y^4} \\ &+ [\beta_r (T - T_\infty) g + \beta_c (C - C_\infty) g] \cos \alpha - Fu^2 \end{aligned} \tag{2}$$

$$\begin{aligned} \frac{\partial T}{\partial x} u + \frac{\partial T}{\partial y} v &= \frac{1}{(\rho C_p)} \frac{\partial^2 T}{\partial y^2} k + \beta \frac{1}{C_p} k_0^2 \left( \frac{T}{T_\infty} \right)^m \exp \left( -\frac{E_0}{k_1 T} \right) (C - C_\infty) \\ &+ \frac{1}{(\rho C_p)} \frac{16}{3} \frac{\sigma^* T_\infty^3}{k^*} \frac{\partial^2 T}{\partial y^2} + \tau \left( D_B \frac{\partial T}{\partial y} \frac{\partial C}{\partial y} + \frac{1}{T_\infty} D_T \left( \frac{\partial T}{\partial y} \right)^2 \right) \end{aligned} \tag{3}$$

$$v \frac{\partial C}{\partial y} + u \frac{\partial C}{\partial x} = D_B \frac{\partial}{\partial y} \left( \frac{\partial C}{\partial y} \right) + \frac{D_T}{T_\infty} \frac{\partial^2 T}{\partial y^2} - k_0^2 \left( \frac{T}{T_\infty} \right)^m \exp \left( -\frac{E_0}{k_1 T} \right) (C - C_\infty) \tag{4}$$

$$\left. \begin{aligned} C = C_w, v = 0, u = 0, T = T_w, \frac{\partial^2 u}{\partial y^2} = 0, \text{ at } y = 0, \\ C \rightarrow C_\infty, u \rightarrow 0, T \rightarrow T_\infty, \frac{\partial u}{\partial y} \rightarrow 0, \text{ as } y \rightarrow \infty. \end{aligned} \right\} \tag{5}$$

For the purpose of converting regulatory equations, Sudarmozhi et al. [35] introduced further similarity transformations:

$$\left. \begin{aligned} \eta = \frac{y}{x} Ra_x^{0.25}, Ra_x = \frac{g \beta_r (T_w - T_\infty) x^3}{\alpha \nu}, u = \frac{\alpha}{x} Ra_x^{0.5} f', \\ v = \frac{\alpha}{4x} \eta Ra_x^{0.25} f' - \frac{3\alpha}{4x} Ra_x^{0.25} f, \phi(\eta) = \frac{C - C_\infty}{C_w - C_\infty}, T = T_\infty + \theta(\eta)(T_w - T_\infty). \end{aligned} \right\} \tag{6}$$

Through the use of terms in (6), the continuity equation (1) is satisfied in a straightforward manner. Terms in (6) can then be skilfully used to convert (2 - 5) as the following:

$$\frac{3}{4}ff'' - \frac{\Lambda_1}{2} \frac{1}{\sqrt{\text{Pr}}} \left( f^{13} + 3\eta f^{12} f'' + \frac{3}{2} ff' f'' + \frac{9}{4} f^2 f''' \right) - \frac{f'^2}{2} - \sqrt{\text{Pr}} \left( Mg + \frac{1}{Da} \right) f' + \frac{\Lambda_2}{2} \frac{1}{\sqrt{\text{Pr}}} \left( \frac{f''^2}{2} - f' f''' - \frac{3}{2} ff^{iv} \right) - Fr f'^2 + \text{Pr}(\theta + \lambda\phi) \cos \alpha - Cs f^v = 0 \quad (7)$$

$$\left( 1 + \frac{4}{3} Ra \right) \theta'' + \frac{3}{4} f \theta' + \chi \Gamma (1 + S\theta)^m \exp\left(-\frac{A}{1+S\theta}\right) \phi + Nb \theta' \phi' + Nt \theta'^2 = 0 \quad (8)$$

$$\frac{1}{Le} \phi'' + \frac{3}{4} f \phi' + \frac{1}{Le} \frac{Nt}{Nb} \theta'' - \Gamma (1 + S\theta)^m \exp\left(-\frac{A}{1+S\theta}\right) \phi = 0 \quad (9)$$

$$\left. \begin{aligned} \text{at } \eta = 0 : \phi = 1, f = 0, f' = 0, \theta = 1, f''' = 0, \\ \text{as } \eta \rightarrow \infty : \theta \rightarrow 0, f'' \rightarrow 0, f' \rightarrow 0, \phi \rightarrow 0. \end{aligned} \right\} \quad (10)$$

where

$$\left. \begin{aligned} \text{Pr} = \frac{\nu}{\alpha}, Mg = \sqrt{\frac{1}{g\beta_T(T_w - T_\infty)}} \frac{\sigma B_0^2}{\rho}, Cs = \sqrt{\frac{g\beta_T(T_w - T_\infty)}{\nu}} \frac{\gamma_1}{\rho\alpha^{3/2}}, \gamma_0 = \gamma_1 \sqrt{x}, Ra = \frac{4\sigma^* T_\infty^3}{kk^*}, \\ Da = \frac{\kappa_0 \sqrt{\alpha g \beta_T (T_w - T_\infty)}}{\nu}, \kappa = \kappa_0 \sqrt{x}, Fr = \frac{C_b}{\sqrt{\kappa}}, \Lambda_1 = \delta_0 \sqrt{g\beta_T(T_w - T_\infty)}, \delta_0 = \frac{\delta_1}{\sqrt{x}}, \\ Nb = \frac{\tau(C_w - C_\infty) D_B}{\alpha}, Le = \frac{\alpha}{D_B}, \Gamma = \frac{k_r^2}{\alpha}, k_r = k_0 x, \Lambda_2 = \delta^* \sqrt{g\beta_T(T_w - T_\infty)}, \delta^* = \frac{\delta_2}{\sqrt{x}}, \\ A = \frac{E_0}{k_2 T_\infty}, S = \frac{T_w - T_\infty}{T_\infty}, Nt = \frac{\tau(T_w - T_\infty) D_T}{\alpha T_\infty}. \end{aligned} \right\}$$

Friction factor, Nusselt and Sherwood numbers are outlined as:

$$\left. \begin{aligned} Cf = \frac{x^2}{\mu \alpha Ra_x} \tau_w \Big|_{y=0}, \tau_w = \mu \frac{\partial u}{\partial y}, \\ Nu = \frac{q_w}{k_f (T_w - T_\infty)} \Big|_{y=0}, q_w = - \left( k_f + \frac{16\sigma^* T^3}{3k^*} \right) \left( \frac{\partial T}{\partial y} \right), \\ Sh = \frac{s_w}{D_B (C_w - C_\infty)} \Big|_{y=0}, s_w = - D_B \left( \frac{\partial C}{\partial y} \right). \end{aligned} \right\} \quad (11)$$

Terms in (6) allows us to rewrite the terms in (11) as

$$\left. \begin{aligned} (Ra_x)^{\frac{1}{4}} Cf = f''(0), \\ (Ra_x)^{-\frac{1}{4}} Nu = - \left( 1 + \frac{4}{3} Ra \right) \theta'(0), \\ (Ra_x)^{\frac{1}{4}} Sh = - \phi'(0). \end{aligned} \right\}$$

### 3. NUMERICAL PROCEDURE

The transformed governing equations (7 - 9) subject to the restrictions (10) are worked out with the *bvp4c* solver in MATLAB. This solver is a finite-difference method designed to obtain the solutions of boundary value problems (BVPs) for ordinary differential equations (ODEs) by employing a collocation technique. It adaptively adjusts mesh points to ensure accuracy and efficiency. Advantages include its robustness in handling nonlinear and stiff BVPs, automatic error control for high precision, flexibility with various boundary conditions, and ease of implementation, making it ideal for complex fluid dynamics problems like those in this study.

### 4. DISCUSSION OF OUTCOMES

This section systematically examines the impacts of key parameters- including couple stress, thermal radiation, thermophoresis, and relaxation time of the fluid- on velocity, temperature, and concentration profiles.

The rise in couple stress within a fluid leads to an increase in internal resistance against deformation, which in turn reduces the fluid's velocity (see Fig. 2). Couple stress arises from micro-rotational effects in complex fluids (e.g., liquid crystals or polymeric fluids), where adjacent fluid elements experience opposing rotational moments. As couple stress increases, these microscopic interactions dissipate more kinetic energy, effectively resisting fluid motion. Physically, this means the fluid exhibits a stronger tendency to resist shear and rotational deformation, resulting in a stiffer response to applied forces and a slower overall flow. This behaviour is particularly relevant in non-Newtonian fluids, where microstructure interactions dominate macroscopic flow properties. Thus, higher couple stress correlates with reduced velocity due to enhanced internal friction and energy dissipation at the microstructural level. In the Oldroyd-B fluid model, the relaxation parameter ( $\Lambda_1$ ) represents the time scale over which polymeric stresses in the fluid decay. When  $\Lambda_1$  increases, the fluid exhibits stronger viscoelastic memory, meaning it retains internal stresses for a longer time, resisting deformation. This increased elastic resistance opposes the flow, effectively reducing the fluid's velocity (see Fig. 3).

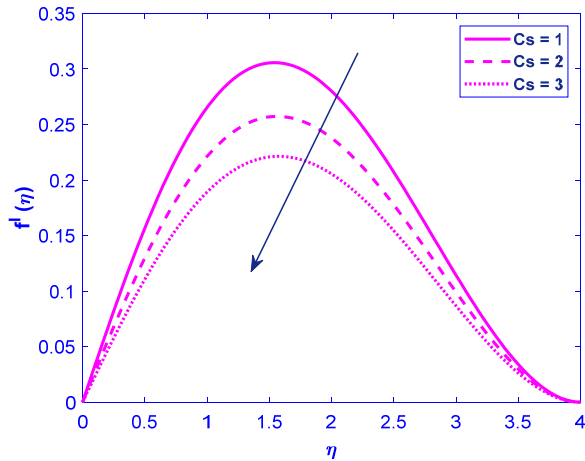


Figure 2. Upshot of  $C_s$  on velocity

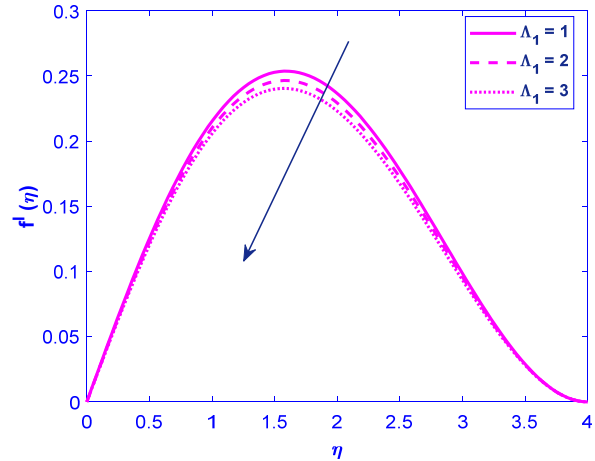


Figure 3. Upshot of  $\Lambda_1$  on velocity

Physically, this can be interpreted as the polymer chains within the fluid becoming more entangled or stretched, enhancing their ability to store elastic energy and thus dampening momentum transfer. Consequently, a higher  $\Lambda_1$  leads to a slower velocity profile, as more energy is dissipated through elastic recoil rather than kinetic motion. This behaviour is typical of viscoelastic fluids, where elasticity competes with viscous flow, slowing down the overall movement. The Forchheimer number ( $Fr$ ) quantifies the relative importance of inertial (non-Darcy) effects compared to viscous (Darcy) effects in porous media flow. A rise in  $Fr$  indicates stronger inertial resistance, often due to higher flow velocity, larger pore-scale turbulence, or increased fluid inertia. As  $Fr$  increases, the inertial drag force opposing the flow becomes more significant, leading to a reduction in the effective fluid velocity (see Fig. 4). Physically, this occurs because energy is dissipated in overcoming additional resistance caused by eddies, flow separation, and momentum exchange at higher velocities. Thus, the velocity decreases to balance the increased inertial dissipation, maintaining equilibrium in the flow system. This effect is particularly notable in high-velocity flows through coarse or fractured porous media. In an exothermic chemical reaction, the activation energy represents the energy barrier that must be overcome for reactants to form products. When the activation energy increases, the reaction rate typically decreases because fewer molecules possess sufficient energy to surpass this higher barrier. As a result, the rate of heat release from the exothermic reaction slows down, leading to a reduction in the overall temperature of the fluid (see Fig. 5).

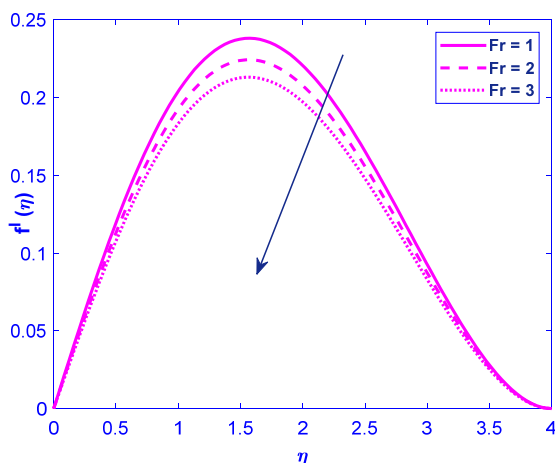


Figure 4. Upshot of  $Fr$  on velocity

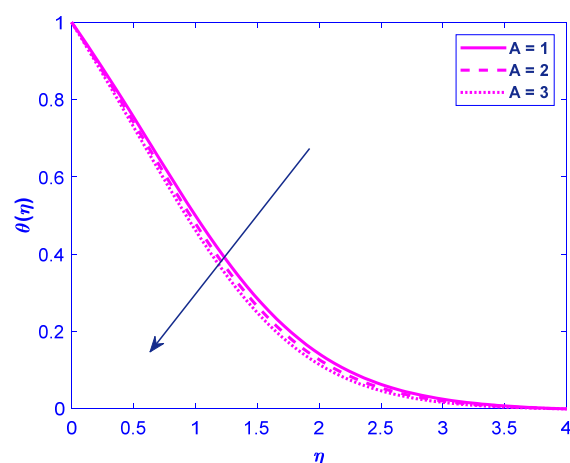


Figure 5. Upshot of  $A$  on temperature

Physically, this means that the system generates less thermal energy per unit time because the reaction becomes less efficient at converting reactants into energy-releasing products. The temperature drop reflects the diminished exothermic output due to the higher energy threshold required for the reaction to proceed. The rise in thermal radiation increases the temperature of a fluid because radiation transfers energy in the form of electromagnetic waves, which are absorbed by the fluid's molecules (see Fig. 6). When these waves are absorbed, the molecules gain kinetic energy, leading to increased vibrational and translational motion, which manifests as a rise in temperature. Physically, this process aligns with the first law of thermodynamics, where energy absorption increases the internal energy of the fluid. The extent of heating depends on the fluid's absorptivity—opaque fluids absorb more radiation, converting it efficiently into thermal energy, while transparent fluids may allow radiation to pass through with minimal heating. This mechanism is crucial in applications like solar heating, where radiative energy directly influences fluid temperature. The rise in the thermophoresis parameter increases fluid temperature because thermophoresis involves the migration of particles from hotter to colder regions due to a temperature gradient (see Fig. 7).

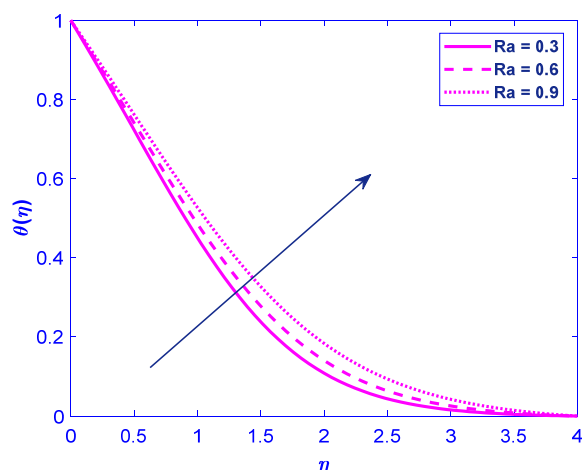


Figure 6. Upshot of  $Ra$  on temperature

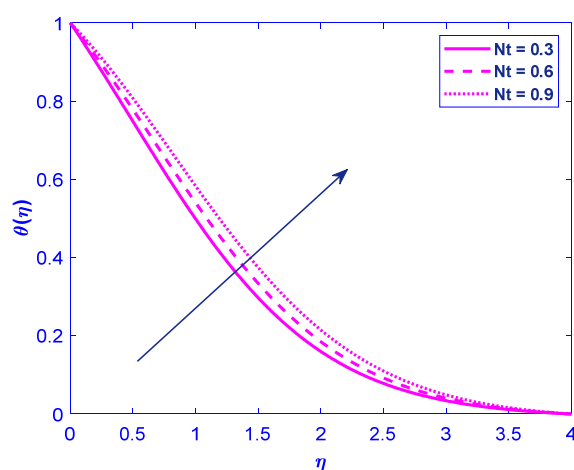


Figure 7. Upshot of  $Nt$  on temperature

When the thermophoresis parameter is enhanced, particles move away from the heated surface, carrying thermal energy with them and redistributing it within the fluid. This movement reduces the thermal boundary layer's resistance, allowing more efficient heat transfer into the fluid and elevating its overall temperature. Physically, this phenomenon indicates that stronger thermophoretic effects enhance convective heat transfer by promoting particle-driven energy dispersion, effectively increasing fluid temperature. The result highlights the significant role of particle migration in modifying thermal dynamics, particularly in nanofluids or dusty gases where thermophoresis is prominent. The rise in the Brownian motion parameter enhances the random movement of nanoparticles within a fluid, leading to greater dispersion. As Brownian motion intensifies, nanoparticles spread more uniformly, reducing localized concentration gradients (See Fig. 8). Physically, this means that increased thermal energy drives nanoparticles away from regions of high concentration, promoting mixing and reducing peak fluid concentration. This effect is particularly significant in nanofluids, where enhanced Brownian motion improves heat transfer by distributing particles more evenly, but simultaneously lowers the maximum concentration due to reduced aggregation. Thus, the parameter inversely influences concentration while improving homogeneity. The rise in the activation energy parameter typically increases the fluid concentration because higher activation energy represents a greater energy barrier that molecules must overcome to participate in reactions or diffusion processes (see Fig. 9).

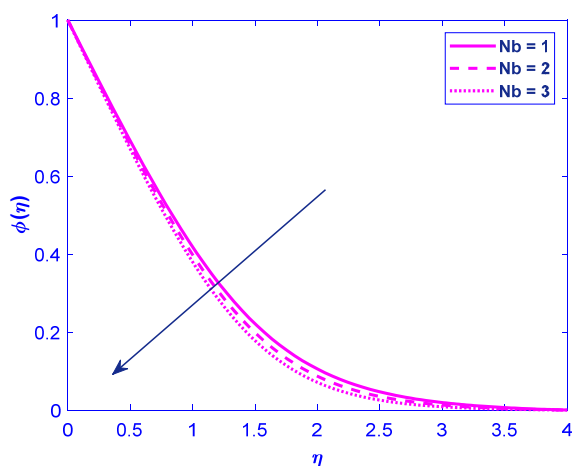


Figure 8. Upshot of  $Nb$  on concentration

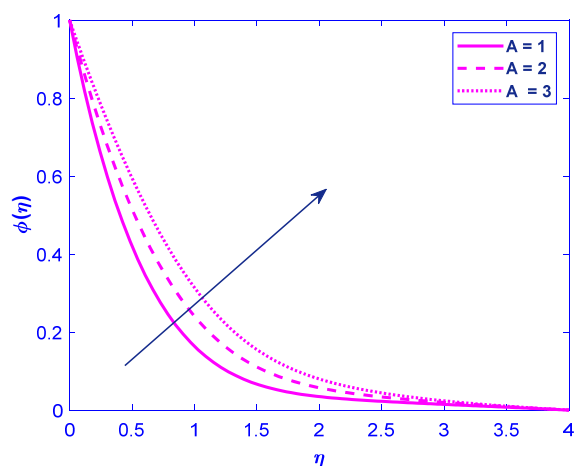


Figure 9. Upshot of  $A$  on concentration

When activation energy increases, fewer molecules possess sufficient kinetic energy to react or diffuse, leading to a slower rate of consumption or removal of the fluid species. As a result, the fluid concentration builds up over time since the outflow or reaction rate is reduced. Physically, this implies that systems with higher activation energy tend to retain more of the fluid phase, as the energy threshold restricts dynamic processes like chemical reactions or mass transfer. This effect is particularly relevant in catalysis, combustion, or transport phenomena, where activation energy governs reaction kinetics and species distribution. The increased concentration reflects a bottleneck in molecular activity due to the heightened energy requirement.

#### 4.1. Multiple linear regression

Important technical characteristics, such as the mass transmission rate, and specific variables, such as the Brownian motion, were linked in this study using the models outlined below:

$$Cf = a_0 + a_1\Lambda_1 + a_2Cs \quad (12)$$

$$Nu = b_0 + b_1Nt + b_2A \quad (13)$$

$$Sh = c_0 + c_1A + c_2Nb \quad (14)$$

We used 25 different sets of variables for each computation to speed up the process of discovering results:

$$Cf = 2.2124 + 0.0832\Lambda_1 - 0.5199Cs \quad (15)$$

$$Nu = 0.2028 - 0.0784Nt + 0.0568A \quad (16)$$

$$Sh = 0.4264 - 0.0886A + 0.232Nb \quad (17)$$

Equation (15) explains that the friction factor raises with an elevation in  $\Lambda_1$  and lowers with an increase in  $Cs$ . The rise in the couple stress parameter decreases the skin friction coefficient in fluid flow due to the additional resistance to rotational deformation offered by the couple stresses. In fluids with microstructures (e.g., liquid crystals or polymeric fluids), couple stresses account for the resistance to particle rotation, effectively introducing an internal damping mechanism. As the couple stress parameter increases, the fluid's microstructure resists local angular deformations more strongly, reducing the velocity gradient near the boundary. Since skin friction is directly related to the velocity gradient at the wall, a lower gradient results in reduced shear stress and thus a lower skin friction coefficient. Physically, this implies that the fluid's internal microstructure absorbs part of the shear energy, leading to a smoother transition in velocity near the wall and weaker frictional drag. This effect is particularly significant in microfluidic and biological flows where microstructure interactions dominate. The friction factor decreases by 59.8% when the value of  $Cs$  ranges from 0.1 to 2.5. Equation (16) demonstrates that the Nusselt number lowers with a spike in  $Nt$  and rises with an elevation in  $A$ . The rise in the thermophoresis parameter decreases the Nusselt number because thermophoresis causes particles to move from hotter to colder regions, creating a concentration gradient near the heated surface. This particle migration reduces the effective thermal conductivity of the fluid near the boundary, as fewer particles are available to enhance heat transfer. Consequently, the temperature gradient at the wall decreases, leading to a lower Nusselt number, which represents the ratio of convective to conductive heat transfer. Physically, this means that thermophoresis suppresses heat transfer by redistributing particles away from the hot surface, thereby weakening thermal convection. The result highlights the trade-off between particle migration effects and thermal performance in nanofluids. The heat transmission rate diminishes by 7.8% as the value of  $Nt$  varies from 0.1 to 2.5. As seen in Equation (17), the Sherwood number decreases as  $A$  spikes and increases as  $Nb$  climbs. The rise in the Brownian motion parameter enhances the Sherwood number in fluid flow because it intensifies the random motion of nanoparticles, leading to greater mass transfer. Brownian motion increases the dispersion of particles within the fluid, reducing concentration gradients and promoting more uniform mixing. This heightened activity enhances the effective mass diffusivity, thereby improving the convective mass transfer rate, which is quantified by the Sherwood number. Physically, this means that as nanoparticles move more vigorously due to thermal fluctuations, they facilitate faster transport of species across the fluid, increasing the overall mass transfer efficiency. The result highlights the importance of microscopic particle dynamics in macroscopic transport phenomena, particularly in nanofluid applications where enhanced mass transfer is desired. It is observed that as  $Nb$  ranges from 0.1 to 2.5, the mass transmission rate drops 2.6%.

#### 4.2 Validation of the results using Artificial Neural Network

In MATLAB, the Bayesian training approach is a regularization method for neural networks that optimizes weights by minimizing a combination of squared errors and weight magnitudes, effectively balancing model complexity and predictive accuracy. This approach treats weights as probabilistic variables, using Bayesian inference to automatically determine optimal regularization parameters, which helps prevent overfitting and improves generalization.

In this study, we rigorously compare our analytical and regression-based results with those generated by a Bayesian-regularized neural network to assess the model's reliability and precision. Our results are exceptionally good, demonstrated by the elevated R-values (approaching 1) in the regression plots (Figs. 10–12), signifying near-perfect correspondence between anticipated and actual values. The error histograms (Figs. 13–15) corroborate this by displaying symmetric, zero-centred distributions with limited dispersion, indicating unbiased and accurate predictions. Furthermore, the function fit plots (Figs. 16–18) illustrate that the neural network effectively represents the fundamental physical trends,

including the inverse relationship between couple stress and skin friction and the positive correlation between Brownian motion and Sherwood number.

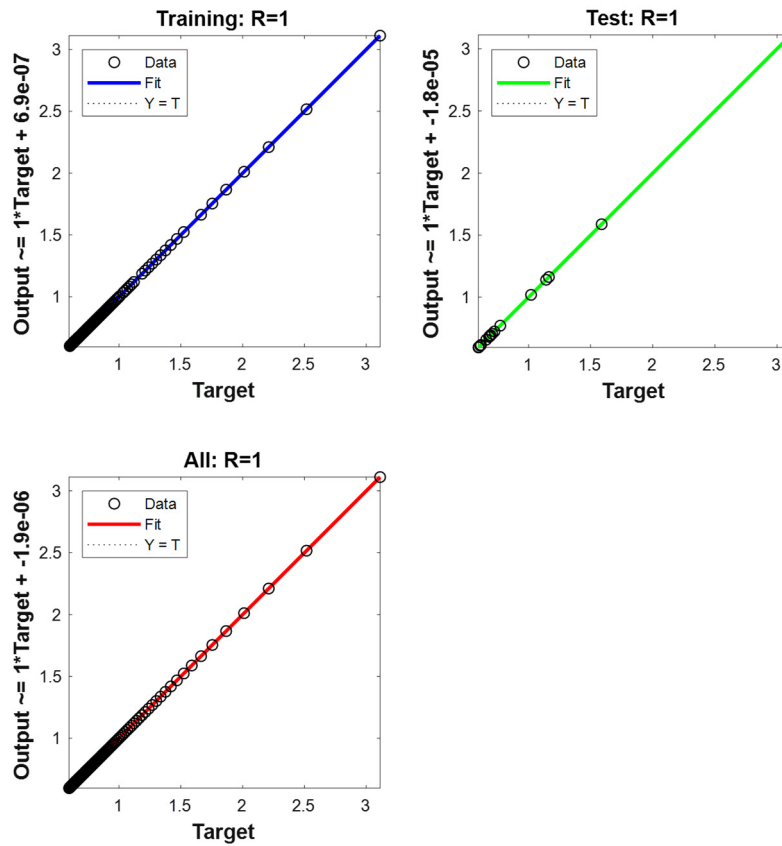


Figure 10. Regression chart for couple stress vs skin friction coefficient

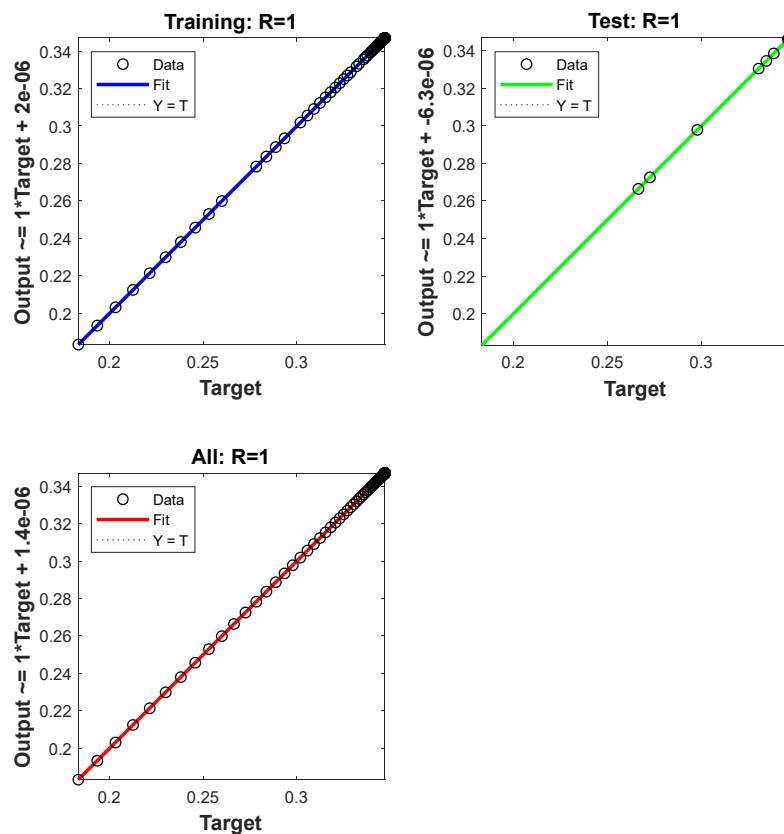


Figure 11. Regression chart for activation energy vs Nusselt number



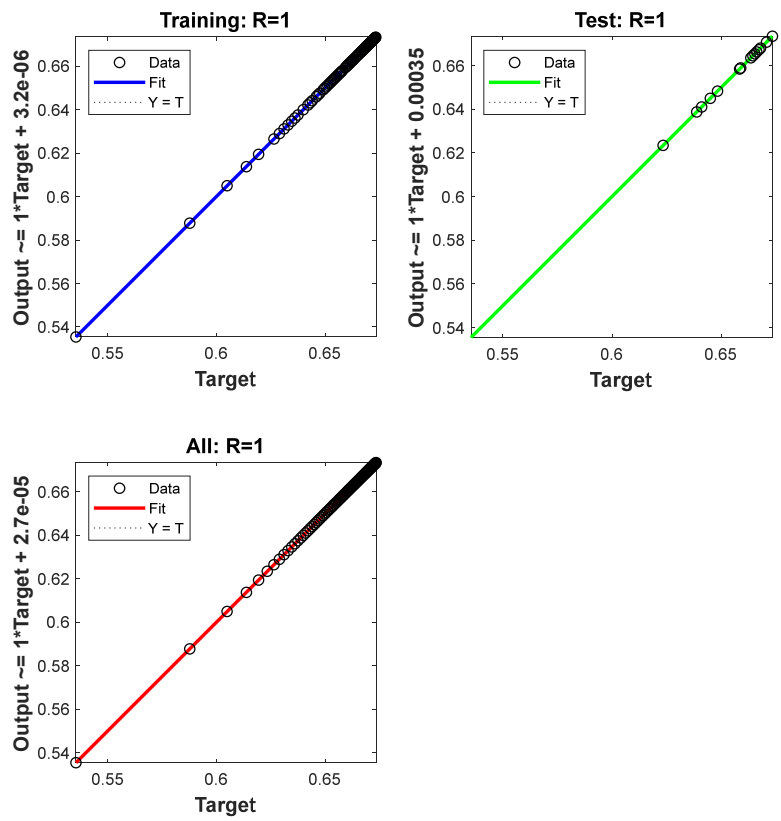


Figure 12. Regression chart for Brownian motion vs Sherwood number

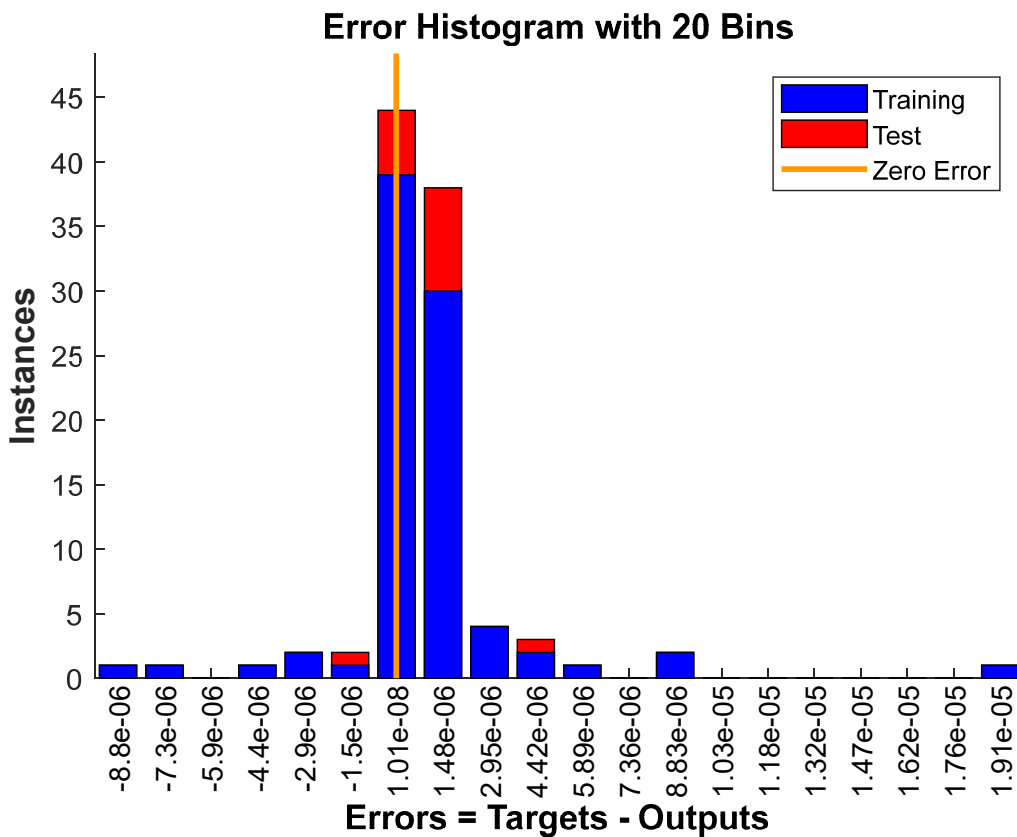


Figure 13. Error histogram for couple stress vs skin friction coefficient

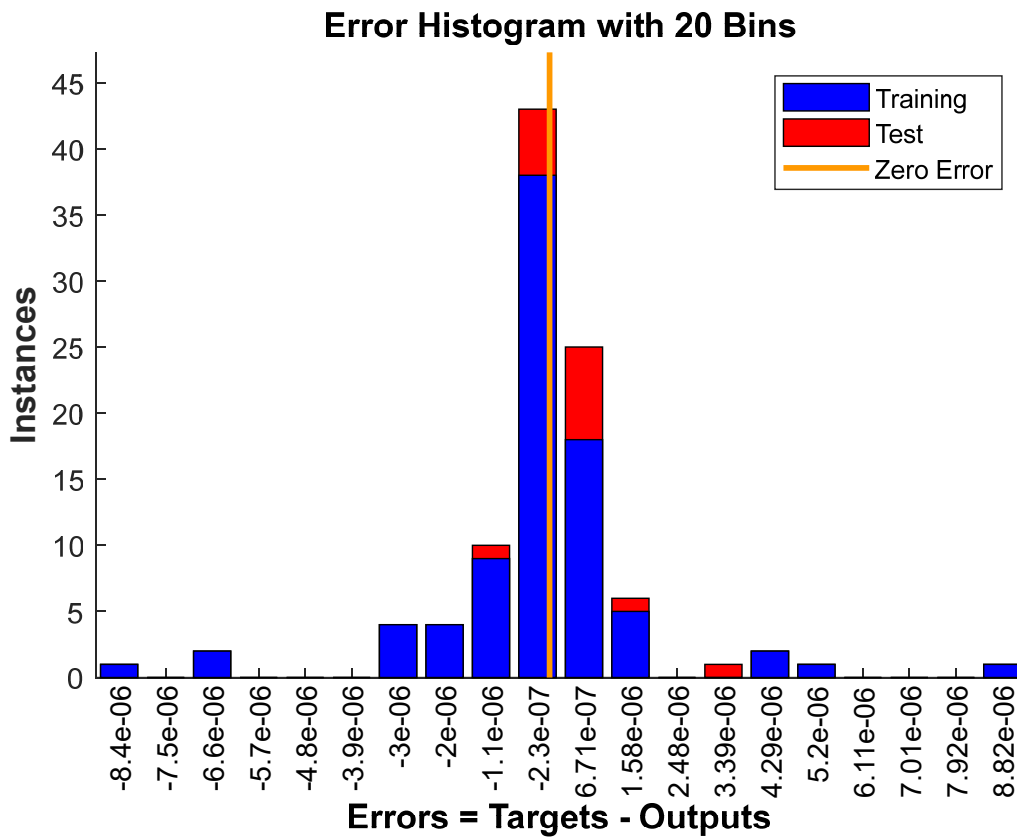


Figure 14. Error histogram for activation energy vs Nusselt number

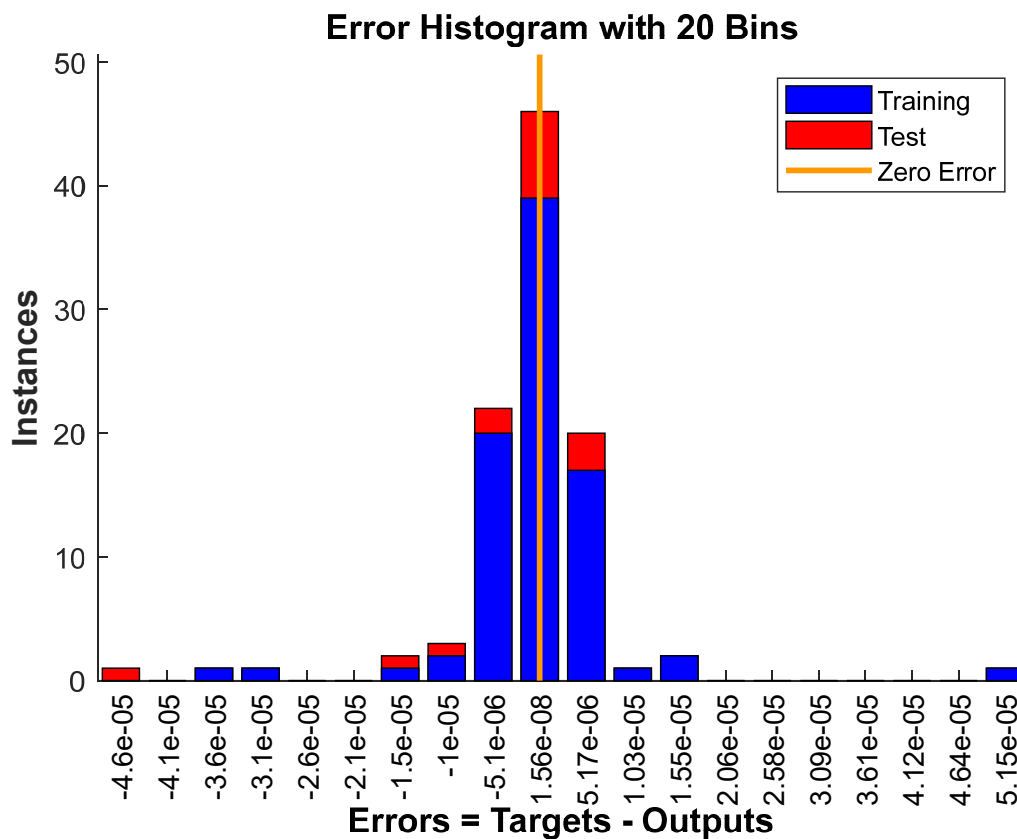


Figure 15. Error histogram for Brownian motion vs Sherwood number

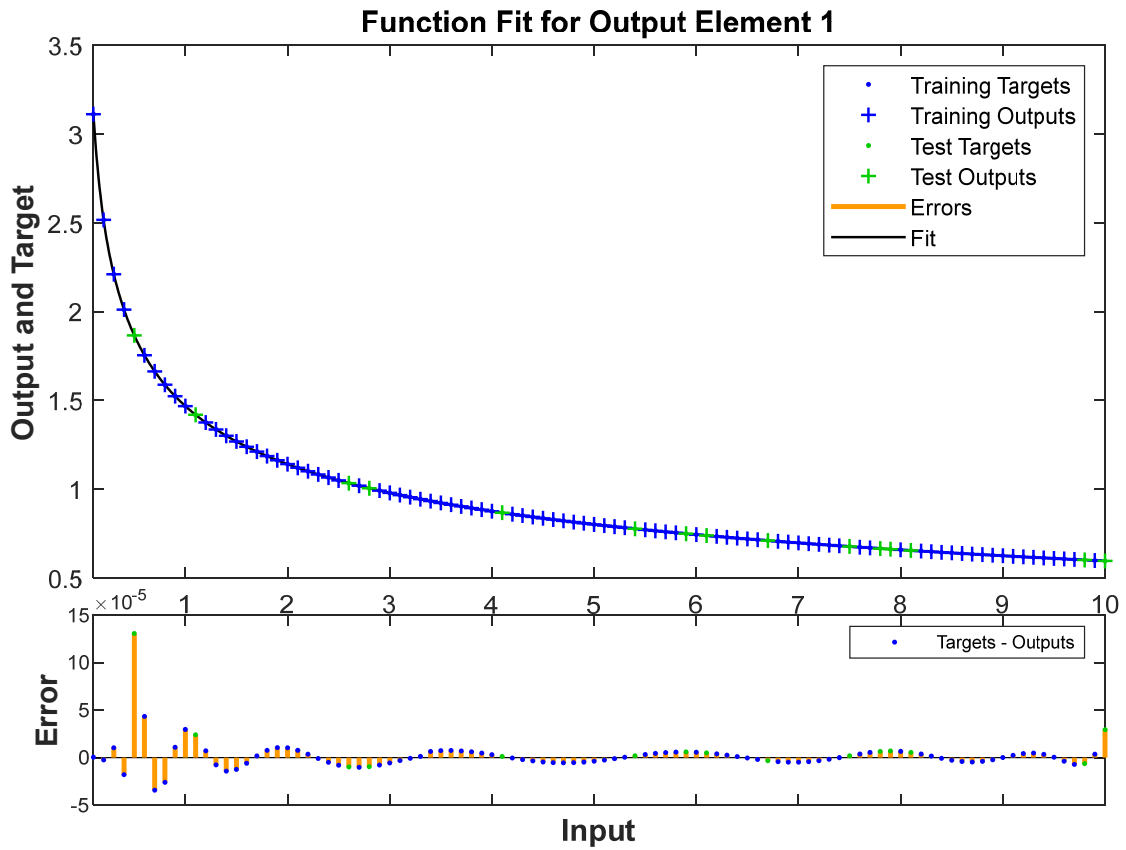


Figure 16. Function Fit plot for couple stress vs skin friction coefficient

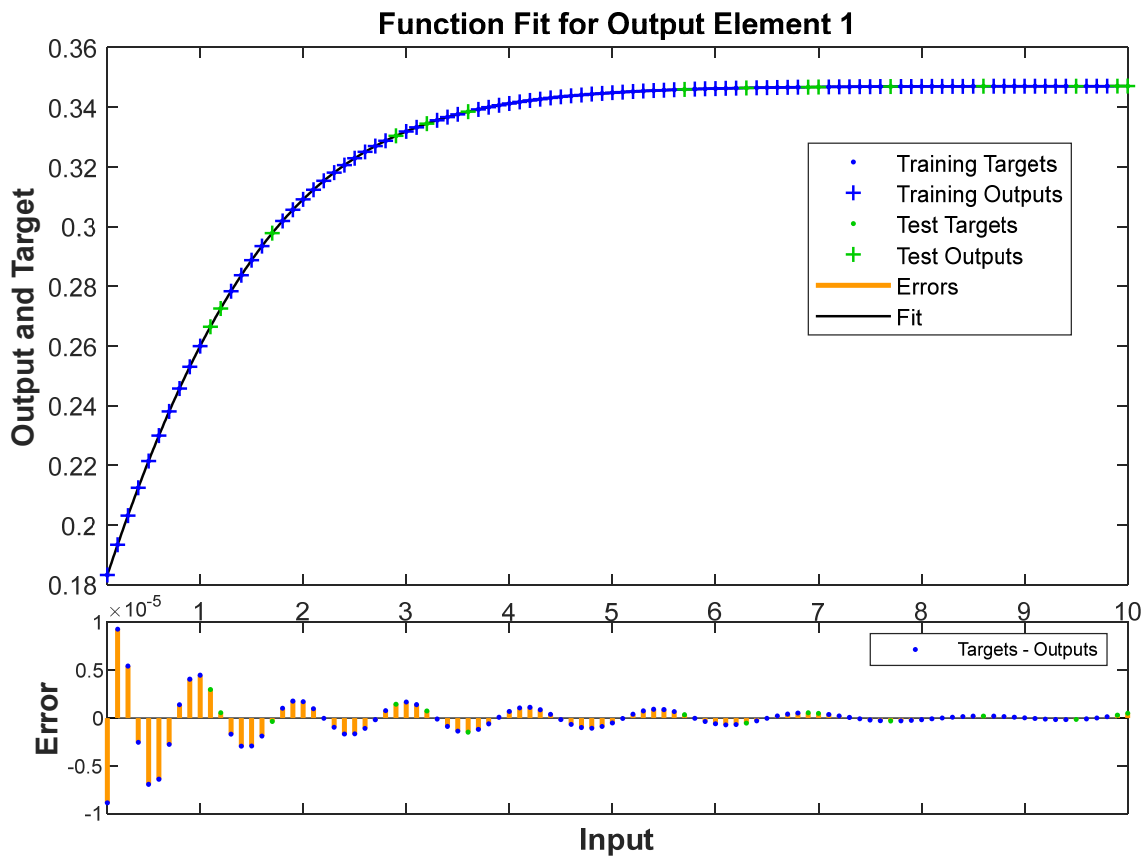


Figure 17. Function Fit plot for activation energy vs Nusselt number

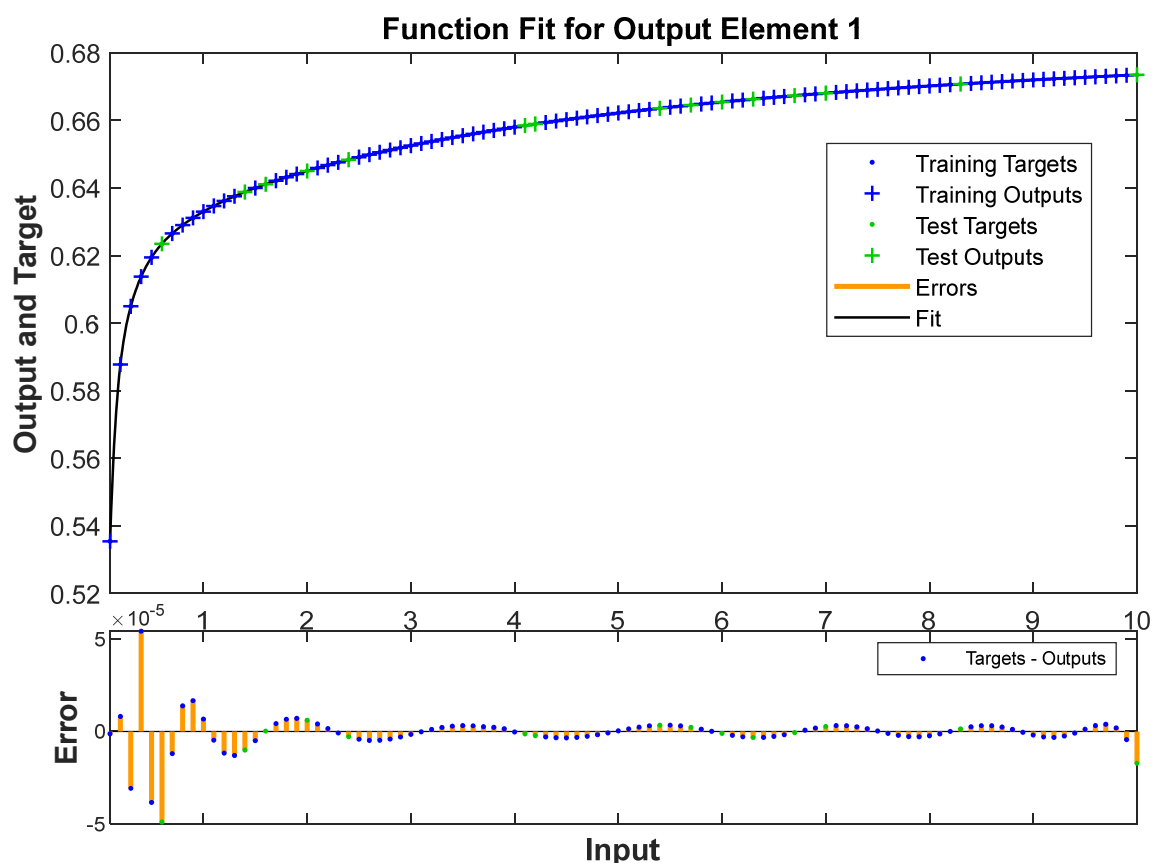


Figure 18. Function Fit plot for Brownian motion vs Sherwood number

## 5. CONCLUSIONS

This study investigates the steady, laminar motion of a non-Newtonian Oldroyd-B nanofluid across an inclined vertical plate, integrating Buongiorno's nanofluid model to account for Thermophoresis and Brownian motion. The research examines the effects of key parameters such as couple stress, relaxation time, Forchheimer number, thermal radiation, thermophoresis, Brownian motion and the activation energy on velocity, temperature and concentration. Multiple linear regression and a Bayesian-regularized artificial neural network (ANN) are employed to model relationships and predict outcomes, offering insights into complex nanofluid dynamics under viscoelastic, magnetic, and exothermic reaction influences. The findings have applications in heat exchangers, polymer processing, enhanced oil recovery, and biomedical systems. Key findings are mentioned below:

- Increasing couple stress reduces velocity by enhancing viscosity and internal friction.
- Higher relaxation time decreases velocity due to increased fluid elasticity, thickening the boundary layer.
- Higher activation energy decreases temperature by reducing exothermic reaction rates.
- Greater thermophoresis raises temperature through enhanced particle migration from warmer to cooler regions.
- Increased Brownian motion reduces particle concentration by enhancing diffusion.
- Higher activation energy increases concentration by reducing particle mobility.
- It is noticed that increasing the couple stress parameter from 0.1 to 2.5 reduces friction factor by 59.8%.
- Increasing the thermophoresis parameter from 0.1 to 2.5 decreases the Nusselt number by 7.8%, reflecting reduced heat transfer,
- Increasing the Brownian motion parameter from 0.1 to 2.5 reduces the mass transmission rate by 2.6%.
- These findings advance the understanding of complex nanofluid systems and provide robust tools for optimizing engineering applications, such as heat transfer devices, polymer processing, and enhanced oil recovery, where precise control of flow and thermal behaviour is critical.

## ORCID

©Gadamsetty Revathi, <https://orcid.org/0000-0001-9419-2637>; ©M. Rekha, <https://orcid.org/0000-0001-8842-530X>

©P. Sridhya Devi, <https://orcid.org/0000-0001-6131-7421>; ©B.Ch. Nookaraju, <https://orcid.org/0000-0002-2699-4037>

## REFERENCES

- [1] J.G. Oldroyd, "On the Formulation of Rheological Equations of State," Proceedings of the Royal Society of London. Series A, **200**, 523-541 (1950). <https://doi.org/10.1098/rspa.1950.0035>

- [2] H. Fröhlich and R. Sack, "Theory of the Rheological Properties of Dispersions," *Proceedings of the Royal Society of London A*, **185**, 415-430 (1946). <https://doi.org/10.1098/rspa.1946.0028>
- [3] F. Mebarek-Oudina and I. Chabani, "Review on nano-fluids applications and heat transfer enhancement techniques in different enclosures," *Journal of Nanofluids*, **11**(2), 155-168 (2022). <https://doi.org/10.1166/jon.2022.1834>
- [4] A. Boudjemline, I. Ahmad, S. Rehman, Hashim and N. Khedher, "Jeffery-Hamel flow extension and thermal analysis of Oldroyd-B nanofluid in expanding channel," *Journal of Non-Equilibrium Thermodynamics*, **48**(1), 75-90 (2023). <https://doi.org/10.1515/jnet-2022-0052>
- [5] M. Yasir, A. Ahmed, M. Khan, A.K. Alzahrani, Z.U. Malik and A.M. Alshehri, "Mathematical modelling of unsteady Oldroyd-B fluid flow due to stretchable cylindrical surface with energy transport," *Ain Shams Engineering Journal*, **14**(1), 101825 (2023). <http://dx.doi.org/10.1016/j.asej.2022.101825>
- [6] F. Sun, X. Wen, X. Si, C. Xie, B. Li, L. Cao, and J. Zhu, "Numerical simulations of the Oldroyd-B fluid flow around triangular cylinders with different orientations," *Journal of Non-Newtonian Fluid Mechanics*, **326**, 105204 (2024). <https://doi.org/10.1016/j.jnnfm.2024.105204>
- [7] L. Liu, S. Zhang, J. Wang, L. Feng and C. Xie, "Construction of the absorbing boundary condition for the flow of Oldroyd-B fluid over a semi-infinite plate with magnetic effect," *Physics of Fluids*, **36**(4), 043118 (2024). <https://doi.org/10.1063/5.0199911>
- [8] C. Fetecau and D. Vieru, "Investigating magnetohydrodynamic motions of Oldroyd-B fluids through a circular cylinder filled with porous medium," *Processes*, **12**(7), 1354 (2024). <https://doi.org/10.3390/pr12071354>
- [9] S. Munir, A. Maqsood, U. Farooq, M. Hussain, M.I. Siddiqui and T. Muhammad, "Numerical analysis of entropy generation in the stagnation point flow of Oldroyd-B nanofluid," *Waves in Random and Complex Media*, **35**(1), 465-481 (2025). <https://doi.org/10.1080/17455030.2021.2023782>
- [10] L. Kang, B. Khan, S.Z. Abbas, W.A. Khan and S.A. Alrub, "Brownian moment and thermophoresis analysis of nanoparticles for Oldroyd-B fluid capturing aspects of radiation phenomenon," *International Journal of Modern Physics B*, **39**(12), 2550092 (2025). <https://doi.org/10.1142/S0217979225500924>
- [11] M. Ahmad, S.U. Khan, Q. Bibi, M. Taj and M.M. Bhatti, "Buoyancy-driven bidirectional forced convection in chemically reactive Oldroyd-B nanofluid: incorporating the Cattaneo-Christov model with an external heat source for improved analysis," *Particulate Science and Technology*, **43**(3), 369-381 (2025). <https://doi.org/10.1080/02726351.2025.2457568>
- [12] M. Yasir, A. Ahmed, M. Khan, M.M.I. Ch and M. Ayub, "Study on time-dependent Oldroyd-B fluid flow over a convectively heated surface with Cattaneo-Christov theory," *Waves in Random and Complex Media*, **35**(1), 144-161 (2025). <https://doi.org/10.1080/17455030.2021.2021316>
- [13] J.K. Madhukesh, B.C. Prasannakumara, S.A. Shehzad, M.I. Anwar and S. Nasir, "Endothermic and exothermic chemical reactions' influences on a nanofluid flow across a permeable microchannel with a porous medium," *International Journal of Ambient Energy*, **45**(1), 2325515 (2024). <https://doi.org/10.1080/01430750.2024.2325515>
- [14] G.K. Ramesh, J.K. Madhukesh, E.H. Aly, et al., "Endothermic and exothermic chemical reaction on MHD ternary (Fe<sub>2</sub>O<sub>4</sub>-TiO<sub>2</sub>-Ag/H<sub>2</sub>O) nanofluid flow over a variable thickness surface," *J. Therm. Anal. Calorim.* **149**, 6503-6515 (2024). <https://doi.org/10.1007/s10973-024-13013-x>
- [15] O.A. Agbolade and E.O. Fatunmbi, "Thermal explosion and distribution of hydromagnetic Eyring-Prandtl double exothermic diffusion-reaction fluid in a porous channel," *Thermal Advances*, **1**, 100005 (2024). <https://doi.org/10.1016/j.thradv.2024.100005>
- [16] K.A. Maleque, "Effects of exothermic/endothermic chemical reactions with Arrhenius activation energy on MHD free convection and mass transfer flow in presence of thermal radiation," *Journal of Thermodynamics*, **2013**(1), 692516 (2013). <https://doi.org/10.1155/2013/692516>
- [17] T.H. Alarabi, S.S. Alzahrani, A. Mahdy and O.A. Abo-Zaid, "Aspects of mass and thermal relaxation time and exothermic chemical processes on the flow of a ternary hybrid Sutterby nanofluid via slant surface with activation energy and linear convection limits," *Proceedings of the Institution of Mechanical Engineers, Part E: Journal of Process Mechanical Engineering*, 09544089241274054 (2024). <https://doi.org/10.1177/09544089241274054>
- [18] M. Shanmugapriya, R. Sundareswaran, S.G. Krishna and M. Pal, "An analysis of effect of higher order endothermic/exothermic chemical reaction on magnetized Casson hybrid nanofluid flow using fuzzy triangular number," *Engineering Applications of Artificial Intelligence*, **133**, 108119 (2024). <https://doi.org/10.1016/j.engappai.2024.108119>
- [19] R.A. Oderinu, S.O. Salawu, A.D. Ohaeghwe, S. Alao, E.I. Akinola and J.A. Owolabi, "Numerical exploration and thermal criticality of a dual exothermic reaction with radiative heat loss in co-axial cylinder configurations," *International Journal of Thermofluids*, **25**, 101039 (2025). <https://doi.org/10.1016/j.ijft.2024.101039>
- [20] I. Khan, R. Zulkifli, T. Chinyoka, Z. Ling and M.A. Shah, "Numerical analysis of radiative MHD gravity-driven thin film third-grade fluid flow with exothermic reaction and modified Darcy's law on an inclined plane," *Mechanics of Time-Dependent Materials*, **29**(1), 1-18 (2025). <https://doi.org/10.1007/s11043-024-09744-x>
- [21] T. Hayat, F. Haider and A. Alsaedi, "Darcy-Forchheimer flow with nonlinear mixed convection," *Applied Mathematics and Mechanics*, **41**, 1685-1696 (2020). <https://doi.org/10.1007/s10483-020-2680-8>
- [22] M.I. Khan, "Transportation of hybrid nanoparticles in forced convective Darcy-Forchheimer flow by a rotating disk," *International Communications in Heat and Mass Transfer*, **122**, 105177 (2021). <https://doi.org/10.1016/j.icheatmasstransfer.2021.105177>
- [23] G. Revathi, G. Veeram, M.J. Babu, K.S. Babu and A. Suneel Kumar, "Darcy-Forchheimer flow of power-law (Ostwald-de Waele type) nanofluid over an inclined plate with thermal radiation and activation energy: an irreversibility analysis," *International Journal of Ambient Energy*, **44**(1), 1980-1989 (2023). <https://doi.org/10.1080/01430750.2023.2200434>
- [24] H.U. Rasheed, W. Khan, M. Kouki, H. Al Garalleh and A. Al Agha, "A mathematical model for three dimensional magnetohydrodynamic thermal nanofluid flow over a permeable Darcy-Forchheimer medium with chemical reaction and activation energy effects," *Multiscale and Multidisciplinary Modeling, Experiments and Design*, **8**(5), 1-13 (2025). <https://doi.org/10.1007/s41939-025-00837-9>
- [25] F.S. Hira, Q. Rubbab, I. Ahmad and A.H. Majeed, "Advanced computational modeling of Darcy-Forchheimer effects and nanoparticle-enhanced blood flow in stenosed arteries," *Engineering Applications of Artificial Intelligence*, **152**, 110737 (2025). <https://doi.org/10.1016/j.engappai.2025.110737>

- [26] M. Yasir, M. Naveed Khan, M.A. Abdelmohimen and N.A. Ahammad, "Thermal transport analysis for entropy generated flow of hybrid nanomaterial: modified Cattaneo-Christov heat and Darcy-Forchheimer," *Multidiscipline Modeling in Materials and Structures*, **21**(2), 291-307 (2025). <https://doi.org/10.1108/MMMS-08-2024-0220>
- [27] N. Khemiri, S. Rehman, T. Saidani and V. Tirth, "Heat transfer analysis of radiated thin-film flow of couple-stress nanofluid embedded in a Darcy-Forchheimer medium with Newtonian heating effects," *Nuclear Engineering and Technology*, **57**(7), 103510 (2025). <https://doi.org/10.1016/j.net.2025.103510>
- [28] S. Abu Bakar, N.S. Wahid, N.M. Arifin and N.S. Khashi'ie, "The flow of hybrid nanofluid past a permeable shrinking sheet in a Darcy-Forchheimer porous medium with second-order velocity slip," *Waves in random and complex media*, **35**(1), 46-63 (2025). <https://doi.org/10.1080/17455030.2021.2020375>
- [29] N. Yasin, S. Ahmad, M. Umair, Z. Shah, N. Vrinceanu and G. Alhawael, "Investigations of conjugate heat transfer and fluid flow in partitioned porous cavity using Darcy-Forchheimer model: Finite element-based computations," *Case Studies in Thermal Engineering*, **72**, 106252 (2025). <https://doi.org/10.1016/j.csite.2025.106252>
- [30] D. Mohanty, G. Mahanta, A.J. Chamkha and S. Shaw, "Numerical analysis of interfacial nanolayer thickness on Darcy-Forchheimer Casson hybrid nanofluid flow over a moving needle with Cattaneo-Christov dual flux," *Numerical Heat Transfer, Part A: Applications*, **86**(3), 399-423 (2025). <https://doi.org/10.1080/10407782.2023.2263906>
- [31] W. Alghamdi and T. Gul, "Darcy-Forchheimer hybrid nanofluid flow in a squeezing inclined channel for drug delivery applications by means of artificial neural network," *Multidiscipline Modeling in Materials and Structures*, **21**(2), 387-404 (2025). <https://doi.org/10.1108/MMMS-07-2024-0202>
- [32] V. Singh, N.B. Naduvinamani, K. Vinutha, B.C. Prasannakumara, J.K. Madhukesh and A. Abdulrahman, "Sodium alginate-based MHD ternary nanofluid flow across a cone and wedge with exothermic/endothermic chemical reactions: A numerical study," *Numerical Heat Transfer, Part A: Applications*, 1-20 (2024). <https://doi.org/10.1080/10407782.2024.2355520>
- [33] T. Muhammad, A. Alsaedi, T. Hayat and S.A. Shehzad, "A revised model for Darcy-Forchheimer three-dimensional flow of nanofluid subject to convective boundary condition," *Results in physics*, **7**, 2791-2797 (2017). <https://doi.org/10.1016/j.rinp.2017.07.052>
- [34] P.S. Reddy, A.J. Chamkha and A. Al-Mudhaf, "MHD heat and mass transfer flow of a nanofluid over an inclined vertical porous plate with radiation and heat generation/absorption," *Advanced Powder Technology*, **28**(3), 1008-1017 (2017). <https://doi.org/10.1016/j.apt.2017.01.005>
- [35] K. Sudarmozi, D. Iranian, I. Khan, A.S. Al-Johani and S.M. Eldin, "Magneto radiative and heat convective flow boundary layer in Maxwell fluid across a porous inclined vertical plate," *Scientific Reports*, **13**(1), 6253 (2023). <https://doi.org/10.1038/s41598-023-33477-5>

### ПОТІК ДАРСІ-ФОРХГАЙМЕРА ОЛДРОЙД-В НАНОРІДИНИ НАД ПОХИЛОЮ ПЛАСТИНКОЮ З ЕКЗОТЕРМІЧНИМИ ХІМІЧНИМИ РЕАКЦІЯМИ ТА МОДЕЛЮВАННЯМ БАЄСІВСЬКОЮ НЕЙРОННОЮ МЕРЕЖЕЮ

Гадамсетгі Реваті<sup>а</sup>, М. Рекха<sup>б</sup>, П. Шрівідья Деві<sup>б</sup>, В.Ч. Нукараджу<sup>с</sup>

<sup>а</sup>Кафедра математики, Інженерно-технологічний інститут Гокараджу Рангараджу, Бачупаллі, Хайдерабад – 500090, Індія

<sup>б</sup>Кафедра електротехніки та електроніки, Інженерно-технологічний інститут Гокараджу Рангараджу, Бачупаллі, Хайдерабад – 500090, Індія

<sup>с</sup>Кафедра машинобудування, Інженерно-технологічний інститут Гокараджу Рангараджу, Бачупаллі, Хайдерабад, - 500 090, Індія

Це дослідження досліджує стаціонарний ламінарний рух неньютонівської нанорідина Олдройда-Б над похилою пластиною, інтегруючи модель нанорідина Буонджорно для врахування броунівського руху та термофорезу. Нова інтеграція парних напружень та інерції Форхгеймера в аналізі, у поєднанні з удосконаленим байєсівсько-регуляризованим моделюванням штучних нейронних мереж, відрізняє цю роботу. Керівні рівняння трансформуються за допомогою змінних подібності та розв'язуються чисельно за допомогою розв'язувача `bvp4c` у `MATLAB`. Систематично проаналізовано вплив парного напруження, часу релаксації, числа Форхгеймера, теплового випромінювання, термофорезу, броунівського руху та енергії активації на профілі швидкості, температури та концентрації. Результати показують, що парне напруження та час релаксації зменшують швидкість, тоді як теплове випромінювання та термофорез підвищують температуру. Броунівський рух зменшує концентрацію, а енергія активації впливає як на температуру, так і на концентрацію протилежно. Моделі множинної лінійної регресії кількісно визначають зв'язки між коефіцієнтом тертя, числами Нуссельта та Шервуда і ключовими параметрами, тоді як байєсівсько-регуляризована штучна нейронна мережа (ШНМ) демонструє високу прогностичну точність (значення  $R \sim 1$ ). Помічено, що збільшення параметра парного напруження з 0,1 до 2,5 зменшує коефіцієнт тертя на 59,8%, збільшення параметра термофорезу з 0,1 до 2,5 зменшує число Нуссельта на 7,8%, що відображає зменшення теплопередачі, а збільшення параметра броунівського руху з 0,1 до 2,5 зменшує швидкість передачі маси на 2,6%.

**Ключові слова:** неньютонівська рідина; термофорез; `bvp4c`; броунівський рух; енергія активації; теплове випромінювання



## INFLUENCE OF LORENTZ FORCE AND ARRHENIUS ACTIVATION ENERGY ON RADIATIVE BIO-CONVECTIVE MICROPOLAR NANOFLUID FLOW WITH MELTING HEAT TRANSFER OVER A STRETCHING SURFACE

Syed Fazuruddin<sup>a</sup>,  Sreenivasulu Arigela<sup>b\*</sup>,  A. Shobha<sup>c</sup>, V. Raja Rajeswari<sup>d</sup>,  K. Venkatadri<sup>b#</sup>

<sup>a</sup>Department of School of Technology Mathematics, The Apollo Knowledge City Campus Saketa, Murukambattu, The Apollo University Chittoor, Andhra Pradesh-517127, India

<sup>b</sup>Department of Mathematics, School of Liberal Arts and Sciences, Mohan Babu University (Erstwhile Sree Vidyanikethan Engineering College), Sree Sainath Nagar, Tirupati, A.P., 517102, India

<sup>c</sup>Department of Applied Mathematics, Sri Padmavathi Mahila Visva Vidyalyam, Tirupati 517502, AP, India

<sup>d</sup>Department of Electronics and Communication Engineering, School of Engineering and Technology, Sri Padmavathi Mahila Visva Vidyalyam, Tirupati 517502, A.P., India

\*Corresponding Author E-mail: [sreenu1184@gmail.com](mailto:sreenu1184@gmail.com); #E-mail: [venkatadri.venki@gmail.com](mailto:venkatadri.venki@gmail.com)

Received July 1, 2025; revised August 7, 2025; accepted August 15, 2025

Novelty of this research is to explore an impact of Lorentz force, Arrhenius activation energy, and Conduction of Melting Heat on the micropolar fluid behaviour of steady radiative bio-convective micropolar nanofluid flow towards a stretchable surface. Using the standard similarity method, we have derived the equations of similarity for the relevant quantities of momentum, angular momentum, temperature, and concentration. The MATLAB tool 'bvp4c' is used to determine solutions to the transformed governing equations. Equations of similarity in four dimensions (momentum, angular momentum, temperature, and concentration) are numerically solved. We have examined, microrotation, velocity, concentration, temperature fields behavior for various parameters. Results show that the motile density of microorganisms decreases when the Peclet number and the microorganism concentration differential parameter are increased. Motility density increases as the Peclet number in microbial concentrations rises. Nanofluids are therefore appropriate as heat transfer fluids due to their surface cooling effect. The numerical scheme applied is validated by comparison with the previous numerical values.

**Keywords:** Melting Heat Transfer; Micropolar nanofluid; Bioconvection; Radiative heat flux; Activation energy

**PACS:** 44.05.+e, 47.11.-j, 41.20.-q, 47.15.Rq, 47.65.-d, 47.55.pb, 44.30.+v

### Nomenclature

<b><i>K</i></b>	Material parameter	<b><i>C</i></b>	concentration
<b><i>Rd</i></b>	Thermal radiation parameter	<b><i>C<sub>w</sub></i></b>	Concentration at the surface
<b><i>Pr</i></b>	Prandtl number	<b><i>C<sub>∞</sub></i></b>	Ambient fluid concentration
<b><i>Nb</i></b>	Brownian Motion parameter	<b><i>C<sub>p</sub></i></b>	Specific heat
<b><i>Nt</i></b>	Thermo Phoresis parameter	<b><i>D<sub>s</sub></i></b>	Microorganism diffusion coefficient
<b><i>Ec</i></b>	Eckert Number	<b><i>f</i></b>	Dimension less stream function
<b><i>Le</i></b>	Lewis number	<b><i>f'</i></b>	Dimension less velocity
<b><i>Da</i></b>	Darcy number	<b><i>k*</i></b>	Mean absorption coefficient
<b><i>M</i></b>	Magnetic parameter	<b><i>Nu</i></b>	Local Nusselt number
<b><i>λ</i></b>	Mixed convection parameter	<b><i>Q<sub>0</sub></i></b>	Heat generation/Absorption parameter
<b><i>θ<sub>w</sub></i></b>	Temperature Ratio parameter	<b><i>s</i></b>	Microorganism field
<b><i>E</i></b>	Activation Energy parameter	<b><i>s<sub>w</sub></i></b>	Microorganism at the surface
<b><i>Lb</i></b>	The Bioconvection Lewis number	<b><i>s<sub>∞</sub></i></b>	Ambient fluid Microorganism
<b><i>Pe</i></b>	Peclet number	<b><i>Sh</i></b>	Local Sherwood number
<b><i>Ω</i></b>	The constant difference constant of microorganism	<b><i>T</i></b>	Fluid temperature
<b><i>S</i></b>	Suction parameter	<b><i>T<sub>w</sub></i></b>	Temperature at the surface
<b><i>Ma</i></b>	Melting parameter	<b><i>T<sub>∞</sub></i></b>	Ambient fluid temperature
<b><i>L</i></b>	Momentum slip parameter	<b><i>U<sub>w</sub></i></b>	Stretching velocity
<b><i>m</i></b>	Micro rotation parameter	<b><i>(u, v)</i></b>	Velocity components along x-axis and y-axis respectively
<b><i>γ<sub>1</sub></i></b>	Thermal Biot number	<b><i>(x, y)</i></b>	Space coordinates
<b><i>γ<sub>2</sub></i></b>	Mass Biot number	<b><i>Wc</i></b>	Cell moving speed
<b><i>Nr</i></b>	Buoyancy Ratio parameter	<b><i>η</i></b>	Dimension less variable
<b><i>Nc</i></b>	Bioconvection Rayley number	<b><i>μ</i></b>	Dynamic viscosity
<b><i>ε</i></b>	Variable thermal conductivity parameter	<b><i>σ*</i></b>	Stefan-Boltzmann constant
<b><i>Re</i></b>	Reynolds number	<b><i>φ</i></b>	Volumetric concentration
<b><i>σ</i></b>	Reaction rate parameter	<b><i>χ</i></b>	Microorganism concentration
<b><i>a</i></b>	Stretching rate	<b><i>ψ</i></b>	Stream function
<b><i>Bh</i></b>	Local microorganism density number		

**Cite as:** S. Fazuruddin, S. Arigela, A. Shobha, V.R. Rajeswari, K. Venkatadri, East Eur. J. Phys. 3, 194 (2025), <https://doi.org/10.26565/2312-4334-2025-3-17>

© S. Fazuruddin, S. Arigela, A. Shobha, V.R. Rajeswari, K. Venkatadri, 2025; CC BY 4.0 license

As micro-organisms move upward on average, the phenomenon of bioconvection occurs. In general, microorganisms have a higher density than water. It is the microorganisms' own self-propelled movement across the upper fluid zone that causes the surface there to thicken to an unstable degree. Exciting circumstances lead to a complex network of currents. Bioconvection is used in a wide variety of fields, but the ones that stand out the most include bio microsystems, biotechnology, environmental systems, biofuels, and petroleum engineering. Using nanoparticles in a bioconvection process calls for the combined properties of buoyant forces and microorganisms. Suspensions containing nanoparticles and gyrotactic microorganisms may grow in a way that is both pleasant and effective in terms of their stability. Microorganisms are often sorted into the chemotactic or oxytactic kind, the gyrotactic, microorganisms, and the geotactic, microorganisms, based on the directions in which they travel. Another key factor in the enhanced stability of nanoparticles is the bioconvection phenomenon. Prokaryotic bacteria move in a variety of ways, including swimming, crawling, gliding, and skimming across solid surfaces and fluid media. Without flagella, rod-shaped bacteria have adapted gliding as a mode of locomotion. Relevant instances include the BH3 stain from *Flexibacter*, as well as cytophaga, oscillatoria, and vitreoscilla. Bioconvection, or the diffusion of lower denseness microorganisms near surface liquid, results in the emergence of stable, chaotic patterns. Algae and other freely moving microorganisms have a tendency to cluster together in the fluid's top layer, where they might contribute to the stratification density and harden the surface. When compared to microbes, nanomaterials move in a way that is distinct. It is essential for microfluidics that bioconvection and water nanofluids interact. There is a significant challenge in developing microfluidic devices due to the mobility of microbes. Maintaining the bacterium's shape, molecular sieving, and enhancing the bacteria's ability to associate with macrophages [1]. Bacterial motility is greatly aided by the S-layer. An important part of a cell's ability to propel itself forward is its form and the stiffness of its wall and surface layers, both of which are maintained in part by the S-layer. The cell is shielded by the S-layer from harmful ions, acids, osmotic stress, enzymes, viruses, and other bacteria. Their cells may adhere to those of other types or to surfaces. Protection from phagocytosis is something they can provide harmful bacteria. Soil, silt, and rotting wood are just a few examples of watery environments that bacteria may adapt to grow in through tiny channels that allow them to glide [2]. Gliding motility, namely its mechanism, is still a matter of some controversy. Circulating discs on the surface of the cells, electro-kinesis, the release of slime, the application of osmotic pressures, the generation of peristaltic waves on the surface, and contractile components are all mentioned in the literature as contributing to bacterial motility [3, 4]. To explain the vitreoscilla's glide-like movement, Costerton et al. [5] proposed this theory. In their paper, Halfen and Castenholz [6] hypothesised that the wavy regime, that is virtually in touch with solid barrier and allows green-blue algae's to glide with such ease. That flexibacter may move by sending off waves from its own surface was substantiated by research published by Humphrey et al. [7]. As one of two mechanisms used by cyanobacteria for locomotion, Hoiczuk [8] described the formation of tiny surface waves that flow along the surface of the filament. Because of these observations, Venkatadri et al. [9] presents a novel investigation of thermomagnetic bioconvection flow involving oxytactic microorganisms within a semi-trapezoidal porous enclosure, particularly targeting magnetic biofuel cell applications. The coupling of magnetic fields, bioconvection, porous media effects, and nanofluid transport offers a strong precedent for studies focusing on multiphysics transport phenomena in non-standard enclosures, especially in contexts involving thermal energy harvesting or biological systems. O'Brien [10] decided to create a mathematical model to investigate bacterial glide behaviour. Using lubrication theory, he determined the flexibacter's maximum speed and the rate at which power was dissipated. They used those findings to suggest a model for *Flavobacterium* gliding, and the math behind it seems sound. Islam and Mignot [11] analyse in depth the role of focal adhesions in the pathogenesis of *Myxococcus xanthus*. An outstanding review study on the gliding processes described in flavobacteria, myxobacteria, mycoplasmas literature was published by Nan and Zusman [12]. An effects of heat and mass transmission, as well as the mobility of microorganisms, on the motion of a nanofluid were examined by Shafiq et al. [13]. When it comes to the boundary layer flow containing gyrotactic nano liquid microorganisms, Elbashbeshy et al. [14] used computational methods to examine the impact of heat production across an incline stretched cylinder. Using computational methods, we examine the bioconvection of a nanofluid via a stretched surface in a porous media containing gyrotactic microorganisms subject to Newtonian heating reported by Pourrajab and Noghrehabadi [15]. In this paper, we investigate the effect of thermosolutal Marangoni on bioconvection in a solution of gyrotactic microorganisms over an inclined stretched sheet explored by Kairi et al. [16]. Compliant thermoelectric coils for use in flexible and biointegrated devices are analysed for thermal and mechanical properties explored by Chen et al. [17]. Over a vertical cone, a numerical solution is found for bioconvection in convectional nanofluid flow including gyrotactic microorganisms explored by Rao et al. [18].

Some fluids, due to the micromotions of their constituent parts, display microscopic phenomena that are the focus of the idea of micropolar fluid. A diluted suspension of stiff macromolecules, each with its own movements supporting stress and body moments and governed by spin inertia, may be found in these fluids. Some fluids, known as micropolar fluids, have notably non-Newtonian hydrodynamics due to the existence of micro-constituents that are capable of rotation. Micropolar fluid, one of numerous types of non-Newtonian fluids, is best suited to characterising both the microstructure-determined local characteristics and the intrinsic particles liquid movement. As a result of these features, micropolar fluid modeling problems widely utilised to mimic complicated processes in a wide variety of liquids, such as polymer, plastic planes, ferrofluid, crystals, biology, etc. Thermo-micropolar fluids theory was developed by Eringen [19], who also created the theory of micropolar fluids and obtained its constitutive equations. In essence, Eringen is responsible for developing the idea of micropolar fluids. Many different kinds of fluids, from suspension solutions to blood rheology and

colloidal fluids, may be studied mathematically with the help of this model. Polymer fluids, liquid suspension, blood, crystals, dusty cloud, etc. includes micropolar liquids (Ahmadi [20]; Hayat et al. [21]). Researchers' curiosity with it has been piqued by the wide variety of industrial processes in which it is used, including polymer extrusion, lubricants, water baths are used to cool metallic plates (Rahman [22]). Lukaszewicz [23] explained a comprehensive theory, micropolar liquids applications.

Phenomenon of melting heat transfer is fundamentally important in many technological and industrial endeavors, such as understanding permafrost melting, magma-solidifications, metal-purifications, etc. Epstein and Choi et al. [24] found that melting affects heat transmission process. In a micropolar fluid, Jacob et al. [25] studied heat melting transfer at the stagnation point of the boundary layer as it moved towards a stretching/shrinking sheet. Powell-Eyring flow with linear surface and heat melting transfer was investigated by Hayat et al. [26]. Khan et al. [27] studied an impact of non-Newtonian flow over a stretched surface on melting heat and mass transfer with non-linear radiation and a magnetic regime. Gireesha et al. [28] proposed MHD flow Casson liquid across a stretched plane at melting heat transfer.

Based on the research that has been done so far, melting stretching sheets have a small number of investigations of MHD Micro-Polar fluid. Revisions to micropolar fluids with gyrotactic microorganisms have received very little attention, as shown by the literature review and by the necessary engineering and industrial applications. An objective of this manuscript is to explore an impact of Lorentz force, Arrhenius activation energy, and Conduction of Melting Heat on the micropolar fluid behavior of steady radiative bio-convective micropolar nanofluid flow towards a stretchable surface. The results of changing any of the controlling variables may be seen in graphical form. Further research in the fields of fuel production, crushed water flow issues, and polymer sheet extrusion may all benefit from the analyses provided in the cited study. Engineering designs, metallurgy industries, and the effectiveness of systems for the flow of thermos fluids all benefit from the findings of this research. Biomedical, industrial, pharmaceutical, and thermal/thermal processes may all benefit greatly from this design.

## 2. MATHEMATICAL CONCEPTUALIZATION

This integrated study constitutes self-motivated bio-convective microorganisms, numerous slips, non-linear radiative micropolar nano fluids. Flow of a fluid, often considered to be laminar, two-dimensional, and incompressible. Figure 1. depicts flow model of the problem. In order to properly evaluate an induced magnetic influence, a high magnetic Reynolds number is required.

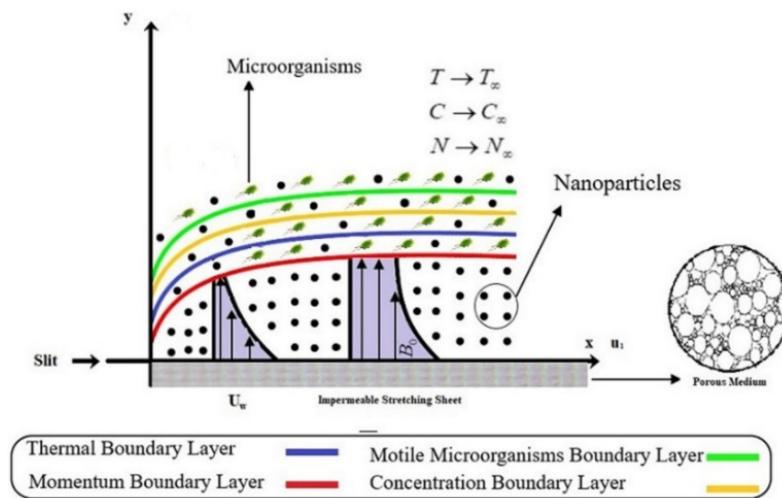


Figure 1. Flow Model

Additionally, the flow is assumed to be a steady-state flow during the development of the model. Velocity of surface material is  $U_w = ax$ ,  $a$  is positive. All these factors taken into account, the governed boundary equations are as follows:

$$\frac{\partial u}{\partial x} + \frac{\partial v}{\partial y} = 0 \quad (1)$$

$$u \frac{\partial u}{\partial x} + v \frac{\partial u}{\partial y} = \left( \frac{\mu + k}{\rho} \right) \frac{\partial^2 u}{\partial y^2} + \frac{k}{\rho} \frac{\partial N}{\partial y} - \frac{\sigma B_0^2}{\rho} u - \frac{v}{\kappa} u + g\beta_r [T - T_\infty] + g\beta_c [C - C_\infty] + g\beta_s [s - s_\infty] \quad (2)$$

$$u \frac{\partial N}{\partial x} + v \frac{\partial N}{\partial y} = \frac{\gamma}{\rho j} \frac{\partial^2 N}{\partial y^2} - \frac{\kappa}{\rho j} \left[ 2N + \frac{\partial u}{\partial y} \right] \quad (3)$$

$$u \frac{\partial T}{\partial x} + v \frac{\partial T}{\partial y} = \alpha \left( \frac{\partial^2 T}{\partial y^2} \right) - \frac{1}{\rho C_p} \frac{\partial q_r}{\partial y} + \tau \left( D_B \frac{\partial C}{\partial y} \frac{\partial T}{\partial y} + \frac{D_T}{T_\infty} \left( \frac{\partial T}{\partial y} \right)^2 \right) + \left( \frac{\mu + k}{\rho C_p} \right) \left( \frac{\partial u}{\partial y} \right)^2 + \frac{Q_0}{\rho C_p} [T - T_\infty] \quad (4)$$

$$u \frac{\partial C}{\partial x} + v \frac{\partial C}{\partial y} = D_m \left( \frac{\partial^2 C}{\partial y^2} \right) + \frac{D_T}{T_\infty} \frac{\partial^2 T}{\partial y^2} - k_c (C - C_\infty) \left( \frac{T}{T_\infty} \right)^n \exp \left( \frac{-E_a}{k_a T} \right) \quad (5)$$

$$u \frac{\partial s}{\partial x} + v \frac{\partial s}{\partial y} + \frac{bW_c}{(C_w - C_\infty)} \left[ \frac{\partial}{\partial y} \left( s \frac{\partial C}{\partial y} \right) \right] = D_s \left( \frac{\partial^2 s}{\partial y^2} \right) \quad (6)$$

Convective boundary conditions

$$u = U_w + L_1 \frac{\partial u}{\partial y},$$

$$v = k \frac{1}{\rho [\beta_m + c_s (T_m - T_0)]} \frac{\partial T}{\partial y} - v_w \quad (7)$$

$$N = -m \frac{\partial u}{\partial y}, -k \frac{\partial T}{\partial y} = h_f (T - T_w), -k \frac{\partial C}{\partial y} = h_m (C - C_w), s = s_w$$

$$u \rightarrow 0, N \rightarrow 0, T \rightarrow T_\infty, C \rightarrow C_\infty, s \rightarrow s_\infty \quad (8)$$

$$\gamma = (\mu + k/2) j = \mu(1 + K/2), \quad K \text{ denotes the material parameter}$$

Thermal conductivity as a function of temperature is defined as

$$k = k_\infty \left( 1 + \varepsilon \frac{T - T_\infty}{T_w - T_\infty} \right)$$

A usual stream functions

$$u = \frac{\partial \psi}{\partial y} \text{ and } v = -\frac{\partial \psi}{\partial x} \quad (9)$$

Considering similarity transformations are

$$u = axf', v = -\sqrt{av} f(\eta), \eta = y \sqrt{\frac{a}{v}}, \psi = x\sqrt{av} f(\eta), \theta(\eta) = \frac{T - T_\infty}{T_w - T_\infty},$$

$$\phi(\eta) = \frac{C - C_\infty}{C_w - C_\infty}, T = T_\infty [1 + (\theta_w - 1)\theta], \chi(\eta) = \frac{s - s_\infty}{s_w - s_\infty}, \theta_w = \frac{T_w}{T_\infty}, \quad (10)$$

Non-linear Radiative heat flux

$$q_r = -\frac{4\sigma^*}{3k^*} \frac{\partial T^4}{\partial y} \quad (11)$$

$$\frac{\partial q_r}{\partial y} = -\frac{16\sigma^*}{3k^*} \left[ 3T^2 \left( \frac{\partial T}{\partial y} \right)^2 + T^3 \frac{\partial^2 T}{\partial y^2} \right] \quad (12)$$

Converted ODEs are

$$[1 + K] f''' - f'^2 + f f'' + Kg - Da f' - Mf' + \lambda(\theta - Nr\phi - Nc\chi) = 0 \quad (13)$$

$$\left[ 1 + \frac{K}{2} \right] g'' + fg' - f'g - K[2g + f''] = 0 \quad (14)$$

$$\left[ (1 + \varepsilon\theta) + \frac{4}{3} Rd(1 + (\theta_w - 1)\theta)^3 \right] \theta'' + \left[ \varepsilon + 4Rd(\theta_w - 1)(1 + (\theta_w - 1)\theta)^2 \theta'^2 \right]$$

$$+ Pr f \theta' + Pr(Nb\theta' \phi' + Nt\theta'^2) + Ec Pr(f'')^2 + Pr Q_0 \theta = 0 \quad (15)$$

$$\phi'' + \text{Pr} \text{Le} f \phi' + \left(\frac{Nt}{Nb}\right) \theta'' - \text{Pr} \text{Le} \sigma (1 + \delta\theta)^n \exp\left(\frac{-E}{1 + \delta\theta}\right) \phi = 0 \tag{16}$$

$$\chi'' + \text{Lb} f \chi' - \text{Pe} [\phi'' (\chi + \Omega) + \phi' \chi'] = 0 \tag{17}$$

The relative boundary conditions are

$$\begin{aligned} f(0) &= S - \frac{Ma}{\text{Pr}} \theta'(0), f'(0) = 1 + L f''(0), g(0) = -m f''(0), \\ \theta'(0) &= -\gamma_1 (1 - \theta(0)), \phi'(0) = -\gamma_2 (1 - \phi(0)), \chi(0) = 1 \end{aligned} \tag{18}$$

$$f'(\infty) = 0, g'(\infty) = 1, h \rightarrow 0, \theta(\infty) = 0, \phi(\infty) = 0, \chi(\infty) = 0 \tag{19}$$

The relation of flow transformations:

$$\begin{aligned} \lambda &= \frac{Gr_T}{\text{Re}_x^2}, \delta = \frac{Gr_C}{\text{Re}_x^2}, \gamma = \frac{Gr_s}{\text{Re}_x^2}, Gr_T = \frac{g\beta_T (T_w - T_\infty) x^3}{\nu^2}, Gr_C = \frac{g\beta_C (C_w - C_\infty) x^3}{\nu^2}, \\ Gr_s &= \frac{g\beta_s (s_w - s_\infty) x^3}{\nu^2}, Rd = \frac{16\sigma^* T_\infty^3}{3kk^*}, Sc = \frac{\nu}{D_B}, Lb = \frac{\nu}{D_s}, Pe = \frac{bW_c}{D_s}, \\ \varepsilon &= \frac{\nu}{\alpha_e}, \Omega = \frac{s_w}{s_w - s_\infty}, Q = \frac{Q_0}{a\rho C_p} \end{aligned}$$

Where  $\lambda_1 = L_1 \sqrt{\frac{a}{\nu}}$ ,  $\lambda_2 = L_2 \sqrt{\frac{a}{\nu}}$ ,  $\lambda_3 = L_3 \sqrt{\frac{a}{\nu}}$ ,  $\lambda_4 = L_4 \sqrt{\frac{a}{\nu}}$

The physical quantities of Cfx, Csx, Nux, Shx are assumed as:

$$Cf = \frac{(\tau_w)_{y=0}}{\rho U_w^2}, Cs = \frac{xM_w}{\mu ja}, Nu = \frac{x(q_w)_{y=0}}{k[T_w - T_\infty]}, Sh = \frac{x(j_w)_{y=0}}{D_M [C_w - C_\infty]}, Bh = \frac{x(p_w)_{y=0}}{D_s [s_w - s_\infty]} \tag{20}$$

Where

$$\begin{aligned} (\tau_w)_{y=0} &= \mu \left[ \frac{\partial u}{\partial y} \right]_{y=0} + K \left( \frac{\partial u}{\partial y} + N \right)_{y=0}, (q_w)_{y=0} = -k \left[ \frac{\partial T}{\partial y} \right]_{y=0} + (q_r)_{y=0}, \\ (j_w)_{y=0} &= -D_B \left[ \frac{\partial C}{\partial y} \right]_{y=0}, (p_w)_{y=0} = -D_s \left[ \frac{\partial s}{\partial y} \right]_{y=0} \end{aligned} \tag{21}$$

The non-dimensional quantities are

$$\begin{aligned} \text{Re}_x^{-\frac{1}{2}} Cf &= f''(0) \left( 1 + M_\lambda \right) \left( 1 + \frac{1}{C_\beta} \right), \text{Re}_x^{-\frac{1}{2}} Cs = \left[ 1 + \frac{K}{2} \right] h'(0), \\ \text{Re}_x^{-\frac{1}{2}} Nu &= - \left[ 1 + Nr\theta_w^{*3} \right] \theta'(0), \text{Re}_x^{-\frac{1}{2}} Sh = -\phi'(0), \\ \text{Re}_x^{-\frac{1}{2}} Bh &= -\chi'(0) \end{aligned} \tag{22}$$

Where  $\text{Re}_x = \frac{xU_w}{\nu}$ .

### 3. NUMERICAL METHOD

Analytical solutions to the modeled equations for a two-point boundary-value problem is impossible because of their extremely nonlinear nature. Computational software MATLAB was used to obtain a numerical solution to this boundary

value problem. In MATLAB, the well-known `bvp4c` is used to regulate the flow with non-standard parameters. With the help of the MATLAB `bvp4c` method, numerical results for the dimensionless nonlinearly correlated ODEs, Eqs. (13)-(17) with boundary constraints (18) and (19) are obtained. To solve first-order ODEs, the `bvp4c` method is used. In this method, the modeled PDEs are transformed into first-order ODEs by taking into account what is appropriate along with boundary conditions, and are then numerically solved using the `bvp4c` package in MATLAB. The largest allowable residual error and step size are  $10^{-6}$  &  $\eta_{\max} = 18$ . The approach of the current numerical technique is broken down into its individual components and illustrated in chart form. The flow chart is depicted in Figure 2.

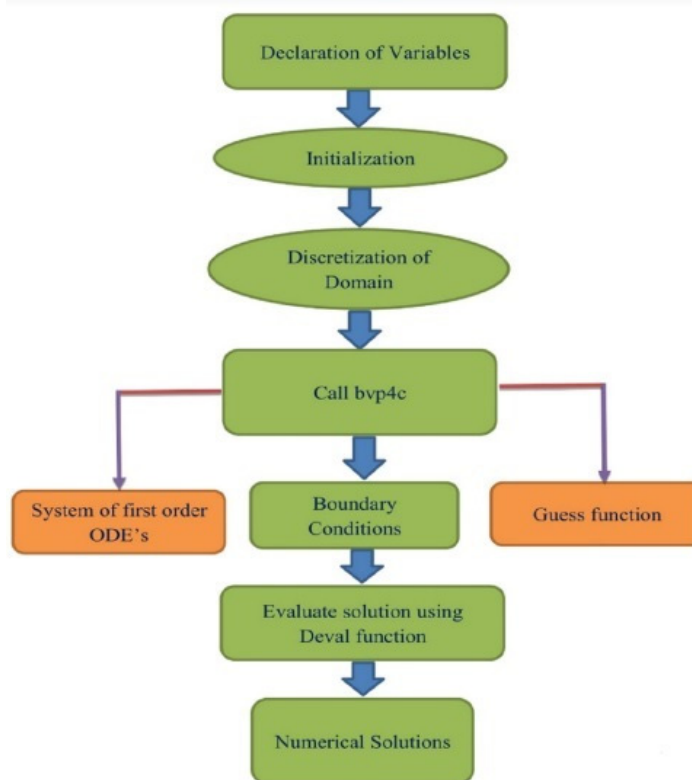


**Figure 2.** Flow chart of the method of the problem

#### 4. RESULTS AND DISCUSSION:

We have addressed the flow of a viscous, incompressible, micropolar fluid in two-dimensional mixed convective boundary layer through a permeable stretching sheet that is contained in bio-convection, activation energy and melting heat transfer. Assigning numerical values to distinct parameters obtained in the mathematical formulation and displaying the numerical results graphically allows, to gain a physical understanding of the problem by discussing the distributions of velocity  $f'(\eta)$ , angular velocity  $g(\eta)$  (microrotation), temperature  $\theta(\eta)$ , concentration  $\phi(\eta)$  and motile organism  $\chi(\eta)$ . We have included figures related to local skin friction coefficient  $\tau$ , couple stress coefficient  $h'(0)$ , Nusselt number  $-\theta'(0)$ , Sherwood number  $-\phi'(0)$  and micro-organism  $-\chi'(0)$ .

Figures 3 and 12 shows material parameter  $K$  influence in the profiles of  $f'(\eta)$  and  $g(\eta)$ . The microrotation profile exhibits the opposite behaviour, whereas the velocity profile improves as a function of the material parameter. Physically speaking, As the value of the material parameter is raised, the fluid's micro concentration rises, causing a change in the flow, and therefore, the boundary layer thickens. Figures 4 and 13 show how the porosity parameter  $K$  affects both the velocity and the angular velocity. Saturated porous medium is the primary focus of this investigation. It is common practice to employ porous medium as insulation for a hot object. Figure 4 shows that when the porosity parameter increases, the velocity decreases. The angular velocity, on the other hand, improves when the porosity parameter rises. This slowing down is explained by the concept of mass conservation and is seen wherever there is an increase in porosity. Figures 5 and 14 show how the velocity and angular velocity change as mixed convection parameter, respectively. Raising mixed convection parameter's value slows air flow. When buoyancy influence on free convection became noticeable, a transition to mixed convection occurs. The buoyancy improves with a raise on mixed convection value. However, when the mixed convection parameter raises, the angular velocity rises along with it. Figures 6 and 15 show the impact of the magnetic field parameter on  $f'(\eta)$  and  $g(\eta)$ . Figure 6 shows that the existence of a magnetic field results in a force called Lorentz, which acts against the flow of the fluid. Figure 15 shows that when the magnetic field strength rises, so does the angular velocity. The Lorentz force, created by the presence of a magnetic field, acts counter to the momentum field in most cases. Increasing the magnetic field has the opposite impact on angular velocity distributions. This is because the



micropolar fluid has elasticity. The results of changing  $m$  are shown in Figure 7 for the velocity part. Figure 7 shows that when  $m$  rises, both velocity and thickness of the boundary layer reduces. Fig's 8 and 16 depicts Bioconvection Rayleigh number impact on velocity and angular velocity profiles. However, the parameter has inverse behaviours on the microrotation function and the velocity function due to the bioconvection Rayleigh number. The microrotation and fluid flow patterns for different Buoyancy levels are shown in Figures 9 and 17, respectively. It has been shown that increasing the values of buoyancy parameters leads to decreasing the velocity profile and increasing the micro-rotation. The fluid flow and microrotation patterns for distinct values of melting parameter are presented as fig's 10 and 18. When the melting parameter is increased, the fluid flow profile and the microrotation profile are both seen to decrease. Excited by the increased temperature, the fluid's molecules begin to move (as the intermolecular forces that normally keep them together diminish). As the Melting parameter is increased, the micropolar fluid is able to overcome the forces holding its molecules together, allowing it to move faster and decreasing its viscosity gradually as it moves away from the wall. The influence of Prandtl number on the velocity and microrotation fields is seen in Figures 11 and 19. Prandtl number parameter is raised, then fluid's velocity raises and the microrotation profiles near the surface diminish while those distant from the surface improve. Fig. 22 illustrates Prandtl number influence on temperature distribution. Physically, smaller Prandtl number results in a thinner thermal boundary layer and a more uniform temperature distribution. Fig. 20 shows how the temperature ratio parameter affects the temperature distributions seen there. Increasing  $\theta_w$  increases both the temperature and related thermal boundary layer thickness. The reason for this is because when  $w$  is increased, the fluid temperature becomes much greater than the surrounding ambient temperature. The temperature field for distinct radiation parameter values are shown in Fig. 21. Temperature rises with increasing  $R_d$  and the corresponding boundary layer thickness, as seen in the figure. Reason being, a thicker thermal boundary layer and higher temperatures result from an increase in the radiation parameter, which supplies more heat to the fluid. Figure 23 demonstrates that when the Eckert number grows, the sheet temperature rises because of the thermal effect's resistance. Since the Eckert number represents a correlation between kinetic energy and heat enthalpy differences. Therefore, when the Eckert number grows, kinetic energy is converted into internal energy through work against the viscous fluid stresses. Fig. 24 depicts the influence of Brownian motion on temperature distributions. The relationship between temperature and the Brownian parameter is well established. Figure 25 depicts the temperature's response to changing the Thermophoresis parameter. It is clear from these graphs that as  $N_t$  grows, so do the temperature profiles. According to the findings, when the Brownian motion parameter is increased, the energy distribution expands, and when the Thermophoresis parameter is increased, the temperature expands. For distinct Thermal Biot number values, the dimensionless temperature profiles are shown in Fig. 26. The fluid temperature rises as the Thermal Biot number ( $\gamma_1$ ) increases. Biot number refers ratio of heat conduction resistance within a body to thermal convection resistance on its surface. When a body is heated or cooled over time by a heat flux at the surface, this ratio reveals whether or not the internal temperature fluctuates considerably in space. Concentration fields at various Lewis numbers are seen in Fig. 27. When compared to thermal boundary layer thickness, the concentration boundary layer thins as  $Le$  rises. To counteract the lower concentration on boundary layer, a resultant species-induced force diminishes with increasing  $Le$ . Figures 28 and 29 show the impact of the controlling factors  $N_b$  and  $N_t$  on the concentration profile. Brownian motion's effects on the boundary layer concentration of nanoparticles are discussed in Fig. 28. Brownian motion decreases the concentration (variations are minimal for higher values of parameter) and solutal boundary layer thickness, as seen in picture. The concentration of nanoparticles diminishes because an increase in Brownian motion speeds up the random motion that disperses them. Fig. 29 depicts the effects of thermophoresis on the concentration profile. For higher levels of the thermophoresis parameter, this figure shows that the concentration profile declines quickly over the whole flow domain. Given that the random mobility of nanoparticles in liquids is analogous to Brownian motion. As a result of the nanoparticles' erratic motion, the rate at which they collide with molecules in the fluid increases, raising the temperature. Figure 30 demonstrates that the concentration dropped under the effect of the reaction rate parameter. Chemical reactions occur at a rate proportional to the concentration of the reactants, according to the law of mass action. According to this, faster chemical reactions occur when there are higher concentrations of reactants, while slower reactions occur when there are lower concentrations of reactants. Since, parameter  $\delta$  as it relates to concentration profiles is shown in Figure 31. With an increase in  $\delta$ , the concentration field weakens. The influence of the activation energy parameter ( $E$ ) on concentration profile was seen in Fig. 32. The study's authors found that a raise in the 'E' resulted in a corresponding increase on concentration. To initiate a chemical reaction, a quantity of energy called the activation energy presents for chemical system including potentials reactant. In order to determine activation energy, one must first apply Arrhenius equation, that explains a change on rate constants w.r.to temperature. A chemical reaction including a mass transfer phenomenon is used in many fields, including geothermal, chemical, chemistry, emulsions, and deterioration of materials. The connection between chemical processes and the movement of mass is intricate. Both flow fluid and mass transferred studied in relation to one another by manufacturing and digesting species reactant at distinct rates, therefore examining the relationship between the two processes. Concentration profiles are improved by the mass Biot number, as shown in Figure 33. These figures show that when the mass Biot number grows, boundary layer thickness at the solutal concentration also increases. Bioconvection parameter influence is deploy in Figure 34. In order to optimise the bioconvection parameter, the density of gyrotactic, motile microorganisms was decreased. The effect of the Peclet number  $Pe$  is seen in Figure 35. The boundary layer thickness of the movable microorganisms has been shown to decrease. The microbes' diffusivity decreases as  $Pe$  increases to its maximum value.

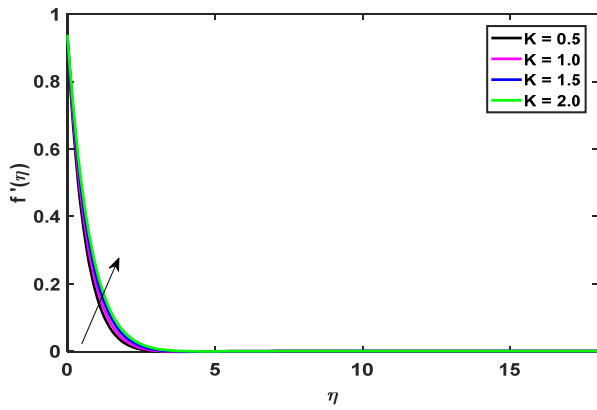


Figure 3. Implementation of K for  $f'(\eta)$

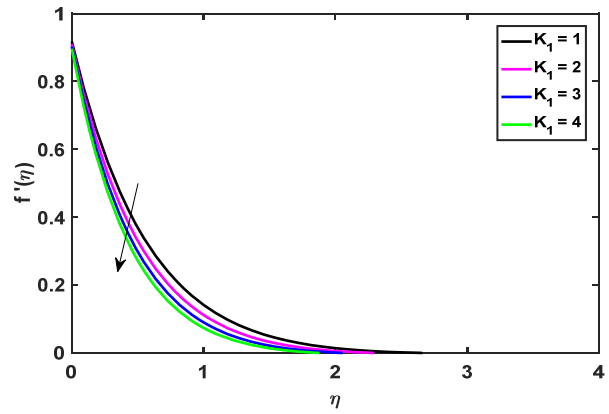


Figure 4. Implementation of  $K_1$  for  $f'(\eta)$

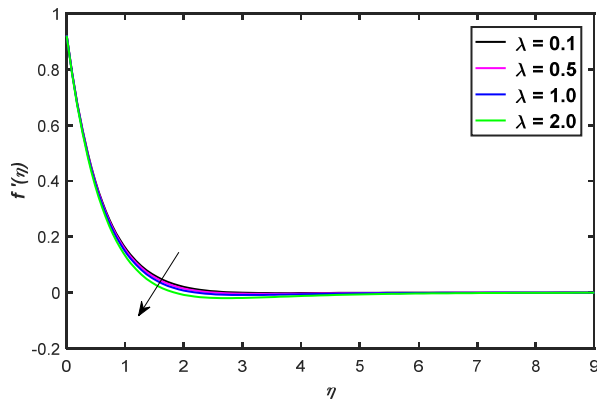


Figure 5. Implementation of  $\lambda$  for  $f'(\eta)$

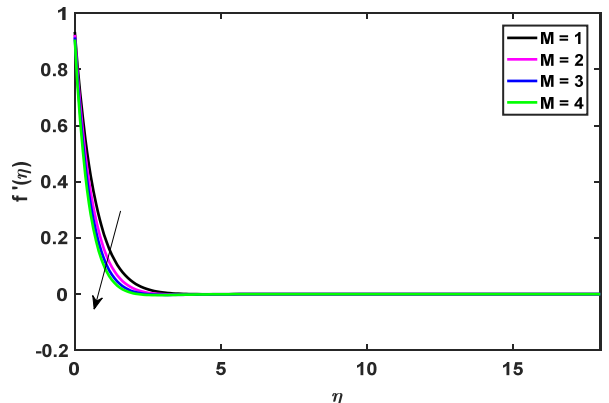


Figure 6. Implementation of M for  $f'(\eta)$

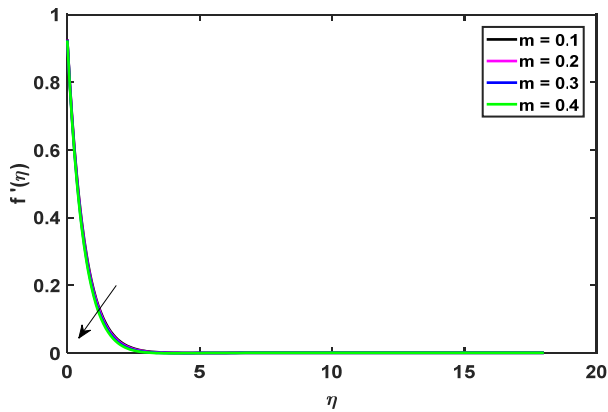


Figure 7. Implementation of m for  $f'(\eta)$

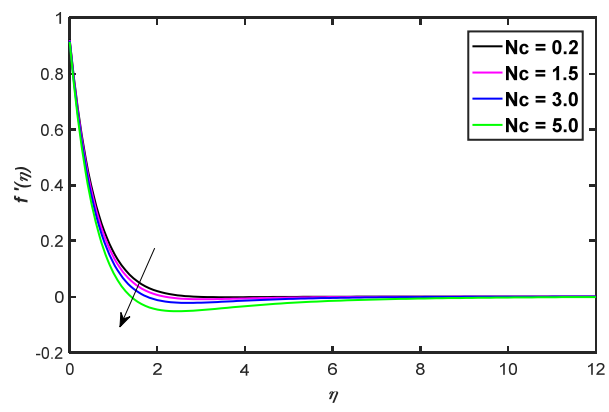


Figure 8. Implementation of  $N_c$  for  $f'(\eta)$

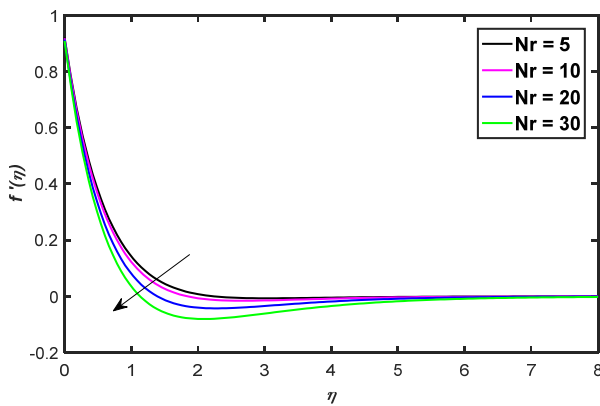


Figure 9. Implementation of  $N_r$  for  $f'(\eta)$

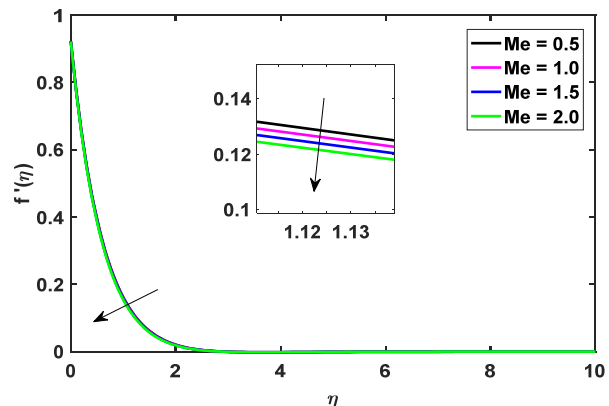


Figure 10. Implementation of  $Me$  for  $f'(\eta)$

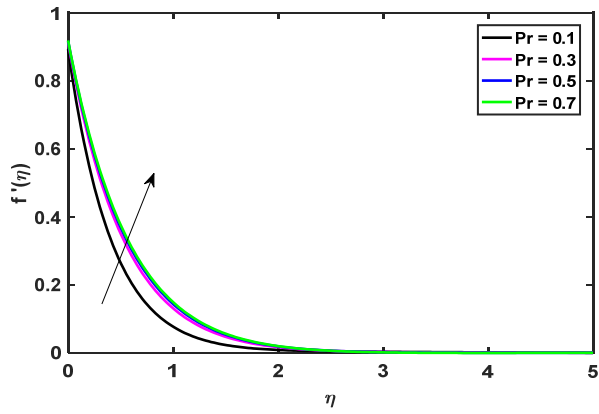


Figure 11. Implementation of Pr for  $f'(\eta)$

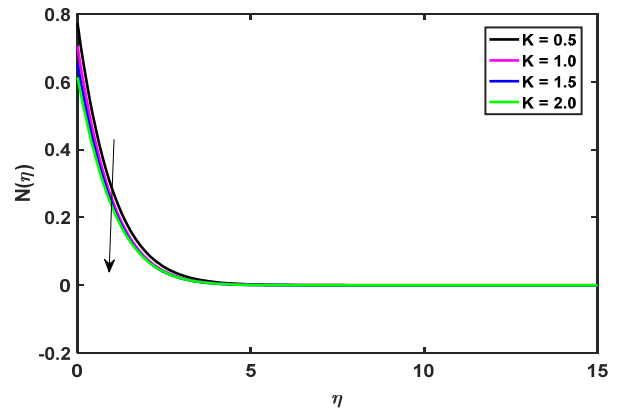


Figure 12. Implementation of K for angular velocity  $g(\eta)$

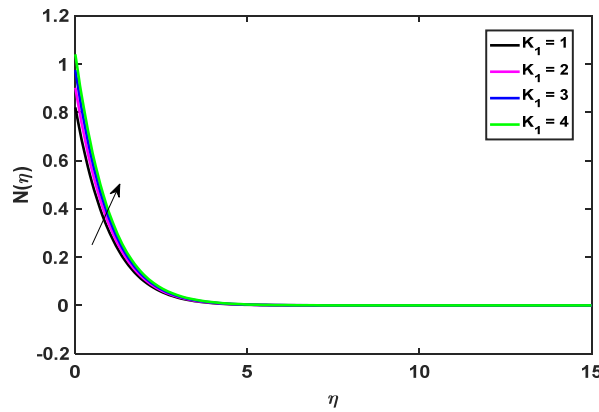


Figure 13. Implementation of  $K_1$  for angular velocity  $g(\eta)$

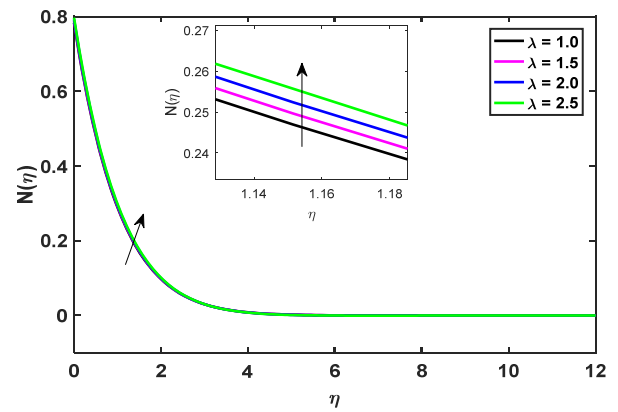


Figure 14. Implementation of  $\lambda$  for angular velocity  $g(\eta)$

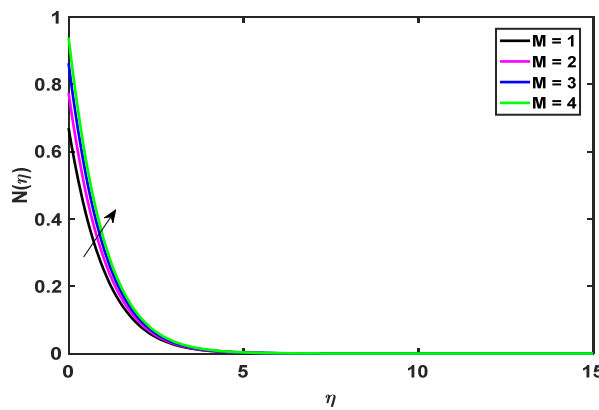


Figure 15. Implementation of M for angular velocity  $g(\eta)$

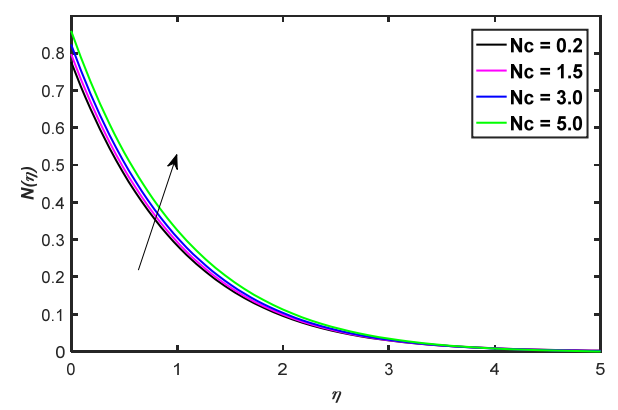


Figure 16. Implementation of  $N_c$  for angular velocity  $g(\eta)$

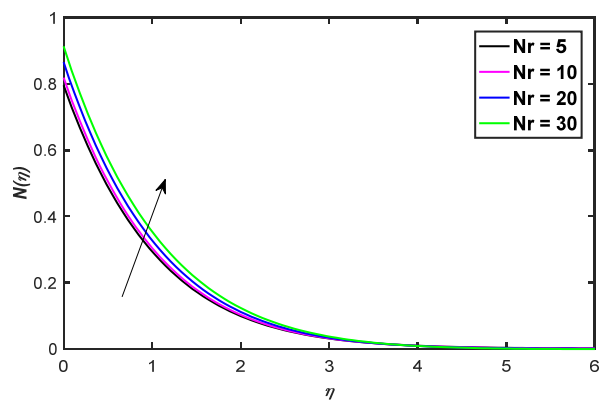


Figure 17. Implementation of  $N_r$  for angular velocity  $g(\eta)$

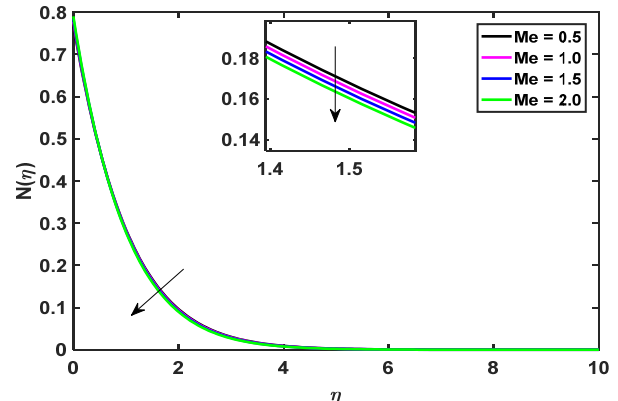


Figure 18. Implementation of  $M_e$  for angular velocity  $g(\eta)$

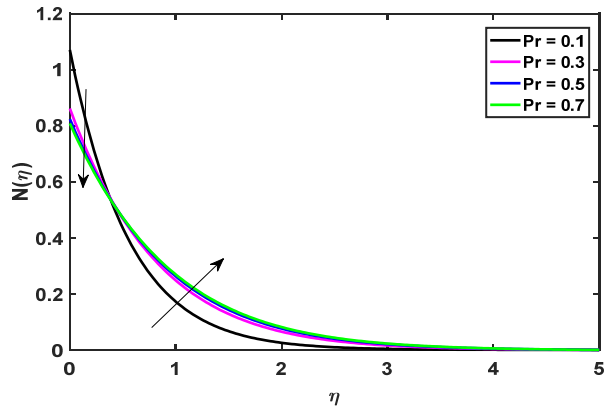


Figure 19. Implementation of Pr for angular velocity  $g(\eta)$

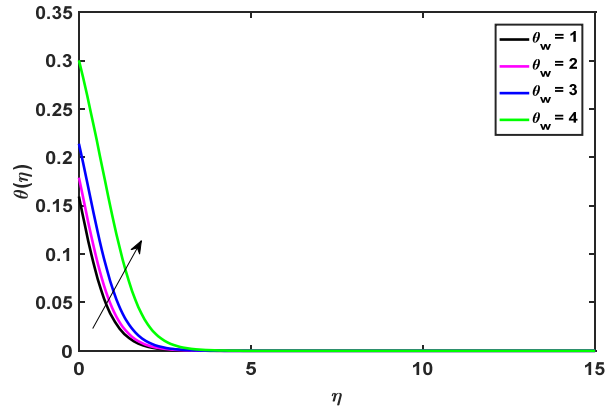


Figure 20. Implementation of  $\theta_w$  for  $\theta(\eta)$

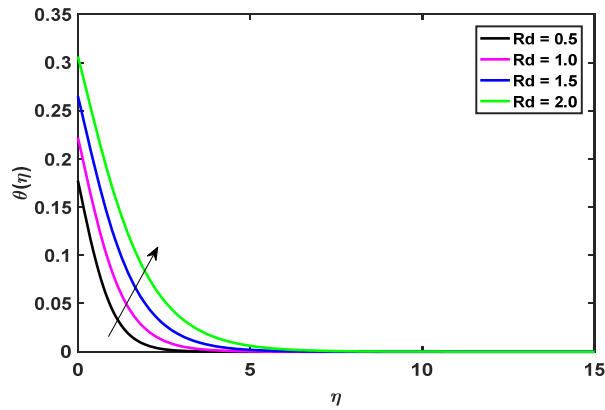


Figure 21. Implementation of Rd for  $\theta(\eta)$

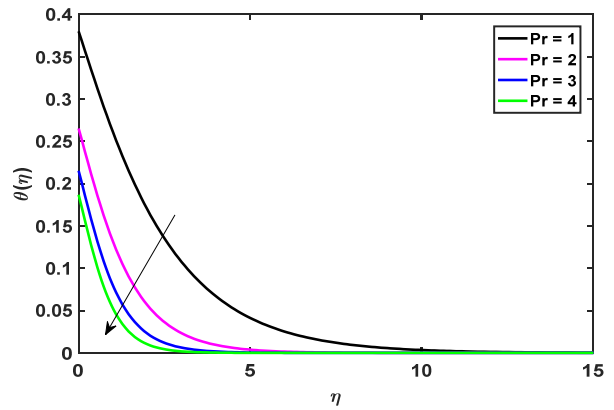


Figure 22. Implementation of Pr for  $\theta(\eta)$

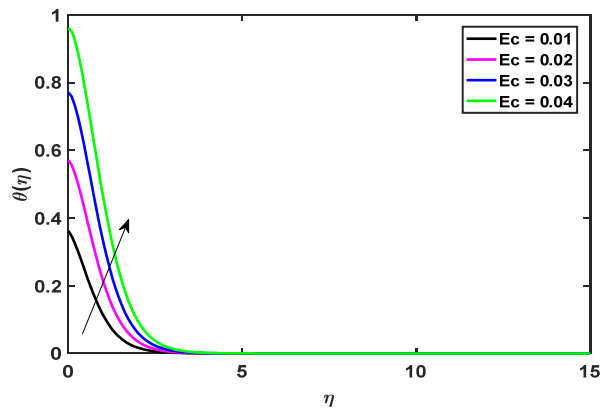


Figure 23. Implementation of Ec for  $\theta(\eta)$

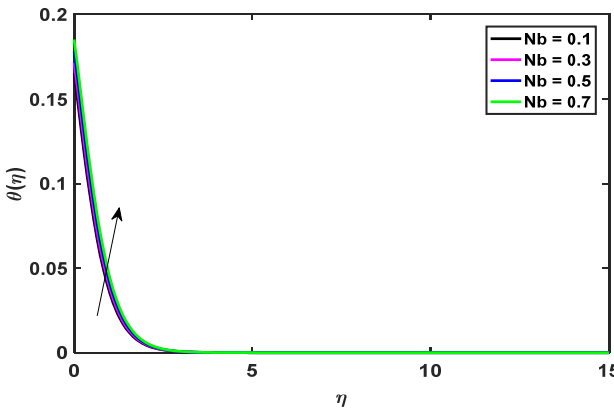


Figure 24. Implementation of Nb for  $\theta(\eta)$

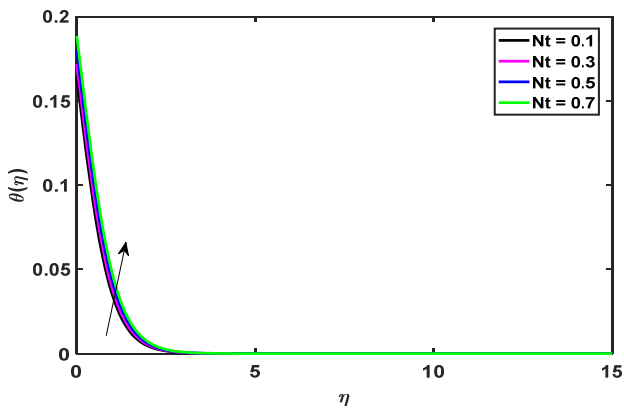


Figure 25. Implementation of Nt for  $\theta(\eta)$

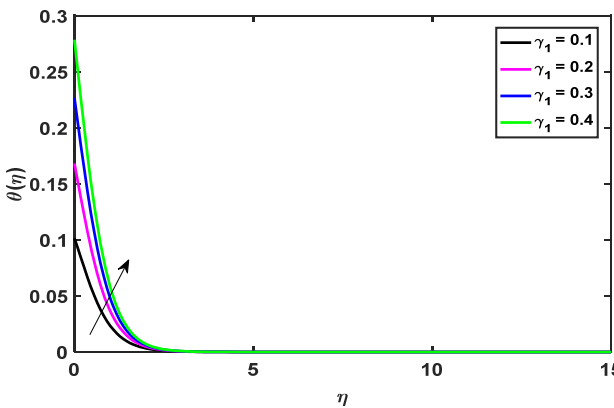


Figure 26. Implementation of  $\lambda_1$  for  $\theta(\eta)$

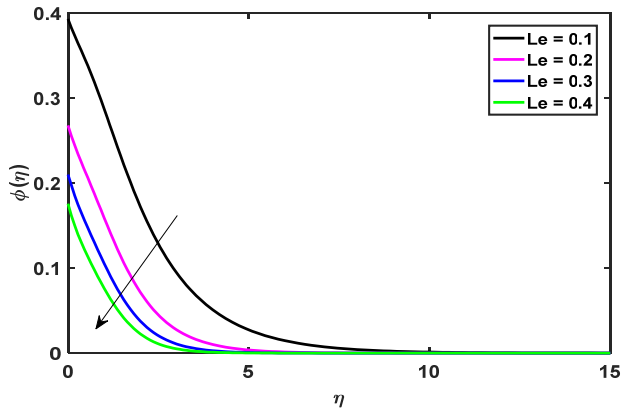


Figure 27. Implementation of  $Le$  for  $\phi(\eta)$

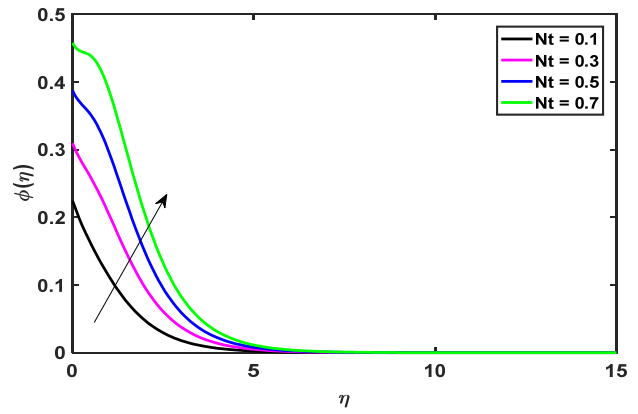


Figure 28. Implementation of  $Nt$  for  $\phi(\eta)$

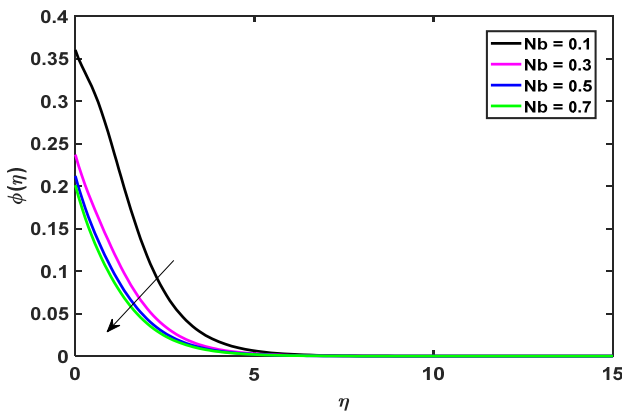


Figure 29. Implementation of  $Nb$  for  $\phi(\eta)$

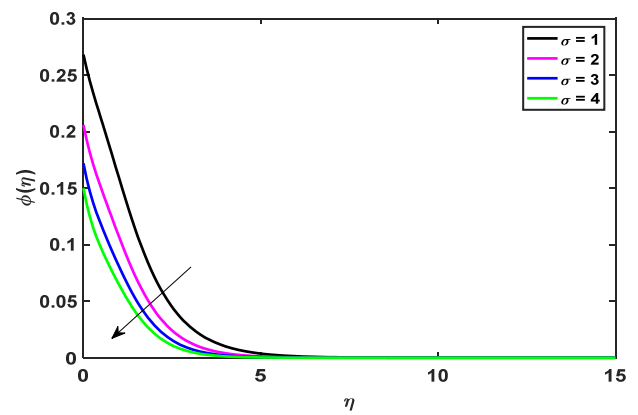


Figure 30. Implementation of  $\sigma$  for  $\phi(\eta)$

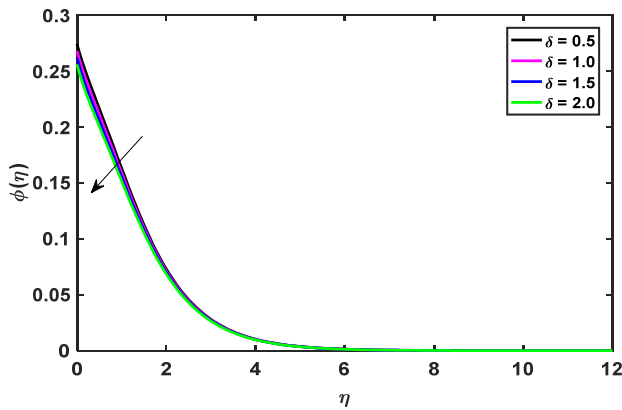


Figure 31. Implementation of  $\delta$  for  $\phi(\eta)$

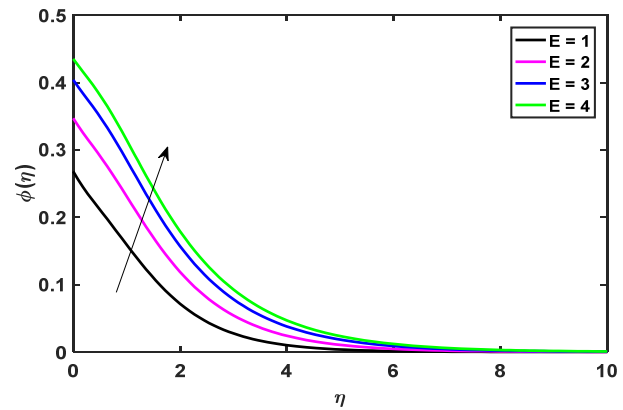


Figure 32. Implementation of  $E$  for  $\phi(\eta)$

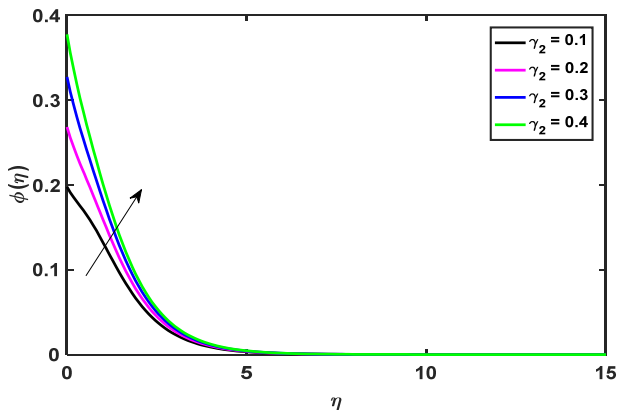


Figure 33. Implementation of  $\lambda_2$  for  $\phi(\eta)$

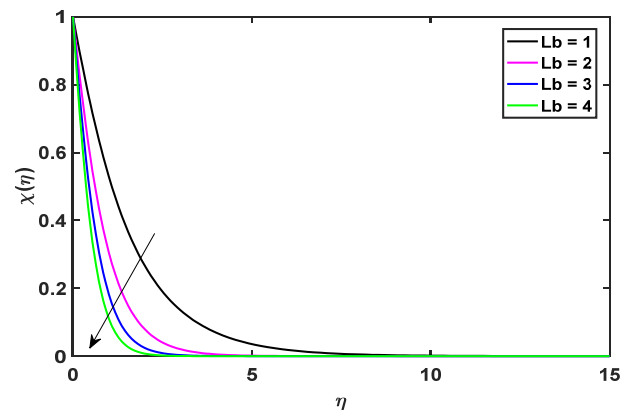


Figure 34. Implementation of  $Lb$  for  $\chi(\eta)$

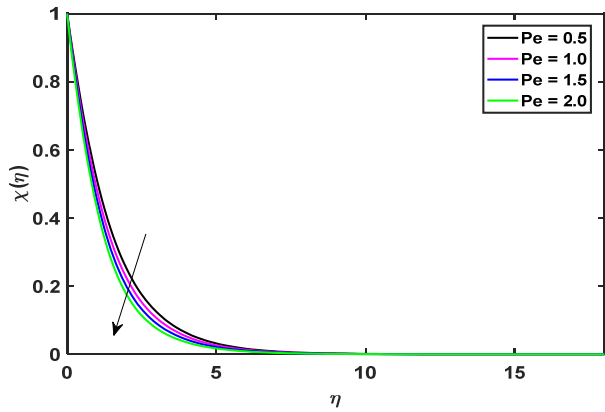


Figure 35. Implementation of Pe for  $\chi(\eta)$

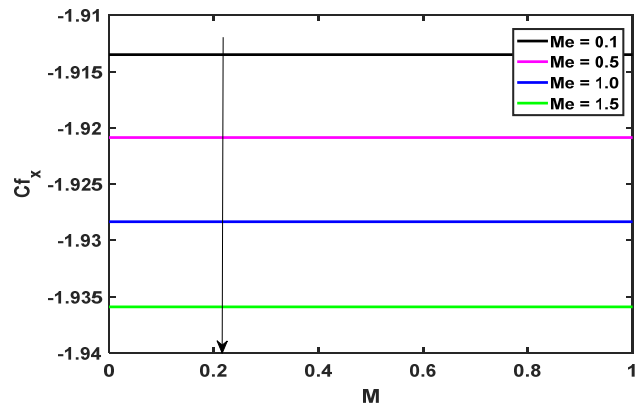


Figure 36. Implementation of Me for Cfx against M

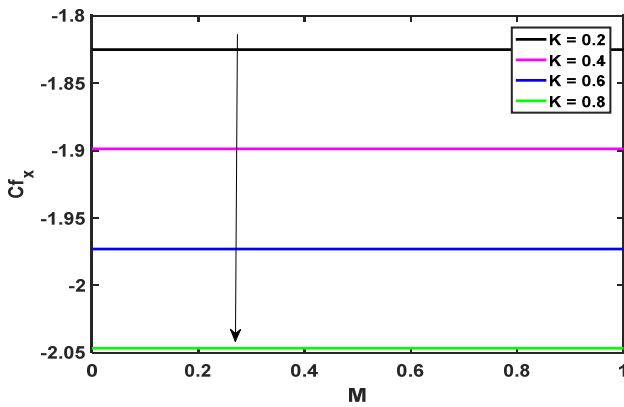


Figure 37. Implementation of K for Cfx against M

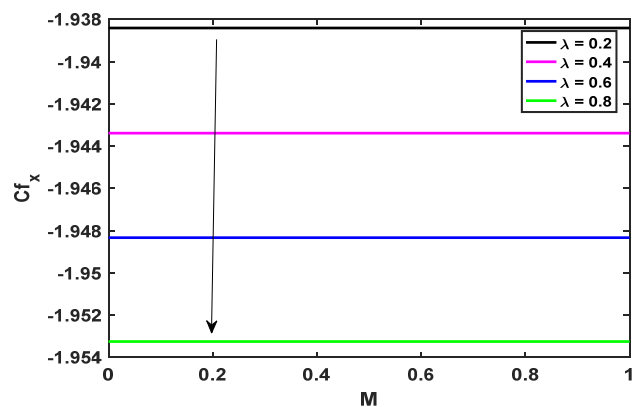


Figure 38. Implementation of  $\lambda$  for Cfx against M

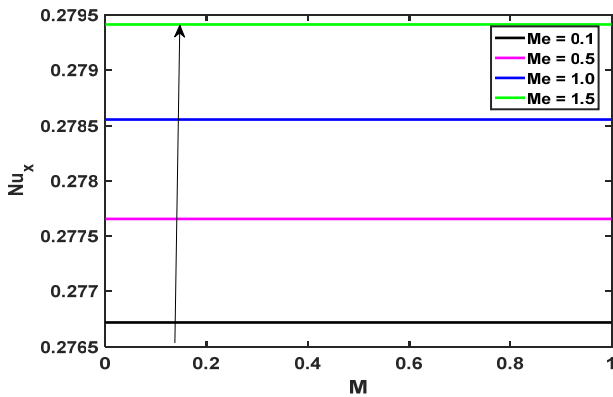


Figure 39. Implementation of Me for Nux against M

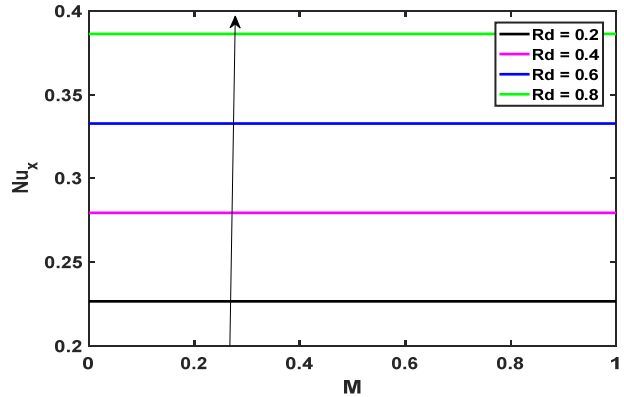


Figure 40. Implementation of Rd for Nux against M

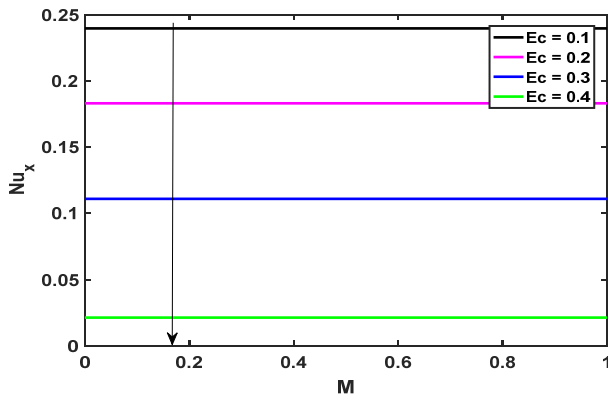


Figure 41. Implementation of Ec for Nux against M

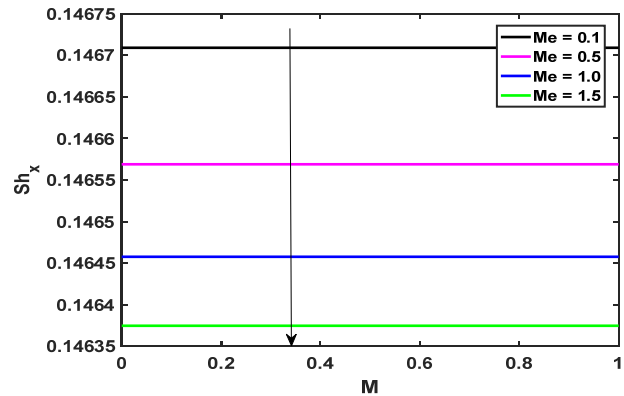


Figure 42. Implementation of Me for Shx against M



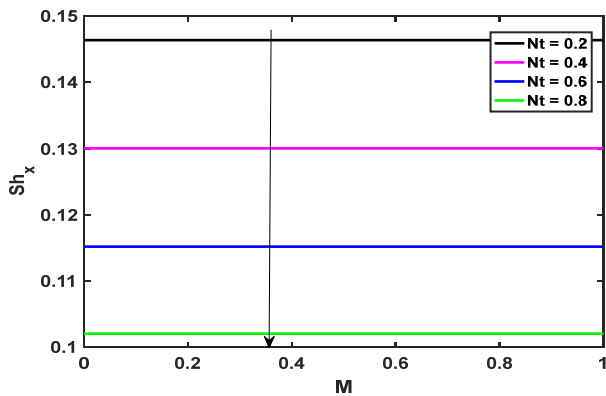


Figure 43. Implementation of Nt for Shx against M

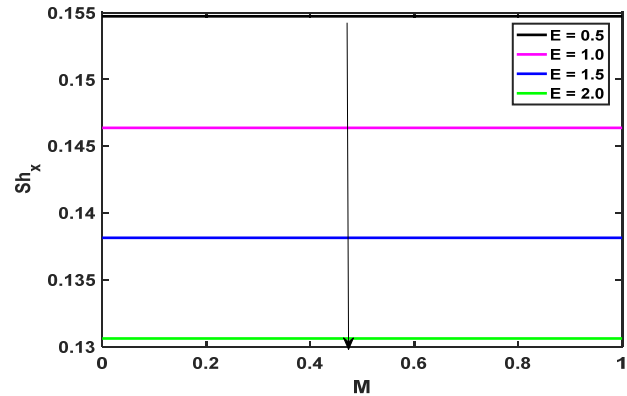


Figure 44. Implementation of E for Shx against M

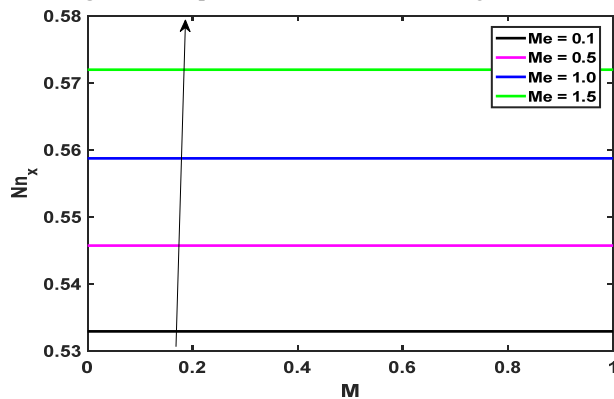


Figure 45. Implementation of Me for Nnx against M

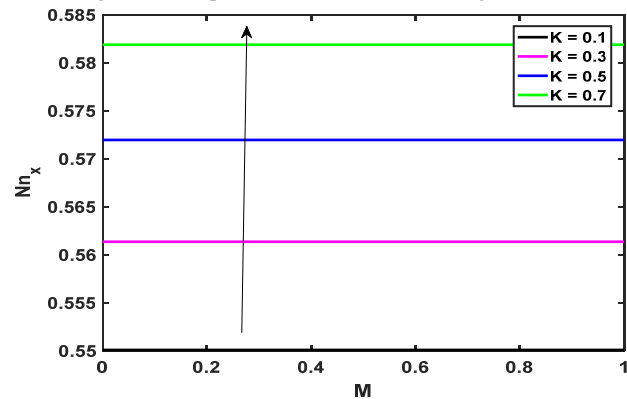


Figure 46. Implementation of K for Nnx against M

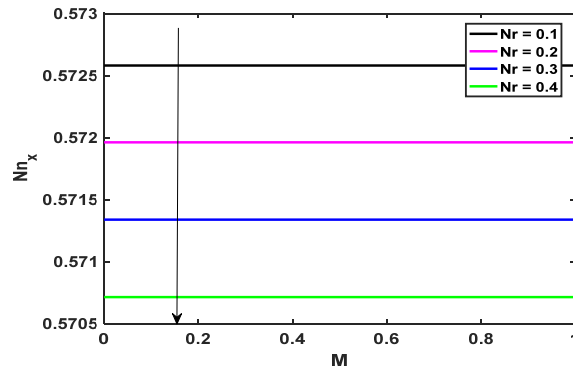


Figure 47. Implementation of Nr for Nnx against M

### 5. FINAL REMARKS

We have addressed the flow of a viscous, incompressible, micropolar fluid in two-dimensional mixed convective boundary layer through a permeable stretching sheet that is contained in bio-convection, activation energy and melting heat transfer. Assigning numerical values to distinct parameters obtained in the mathematical formulation and displaying the numerical results graphically allows, to gain a physical understanding of the problem by discussing the distributions of velocity  $f'(\eta)$ , angular velocity  $g(\eta)$  (microrotation), temperature  $\theta(\eta)$ , concentration  $\phi(\eta)$  and motile organism  $\chi(\eta)$ . We have included figures related to local skin friction coefficient  $\tau$ , couple stress coefficient  $h'(0)$ , Nusselt number  $-\theta'(0)$ , Sherwood number  $-\phi'(0)$  and micro-organism  $-\chi'(0)$ . The parameters for bioconvection and the Peclet number both resulted in a decrease in the density of motile gyrotactic microorganisms. The activation energy parameter and the mass biot number both enhance while the Brownian motion parameter and the Lewis number both decrease the concentration profile. Parameters for Brownian motion and thermophoresis, radiation, and the thermal biot number all contribute to a steeper temperature profile.

**Data Availability Statement:** The datasets used and/or analyzed during the current study are available from the corresponding author upon reasonable request.

**Conflict of Interest:** Authors have no conflict of Interest at this stage.

## ORCID

©Sreenivasulu Arigela, <https://orcid.org/0009-0003-1591-0138>; ©A. Shobha, <https://orcid.org/0009-0006-3177-5564>; ©K. Venkatadri, <https://orcid.org/0000-0001-9248-6180>

## REFERENCES

- [1] S. Mesnage, E.T. Couture, P. Gounon, M. Mock, and A. Fouet, "The capsule and S-layer: two independent and yet compatible macromolecular structures in *Bacillus anthracis*," *J. Bacteriol.* **180**, 52–58 (1998). <https://doi.org/10.1128/jb.180.1.52-58.1998>
- [2] D. Kaiser, "Bacterial motility: how do pili pull? *Curr. Biol.* **10**, 777–780 (2000). [https://doi.org/10.1016/S0960-9822\(00\)00764-8](https://doi.org/10.1016/S0960-9822(00)00764-8)
- [3] A.L. Koch, "The sacculus contraction/expansion model for gliding motility." *J. Theor. Biol.* **142**, 95–112 (1990). [https://doi.org/10.1016/S0022-5193\(05\)80015-3](https://doi.org/10.1016/S0022-5193(05)80015-3)
- [4] I.R. Lapidus, and H.C. Berg, "Gliding motility of *Cytophaga* sp. strain U67," *J. Bacteriol.* **151**, 384–398 (1982). <https://doi.org/10.1128/jb.151.1.384-398.1982>
- [5] J.W. Costerton, R.G.E. Murray, and C.F. Rabino, "Observations on the motility and the structure of vitreoscilla," *Can. J. Microbiol.* **7**, 329–339 (1961). <https://doi.org/10.1139/m61-040>
- [6] L.N. Halfen, and R.W. Castenholz, "Gliding in the blue-green alga: a possible mechanism," *Nature*, **225**, 1163–1165 (1970). <https://doi.org/10.1038/2251163a0>
- [7] B.A. Humphrey, M.R. Dickson, and K.C. Marshall, "Physicochemical and in situ observations on the adhesion of gliding bacteria to surfaces," *Arch. Microbiol.* **120**, 231–238 (1979). <https://doi.org/10.1007/BF00423070>
- [8] E. Hoiczuk, "Gliding motility in cyanobacteria: observations and possible explanations," *Arch. Microbiol.* **174**, 11–17 (2000). <https://doi.org/10.1007/s002030000187>
- [9] K. Venkatadri, P. Rajarajeswari, O.A. Béq, V.R. Prasad, H.J. Leonard, and S. Kuharat, "Thermomagnetic Bioconvection Flow in a Semitrapezoidal Enclosure Filled with a Porous Medium Containing Oxytactic Micro-Organisms: Modeling Hybrid Magnetic Biofuel Cells," *ASME. J. Heat Mass Transfer.* **147**(5): 051201 (2025). <https://doi.org/10.1115/1.4067607>
- [10] R.W. O'Brien, "The gliding motion of a bacterium, *Flexibactor* strain BH 3," *J. Aust. Math. Soc. (Ser B)*, **23**(1), 2–16 (2009). <https://doi.org/10.1017/S0334270000000035>
- [11] S.T. Islam, and T. Mignot, "The mysterious nature of bacterial surface (gliding) motility: a focal adhesion-based mechanism in *Myxococcus xanthus* Semin," *Cell Dev. Biol.* **46**, 143–154 (2015). <https://doi.org/10.1016/j.semcd.2015.10.033>
- [12] B. Nan, and D.R. Zusman, "Novel mechanisms power bacterial gliding motility," *Mol. Microbiol.* **101**, 186–193 (2016). <https://doi.org/10.1111/mmi.13389>
- [13] A. Shafiq, G. Rasool, C.M. Khalique, and S. Aslam, "Second grade bioconvectivenanofluid flow with buoyancy effect and chemical reaction," *Symmetry*, **12**(4), 621 (2020). <https://doi.org/10.3390/sym12040621>
- [14] E.M.A. Elbasheshy, H.G. Asker, and B. Nagy, "The effects of heat generation absorption on boundary layer flow of a nanofluid containing gyrotactic microorganisms over an inclined stretching cylinder," *Ain. Shams. Eng. J.* **13**, 101690 (2022). <https://doi.org/10.1016/j.asej.2022.101690>
- [15] R. Pourrajab, and A. Noghrehabadi, "Bioconvection of nanofluid past stretching sheet in a porous medium in presence of gyrotactic microorganisms with newtonian heating," in: *MATEC Web of Conferences*, **220**, pp. 01004, (EDP Sciences, 2018).
- [16] R.R. Kairi, S. Shaw, S. Roy, and S. Raut, "Thermosolutal marangoni impact on bioconvection in suspension of gyrotactic microorganisms over an inclined stretching sheet," *J. Heat Transfer*, **143**(3), 031201 (2021). <https://doi.org/10.1115/1.4048946>
- [17] K. Li, L. Chen, F. Zhu, and Y. Huang, "Thermal and mechanical analyses of compliant thermoelectric coils for flexible and Bio-Integrated devices," *J. Appl. Mech.* **88**(2), 021011 (2021). <https://doi.org/10.1115/1.4049070>
- [18] M.V.S. Rao, K. Gangadhar, A.J. Chamkha, and P. Surekha, "Bioconvection in a convectonal nanofluid flow containing gyrotactic microorganisms over an isothermal vertical cone embedded in a porous surface with chemical reactive species," *Arab J. Sci. Eng.* **46**, 2493–2503 (2021). <https://doi.org/10.1007/s13369-020-05132-y>
- [19] A.C. Eringen, "Theory of Thermo-Microfluids," *Journal of Mathematical Analysis and Applications*, **38**, 480-496 (1972). [https://doi.org/10.1016/0022-247X\(72\)90106-0](https://doi.org/10.1016/0022-247X(72)90106-0)
- [20] G. Ahmadi, "Self-Similar Solution of Incompressible Micropolar Boundary Layer Flow over a Semi-Infinite Plate," *International Journal of Engineering Science*, **14**, 639-646 (1976). [https://doi.org/10.1016/0020-7225\(76\)90006-9](https://doi.org/10.1016/0020-7225(76)90006-9)
- [21] T. Hayat, M. Mustafa, and S. Obaidat, "Soret and Dufour Effects on the Stagnation Point Flow of a Micropolar Fluid toward a Stretching Sheet," *Journal of Fluid Engineering*, **133**, 1-9 (2011). <https://doi.org/10.1115/1.4003505>
- [22] M.M. Rahman, "Convective Flows of Micropolar Fluids from Radiate Isothermal Porous Surface with Viscous Dissipation and Joule Heating," *Communications in Nonlinear Science and Numerical Simulation*, **14**, 3018-3030 (2009). <https://doi.org/10.1016/j.cnsns.2008.11.010>
- [23] G. Lukaszewicz, "Micropolar Fluids: Theory and Applications," (Birkhauser, Boston, 1999). <https://doi.org/10.1007/978-1-4612-0641-5>
- [24] M. Epstein, and D.H. Cho, "Melting heat transfer in steady laminar flow over a fat plate," *J. Heat Transfer.* **98**, 3 (1976). <https://doi.org/10.1115/1.3450595>
- [25] A. Yacob, A. Ishak, and I. Pop, "Melting heat transfer in boundary layer stagnation-point flow towards a stretching/shrinking sheet in a micropolar fluid," *Comput. Fluids*, **47**, 16–21 (2011). <https://doi.org/10.1016/j.compfluid.2011.01.040>
- [26] T. Hayat, M. Farooq, A. Alsaedi, and Z. Iqbal, "Melting heat transfer in the stagnation point flow of powell-eyring fluid," *J. Thermo Phys. Heat Transfer.* **27**(4), 761–766 (2013). <https://doi.org/10.2514/1.T4059>
- [27] W. A. Khan, M. Khan, M. Irfan, and A.S. Alshomrani, "Impact of melting heat transfer and nonlinear radiative heat flux mechanisms for the generalized Burgers fluids," *Results Phys.* **7**, 4025–4032 (2017). <https://doi.org/10.1016/j.rinp.2017.10.004>
- [28] B. Gireesha, B.M. Shankaralingappa, B.C. Prasannakumara, and B. Nagaraja, "MHD flow and melting heat transfer of dusty Casson fluid over a stretching sheet with Cattaneo Christov heat flux model," *Int. J. Ambient Energy*, **6**, 1–22 (2020). <https://doi.org/10.1080/01430750.2020.1785938>

**ВПЛИВ СИЛИ ЛОРЕНЦЯ ТА ЕНЕРГІЇ АКТИВАЦІЇ АРРЕНІУСА НА РАДІАЦІЙНИЙ БІОКОНВЕКТИВНИЙ ПЛІН МІКРОПОЛЯРНОЇ НАНОРІДИНИ З ПЛАВЛЕННЯМ НАД ПОВЕРХНЕЮ, ЩО РОЗТЯГУЄТЬСЯ**  
**Сайєд Фазуруддін<sup>a</sup>, Срінівасулу Арігела<sup>b</sup>, А. Шобха<sup>c</sup>, В. Раджа Раджесварі<sup>d</sup>, К. Венкатадрі<sup>b</sup>**

<sup>a</sup>Факультет технологічної школи математики, Кампус міста знань Аполло Сакета, Мурукамбатту, Університет Аполло Чіттор, Андхра-Прадеш-517127, Індія

<sup>b</sup>Факультет математики, Школа вільних мистецтв і наук, Університет Мохана Бабу (Колишній інженерний коледж Шрі Відьянікетан), Срі Сайнат Нагар, Тірупаті, А.П., 517102, Індія.

<sup>c</sup>Кафедра прикладної математики, Шрі Падмаваті Махіла Вішва Відьялям, Тірупаті 517502, АР, Індія

<sup>d</sup>Кафедра електроніки та комунікаційної техніки, Школа інженерії та технологій, Шрі Падмаваті Махіла Вішва Відьялям, Тірупаті 517502, А.Р., Індія

Новизна цього дослідження полягає у вивченні впливу сили Лоренца, енергії активації Арреніуса та теплопровідності плавлення на поведінку мікрополярної рідини стаціонарного радіаційного біоконвективного потоку мікрополярної нанорідини до розтягнутої поверхні. Використовуючи стандартний метод подібності, ми вивели рівняння подібності для відповідних величин імпульсу, кутового моменту, температури та концентрації. Інструмент MATLAB 'bvp4c' використовується для визначення розв'язань перетворених керівних рівнянь. Рівняння подібності у чотирьох вимірах (імпульс, кутовий момент, температура та концентрація) розв'язані чисельно. Ми дослідили поведінку полів мікрообертання, швидкості, концентрації та температури для різних параметрів. Результати показують, що щільність рухомості мікроорганізмів зменшується зі збільшенням числа Пекле та параметра різниці концентрацій мікроорганізмів. Щільність рухомості збільшується зі збільшенням числа Пекле в мікробних концентраціях. Тому нанорідини є придатними як рідини для теплопередачі завдяки їхньому ефекту охолодження поверхні. Застосована числова схема підтверджена шляхом порівняння з попередніми числовими значеннями.

**Ключові слова:** теплопередача плавлення; мікрополярна нанорідина; біоконвекція; радіаційний тепловий потік; енергія активації

## EFFECTS OF NATURAL CONVECTION AND RADIATION ON MHD STAGNATION POINT NANO-FLUID FLOW PAST A STRETCHABLE SURFACE WITH VELOCITY SLIP AND NEWTONIAN HEATING

**G.P. Gifty<sup>a</sup>, S.B. Padhi<sup>a</sup>, B.K. Mahatha<sup>b</sup>,  G.K. Mahato<sup>c\*</sup>**

<sup>a</sup>*Department of Mathematics, Centurion University of Technology and Management, Odisha, India*

<sup>b</sup>*Rajkiyakrit +2 High School, Latbedhwa, Koderma, Jharkhand, India*

<sup>c</sup>*Department of Mathematics, Amity Institute of Applied Sciences, Amity University Jharkhand, Ranchi-835303, India*

<sup>\*</sup>*Corresponding author E-mail: [mahatogk@gmail.com](mailto:mahatogk@gmail.com)*

Received June 6, 2025; revised August 7, 2025; accepted August 11, 2025

MHD stagnation point natural convection flow of a viscous, incompressible, electrically conducting, and heat radiating nanofluid past a stretchy surface with velocity slip and Newtonian heating in the presence of a transverse magnetic field is examined. Governing nonlinear partial differential equations are solved with the help of Matlab's bvp4c technique. To confirm robustness and accuracy of the result, the numerical findings in this study are compared with the existing literature, and they are found to be in good agreement. Effects of various parameters on velocity, temperature, and species concentration are computed and presented in the form of graphs whereas the effects on skin friction, the heat transfer rate and mass transfer rate are tabulated. As a result of enhanced thermal energy accumulation or diffusion, nanofluid temperature is increased by Brownian motion, thermophoretic diffusion, velocity slip, convective heating, nonlinear thermal radiation, and Prandtl number. Rate of heat transfer is getting enhanced by temperature ratio, convective heating, and thermal Grashof number due to increased thermal gradients and buoyancy-driven heat transport. Such nanofluid flows have the potential to be used in a number of heat transfer processes such as renewable energy devices including MHD power generators, etc.

**Keywords:** MHD, Nano-Fluid, Natural Convection, Radiation, Velocity Slip, Newtonian Heating

**PACS:** 47.11.-j, 47.10.ab, 02.30.Jr

### INTRODUCTION

Magnetohydrodynamics deals with the study of the dynamic flow of the fluids that conduct electricity. It connects the fluid dynamics and the electromagnetism. It has various applications especially in the field of marine propulsion, astrophysical simulations, forecasting of the space weather etc., Nandini *et al.* [1] made an analysis of the effects of nonlinear radiation in a Darcy-forchheimer model in a rotating channel. The parameters of rotation, magnetic, stretching ratio, Reynolds number, and fluid velocity are all inversely related. In contrast to the parameters of rotation and magnetic field, the Nusselt parameter is correlated with Reynolds number. The fluid temperature is inversely correlated with Reynolds number and similar to rotation and magnetic field. The Reynolds number and magnetic field have a comparable relationship with skin friction. Ouyang *et al.* [2] found that in contrast to the dihybrid nanofluid, they discovered that the trihybrid nanofluid responded favorably to every parameter. Hasana *et al.* [3] taking the radiative heat flux and exothermic chemical reactions found that the Rayleigh number and the nanofluid's velocity are directly correlated. While it is in opposition to thermal radiation, the Frank-Kemenetskii number is proportional to fluid velocity. It is found that the Rayleigh number's critical value is  $3 \times 10^4$ . Heat transfer is at its highest when the nanoparticle's volume fraction is 3%. Shilpa *et al.* [4] took the Carreaaternary hybrid nano fluid for their study on Artificial neural network to find the rate of heat and mass transfer in MHD flow across a vertical cylinder. They discovered that the rate at which heat was transported was significantly higher when they substituted ternary nanoparticles for standard nanoparticles. Accelerated Schmidt number and chemical reaction parameters exacerbate the rate of mass transfer in nanofluids. Additionally, these characteristics raise the fluid's concentration. Khan *et al.* [5] considering the radiating couple stress on the MHD nanofluid flow, discovered that, in contrast to fractional parameters, velocity is proportional to Grashof number, couple stress, and thermal variables. Skin friction varies similarly in response to pressure gradients. The Nusselt number appears to increase exponentially in relation to the Reynolds and Eckert numbers. As the fractional parameter grows, the Bejan number rises as well. Vaidya *et al.* [6] considering gold nanoparticles for thermal radiation in cancer treatment process in flow of Phan-Thien-Tanner MHD found that the fluid flow is enhanced by the Weissenberg number and magnetic parameter, but it is inhibited by the Hall parameter. The fluid's temperature is directly correlated with the thermal radiation parameter. The Weissenberg number and shear stress are connected. Fatunmbi *et al.* [7] considering micropolar water-based iron oxide and silver nanoparticles in the fluid found that when on increasing the suction/injection and magnetic parameters results in a significant decrease in fluid flow. When the heat generation parameter is raised, the fluid's temperature rises; conversely, when the heat exponent is raised, the opposite occurs. Heat transmission in the nanofluid is accelerated by radiation. Saranya *et al.* [8] found that when two disks are rotated the rate of flow is enhanced. They discovered that raising the Reynolds number improved micro rotation. The fluid's temperature is directly correlated with its Reynolds

number and thermal radiation. When vortex viscosity and magnetic field act on the fluid, fluid velocity decreases; conversely, when the volume fraction of the nanoparticle increases, the opposite occurs. Iqbal *et al.* [9] made a study taking microorganisms and the bioconvective flow into consideration. As the thermophoretic effect increases, the temperature rises. The Nusselt number rises in tandem with the Prandtl number. The fluid's velocity and its Forchheimer number are inversely correlated. When the fluid's temperature is raised, radiation raises it. The Pecelt number has an inverse relationship with the fluid's concentration. Alqurashi *et al.* [10] using chemical engineering applications in mixed convection mode, made a detailed study and found that the fluid's velocity is correlated with the mixed convection coefficient and in opposition to the Darcy number and relaxation time coefficient. When the Eckert number and radiation are increased, the temperature rises. The fluid's concentration rises as the thermophoresis parameter rises, but the opposite is true for the Lewis number and chemical reaction coefficient.

Nanofluid is obtained by dispersing nanoparticles like copper, gold, silver etc., in base fluids like water, glycol etc., these nanofluid enhance the thermal properties by increasing the rate of heat and mass transfer. It is mostly used as a coolant in various industries like nuclear reactors, electronic coolings, solar energy, aerospace engineering, etc., Afifi *et al.* [11] studied effects of FEM and AGM in the convection mode in the fluid flow. When the relaxation to retardation ratio rises, the temperature always rises; however, when the Prandtl number falls, the temperature falls. As mass diffusion decreases, increasing the Schimdt number lowers the fluid's concentration. The relationship between velocity and Hartmann number is inverse. Suma *et al.* [12] studied the rate of heat transfer when using a rectangular lid-driven enclosure with a circular hollow cylinder for a nanofluid flow. As the Richardson number rises, so does the rate of heat transmission. A higher magnetic field improves fluid flow. Temperature increases with non-dimensional time. Irfan *et al.* [13] studied the effect of radiation in a bioconvective mode in fluid flow "Numerical study of nonlinear thermal radiation and Joule heating on MHD bioconvection Carreau nanofluid with gyrotactic microorganisms." Increasing Brownian diffusion raises the temperature. Hiking the Prandtl and Lewis numbers is given more attention. The biconvection Lewis number increases motile microorganisms. Suma *et al.* [14] studied "Optimization and sensitivity analysis of unsteady MHD mixed convective heat transfer in a lid-driven cavity containing a double-pipe circular cylinder using nanofluids." Heat transfer and non-dimensional time are related. When compared to heater length, fluid flow and Nusselt number are exactly related to the solid volume %. As the rate of application of the magnetic field increases, the Lorentz force reduces fluid flow. P. Deepalakshmi *et al.* [15] taking the couple stress into consideration made a detailed study on the fluid flow in a porous medium. Radiation and the slip parameter raise temperature, but the Prandtl number has the opposite effect. Heat diffusion has no effect on concentration. Heat source/sink and transfer rate are related, however radiation causes the reverse effect. Pressure decline is accelerated by the Hartmann number. Habiba *et al.* [16] used n-decane nanofluid for their study in a convective mode focusing on magnetic and radiation parameter. Fluid flow is analogous to Hartmann number. Nusselt number and vortex energy are enhanced by Richardson number. Radiation causes an increase in heat transfer. Many researchers [17-21] have contributed in this area of research.

Free convection is a process of heat transfer which happens naturally without any external force generally due to temperature gradient when the density differs. It has its application in the field of building designs, nuclear reactors etc., Hameed *et al.* [22] used Casson based Copper hydroxide nanofluid in a semi- parabolic surface. Rayleigh number increases heat and velocity transfer. The boundary layer thickens and the Nusselt number is increased by the corrugation number. The temperature drops by 8% because of the angle of inclination. Zeb *et al.* [23] used Prandtl fluid for their investigation. Pressure gradient is the opposite of velocity, which is exactly proportional to Prandtl numbers. The magnetic field reduces velocity. The application of radiation accelerates the rate of heat exchange. The concentration of the nanofluid rises as a result of a chemical reaction. Afifi *et al.* [24] used a hexagonal cavity with circular obstacles to study the rate of heat transfer in nanofluid. Hartmann number increasing in a range from 0 to 20, depletes the fluid flow as the maximum flow is obtained when it is at zero. Heat transferred by having a greater number of obstacles on Nusselt number. Maximum oscillation will lead to hike in velocity. When the obstacles are removed the stream function is at maximum. Saghafian *et al.* [25] applying heat flux constantly on vertical plate the rate of heat transfer was examined. Nusselt number is in corelation with maximum wall temperature. Mass flow increases with time but decreases with magnetic field and Hartmann number. Neiri *et al.* [26] investigated "Numerical Simulation of Natural Convection in a Chamfered Square Cavity with Fe3O4-Water Nanofluid and Magnetic Excitation." Temperature and velocity deaccelerate with Hartmann number.

Thermal radiation in nanofluid is rate of heat transfer through electromagnetic waves. It enhances heat transfer and also plays a vital role in the case of heat transfer where no contact is required. It has application in nuclear reactors, electronic cooling systems, etc. Ali *et al.* [27] used Casson fluid for their investigation to find out the effect of thermal radiations. Unsteady parameter, nanoparticle concentration, Casson fluid, Grashof number, Darcy number helps to increase velocity whereas magnetic field depletes it. Khan *et al.* [28] investigated "Impact of multiple slips and thermal radiation on heat and mass transfer in MHD Maxwell hybrid nanofluid flow over porous stretching sheet." Eckert number, thermal relaxation, velocity slip and Grashof number stimulates skin friction. Hybrid nanofluid possess more skin friction as compared to mono nanofluid. Deborah number, magnetic field, radiation and concentration slip parameters, all are responsible for the decline in Nusselt number. Grasshof number and radiation are inversely proportional to Sherwood number. Manjunatha *et al.* [29] made an investigation on the rate of heat transfer applying magnetic field and radiation. Solid volume fraction increased velocity. Temperature of clear fluid is more than nanofluid. Boundary layer thickness of



*Cu – water* is more than that of clear fluid. When magnetic field is applied, rotation, heat source and skin friction increase. Alsemiry *et al.* [30] studied the Thermodiffusion Effects investigated on ANN-Based Prediction and RSM Optimization and applying couple stress. Dufour number accelerate temperature and rate of heat transfer. Velocity is enhanced by mixed convection and slip parameter. Khan *et al.* [31] studied the effect of thermal stratification on an inclined surface. Temperature increases for Deborah number but decreases for Prandtl number. Velocity depletes for Deborah number. Radiation and thermal stratification, boost temperature. Concentration of  $Fe_3O_4$  in the fluid enhances temperature while it reduces velocity.

The stretching sheet in nanofluid flow refers to as the flat surface which keeps moving in a particular direction which generates boundary flow. It has its application in textile industry, thin film coating, biomedical engineering, etc. Li *et al.* [32] used ternary hybrid nanofluid in a Cattaneo-Christov heat flux model. Magnetic field when applied to the fluid, deaccelerated the velocity but increased the temperature and the boundary layer thickened. Biot number and Prandtl number increased the temperature while thermal relaxation brought down the temperature. Skin friction augmented by magnetic field. Mishra *et al.* [33] made an investigation in a spinning disk the effect of radiation. Due to magnetic field and porous matrix, the concentration of nanoparticles increases and hence oppose the fluid velocity and flow. There is great absorption of thermal radiation in the presence of silver nanoparticles leading to increase in temperature. Nusselt number is enhanced by radiation. Sait *et al.* [34] using electroosmotic effects with boundary slip studied the effect of the heat flow. Hartmann number increased the viscosity in the fluid leading to rise in pressure and shear stress while the temperature dropped. Velocity declined due to Prandtl numbers. Slip parameter and magnetic parameter have opposite actions on pressure gradient. Ouyang *et al.* [35] used ternary nanofluid for their study. Presence of nanoparticle increases the thermal conductivity in the fluid leading to rise in heat absorption. Suction/injection parameter has opposite effects on Nusselt number and temperature. Skin friction is enhanced by suction/injection factor.

Based on the reviewed literature, the authors are inspired to explore the boundary layer MHD stagnation point natural convection flow of a viscous, incompressible, electrically conducting, and heat radiating nanofluid past a stretchy surface with velocity slip and Newtonian heating in the presence of a transverse magnetic field. The primary objective of this study is to investigate the boundary layer MHD stagnation point natural convection flow and heat transfer characteristics of a viscous, incompressible, and electrically conducting nanofluid with thermal radiation effects. The analysis focuses on the influence of a transverse magnetic field, velocity slip, and Newtonian heating over a stretching surface, aiming to understand the combined impact of these parameters on the fluid flow and thermal behavior.

### MATHEMATICAL MODEL

Consider the boundary layer, Magnetohydrodynamic (MHD), stagnation-point, natural convection flow of a viscous, incompressible, electrically conducting, and heat-radiating nanofluid past a stretching surface, in the presence of a uniform transverse magnetic field  $B_0$ . The  $x$ -axis is aligned along the horizontal direction of the stretching sheet, while the  $y$ -axis is perpendicular to it. Two equal and opposite forces act on the sheet, stretching it along its length with a velocity  $U_w(x)$ , keeping the origin fixed. The free-stream velocity of the nanofluid is taken as  $U_\infty(x)$ . The surface of the sheet is subject to convective heating from a hot fluid at temperature  $T_f$ , with a heat transfer coefficient  $h_f$ . The significant temperature difference between the ambient fluid temperature  $T_\infty$  and the boundary layer temperature  $T_w$  is assumed to generate substantial thermal radiation effects within the flow field. Partial velocity slip at the fluid–solid interface is considered, meaning the fluid velocity at the surface does not necessarily match the surface velocity due to slip effects. The magnetic Reynolds number of the nanofluid is assumed to be sufficiently small, allowing the neglect of any induced magnetic fields relative to the imposed magnetic field. The nanoparticle volume fraction at the sheet's surface and far from the boundary layer are denoted by  $C_w$  and  $C_\infty$ , respectively.

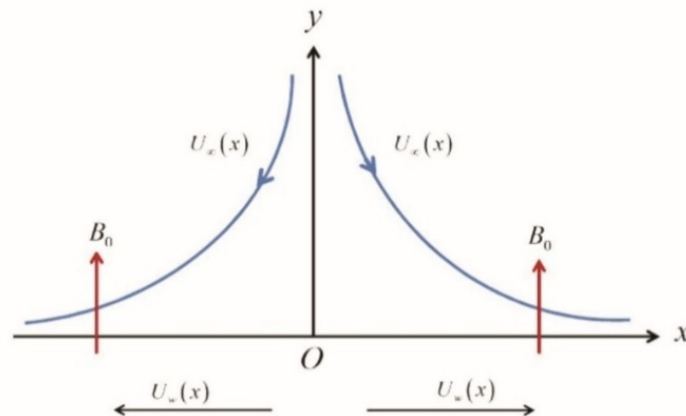


Figure 1. Schematic diagram of the physical configuration

Based on the assumptions aforementioned, equations governing to the present problem, using Rosseland's approximation, are given by:



$$\frac{\partial u}{\partial x} + \frac{\partial v}{\partial y} = 0 \tag{1}$$

$$u \frac{\partial u}{\partial x} + v \frac{\partial u}{\partial y} = v \frac{\partial^2 u}{\partial y^2} + U_\infty \frac{\partial U_\infty}{\partial x} + \frac{\sigma B_0^2}{\rho_f} (U_\infty - u) + \frac{1}{\rho_f} [(1 - C_\infty) \rho_{f\infty} \beta g (T - T_\infty) - (\rho_p - \rho_{f\infty}) g (C - C_\infty)] \tag{2}$$

$$u \frac{\partial T}{\partial x} + v \frac{\partial T}{\partial y} = \alpha_m \frac{\partial^2 T}{\partial y^2} + \tau \left\{ D_B \frac{\partial C}{\partial y} \frac{\partial T}{\partial y} + \frac{D_T}{T_\infty} \left( \frac{\partial T}{\partial y} \right)^2 \right\} + \frac{\partial}{\partial y} \left( \frac{16\sigma^* T^3}{3\alpha^*} \frac{\partial T}{\partial y} \right) \tag{3}$$

$$u \frac{\partial C}{\partial x} + v \frac{\partial C}{\partial y} = D_B \frac{\partial^2 C}{\partial y^2} + \frac{D_T}{T_\infty} \frac{\partial^2 T}{\partial y^2} \tag{4}$$

where  $u$  and  $v$  are the velocity components along the  $x$  and  $y$  axes, respectively,  $\alpha_m = \frac{k}{(\rho c)_f}$  is the thermal diffusivity of the fluid,  $\nu$  is the kinematic viscosity,  $D_B$  is the Brownian diffusion coefficient,  $D_T$  is the thermophoretic diffusion coefficient and  $\tau = \frac{(\rho c)_p}{(\rho c)_f}$  is the ratio between the effective heat capacity of the nanoparticle material and heat capacity of the fluid with  $\rho$  being the density,  $c$  is the specific heat at constant pressure,  $\rho_p$  is the density of the particles,  $\sigma^*$  is the Stefan-Boltzmann constant,  $\alpha^*$  is the Rosseland mean absorption coefficient.

The current situation is governed by the following boundary conditions:

$$\left. \begin{aligned} u = U_w + L \frac{\partial u}{\partial y} = cx + L \frac{\partial u}{\partial y}, v = 0, -k \frac{\partial T}{\partial y} = h(T_f - T), C = C_w \quad \text{at} \quad y = 0 \\ u \rightarrow U_\infty = ax, v = 0, T \rightarrow T_\infty, C \rightarrow C_\infty \quad \text{at} \quad y \rightarrow \infty \end{aligned} \right\} \tag{5}$$

where  $U_w = cx$  ( $c > 0$ ),  $L$ ,  $k$ , and  $U_\infty = ax$  ( $a > 0$ ) are, respectively, the velocity of the stretching sheet, slip length, thermal conductivity of the nanofluid, and free stream velocity of the nanofluid.

The dimensionless and similarity variables are listed below:

$$\eta = y\sqrt{\frac{a}{\nu}}, \quad \psi = \sqrt{a\nu} x f(\eta), \quad \theta(\eta) = \frac{T - T_\infty}{T_f - T_\infty}, \quad \phi(\eta) = \frac{C - C_\infty}{C_w - C_\infty} \tag{6}$$

Equation (1) is satisfied in the same way that equation (6) is applied. The following are the types of equations (2), (3), and (4), as well as the boundary conditions (5):

$$f''' + ff'' - f'^2 + 1 + M(1 - f') + Gr\theta - Nr\phi = 0 \tag{7}$$

$$\left[ 1 + \frac{4}{3N_R} \{1 + (\theta_w - 1)\theta\}^3 \right] \theta'' + Pr f \theta' + Pr Nb \phi' \theta' + \left[ Pr Nt + \frac{4}{N_R} (\theta_w - 1) \{1 + (\theta_w - 1)\theta\}^2 \right] \theta'^2 = 0 \tag{8}$$

$$\phi'' + Le Pr f \phi' + \frac{Nt}{Nb} \theta'' = 0 \tag{9}$$

Boundary conditions are used in non-dimensional formats as

$$\left. \begin{aligned} f(\eta) = 0, f'(\eta) = \alpha + Af''(\eta), \theta'(\eta) = -Bi[1 - \theta(\eta)], \phi(\eta) = 1, \text{ at } \eta = 0 \\ f'(\eta) \rightarrow 1, \theta(\eta) \rightarrow 0, \phi(\eta) \rightarrow 0 \text{ at } \eta \rightarrow \infty. \end{aligned} \right\} \tag{10}$$

The non-dimensional governing parameters in this case are defined as follows:

$$\left. \begin{aligned} M = \frac{\sigma B_0^2}{\rho_f a}, Le = \frac{\alpha}{D_B}, Pr = \frac{\nu}{\alpha}, \alpha = \frac{c}{a}, A = L\sqrt{\frac{a}{\nu}}, Nb = \frac{(\rho c)_p D_B (C_w - C_\infty)}{(\rho c)_f \nu}, Nt = \frac{(\rho c)_p D_T (T_m - T_\infty)}{(\rho c)_f \nu T_\infty}, \\ Gr = \frac{(1 - C_\infty) \beta \rho_{f\infty} g (T_m - T_\infty)}{\rho_f U_\infty a}, Nr = \frac{(\rho_p - \rho_{f\infty}) g (C_w - C_\infty)}{\rho_f U_\infty a}, N_R = \frac{k \alpha^*}{4\sigma^* T_\infty^3}, \theta_w = \frac{T_w}{T_\infty}, Bi = \frac{h}{k} \sqrt{\frac{\nu}{\alpha}}. \end{aligned} \right\} \tag{11}$$

where  $M, Le, Pr, \alpha, A, Nb, Nt, Gr, Nr, N_r, \theta_w, Bi$  are, respectively, the magnetic parameter, Lewis number, Prandtl number, ratio of rates of stretching velocity and free stream velocity, velocity slip parameter, Brownian motion parameter, thermophoresis parameter, thermal Grashof number, solutal Grashof number, radiation parameter, temperature ratio parameter, and Biot number.

On the basis of above quantities, the coefficient of skin friction  $C_f$ , local Nusselt number  $Nu_x$ , and local Sherwood number  $Sh_x$  are defined as:

$$C_f = \frac{\tau_w}{\rho u_w^2}, Nu_x = \frac{xq_w}{k(T_m - T_\infty)}, Sh_x = \frac{xh_m}{D_B(C_w - C_\infty)} \tag{12}$$

where the wall shear stress  $\tau_w$ , wall heat-flux  $q_w$  and wall mass-flux  $h_m$  are given by

$$\tau_w = \mu \left( \frac{\partial u}{\partial y} \right)_{y=0}, q_w = -k \left( \frac{\partial T}{\partial y} \right)_{y=0}, h_m = -D_B \left( \frac{\partial C}{\partial y} \right)_{y=0} \tag{13}$$

We get the following results by using similar variables and the above equations.

$$C_f \sqrt{Re_x} = f''(0), \frac{Nu_x}{\sqrt{Re_x}} = -\theta'(0), \frac{Sh_x}{\sqrt{Re_x}} = -\phi'(0) \tag{14}$$

where  $Re_x$  is the local Reynolds number.

**NUMERICAL PROCEDURE**

Non-linear ordinary differential equations are found from the controlling non-linear partial differential equations (1) - (5) with the help of suitable similarity transformation. These equations (7) - (9) together with boundary conditions (10) are solved, numerically, using MATLAB's bvp4c routine. To confirm robustness and accuracy of the result, the same scheme is applied to the present problem taking  $Gr = Nr = 0$  and the numerical values of coefficient of skin-friction, Nusselt number and Sherwood number has been calculated and compared with the results obtained by Mahatha *et al.* [36], and they are found to be in good agreement.

**Table 1.** Computations showing comparison with Mahatha *et al.* [36] taking  $Gr = Nr = 0$ .

								Mahatha <i>et al.</i> [36]			Present Finding		
$M$	$N_r$	$\theta_w$	$Nb$	$Nt$	$\alpha$	$A$	$Bi$	$-C_f \sqrt{Re_x}$	$\frac{Nu_x}{\sqrt{Re_x}}$	$\frac{Sh_x}{\sqrt{Re_x}}$	$-C_f \sqrt{Re_x}$	$\frac{Nu_x}{\sqrt{Re_x}}$	$\frac{Sh_x}{\sqrt{Re_x}}$
2 6 10	5	2	0.1	0.1	2	0.5	0.5	1.0559954	0.56564827	1.9085476	1.0559954	0.56564827	1.9085476
								1.19783053	0.56360081	1.85031759	1.19783053	0.56360081	1.85031759
								1.28411476	0.56236343	1.81727632	1.28411476	0.56236343	1.81727632
	10 15							1.0559954	0.56564827	1.90854760	1.05599540	0.56564827	1.90854760
								1.05599540	0.47273451	1.89617746	1.05599540	0.47273451	1.89617746
								1.05599540	0.44257262	1.89169667	1.05599540	0.44257262	1.89169667
		2 3 4						1.05599540	0.56564827	1.90854760	1.05599540	0.56564827	1.90854760
								1.05599540	0.73300040	1.94109901	1.05599540	0.73300040	1.94109901
								1.05599540	1.09573572	1.98983165	1.05599540	1.09573572	1.98983165
			0.1 0.2 0.3					1.05599540	0.56564827	1.90854760	1.05599540	0.56564827	1.90854760
								1.05599540	0.54620893	2.00630565	1.05599540	0.54620893	2.00630565
								1.05599540	0.52186269	2.03933398	1.05599540	0.52186269	2.03933398
				0.1 0.3 0.5				1.05599540	0.56564827	1.90854760	1.05599540	0.56564827	1.90854760
								1.05599540	0.55916364	1.69574713	1.05599540	0.55916364	1.69574713
								1.05599540	0.55107685	1.57321616	1.05599540	0.55107685	1.57321616
					1.5 2.0 2.5			0.52197609	0.56129753	1.79227818	0.52197609	0.56129753	1.79227818
								1.05599540	0.56564827	1.90854760	1.05599540	0.56564827	1.90854760
								1.60080045	0.56927362	2.01863199	1.60080045	0.56927362	2.01863199
						0.1 0.3 0.5		1.87844309	0.57087930	2.07184081	1.87844309	0.57087930	2.07184081
								1.34862035	0.56768153	1.96865917	1.34862035	0.56768153	1.96865917
								1.05599540	0.56564827	1.90854760	1.05599540	0.56564827	1.90854760
							0.5 1.0 1.5	1.05599540	0.56564827	1.90854760	1.05599540	0.56564827	1.90854760
								1.05599540	0.99831813	1.86710996	1.05599540	0.99831813	1.86710996
								1.05599540	1.31203155	1.85838165	1.05599540	1.31203155	1.85838165

**RESULTS AND DISCUSSION**

To get insight into the flow pattern, the effects of various flow parameters on fluid velocity, temperature and concentration have been depicted in graphical form from Figures 2-37. It is evident from Fig. 2-13 that on increasing  $M, \theta_w, A, N_r$ , there is a decrease in fluid velocity while on increasing  $Nb, Nt, \alpha, Bi, Le, Gr, N_r$  and  $Pr$ , an increment on fluid velocity is seen. This implies that magnetic field, temperature ratio, velocity slip, solutal Grashof number have the tendency to retard the fluid velocity while Brownian diffusion, thermophoretic diffusion, stretching ratio, convective heating, Lewis number, thermal Grashof number, non-linear radiation and Prandtl number have the reverse

effect on it. The application of a transverse magnetic field induces a Lorentz force that opposes the motion of the electrically conducting fluid, acting as a resistive (drag) force and thereby reducing the fluid velocity. Though typically promoting flow due to solutal buoyancy, under certain conditions (e.g., adverse concentration gradients), it may counteract thermal buoyancy, thereby slowing the flow. Brownian diffusion enhances nanoparticle motion, which contributes to increased thermal conductivity and energy transport, indirectly supporting momentum transfer and increasing velocity. Thermophoretic diffusion drives nanoparticles away from heated regions, enhancing momentum in the fluid layers and increasing the overall velocity. Greater surface heating enhances buoyancy-driven flow, thus increasing velocity on increasing convective heating. Thermal Grashof number represents buoyancy effects due to temperature differences. Higher values increase upward motion and accelerate fluid flow. Radiative heat enhances thermal energy in the system, increasing buoyancy and promoting fluid acceleration.

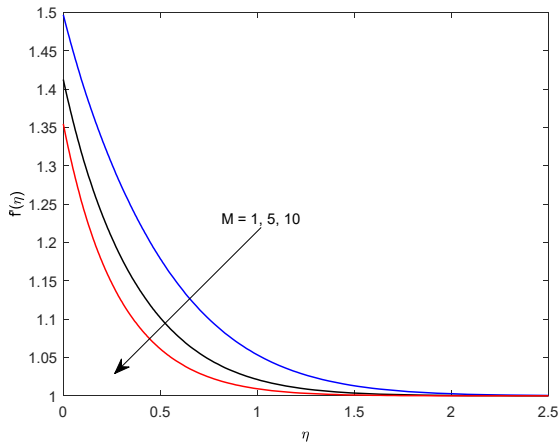


Figure 2. Velocity profile for  $M$

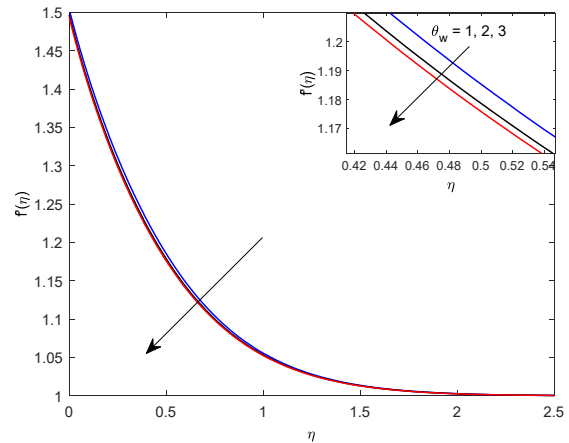


Figure 3. Velocity profile for  $\theta_w$

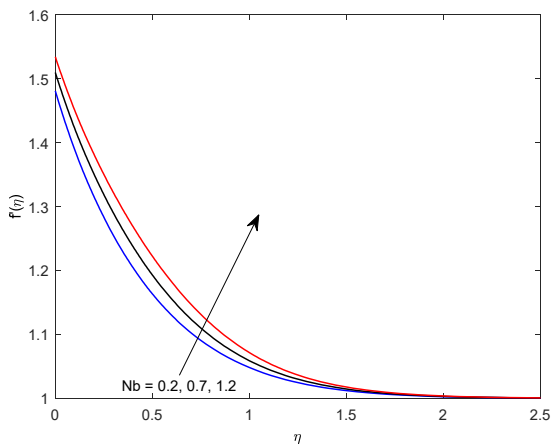


Figure 4. Velocity profile for  $Nb$

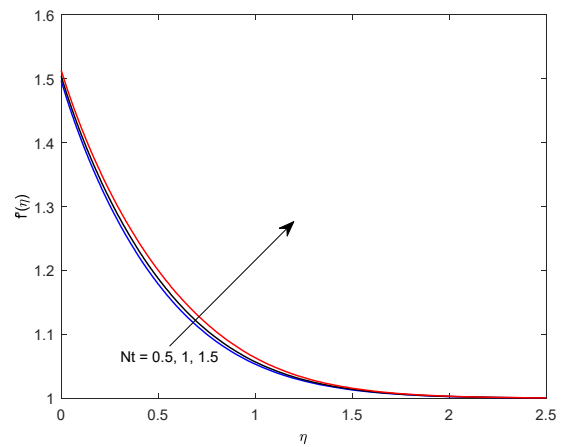


Figure 5. Velocity profile for  $Nt$

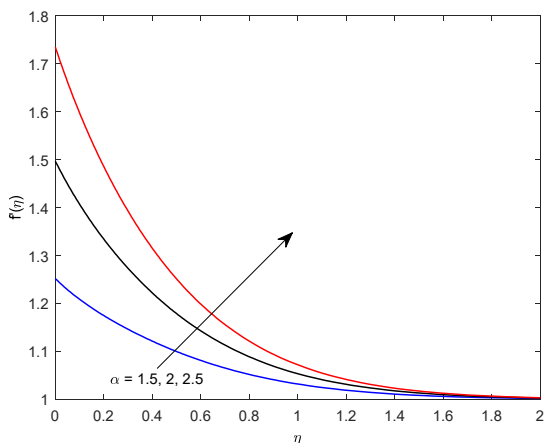


Figure 6. Velocity profile for  $\alpha$

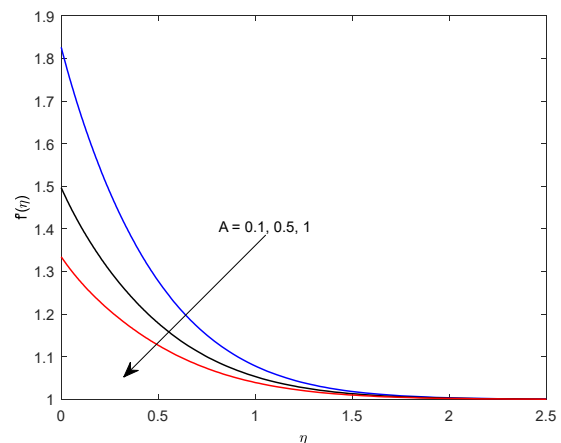


Figure 7. Velocity profile for  $A$

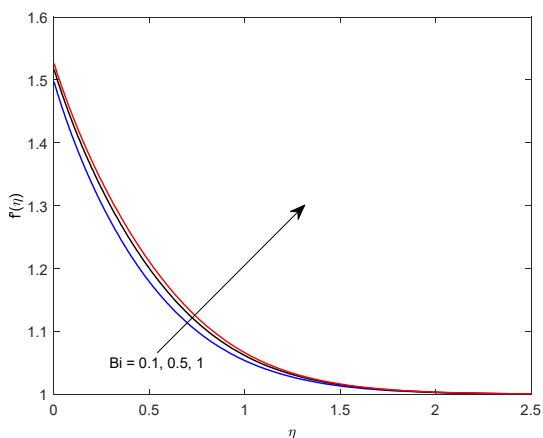


Figure 8. Velocity profile for  $Bi$

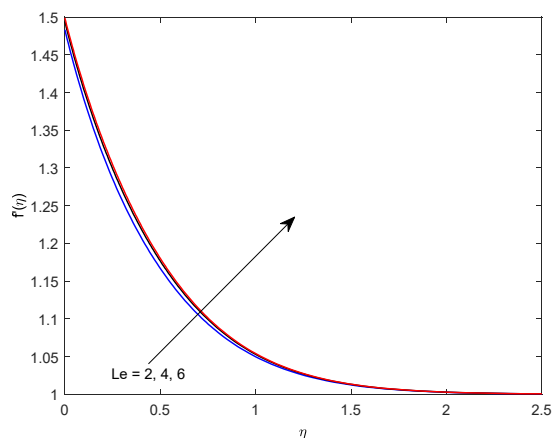


Figure 9. Velocity profile for  $Le$

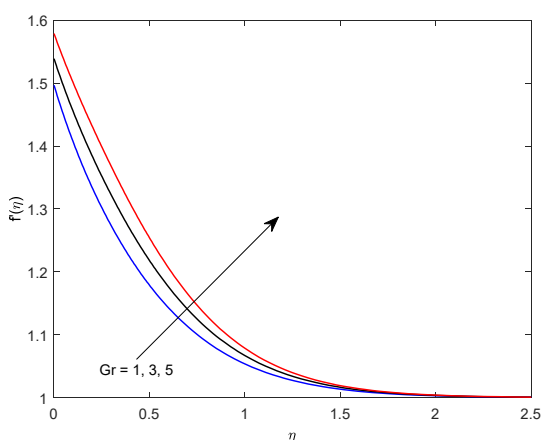


Figure 10. Velocity profile for  $Gr$

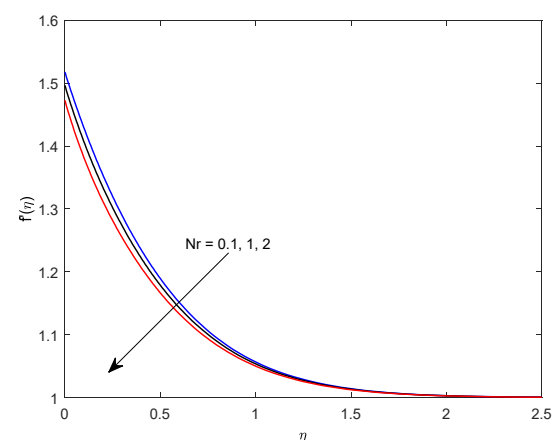


Figure 11. Velocity profile for  $Nr$

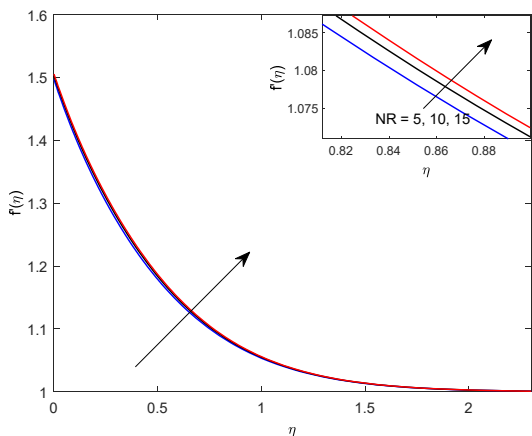


Figure 12. Velocity profile for  $N_R$

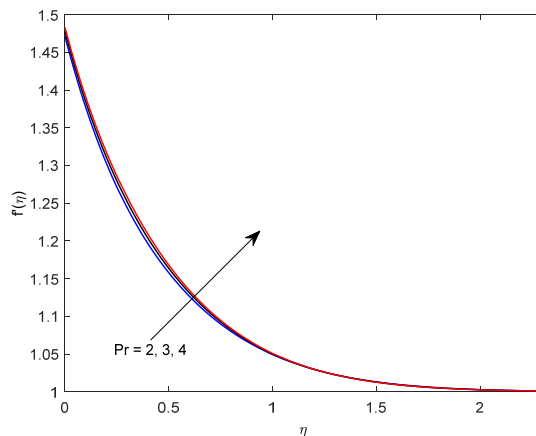


Figure 13. Velocity profile for  $Pr$

Figs. 14-25 represents the effects of various flow parameters on fluid temperature. It is clearly seen from fig. 14-25 that on increasing  $M$ ,  $Nb$ ,  $Nt$ ,  $A$ ,  $Bi$ ,  $Le$ ,  $Nr$ ,  $N_R$  and  $Pr$ , fluid temperature is getting increased while it is decreasing  $\theta_w$ ,  $\alpha$ ,  $Gr$ . This implies that the fluid temperature is getting enhanced by Brownian diffusion, thermophoretic diffusion, velocity slip, convective heating, Lewis number, non-linear thermal radiation and Prandtl number. While reverse trend is visible in temperature profiles for temperature ratio, stretching ratio and thermal Grashof number. Brownian motion of nanoparticles enhances random thermal agitation within the fluid, promoting increased thermal conductivity and leading to a rise in fluid temperature. Thermophoresis causes particles to move from hot to cold regions, redistributing energy within the boundary layer. This enhances the thermal boundary layer thickness and increases the temperature. Stronger convective heating at the surface introduces more heat into the fluid, increasing its temperature near the wall and throughout the boundary layer. Thermal radiation provides an additional mode of energy transport. With nonlinear radiation, this effect becomes more pronounced at higher temperatures, leading to significant heat gain in the fluid. While

$Gr$  promotes buoyancy-driven flow, a high  $Gr$  accelerating the fluid away from the heated surface, reducing residence time and resulting in lower temperatures within the thermal boundary layer.

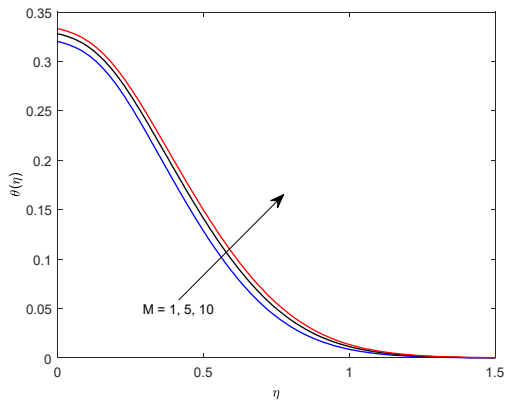


Figure 14. Temperature profile for  $M$

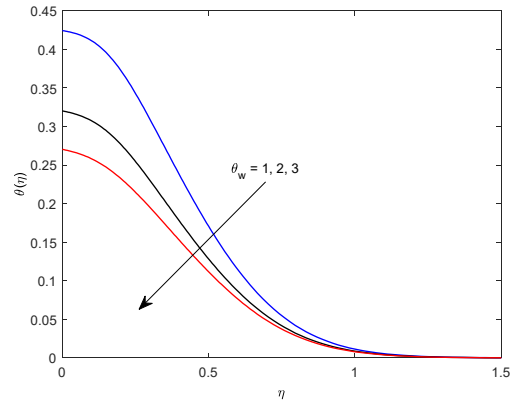


Figure 15. Temperature profile for  $\theta_w$

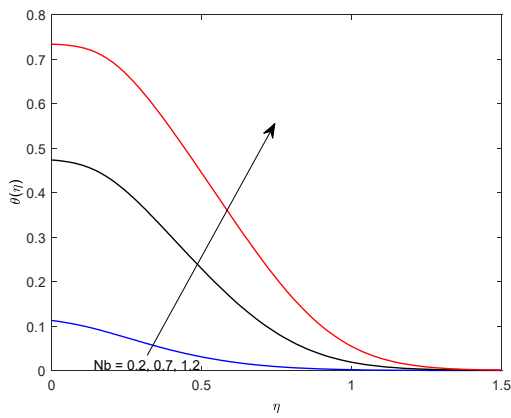


Figure 16. Temperature profile for  $Nb$

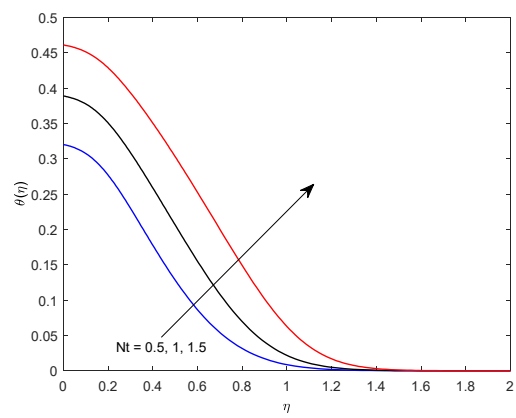


Figure 17. Temperature profile for  $Nt$

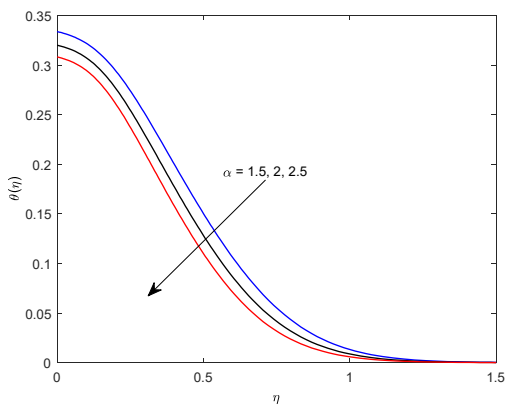


Figure 18. Temperature profile for  $\alpha$

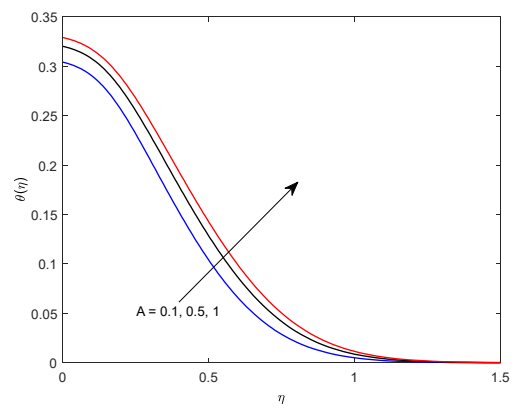


Figure 19. Temperature profile for  $A$

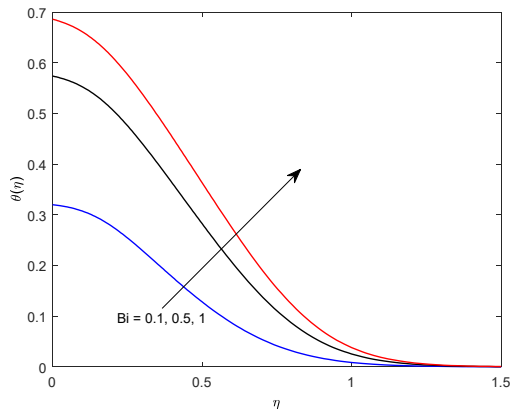


Figure 20. Temperature profile for  $Bi$

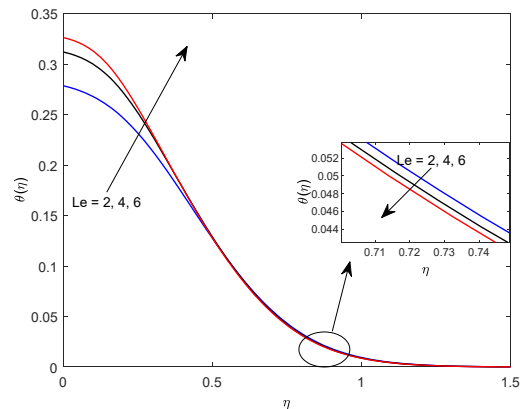


Figure 21. Temperature profile for  $Le$

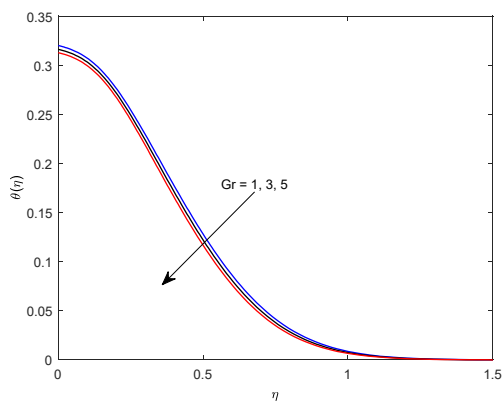


Figure 22. Temperature profile for  $Gr$

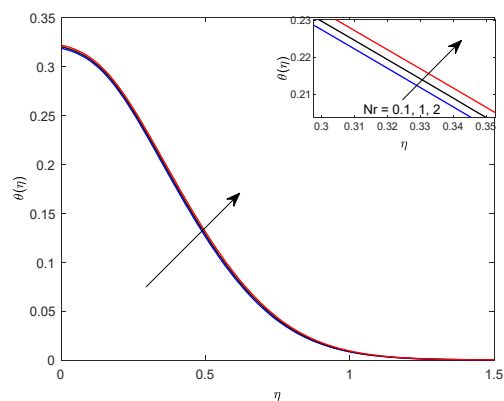


Figure 23. Temperature profile for  $Nr$

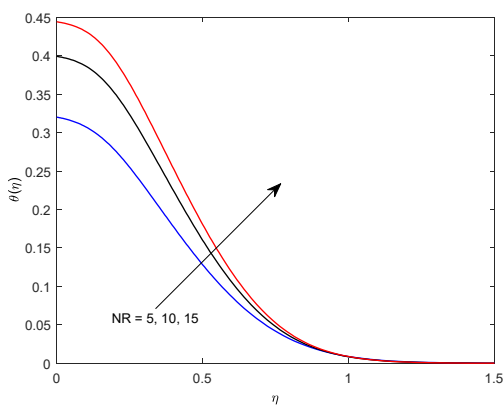


Figure 24. Temperature profile for  $N_R$

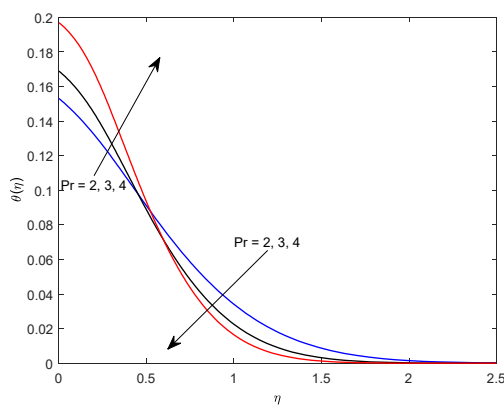


Figure 25. Temperature profile for  $Pr$

It is visible from Fig. 26-37 that with the increase in  $M$ ,  $\theta_w$ ,  $A$ ,  $Nr$ , there is an increment in the concentration profiles while there is a decrement on increasing  $Nb$ ,  $Nt$ ,  $\alpha$ ,  $Bi$ ,  $Le$ ,  $Gr$ ,  $N_R$  and  $Pr$  in the boundary layer region.

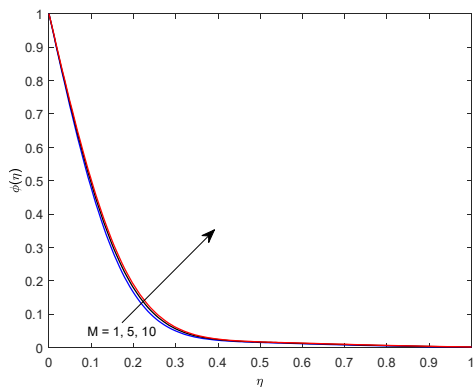


Figure 26. Concentration profile for  $M$

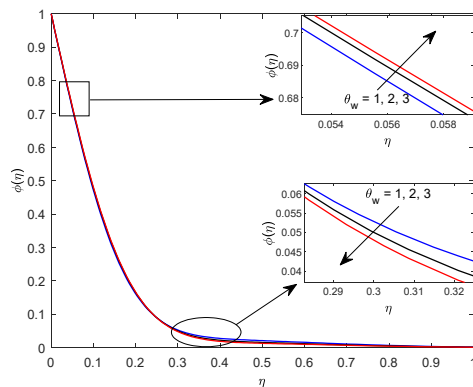


Figure 27. Concentration profile for  $\theta_w$

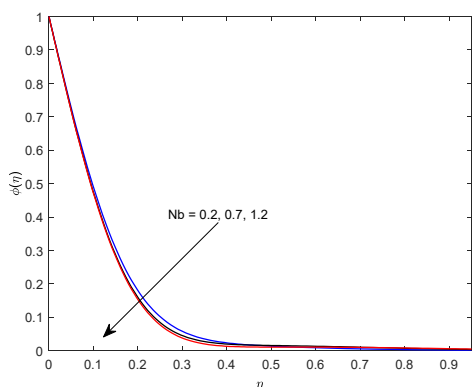


Figure 28. Concentration profile for  $Nb$

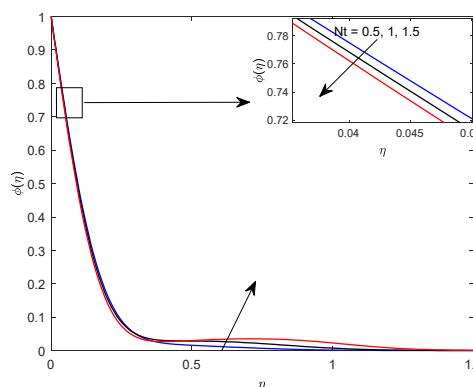


Figure 29. Concentration profile for  $Nt$



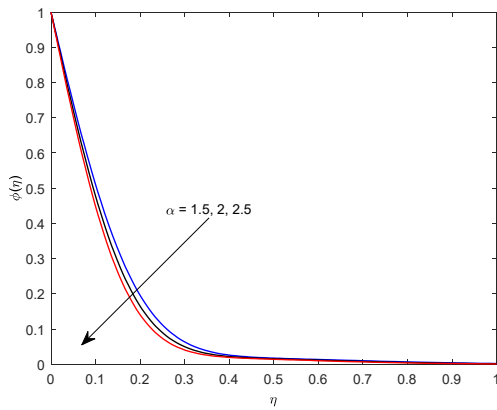


Figure 30. Concentration profile for  $\alpha$

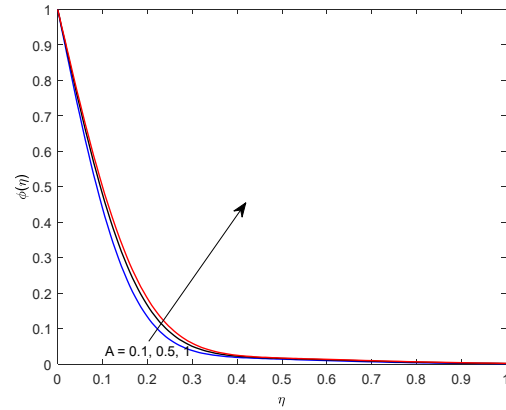


Figure 31. Concentration profile for  $A$

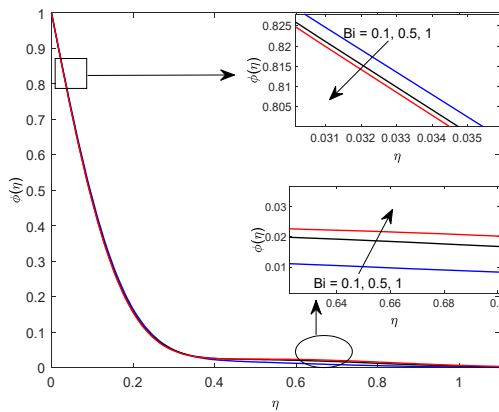


Figure 32. Concentration profile for  $Bi$

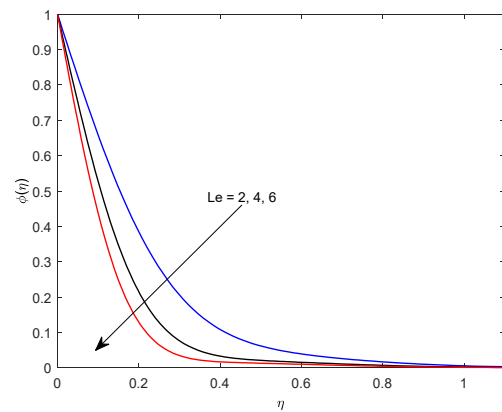


Figure 33. Concentration profile for  $Le$

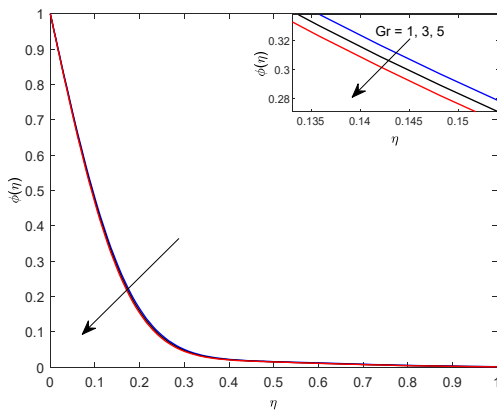


Figure 34. Concentration profile for  $Gr$

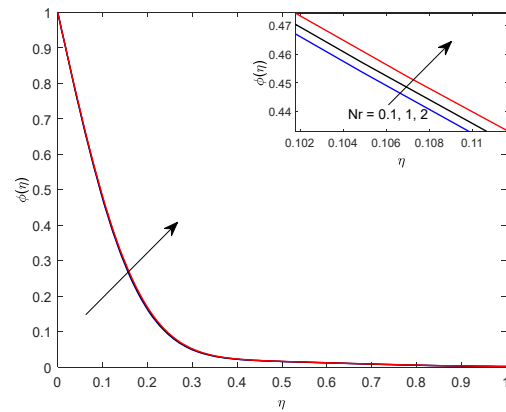


Figure 35. Concentration profile for  $Nr$

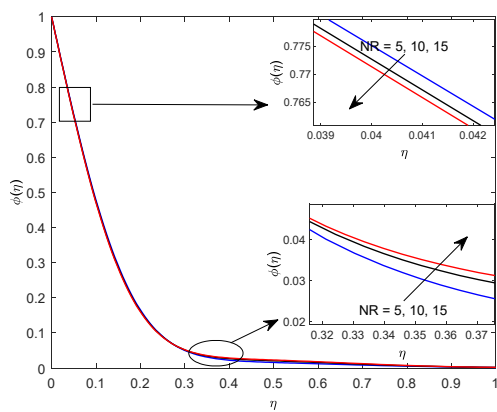


Figure 36. Concentration profile for  $N_R$

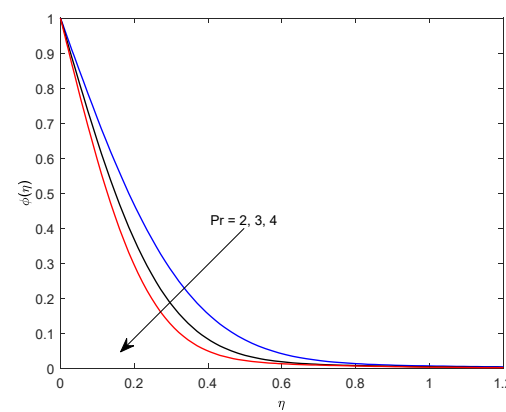


Figure 37. Concentration profile for  $Pr$

This shows that the magnetic field, temperature ratio, velocity slip and solutal Grashof number are the cause for the rise in concentration of fluid. On the other hand, Brownian motion, thermophoretic diffusion, stretching parameter,

Newtonian heating, Lewis number, Grasshof number, Prandtl number and non-linear radiation. These are the cause in concentration profile. The application of a magnetic field generates a Lorentz force that opposes fluid motion. This suppresses convective transport and slows the fluid, allowing more time for mass to accumulate near the surface, thereby increasing concentration. As solutal Grasshof number measures buoyancy effects due to concentration differences. A higher value promotes solutal buoyancy-driven flow, which enhance concentration near the surface due to a stronger diffusion gradient. Brownian diffusion promotes random motion of nanoparticles, which tends to spread out concentration gradients and leads to a decrease in the local concentration near the surface. Thermophoresis drives particles from hot to cold regions, often away from the surface, thereby reducing the concentration in the boundary layer. Strong surface heating increases thermal energy, which activate both thermophoretic and Brownian effects, enhancing mass diffusion and reducing concentration near the wall. Enhanced buoyancy due to temperature differences promotes faster upward fluid motion, which dilutes concentration near the surface by enhancing convective mass transport. A high Prandtl number implies slower thermal diffusion, which may indirectly increase convective effects and enhance species dispersion, thus lowering concentration. Increased radiative heat flux intensifies temperature gradients, which promote stronger thermophoretic effects, pushing nanoparticles away from the wall and decreasing concentration in the near-wall region.

To get more physical insight, the effects of various physical entities on skin friction, rate of heat transfer and rate of mass transfer have been calculated and listed in Table 2.

**Table 2.** Numerical values of the coefficient of skin friction, Nusselt number and Sherwood number against different values of flow parameters

$M$	$N_R$	$\theta_w$	$Pr$	$Nb$	$Nt$	$\alpha$	$A$	$Bi$	$Le$	$Gr$	$Nr$	$C_f \sqrt{Re_x}$	$Re_x^{-1/2} Nu_x$	$Re_x^{-1/2} Sh_x$
1	5	2	6.785	0.5	0.5	2	0.5	0.1	5	1	1	1.00647243	0.10969678	5.71847394
5												1.17545046	0.10916806	5.52978961
10												1.29087133	0.10881602	5.40032863
	5											1.00647243	0.10969678	5.71847394
	10											0.99539217	0.08202349	5.78274036
	15											0.98883774	0.0704694	5.81704256
		1										0.99178448	0.07291539	5.80510782
		2										1.00647243	0.10969678	5.71847394
		3										1.01305281	0.14412317	5.67286711
			2									1.05697201	0.11931776	2.94310389
			3									1.04442418	0.11850775	3.66004079
			4									1.03394039	0.1170332	4.27679022
				0.2								1.03810586	0.12133854	5.59760324
				0.7								0.98054756	0.09757684	5.74929635
				1.2								0.93176267	0.06360343	5.76595794
					0.5							1.00647243	0.10969678	5.71847394
					1							0.9919851	0.10477874	5.90396126
					1.5							0.9735596	0.09873209	6.06812004
						1.5						0.49631091	0.10877109	5.28764785
						2						1.00647243	0.10969678	5.71847394
						2.5						1.53026552	0.11047703	6.11135321
							0.1					1.73817223	0.11074986	6.2560944
							0.5					1.00647243	0.10969678	5.71847394
							1					0.66538584	0.10909963	5.43657748
								0.1				1.00647243	0.10969678	5.71847394
								0.3				0.96674662	0.26068122	5.83954402
								0.5				0.94784719	0.35745004	5.88242681
									2			1.03339216	0.11235762	3.57004164
									4			1.01203843	0.11024239	5.10455488
									6			1.002337	0.1092959	6.27206578
										1		1.00647243	0.10969678	5.71847394
										3		0.92209211	0.10994859	5.81105052
										5		0.84229688	0.11017426	5.89685957
											0.1	0.9640686	0.10979618	5.76159899
											1	1.00647243	0.10969678	5.71847394
											2	1.05443945	0.10958192	5.66923073

It is evident from Table 2 that the skin friction is getting hiked by magnetic field, temperature ratio, stretching ratio and linear non-thermal radiation whereas it experiences reverse effect by solutal Grasshof number, Prandtl number, Brownian motion, thermophoretic diffusion, velocity slip, convective heating, Lewis number and thermal Grasshof number. The Lorentz force acts against the flow, increasing resistance and thereby enhancing wall shear stress, which

leads to higher skin friction. Increased stretching of the surface amplifies tangential stress and fluid acceleration near the wall, raising skin friction. Radiation alters energy distribution in the flow, potentially increasing momentum transfer near the surface, which raises wall shear stress. Enhanced solutal buoyancy may weaken the surface shear due to rising flow, leading to a drop in friction at the wall. Higher Pr reduces thermal diffusivity, thinning the velocity boundary layer and thereby reducing friction drag. Brownian motion and thermophoretic diffusion disrupt the uniformity of momentum transport, reducing shear at the wall. Slip condition reduces direct contact between the fluid and surface, decreasing the frictional force. Convective heating increases thermal energy and buoyancy, which may redistribute momentum and reduce skin friction. Strong thermal buoyancy lifts fluid away from the wall, reducing wall shear stress.

Temperature ratio, stretching ratio, convective heating and thermal Grashof number have the tendency to enhance the rate of heat transfer at the surface while magnetic field, solutal Grashof number, Prandtl number, Brownian motion, thermophoretic diffusion, velocity slip, Lewis number and thermal radiation have a reverse effect on heat transfer. A higher wall temperature promotes a stronger thermal gradient, enhancing heat transfer. Stretching increases convective effects, improving surface heat transfer. Convective heating directly enhances surface heat input, increasing the temperature gradient and rate of heat transfer. Thermal Grashof number boosts thermal buoyancy-driven convection, enhancing heat transfer from the surface. The resistive Lorentz force suppresses fluid motion, weakening convection and reducing heat transfer. Solutal Grashof Number may oppose thermal buoyancy in some regimes, reducing heat transfer effectiveness. Higher Pr means lower thermal diffusivity, resulting in thinner thermal boundary layers, which can reduce heat transfer if the flow is not accelerated proportionally. Brownian motion and thermophoretic diffusion increase thermal boundary layer thickness due to nanoparticle interactions, reducing the surface heat gradient. Velocity Slip decreases the transfer of thermal energy from the wall to fluid. Nonlinear thermal radiation reduces the effective thermal gradient at the wall by redistributing heat into the fluid bulk, lowering surface heat flux. Solutal Grashof number, Prandtl number, Brownian diffusion, thermophoretic diffusion, stretching ratio, Newtonian heating, Lewis number and thermal Grashof number accelerate the rate of mass transfer whereas magnetic field, temperature ratio, velocity slip and thermal radiation deaccelerate the rate of mass transfer. Solutal Grashof number enhances concentration-driven buoyancy, promoting species transport and increasing mass transfer rate. Brownian motion and thermophoretic diffusion intensify particle diffusion and migration, thus enhancing mass transfer at the wall. Newtonian heating promotes both thermal and concentration gradients, especially when mass transfer is coupled with temperature effects. Thermal Grashof number boosts upward convection, carrying species away from the surface and enhancing mass transfer. Magnetic field slows fluid motion due to Lorentz force, reducing convective mass transport. Temperature ratio may alter thermal stratification, diminishing thermophoretic effects and lowering mass transfer. Velocity slip reduces surface interaction, limiting mass exchange between the surface and fluid. Thermal radiation alters temperature distribution, which affects species migration driven by thermal gradients, potentially weakening mass transfer.

## CONCLUSIONS

The present study comprehensively investigates the influence of various flow parameters on the velocity, temperature, and concentration fields, as well as on the skin friction coefficient, rate of heat transfer, and rate of mass transfer in a boundary layer MHD stagnation-point flow of a nanofluid over a stretching surface, incorporating velocity slip, Newtonian heating, and thermal radiation effects. The key conclusions drawn from the study are summarized below:

- “Due to enhanced resistive or damping forces, magnetic field, temperature ratio, velocity slip, and solutal Grashof number reduces the nanofluid velocity. On the other hand, convective heating, thermal Grashof number, nonlinear radiation, and Prandtl number induces the nanofluid velocity, owing to strengthened convective or thermal driving mechanisms”.
- “Fluid temperature is increased by Brownian motion, thermophoretic diffusion, velocity slip, convective heating, nonlinear thermal radiation, and Prandtl number, as these enhance thermal energy accumulation or diffusion whereas it is decreased with increasing temperature ratio, and thermal Grashof number due to the thinning of the thermal boundary layer or enhanced convective cooling”.
- “An increase in nanofluid concentration profiles on increasing magnetic field, temperature ratio, velocity slip, and solutal Grashof number, indicating suppressed mass diffusion or accumulation near the wall. On the other hand, decreased concentration is observed with increasing Newtonian heating, thermal Grashof number, Prandtl number, and nonlinear radiation due to enhanced mass diffusion or particle migration away from the surface”.
- “Due to enhanced resistive or surface-driven momentum input, magnetic field, temperature ratio, and linear non-thermal radiation enhances the skin friction while a reduction due to solutal Grashof number, Prandtl number, Brownian motion, thermophoretic diffusion, velocity slip, convective heating, Lewis number, and thermal Grashof number, indicates momentum thinning or reduced wall interaction”.
- “Rate of heat transfer is getting enhanced by temperature ratio, convective heating, and thermal Grashof number due to increased thermal gradients and buoyancy-driven heat transport whereas it is reduced by magnetic field, solutal Grashof number, Prandtl number, Brownian motion, thermophoretic diffusion, velocity slip, and thermal radiation, owing to boundary layer thickening or damping effects”.
- “Mass transfer increases with solutal Grashof number, Prandtl number, Brownian motion, thermophoretic diffusion, Newtonian heating, and thermal Grashof number due to intensified concentration gradients and diffusive transport.

It decreases with magnetic field, temperature ratio, velocity slip, and thermal radiation, reflecting inhibited mass transport and particle dispersion”.

#### ORCID

©G.K. Mahato, <https://orcid.org/0000-0003-4549-0042>

#### REFERENCES

- [1] M. Nandini, B.N. Hanumagowda, G. Saini, S.V.K. Varma, J.V. Tawade, N.V. Satpute, R. Ghodhbani, *et al.*, “Non-linear thermal radiation impacts on MHD nanofluid flow in a rotating channel with Darcy-forcheimer model: An entropy analysis,” *J. Rad. Res. Appl. Sci.* **18**(1), 101228 (2025). (2024). <https://doi.org/10.1016/j.jrras.2024.101228>
- [2] Y. Ouyanga, Md. Faisal, Md. Basir, K. Naganthran, and I. Pop, “Numerical analysis of MHD ternary nanofluid flow past a permeable stretching/shrinking sheet with velocity slip,” *Alexandria Engineering Journal*, **116**, 427-438 (2025). <https://doi.org/10.1016/j.aej.2024.12.089>
- [3] Md.M. Hasan, M.J. Uddin, and S.A. Faroughi, “Magnetohydrodynamic nanofluids flow and heat transfer with radiative heat flux and exothermic chemical reactions,” *International Journal of Thermofluids*, **26**, 101114 (2025). <https://doi.org/10.1016/j.ijft.2025.101114>
- [4] Shilpa, R. Mehta, and K. Senthilvadivu, “Artificial neural network analysis on heat and mass transfer in MHD Carreau ternary hybrid nanofluid flow across a vertical cylinder: A numerical computation,” *International Journal of Thermofluids*, **27**, 101171 (2025). <https://doi.org/10.1016/j.ijft.2025.101171>
- [5] Z.H. Khan, O.D. Makinde, M. Usman, A. Rashid, and W.A. Khan, Fractional order analysis of radiating couple stress MHD nanofluid flow in a permeable wall channel. *Journal of Taibah University for Science*, **19**(1), 2485396 (2025). <https://doi.org/10.1080/16583655.2025.2485396>
- [6] H. Vaidya, M. Bakouri, D. Tripathi, I. Khan, A.M. Alqahtani, K.V. Prasad, and R. Choudhari, “Significance of thermal radiation on peristaltic flow of Phan-Thien-Tanner MHD nanofluid containing gold nanoparticles with applications in cancer medications,” *Journal of Radiation Research and Applied Sciences*, **18**(1), 101212 (2024). <https://doi.org/10.1016/j.jrras.2024.101212>
- [7] E.O. Fatunmbi, A.M. Obalalu, S.O. Salawu, U. Khand, N. Abdullah, S. Elattar, and R. Ghodhbani, Refka, “Aspects of heat transfer hybridized micropolar water-based iron oxide and silver nanoparticles across a stretching bidirectional sheet with thermal radiation,” *Journal of Radiation Research and Applied Sciences*, **18**, 101220 (2024). <https://doi.org/10.1016/j.jrras.2024.101220>
- [8] S. Saranya, P. Ragupathi, and Q.M. Al-Mdallal, “Impact of micropolar effects on nanofluid flow between two disks,” *International Journal of Thermo-fluids*, **26**, 101050 (2025). <https://doi.org/10.1016/j.ijft.2024.101050>
- [9] M.A. Iqbal, N. Khan, A.H. Alzahrani, and Y. Khan, “Thermophoretic particle deposition in bioconvection flow of nanofluid with microorganisms and heat source: Applications of nanoparticle and thermal radiation,” *Journal of Radiation Research and Applied Sciences*, **18**, 101305 (2025). <https://doi.org/10.1016/j.jrras.2025.101305>
- [10] M.S. Alqurashi, F.S. Bayones, S.M. Abo-Dahab, A.M. Abd-Alla, and M.S. Soliman, “Mixed convection effect on MHD Oldroyd-B nanofluid flow over a stretching sheet through a porous medium with viscous dissipation-chemical engineering applications,” *Alexandria Engineering Journal*, **125**, 507-525 (2025). <https://doi.org/10.1016/j.aej.2025.04.056>
- [11] M.D. Affif, A. Jahangiri, and M. Ameri, “Numerical and analytical investigation of Jeffrey nanofluid convective flow in magnetic field by FEM and AGM,” *International Journal of Thermofluids*, **25**, 100999 (2024). <https://doi.org/10.1016/j.ijft.2024.100999>
- [12] U.K. Suma, M.M. Billah, A.R. Khan, and K.E. Hoque, “Magnetohydrodynamic mixed convective heat transfer augmentation in a rectangular lid-driven enclosure with a circular hollow cylinder utilizing nanofluids,” *International Journal of Thermofluids*, **25**, 101014 (2024). <https://doi.org/10.1016/j.ijft.2024.101014>
- [13] Md. Irfan, T. Muhammad, M. Rashid, M.S. Anwar, S.S. Abas, and P.V.S. Narayana, “Numerical study of nonlinear thermal radiation and Joule heating on MHD bioconvection Carreau nanofluid with gyrotactic microorganisms,” *Journal of Radiation Research and Applied Sciences*, **18**, 101254 (2024). <https://doi.org/10.1016/j.jrras.2024.101254>
- [14] U.K. Suma, M.M. Billah, and A.R. Khan, “Optimization and sensitivity analysis of unsteady MHD mixed convective heat transfer in a lid-driven cavity containing a double-pipe circular cylinder using nanofluids,” *International Journal of Thermofluids*, **27**, 101197 (2025). <https://doi.org/10.1016/j.ijft.2025.101197>
- [15] P. Deepalakshmi, G. Shankar, E.P. Siva, D. Tripathi, and A.O. Beg, “MHD analysis of couple stress nanofluid through a tapered non-uniform channel with porous media and slip-convective boundary effects,” *International Journal of Thermofluids*, **27**, 101208 (2025). <https://doi.org/10.1016/j.ijft.2025.101208>
- [16] U. Habiba, M.N. Hudha, B. Neogi, S. Islam, and M.M. Rahman, “Numerical exploration on n-decane nanofluid based MHD mixed convection in a lid driven cavity: impact of magnetic field and thermal radiation,” *International Journal of Thermofluids*, **27**, 101209 (2025). <https://doi.org/10.1016/j.ijft.2025.101209>
- [17] B.K. Mahatha, R. Nandkeolyar, G.K. Mahato, and P. Sibanda, “Dissipative Effects in Hydromagnetic Boundary Layer Nanofluid Flow Past A Stretching Sheet with Newtonian Heating,” *Journal of Applied Fluid Mechanics*, **9**(4), 1977-1989 (2016). <https://doi.org/10.18869/acadpub.jafm.68.235.24451>
- [18] R. Nandkeolyar, B.K. Mahatha, G.K. Mahato, and P. Sibanda, “Effect of Chemical Reaction and Heat Absorption on MHD Nanoliquid Flow Past a Stretching Sheet in the Presence of a Transverse Magnetic Field,” *Magnetochemistry*, **4**(1), 1-14 (2018). <https://doi.org/10.3390/magnetochemistry4010018>
- [19] G.K. Mahato, B.K. Mahatha, R. Nandkeolyar, and B. Patra, “The Effects of Chemical Reaction on Magnetohydrodynamic Flow and Heat transfer of a Nanofluid past a Stretchable Surface with Melting,” *AIP Conference Proceedings*, **2253**, 020011 (2020). <https://doi.org/10.1063/5.0019205>
- [20] G.K. Mahato, B.K. Mahatha, S. Ram, and S.B. Padhi, “Radiative and Convective Heat Transfer on MHD Stagnation point Nanofluid Flow past a Stretchable Surface with Melting,” *AIP Conference Proceedings*, **2435**, 020037 (2022). <https://doi.org/10.1063/5.0083936>
- [21] B.K. Mahatha, S.B. Padhi, G.K. Mahato, and S. Ram, “Radiation, Chemical Reaction and Dissipative Effects on MHD Stagnation Point Nano-Fluid Flow Past a Stretchable Melting Surface,” *AIP Conference Proceedings*, **2435**, 020040 (2022). <https://doi.org/10.1063/5.0083933>

- [22] R.H. Hameed, R.A. Hussein, Q.H. Al-Salami, M.A. Alomari, A.M. Hassan, F.Q.A. Alyousuf, F. Alqurashi, *et al.*, "Free convection investigation for a Casson-based  $Cu - H_2O$  nanofluid in semi parabolic enclosure with corrugated cylinder," *Heliyon*, **11**, e40960 (2024). <https://doi.org/10.1016/j.heliyon.2024.e40960>
- [23] S. Zeb, Z. Ullah, A.B. Albidah, I. Khan, and W.A. Khan, "The significance of heat transfer through natural convection in stagnation point flow of prandtl fluid," *Results in Physics*, **68**, 108087 (2024). <https://doi.org/10.1016/j.rinp.2024.108087>
- [24] M.D Afifi, A. Jahangiri, and Md. Ameri, "Investigation of natural convection heat transfer in MHD fluid within a hexagonal cavity with circular obstacles," *International Journal of Thermofluids*, **25**, 101024 (2024). <https://doi.org/10.1016/j.ijft.2024.101024>
- [25] M. Saghafian, M. Moslehi, and O.A. Akbari, "Magneto hydrodynamic unsteady natural convection slip flow in a vertical parallel plate microchannel heated with constant heat flux," *Heliyon*, **11**, e41502 (2024). <https://doi.org/10.1016/j.heliyon.2024.e41502>
- [26] R. Neiri, A.E.A. Awouda, A.A. Musa, H.G. Alshomrani, and F. Nasri, "Numerical Simulation of Natural Convection in a Chamfered Square Cavity with  $Fe_3O_4$ -Water Nanofluid and Magnetic Excitation," *Engineering, Technology & Applied Science Research*, **15**(1), 20523–20528 (2025). <https://doi.org/10.48084/etasr.9775>
- [27] A. Ali, Rabia, S. Hussain, and M. Ashraf, "Theoretical investigation of unsteady MHD flow of Casson hybrid nanofluid in porous medium: Applications of thermal radiations and nanoparticle," *Journal of Radiation Research and Applied Sciences*, **17**(1), 101029 (2024). <https://doi.org/10.1016/j.jrras.2024.101029>
- [28] Z.H. Khan, W.A. Khan, S.M. Ibrahim, K. Swain, Z. Huang, "Impact of multiple slips and thermal radiation on heat and mass transfer in MHD Maxwell hybrid nanofluid flow over porous stretching sheet," *Case Studies in Thermal Engineering*, **61**, 104906 (2024). <https://doi.org/10.1016/j.csite.2024.104906>
- [29] N. Manjunatha, M.G. Reddy, A. Aloqaily, S. Aljohani, A.R. Reddy, F. Ali, and N. Mlaiki, "Radiation effects on rotating system free convective nanofluid unsteady flow with heat source and magnetic field," *Partial Differential Equations in Applied Mathematics*, **13**, 101083 (2025). <https://doi.org/10.1016/j.padiff.2025.101083>
- [30] R.D. Alsemiry, S.E. Ahmed, M.R. Eid, and M.E. Essam, "ANN-Based Prediction and RSM Optimization of Radiative Heat Transfer in Couple Stress Nanofluids with Thermodiffusion Effects," *Process*, **13**(4), 1055 (2025). <https://doi.org/10.3390/pr13041055>
- [31] A. Khan, Hashim, M. Farooq, W. Jamshed, B.M. Makhdom, and N.A.A.M. Nasir, "Nonlinear convective heat transfer in Maxwell nanofluids with quadratic thermal stratification over a Magnetized inclined Surface: Applications towards engineering Industry," *Ain Shams Engineering Journal*, **16**, 103432 (2025). <https://doi.org/10.1016/j.asej.2025.103432>
- [32] W. Li, S.A. Khan, M. Shafqat, Q. Abbas, T. Muhammad, and M. Imran, "Computational analysis for efficient thermal transportation of ternary hybrid nanofluid flow across a stretching sheet with Cattaneo-Christov heat flux model," *Case Studies in Thermal Engineering*, **66**, 105706 (2024). <https://doi.org/10.1016/j.csite.2024.105706>
- [33] S.R. Mishra, I. Haq, R. Baithalu, S. Panda, and A. Saeed, "Transient radiative flow of hybrid nanofluid under slip effects over an impermeable spinning disk with porous material," *Partial Differential Equations in Applied Mathematics*, **14**, 101154 (2025). <https://doi.org/10.1016/j.padiff.2025.101154>
- [34] S.M. Sait, A. Riaz, S. Shaheen, R. Ellahi, and S. Akram, "Thermally induced cilia flow of Prandtl nanofluid under the influence of electroosmotic effects with boundary slip," *Journal of Taibah University for Science*, **19**, 2484877 (2025). <https://doi.org/10.1080/16583655.2025.2484877>
- [35] Y. Ouyang, Md. Faisal, Md. Basir, K. Naganthran, and I. Pop, "Exploring velocity slip and stability in unsteady ternary nanofluid flow past a permeable stretching/shrinking sheet," *Journal of Taibah University for Science*, **19**, 2487302 (2025). <https://doi.org/10.1080/16583655.2025.2487302>
- [36] B.K. Mahatha, R. Nandkeolyar, G. Nagaraju, and M. Das, "MHD stagnation point flow of a nanofluid with velocity slip, Non-linear radiation and Newtonian heating," *Procedia Engineering*, **127**, 1010-1017 (2015). <https://doi.org/10.1016/j.proeng.2015.11.450>

## ВПЛИВ ПРИРОДНОЇ КОНВЕКЦІЇ ТА ВИПРОМІНЮВАННЯ НА МГД-ТЕЧІЮ НАНОРІДИНИ В ТОЧЦІ ЗАСТОЮ, ЩО ПРОТІКАЄ ПОВЗ РОЗТЯГУВАНУ ПОВЕРХНЮ ІЗ ШВИДКІСИМ КОВЗАННЯМ І НЬЮТОНІВСЬКИМ НАГРІВАННЯМ

Г.П. Гіфті<sup>а</sup>, С.Б. Падхі<sup>а</sup>, Б.К. Махатха<sup>а</sup>, Г.К. Махато<sup>с</sup>

<sup>а</sup>Кафедра математики, Технологічний та менеджментний університет Центуріон, Одіша, Індія

<sup>б</sup>Середня школа Раджкіякрит +2, Латбедхва, Кодерма, Джаркханд, Індія





<sup>с</sup>Кафедра математики, Інститут прикладних наук Амїті, Університет Амїті, Джаркханд, Ранчі-835303, Індія

Досліджується природний конвекційний потік в'язкої, нестисливої, електропровідної та випромінюючої тепло нанорідини в точці застою МГД повз розтягвану поверхню з ковзанням за швидкістю та ньютонівським нагріванням у присутності поперечного магнітного поля. Розв'язуються відповідні нелінійні диференціальні рівняння в частинних похідних за допомогою методу `bvp4c` Matlab. Для підтвердження надійності та точності результату, числові результати цього дослідження порівнюються з існуючою літературою, і було виявлено, що вони добре узгоджуються. Вплив різних параметрів на швидкість, температуру та концентрацію речовин обчислюється та представляється у вигляді графіків, тоді як вплив тертя поверхні, швидкість теплопередачі та швидкість масопередачі зведено в таблиці. В результаті посиленого накопичення або дифузії теплової енергії температура нанорідини збільшується внаслідок броунівського руху, термофоретичної дифузії, швидкісного ковзання, конвективного нагрівання, нелінійного теплового випромінювання та числа Прандтля. Швидкість теплопередачі збільшується внаслідок співвідношення температур, конвективного нагрівання та теплового числа Грасгофа завдяки збільшенню теплових градієнтів та теплопередачі, зумовленої плавучістю. Такі потоки нанорідин мають потенціал для використання в низці процесів теплопередачі, таких як пристрої відновлюваної енергії, включаючи МГД-генератори, тощо.

**Ключові слова:** МГД; нанорідина; природна конвекція; випромінювання; швидкісне ковзання; ньютонівське нагрівання



## IMPACT OF COMBINED CHEMICAL REACTIONS AND THERMAL DISPERSION ON CONVECTIVE FLOW IN HYBRID NANOFLUID POROUS MEDIUM

 Zohra Terbiche<sup>a</sup>,  Hamza Ali Agha<sup>a,b,\*</sup>,  Soufiane Rahal<sup>a</sup>,  Nadir Boutalbi<sup>b</sup>

<sup>a</sup>Biomaterials and Transport Phenomena Laboratory (LBMP), Faculty of technology, University Yahia Fares of Medea, Pole Urbain Medea, 26000, Algeria

<sup>b</sup>Mechanic, Materials and Energetic Laboratory (L2ME), Faculty of technology, University A. MIRA of Bejaia, Targua Ouzmour Bejaia, 06000, Algeria

\*Corresponding author: [aliagha.hamza@univ-medea.dz](mailto:aliagha.hamza@univ-medea.dz)

Received May 1, 2025; revised May 26, 2025; in final form June 12, 2025; accepted June 19, 2025

The present study is characterized by numerical analysis concerning thermal dispersion's influence on heat and mass transfer flow towards a stretching plate in a saturated porous medium filled with Cu/Al<sub>2</sub>O<sub>3</sub>-water hybrid nanofluid, considering the presence of homogeneous (HOM)-heterogeneous (HET) chemical reactions. A new model of (HOM-HET) chemical reactions is constructed where the (HET) reactions occur on the surfaces of the solid matrix within the porous medium and the plate, following first-order kinetics. In contrast, the homogeneous (HOM) reaction takes place in the fluid phase and is described by isothermal cubic autocatalytic kinetics. The momentum, energy, and mass transfer phenomena are governed by a set of partial differential equations with appropriate similarity transformations that yield four coupled nonlinear ordinary differential equations. The resulting system of governing equations is solved numerically through a computationally efficient finite-difference scheme. The numerical results are validated through comparison with available data, showing good agreement. The numerical results demonstrate the influence of physical control parameters on the flow dynamics, thermal distribution, and solute concentration profiles. Furthermore, key solution characteristics, including the Nusselt number and skin friction coefficient, are tabulated.

**Keywords:** Hybrid nanofluid; Thermal dispersion; Stagnation-point flow; Porous medium

**PACS:** 47.11.-j, 63.20.D, 47.55.P, 44.30.+v

### Nomenclature

A, B	Chemical species	$K_c$	Homogeneous reaction parameter
$D_A, D_B$	Diffusion coefficients of species A and B, respectively	$K_s$	Heterogeneous reaction parameter
a, b	Concentration of chemical species A and B, respectively	$K_{cv}$	Surface-catalyzed parameter
$a_0, b_0$	Initial concentration of species A and B, respectively	$Sc$	Schmidt number
$c_p$	Specific heat at constant temperature	$Nu_x$	Local Nusselt number
$d$	Mean particle diameter	$Pr$	Prandtl number
$G, H$	Dimensionless concentrations of chemical species A and B	$Re_x$	Reynolds number
$K$	Permeability of the porous medium	$S$	Interfacial area
$K_1$	Parameter of the porous medium	$T$	Fluid temperature
$k_c$	Reaction rate constant of homogeneous reaction	$T_\infty$	Ambient temperature attained as $y$ tends to infinity
$k_s$	Reaction rate constant of homogeneous reaction	$U_w$	Stretching sheet velocity
$k_{hnf}$	Thermal conductivity of hybrid nanofluid	$U_\infty$	Free stream velocity
$k_f$	Thermal conductivity of pure water	$u, v$	Velocity components in the $x$ and $y$ directions
$k_{s1}$	Thermal conductivity of copper nanoparticle	$x, y$	Cartesian coordinates
$k_{s2}$	Thermal conductivity of alumina nanoparticle		

### Greek symbols

$\alpha_d$	Dispersion diffusivity	$\nu_{hnf}$	Kinematic viscosity of hybrid fluid
$\alpha_{eff}$	Effective thermal diffusivity	$\nu_f$	Kinematic viscosity of base fluid
$\alpha_{hnf}$	Molecular diffusivity of nanofluid	$\theta$	Dimensionless temperature
$\gamma$	Dispersion coefficient of the porous medium	$\rho$	Density
$\eta$	Similarity variable	$\psi$	Stream function.
$\lambda$	Positive constant	$\delta$	Ratio of the diffusion coefficient
$\mu_{hnf}$	Dynamic viscosity of the hybrid nanofluid	$\varepsilon$	Velocity ratio parameter

## INTRODUCTION

The interaction between nanofluid flow and heat/mass transfer through a porous medium is a multifaceted process governed by intricate fluid dynamics as well as thermal and mass transfer phenomena. The presence of nanoparticles such as metals, carbides, oxides, or carbon nanotubes in a base fluid such as water, ethylene glycol, oil, or toluene can affect the flow behavior, leading to changes in heat and mass transfer rates and patterns by increasing the thermal properties of the base fluid. Analysing heat and mass transfer characteristics in porous media filled with nanofluid is crucial for various engineering applications including heat exchangers, thermal management systems, enhanced energy recovery, geothermal energy extraction, and chemical engineering. Advanced computational modeling and experimental studies are employed



to analyze and optimize these processes for improved efficiency and performance in practical applications. Comprehensive reviews on nanofluid-saturated porous media have been conducted by Khanafer and Vafai [1], Vafai and coworkers [2,3], and by Nield and Bejan [4].

In addition, the convective flow of a nanofluid through a porous medium over stretching objects is widely studied by several researchers because of the importance of this phenomenon, which is prevalent in various engineering and environmental applications. In this context, Sowmiya and Kumar [5] discussed numerically the influence of magnetic field and thermal radiation in porous medium filled with Williamson nanofluid within a stretching cylinder. The objective of this study was to investigate the impact of rheological characteristics on flow behavior in a cylinder geometry. Khalil et al. [6] studied numerically ( $\text{Fe}_3\text{O}_4\text{-Cu}$ ) hybrid nanofluid flow in a porous medium over an exponentially stretching plate in presence of Joule heating and thermal radiation. Dulal Pal and Mandal [7] presented the effects of thermal radiation on mixed convection towards a stagnation-point flow over a moving plate in a porous medium with heat generation and viscous dissipation. This study revealed that the suction parameter reduces the dynamic behavior and temperature profiles in the stretching-sheet situation, whereas the opposite tendency arises in the shrinking-sheet case. Adigun et al. [8] discussed the magnetohydrodynamic (MHD) stagnation-point flow of a viscoelastic nanofluid past an inclined cylinder stretching linearly. Nandi et al. [9] explored the impact of nonlinear thermal radiation and heat generation on MHD stagnation point flow of nanofluid containing  $\text{Fe}_3\text{O}_4$ , Cu and Ag nanoparticles along a permeable stretching plate embedded in a porous medium. Asogwa et al. [10] examined the external thermal radiation effects on electromagnetohydrodynamic (EMHD) boundary layer flow of non-Newtonian nanofluid over reactive stretching surface, considering combined thermal transport properties. They found that the control parameters play an important role in modification of the dynamic, heat and mass behaviors.

Another level of complexity emerges in flow within porous media when dispersion mechanisms are taken into account. This complexity can manifest as significant thermal dispersion, wherein heat undergoes molecular diffusion as a result of mixing and recirculation of local fluid currents induced by the complicated flow paths through the porous medium. In this context, Kameswaran and Sibanda [11] investigate numerically via the shooting technique the effects of thermal dispersion on non-Newtonian power-law nanofluid flow over an impermeable vertical plate. From this work, the results reveal that under a constant thermal dispersion parameter, the thermal boundary layer thickness reduces with increasing power-law index values, a trend consistent in both aiding and opposing buoyancy situations. Bouaziz and Hanini [12] mainly explore thermal and solute dispersions in the simultaneous heat and mass transfer along a vertical plate immersed into a non-Darcy saturated porous medium with a Buongiorno nanofluid. Sheremet et al. [13] studied the effect of thermal dispersion on transient natural convection in a wavy-walled porous cavity using the Tiwari and Das nanofluid model. A numerical analysis was achieved by RamReddy and Venkata [14] to study the combined effects of double dispersion and the convective boundary condition on natural convection flow over vertical frustum of a cone in a nanofluid saturated non-Darcy porous medium. They take into account the Brownian motion and thermophoresis mechanisms. Sudhagar et al. [15] studied the impact of thermal dispersion on the mixed convective boundary layer nanofluid flow past over an isothermal vertical wedge implanted in a porous medium. They observed that the presence of thermal dispersion could affect fluid flow and temperature profiles. Awad et al. [16] investigate free convection nanofluid flow in a porous layer with double dispersion effects. They have use the Forchheimer extension for porous medium and Buongiorno nanofluid, which incorporates Brownian motion and thermophoresis parameters. Meena et al. [17] investigate mixed convection flow over a vertical cone in a saturated porous medium with the presence of thermal and solutal dispersion effects. Khashi'ie et al. [18] numerically analyze the mixed convection flow of  $\text{Cu-Al}_2\text{O}_3/\text{water}$  nanofluid along a vertical plate embedded in a porous medium under the presence of thermal dispersion. They take into consideration the assisting and opposing flows, and they found that in the opposing buoyancy region, dual solutions are expected, and the presence of nanoparticles and thermal dispersion can modify the dynamic and thermal behavior in the boundary layers.

Furthermore, chemically reactive flows in porous media have received increasing interest over the last three decades. The combined impact of homogeneous and heterogeneous reactions pertains to scenarios where both categories of reactions take occur simultaneously within a chemical or physical system. Homogeneous reactions take place in a single phase, typically the gas or liquid phase, while heterogeneous reactions involve interfaces between different phases, such as gas-solid or liquid-solid reactions. Understanding the interaction between these reactions is essential in various fields, including chemistry, chemical engineering, combustion and catalysis. The reactive transport is usually described by partial differential equations [19]. The first model describing the isothermal homogeneous-heterogeneous reactions in boundary layer flow of a viscous fluid was developed by Chaudhary and Merkin [20,21]. In this area of interest, Alzahrani et al. [22] investigate the thermal evaluation of viscoelastic nanofluid flow past a porous surface with a heat source/sink and the presence of homogeneous and heterogeneous reactions. They found that for higher values of homogeneous and heterogeneous reaction parameters, mass transfer is greater in fluid flow with aggregation conditions. Liu et al. [23] discussed the impact of catalytic homogeneous-heterogeneous reactions in a Darcy porous medium. They found that an increase in the interfacial area of porous media enhances the rate of surface-catalyzed reactions, thereby significantly shortening chemical reaction time. The influence of induced magnetic field on Darcy-Forchheimer nanofluid flows comprising carbon nanotubes with homogeneous-heterogeneous reactions was performed by Bashir et al. [24]. The goal of this study is to conduct a comparative analysis of Darcy-Forchheimer nanofluid flows containing CNTs of both multi-wall (MWCNTs) and single-wall carbon nanotubes (SWCNTs) immersed in two different base fluids over a stretched

surface. Irfan et al. [25] examined the interplay of coupled homogeneous-heterogeneous reactions and non-Fourier heat flux (Cattaneo-Christov model) in a non-Newtonian fluid with variable thermal conductivity. Their analysis revealed that the thermal relaxation parameter significantly modulates the temperature distribution, whereas the concentration profile demonstrates an inverse correlation between the Schmidt number and the homogeneous reaction parameter. The influence of nanoparticle aggregation on heat transfer phenomena of second grade nanofluid flow over melting surface subject to homogeneous-heterogeneous reactions was investigated by Sunthrayuth et al. [26]. They showed that higher mass transfer for fluid flow with aggregation condition is observed for increased values of heterogeneous and homogeneous reaction parameters. Abbas and Sheikh [27] studied numerically the stagnation point flow of ferrofluid over a flat plate with non-linear slip boundary condition in the presence of homogeneous-heterogeneous reactions. Hayat et al. [28] studied the phenomenon of melting heat transfer in the presence of homogeneous-heterogeneous reactions and a magnetic field in flow along a stretching surface with variable thickness.

In view of all the above-mentioned applications and from the literature context of study, it is observed that hybrid nanofluid reactive flow over a porous stretchable sheet in the presence of thermal dispersion has not yet been investigated. The purpose of the current paper is to emphasize the effects of thermal dispersion on Darcy convection boundary layer flow over a stretching plate in the presence of coupled homogeneous-heterogeneous reactions (H-H-R). Cu/Al<sub>2</sub>O<sub>3</sub> hybrid nanoparticles are used in the base fluid. The behavior of different profiles has been examined and displayed graphically. Moreover, the interesting features of the solutions in terms of the number of Nusselt and skin friction coefficient are calculated.

### PROBLEM STATEMENT

Consider a two-dimensional steady boundary layer flow over a stretching sheet in a laminar and incompressible nanofluid of constant ambient temperature  $T_\infty$ . In this study, a water-based nanofluid containing two types of nanoparticles Cu /Al<sub>2</sub>O<sub>3</sub> is used as working fluid. The nanoparticles are assumed to have a uniform shape and size. Figure 1 describes the physical model and the coordinate system, where the  $x$  and  $y$  axes are measured along the surface of the sheet and normal to it, respectively. The stretching velocity  $U_w(x)$  and the ambient fluid velocity,  $U_\infty(x)$ , is assumed to increase linearly from the stagnation point, i.e.,  $U_w(x) = \lambda x$  and  $U_w(x) = cx$ , where  $\lambda$  and  $c$  are constant with  $c > 0$ . We note that  $\lambda > 0$  correspond to stretching sheet.

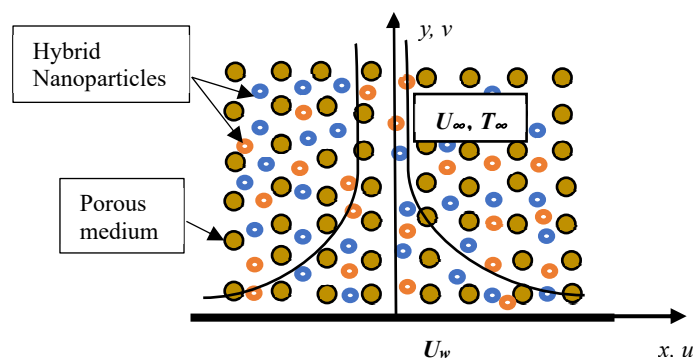


Figure 1. Physical Sketch of the model

It is supposed that the temperature at the surface,  $T_w$ , varies along the sheet and changes with position  $x$ . Additionally, the base fluid and nanoparticles are in thermal equilibrium, with no slip occurring between them.

The Darcy model is used to describe the reactive flow in porous medium, which contains a reactive species ( $A$ ) that reacts to form some product ( $B$ ) when in contact with the plate surface. In particular, the following two types of reactions are applied:

- An isothermal cubic autocatalytic reaction which takes place in the porous medium, this reaction is given schematically by  $A + 2B \rightarrow 3B$ ,  $rate = k_c ab^2$ .
- A single first-order exothermic catalytic reaction on the plate surface whereby reactant ( $A$ ) is converted to a product ( $B$ );  $A \rightarrow B$ ,  $rate = k_s a$

These two basic models are widely used by several researchers, for more details, see [20, 25].

Notably, the porous medium and stretching surface share the same catalytic material, enabling heterogeneous reactions to occur on the solid matrix of the porous medium. These surface-catalyzed reactions are governed by the kinetic model outlined in [23]  $r_p = -Sk_s$ .

The boundary layer equations, incorporating the momentum, energy, and mass equations, can be expressed in dimensional form as follows, according to the previously stated assumptions:

$$\frac{\partial u}{\partial x} + \frac{\partial v}{\partial y} = 0, \quad (1)$$

$$u \frac{\partial u}{\partial x} + v \frac{\partial u}{\partial y} = U_{\infty} \frac{dU_{\infty}}{dx} + \frac{\mu_{hnf}}{\rho_{hnf}} \frac{\partial^2 u}{\partial y^2} + \frac{\mu_{hnf}}{\rho_{hnf} K} (U_{\infty}(x) - u), \tag{2}$$

$$u \frac{\partial T}{\partial x} + v \frac{\partial T}{\partial y} = \frac{\partial}{\partial y} \left( \alpha_{eff} \frac{\partial T}{\partial y} \right), \tag{3}$$

$$u \frac{\partial a}{\partial x} + v \frac{\partial a}{\partial y} = D_A \frac{\partial^2 a}{\partial y^2} - k_c a b^2 - S k_s a, \tag{4}$$

$$u \frac{\partial b}{\partial x} + v \frac{\partial b}{\partial y} = D_B \frac{\partial^2 b}{\partial y^2} + k_c a b^2 + S k_s a. \tag{5}$$

Here  $x$  and  $y$  are distances along and perpendicular to the surface,  $u$  and  $v$  are the velocity components in the  $x$  and  $y$  directions, respectively.  $T$  is the temperature,  $K$  is permeability of porous medium,  $\mu_{hnf}$  is the viscosity of the hybrid nanofluid,  $\rho_{hnf}$  is the density of the hybrid nanofluid,  $\alpha_{eff}$  characterize the effective thermal diffusivity which is the sum of the molecular diffusivity  $\alpha_{mf}$  of hybrid nanofluid and the dispersion diffusivity  $\alpha_d$ , where  $\alpha_d = \gamma u d$ . Here  $\gamma$  is the thermal dispersion coefficient,  $u$  is stream-wise velocity and  $d$  denotes to the mean particle diameter. Note that, this model is valid for fluids and nanofluids as mentioned in [12, 18, 29, 30 and 31]. ( $D_A, D_B$ ) the diffusion species coefficients of reactant ( $A$ ) and product ( $B$ ), ( $a, b$ ) are the concentration of chemical species of ( $A$ ) and ( $B$ ), respectively.  $k_c$  and  $k_s$  denote the rate constants of homogeneous and heterogeneous reactions, respectively.  $S$  is the interfacial area of the porous media.

The correlations of the hybrid nanofluid are presented in Table 1, where  $s_1$  and  $s_2$  denotes the copper and alumina nanoparticles, respectively,  $\phi_1$  and  $\phi_2$  are the volumetric concentration of Cu and  $Al_2O_3$  nanoparticles, accordingly. In addition, the subscript  $f$  denotes the base fluid. In Table 1,  $\phi_{hnf} = \phi_1 + \phi_2$  where  $\phi_{hnf} = 0$  corresponds to a regular fluid (pure water). The thermophysical properties of the water and respective nanoparticles are detailed in Table 2.

The boundary conditions associated with the above problem are as follows:

$$u = U_w(x) = \lambda x; v = 0; T_w = T_{\infty} + w \left( \frac{x}{l} \right)^2; D_A \frac{\partial a}{\partial y} = -D_B \frac{\partial b}{\partial y} = k_s a; \text{ as } y = 0, \tag{6}$$

$$u = U_{\infty}(x) = cx; T \rightarrow T_{\infty}; a \rightarrow a_0; b \rightarrow 0 \text{ as } y \rightarrow \infty. \tag{7}$$

**Table 1.** The correlations of hybrid nanofluids (see Babu et al. [32] and Takabi and Salehi 33]).

Properties	Nanofluids
Density ( $\rho$ )	$\rho_{hnf} = (1 - \phi_{hnf}) \rho_f + \phi_1 \rho_{s1} + \phi_2 \rho_{s2}$
Capacity Heat ( $\rho c_p$ )	$(\rho c_p)_{hnf} = (1 - \phi_{hnf}) (\rho c_p)_f + \phi_1 (\rho c_p)_{s1} + \phi_2 (\rho c_p)_{s2}$
Dynamic Viscosity ( $\mu$ )	$\mu_{hnf} = \frac{\mu_f}{(1 - \phi_{hnf})^{2.5}}$
Thermal Conductivity ( $k$ )	$\frac{k_{hnf}}{k_f} = \frac{\left[ \left( \frac{\phi_1 k_{s1} + \phi_2 k_{s2}}{\phi_{hnf}} \right) + 2k_f + 2(\phi_1 k_{s1} + \phi_2 k_{s2}) - 2\phi_{hnf} k_f \right]}{\left[ \left( \frac{\phi_1 k_{s1} + \phi_2 k_{s2}}{\phi_{hnf}} \right) + 2k_f - (\phi_1 k_{s1} + \phi_2 k_{s2}) + \phi_{hnf} k_f \right]}$

**Table 2.** Thermophysical properties of water and nanoparticles (Oztop and Abu-Nada [34]).

Physical properties	Water	Cu	$Al_2O_3$
$c_p$ (J/kg K)	4179	385	765
$\rho$ (kg/m <sup>3</sup> )	997.1	8933	3970
$k$ (W/m.K)	0.613	400	40

The governing Eqs. (1-5) subject to the boundary conditions (6-7) can be expressed in a nondimensional form by introducing the following transformations [38] and [39]:

$$\eta = \left( \frac{c}{v_f} \right)^{\frac{1}{2}} y; \psi = (v_f c)^{\frac{1}{2}} x f(\eta); \theta(\eta) = \frac{T - T_{\infty}}{T_w - T_{\infty}}; G = \frac{a}{a_0}; H = \frac{b}{a_0}$$

$G$  and  $H$  are dimensionless concentrations of species (A) and (B), respectively.

$\psi$  is the stream function defined as  $u = \frac{\partial \psi}{\partial y}$ ;  $v = -\frac{\partial \psi}{\partial x}$ .

Equations (1–5) can be reduced to a set of ordinary differential equations by applying the similarity variables defined above.

$$f''' + K_1(1-f') + A_1(1+ff'' - f'^2) = 0 \quad (8)$$

$$\frac{k_{hmf}/k_f}{A_2} \theta'' + Ds(f'\theta')' + Pr(f\theta' - 2f'\theta) = 0 \quad (9)$$

$$\frac{1}{Sc} G'' - K_c GH^2 - K_{sv}G + fG' = 0 \quad (10)$$

$$\frac{\delta}{Sc} H'' + K_c GH^2 + K_{sv}G + fH' = 0 \quad (11)$$

Building on the work of Chaudhary and Merkin [20, 21], we consider a common practical situation where the diffusion coefficients  $D_A$  and  $D_B$  for chemical species (A) and (B) are of similar magnitude and size. Consequently, we assume  $D_A = D_B$ , leading to  $\delta = 1$ . Under this assumption, the following relation is obtained:

$$G(\eta) + H(\eta) = 1 \quad (12)$$

Equations (10) and (11) under this assumption reduce to:

$$\frac{1}{Sc} G'' - K_c G(1-G)^2 - K_{sv}G + fG' = 0 \quad (13)$$

Given the boundary conditions (6–7), which are now written as:

$$f = 0; f' = \varepsilon; \theta = 1; G' = K_s G; \delta H' = K_s G \quad \text{as } \eta = 0 \quad (14)$$

$$f' \rightarrow 1; \theta \rightarrow 0; G \rightarrow 1; H \rightarrow 0 \quad \text{as } \eta \rightarrow \infty. \quad (15)$$

In the equations above,  $K_1$  porous medium parameter, Thermal dispersion parameter, Prandtl number,  $\varepsilon$  is the velocity ratio parameter,  $K_c$ ,  $K_s$  are the homogeneous and heterogeneous reaction parameter, respectively.  $K_{sv}$  represent the surface-catalyzed parameter,  $\delta$  is the ratio of diffusion coefficients, the Schmidt number  $Sc$ .

$$K_1 = \frac{v_f}{Kc}; Ds = \frac{\gamma d U_\infty}{\alpha_f}; Pr = \frac{v_f}{\alpha_f}; \varepsilon = \frac{c}{\lambda}; K_c = \frac{k_c a_0^2}{c}; K_s = \left(\frac{v_f}{c}\right)^{\frac{1}{2}} \frac{k_s}{D_A}; K_{sv} = S_v K_s; Sc = \frac{v_f}{D_A} S_v = \frac{SD_A}{(c\nu)^{\frac{1}{2}}}, \delta = \frac{D_B}{D_A},$$

$$A_1 = (1 - \phi_{hmf})^{2.5} \left( (1 - \phi_{hmf}) + \phi_1 \frac{\rho_{s1}}{\rho_f} + \phi_2 \frac{\rho_{s2}}{\rho_f} \right), A_2 = \left( (1 - \phi_{hmf}) + \phi_1 \frac{(\rho c_p)_{s1}}{(\rho c_p)_f} + \phi_2 \frac{(\rho c_p)_{s2}}{(\rho c_p)_f} \right)$$

The physical quantities of interest are the skin friction coefficient  $C_f$  and the local Nusselt number  $Nu_x$ , which are defined as:

$$C_f = \frac{\mu_{hmf}}{\rho_f U_\infty^2} \left( \frac{\partial u}{\partial y} \right)_{y=0}; \quad Nu_x = \frac{x k_{hmf}}{k_f (T_w - T_\infty)} \left( -\frac{\partial T}{\partial y} \right)_{y=0}$$

With  $\mu_{hmf}$  and  $k_{hmf}$  being the dynamic viscosity and thermal conductivity of the nanofluids, respectively. Applying the similarity transformations, we obtain:

$$Re_x^{1/2} C_f = \frac{1}{(1 - \phi_{hmf})^{2.5}} f''(0) \quad (16)$$

$$Re_x^{-1/2} Nu_x = -\frac{k_{hmf}}{k_f} \theta'(0) \quad (17)$$

## RESULTS AND DISCUSSIONS

The governing ordinary differential equations (8, 9, and 13), along with the boundary conditions (14–15), were numerically solved using the finite difference scheme implemented through the bvp4c package in Matlab. This package

utilizes the three-stage Lobatto collocation formula, ensuring a continuous solution with fourth-order accuracy. Mesh selection and error control are determined based on the residual of the continuous solution. This method has proven successful in numerous research endeavors as [35] and [36]. For further insights, refer to [37].

In order to verify the accuracy of our present technique, we have compared obtained numerical solutions, through the skin friction coefficient and local Nusselt number for the case where the stretched surface is isothermal and without thermal dispersion effects. From the table 3, it is seen that the present results are in excellent agreement with both results presented by Bachok [38], Nandkeolyar et al. [39] and Yacob et al. [40].

**Table 3.** Values of  $Re_x^{-1/2} Nu_x$  and  $Re_x^{1/2} Cf$  for some values of  $\phi_1, \phi_2$  and  $\epsilon$

		(Cu-water)					
		Bachok [38].		Nandkeolyar et al. [39].		Present work	
$\epsilon$	$\phi_1$	$Re_x^{1/2} Cf$	$Nu_x Re_x^{-1/2}$	$Re_x^{1/2} Cf$	$Nu_x Re_x^{-1/2}$	$Re_x^{1/2} Cf$	$Nu_x Re_x^{-1/2}$
0	0.1	1.8843	1.4043	1.8832	1.404329	1.884323	1.404327
	0.2	2.6226	1.6692	2.6227	1.669343	2.622743	1.669337
0.5	0.1	1.0904	1.8724	1.0904	1.872389	1.090452	1.872386
	0.2	1.5177	2.1377	1.5177	2.157696	1.517773	2.157690
		(Al <sub>2</sub> O <sub>3</sub> -water)					
		Bachok [38].		Yacob et al. [40].		Present work	
$\epsilon$	$\phi_2$	$Re_x^{1/2} Cf$	$Nu_x Re_x^{-1/2}$	$Re_x^{1/2} Cf$	$Nu_x Re_x^{-1/2}$	$Re_x^{1/2} Cf$	$Nu_x Re_x^{-1/2}$
0	0.1	1.6019	1.3305	1.6019	1.3305	1.6020	1.3305
	0.2	2.0584	1.5352	2.0584	1.5352	2.0584	1.5352
0.5	0.1	0.9271	1.8278	-	-	0.9270	1.8279
	0.2	1.1912	2.0700	-	-	1.1912	2.0700

The parametric study results reported in this section are displayed using graphical illustrations to highlight the effect of several parameters such as  $K_1, D_s, K_c, K_{sv}, K_s, \phi_1, \phi_2$  as well as stretching parameter  $\epsilon$  on velocity, temperature, and concentration. Numerical computations are done for  $0.5 \leq K_1 \leq 4.0; 0.0 \leq D_s \leq 3.0; 0.05 \leq \phi_1, \phi_2 \leq 0.09; 0.5 \leq K_c \leq 1.5; 0.0 \leq K_s \leq 5; 0.1 \leq K_{sv} \leq 0.5; 0.5 \leq \epsilon \leq 4.0$ .

The variation of non-dimensional velocity distribution against the similarity variable  $\eta$  is shown respectively in Figure 2 for a few sets of values of  $\epsilon$  and  $K_1$ .

Figure 2 depicts the dynamic behavior of axial velocity for different values of  $K_1$  and  $\epsilon$ . The curves corresponding to various values of  $\epsilon$  exhibit a slight vertical shift for a given  $K_1$ . From this figure, as the porous medium parameter increases, the velocity decreases and consequently the dynamic boundary layer becomes thicker. This effect physically is due to the enhanced resistance imposed by the porous medium in term of permeability on the fluid flow. Additionally, the presence of nanoparticles in a nanofluid can also influence flow through porous media, potentially leading to changes in permeability due to particle interactions with the pore walls or the formation of particle bridges. The same tendency was observed by Kameswaran et al. [41] for single nanoparticles (Al<sub>2</sub>O<sub>3</sub> / water) nanofluids. Furthermore, a higher stretching parameter promotes faster flow and results in a larger momentum boundary layer.

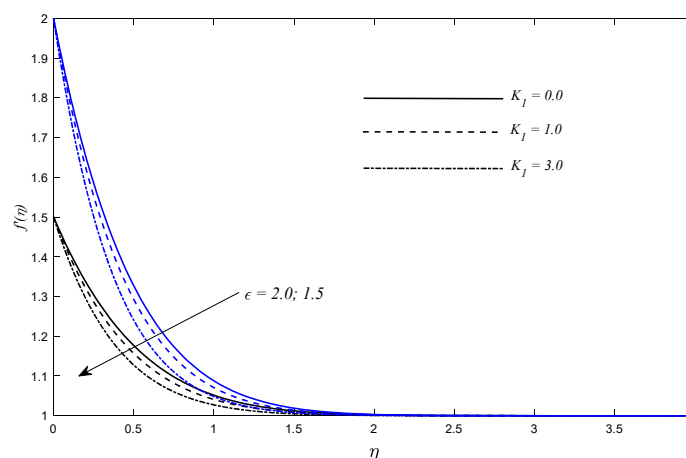


**Figure 2.** Variation of velocity profiles with  $\eta$ , for varying  $\epsilon$  and  $K_1$  ( $D_s = 1.0, Pr = 6.2, K_c = K_s = 0.5, Sc = 1.0, K_{sv} = 0.1, \phi_1 = \phi_2 = 0.02$ )

The temperature distributions against the space variable  $\eta$  are demonstrated in Figure 3 for some values of thermal dispersion  $D_s$  and stretching parameter  $\epsilon$ . A notable observation from this figure is that the temperature profiles gradually

approach zero as the distance from the boundary increases, ensuring compliance with the boundary conditions. An analysis of this figure reveals that the temperature profiles increase in direct proportion to the thermal dispersion parameter. In addition, the increasing in thermal dispersion term leads to enhance the thermal boundary layer thickness. These outcomes are subjectively like those got by Sudhagar et al. [15] on account of a Buongiorno nanofluid. The effect of thermal dispersion increases the temperature, bringing about surpassing flow rates at the surface. This is in agreement with the expected physical behavior. Besides, the augmentation in stretching parameter leads to reduction in the dimensionless temperature.

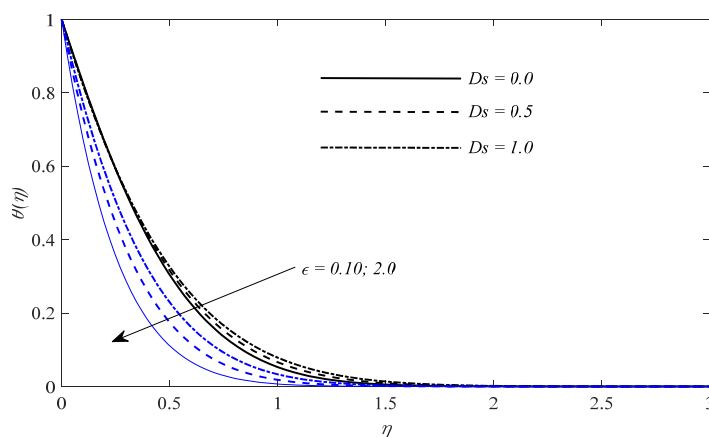


**Figure 3.** Variation of temperature profiles with  $\eta$ , for varying  $\epsilon$  and  $D_s$

( $K_1=1.0$ ;  $K_c = K_s = 0.5$ ,  $Sc=1.0$ ,  $K_{sv}=0.1$ ,  $\phi_1=\phi_2=0.1$ )

The numerical results for the mass transport of chemical species (A) are presented in Figures 4-6 for different values of some governing parameters, namely  $K_c$ ,  $K_{sv}$  and  $K_s$ . Figure 4 represents the effects of the parameter surface-catalyzed  $K_{sv}$  and homogeneous reaction parameters  $K_c$  on the dimensionless concentration  $G(\eta)$ . The numerical results show that an improvement in  $K_{sv}$  and  $K_c$  reduces the concentration, causing the mass boundary layer becomes to thicken. Physically, when the reaction interface on solid matrix of the porous medium augment, the catalyzed reaction accelerates and the concentration of species (A) reaches its lowest a fixed position  $\eta$  gradually. Liu et al. observed the similar results for  $Al_2O_3$ -water nanofluid (see [23]). The impact of both the stretching parameter and the heterogeneous reaction parameter is displayed in Figure 5.

From this figure, it is observed that for  $\epsilon = 0.1$  the concentration of the species (A) is lower compared to the concentration when  $\epsilon = 3.0$  at ( $\eta = 0$ ) which means that when the stretching velocity is slow, the reaction on the sheet becomes faster. In addition, the augmentation in  $K_s$  promotes the catalytic reaction at the surface of the sheet. Consequently, the mass transfer becomes more important, and the boundary layer becomes thicker. Figure 6 illustrates the influence of the combined effect of  $K_c$ ,  $K_{sv}$ , and  $K_s$  on the decay of the concentration profile when the spatial variable ( $\eta$ ) is equal to zero. It is observed that an increase in homogeneous and heterogeneous reaction parameters leads to a decrease in the concentration of species and the mass transfer rate to the plate. Furthermore, it is observed that the concentration at the surface decreases as the strength of the HOM-HET reactions increases. It is worth noting that the surface catalytic parameter has a significant influence on the surface concentration. The intense surface catalytic reaction on porous media leads to a lower wall concentration.

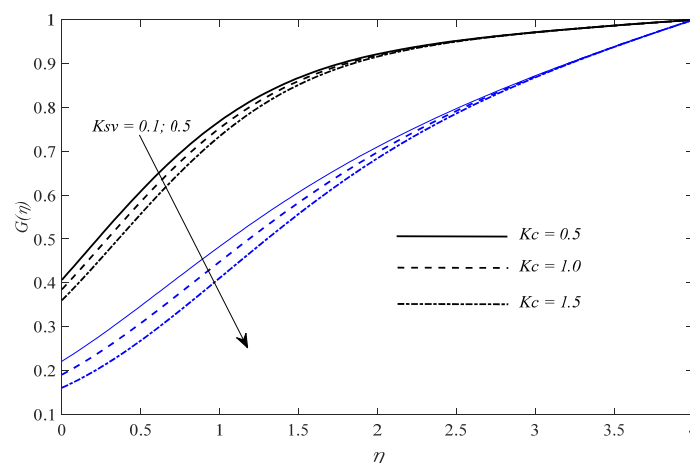


**Figure 4.** Effect of  $K_{sv}$  and  $K_c$  on the concentration profiles.

( $K_1 = 1.0$ ,  $D_s = 1.0$ ,  $Pr = 6.2$ ,  $Sc = 1.0$ ,  $\phi_1 = \phi_2 = 0.05$ ).



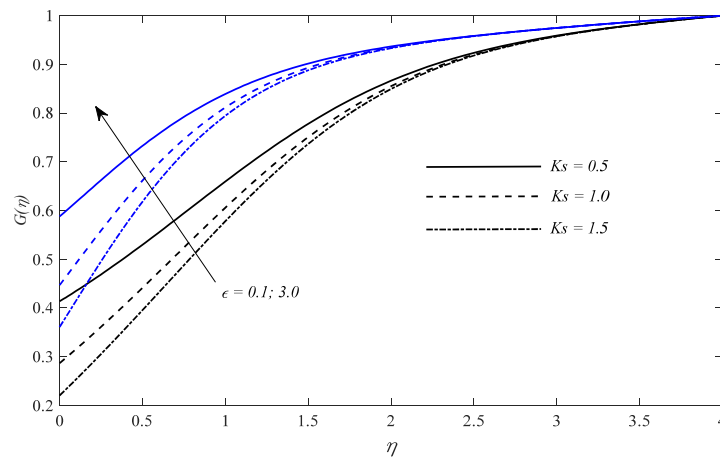


**Figure 5.** Effect of  $K_s$  and  $\epsilon$  on the concentration profiles. ( $K_1 = 1.0$ ,  $D_s = 1.0$ ,  $Pr = 6.2$ ,  $K_c = 0.5$ ,  $Sc = 1.0$ ,  $K_{sv} = 0.1$ ,  $\phi_1 = \phi_2 = 0.05$ ).

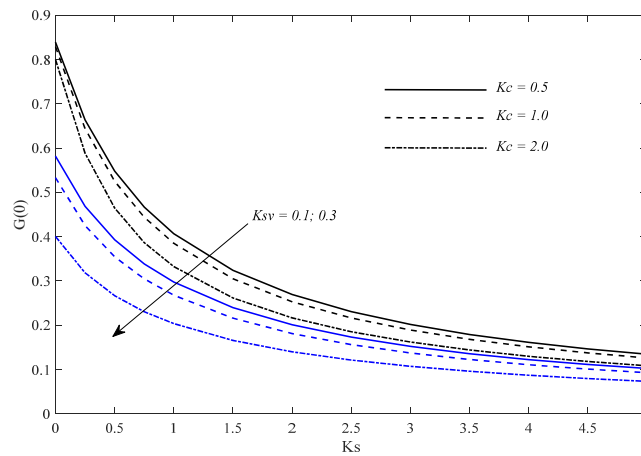


**Figure 6.** Effect of  $K_{sv}$ ,  $K_c$  and  $K_s$  on the concentration profiles  $G(0)$  ( $K_1 = 1.0$ ,  $D_s = 1.0$ ,  $Pr = 6.2$ ,  $Sc = 1.0$ ,  $\phi_1 = \phi_2 = 0.05$ ;  $\epsilon = 2$ )

The effects of increase in the values of  $\epsilon$ ,  $\phi_1$ ,  $\phi_2$ ,  $K_1$ , and  $D_s$  on the skin friction, which is proportional  $f''(0)$ , and the Nusselt number which measures the rate of heat transfer at the plate and can be measured as a variation in  $\theta''(0)$  as mentioned in Eqs (16 and 17). Some values of these interest quantities are calculated in Table 4.

**Table 4.** Values of  $Re_x^{-1/2} Nu_x$  and  $Re_x^{1/2} C_f$  for selected values of parameters.  $K_c = K_s = 1.0$ ,  $K_{sv} = 0.10$ ,  $Sc = 0.5$ .

$\epsilon$	$\phi_1 = \phi_2$	$K_1$	$D_s$	$Re_x^{1/2} C_f$	$Re_x^{-1/2} Nu_x$
0.5	0.05	1.0	1.0	0.6507	1.7270
1.5	-	-	-	-0.6507	1.7040
2.0	-	-	-	-1.3013	1.6835
4.0	-	-	-	-3.9040	1.5925
2	0.01	1.0	1.0	-2.2333	1.4151
-	0.05	-	-	-2.5974	1.6835
-	0.07	-	-	-2.7600	1.8294
-	0.09	-	-	-2.9116	1.9841
2	0.05	0.5	1.0	-2.4716	1.6936
-	-	1.0	-	-2.5974	1.6835
-	-	2.0	-	-2.8331	1.6654
-	-	4.0	-	-3.2551	1.6359
2	0.05	1.0	0.0	-2.5874	2.9281
-	-	-	0.5	-2.5874	2.0904
-	-	-	1.0	-2.5874	1.6835
-	-	-	3.0	-2.5874	1.0403

It can be seen the augmentation in the stretching parameter and volume fraction of the hybrid of nanoparticles leads to enhance the heat exchange between the surface of plate and the fluid on porous medium. This augmentation is due to

presence of nanoparticles, which include a higher thermal conductivity as compared with clear nanofluid ( $\phi_1 = \phi_2 = 0$ ). On the other hand, when the thermal dispersion and porous medium parameter rise up the heat transfer rate decrease. Regarding the skin friction coefficient, it can be observed that the presence on nanoparticles can ameliorate the skin friction. Whereas, the stretching velocity speed up the friction coefficient decrease. The same tendency observed for porous medium parameter. Physically, this effect is due to the presence of hybrid nanoparticles, which gives a higher drag force in opposition to the flow in porous medium.

### CONCLUDING REMARKS

In this work, we studied the impact of thermal dispersion under the presence of coupled homogeneous-heterogeneous reactions on a convective flow through a porous medium filled by hybrid nanofluid. Copper (Cu) and aluminum oxide ( $Al_2O_3$ ) were taken as nanoparticles and water as the base fluid. We used the Darcy model in the momentum equation and we supposed non-uniform boundary conditions in term of temperature and velocity. The partial differential equations are converted into ordinary differential equations applying appropriate similarity transformations. Validated by some results shown in the literature. The important results of this parametric study are summarized below:

- The presence of thermal dispersion plays a significant role in the modification temperature field and heat transfer rate.
- The homogeneous and heterogeneous reactions parameters cause a decrease in the species concentration and the rate of mass transfer at the plate.
- The presence of porous medium parameter leads to decrease the velocity near the plate and the local Nusselt Number.
- The presence of hybrid nanoparticles in working fluid enhance the both of skin friction coefficient and the heat transfer rate.
- The changing in the stretching parameter leads to improve the dynamic behavior and the heat transport near the sheet.

### ORCID

• Zohra Terbiche, <https://orcid.org/0009-0000-5241-326X>; • Hamza Ali Agha, <https://orcid.org/0009-0002-2152-886X>  
 • Soufiane Rahal, <https://orcid.org/0000-0002-3252-8921>; • Nadir Boutalbi, <https://orcid.org/0009-0000-0382-5671>

### REFERENCES

- [1] K. Khanafer and K. Vafai, *J. Therm. Anal. Calorim.* **135**, 1479 (2019). <https://doi.org/10.1007/s10973-018-7565-4>
- [2] K. Vafai, *Handbook of porous media*, third Ed., (CRC Press, New York, 2015). <https://doi.org/10.1201/b18614>
- [3] Y. Mahmoudi, K. Hooman and K. Vafai, *Convective Heat Transfer in Porous Media*, first Ed., (CRC Press, New York, 2019). <https://doi.org/10.1201/9780429020261>
- [4] D.A. Nield and A. Bejan, *Convection in Porous Media*, fifth Ed., (Springer, New York, 2017). <https://doi.org/10.1007/978-3-319-49562-0>
- [5] C. Sowmiya and B.R. Kumar, *Therm. Sci. Eng. Prog.* **53**, 102772 (2024). <https://doi.org/10.1016/j.tsep.2024.102772>
- [6] S. Khalil, T. Abbas and R. Nawaz, *Nano-Struct. Nano-Objects*, **40**, 101350 (2024). <https://doi.org/10.1016/j.nanoso.2024.101350>
- [7] D. Pal, and G. Mandal, *J. Pet. Sci. Eng.* **126**, 16 (2015). <https://doi.org/10.1016/j.petrol.2014.12.006>
- [8] J.A. Adigun, A. Adeniyani and I.O. Abial, *Int. Commun. Heat Mass Transfer*, **126**, 105479 (2021). <https://doi.org/10.1016/j.icheatmasstransfer.2021.105479>
- [9] S. Nandi, B. Kumbhakar, and S. Sarkar, *Int. Commun. Heat Mass Transfer*, **130**, 105791 (2022). <https://doi.org/10.1016/j.icheatmasstransfer.2021.105791>
- [10] K.K. Asogwa, B.S. Goud, Y.D. Reddy and A.A. Ibe, *Results Eng.* **15**, 100518 (2022). <https://doi.org/10.1016/j.rineng.2022.100518>
- [11] P.K. Kameswaran, P. Sibanda, *Bound. Value Probl.* 2013 (2013) 1-12. <https://doi.org/10.1186/1687-2770-2013-243>
- [12] A.M. Bouaziz, S. Hanini, *J. Mech.* **32** (2016) 441 – 451. <https://doi.org/10.1017/jmech.2016.18>
- [13] M.A. Sheremet, I. Pop, and N. Bachok, *Int. J. Heat Mass Transfer* **92**, 1053 (2016). <https://doi.org/10.1016/j.ijheatmasstransfer.2015.09.071>
- [14] Ch. RamReddy and Ch. Venkata Rao, *Nonlinear Eng.* **6**, 277 (2017). <https://doi.org/10.1515/nleng-2016-0071>
- [15] P. Sudhagar, P.K. Kameswaran, and B.R. Kumar, *J. Porous Media*, **23**, 923 (2020). <https://doi.org/10.1615/JPorMedia.2020024874>
- [16] F.G. Awad, P. Sibanda and P.V.S.N. Murthy, *ASME J. Heat Mass Transfer*, **137**, 104501 (2015). <https://doi.org/10.1115/1.4024895>
- [17] Om P. Meena, P. Janapatla and G. Kumar, *Appl. Math. Comput.* **430**, 127072 (2022). <https://doi.org/10.1016/j.amc.2022.127072>
- [18] N.S. Khashi'ie, N.Md. Arifin, and I. Pop, *Int. Commun. Heat Mass Transfer*, **118**, 104866 (2020). <https://doi.org/10.1016/j.icheatmasstransfer.2020.104866>
- [19] X. Song, L.D. Schmidt and R. Aris, *Chem. Eng. Sci.* **46**, 1203 (1991). [https://doi.org/10.1016/0009-2509\(91\)85049-4](https://doi.org/10.1016/0009-2509(91)85049-4)
- [20] M.A. Chaudhary, and J.H. Merkin, *Fluid Dyn. Res.* **16**, 311 (1995). [https://doi.org/10.1016/01695983\(95\)00015-6](https://doi.org/10.1016/01695983(95)00015-6)
- [21] J.H. Merkin, *Math. Comput. Model. Dyn.* **24**, 125 (1996). [https://doi.org/10.1016/08957177\(96\)00145-8](https://doi.org/10.1016/08957177(96)00145-8)
- [22] F. Alzahrani, R.J.P. Gowda, R.N. Kumar, and M.I. Khan, *J. Indian Chem. Soc.* **99**, 100458 (2022). <https://doi.org/10.1016/j.jics.2022.100458>
- [23] Ch. Liu, M. Pan, L. Zheng and P. Lin, *Int. Commun. Heat Mass Transfer*, **110**, 104434 (2020). <https://doi.org/10.1016/j.icheatmasstransfer.2019.104434>
- [24] S. Bashir, I.M. Almanjahie, M. Ramzan, A.N. Cheema, M. Akhtar and F. Alshahrani, *Heliyon*, **10**, e24718 (2024). <https://doi.org/10.1016/j.heliyon.2024.e24718>
- [25] M. Irfan, M. Khan and W.A. Khan, *J. Braz. Soc. Mech. Sci. Eng.* **41**, 135 (2019). <https://doi.org/10.1007/s40430-019-1619-9>

- [26] P. Sunthrayuth, S.A. Abdelmohsen, M.B. Rekha, K.R. Raghunatha, A.M. Abdelbacki, M.R. Gorji and B.C. Prasannakumara, *Case Stud. Therm. Eng.* **32**, 32101897 (2022). <https://doi.org/10.1016/j.csite.2022.101897>
- [27] Z. Abbas and M. Sheikh, *Chin. J. Chem. Eng.* **25**, 11 (2017). <https://doi.org/10.1016/j.cjche.2016.05.019>
- [28] T. Hayat, M.I. Khan, A. Alsaedi and M.I. Khan, *J. Mol. Liq.* **223**, 960 (2016). <https://doi.org/10.1016/j.molliq.2016.09.019>
- [29] O. Plumb, in: *Proc. First ASME/JSME Thermal Engineering Joint Conference 2*, (Honolulu, HI, USA, 1983), pp. 17–21.
- [30] J.T. Hong and C.L. Tien, *Int. J. Heat Mass Transfer*, **30**, 143 (1987). [https://doi.org/10.1016/0017-9310\(87\)90067-6](https://doi.org/10.1016/0017-9310(87)90067-6)
- [31] S. Yagi, D. Kunii and K. Endo, *Int. J. Heat Mass Transfer*, **7**, 333 (1964). [https://doi.org/10.1016/0017-9310\(64\)90109-7](https://doi.org/10.1016/0017-9310(64)90109-7)
- [32] J.R. Babu, K.K. Kumar and S.S. Rao, *Renewable Sustainable Energy Rev.* **77**, 551 (2017). <https://doi.org/10.1016/j.rser.2017.04.040>
- [33] B. Takabi and S. Salehi, *Adv. Mech. Eng.* **6**, 147059 (2014). <https://doi.org/10.1155/2014/147059>
- [34] H.F. Oztop and E. Abu-Nada, *Int. J. Heat Fluid Flow*, **29**, 1326 (2008). <https://doi.org/10.1016/j.ijheatfluidflow.2008.04.009>
- [35] H. Ali Agha, M.N. Bouaziz and S. Hanini, *J. Mech.* **31**, 607 (2015). <https://doi.org/10.1017/jmech.2015.28>
- [36] M. Hussain, A. Ali, S.W. Yao, A. Ghaffar, and M. Inc, *Case Stud. Therm. Eng.* **31**, 101809 (2022). <https://doi.org/10.1016/j.csite.2022.101809>
- [37] L. Shampine, I. Gladwell, and S. Thompson, *Solving ODEs with matlab*, first Ed., (Cambridge University Press, United Kingdom, 2003). <https://doi.org/10.1017/S0025557200178088>
- [38] N. Bachok, A. Ishak and I. Pop, *Nanoscale Res. Lett.* **6**, 623 (2011). <https://doi.org/10.1186/1556-276X-6-623>
- [39] R. Nandkeolyar, S.S. Motsa and P. Sibanda, *J. Nanotechnol. Eng. Med.* **4**, 041002 (2013). <https://doi.org/10.1115/1.4027435>
- [40] N.A. Yacob, A. Ishak and I. Pop, *Int. J. Thermal. Sci.* **50**, 133 (2011). <https://doi.org/10.1016/j.ijthermalsci.2010.10.008>
- [41] P.K. Kameswaran, S. Shaw, P. Sibanda and P.V.S.N. Murthy, *Int. J. Heat Mass Transfer*, **57**, 465 (2013). <https://doi.org/10.1016/j.ijheatmasstransfer.2012.10.047>

### ВПЛИВ КОМБІНОВАНИХ ХІМІЧНИХ РЕАКЦІЙ ТА ТЕПЛОВОЇ ДИСПЕРСІЇ НА КОНВЕКТИВНИЙ ПОТІК У ПОРИСТОМУ СЕРЕДОВИЩІ З ГІБРИДНОЮ НАНОРІДИНОЮ

Зохра Тербіше<sup>a</sup>, Хамза Алі Ага<sup>a,b</sup>, Суфіан Рахал<sup>a</sup>, Надір Бутальбі<sup>b</sup>

<sup>a</sup>Лабораторія біоматеріалів та явищ переносу (ЛВМРТ), Технологічний факультет, Університет Яхія Фарес Медейський, Поле Урбен Медейський, 26000, Алжир

<sup>b</sup>Лабораторія механіки, матеріалів та енергетики (L2ME), Технологічний факультет, Університет А. МіРА з Беджаї, Таргуа Узмур Беджая, 06000, Алжир

Це дослідження характеризується чисельним аналізом впливу теплової дисперсії на потік тепло- та масопереносу до розтягнутої пластини в насиченому пористому середовищі, заповненому гібридною нанорідиною Cu/Al<sub>2</sub>O<sub>3</sub>-вода, враховуючи наявність гомогенних (НОМ)-гетерогенних (НЕТ) хімічних реакцій. Побудовано нову модель хімічних реакцій (НОМ-НЕТ), де реакції (НЕТ) відбуваються на поверхнях твердої матриці в пористому середовищі та пластині, дотримуючись кінетики першого порядку. На відміну від цього, гомогенна реакція (НОМ) відбувається в рідкій фазі та описується ізотермічною кубічною автокаталітичною кінетикою. Явища імпульсу, енергії та масопереносу визначаються набором диференціальних рівнянь з частинними похідними з відповідними перетвореннями подібності, які дають чотири зв'язані нелінійні звичайні диференціальні рівняння. Отримана система рівнянь, що визначає, розв'язується чисельно за допомогою обчислювально ефективною схеми скінченних різниць. Числові результати перевірено шляхом порівняння з наявними даними, що показує хорошу узгодженість. Числові результати демонструють вплив фізичних параметрів керування на динаміку потоку, розподіл тепла та профілі концентрації розчинених речовин. Крім того, ключові характеристики розчину, включаючи число Нуссельта та коефіцієнт тертя поверхні, зведені в таблиці.

**Ключові слова:** гібридна нанорідина; термічна дисперсія; потік у точці застою; пористе середовище

## TWO-PHASE INCLINED MHD BLOOD FLOW IN POROUS TUMOR REGION WITH CONCENTRATION AND VOLUME FRACTION

 **D. Kumar<sup>a\*</sup>**,  **M. Garvandha<sup>a</sup>**, **S. Kumar<sup>b</sup>**, **N. Deo<sup>c</sup>**

<sup>a</sup>*Department of Computer and Information Science, University of Technology and Applied Sciences-Shinas, Oman*

<sup>b</sup>*Dr. Bhimrao Ambedkar University, Agra, India*

<sup>c</sup>*Oncology Unit, Synergy Hospital, Agra, India*

\*Corresponding Author e-mail: [devendra.kumar@utas.edu.om](mailto:devendra.kumar@utas.edu.om)

Received May 5, 2025; revised June 20, 2025; accepted July 7, 2025

There are different approaches for treating invasive and non-invasive tumors. The flowing fluid (blood) provides the required nutrients to the tumors and absorbs the suspensions. Drug delivery systems are dependent on the medium (flowing fluid) that carries the drugs. The blood vessels usually carry drugs to the targeted regions that treat the affected region. This situation varies the concentration of the tumor surrounding the medium. The system is monitored under a magnetic field that is applied at an angle ( $0 < \alpha < 90$ ). The system of the blood flow surrounding a tumor is governed by partial differential equations (PDEs). The Governing equations are solved using the mathematical function PDEPE in MATLAB. The effects of different parameters, concentration parameters, inclined magnetic field, porosity, on fluid (blood) velocity, and medication (drug) velocity in the presence of volume fraction. Flow patterns so obtained show significant effects that help to treat the deceased regions clinically. The numerical results are interpreted through the graphs drawn.

**Keywords:** *Two-Phase Inclined MHD Blood Flow; Porous Tumor Regions; Concentration; Volume Fraction*

**PACS:** 02.30.Jr, 47.56.+r, 52.65.Kj, 47.70.Fw

### INTRODUCTION

Cancer in the present is a big threat to the whole society, as this is the only cause of death compared to HIV, TB, and Malaria altogether. The cancer region (tumor region) is treated using different therapies like radiotherapy, immunotherapy, chemotherapy, and targeted therapy. There are ways to send the drugs, like external agents (medicines/drug particles) through the drug carriers, like blood flow. Life expectancy is very unpredictable due to huge deaths from cancer, heart attacks, and many other diseases, even after a massive development in medical science. This challenge is mounting day by day, so the required services and infrastructure are needed more [1]. Several deaths are predicted due to the late detection of tumors, which are fed by the flowing fluid (blood-carrying suspensions) surrounding the tumor spheroids. Surrounding the tumor spheroids multiphase fluid flow system occurs. Tumors are found at the apex of bifurcation in bifurcated arteries. The volume fraction is the space occupied by each phase, and the laws of conservation of mass and momentum are satisfied by each phase individually.

Plenty of researchers have tried to contribute to the understanding of the Two-phase flow behavior of fluid. Singh and Singh [2] studied a fluid suspended with dust particles. Heat and mass transfer effects were seen in the presence of volume fraction along with a magnetic field applied normally to the flow channel. Byrne and King [3] studied two-phase solid tumor growth. Bogdanov et al. [4] investigated two-phase flow through porous media. Prakash et al. [5] investigated the blood flow behavior in bifurcated arteries. The authors applied an external heat source to the flowing system. The authors provided the blood flow variations in the presence of different parameters. Chaudhary et al. [6], Abbas et al. [7], and Madhura and Shweta [8] provided their investigations on two-phase studies with volume fractions. Volume fractions play a vital role when fluid flows through porous media. There are pores in a medium that absorb the suspension-like drug, which is carried by blood in case of flow through the tumor spheroids. That enhances the size of the tumor. Chen et al. [9] used positron emission tomography to understand tumor permeability and blood flow transactions. Thulborn et al. [10] studied the view of chemoradiation, the number of drugs used during chemotherapy, tumor cell volume, and amount of cell killing volume. Thus, further studies of volume fraction along with heat stress create significant scope in tumor studies. Wirthl et al. [11] and Bera et al. [12] examined tumor development under the multiphase system. Flowing fluids carrying the nanoparticle suspension. The magnetic field is applied under thermal conditions. Kumar et al. [13] studied blood flowing through the apex of a bifurcated artery with a tumor. The amount of drug is applied that creates chemical reactions, and this supports tumor treatments. Heat transfer is applied where an inclined magnetic field supports the study.

Darvishi et al. [14] provided a cost-effective drug delivery system for tumor treatments using magnetized nanoparticles, which is nothing but monitoring of drugs as a model of volume fraction in the presence of heat and mass transfer. Most recently Wang et al. [15] investigated the impacts of porosity and volume fraction to understand the atomic behavior of cancer cells. The authors have used the molecular dynamics method in the formation of hematogenous metastasis. Yadav et al. [16] have investigated a two-phase blood flow study through the porous channel.

Maslov et al. [17] discussed drug deliveries in terms of their concentration. The authors focused on heavy concentrations of the drugs affecting drug distribution and the local region biologically. The findings say that high

concentrations give good agreement with high concentrations. Shakya [18] identified the role of chemistry in cancer treatment. The harmful disease for the whole of humanity, cancer, is treated by several therapies using external drugs in the form of tablets. Chemical reactions are observed to serve the badly affected regions. Recent chemistry roles are developing the efficacy of drug delivery systems, and it has been proven to be cost-effective, too. Ezike et al. [19] investigated and compared the systematic drug delivery systems with the usual ones. The authors did a critical review of their observations that the targeted, biocompatible, biologically acceptable drugs are giving better results in the form of nanomaterials. They found that the clinically administered drugs that change and affect the biological environment can be administered well to treat the patients without harming them. In the critical review of Jain [20], fluid(blood) transport plays a key role in growth, metastasis, identification, and survival from tumor decreases. Radiotherapy requires a rich amount of oxygen in the tumor environment. In contrast, chemotherapy and immune therapy require a significant number of drugs that can be carried out through the blood vessels, along with blood. Thus, this study of blood transport with drug suspensions with different parameters becomes a necessity. In the present investigation, a single-phase study of blood flow in a bifurcated region is further studied with some drug-loaded (concentration) suspension with fluid. Thus, the two-phase flow behavior of flowing biofluid in the tumor-surrounded region is investigated as a drug delivery system.

**MATHEMATICAL FORMULATION**

The flow channel is considered as a conducting parallel plate channel at  $2b$  apart. The flowing fluid blood of density  $\rho$  is considered Newtonian, homogeneous, and viscous. The flowing channel has a tumor region of rectangular shape, having pores surrounding it. The non-conducting drug mixture is loaded into the blood. The flowing region is under an external magnetic field  $B_0$  applied at an inclination of angle  $\alpha$ . Mostly, these tumors are found at the apex of the bifurcation of the arterial flow (channel), where the angle of bifurcation is zero. The magnetic field produced due to induction is negligible, and the Reynolds number  $Re$  is kept low to maintain the flow laminar.

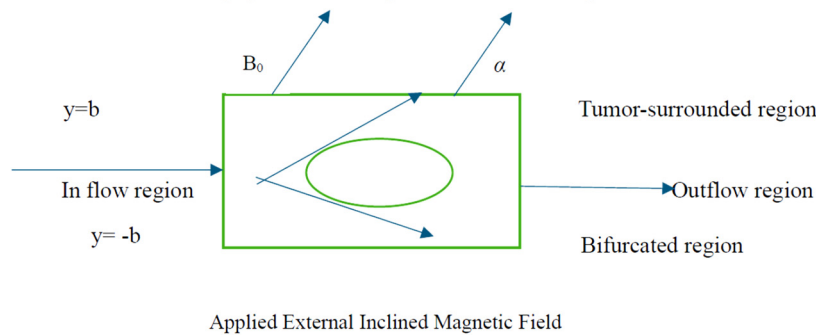


**Figure 1.** Schematic diagram of the flowing fluid surrounding the tumor spheroid

Blood flow through a porous medium under a magnetic field and mass transfer, followed by the assumptions considered in the mathematical formulation, is taken as two-dimensional boundary layers. Let  $u^*$  and  $v^*$  are the velocity of blood and suspension (drug), respectively, at time  $t$  in the flow field.  $\eta$  is the viscosity of the blood while  $p^*$  is pressure.  $\beta'$  is the volumetric expansion parameter for concentration,  $\alpha$  is the angle of inclination of the applied magnetic field, and  $K^*$  is a porosity parameter.

$$(1 - \phi^*) \frac{\partial u^*}{\partial t^*} = (1 - \phi^*) \left( -\frac{1}{\rho} \frac{\partial p^*}{\partial x^*} + \frac{\eta}{\rho} \frac{\partial^2 u^*}{\partial y^{*2}} \right) + g\beta'(C - C_{\infty})^* + K'N(u^* - v^*) - \frac{\sigma B_0^2 \sin^2 \alpha}{\rho} u^* - \frac{1}{K^*} u^* \tag{1}$$

$$m_p \frac{\partial v^*}{\partial t^*} = K'(u^* - v^*) \tag{2}$$

$$\frac{\partial C^*}{\partial t^*} = D \frac{\partial^2 C^*}{\partial y^{*2}} \tag{3}$$

$D$  is for diffusion of drug particles  
 The non-dimensional variables are

$$x = \frac{x^*}{b}, y = \frac{y^*}{b}, u = \frac{u^*}{m/2b\rho}, v = \frac{v^*}{m/2b\rho}, h = \frac{-(dp^*/dx^*)}{(\eta m/2b^3\rho)}, \tau = \frac{\eta}{\rho}, t = \frac{t^*}{\left(\frac{b^2\rho}{\eta}\right)}, C = \frac{C^*(2b^3\rho^2)}{m\eta}, K = \frac{K^*}{\left(\frac{b^2\rho}{\eta}\right)}$$

The non-dimensional governing equations of motion are:

$$\frac{\partial u}{\partial t} = h + \frac{\partial^2 u}{\partial y^2} + \frac{1}{(1-\phi)} \left( g\beta' C - M^2 \sin^2 \alpha u - R(u - v) - \frac{u}{K} \right) \tag{4}$$

$$G \frac{\partial v}{\partial t} = u - v, \tag{5}$$

$$\frac{\partial C}{\partial t} = \frac{1}{Sc} \frac{\partial^2 C}{\partial y^2} \tag{6}$$

$$Sc \text{ (Schmidt number)} = \frac{\eta}{D\rho}, \quad M^2 \text{ (Magnetic Field Parameter)} = \frac{kn}{\sigma b^2}, \quad (\text{Porosity parameter}) = \frac{kn}{\sigma b^2},$$

$$G \text{ (Particle Mass Parameter)} = \frac{m_p \mu}{\rho h^2 K}, \quad R \text{ (Particle Concentration Parameter)} = \frac{K' N h^2}{\mu}$$

The boundary conditions are:

$$u = e^{-\lambda^2 t}, v = e^{-\lambda^2 t}, C = e^{-\lambda^2 t} \text{ at } y = -1$$

$$u \rightarrow 0, \quad v \rightarrow 0, \quad C = 0 \text{ at } y = 1 \tag{7}$$

The governing PDEs are solved by the function PDEPE in MATLAB. The PDEPE solver available in MATLAB is an easy and practical tool for simulating and visualizing models, serving as an alternative approach for solving initial boundary value problems (IBVP) related to parabolic and hyperbolic equations. The PDEPE is a built-in function that employs a second-order spatial discretization technique, which is developed by utilizing the  $x$ -Mesh and  $t$ -Span parameters. The accuracy, consistency, and expense of the computational approach rely on the mesh size employed. The function PDEPE operates in tandem with the stiff ODE solver ode15 for effective calculations, utilizing time step values that are dynamically modified to maintain the precision of the PDE solutions.

**RESULTS AND DISCUSSION**

The transport of biofluid (blood) and the suspensions (drug material) is investigated in terms of velocity profiles for the different phases against different parameters through Figures 2 to 10. In this investigation of numerical results, some of the values are considered fixed values  $t = 1, \tau = 0.25, h=0.5, K = 2, R = 0.5$ (concentration),  $G = 0.8$ (particle mass),  $\lambda = 1, M=0.5, \alpha = 30^\circ, \phi = 0.2$ .

The amount of drug is loaded in the fluid for treating the affected tumor-surrounded region, which is mathematically formulated as a concentration amount. Thus, fluid concentration will change the viscosity of the fluid even if the flow is Newtonian. Figures 2-7 represent the velocity profiles for the drug-carrying fluid (blood) and suspension (drug) in the affected region for the magnetic field intensity  $M(0.5, 1, 1.5)$ , concentration of drug amount  $R(0.5, 1, 1.5)$ , and decay parameter  $\lambda(0.8, 0.9, 1.0)$ , angle of inclination of the applied magnetic field  $\alpha(30^\circ, 45^\circ, 60^\circ)$ , added particle mass  $G(0.8, 1, 1.2)$  and the Schmidt number  $Sc(2, 2.4, 2.8)$ . The flow regions are considered in the entire channel region between  $y = -1$  and  $y = 1$ . Velocity profiles are showing decreasing trends against increasing values of the parameters, respectively. Suspension particle (drug) velocity is less than that of the drug carrier. Velocity at the walls is almost zero due to the drag force at the slip region.

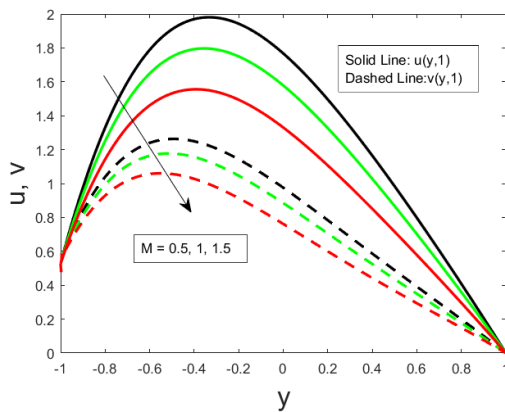


**Figure 2.** Fluid and suspension velocity for magnetic field M

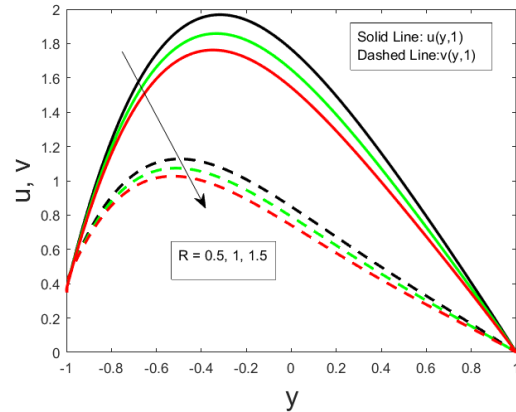


**Figure 3.** Fluid and suspension velocity for particle concentration R

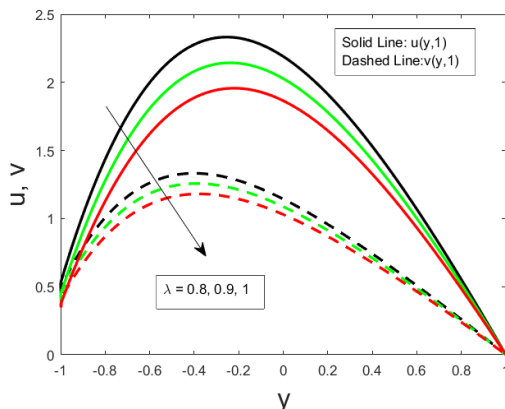


**Figure 4.** Fluid and suspension velocity for decay parameter  $\lambda$ .

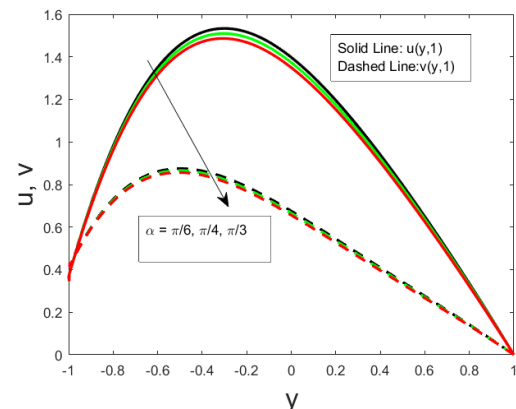


**Figure 5.** Fluid and suspension velocity for the angle of inclination  $\alpha$



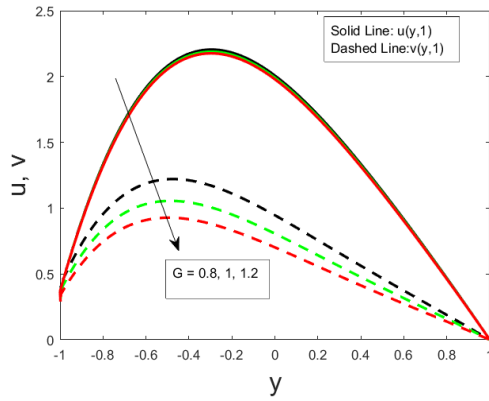


**Figure 6.** Fluid and suspension velocity for particle mass parameter  $G$

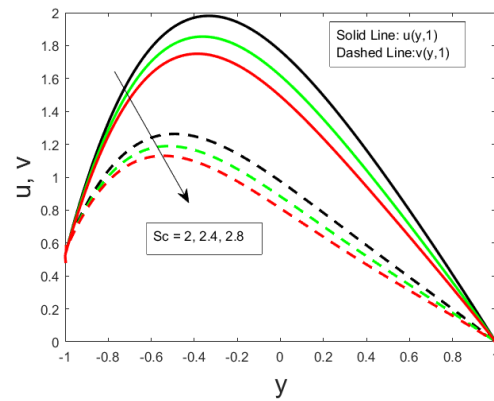


**Figure 7.** Fluid and suspension velocity to Schmidt number  $Sc$

Figures 8-10 are structured to represent the velocity profiles for the drug-carrying fluid (blood) and medication (drug) in the affected region for the volumetric expansion coefficient  $\beta'$  (1.5, 2, 2.5), volume fraction parameter  $\phi$  (0.01, 0.1, 0.2) and porosity parameter  $K$  (1.5, 2, 2.5). The flow regions are considered the entire channel region between  $y = -1$  and  $y = 1$ . Velocity profiles are showing decreasing trends against increasing values of the parameters, respectively. Suspension particle (drug) velocity is less than that of the drug carrier. Velocity at the walls is almost zero due to the drag force at the slip region.

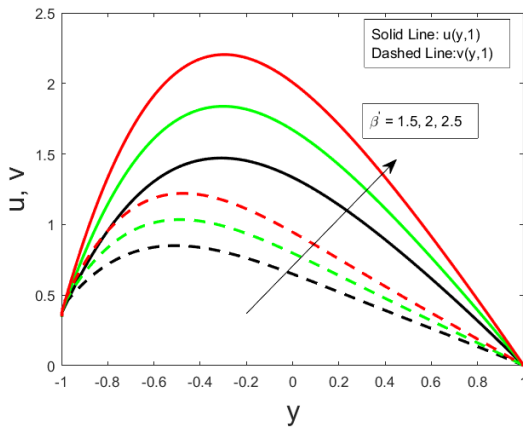


**Figure 8.** Fluid and suspension velocity for volumetric expansion due to concentration  $\beta'$

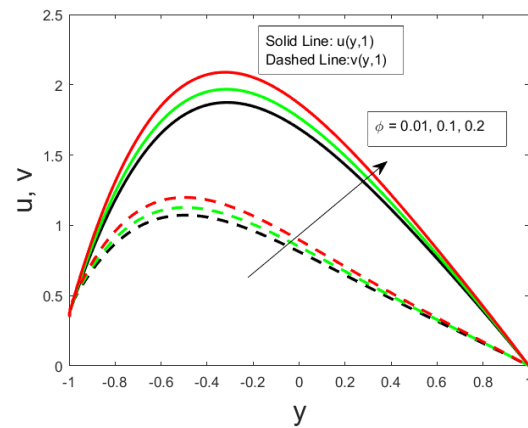


**Figure 9.** Fluid and suspension velocity for volume fraction  $\phi$

Figures 11 and 12 are depicted for the concentration profile against the Schmidt number  $Sc$  (2, 2.4, 2.8) and the decay parameter  $\lambda$  (1, 1.1, 1.2). Both parameters decrease the concentration profile for increasing values. This indicates that once the diffusion of the drug is reduced, the concentration will also be reduced. Moreover, due to the flow force fraction, one of the boundaries of the tumor region is concentrated more, which increases the drug load. This will improve the efficacy of drug delivery.

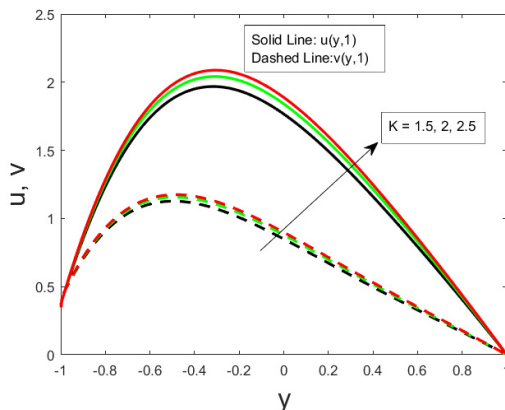


**Figure 10.** Fluid and suspension velocity for porosity parameter  $K$

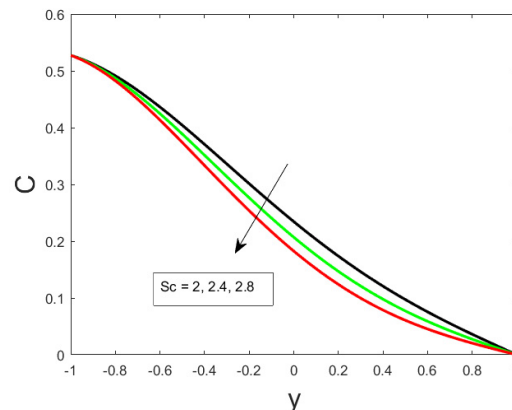


**Figure 11.** Concentration profile to Schmidt number  $Sc$

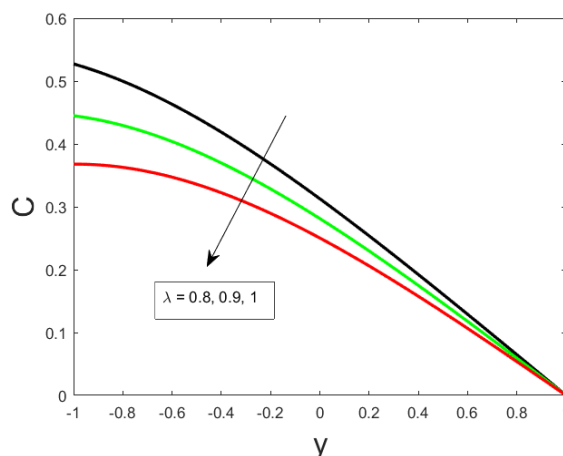


Figure 12. Concentration profile for decay parameter  $\lambda$

### CONCLUSION

The present investigation is conducted to see the effect of volume fraction and high drug concentration on two-phase flow behavior in the tumor surrounding regions. Effects of various parameters on flow profiles of blood-carrying medications (drug) and concentration profiles are concluded as:

- The concentrated drug is flowing in the entire affected region along with a mixture of many flowing components.
- The flowing two-phase fluid (blood) along with the medications (drug particles) mixed with are, is transported with varying velocity profiles with a pulsating nature, with almost zero at the boundaries and maximum in the middle of the channel.
- The drug-carrying fluid supports the transport of the drug in the affected region as the medication velocity is less than that of the drug carrier.
- The increasing magnetized region ( $M$ ) that is applied at different increasing angles ( $\alpha$ ) gives a reduced flow as the high concentration is used within the flow channel to treat the affected region.
- Increasing values of  $R$  (particle concentration parameter),  $\lambda$  (decay parameter),  $G$  (suspension mass parameter),  $Sc$  (Schmidt Number) reduces the velocity of both phases. In the presence of dense medications (heavy drug load), low diffusions, and reduced flow rates give good indications to reduce inflammations.
- Rising values of  $K$  (porosity parameter),  $\beta'$  (volumetric expansion parameter for concentration),  $\phi$  (volume fraction parameter) increases the velocity for both the fluid phases. These increasing velocities need to be monitored during treatment as flow rates will increase, which will lead to a jump in pressure on the walls of the fluid carrier.
- Increasing  $\lambda$ , and  $Sc$  (Schmidt number) reduces the concentration profile of the affected area as diffusion is reduced.

The above results are based on a mathematical formulation and computational approach. Further, these numerical approaches need to be validated clinically by the medical community.

### Acknowledgment

This research project was funded by the University of Technology and Applied Sciences, Shinas, through the Internal Research Funding Program-2024, grant number (UTAS-Shinas-cy01-2024-005).

### Conflict of Interest

There is no conflict of interest.

### ORCID

©D. Kumar, <https://orcid.org/0000-0002-2346-8445>; ©M. Garvandha, <https://orcid.org/0000-0002-4751-5840>

### RERERENCES

- [1] World Health Organization News 01-02-2024. <https://www.who.int/news/item/01-02-2024-global-cancer-burden-growing--amidst-mounting-need-for-services>.
- [2] N.P. Singh and A.K. Singh, "MHD Effects on heat and mass transfer in the flow of a dusty viscous fluid with volume fraction," *Indian Journal of Pure and Applied Physics*, **39**, 496-509 (2001).
- [3] H.M. Byrne and J.R. King, "A Two-Phase Model of Solid Tumour Growth," *Applied Mathematics Letters*, **16**, 567-573 (2003). [https://doi.org/10.1016/S0893-9659\(03\)00038-7](https://doi.org/10.1016/S0893-9659(03)00038-7)
- [4] I.I Bogdanov, V.V. Mourzenko, J.F. Thovert and P.M. Adler, "Two-phase flow through fractured porous media," *Physical Review E*, **68**, 767-782 (2003). <https://doi.org/10.1103/PhysRevE.68.026703>

- [5] O. Prakash, S.P. Singh, D. Kumar and Y. Dwivedi, "A study of effects of heat source on MHD blood flow through a bifurcated artery," *AIP Advances*, **1**, 042128 (2011). <https://doi.org/10.1063/1.3658616>
- [6] A. Chaudhuri, C.F. Osterhoudt and D. Sinha, "Determination of Volume Fractions in Two-Phase Flows from Sound Speed Measurement," in: *ASME 2012 Noise Control and Acoustics Division Conference*, (New York, USA, 2012), pp. 559-567. <https://doi.org/10.1115/NCAD2012-1381>
- [7] Z. Abbas, J. Hasnain and M. Sajid, "MHD two-phase fluid flow and heat transfer with partial slip in an inclined channel," *Thermal Science*, **20**(5), 1435-1446 (2016). <https://doi.org/10.2298/TSCI130327049A>
- [8] K.R. Madhura and D.S. Swetha, "Influence of Volume Fraction of Dust Particles on Dusty Fluid Flow through Porous Rectangular Channel," *International Journal of Mathematics Trends and Technology (IJMTT)*, **50**(5), 261-275 (2017). <https://doi.org/10.14445/22315373/IJMTT-V50P543>
- [9] H. Chen, X. Tong, L. Lang, O. Jacobson, B. C. Yung, X. Yang, R. Bai, *et al.*, "Quantification of Tumor Vascular Permeability and Blood Volume by Positron Emission Tomography," *Theranostics*, **7**(9), 2363-2376 (2017). <https://doi.org/10.7150/thno.19898>
- [10] K.R. Thulborn, A. Lu, I.C. Atkinson, M. Pauliah, K. Beal, T.A. Chan, A. Omuro, *et al.*, "Residual Tumor Volume, Cell Volume Fraction, and Tumor Cell Kill During Fractionated Chemoradiation Therapy of Human Glioblastoma using Quantitative Sodium MR Imaging," *Clinical cancer research: an official journal of the American Association for Cancer Research*, **25**(4), 1226-1232 (2019). <https://doi.org/10.1158/1078-0432.CCR-18-2079>
- [11] B. Wirthl, J. Kremheller, B.A. Schrefler and W.A. Wall, "Extension of a multiphase tumor growth model to study nanoparticle delivery to solid tumors," *PLoS One*, **15**(2), e0228443 (2020). <https://doi.org/10.1371/journal.pone.0228443>
- [12] A. Bera, S. Dutta, J.C. Misra and G.C. Shit, "Computational modeling of the effect of blood flow and dual phase lag on tissue temperature during tumor treatment by magnetic hyperthermia," *Mathematics and Computers in Simulation*, **188**, 389-403 (2021). <https://doi.org/10.1016/j.matcom.2021.04.020>
- [13] D. Kumar, B. Satyanarayana, R. Kumar, S. Kumar and N. Deo, "Application of heat source and chemical reaction in MHD blood flow through permeable bifurcated arteries with inclined magnetic field in tumor treatments," *Results in Applied Mathematics*, **10**, 100151 (2021). <https://doi.org/10.1016/j.rinam.2021.100151>
- [14] V. Darvishi, M. Navidbakhsh and S. Amanpour, "Heat and mass transfer in the hyperthermia cancer treatment by magnetic nanoparticles," *Heat and Mass Transfer*, **58**(6), 1029-1039 (2022). <https://doi.org/10.1007/s00231-021-03161-3>
- [15] H. Wang, A.A. Alizadeh, A.M. Abed, A. Piranfar, G.F. Smaism, S. K. Hadrawi and M. Hekmatifar, "Investigation of the effects of porosity and volume fraction on the atomic behavior of cancer cells and microvascular cells of 3DN5 and 5OTF macromolecular structures during hematogenous metastasis using the molecular dynamics method," *Computers in Biology and Medicine*, **158**, 106832 (2023). <https://doi.org/10.1016/j.compbiomed.2023.106832>
- [16] N. Yadav, S. Jaiswal and P.K. Yadav, "Two-phase magnetohydrodynamic blood flow through the curved porous artery," *Physics of Fluids*, **36**, 091924 (2024). <https://doi.org/10.1063/5.0225245>
- [17] M.Y. Maslov, E.R. Edelman, A.E. Wei, M.J. Pezone and M.A. Lovich, "High concentrations of drug in target tissues following local controlled release are utilized for both drug distribution and biological effect: An example with epicardial inotropic drug delivery," *Journal of Controlled Release*, **171**(2), 201-207 (2013). <https://doi.org/10.1016/j.jconrel.2013.06.038>
- [18] B. Shakya, "The Role of Chemistry in Cancer Chemotherapy: A Mini Review," *Amrit Journal*, **3**, 49-56 (2023). <https://doi.org/10.3126/amritj.v3i1.61541>
- [19] T.C. Ezike, U.S. Okpala, U.L. Onoja, C.P. Nwike, E.C. Ezeako, O.J. Okpara, C.C. Okoroafor, *et al.*, "Advances in drug delivery systems, challenges, and future directions," *Heliyon*, **9**(6), e17488 (2023). <https://doi.org/10.1016/j.heliyon.2023.e17488>
- [20] R.K. Jain, "Transport Phenomena in Tumors," *Advances in Chemical Engineering*, **19**, 129-200 (1994). [https://doi.org/10.1016/s0065-2377\(08\)60214-8](https://doi.org/10.1016/s0065-2377(08)60214-8)

## ДВОФАЗНИЙ ПОХИЛИЙ МГД-ПОТОК КРОВІ В ПОРИСТІЙ ДІЛЯНЦІ ПУХЛИНИ З КОНЦЕНТРАЦІЄЮ ТА ОБ'ЄМНОЮ ФРАКЦІЄЮ

Д. Кумар<sup>а</sup>, М. Гарвандха<sup>а</sup>, С. Кумар<sup>б</sup>, Н. Део<sup>с</sup>

<sup>а</sup>Кафедра комп'ютерних та інформаційних наук, Університет технологій та прикладних наук-Шинас, Оман

<sup>б</sup>Університет доктора Бхімрао Амбедкара, Агра, Індія

<sup>с</sup>Онкологічне відділення, лікарня Supergy, Агра, Індія

Існують різні підходи до лікування інвазивних та неінвазивних пухлин. Рідина, що тече (кров), забезпечує пухлини необхідними поживними речовинами та поглинає суспензії. Системи доставки ліків залежать від середовища (рідини, що тече), яке переносить ліки. Кровоносні судини зазвичай переносять ліки до цільових ділянок, які лікують уражену ділянку. Ця ситуація змінює концентрацію пухлини навколо середовища. Система контролюється під дією магнітного поля, яке прикладається під кутом ( $0 < \alpha < 90$ ). Система кровотоку навколо пухлини визначається диференціальними рівняннями в частинних похідних (РЧП). Визначальні рівняння розв'язані за допомогою математичної функції PDEPE в MATLAB. Вплив різних параметрів, параметрів концентрації, похилого магнітного поля, пористості, на швидкість рідини (крові) та швидкість ліків (препаратів) за наявності об'ємної фракції. Отримані таким чином картини потоку демонструють значний вплив, що допомагає клінічно лікувати уражені ділянки. Числові результати інтерпретуються за допомогою побудованих графіків.

**Ключові слова:** двофазний похилий МГД-потік; пористі ділянки пухлини; концентрація; об'ємна частка

## BENJAMIN—FEIR INSTABILITY OF INTERFACIAL GRAVITY–CAPILLARY WAVES IN A TWO-LAYER FLUID. PART I

Olga Avramenko<sup>a\*,b</sup>, Volodymyr Naradovyi<sup>c</sup>

<sup>a</sup>National University of Kyiv-Mohyla Academy, 2 Skovorody, Kyiv, 04070, Ukraine

<sup>b</sup>Vytautas Magnus University, 58 K. Donelaičio g., Kaunas 44248, Lithuania

<sup>c</sup>Volodymyr Vynnychenko Central Ukraine State University, 1 Shevchenka, Kropyvnytskyi, 25006, Ukraine

\*Corresponding Author e-mail: [o.avramenko@ukma.edu.ua](mailto:o.avramenko@ukma.edu.ua)

Received June 1, 2025; revised July 27, 2025; accepted August 21, 2025

This study presents a detailed investigation of the modulational stability of interfacial wave packets in a two-layer inviscid incompressible fluid with finite layer thicknesses and interfacial surface tension. The stability analysis is carried out for a broad range of density ratios and geometric configurations, enabling the construction of stability diagrams in the  $(\rho, k)$ -plane, where  $\rho$  is the density ratio and  $k$  is the carrier wavenumber. The Benjamin–Feir index is used as the stability criterion, and its interplay with the curvature of the dispersion relation is examined to determine the onset of modulational instability. The topology of the stability diagrams reveals several characteristic structures: a localized *loop* of stability within an instability zone, a global *upper* stability domain, an elongated *corridor* bounded by resonance and dispersion curves, and a degenerate *cut* structure arising in strongly asymmetric configurations. Each of these structures is associated with a distinct physical mechanism involving the balance between focusing/defocusing nonlinearity and anomalous/normal dispersion. Systematic variation of layer thicknesses allows us to track the formation, deformation, and disappearance of these regions, as well as their merging or segmentation due to resonance effects. Limiting cases of semi-infinite layers are analyzed to connect the results with known configurations, including the ‘half-space–layer’, ‘layer–half-space’, and ‘half-space–half-space’ systems. The influence of symmetry and asymmetry in layer geometry is examined in detail, showing how it governs the arrangement and connectivity of stable and unstable regions in parameter space. The results provide a unified framework for interpreting modulational stability in layered fluids with interfacial tension, highlighting both global dispersion-controlled regimes and localized stability islands. This work constitutes Part I of the study; Part II will address the role of varying surface tension, which is expected to deform existing stability domains and modify the associated nonlinear–dispersive mechanisms.

**Keywords:** Modulational stability; Interfacial waves; Two-layer fluid; Benjamin–Feir instability; Surface tension

**PACS:** 47.20.Dr, 47.20.Ky, 47.35.Bb, 47.35.Pq

### 1. INTRODUCTION

This study investigates wave packet propagation along a two-layer fluid interface with surface tension, focusing on modulational instability as a fundamental nonlinear mechanism. First described by Benjamin [1] and formulated via the nonlinear Schrödinger (NLS) equation by Zakharov [2], modulational instability plays a central role in nonlinear wave evolution. Classical multiple-scale derivations of the NLS equation for modulated wave packets in layered fluids were carried out by Hasimoto and Ono [3] for a single layer and by Nayfeh [4] for a two-layer configuration, with later refinements for interfacial waves by Grimshaw and Pullin [5] and Selezov et al. [6]. These works established the theoretical basis for studying stability boundaries in terms of nonlinear–dispersive balances; however, they did not include the specific ‘layer with a solid bottom – layer with a rigid lid’ (La–La) configuration considered here.

A broad range of studies has addressed nonlinear wave propagation in two-layer and interfacial systems. Oikawa [7] analyzed resonant interactions between internal gravity waves and surface wave packets, while Ablowitz and Haut [8] developed coupled NLS models for interfacial flows with a free surface. Christodoulides and Dias [9] investigated the stability of capillary–gravity interfacial waves between two bounded fluid layers, including limiting configurations such as ‘lower half-space–upper layer with rigid lid’ and ‘half-space–half-space’. Avramenko et al. [10] examined dispersion relations in a two-layer liquid with a finite-depth free surface, and Panda and Martha [11] incorporated surface tension in scattering problems over a permeable bottom. Purkait and Debsarma [12] studied oblique wave packet interactions in a two-layer fluid with an infinitely deep lower layer, finding that instability growth rates depend strongly on upper layer thickness. More recent works by Li et al. [13, 14, 15, 16] and Pal and Dhar [17, 18] extended the multiple-scale framework to include arbitrary depths, surface tension, and background currents, revealing significant modifications of instability thresholds and growth rates. While these studies identify key physical mechanisms in specific configurations, none systematically characterizes modulational stability in a La–La system with arbitrary finite thicknesses.

Benjamin–Feir type instability of internal gravity waves has also been widely investigated in geophysical and atmospheric contexts, revealing diverse instability mechanisms. Talipova et al. [19] demonstrated modulational instability of long internal waves in horizontally inhomogeneous oceans, while Liang et al. [20] identified inherent instability via resonant harmonic generation. Chow et al. [21] analyzed instability in smoothly stratified shallow fluids, and Voelker

and Schlutow [22] reported cascades of modulation and shear instabilities in vertically sheared flows. Kuklin and Poklonskiy [23] examined anomalous amplitude waves in the ocean, showing their persistence, enhanced modulation instability, and ability to propagate over long distances. Recent rigorous analyses, such as Bianchini et al. [24] for the Boussinesq system and Lashkin and Cheremnykh [25] for atmospheric waves, provide quantitative thresholds for instability onset. Although these studies deepen understanding of modulational instability in complex media, the combined effects of finite thickness and surface tension in the La–La configuration remain unexplored.

There has also been sustained interest in the role of surface tension and higher-order effects in wave stability. Ionescu and Pusateri [26] and Düll [27] examined global regularity and the validity of the NLS approximation for water waves with capillarity, while Sedletsky [28] derived a fifth-order NLS equation for finite-depth gravity–capillary waves. Ablowitz et al. [29] analyzed six-wave interactions and resonances, demonstrating the complexity of nonlinear–dispersive interplay with surface tension. However, no comprehensive topological description of modulational stability diagrams has been given for a two-layer finite-depth La–La system.

The present paper (Part I) addresses this gap using multiscale expansion with symbolic computation, verifying results through limiting transitions to the ‘half-space–layer’ (HS–La), ‘layer–half-space’ (La–HS), and ‘half-space–half-space’ (HS–HS) configurations. A companion study (Part II) will focus on the influence of surface tension magnitude on the topology of stability boundaries, revealing additional stabilization and destabilization mechanisms.

## 2. PROBLEM FORMULATION AND SOME PRELIMINARY BACKGROUND

### 2.1. Wave packets in a two-layer fluid and their modulational stability condition

We consider the propagation of wave packets along the interface  $z = \eta(x, t)$  between two incompressible fluid layers,  $\Omega_1$  and  $\Omega_2$ , with densities  $\rho_1$  and  $\rho_2$ , respectively. The effect of interfacial surface tension  $T$  acting on  $\eta(x, t)$  is taken into account. In the undisturbed state, the domains are  $\Omega_1 = \{(x, z) : |x| < \infty, -h_1 < z < 0\}$ ,  $\Omega_2 = \{(x, z) : |x| < \infty, 0 < z < h_2\}$ , where  $h_1$  and  $h_2$  denote the layer thicknesses (Figure 1).

The problem is formulated in dimensionless variables by introducing characteristic scales based on gravitational acceleration  $g$ , the density of the lower fluid  $\rho_1$ , and a reference surface tension  $T_0$ . The characteristic length, time, and mass are defined as  $L = (T_0/(\rho_1 g))^{1/2}$ ,  $t_0 = (L/g)^{1/2}$ , and  $m_0 = \rho_1 L^3$ . Dimensionless variables (denoted by an asterisk) are then introduced as  $(x^*, z^*, h_1^*) = (x, z, h_1)/L$ ,  $(\rho_1^*, \rho_2^*) = (\rho_1, \rho_2)/\rho_1$ ,  $t^* = t/t_0$ ,  $T^* = T/T_0$ ,  $\eta^* = \eta/(\alpha L)$ , and  $(\phi_1^*, \phi_2^*) = (\phi_1, \phi_2)/(\alpha L^2/t_0)$ , where  $\alpha = a/l$  is the small wave–steepness parameter, with  $a$  the maximum interface displacement and  $l$  the wavelength, and  $\rho = \rho_2/\rho_1$  is the density ratio. In the analytical derivations the parameter  $T$  is retained explicitly, while in the numerical analysis and in all stability diagrams presented below the dimensionless surface tension coefficient is fixed at  $T = 1$ .

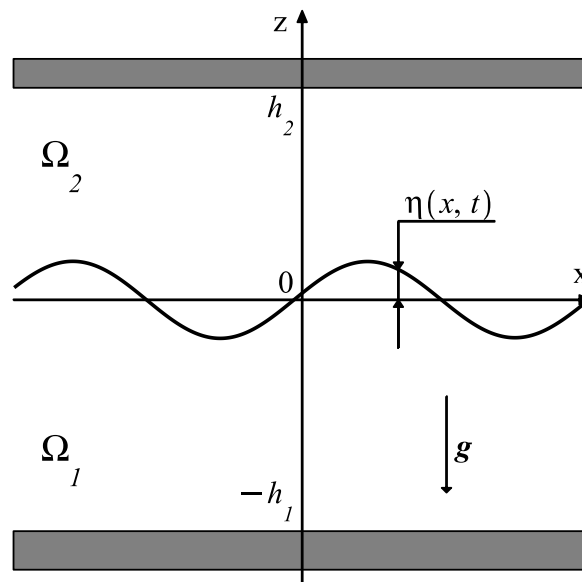


Figure 1. Statement of the problem.

In nondimensional variables, the problem is formulated in terms of the velocity potentials  $\phi_j(x, z, t)$  and the interface displacement  $\eta(x, t)$ , with the governing equations and boundary conditions given by

$$\begin{aligned} \Delta \phi_j &= 0, & (x, z) \in \Omega_j, \\ \eta_{,t} - \phi_{j,z} &= -\alpha \eta_{,x} \phi_{j,x}, & z = \alpha \eta(x, t), \end{aligned}$$

$$\begin{aligned} \phi_{1,t} - \rho\phi_{2,t} + (1 - \rho)\eta + \frac{1}{2}\alpha(\nabla\phi_1)^2 - \frac{1}{2}\alpha\rho(\nabla\phi_2)^2 - T\left[1 + (\alpha\eta_{,x})^2\right]^{-3/2}\eta_{,xx} &= 0, & z = \alpha\eta(x, t), \\ \phi_{1,z} &= 0, & z = -h_1, \\ \phi_{2,z} &= 0, & z = h_2. \end{aligned} \quad (1)$$

Following the multiple-scale method, we represent the unknown fields as

$$(\eta, \phi_j) = \sum_{n=1}^3 \alpha^{n-1} (\eta_n, \phi_{jn}) + O(\alpha^3),$$

with slow variables  $x_n = \alpha^n x$ ,  $t_n = \alpha^n t$  ( $n = 0, 1, 2$ ), and expansion coefficients  $\eta_n, \phi_{jn}$ .

From the first approximation of the problem (1) we obtain the dispersion relation

$$\omega^2 = \frac{k(1 - \rho + Tk^2)}{\coth kh_1 + \rho \coth kh_2}, \quad (2)$$

where  $k$  is the carrier wave number and  $\omega$  the carrier frequency.

The second-order problem yields the amplitude of the second harmonic in the form

$$\Lambda = 0.5k\omega^2 \frac{\rho \coth^2 kh_2 - \coth^2 kh_1 + 4\rho \coth 2kh_2 \coth kh_2 - 4 \coth 2kh_1 \coth kh_1 - 3(\rho - 1)}{4Tk^3 - k\rho + k - 2\omega^2(\rho \coth 2kh_2 + \coth 2kh_1)}. \quad (3)$$

At third order, the solvability condition together with (2) and (3) gives the nonlinear Schrödinger equation

$$iA_{,t} + i\omega' A_{,x} + 0.5\omega'' A_{,xx} = -\alpha\omega^{-1} J A^2 \bar{A}, \quad (4)$$

where  $\bar{A}$  is the complex conjugate of  $A$ ,  $\omega' = \partial\omega/\partial k$  is the group velocity, and  $\omega'' = \partial^2\omega/\partial k^2$ .

The Benjamin–Feir index  $J$  is explicitly

$$\begin{aligned} J = & -\frac{1}{16(1 - \rho) [\rho \coth kh_2 + \coth kh_1]} \left\{ 2k\omega^2(1 - \rho)\Lambda [-3\rho \coth^2 kh_2 + 3 \coth^2 kh_1 - 1 + \rho] \right. \\ & - 4k\omega^4 \left[ \rho (\coth^2 kh_2 - 1) - (\coth^2 kh_1 - 1) \right]^2 \\ & \left. - 4k^2\omega^2(1 - \rho) [\rho \coth^3 kh_2 + \coth^3 kh_1 - 2\rho \coth kh_2 - 2 \coth kh_1] - 3Tk^5(1 - \rho) \right\}. \end{aligned} \quad (5)$$

A purely temporal solution of (4) reads  $A(t) = a \exp(i\alpha a^2 \omega^{-1} J t)$ , where  $a$  is a constant envelope amplitude. Following [4], the modulational stability condition is obtained by linearizing equation (4) around a uniform envelope solution and analysing the evolution of small harmonic sideband perturbations. The sign of the product  $J\omega''$  determines the outcome: stability occurs when

$$J\omega'' < 0, \quad (6)$$

while  $J\omega'' > 0$  indicates modulational instability.

The criterion (6) provides a simple yet powerful diagnostic for determining whether a quasi-monochromatic wave packet is modulationally stable or unstable. If  $J\omega'' < 0$ , the effects of nonlinearity and dispersion counteract each other, preventing the growth of sideband perturbations and ensuring the persistence of a uniform packet. Conversely, when  $J\omega'' > 0$ , nonlinearity and dispersion act in unison, amplifying small sideband disturbances. This cooperative interaction leads to the exponential growth of modulation, breakdown of the initial packet, and, in many cases, the emergence of localized structures such as envelope solitons or wave focusing events. The sign of  $J$  is determined by the balance between focusing/defocusing nonlinearity, while  $\omega''$  reflects the curvature of the dispersion relation and thus the type of dispersion (normal or anomalous) present in the system.

## 2.2. Limiting cases

The La–La system with finite layer thicknesses  $h_1$  and  $h_2$  reduces in several limiting cases to previously studied configurations: (i)  $h_1 \rightarrow \infty \Rightarrow$  HS–La [30]; (ii)  $h_2 \rightarrow \infty \Rightarrow$  La–HS [31]; (iii)  $h_1, h_2 \rightarrow \infty \Rightarrow$  HS–HS [4]. All key relations—the dispersion relation (2), the second-harmonic amplitude (3), the evolution equation (4), the Benjamin–Feir index (5), and the modulational stability condition (6)—degenerate to their known forms in these limits.

In agreement with [4, 9, 31], the condition  $J = 0$  as  $k \rightarrow \infty$  yields two vertical asymptotes at

$$\rho = \frac{2 - \sqrt{2}}{2 + \sqrt{2}} \approx 0.1716, \quad \rho = \frac{2 + \sqrt{2}}{2 - \sqrt{2}} \approx 5.8275. \quad (7)$$



In the special case  $\rho = 1$  (equal densities), the gravitational restoring mechanism vanishes, but for  $T > 0$  the interface still supports waves due solely to surface tension. This regime models a homogeneous medium with a purely capillary interface, exhibiting nontrivial dispersion distinct from both surface and internal waves.

The limit  $\rho \rightarrow 1$  of  $J$  is

$$\lim_{\rho \rightarrow 1} J = \begin{cases} \frac{4k \coth^3 kh - \coth^2 kh - 5k \coth kh + 1}{8 \coth^2 kh} T k^4, & h_1 = h_2 = h, \\ -\infty, & h_1 \neq h_2. \end{cases} \quad (8)$$

For  $h_1 \neq h_2$ ,  $J \rightarrow -\infty$  for all  $k$ , making  $\rho = 1$  a universal boundary between stable and unstable regimes. For  $h_1 = h_2$ , the limit is finite and sign-changing with  $k$ , so  $\rho = 1$  does not universally separate stability and instability; the outcome depends on local spectral properties.

### 3. ANALYSIS OF THE EVOLUTION OF MODULATIONAL STABILITY DIAGRAMS WITH VARYING LAYER THICKNESSES

#### 3.1. Notation overview for stability diagrams

This subsection provides a general description of the notation and principles used in constructing modulational stability diagrams in the  $(\rho, k)$  parameter plane for a La–La system. Each diagram contains two principal regions: the zones of linear instability, indicated by a dark shade, and the zones of linear stability. The latter are further subdivided into subregions of nonlinear stability, shown as unshaded areas, and modulational instability (i.e., instability of the wave packet envelope or Benjamin–Feir instability), displayed in a light shade.

The boundary between linear stability and instability is determined by the condition  $k > k_c = \sqrt{(\rho - 1)/T}$ , and the curve  $k = k_c$ , drawn in black, divides the  $(\rho, k)$  plane into a region of linear instability (below this curve) and a region of linear stability (above and to the left). Within the linear stability region, the modulational behaviour is determined by the sign of the product  $J\omega''$ . The subdivision into zones is carried out by the curves  $J = 0$  (red),  $J \rightarrow \infty$  (blue), and  $\omega'' = 0$  (green), corresponding respectively to changes in the sign of the nonlinearity, resonant conditions, and changes in the sign of the second derivative of the carrier frequency  $\omega''$  with respect to the wavenumber  $k$ , or, equivalently, of the group velocity.

Figures 2 and 3 present  $4 \times 4$  matrix-format stability diagrams for various combinations of lower-layer thickness  $h_1$  and upper-layer thickness  $h_2$ . Figure 2 covers  $h_1, h_2 \in \{1, 2, 3, 4\}$ , allowing one to trace topological changes with small increments in the system geometry. Figure 3 covers  $h_1, h_2 \in \{1, 5, 9, 13\}$ , enabling the study of cases with pronounced thickness contrasts and analysis of limiting regimes. The case  $h_1 = 1, h_2 = 1$  appears in both matrices (Figs. 2a and 3a), facilitating the understanding of stability/instability evolution with changing geometric parameters. These diagrams are analysed in detail in the following sections.

Examining the diagonal cells of the matrices in Figs. 2 and 3 reveals the evolution of characteristic curves and the stability/instability ratio as  $h_1$  and  $h_2$  increase synchronously. This approach identifies key topological transitions in a symmetric two-layer system as it approaches the HS–HS limit (see Sec. 3.2). Analysis of the first column tracks the effect of increasing  $h_1$  at fixed  $h_2 = 1$ , characterising transitions in an asymmetric system towards the HS–La limit (see Sec. 3.3). Analysis of the first row shows the changes occurring when  $h_2$  increases at fixed  $h_1 = 1$ , identifying transitions towards the La–HS limit (see Sec. 3.4). In this context, several recurrent topological structures will be encountered, namely the *upper stability region*, the *stability corridor*, the *loop*, and the *cut*, which will serve as reference features in the subsequent analysis.

#### 3.2. Modulational stability diagrams for equal layer thicknesses

We now examine how the topology of modulational stability diagrams changes as the equal layer thicknesses  $h_1 = h_2 = h$  increase. The diagonal entries of the matrix plots in Figs. 2 and 3 trace this evolution from thin layers to the deep-water limit (HS–HS). In all cases, the principal curves are:  $J = 0$  (red),  $\omega'' = 0$  (green),  $\omega = 0$  (black), and  $J \rightarrow \infty$  (blue). The sign combinations of  $J$  and  $\omega''$  determine stability: instability of the Benjamin–Feir type for  $J > 0, \omega'' > 0$ ; the opposite instability for  $J < 0, \omega'' < 0$ ; and stability when the two effects compensate ( $J > 0, \omega'' < 0$  or  $J < 0, \omega'' > 0$ ). In the following analysis we will also refer to recurrent localized features emerging from these curves, namely the *upper stability region*, the *stability corridor*, and the *loop*.

**Small thicknesses ( $h = 1, 2$ ).** For  $h = 1$  (Fig. 2a), the diagram exhibits the basic topology: a U-shaped  $J = 0$  curve, a green  $\omega'' = 0$  line starting at  $(\rho = 1, k = 0)$ , and a black  $\omega = 0$  curve slightly below it. The region below  $J = 0$  and bounded on the right by  $\omega'' = 0$  is modulationally unstable (Benjamin–Feir type), while the upper region above  $J = 0$  is stable. A second stability region occurs between  $\omega'' = 0$  and  $\omega = 0$  for  $\rho > 1$ .

At  $h = 2$  (Fig. 2f), all four characteristic curves appear, with the  $J \rightarrow \infty$  line and a new branch of  $\omega'' = 0$  forming, at small  $\rho$ , a narrow stability corridor separating two instability zones. The overall arrangement to the right of  $\rho = 1$  remains close to the  $h = 1$  case.

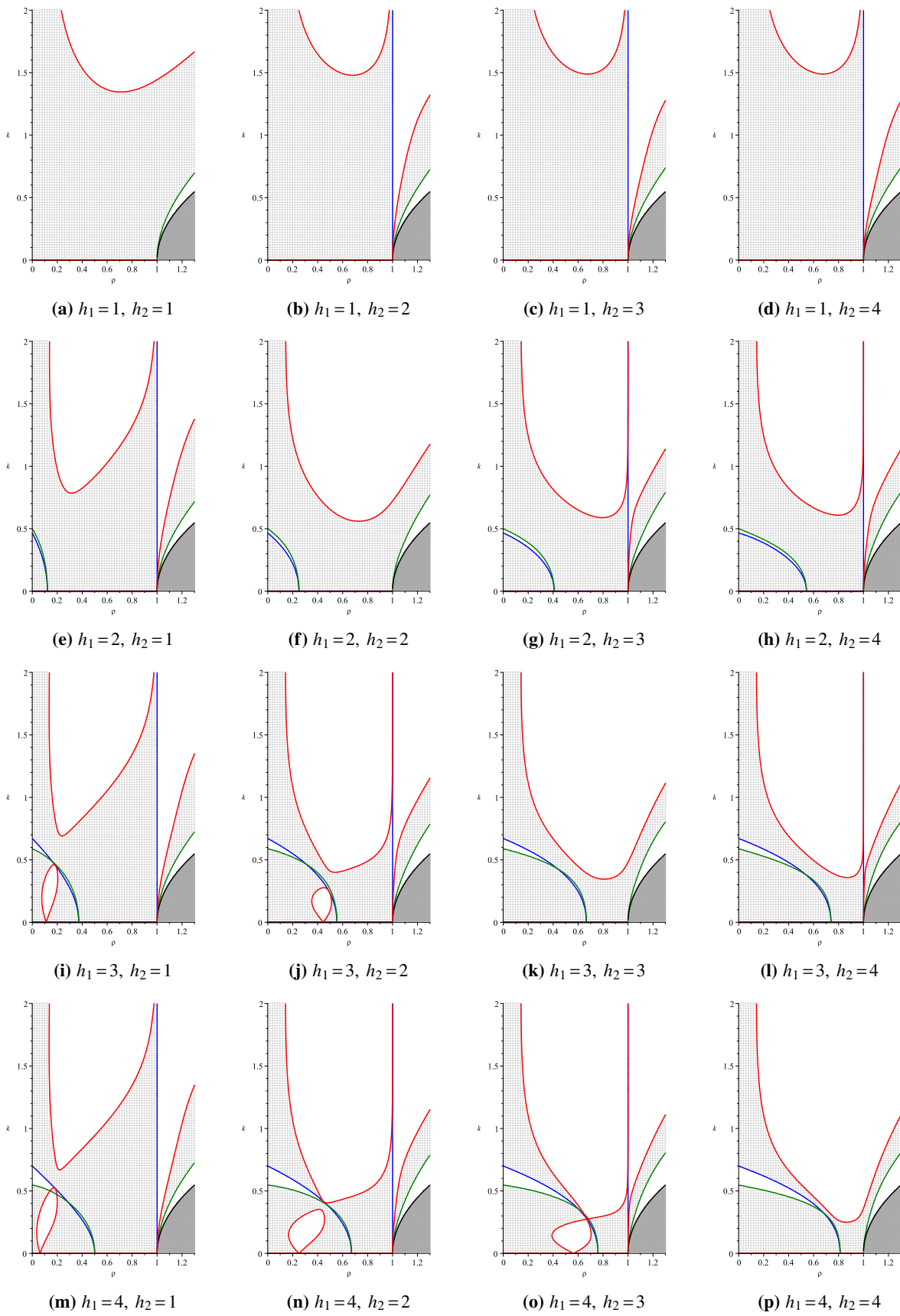


Figure 2. Modulational stability diagrams for all combinations of  $h_1, h_2 \in \{1, 2, 3, 4\}$ .

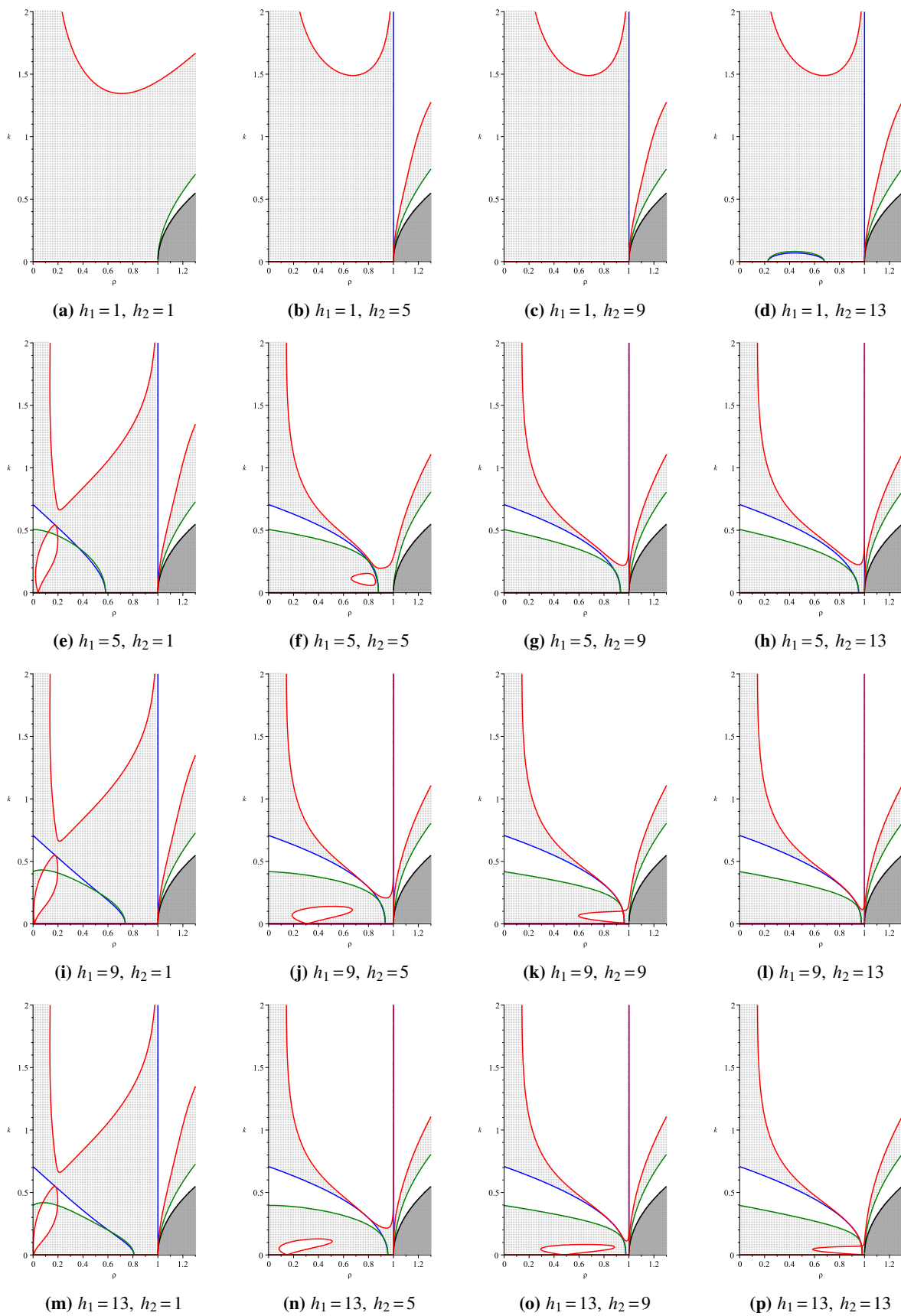


Figure 3. Modulational stability diagrams for all combinations of  $h_1, h_2 \in \{1, 5, 9, 13\}$ .

**Intermediate thicknesses** ( $h = 3, 4, 5$ ). For  $h = 3$  and  $h = 4$  (Figs. 2k,p), the blue and green curves diverge further at small  $\rho$ , enlarging the range of stability by compensation. For  $h = 3$ , their intersections enclose a lens-shaped stability region; at  $h = 4$ , the stability corridor shifts rightwards and partially merges with regions to the right of  $\rho = 1$ . The U-shaped  $J = 0$  curve deforms and shifts to smaller  $k$ , lowering and displacing the upper region.

At  $h = 5$  (Fig. 3f), a qualitative change occurs: an isolated closed  $J = 0$  curve (a loop) appears in the lower-left diagram, enclosing a local stability island inside an instability zone (isola-bifurcation between  $h = 4$  and  $h = 5$ ). The stability corridor continues to widen and link distinct stable zones.

**Large thicknesses and deep-water limit** ( $h = 9, 13, \infty$ ). For  $h = 9$  (Fig. 3k), the stability corridor closes into an elongated loop bounded by  $J \rightarrow \infty$  and  $\omega'' = 0$ , forming a stability island in  $(\rho, k)$  space. The  $J = 0$  loop persists inside the main instability zone. At  $h = 13$  (Fig. 3p), the left-side curves  $J = 0$ ,  $J \rightarrow \infty$ , and  $\omega'' = 0$  nearly coincide, producing extremely narrow alternating stability/instability bands and stretching the loop towards the  $k$ -axis.

In the limit  $h \rightarrow \infty$ , the configuration converges to the HS–HS topology [4]: the loop disappears,  $J = 0$ ,  $J \rightarrow \infty$ , and  $\omega'' = 0$  take their deep-water forms, and the  $(\rho, k)$  plane splits into large continuous stable and unstable regions without isolated resonance islands.

### 3.3. Modulational stability diagrams for varying lower-layer thickness at fixed upper-layer thickness

We now investigate the influence of increasing lower-layer thickness  $h_1$  while keeping the upper-layer thickness fixed at  $h_2 = 1$ . The first columns of the matrix plots in Figs. 2 and 3 show the evolution of characteristic curves ( $J = 0$ ,  $J \rightarrow \infty$ ,  $\omega'' = 0$ ,  $\omega = 0$ ) and the associated stability/instability regions. As in the symmetric case, stability is determined by the sign combinations of  $J$  and  $\omega''$ , and localised structures such as the *stability corridor*, *loop*, and *upper* stability region are defined in Sec. 3.1 and referred to here without repetition. A distinctive feature of all asymmetric configurations is that  $\rho = 1$  acts as a universal boundary between stability and instability, since  $\lim_{\rho \rightarrow 1} J = -\infty$  for  $h_1 \neq h_2$ , regardless of  $k$ , as follows from Eq. (8).

**Small lower-layer thicknesses** ( $h_1 = 2, 3$ ). Transitioning from the symmetric  $h_1 = h_2 = 1$  case to  $h_1 = 2$  (Fig. 2e) produces a narrow stability corridor at small  $\rho$ , bounded by  $J \rightarrow \infty$  and a new branch of  $\omega'' = 0$ . Compared to the symmetric configuration, the corridor is much narrower due to the limited range of compensation between nonlinearity and dispersion in the asymmetric geometry. At  $h_1 = 3$  (Fig. 2i), a loop appears below the corridor, tangent to  $k = 0$  and surrounded by an instability zone. The corridor itself develops two intersections between  $J \rightarrow \infty$  and  $\omega'' = 0$ , segmenting it into alternating stable and unstable strips. The upper stability region shifts and elongates towards the loop, suggesting possible merging for larger  $h_1$ .

**Intermediate lower-layer thicknesses** ( $h_1 = 4, 5$ ). For  $h_1 = 4$  (Fig. 2m), the corridor widens as  $J \rightarrow \infty$  and  $\omega'' = 0$  diverge, extending the parameter range for stability by resonance compensation. The loop enlarges, tilts, and shifts rightwards along  $k = 0$ , indicating stability for higher  $\rho$  and longer waves. Partial overlap between the loop and corridor creates a composite stability domain with internal segmentation. At  $h_1 = 5$  (Fig. 3e), these tendencies strengthen: the loop expands further and its contact point with  $k = 0$  moves right; the corridor stretches towards larger  $\rho$  and overlaps more with the loop, forming an extended multi-mechanism stability region separated from the upper zone by the  $J \rightarrow \infty$  resonance line.

**Large lower-layer thicknesses** ( $h_1 = 9, 13$ ). For  $h_1 = 9$  (Fig. 3i), the loop continues to grow and retain its tilt, with the contact point shifting further along  $k = 0$ . The corridor extends towards higher  $\rho$ , increasing its overlap with the loop and producing a complex composite stability structure with narrow intervening instability bands. At  $h_1 = 13$  (Fig. 3m), the  $J = 0$ ,  $J \rightarrow \infty$ , and  $\omega'' = 0$  curves in the left part of the diagram move closer together, narrowing the corridor and increasing sensitivity to parameter variations, while the loop remains prominent.

**Deep lower-layer limit** ( $h_1 \rightarrow \infty$ ). In the limit of an infinitely deep lower layer, the configuration approaches the HS–La model [30]. Here, the loop root lies at  $(\rho, k) = (0, 0)$ , the corridor broadens and extends to  $(1, 0)$ , and the upper stability region approaches but does not merge with the loop due to the intervening  $J \rightarrow \infty$  resonance barrier. With the influence of the lower boundary removed, stability and instability are controlled solely by the interfacial mode and the upper layer, without additional isolated structures.

### 3.4. Modulational stability diagrams for varying upper-layer thickness at fixed lower-layer thickness

We now examine how the topology of modulational stability diagrams changes when the upper-layer thickness  $h_2$  increases while the lower-layer thickness remains fixed at  $h_1 = 1$ . The first rows of Figs. 2 and 3 trace this evolution. The principal curves ( $J = 0$ ,  $J \rightarrow \infty$ ,  $\omega'' = 0$ ,  $\omega = 0$ ) and the sign combinations of  $J$  and  $\omega''$  determine the stability regimes, as described in Sec. 3.1. In this asymmetric setting, most recurrent structures disappear: only the *upper* stability region persists, intersected by the universal boundary  $\rho = 1$  corresponding to the vertical  $J \rightarrow \infty$  resonance line. For sufficiently large  $h_2$ , a new degenerate structure, the *cut*, emerges from a local degeneracy of  $\omega''$  without a change in dispersion type.

**Small to moderate upper-layer thicknesses** ( $h_2 = 2, 3, 4, 5, 9$ ). For all these cases (Figs. 2b–d, 3b,c), the U-shaped  $J = 0$  branch lies in the left part of the diagram, while an additional  $J = 0$  branch emerges from  $(\rho = 1, k = 0)$  and interacts

with the vertical  $J \rightarrow \infty$  line, producing a stability region absent in symmetric configurations. The lower instability zone (Benjamin–Feir type) persists, while the U-shaped branch and the upper stability region above it shift slowly towards larger  $k$ , indicating reduced stability for long waves. The right-hand stability zone ( $J > 0$ ,  $\omega'' < 0$ ) bounded by  $\omega'' = 0$  and  $\omega = 0$  changes little with  $h_2$ .

**Strongly asymmetric case ( $h_2 = 13$ ).** For  $h_2 = 13$  (Fig. 3d), a new local structure appears in the lower part of the diagram: a closed  $\omega'' = 0$  contour (cut) enclosing a small modulationally unstable area within the main instability zone. Unlike standard  $\omega'' = 0$  contours, the cut does not change the sign of  $\omega''$ ; instead, it modifies the shape and connectivity of instability zones and reflects a local degeneracy of the dispersion relation. This structure is characteristic of strong thickness asymmetry and elongates with increasing  $h_2$ . In the limit  $h_2 \rightarrow \infty$ , it closes between  $(0, 0)$  and  $(0, 1)$ , yielding the La–HS configuration [31].

#### 4. ANALYSIS AND DISCUSSION OF THE FORMATION AND DEFORMATION OF PRINCIPAL STABILITY REGIONS

This section reviews the main stability domains in modulational diagrams of a two-layer fluid: a localized *loop*, the *upper* region bounded by  $J = 0$ , and the *corridor* between  $J \rightarrow \infty$  and  $\omega'' = 0$ ; in strongly asymmetric cases a degenerate *cut* also appears. Their occurrence, location in the  $(\rho, k)$ -plane, and underlying physical mechanisms are discussed.

##### 4.1. Conditions for the appearance and placement of the loop

The *loop* appears when the lower layer is at least as thick as the upper one and the overall depth is sufficient to approach the deep-water regime for internal waves. In these cases, the loop originates from solutions of a single condition corresponding to the  $J = 0$  curve. This zone represents a localized balance between focusing or defocusing nonlinearity and anomalous or normal dispersion, in which modulational perturbations are effectively neutralized.

For symmetric configurations ( $h_1 = h_2$ ), the loop first emerges at relatively large thicknesses (e.g.,  $h \geq 5$  in our results) and persists for larger  $h$ . With strongly asymmetric large-thickness configurations, it can also occur when the lower layer is only slightly thicker than the upper. In thin-layer cases (e.g.,  $h_1 = 2$ ,  $h_2 = 1$ ), boundary effects from the free surface and bottom prevent the  $J = 0$  curve from forming a closed contour, leaving only open structures such as the stability corridor.

The loop typically lies beneath the stability corridor, but in some configurations with a much thicker lower layer it partially overlaps the corridor, producing intricate interleaving of stable and unstable regions. Its point of contact with the  $k = 0$  axis—when present—marks a long-wave limit of localized stability. This contact point shifts with the  $h_1/h_2$  ratio: to lower  $\rho$  for strongly asymmetric cases, toward  $\rho \approx 0.5$  for moderately asymmetric ones, and toward  $\rho \approx 1$  for nearly symmetric layers, without reaching  $(0, 1)$ . In certain symmetric or near-symmetric large-thickness cases, the loop remains entirely detached from the  $k = 0$  axis and may approach the corridor boundary instead.

In the limiting HS–HS configuration ( $h_1, h_2 \rightarrow \infty$ ), the loop vanishes, merging with the  $k = 0$  axis. Here, boundary effects are absent and stability properties are determined solely by the global dispersion characteristics, with no isolated localized stability regions.

##### 4.2. Influence of geometric parameters on the upper stability region

The *upper* stability region occupies the part of the  $(\rho, k)$ -plane above the red  $J = 0$  curve. For equal layer thicknesses it spans  $0.1716 \leq \rho \leq 5.8275$  as  $k \rightarrow \infty$ , with limits given by  $\rho = \frac{2-\sqrt{2}}{2+\sqrt{2}}$  and  $\rho = \frac{2+\sqrt{2}}{2-\sqrt{2}}$ , in agreement with the relations in (7). For unequal thicknesses the high- $k$  range splits:  $0.1716 \leq \rho \leq 1$  contains the main upper region, while  $1 \leq \rho \leq 5.8275$  contains a other stability zone.

The shape of the upper region depends asymmetrically on the thickness ratio  $h_1/h_2$ . When the lower layer is thicker, its dispersion dominates, producing a downward shift of the lower boundary toward the stability corridor and, in some cases, a “pulling” of the upper region toward a coexisting loop (e.g.,  $h_1 > h_2$  with moderate asymmetry). When the upper layer is thicker, the stabilizing mechanism changes: the loop does not form, the pulling effect disappears, and the geometry of the upper region is altered accordingly.

This asymmetry, seen for various  $(h_1, h_2)$  pairs, reflects the different contributions of the two layers to the dispersion of the internal mode.

##### 4.3. Conditions for emergence, extent, and width of the stability corridor

The *stability corridor* is defined as the  $(\rho, k)$  region bounded by the blue  $J = \infty$  and green  $\omega'' = 0$  curves. It appears only when the lower layer thickness exceeds a certain threshold: for  $h_1 = 1$  the corridor is absent for all tested  $h_2$  values, while a very narrow corridor forms at  $h_1 = 2$  and expands with increasing  $h_2$ . Further increase to  $h_1 = 3$ – $4$  significantly widens the corridor at small  $\rho$ , extending its reach toward higher  $\rho$  values; for large  $h_1$  and  $h_2$  (e.g., 5–13) it becomes broad and nearly uniform, with intersection points of its boundaries shifting rightward and nearly merging.

When present, the corridor may intersect with a stability loop, producing complex local–global stability patterns. Its absence at small  $h_1$  is explained by the dominant influence of the free surface and bottom boundaries, which prevents the

formation of a bounded region enclosed by the  $J = \infty$  and  $\omega'' = 0$  curves. As  $h_1$  grows, the lower layer increasingly governs the dispersion, leading to the appearance and gradual broadening of the corridor; in the deep-water limit, it attains a wide, homogeneous form with minimal influence from intersection points.

#### 4.4. The cut as a degenerate stability region

The *cut* denotes a local topological structure on the modulational stability diagram in the form of a closed branch of the  $\omega'' = 0$  curve, isolating a small region of modulational instability ( $J > 0$ ,  $\omega'' > 0$ ) from the surrounding zone with identical parameter signs. Unlike standard  $\omega'' = 0$  contours, where  $\omega''$  changes sign across the curve, the cut is degenerate: near the point  $(k_0, \rho_0)$  with  $\omega'' = 0$ , the sign of  $\omega''$  remains the same on both sides. This feature appears for very thick upper layers combined with a thin lower layer, most clearly for  $h_1 = 1$ ,  $h_2 = 13$  (Fig. 3d), where it lies near the bottom of the diagram and touches the  $k = 0$  axis. For even thinner lower layers, the effect is expected at smaller  $h_2$ , potentially yielding more complex degenerate structures. Such regions are highly sensitive to density variations and may reveal additional mechanisms of modulational stability and instability.

### CONCLUSIONS

A comprehensive topological classification of modulational stability diagrams for wave packets at the interface of a two-layer fluid with interfacial tension has been developed in the  $(\rho, k)$  parameter space for a wide range of layer-thickness ratios. The stability landscape is governed by the interplay of four characteristic curves:  $J = 0$  (change of nonlinearity sign),  $\omega'' = 0$  (change of dispersion type),  $J = \infty$  (resonance condition), and  $\omega = 0$  (linear existence limit). Depending on system geometry, four distinct stability structures are identified: a localized closed loop, a global upper stability region, an elongated corridor between resonance and dispersion curves, and a degenerate cut structure. Each reflects a specific balance between focusing/defocusing nonlinearity and anomalous/normal dispersion.

The loop appears when the lower layer is sufficiently thick, often in symmetric or near-symmetric configurations, and marks a narrow parameter interval of complete nonlinear–dispersive compensation; it vanishes in the deep-water HS–HS limit. The upper stability region changes shape and position with layer-thickness ratio: when the lower layer is thicker, its boundary shifts toward the loop, whereas with a thicker upper layer the loop is absent. The stability corridor forms only above a threshold lower-layer thickness, widens with increasing depths, and can partially overlap with the loop to create multi-component stability zones. The cut arises when a very thick upper layer is combined with a thin lower layer, corresponding to a local degeneracy of  $\omega''$  without change in dispersion type.

These results provide a unified interpretation of modulational stability in terms of global and local nonlinear–dispersive balances, identifying conditions where stability is controlled either by localized parameter islands or by global spectral properties. In a companion study (Part II), we will investigate how the magnitude of interfacial surface tension modifies the topology of stability boundaries, thereby uncovering additional stabilization and destabilization mechanisms that arise from the combined action of capillary and gravitational effects.

### Acknowledgments

Olga Avramenko thanks the Research Council of Lithuania for supporting this work.

### ORCID

 Olga Avramenko, <https://orcid.org/0000-0002-7960-1436>;  Volodymyr Naradovyi, <https://orcid.org/0000-0001-5187-8831>

### REFERENCES

- [1] T. B. Benjamin, and J. E. Feir, *J. Fluid Mech.* **27**(3), 417–430 (1967). <https://doi.org/10.1017/S002211206700045X>
- [2] V. E. Zakharov, *J. Appl. Mech. Tech. Phys.* **9**, 190–194 (1968). <https://doi.org/10.1007/BF00913182>
- [3] H. Hasimoto, and H. Ono, *J. Phys. Soc. Jpn.* **33**(3), 805–811 (1972). <https://doi.org/10.1143/JPSJ.33.805>
- [4] A. H. Nayfeh, *J. Appl. Mech.* **43**(4), 584–588 (1976). <https://doi.org/10.1115/1.3423936>
- [5] R. H. J. Grimshaw, and D. I. Pullin, *J. Fluid Mech.* **160**, 297–315 (1985). <https://doi.org/10.1017/S0022112085003494>
- [6] I. Selezov, O. Avramenko, C. Kharif, and K. Trulsen, *C. R. Mécanique* **331**(3), 197–201 (2003). [https://doi.org/10.1016/S1631-0721\(03\)00043-3](https://doi.org/10.1016/S1631-0721(03)00043-3)
- [7] M. Oikawa, M. Okamura, and M. Funakoshi, *J. Phys. Soc. Jpn.* **58**(18), 4416–4430 (1989). <https://doi.org/10.1143/JPSJ.58.4416>
- [8] M. J. Ablowitz, and N. S. Haut, *Theor. Math. Phys.* **159**, 689–697 (2009). <https://doi.org/10.1007/s11232-009-0057-8>
- [9] P. Christodoulides, and F. Dias, *Phys. Fluids* **7**(12), 3013–3027 (1995). <https://doi.org/10.1063/1.868678>
- [10] O. V. Avramenko, V. V. Naradovyi, and I. T. Selezov, *J. Math. Sci.* **212**, 131–141 (2016). <https://doi.org/10.1007/s10958-015-2654-4>
- [11] S. Panda, and S. C. Martha, *Math. Model. Anal.* **22**(6), 827–851 (2017). <https://doi.org/10.3846/13926292.2017.1386239>



- [12] A. Purkait, and D. Suma, Ocean Dyn. **69**(1), 21–27 (2019). <https://doi.org/10.1007/s10236-018-1227-8>
- [13] S. Li, A. Cao, J. Song, Ch. Yu, and J. Chen, Phys. Fluids **32**(7), 072104 (2020). <https://doi.org/10.1063/5.0013225>
- [14] S. Li, J. Song, and A. Cao, Chin. Phys. B **29**(12), 124702 (2020). <https://doi.org/10.1088/1674-1056/abb3e4>
- [15] S. Li, J. Chen, A. Cao, and J. Song, Chin. Phys. B **28**, 124701 (2019). <https://doi.org/10.1088/1674-1056/ab53cf>
- [16] S. Li, X. Xie, D. Chen, and J. Song, Phys. Fluids **34**, 092105 (2022). <https://doi.org/10.1063/5.0098077>
- [17] T. Pal, and A. K. Dhar, Ocean Dyn. **72**, 241–257 (2022). <https://doi.org/10.1007/s10236-022-01503-1>
- [18] T. Pal, and A. K. Dhar, Ocean Dyn. **74**, 133–147 (2024). <https://doi.org/10.1007/s10236-023-01594-4>
- [19] T. G. Talipova, E. N. Pelinovsky, and C. Kharif, JETP Lett. **94**, 182–186 (2011). <https://doi.org/10.1134/S0021364011150124>
- [20] Y. Liang, A. Zareei, and M.-R. Alam, J. Fluid Mech. **811**, 400–420 (2017). <https://doi.org/10.1017/jfm.2016.754>
- [21] K. W. Chow, H. N. Chan, and R. H. J. Grimshaw, Nat. Hazards Earth Syst. Sci. **19**, 583–587 (2019). <https://doi.org/10.5194/nhess-19-583-2019>
- [22] G. S. Voelker, and M. Schlutow, Geophys. Astrophys. Fluid Dyn. (submitted, 2023). <https://doi.org/10.48550/arXiv.2309.17392>
- [23] V. M. Kuklin, and E. V. Poklonskiy, East Eur. J. Phys. **4**, 41–46 (2019). <https://doi.org/10.26565/2312-4334-2019-4-04>
- [24] R. Bianchini, A. Maspero, and S. Pasquali, arXiv:2507.10390 (2025). <https://doi.org/10.48550/arXiv.2507.10390>
- [25] V. M. Lashkin, and O. K. Cheremnykh, Phys. Rev. E **110**, 024216 (2024). <https://doi.org/10.1103/PhysRevE.110.024216>
- [26] A. D. Ionescu, and F. Pusateri, Mem. Am. Math. Soc. **256**, 1227 (2018). <https://doi.org/10.1090/memo/1227>
- [27] W.-P. Düll, Arch. Ration. Mech. Anal. **239**, 831–914 (2021). <https://doi.org/10.1007/s00205-020-01586-4>
- [28] Y. Sedletsky, Ukr. J. Phys. **66**(1), 41–54 (2021). <https://doi.org/10.15407/ujpe66.1.41>
- [29] M. J. Ablowitz, X. D. Luo, and Z. H. Musslimani, J. Fluid Mech. **961**, A3 (2023). <https://doi.org/10.1017/jfm.2023.128>
- [30] O. Avramenko, and V. Naradovyi, J. Appl. Math. Comput. Mech. **24**(2), 5–17 (2025). <https://doi.org/10.17512/jamcm.2025.2.01>
- [31] O. Avramenko, and V. Naradovyi, Rend. Mat. Appl. (7) **47**, 55–69 (2026). <https://doi.org/10.48550/arXiv.2411.15168>

## НЕСТІЙКІСТЬ БЕНДЖАМІНА–ФЕЙРА МІЖФАЗНИХ ГРАВІТАЦІЙНО-КАПІЛЯРНИХ ХВИЛЬ У ДВОШАРОВІЙ РІДИНІ

Ольга Авраменко<sup>a,b</sup>, Володимир Наратовий<sup>c</sup>

<sup>a</sup>Національний університет "Кієво-Могилянська академія вул. Сковороди, 2, Київ, 04070, Україна


<sup>b</sup>Університет Вітовта Великого, вул. К. Донелайчо, 58, Каунас, 44248, Литва

<sup>c</sup>Центральноукраїнський державний університет імені Володимира Винниченка,  
вул. Шевченка, 1, Кропивницький, 25006, Україна

У цій роботі подано детальне дослідження модуляційної стійкості хвильових пакетів на межі розділу двошарової ідеальної нестисливої рідини зі скінченною товщиною шарів і міжфазним поверхневим натягом. Аналіз стійкості виконано для широкого діапазону відношень густин та геометричних конфігурацій, що дозволяє побудувати діаграми стійкості на площині  $(\rho, k)$ , де  $\rho$  — відношення густин, а  $k$  — хвильове число основної гармоніки. Як критерій стійкості використано індекс Бенджаміна–Фейра, взаємодія якого з кривизною дисперсійного співвідношення визначає момент виникнення модуляційної нестійкості. Топологія діаграм стійкості виявляє кілька характерних структур: локалізовану замкнену петлю стійкості всередині області нестійкості, глобальну верхню область стійкості, витягнутий коридор, обмежений резонансною та дисперсійною кривими, а також вироджену структуру типу розріз, що виникає у сильно асиметричних випадках. Кожна з цих структур відповідає певному фізичному механізму, пов'язаному з балансом між фокусувальною/дефокусувальною нелінійністю та нормальною/аномальною дисперсією. Систематична зміна товщини шарів дозволяє простежити формування, деформацію та зникнення цих областей, а також їх об'єднання чи сегментацію внаслідок резонансних ефектів. Розглянуто граничні випадки напівнескінчених шарів для узгодження отриманих результатів із відомими конфігураціями, включно з системами типу "півпростір–шар", "шар–півпростір" та "півпростір–півпростір". Особливу увагу приділено впливу симетрії та асиметрії геометрії шарів, що визначає розташування та зв'язність стійких і нестійких областей у параметричному просторі. Отримані результати формують єдину концептуальну основу для інтерпретації модуляційної стійкості у двошарових рідинах з поверхневим натягом, підкреслюючи як глобальні режими, керовані дисперсією, так і локалізовані острови стійкості. Ця робота становить Частина I дослідження; Частина II буде присвячена ролі змінного поверхневого натягу, який, як очікується, деформує наявні області стійкості та змінює відповідні нелінійно-дисперсійні механізми.

**Ключові слова:** модуляційна стійкість; міжфазні хвилі; двошарова рідина; нестійкість Бенджаміна–Фейра; поверхневий натяг

## INFLUENCE OF THERMAL RADIATION EFFECT ON MHD MASS TRANSFER FLOW PAST A POROUS VERTICAL PLATE IN PRESENCE OF CONSTANT HEAT FLUX

T.K. Chutia<sup>a</sup>,  K. Choudhury<sup>b\*</sup>, K. Chamuah<sup>a</sup>, S. Ahmed<sup>b</sup>

<sup>a</sup>Department of Mathematics, Moridhal College, Assam, India

<sup>b</sup>Department of Mathematics, University of Science & Technology Meghalaya, India

\*Corresponding Author E-mail: [kangkan22@gmail.com](mailto:kangkan22@gmail.com)

Received June 22, 2025; revised August 18, 2025; accepted August 20, 2025

In this work, we have undertaken to study heat and mass transfer in MHD convective flow past an infinite plate with porous media in existence of radiation, thermal diffusion effect and heat sink. A uniform strength of magnetic field was used transversely in the fluid region. The novelty of this study is to look into the effect of radiation (Rosseland approximation) and heat sink on natural convective flow in the presence of viscous dissipation and Joule heating with constant heat flux and constant suction velocity, past a continuously moving vertical plate in a porous medium. The principal equations are solved by perturbation technique to get statements for velocity, temperature, and concentration fields. In this paper we also consider several physical quantities on the flow domain graphically as well as tabularly which have been studied previously by other researchers except few new cases like light velocity and temperature relationship from different sources such as density gradient effect which are being discussed herein for first time. However, the current investigation has a wide impact on several engineering processes like glass blowing, paper production, extrusion of plastic sheets, etc.

**Keywords:** MHD; Heat transfer; Thermal diffusion; Porous media; Thermal radiation

AMS subject classification: 76W05

PACS: 44.25.+f

### INTRODUCTION

The magnetic field strength is often enhanced by a progressive, stable, and sustained current. In this case, considering that a spacecraft must navigate through these regions, which are known to be difficult to navigate, it is important to be able to predict their trajectories. The elements of any spacecraft designed for Mars missions include ion thrusters, attitude control systems (or gyros), power generation and transmission systems, vehicle components such as avionics or sensors etc. Consequently, spacecraft design must take into account the effects of MHD so that controllers can achieve advantageous performance before reaching Mars. Some of them are like Alfvén (1942), Ahmed and Choudhury (2019), Seth et al. (2016), Mansour (1990), Seth et al. (2011), Choudhury and Agarwalla (2023), Saikia et al. (2024), Choudhury et al. (2022), Prasad et al. (2023), Balamurugan et al. (2022) etc. Thermal radiation is known to dramatically affect the characteristics of MHD flow. It is a type of electromagnetic wave that has characteristics similar to visible light for its intensity and wavelength but cannot be seen with the naked eye. Thermal radiation can carry energy as heat, infrared, ultraviolet, and X-rays. This induces electric currents in conductors, which generate heat by Joule heating. MHD flow in a viscous incompressible fluid past an impulsively started oscillating plate has been investigated by Appidi et al. (2021). The temperature gradient and stress distributions were computed for different values of space angle of the plates in order to determine the effect of radiation on the MHD flow. They found that both thermal radiation and heat source effect MHD flow and that their effects depend on their spatial distribution at the interface between two media.

The Soret effect or thermal-diffusion effect is an experimental study of the pressure drop under temperature gradient from the solid surface to the fluid. It was originated by the renowned chemist Charles Soret in 1879. The Soret effect is utilized for isotope separation and in mixtures of gases with a very light molecular weight, like H<sub>2</sub> and He. Wide-ranging literature on various features of thermal diffusion on mass transfer related problems can be found in Kafousias and Williams (1998), Ahmed et al. (2013, 2018, 2021), Ahmed and Sengupta (2011), and Chamuah and Ahmad (2021).

The present work generalizes the work done by Chamuah and Ahmed (2021) by including heat sink in MHD convective flow through a porous media. The novelty of this study is to look into the effect of radiation (Rosseland approximation) and heat sink on natural convective flow in the presence of viscous dissipation and Joule heating with constant heat flux and constant suction velocity, past a continuously moving vertical plate in a porous medium. Heat transfer and mass transfer are governed by the same equations, however they different forms. We can rewrite these equations in a simpler way where similarity parameters are used to get rid of their dimensionality. Perturbation techniques are applied to solve these equations and graphically results on plots and tables are shown. However, a comparison with an already published paper has been shown to ensure the accuracy of our present work.

### BASIC EQUATIONS

The vector equations that describe the motion of an incompressible viscous electrically conducting Newtonian fluid through the porous medium are:

Equation of continuity:

$$\vec{\nabla} \cdot \vec{q} = 0 \tag{1}$$

Gauss's law of magnetism:

$$\vec{\nabla} \cdot \vec{B} = 0 \tag{2}$$

Ohm's law:

$$\vec{J} = \sigma(\vec{E} + \vec{q} \times \vec{B}) \tag{3}$$

Momentum equation:

$$\rho(\vec{q} \cdot \vec{\nabla})\vec{q} = \rho\vec{g} - \vec{\nabla}p + \vec{J} \times \vec{B} + \mu\nabla^2\vec{q} - \frac{\mu\vec{q}}{K'} \tag{4}$$

Energy equation:

$$\rho C_p (\vec{q} \cdot \vec{\nabla})T = \kappa\nabla^2T + \phi + \frac{\vec{J}^2}{\sigma} - Q'(T - T_\infty) - \vec{\nabla} \cdot \vec{q}_r \tag{5}$$

Species continuity equation:

$$(\vec{q} \cdot \vec{\nabla})C = D_M \nabla^2C + \frac{D_M K_T}{T_M} \nabla^2T \tag{6}$$

Equation of state

$$\rho_\infty = \rho \left[ 1 + \beta(T - T_\infty) + \bar{\beta}(C - C_\infty) \right] \tag{7}$$

Radiation heat flux as per Rosseland approximation

$$\vec{q}_r = -\frac{4\sigma^*}{3\kappa^*} \vec{\nabla}T^4 \tag{8}$$

All the physical quantities are defined in the nomenclature.

### MATHEMATICAL FORMULATION

The convective flow through a porous vertical plate with uniform suction is investigated by considering the two-dimensional motion of an incompressible fluid. The investigation is based on the following basic premises:

1. Entire fluid properties without density are constant.
2. Plate is electrically insulated.
3. No peripheral electric field is functional to system.
4. Electric potential needed to create Lorentz force be zero.
5. Magnetic field induced by conducting wire parallel to z direction.

We now introduce a Cartesian coordinate system  $(x', y', z')$  with  $X$  - axis along with the plate in the upward vertical direction,  $Y$  - axis normal to the plate directed into the fluid region, and  $Z$  - axis along the width of the plate and the induced magnetic field is negligible. The prototype of the problem is shown in Figure A.

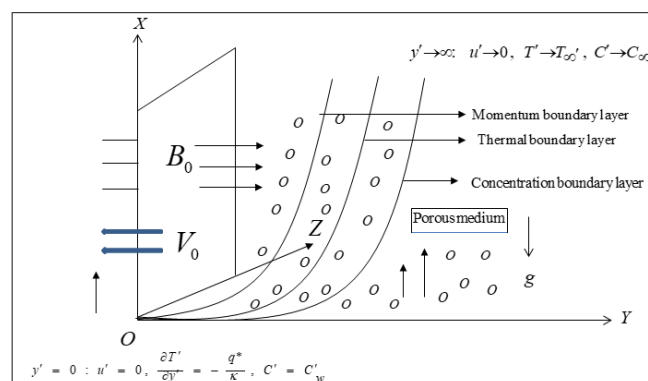


Figure A. Physical model of the problem

The rate of radiative heat flux in an optically thin gray gas is given by

$$\frac{\partial q_r^*}{\partial y'} = -\frac{16\sigma^* T_\infty'^3}{3k^*} \frac{\partial^2 T'}{\partial y'^2} \quad (9)$$

Where  $k^*$  and  $\sigma^*$  be respectively absorption coefficient and Stefan-Boltzmann constant.

Based on the preceding axioms, and the usual boundary layer estimates, the governing equations yield the forms as follows:

$$\frac{\partial v'}{\partial y'} = 0 \quad (10)$$

$$v' \frac{\partial u'}{\partial y'} = g\beta(T' - T_\infty') + g\bar{\beta}(C' - C_\infty') + v' \frac{\partial^2 u'}{\partial y'^2} - \frac{\sigma B_o^2 u'}{\rho} - \frac{vu'}{K'} \quad (11)$$

$$\rho C_p v' \frac{\partial T'}{\partial y'} = \kappa \frac{\partial^2 T'}{\partial y'^2} + \mu \left( \frac{\partial u'}{\partial y'} \right)^2 + \sigma B_o^2 u'^2 - \frac{\partial q_r'}{\partial y'} - Q'(T' - T_\infty') \quad (12)$$

$$v' \frac{\partial C'}{\partial y'} = D_M \frac{\partial^2 C'}{\partial y'^2} + \frac{D_M K_T}{T_M} \frac{\partial^2 T'}{\partial y'^2} \quad (13)$$

with boundary conditions

$$y' = 0: u' = U, \quad \frac{\partial T'}{\partial y'} = -\frac{q^*}{\kappa}, \quad C' = C_w' \quad (14)$$

$$y' \rightarrow \infty: u' \rightarrow 0, \quad T' \rightarrow T_\infty', \quad C' \rightarrow C_\infty' \quad (15)$$

$$\text{Equation (10) yields } v' = \text{a constant} = -V_o \quad (V_o > 0) \quad (16)$$

Non-dimensional parameters:

$$u = \frac{u'}{U}, \quad y = \frac{V_o y'}{v}, \quad \theta = \frac{T' - T_\infty'}{\frac{q^* v}{\kappa V_o}}, \quad \phi = \frac{C' - C_\infty'}{C_w' - C_\infty'}, \quad Gr = \frac{v^2 g \beta q^*}{\kappa U V_o^3}, \quad Ec = \frac{\rho U^2 V_o}{q^*}, \quad Pr = \frac{\mu C_p}{\kappa},$$

$$Gm = \frac{g \bar{\beta} (C_w' - C_\infty') v}{U V_o^2}, \quad Sc = \frac{v}{D_M}, \quad k_p = \frac{K' V_o^2}{v^2}, \quad M = \frac{\sigma B_o^2 v}{\rho V_o^2}, \quad R = \frac{16 v k^* \sigma^* T_\infty'^3}{\rho C_p V_o^2},$$

$$Q = \frac{Q' v}{\rho C_p V_o^2}, \quad Sr = \frac{D_M K_T q^*}{T_M \kappa V_o (C_w' - C_\infty')}$$

Dimensionless governing equations are

$$\frac{d^2 u}{dy^2} + \frac{du}{dy} - \xi u = -Gr\theta - Gm\phi \quad (17)$$

$$\frac{d^2 \theta}{dy^2} + \lambda_1 \frac{d\theta}{dy} - \lambda_2 \theta = -Ec\lambda_3 u'^2 - Ec\lambda_4 u^2 \quad (18)$$

$$\frac{d^2 \phi}{dy^2} + Sc \frac{d\phi}{dy} = -ScSr \frac{d^2 \theta}{dy^2} \quad (19)$$

$$\text{Where } \xi = M + \frac{1}{k_p}; \lambda_1 = \frac{Pr}{1+R}; \lambda_2 = \frac{QPr}{1+R}; \lambda_3 = \frac{1}{1+R}; \lambda_4 = \frac{M}{1+R}$$

with boundary conditions

$$y = 0: u = 1, \quad \frac{d\theta}{dy} = -1, \quad \phi = 1 \quad (20)$$

$$y \rightarrow \infty : u \rightarrow 0, \theta \rightarrow 0, \phi \rightarrow 0 \tag{21}$$

**METHOD OF SOLUTION**

We assume the solutions to equations (17) to (19) as

$$u = u_o(y) + Ec u_1(y) + O(Ec^2) \tag{22}$$

$$\theta = \theta_o(y) + Ec \theta_1(y) + O(Ec^2) \tag{23}$$

$$\phi = \phi_o(y) + Ec \phi_1(y) + O(Ec^2) \tag{24}$$

Here  $Ec$ , the Eckert number ( $Ec \ll 1$ ). By substituting equations (22) to (24) into equations (17) to (19) and equating the coefficient of analogous terms while deserting the terms of  $O(Ec^2)$ , the succeeding equations are derived.

$$\frac{d^2 u_o}{dy^2} + \frac{du_o}{dy} - \xi u_o = -Gr \theta_o - Gm \phi_o \tag{25}$$

$$\frac{d^2 \theta_o}{dy^2} + \lambda_1 \frac{d\theta_o}{dy} - \lambda_2 \theta_o = 0 \tag{26}$$

$$\frac{d^2 \phi_o}{dy^2} + Sc \frac{d\phi_o}{dy} = -ScSr \frac{d^2 \theta_o}{dy^2} \tag{27}$$

$$\frac{d^2 u_1}{dy^2} + \frac{du_1}{dy} - \xi u_1 = -Gr \theta_1 - Gm \phi_1 \tag{28}$$

$$\frac{d^2 \theta_1}{dy^2} + \lambda_1 \frac{d\theta_1}{dy} - \lambda_2 \theta_1 = -\lambda_3 u_o'^2 - \lambda_4 u_o^2 \tag{29}$$

$$\frac{d^2 \phi_1}{dy^2} + Sc \frac{d\phi_1}{dy} = -ScSr \frac{d^2 \theta_1}{dy^2} \tag{30}$$

with boundary conditions

$$y = 0 : u_o = 1; \theta_o' = -1; \phi_o = 1; u_1 = 0; \theta_1' = 0; \phi_1 = 0; \tag{31}$$

$$y \rightarrow \infty : u_o \rightarrow 0; \theta_o \rightarrow 0; \phi_o \rightarrow 0; u_1 \rightarrow 0; \theta_1 \rightarrow 0; \phi_1 \rightarrow 0; \tag{32}$$

Solutions to the equations (25)-(30) under the conditions (31) and (32) are

$$u_o = p_3 e^{-p_1 y} - p_4 e^{-Scy} + p_6 e^{-p_5 y} \tag{33}$$

$$\theta_o = \frac{1}{p_1} e^{-p_1 y} \tag{34}$$

$$\phi_o = (1 - p_2) e^{-Scy} + p_2 e^{-p_1 y} \tag{35}$$

$$u_1 = p_{27} e^{-p_5 y} + p_{21} e^{-p_1 y} + p_{22} e^{-2p_1 y} + p_{23} e^{-2Scy} + p_{24} e^{-(p_1 + p_5)y} + p_{25} e^{-(p_1 + Sc)y} - p_{26} e^{-Scy} \tag{36}$$

$$\theta_1 = p_{13} e^{-p_1 y} - p_7 e^{-2p_5 y} - p_8 e^{-2p_1 y} - p_9 e^{-2Scy} - p_{10} e^{-(p_1 + p_5)y} + p_{11} e^{-(p_1 + Sc)y} + p_{12} e^{-(p_5 + Sc)y} \tag{37}$$

$$\phi_1 = p_{20} e^{-Scy} - p_{14} e^{-p_1 y} + p_{15} e^{-2p_5 y} + p_{16} e^{-2p_1 y} + p_{17} e^{-2Scy} + p_{18} e^{-(p_1 + p_5)y} - p_{19} e^{-(p_1 + Sc)y} \tag{38}$$

where

$$p_1 = \frac{\lambda_1 + \sqrt{\lambda_1^2 + 4\lambda_2}}{2}, p_2 = \frac{ScSr}{Sc - p_1}, p_3 = \frac{-Gr - p_2 Gm}{p_1^2 - p_1 - \xi}, p_4 = \frac{Gm(1 - p_2)}{Sc^2 - Sc - \xi}, p_5 = \frac{1 + \sqrt{1 + 4\xi}}{2},$$

$$p_6 = 1 + p_3 + p_4, p_7 = \frac{\lambda_3 p_5^2 p_6^2 + \lambda_4 p_6^2}{4p_5^2 - 2\lambda_1 p_5 - \lambda_2}, p_8 = \frac{\lambda_3 p_1^2 p_3^2 + \lambda_4 p_3^2}{4p_1^2 - 2\lambda_1 p_1 - \lambda_2}, p_9 = \frac{\lambda_3 Sc^2 p_4^2 + \lambda_4 p_4^2}{4Sc^2 - 2\lambda_1 Sc - \lambda_2},$$

$$\begin{aligned}
p_{10} &= \frac{2\lambda_3 p_1 p_3 p_5 p_6 + 2\lambda_4 p_3 p_6}{(p_1 + p_5)^2 - \lambda_1 (p_1 + p_5) - \lambda_2}, p_{11} = \frac{2\lambda_3 p_1 p_3 p_4 Sc + 2\lambda_4 p_3 p_4}{(p_1 + Sc)^2 - \lambda_1 (p_1 + Sc) - \lambda_2}, \\
p_{12} &= \frac{2\lambda_3 p_4 p_5 p_6 Sc + 2\lambda_4 p_4 p_6}{(p_5 + Sc)^2 - \lambda_1 (p_5 + Sc) - \lambda_2}, \\
p_{13} &= \frac{1}{p_5} [2p_5 p_7 + 2p_1 p_8 + 2Scp_9 + (p_1 + p_5)p_{10} - (p_1 + Sc)p_{11} - (p_5 + Sc)p_{12}], \\
p_{14} &= \frac{ScSr p_1^2 p_{13}}{p_1^2 - Scp_1}, p_{15} = \frac{4ScSr p_5^2 p_7}{4p_5^2 - 2Scp_5}, p_{16} = \frac{4ScSr p_1^2 p_8}{4p_1^2 - 2Scp_1}, p_{17} = \frac{4Sc^3 Sr p_9}{2Sc^2}, \\
p_{18} &= \frac{ScSr (p_1 + p_5)^2 p_{10}}{(p_1 + p_5)^2 - Sc(p_1 + p_5)}, p_{19} = \frac{ScSr (p_1 + Sc)^2 p_{11}}{(p_1 + Sc)^2 - Sc(p_1 + Sc)}, p_{20} = p_{14} - p_{15} - p_{16} - p_{17} - p_{18} + p_{19}, \\
p_{21} &= \frac{Gmp_{14} - Grp_{13}}{p_1^2 - p_1 - \xi}, p_{22} = \frac{Grp_8 - Gmp_{16}}{4p_1^2 - 2p_1 - \xi}, p_{23} = \frac{Grp_9 - Gmp_{17}}{4Sc^2 - 2Sc - \xi}, p_{24} = \frac{Grp_{10} - Gmp_{18}}{(p_1 + p_5)^2 - (p_1 + p_5) - \xi}, \\
p_{25} &= \frac{-Grp_{11} + Gmp_{16}}{(p_1 + Sc)^2 - (p_1 + Sc) - \xi}, p_{26} = \frac{Gmp_{20}}{Sc^2 - Sc - \xi}, p_{27} = p_{26} - p_{21} - p_{22} - p_{23} - p_{24} - p_{25}
\end{aligned}$$

**Skin friction:**

Skin friction is given by

$$\tau = -\left. \frac{\partial u}{\partial y} \right|_{y=0} = -[\tau_0 + Ec\tau_1] \quad (39)$$

Where

$$\tau_0 = -p_1 p_3 + Scp_4 - p_5 p_6$$

$$\tau_1 = -p_5 p_{27} - p_1 p_{21} - 2p_1 p_{22} - 2Scp_{23} - (p_5 + p_1) p_{24} - (Sc + p_1) p_{25} + Scp_{26}$$

**Plate temperature:**

The dimensionless temperature field is,

$$\theta(y) = \theta_0(y) + Ec\theta_1(y)$$

Non-dimensional plate temperature is given by,

$$\theta_w = \theta_0(0) + Ec\theta_1(0) \quad (40)$$

**Sherwood number:**

Sherwood number is given by

$$Sh = -\left. \frac{\partial \phi}{\partial y} \right|_{y=0} = -[Sh_0 + EcSh_1] \quad (41)$$

Where

$$Sh_0 = -Sc(1 - p_2) - p_1 p_2$$

$$Sh_1 = -Scp_{20} + p_1 p_{14} - 2p_5 p_{15} - 2p_1 p_{16} - 2Scp_{17} - (p_1 + p_5) p_{18} + (p_1 + Sc) p_{19}$$

**RESULTS AND DISCUSSIONS**

The numerical computations have been carried out for the representative velocity, temperature, concentration, skin friction, and plate temperature at the wall for different values of the physical parameters involved in the problem. The influence the flow parameters Prandtl number, Schmidt number, thermal radiation, Soret number, thermal Grashof number and mass Grashof number on these fields have been depicted in Figures 1 to 15. Numerical results of shear stress and plate temperature are presented in Table 1 and Table 2. The default values for the flow parameters are chosen as

$$Pr = 0.71, Sc = 0.6, R = 1, K = 1, Sr = 1, Gr = 10, Gm = 5, M = 1.5, E = 0.01, Q = 5$$



The drag-like force called Lorentz force produces a kind of friction on the flow and thus opposes the transport phenomenon. With the increasing values of magnetic parameter, the fluid velocity decreases significantly which is seen from Figure 1. This observation implies that applying a transverse magnetic field decelerate fluid motion. This observation is consistent with the physical fact that a magnetic body force develops due to the interaction of the fluid velocity and magnetic field, which serves as a resistive force to the flow, and as a consequence fluid flow gets decelerated. The velocity distribution due to Soret number shows statistical characteristic features in which it can be observed from Figure 2 that with temperature gradients inducing significant mass diffusion effects, the fluid velocity increases. The effect of thermal radiation on flow phenomena is depicted in Figure 3 where it is seen that with increase in thermal radiation rate, decrease in energy transport to fluid takes place and hence decelerates motion of fluid particles. The effect of heat sink on fluid velocity is seen in Figure 4. It has been observed that fluid velocity decreases marginally with small increase in heat sink whereas it decreases significantly with significant rise in heat sink. So, with large amount of heat absorption the fluid motion decreases rapidly. In this portion of the experiment, the effect of Prandtl number and Schmidt number on the velocity profile is discussed.

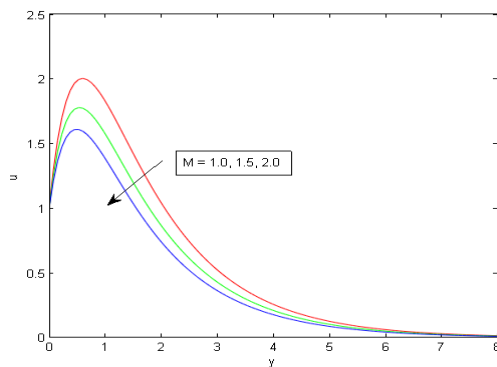


Figure 1. Rate of movement for variations in M

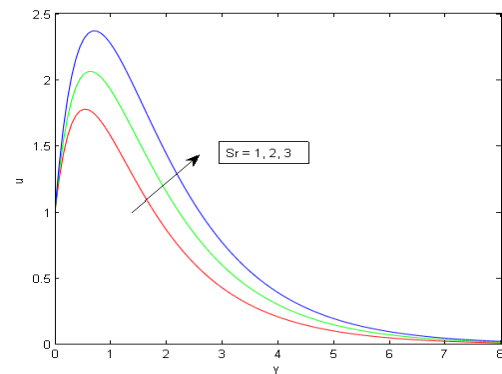


Figure 2. Rate of movement for variations in Sr

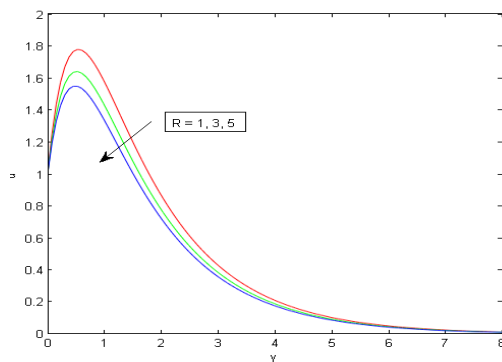


Figure 3. Rate of movement for variations in R

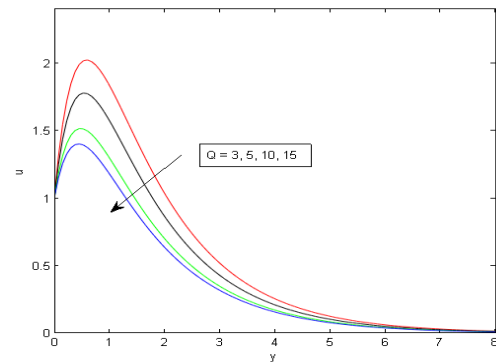


Figure 4. Rate of movement for variations in Q

In Figure 5, it was observed that as the Schmidt number increases, momentum diffusivity increases, resulting in lower fluid velocities. This result was verified by plotting velocity versus Schmidt number in Figure 6, which showed an increase in fluid velocity with increasing values of Prandtl number.

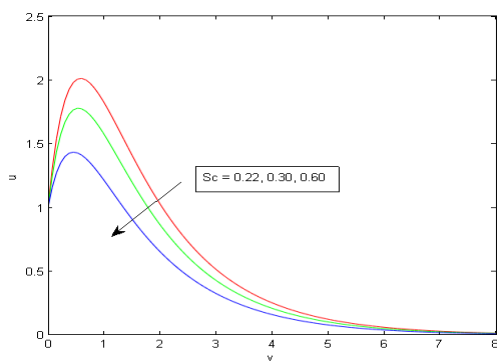


Figure 5. Rate of movement for variations in Sc

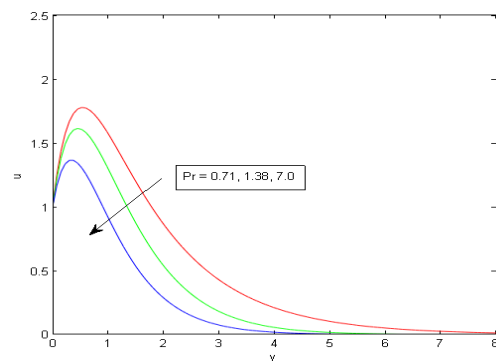


Figure 6. Rate of movement for variations in Pr

The effects of Grashof numbers are depicted in Figures 7 and 8 where it was seen that both thermal buoyancy force and mass buoyancy force have similar effects on the flow domain as well as any one of these forces dominates over another depending upon specific conditions. Thermal buoyancy force (Figure 7) and solutal buoyancy force (Figure 8)

cause the velocity field to rise substantially. This happens due to the direct proportionality of buoyancy force to those of Grashof numbers.

The heat transfer rate of a fluid is controlled by the momentum and thermal insulation of the interface between the fluid and its surroundings. The influence of the heat conductivity on temperature distribution is displayed in Figures 9 and 10. It has been observed that high conductivity fluids such as molten salt have low thermal diffusivity, which results in fast changes in temperatures. Thermal radiation also affects fluid temperature distribution because low thermal conductivity materials absorb large amounts of radiant energy due to higher temperatures compared to fluids having high thermal conductivity. Figure 11 shows another example where fluid temperature can be affected by heat sink coefficient. It is observed from Figure 12 that fluid temperature is reduced due to the increasing values of Eckert number.

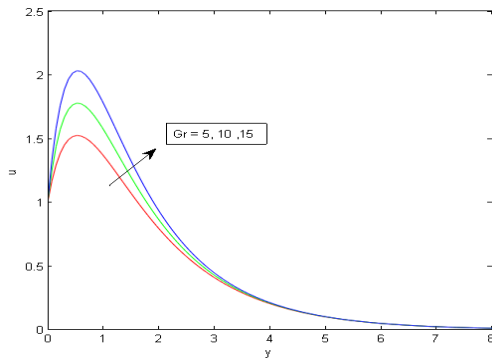


Figure 7. Rate of movement for variations in Gr

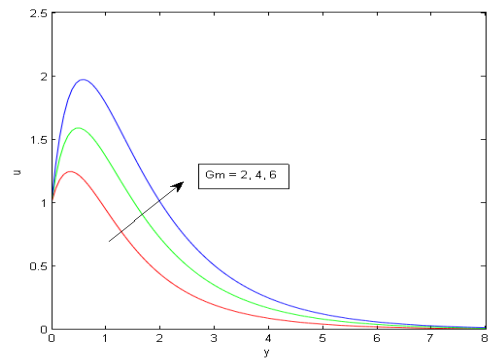


Figure 8. Rate of movement for variations in Gm

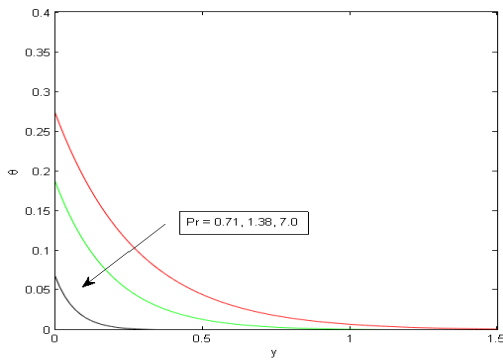


Figure 9. Temperature field for variations in Pr

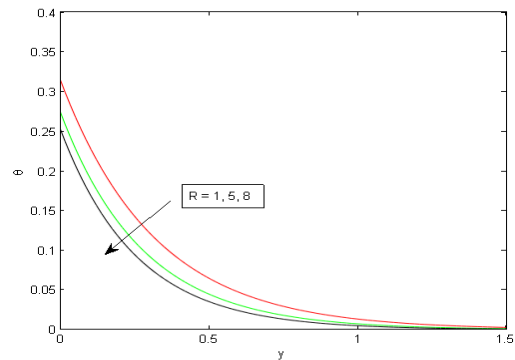


Figure 10. Temperature field for variations in R

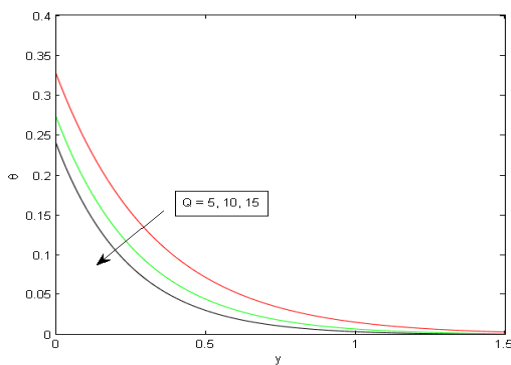


Figure 11. Temperature field for variations in Q

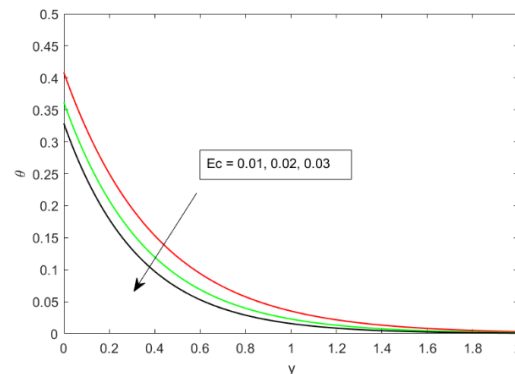


Figure 12. Temperature field for variations in Ec

The concentration profiles are plotted in Figures 13, 14 and 15. In Figure 13, it is seen that the concentration of the fluid falls with increasing values of Schmidt number due to low mass diffusivity. It is noted that an increase in Schmidt number means a fall in mass diffusivity. Thus, the concentration on the plate falls because of low mass diffusivity. This observation is compatible with the physical reality that increasing Schmidt number causes a decrease in mass diffusivity, which causes a decrease in fluid concentration. Figure 14 indicates that an increase in Soret number leads to an increase in the fluid concentration. Figure 15 shows that the influence of heat sink is to decrease the fluid concentration.

As we can see from Table 1, as R, Sc and Q increase, skin friction increases. In addition to this, it is inferred from Table 1 that the skin friction gets diminished for increasing magnetic parameter M. This indicates that the imposition of a transverse magnetic field inhibits viscous drag due to its application on thin films with high aspect ratio. Henceforth, the coefficient of momentum at the planar surface becomes larger for increasing M. Table 2 shows that plate temperature

increases when Pr increase. The temperature of the plate decreases due to the effect of the magnetic field  $M$  as it is applied transversely to the fluid region and the similar effect found for Eckert number  $Ec$ .

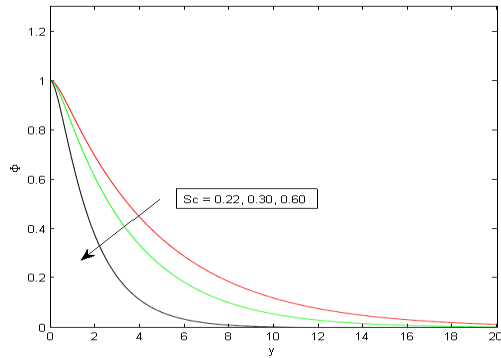


Figure 13. Concentration profile for variations in  $Sc$

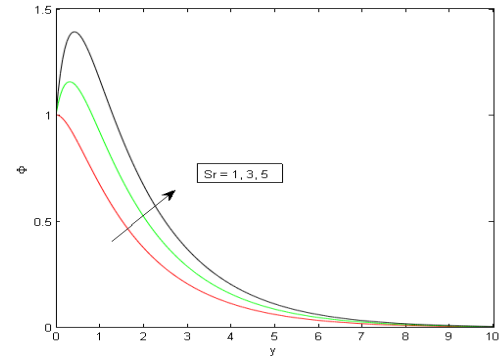


Figure 14. Concentration profile for variations in  $Sr$

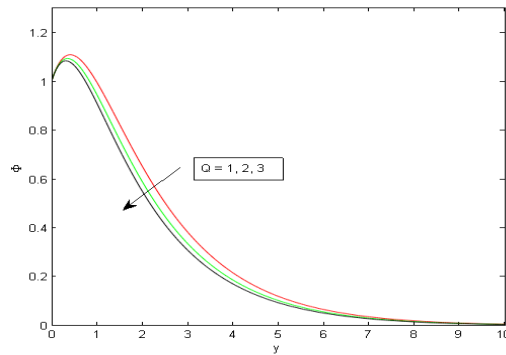


Figure 15. Concentration profile for variations in  $Q$

Table 1: Shear stress  $\tau$  at the plate for the values of  $Pr = 0.71, Sc = 0.6, R = 1, K = 1, Sr = 1, Gr = 10, Gm = 5, M = 1.5, E = 0.01, Q = 5$

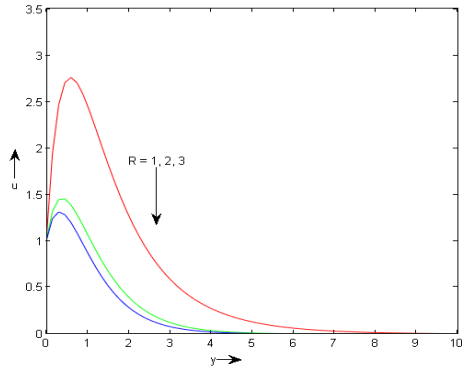
Sc	M	R	Q	Sr	$\tau$
<b>0.30</b>	1.5	1	5	1	2.8377
<b>0.60</b>	1.5	1	5	1	7.2121
<b>0.78</b>	1.5	1	5	1	9.3817
0.60	<b>1</b>	1	5	1	3.1568
0.60	<b>2</b>	1	5	1	2.8376
0.60	<b>3</b>	1	5	1	2.1771
0.60	1.5	<b>2</b>	5	1	5.3559
0.60	1.5	<b>3</b>	5	1	6.1846
0.60	1.5	<b>5</b>	5	1	7.2657
0.60	1.5	1	<b>2</b>	1	5.5559
0.60	1.5	1	<b>4</b>	1	6.7606
0.60	1.5	1	<b>6</b>	1	8.3296
0.60	1.5	1	5	<b>1</b>	4.2394
0.60	1.5	1	5	<b>2</b>	4.6924
0.60	1.5	1	5	<b>3</b>	4.8447

Table 2: Plate temperature  $\theta(0)$  for changed values of the parameters Pr, M, Ec

Pr	M	Ec	$\theta(0)$
<b>0.71</b>	1	0.01	0.2262
<b>1.38</b>	1	0.01	0.4252
<b>7.0</b>	1	0.01	0.4496
0.71	<b>1</b>	0.01	0.2262
0.71	<b>2</b>	0.01	0.0540
0.71	<b>3</b>	0.01	0.0239
0.71	1	<b>0.01</b>	0.2262
0.71	1	<b>0.02</b>	0.0540
0.71	1	<b>0.03</b>	0.0240

**COMPARISON**

Figure 16 is plotted to make a comparison of the current work with the previously published result of Chamuah and Ahmed (2021). Figure 16 displays the variations in velocity profile due to radiation, in absence of heat sink i. e.,  $Q=0$ . Figure 17 (Figure 4 of (2021)) shows the velocity field due to radiation. It is seen that both the figures are identical and indicates a decrease in velocity due to radiation.



**Figure 16.** Velocity field for radiation parameter

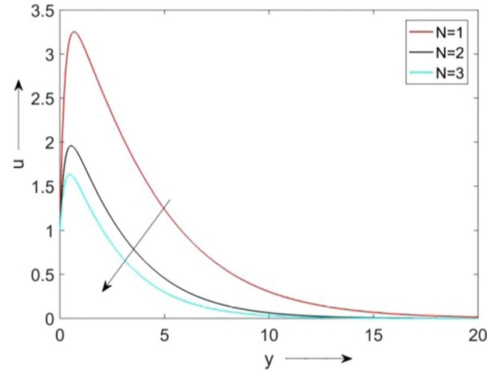


**Figure 17:** Figure 4 of Chamuah & Ahmed (2021)

**CONCLUSIONS**

The present study leads to attain at the subsequent conclusions:

1. Fluid velocity diminutions due to imposition of magnetic field and thus magnetic field can be effectively used in controlling the fluid motion.
2. Fluid motion enhances due to thermal Grashof number, mass Grashof number and thermal diffusion while the trend is reversed with the increase in thermal radiation, heat sink and Schmidt number.
3. Temperature of the fluid drops under the influence of Prandtl number, thermal radiation, and heat sink.
4. Concentration of the fluid grows with Soret number whereas it decreases due to heat absorption and Schmidt number.
5. Skin friction at the wall rises for increasing values of Soret number, Schmidt number, radiation, and heat sink parameter. In the other hand, it is reduced due to the application of transverse magnetic field.

**List of Symbols**

$\vec{q}$	velocity vector	$C_\infty$	free stream concentration
$\rho$	density, $kg/m^3$	$\sigma$	electrical conductivity, $1/(ohm.m)$
$\nu$	kinematic viscosity, $m^2/s$	$\vec{E}$	electrical field
$\vec{J}$	current density	$\beta$	thermal expansion coefficient, $1/k$
$\vec{g}$	acceleration vector	$\bar{\beta}$	solotal expansion coefficient, $1/kmol$
$\vec{B}$	magnetic flux density vector	$T_\infty$	free stream concentration, k
$\kappa$	thermal conductivity, $W/m.K$	$C_\infty$	free stream concentration, kmol
$\kappa^*$	mean absorption coefficient, $1/m$	$B_o$	applied magnetic field strength, Tesla
$\varphi$	energy viscous dissipation per unit volume	$\mu$	viscosity coefficient, $kg/ms$
$p$	fluid pressure	$\theta$	non-dimensional temperature
$U$	velocity of free stream	$\phi$	non-dimensional concentration
$K$	porosity parameter	Pr	Prandtl number
$q^*$	heat flux, $W/m^2$	Q	heat sink
$\vec{q}_r$	radiation heat flux	Sc	Schmidt number
$\vec{J}^2/\sigma$	energy of ohmic dissipation per unit volume	Gr	thermal Grashof number
$T$	fluid temperature, K;	M	magnetic parameter
$C$	concentration, $kmol/m^3$	Gm	solotalGrashof number
$C_w$	plate species concentration	R	radiation
$Ec$	Eckert number	Sr	Soret number

**ORCID**

## REFERENCES

- Ahmed, N. "MHD Convection with Soret and Dufour Effects in a Three-Dimensional Flow Past an Infinite Vertical Porous Plate," *Can. J. Phys.*, **88**(9), 663-674 (2010). <https://doi.org/10.1139/P10-056>
- Ahmed, N. & Choudhury, K. "Heat and mass transfer in three-dimensional flow through a porous medium with periodic permeability," *Heat transfer Asian research*, **48**(2), 644-662 (2019). <https://doi.org/10.1002/htj.21399>
- Ahmed, N. & Dutta, M. "Natural convection in transient MHD dissipative flow past a suddenly started infinite vertical porous plate: A Finite Difference Approach," *Heat Transfer Research*, **49**(6), 491-508 (2018). <https://doi.org/10.1615/HeatTransRes.2018016823>
- Ahmed, N., Sengupta, S. & Datta, D. "An Exact Analysis for MHD Free Convection Mass Transfer Flow Past an Oscillatory Plate Embedded in a Porous Medium," *Chem. Eng. Commun.* **200**, 494-513 (2013). <https://doi.org/10.1080/00986445.2012.709474>
- Ahmed, N. & Sengupta, S. "Thermo-diffusion and Diffusion-thermo effects on a Three-Dimensional MHD Mixed Convection Flow Past an Infinite Vertical Porous Plate with Thermal Radiation," *Magnetohydrodynamics*, **47**(1), 41-60 (2011).
- Alfvén, H. "Discovery of Alfvén waves," *Nature*, **150**, 405-406 (1942).
- Appidi, L., B.S. Malga & P.P. Kumar, "Effect of thermal radiation on an unsteady MHD flow over an impulse vertical infinite plate with variant temperature in existence of Hall current," **51**(3), 2367-2382 (2021). <https://doi.org/10.1002/htj.22402>
- Balamurugan, K.S., Varma, N., & Prasad, J.L. "Entropy generation analysis on forced and free convection flow in a vertical porous channel with aligned magnetic field and Navier slip," *Heat Transfer*, **52**(7), 4619-4639 (2023). <https://doi.org/10.1002/htj.22897>
- Chamuah, K. & Ahmed, N. "MHD free convective dissipative flow past a porous plate in a porous medium in the presence of radiation and thermal diffusion effects," *Heat transfer*, **51**(2), 1964-1981 (2022). <https://doi.org/10.1002/htj.22383>
- Choudhury, K. & Agarwalla, S. "Hydromagnetic convective flow past a porous vertical plate with constant heat flux and heat sink," *Mathematics in Engineering, Science and Aerospace*, **14**(2), 579-595 (2023).
- Choudhury, K., Agarwalla, S. & Ahmed, N., "Diffusion-thermo effect on MHD dissipative flow past a porous vertical plate through porous media," *Heat Transfer*, **51**, 6836-6855 (2022). <https://doi.org/10.1002/htj.22626>
- Kafoussias, N. G., & Williams, E.W. "Thermal Diffusion and Diffusion Thermo Effects on Mixed Free Forced Convective and Mass Transfer Boundary Layer Flow with Temperature Dependent Viscosity," *Int. J. Eng. Sci.*, **33**, 1369-1384 (1998). [https://doi.org/10.1016/0020-7225\(94\)00132-4](https://doi.org/10.1016/0020-7225(94)00132-4)
- Mansour, M. A. "Radiation and free convection effects on the oscillatory flow past a moving vertical porous plate," *Astrophys. Space Sci.*, **166**(2), 269-275 (1990). <https://doi.org/10.1007/BF01094898>
- Prasad, J.L., Rao, Venkateswara I. V., Balamurugan, K.S. & Dharmiah, G. "Radiative Magnetohydrodynamic flow over a vertical cone filled with convective nanofluid," *Communications in Mathematics and Applications*, **13**(2), 449-459. (2022). <https://doi.org/10.26713/cma.v13i2.1795>
- Saikia, D J, Ahmed, N. & Bordoloi, R. "Natural convective MHD mass transfer flow past an infinite vertical porous plate embedded in a porous medium with thermal diffusion and chemical reaction," *Special Topics & Reviews in Porous Media*, **14**(2), 63-75 (2023). <https://doi.org/10.1615/SpecialTopicsRevPorousMedia.2023045885>
- Seth, G. S., Ansari, M. S. & Nandkeolyan, R. "MHD Natural convection flow with radiation heat transfer past an impulsively moving plate with ramped temperature," *Heat Mass Transfer*, **47**, 551-561 (2011). <https://doi.org/10.1007/s00231-010-0740-1>
- Seth, G. S., Sharma, R. & Kumbhakar, B. "Heat and mass transfer effects on unsteady MHD natural convection flow of a chemically reactive and radiating fluid through a porous medium past a moving vertical plate with arbitrary ramped temperature," *J. Appl. Fluid Mech.*, **9**(1), 103-117 (2016). <https://doi.org/10.18869/acadpub.jafm.68.224.23961>

**ВПЛИВ ТЕПЛОГО ВИПРОМІНЮВАННЯ НА МГД-МАСООБМІННИЙ ПОТІК ПОВЗ ПОРИСТУ ВЕРТИКАЛЬНУ ПЛАСТИНУ ЗА НАЯВНОСТІ ПОСТІЙНОГО ТЕПЛОГО ПОТОКУ****Т.К. Чутія<sup>а</sup>, К. Чоудхурі<sup>б</sup>, К. Чамуа<sup>а</sup>, С. Ахмед<sup>б</sup>**<sup>а</sup>*Кафедра математики, Коледж Морідхал, Ассам, Індія*<sup>б</sup>*Кафедра математики, Університет науки і технологій Меххалаї, Індія*

У цій роботі ми взялися за вивчення тепло- та масообміну в конвективному потоці МГД повз нескінченну пластину з пористим середовищем за наявності випромінювання, ефекту термодифузії та тепловідведення. Рівномірна напруженість магнітного поля використовувалася поперечно в області рідини. Новизна цього дослідження полягає у вивченні впливу випромінювання (наближення Росселенда) та тепловідведення на природний конвективний потік за наявності в'язкої дисипації та джоулевого нагрівання з постійним тепловим потоком та постійною швидкістю всмоктування повз безперервно рухоми вертикальному потоці в пористому середовищі. Основні рівняння розв'язуються методом збурень для отримання формулювань для полів швидкості, температури та концентрації. У цій статті ми також розглядаємо кілька фізичних величин в області потоку графічно, а також таблично, які раніше вивчалися іншими дослідниками, за винятком кількох нових випадків, таких як залежність швидкості світла від температури з різних джерел, таких як ефект градієнта густини, які обговорюються тут вперше. Однак, поточне дослідження має широкий вплив на кілька інженерних процесів, таких як видування скла, виробництво паперу, екструзія пластикових листів тощо.

**Ключові слова:** МГД; теплопередача; термодифузія; пористі середовища; теплове випромінювання

# FIRST-PRINCIPLES INVESTIGATION OF SEMICONDUCTING $\text{Cu}_2\text{ZnSnX}_4$ ( $X = \text{S, Se}$ ) ECO-FRIENDLY MATERIALS FOR THE NEXT GENERATION OF PHOTOVOLTAIC APPLICATIONS

 Bhanu Prakash<sup>a</sup>, Ajeet Singh<sup>b</sup>, Tarun Kumar Joshi<sup>c</sup>,  Banwari Lal Choudhary<sup>a</sup>, Naincy Pandit<sup>d</sup>,  
 Ajay Singh Verma<sup>e,f,\*</sup>

<sup>a</sup>Department of Physical Sciences, Banasthali Vidyapith, Banasthali, Rajasthan 304022, India

<sup>b</sup>Department of Physics, Deva Nagri College, Meerut, UP, 250002, India

<sup>c</sup>Department of Physics, Swami Vivekanand Govt. P. G. College, Neemuch, Madhya Pradesh, 458441, India

<sup>d</sup>Department of Physics, School of Allied Sciences, Dev Bhoomi Uttarakhand University, Dehradun 248007, India

<sup>e</sup>Department of Physics, Anand School of Engineering & Technology, Sharda University Agra, Keetham, Agra 282007, India

<sup>f</sup>University Centre for Research & Development, Department of Physics, Chandigarh University, Mohali, Punjab, 140413, India

\*Corresponding Author E-mail: [ajay\\_phy@rediffmail.com](mailto:ajay_phy@rediffmail.com)

Received April 30, 2025; revised June 11, 2025; accepted June 19, 2025

The quaternary general form  $\text{A}_2\text{BCX}_4$ -based semiconducting materials with Kesterite-type structures are promising candidates for thin film-based solar cell devices. We examined the structural, electrical, optical, elastic, thermodynamic, and thermoelectric characteristics of  $\text{Cu}_2\text{ZnSnX}_4$  ( $X = \text{S, Se}$ ) using the FP-LAPW technique with an implanted Wien2k code. The Burke-Ernzerhof-generalized gradient approach (PBE-GGA) and Trans-Blaha modified Becke-johnson (TB-mBJ) are used to manage the exchange and correlation potentials. The results show that  $\text{Cu}_2\text{ZnSnS}_4$  and  $\text{Cu}_2\text{ZnSnSe}_4$  compounds have stable structures with direct bands at 1.51 eV and 1.29 eV, respectively. The optical characteristics of these compounds were estimated using the dielectric function, allowing for an analysis of their reflectivity, refractive index, and absorption. Elastic parameters such as the Bulk, Young, Pugh, and Poisson ratios demonstrate that they are ductile and can be formed as thin films, a significant characteristic of Photovoltaic applications. Furthermore, we calculated various thermodynamic parameters entropy, and constant volume under pressure and temperature. We also determined the  $\text{Cu}_2\text{ZnSnX}_4$  ( $X = \text{S, Se}$ ) exhibits good thermoelectric performance concerning the figure of merit at 300K which is nearly unity. According to our findings, these materials are viable candidates for future clean green solar energy applications.

**Keywords:** Wien2k-DFT;  $\text{Cu}_2\text{ZnSnS}_4$  Solar cell; Structural, Elastic; Thermoelectric properties

**PACS:** 62.20.Dc, 63.10.+a, 63.20.-e, 77.22.Ch, 78.20.Ci

## 1. INTRODUCTION

The most abundant natural resource of energy is sunlight, and the conversion of light into electricity in solar cells is one of the significant suitably developed renewable energy technologies. The research of absorber materials used in solar cells recently became regarded as a pertinent topic offering some solutions to the challenges of energy demand and climate change. Photovoltaic (PV) devices for thin film-based solar cell technologies are being developed as active research areas [1]. Initially, in the year 1954, the first crystalline silicon-based solar cell production was done with an efficiency of 6% [2]. However, after that there are various photovoltaic solar cells have been developed including organic solar cells [3], inorganic solar cells [4], and thin film solar cells, CdTe [5], CIGS [6], GaAs [7], and perovskite [8] based solar cells. Researchers faces many problems such as metal toxicity, expensive materials, rare abundance in nature, and stability of the structure. Therefore, eco-friendly solar cells are one of the strategies to gain high Power Conversion Efficiency (PCE) in larger production of photovoltaic applications. Copper (Cu), Zinc (Zn), Tin (Sn), Sulphur (S), and Selenium (Se)-based solar cells are among the most promising materials for large-scale solar cell production.

They have all appropriate inherent properties as environmentally friendly, non-toxic in nature, wide optimal Bandgap, and high absorption coefficient materials. The semiconducting kesterite phase material  $\text{Cu}_2\text{ZnSnX}_4$  ( $X = \text{S/Se}$ ) has both physical and chemical properties that are similar to CIGS. The optimal energy band gap of semiconducting  $\text{Cu}_2\text{ZnSnS}_4$  materials is around 1.50 eV, possessing a prominent absorption coefficient in the sequence of  $10^4 \text{ cm}^{-1}$  [9-12]. Consequently, thin film-based materials reported experimentally and theoretically power conversion efficiency of semiconducting inorganic  $\text{Cu}_2\text{ZnSnX}_4$  ( $X = \text{S, Se}$ ) reached around 12.6% [13] and 32.2% [14]. So, several investigations (both experimental and theoretical) have been published in the past few years on the fabrication, structure, optical, and electrical characteristics of quaternary  $\text{I}_2\text{-II-IV-VI}_4$  semiconductors. In an experimental study, Benachour et al. [15] synthesized CZTS using the simple sol-gel method, and a thin film was deposited with the help of a dip-coated technique. This study showed that CZTS thin films crystallize into the pure form kesterite phase, and it further showed that annealing reduces the optical energy band gap from 1.62 to 1.50 eV. They eventually concluded that these CZTS thin films could potentially be helpful for PV. Xiong et al. [16] have prepared the CZTS film by using the simple sol-gel method with the help of the spin coating technique. This investigation represents the association between the CZTS thin film crystal structure, surface structure, and optimum annealing temperature. Additionally, they depict the compound's elemental composition. Luckert et al. [17] have fabricated a CZTSe thin film by using



magnetron sputtering. In this study, XRD and Raman's conclusions were analyzed to show the material's outstanding structural quality. By using optical absorption investigation at ambient temperature, the value of the band gap came out to be near to 1.00 eV. Other than this, the experimental longitudinal optical (LO) phonon energy was found to be 28 MeV. Wibowo et al. [18] used a technique of pulsed laser deposition (PLD) to synthesize quaternary CZTSe thin films and examined their optical, structural, and electrical characteristics. Furthermore, it has been found that CZTSe is a possible solar-absorber material due to its high  $10^4 \text{ cm}^{-1}$  absorption coefficient and 1.50 eV optical bandgap. Furthermore, modelling helps investigators to perform theoretical investigations into the fundamental properties of relevant materials. In theoretical studies, it has been shown that the physical properties such as structural, optical, elastic, electronic, thermal, and thermoelectric characteristics of CZTS and CZTSe by using the first principles calculations. Jyothirmal et al. [19] have investigated kesterite CZTS/ CZTSe first principles calculation by DFT. They found structural stability and an optical direct band gap. Also, a high absorption coefficient was found with the record efficiency of CZTSe-based thin film solar cells achieved by 25.81% (pure CZTSe) for solar energy harvesting. HE et al. [20] have explored the elastic and thermal properties of CZTS and CZTSe by applying the density functional theory (DFT) approach. This study demonstrates that both compounds exhibit ductile behavior because of their elevated bulk modulus to shear modulus ratio. They also calculated thermal characteristics, thermal expansion coefficient, and Debye temperature by the Debye model and also found thermal capacity around  $200 \text{ J}/(\text{mol}\cdot\text{K})$  at above 300 K. Nouri et al. [21] used DFT simulations with the GGA + U technique to investigate the electronic, optical, structural, nonlinear, linear, and thermoelectric characteristics of  $\text{Cu}_2\text{MnSnS}_4$ ,  $\text{Cu}_2\text{FeSnS}_4$ , and  $\text{Cu}_2\text{CoSnS}_4$  materials.  $\text{Cu}_2\text{MnSnS}_4$  material has higher electrical conductivity and power factor than  $\text{Cu}_2\text{CoSnS}_4$  and  $\text{Cu}_2\text{FeSnS}_4$  at temperatures ranging from 300 to 800K, owing to its significant carrier mobility and high concentration. As a consequence, this study's shows the p-type behaviour of kesterite CMTS, CCTS materials and CFTS which was demonstrated by Seebeck coefficient. This study shows that these materials might be used in optoelectrical, and thermo-electric conversion-based devices. [22] Because of its remarkable characteristics, Earth's abundant elements, non-toxicity in nature, and eco-friendly  $\text{Cu}_2\text{ZnSnS}/\text{Se}_4$  are considered absorbing materials of the solar cell with high efficiency. Latest studies on inorganic semiconducting compounds ensure that these compounds are potential candidates for solar cell absorbing material and also thermoelectric compounds. As a result, it is reasonable to use First-principles methods to explore the optical and electronic properties of tetragonal  $\text{Cu}_2\text{ZnSnX}_4$  ( $X = \text{S}/\text{Se}$ ) materials. After reviewing the literature, we noticed that the selected compounds had gained attention. Thus, in this study, we examined the structural, optical, electronic, elastic, thermal, and thermoelectric characteristics.

## 2. COMPUTATIONAL DETAILS

The computations were carried out by employing a full potential linear augmented plane wave (FP-LAPW) within density functional theory (DFT) techniques [23] as accomplished in the Wien2K package. [24] The exchange-correlation potential was examined by using Perdew-Burke-Ernzerhof (PBE-GGA). In addition, we used the Tran-Blaha altered Becky Johnson potential (TB-mBJ) for the electronic and optical characteristics.[25] To increase accuracy, the lattice parameters of both compounds were calculated by using total-dependent geometrical optimization. By this, we optimized the atomic location and lattice constant until the residual force was less than  $10^{-3} \text{ Ry Bohr}^{-1}$ . The required energy for separating the valence states and core was -0.6 Ry and  $\text{RK}_{\text{max}}=7$ . Where  $\text{R}_{\text{max}}$  is the radius of the tiniest muffin tin sphere and  $\text{K}_{\text{max}}$  is known as plane wave cutoff. This energy is also referred as "cutoff energy." A  $5 \times 5 \times 5$  Monkhorst [26] pack k-grid mesh was examined and for the muffin tin sphere, the value of  $l_{\text{max}}$  was limited to  $l_{\text{max}}=10$  and  $G_{\text{max}}=12$ . The values associated with muffin tin radii ( $\text{R}_{\text{mt}}$ ) for  $\text{Cu}_2\text{ZnSnS}_4$  (Cu<sub>1</sub>, Cu<sub>2</sub>, Zn, Sn, S) are 2.40 Å, 2.40 Å, 2.40 Å, 2.49 Å, 1.97 Å and  $\text{Cu}_2\text{ZnSnSe}_4$  (Cu<sub>1</sub>, Cu<sub>2</sub>, Zn, Sn, Se) are 2.35 Å, 2.35 Å, 2.35 Å, 2.43 Å, 2.23 Å respectively. (Å = Bohr radius) The volume optimization was performed by using a 3500 k-point mesh in the Brillion zone. However, the physical characteristics of the chosen compounds, like their optical and electronic properties, were estimated by using a 10000 k-point mesh in the irreducible Brillion zone (IBZ). The elastic characteristics have been investigated by employing the *IRElast* package incorporated in WIEN2k. [27] Thermal properties were determined as well by using the Gibbs2 [20] package at various temperatures and pressures up to 10 GPa, and thermoelectric parameters were estimated by employing the BoltzTrap method [28].

## 3 RESULTS AND DISCUSSIONS

### 3.1 Structural properties

The suggested family crystallizes in a variety of forms, including cubic, hexagonal, and tetragonal phases. It has been proposed that the tetragonal structure, which is composed of the kesterite and stannite phases, is the most stable under ambient conditions. Figure 1. depicts the proposed material structural configurations of quaternary I<sub>2</sub>, II, IV, and VI<sub>4</sub>. These materials refer to the I-4 space group with tetragonal symmetry. In all structures, the Sulphur (S) or Selenium (Se) group (VI) atom is surrounded by the two atoms of Copper (Cu), one group of (IV) atom, Tin (Sn) and Zinc (Zn) group (II) atom. The Cu atom is in the separate positions 2a (0, 0, 0) and 2c (0, 0.50, 0.25), Zinc 2d (0, 0.5, 0.75), Sn 2b (0, 0, 0.5) and S/Se 8g (0.756 0.243, 0.128) Wyckoff positions respectively. Table 1 displays the computed lattice parameters for each material. The optimization process was done by using Birch Murnaghan equation of state employed by simulation code. [29]

$$E(V) = E_0 + \frac{9V_0 B_0}{16} \left\{ \left[ \left( \frac{V_0}{V} \right)^{2/3} - 1 \right]^3 B'_0 + \left[ \left( \frac{V_0}{V} \right)^{2/3} - 1 \right]^2 \times \left[ 6 - 4 \left( \frac{V_0}{V} \right)^{2/3} \right] \right\} \quad (1)$$

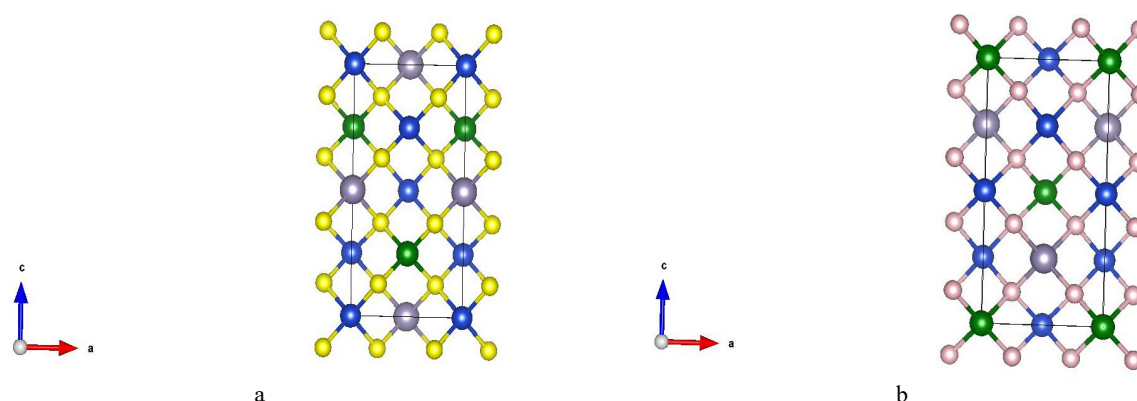


**Figure 1.** a) The optimized crystal structures of  $\text{Cu}_2\text{ZnSnX}_4$  ( $X = \text{S, Se}$ ) materials. where blue atom shown Cu, green shown Zn, grey shown Sn, yellow/light pink shown by S/Se

Volume optimization (Fig. 2) of  $\text{Cu}_2\text{ZnSnX}_4$  ( $X = \text{S, Se}$ ) has been completed by using the PBE-GGA [30]. Table 1 shows the computed structural characteristics, which correlate well with the experimental data.

**Table 1.** Calculated structural parameters compared with experimentally calculated values

Compounds	Lattice Constants Cal.		Lattice Constants Exp.		c/a	B[Gpa]	B'	v	E <sub>0</sub> [Ry]
	a	c	a	c					
$\text{Cu}_2\text{ZnSnS}_4$	5.42	10.81	5.426 <sup>a</sup>	10.816 <sup>a</sup>	1.993	100.00	5.00	1030.56	-25764.44
$\text{Cu}_2\text{ZnSnSe}_4$	5.69	11.33	5.692 <sup>b</sup>	11.340 <sup>b</sup>	1.992	99.99	4.84	1235.23	-42012.64

<sup>a</sup> reference 31, <sup>b</sup> reference 32

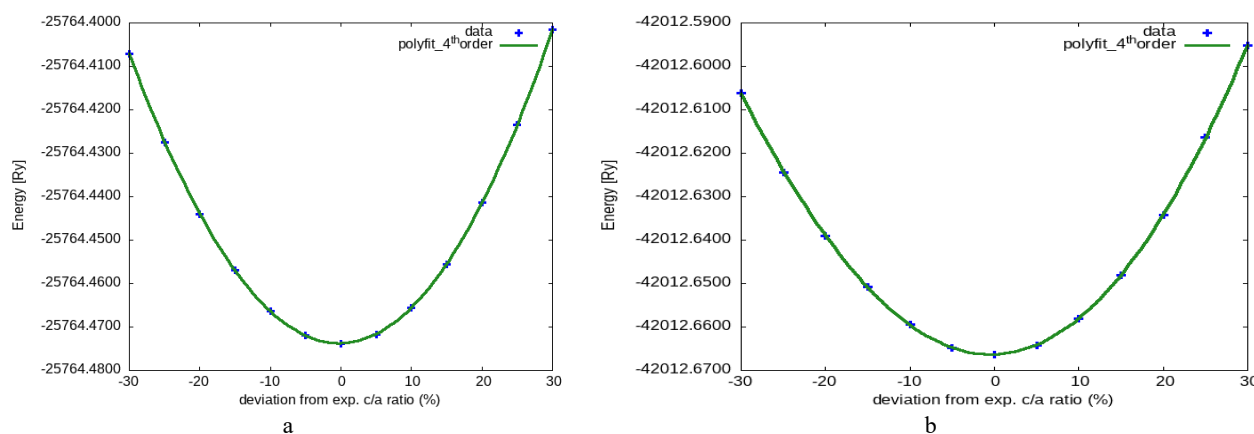


**Figure 2.** Volume optimization curve for a)  $\text{Cu}_2\text{ZnSnS}_4$  and b)  $\text{Cu}_2\text{ZnSnSe}_4$

### 3.2 Electronic properties

To further understand the electronic behavior of the materials we selected, we calculated energy bands and the total and predicted density of states in Figures 3,4. Because the electronic band structure influences a material's many optical and thermoelectric characteristics. Figures 3a and 3b depict the structure of the bands of  $\text{Cu}_2\text{ZnSnS}_4$  and  $\text{Cu}_2\text{ZnSnSe}_4$  plotted along the wave vector  $k$  and the energy function for these materials in the Full-Brillion Zone. One can deduce a material's conductivity, insulator status, and the direct or indirect characteristics of the energy band gap from these curves. We calculated self-consistent fields (SCF) for the compounds under consideration using optimized lattice parameters and the PBE-GGA functional. Furthermore, we employed the WIEN2k Code utilizing the TB-mBJ method over PBE to get the bandgap nearer compared to the experimental data. Hence, the energy band gap of  $\text{Cu}_2\text{ZnSnS}_4$  ( $\text{Cu}_2\text{ZnSnSe}_4$ ) is found at 1.51/1.29 eV respectively. [33-34] The conventional PBE-GGA potential periodically underestimates the electronic band gap value in DFT computations. Thus, in addition to the PBE-GGA method, we use the BJ potential to calculate the band gap.

We calculated the total and partial densities of states of  $\text{Cu}_2\text{ZnSnX}_4$  ( $X = \text{S, Se}$ ) using the TB-mBJ approach to gain a fundamental understanding of the electronic structure in Figure 4a and Figure 4b. As well as, to better understand the (DOS) of this  $\text{Cu}_2\text{ZnSnS}_4$ ( $\text{Cu}_2\text{ZnSnSe}_4$ ) plot, we describe it into three portions: the conduction band portion 0 – 6.0 eV

(0 eV –5.0 eV), Upper Valance Band (UVB) portion from -2.0 eV to 0 eV (-2.5 to 0), and Lower Valance Band (LVB) portion -8.0 eV to -2.0 eV (-7.5 to -2.5). As shown in figure, three huge peaks were formed in the lower valence band portion, separated from one another by a small energy difference. These peaks are formed by the large contribution of the Zinc (Zn), and Tin (Sn) as well as smaller contributions from the atoms of copper (Cu) and Sulphur (S), Selenium (Se). Zn p and Sn orbitals plays a significant role in these peaks, while Cu d orbitals and S(Se) d orbitals only contribute somewhat in  $\text{Cu}_2\text{ZnSnS}_4$  ( $\text{Cu}_2\text{ZnSnSe}_4$ ). These spikes correspond to the substance's lower-lying band on this band diagram. On the other hand, a single peak of Cu and S(Se) indicates the major contribution within the upper valence band portion. In this portion, the contributions of the rest of the elements Zn and Sn atoms are insignificant. The dominant states at the conduction band minima are produced by hybridizing the tin atom's s- and p-states, respectively. Cu and Zn atoms make little of an impact in this area.

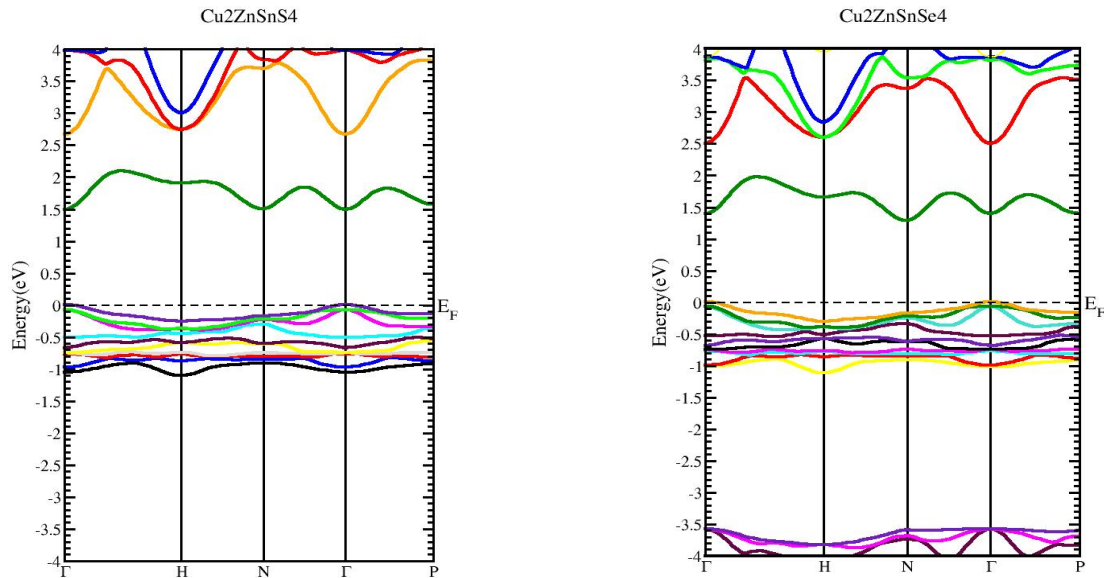


Figure 3. Band Structure of  $\text{Cu}_2\text{ZnSnS}_4$  and  $\text{Cu}_2\text{ZnSnSe}_4$

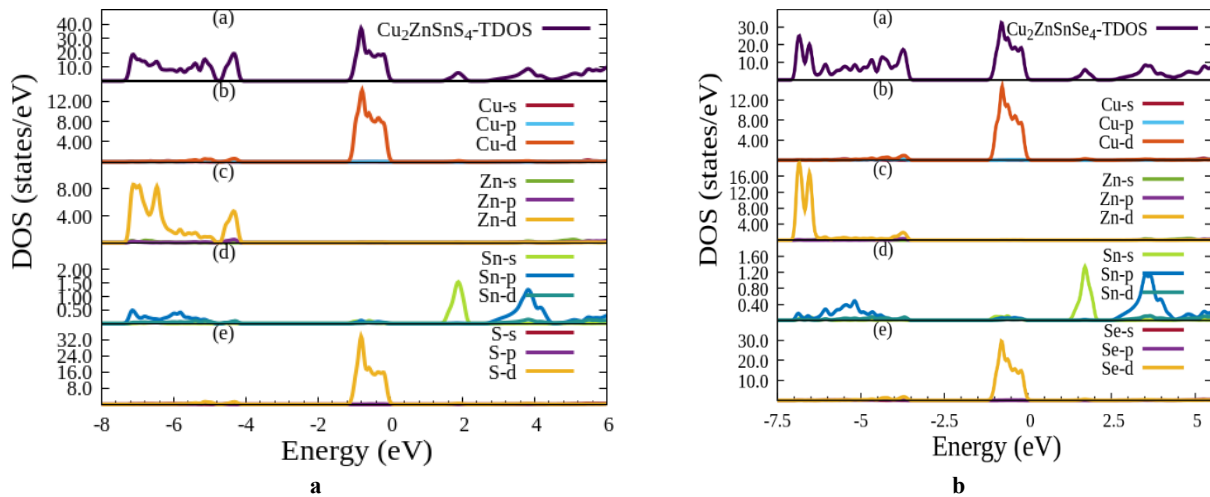


Figure 4. Total and partial density of states plots for  $\text{Cu}_2\text{ZnSnX}_4$  (X= S, Se)

### 3.3 Optical properties

To reveal a material potential for use in photodetectors, optoelectronics, photovoltaics, and other applications, it is essential to understand each of the ways that light interacts with it, including emission, diffusion, and absorption. The possible usage of the material under investigation in photovoltaic and other optoelectronic devices can be identified by studying its optical characteristics. The selected compounds' dielectric function  $\epsilon(\omega)$  is closely associated with optical characteristics. [35]

$$\epsilon(\omega) = \epsilon_1(\omega) + i\epsilon_2(\omega) \quad (2)$$

As a result, its complexity is evident. Here,  $\omega$  indicates the incident electromagnetic radiation's angular frequency. The imaginary component  $\epsilon_2(\omega)$  represents the optical absorption of the material. Similarly, the real component,  $\epsilon_1(\omega)$ , determines electronic polarization and also anomalous dispersion. Here, the expression for  $\epsilon_2(\omega)$  is as follows: [35]

$$\varepsilon_2(\omega) = \frac{4e^2\pi^2}{\omega^2 m^2} \sum_{i,j} \int | \langle i | M | j \rangle |^2 f_i (1 - f_j) \cdot \delta(E_f - E_i - \hbar\omega) d^3k \quad (3)$$

However, electronic charge ( $e$ ), angular frequency ( $\omega$ ), mass of electrons ( $m$ ), and ( $\hbar$ ) stand for and decreased Planck's constant ( $\hbar$ ). Also, ( $M$ ) such as the momentum operator, while  $i$  and  $j$  denote the initial (VB) and final (CB) bands. The Fermi distribution function for the initial state is denoted by ( $f_i$ ), whereas  $\delta(E_f - E_i - \hbar\omega)$  indicates the energy variations between both the initial and the final states at the  $k$  point after collecting a coming photon of energy  $\hbar\omega$ .

$$\varepsilon_1(\omega) = 1 + \frac{2}{\pi} P \int_0^\infty \frac{\omega' \varepsilon_2(\omega')}{\omega'^2 - \omega^2} d\omega' \quad (4)$$

$\varepsilon_1(\omega)$ , is the real component of the dielectric tensor, can be calculated by applying the Kramers-Kronig equation [35] to the  $\varepsilon_2(\omega)$  which is the imaginary component of the dielectric tensor.

Here,  $P$  corresponds to the integral's principal value. We explored the dielectric tensor  $\varepsilon(\omega)$  to know how materials respond to incident radiation. Furthermore, we also calculated several optical parameters like refractive index, extinction coefficient, and reflectivity. Figures 5a–d depict the estimated optical characteristics of these compounds as a function of photon energies ranging to 10 eV.

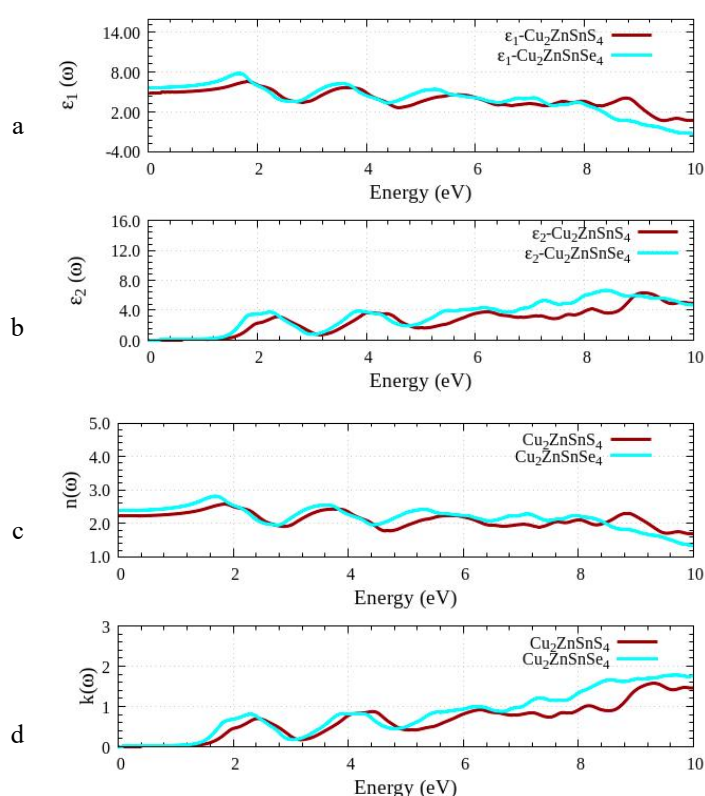


**Figure 5.** Dielectric constant for  $\text{Cu}_2\text{ZnSnX}_4$  ( $X = \text{S}, \text{Se}$ ). a and b, real part ( $\varepsilon_1$ ) and imaginary ( $\varepsilon_2$ ). c and d, refractive index and extinction coefficient

Now, Figure 5(a) shows the computed  $\varepsilon_1(\omega)$  spectra with photon energy. According to this figure, the static dielectric constants of  $\text{Cu}_2\text{ZnSnS}_4$  ( $\text{Cu}_2\text{ZnSnSe}_4$ ) are  $\varepsilon_1(0) = 4.91/5.65$  at zero photon energy. Additionally, the major peaks for  $\text{Cu}_2\text{ZnSnS}_4$  and  $\text{Cu}_2\text{ZnSnSe}_4$  were seen in the  $\varepsilon_1(\omega)$  spectrum at around 1.91 and 1.72 eV, respectively. The higher the value  $\varepsilon_1(0)$ , the greater the material's reactivity to the incoming electromagnetic radiation. Figure 5(a) shows the changes in  $\varepsilon_1(\omega)$  of the compounds under investigation based on the energy of incoming radiation. According to the results, as the energy value rises, the value of  $\varepsilon_1(\omega)$  first increases gradually for these compounds; after reaching its peak, it decreases with a few fluctuations and goes negative in the region of 10 eV; eventually, a slight rise towards zero is noticeable. Figure 5b illustrates that the acceptable threshold energy of  $\varepsilon_2(\omega)$  in each of these materials ranges between 1.10 and 1.6 eV. It is discovered that the optical band gap of a compound, which is indicated by the threshold energy value, is extremely closer to the calculated band gap. It demonstrates how accurate these findings are. After that, Figures 5c and 5d shows the refractive index  $n(\omega)$  and extinction coefficient  $k(\omega)$  of  $\text{Cu}_2\text{ZnSnS}_4$  and  $\text{Cu}_2\text{ZnSnSe}_4$  compounds, respectively. The optical parameter  $n(\omega)$  impacts how light flows via the specimen. It also defines a material's ability to absorb the radiation impacting it.  $\text{Cu}_2\text{ZnSnS}_4$  and  $\text{Cu}_2\text{ZnSnSe}_4$  have static refractive index, which is found be 2.21 and 2.37, respectively. Figures 5(a-b) and (c-d) shows that when incident radiation energy increases, so does  $n(\omega)$  and  $\varepsilon_1(\omega)$ . The damping of oscillations in the electric vector of incoming electromagnetic radiation is correlated with the extinction coefficient of a specimen ( $k(\omega)$ ).



Figure 5(d) shows that  $k(\omega)$  has numerous peaks at frequencies where  $\varepsilon_1(\omega)$  has drained or zeroes out. After reaching its maximum value, it keeps getting smaller as the energy of the incident radiation rises.

The reflectivity,  $R(\omega)$  and energy loss;  $E_{\text{loss}}(\omega)$  of these compounds are shown in Figures 6(a) and (b). According to these graphs, the reflectance  $R(0)$  of  $\text{Cu}_2\text{ZnSnS}_4$  and  $\text{Cu}_2\text{ZnSnSe}_4$  is 0.143 and 0.166 respectively. The reflectivity  $R(\omega)$  value initially progresses slowly in the visible ranges and IR region. On the other side, the term " $E_{\text{loss}}$ " refers to the energy degradation of an electron passing through a compound. The peaks in these pictures exactly matches with these materials' plasma resonance. The observed peaks of  $E_{\text{loss}}(\omega)$  of these compounds are situated in the high-frequency visual range between 8 and 10.0 eV, as shown in Figure 6b.

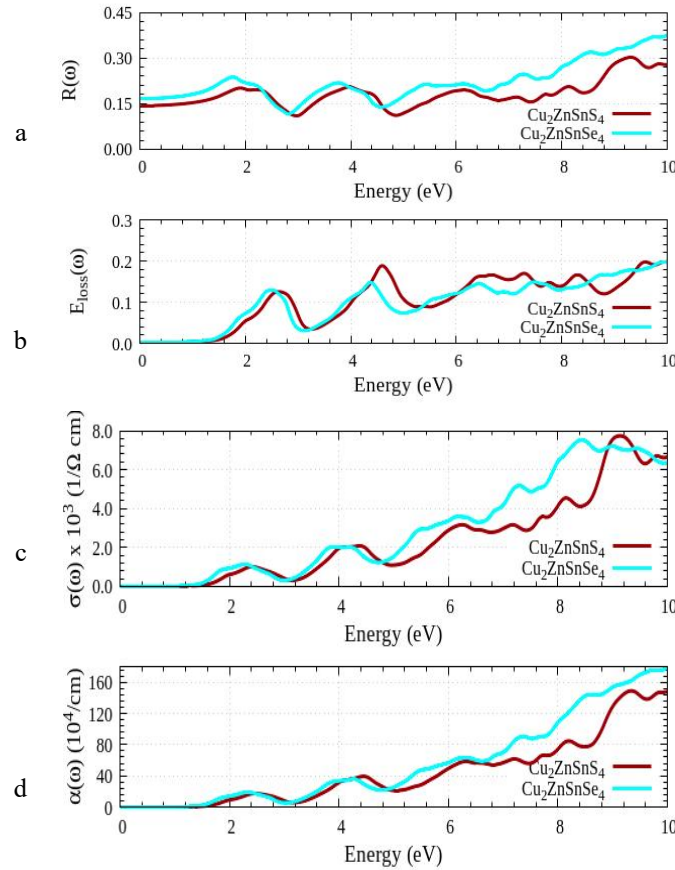


**Figure 6.** a) Reflectivity  $R(\omega)$ , b) Energy loss function  $E_{\text{loss}}(\omega)$ , c) Optical conductivity  $\sigma(\omega)$  and d) Absorption coefficient  $\alpha(\omega)$  for  $\text{Cu}_2\text{ZnSnX}_4$  ( $X = \text{S, Se}$ )

The optical conductivity of a substance can provide insight into how well electrons conduct when exposed to electromagnetic radiation. Figures 6c shows the optical conductivity spectrum; it has the maximum values of optical conductivity  $\sigma(\omega)$  are 7.73 and 7.52 found at 9.10 eV and 8.40 eV respectively. The absorption coefficient  $\alpha(\omega)$  indicates how much incoming electromagnetic radiation is absorbed by a material's unit thickness. The higher a material's absorption coefficient, the more efficiently it moves electrons from its VB to the CB of the material. Each of these materials has the greatest conductivity and absorption coefficient within the visible spectrum. Figures 6d show the changes in the  $\alpha(\omega)$  with incident EM radiation for the selected materials. These figures shows that the optical conductivity appears to be the least in the same range of incoming energy where absorption exhibits its minimal value. Additionally, it has been found that the optical conductivity exhibits peaks at the same frequencies of incident light where absorption does, validating theoretical perception and showing the precision of the suggested results.

### 3.4 Elastic properties

Elastic characteristics offer crucial information about how that material behaves mechanically. These characteristics can be acquired through first-principles research based on DFT. These characteristics can be acquired by understanding stiffness constants, which define how a crystal behaves to forces from the outside and have significant effects on the choosing of suitable compounds. We have optimized the internal structure with changing parameters and deformed symmetry-dependent strain configurations of varied magnitudes using the equilibrium structure in the stiffness constant computations. The determination of elasticity of tetragonal  $\text{Cu}_2\text{ZnSnX}_4$  ( $X = \text{S, Se}$ ) materials is the main goal of the study. Furthermore, Elastic constants  $C_{ij}$  in the Wien2K code constitute the basis for calculating elastic parameters through the M. Jamal methodology. (x) The six distinct elastic constants associated with these tetragonal compounds are  $C_{11}$ ,  $C_{12}$ ,  $C_{13}$ ,  $C_{33}$ ,  $C_{44}$ , and  $C_{66}$  [36].

Despite any kind of uniform elastic deformation, a crystal needs positive strain energy to remain mechanically stable. The mechanical stability criterion for tetragonal compounds can be used to get the aforementioned elastic constant limitations [37].

$$\begin{aligned} C_{11} > 0, C_{33} > 0, C_{44} > 0, C_{66} > 0 \quad (C_{11} - C_{12}) > 0, \\ (C_{11} + C_{33} - 2C_{13}) > 0, (2C_{11} + C_{33} + 2C_{12} + 4C_{13}) > 0. \end{aligned} \quad (5)$$

Applying the VRH (Voigt, Reuss, and Hill) approximation, we were able to determine the macroscopic mechanical characteristics of the  $\text{Cu}_2\text{ZnSnX}_4$  ( $X = \text{S, Se}$ ) compounds. [38] In this case,  $G$  denotes durability against plastic deformation, while  $B$  denotes resistance to breaking. Considering a tetragonal structure and the Voigt and Reuss approximation, the Bulk ( $B$ ) and Shear ( $G$ ) modulus of the material are such as,

$$B_V = \frac{2C_{11} + 2C_{12} + C_{33} + 4C_{13}}{9} \quad (6)$$

$$B_R = \frac{C^2}{M} \quad (7)$$

$$G_V = \frac{M + 3C_{11} - 3C_{12} + 12C_{44} + 63C_{66}}{30} \quad (8)$$

$$G_R = \frac{15}{\frac{18B_V}{C^2} + \frac{6}{C_{11} - C_{12}} + \frac{6}{C_{44}} + \frac{3}{C_{66}}} \quad (9)$$

In which,  $M = C_{11} + C_{12} + 2C_{33} - 4C_{33}$  and  $C^2 = (C_{11} + C_{12}) C_{33} - 2C_{13}^2$ .

Hill [39-40] suggested an approximation for the real value of a modulus based on the average of two independent modulus computed using the VRH technique.

$$B = \left( \frac{B_V + B_R}{2} \right) \quad (10)$$

$$G = \left( \frac{G_V + G_R}{2} \right) \quad (11)$$

Equations including Young's modulus ( $E$ ) and Poisson's ratio ( $\nu$ ), as well as  $B/G$  ratio, are used to determine the further parameters, which are measurements required to determine the hardness of a material, brittleness, or ductility [41-42].

$$E = \left( \frac{9BG}{3B + G} \right) \quad (12)$$

$$\nu = \left( \frac{3B - 2G}{2(3B + G)} \right) \quad (13)$$

Using the elastic constants, one can calculate the Debye temperature ( $\theta_D$ ), which is strongly connected to physical characteristics such as melting point and specific heat of materials.

The calculations of Debye temperature [43] are based on the average sound velocity.

$$\theta_D = \frac{h}{k} \left[ \left( \frac{3n}{4\pi} \right) \left( \frac{N_A \rho}{M} \right) \right]^{-1/3} v_m \quad (14)$$

The letters ( $h$ ) and ( $k$ ) represent the Planks constant and Boltzmann constant, respectively, while ( $n$ ) represents the number of atoms, ( $N_A$ ) the Avogadro number, ( $\rho$ ) the compound's density, and ( $M$ ) the molecular mass. The usual sound speed is defined in [44].

$$V_m = \left[ \frac{1}{3} \left( \frac{2}{V_{t3}} + \frac{1}{V_{l3}} \right) \right]^{-1/3} \quad (15)$$

Sound velocities such as transverse  $V_t$  and longitudinal  $V_l$ , may be calculated using Navier's relation and the elastic constants  $B$  and  $G$  [43].

$$V_t = \sqrt{\frac{G}{\rho}} \quad (16)$$

$$V_l = \sqrt{\frac{3B + 4G}{3\rho}} \quad (17)$$

For the tetragonal  $\text{Cu}_2\text{ZnSnX}_4$  ( $X = \text{S, Se}$ ) compounds, the mechanical stability needs to be given in Eq. (7) is satisfied. Tables 3 and 4 summarize the elastic constants and other elastic parameters. We discovered that the bulk modulus ( $B$ ) computed using elastic constants and the bulk modulus ( $B$ ) computed with volume optimization (EOS) computations are equivalent. When values of shear modulus exceed a certain threshold, they tend to imply enhanced resistance to reversible distortion. To comprehend the deformation caused by shear stress, information about the shear modulus is



required. A substance's stiffness is governed by its Young's modulus, the greater the modulus, the stronger the material. The values of Poisson's ratio and bulk modulus to shear modulus ratio indicate polycrystalline materials' ductility and brittleness. Pugh [45] states that the critical values for Poisson's ratio and B/G are [1.75] and [0.25 to 0.50]. A substance turns ductile when it passes the critical point; otherwise, it becomes brittle. They are brittle if their ductility does not continue past the critical point. Table 3 shows that a stiff material has the largest Young's modulus value, but a ductile material has a high B/G and Poisson's ratio, respectively.

**Table 2.** Bulk modulus (B), Young's modulus (Y), shear modulus (G), and Poisson's ratio ( $\nu$ ) were computed together with the elastic constants

Elastic constant	C11	C12	C13	C33	C44	C66	B	G	Y	$\nu$
<b>Cu<sub>2</sub>ZnSnS<sub>4</sub></b>	137.48	98.92	95.57	106.09	78.82	91.29	104.77	40.08	106.64	0.33
<b>Cu<sub>2</sub>ZnSnSe<sub>4</sub></b>	94.11	67.90	65.70	89.62	96.22	88.74	75.10	44.20	110.85	0.25

**Table 3.** Computed average elastic wave velocity ( $V_l$ ,  $V_t$ ,  $V_m$ , and Debye temperature ( $\theta_D$ ) under zero pressure, as well as longitudinal and transverse wave velocities

Compound	$V_l$ (m/s)	$V_t$ (m/s)	$V_m$ (m/s)	$\theta_D$ (K)
Cu <sub>2</sub> ZnSnS <sub>4</sub>	5873.87	2956.44	3315.27	364.28
Cu <sub>2</sub> ZnSnSe <sub>4</sub>	4862.86	2792.51	3101.67	324.88

### 3.5 Thermal properties

The quasiharmonic Debye model provides the thermodynamic characteristics of kesterite-type CZTS at various temperatures and pressures. We utilized the Gibbs2 method to calculate selected material (CZTS/CZTSe) thermal characteristics at temperatures ranging from 0 to 800 K and investigated the impact of pressure at 0-10 GPa. [46] For both materials, we investigated the relationship between Volume (V) and Bulk modulus (B) as a function of pressure and temperature. Figure 7 (a, b) and Figure 8 (a, b) clearly shows the changes in bulk modulus with changing temperatures for both compounds at different pressures [47].

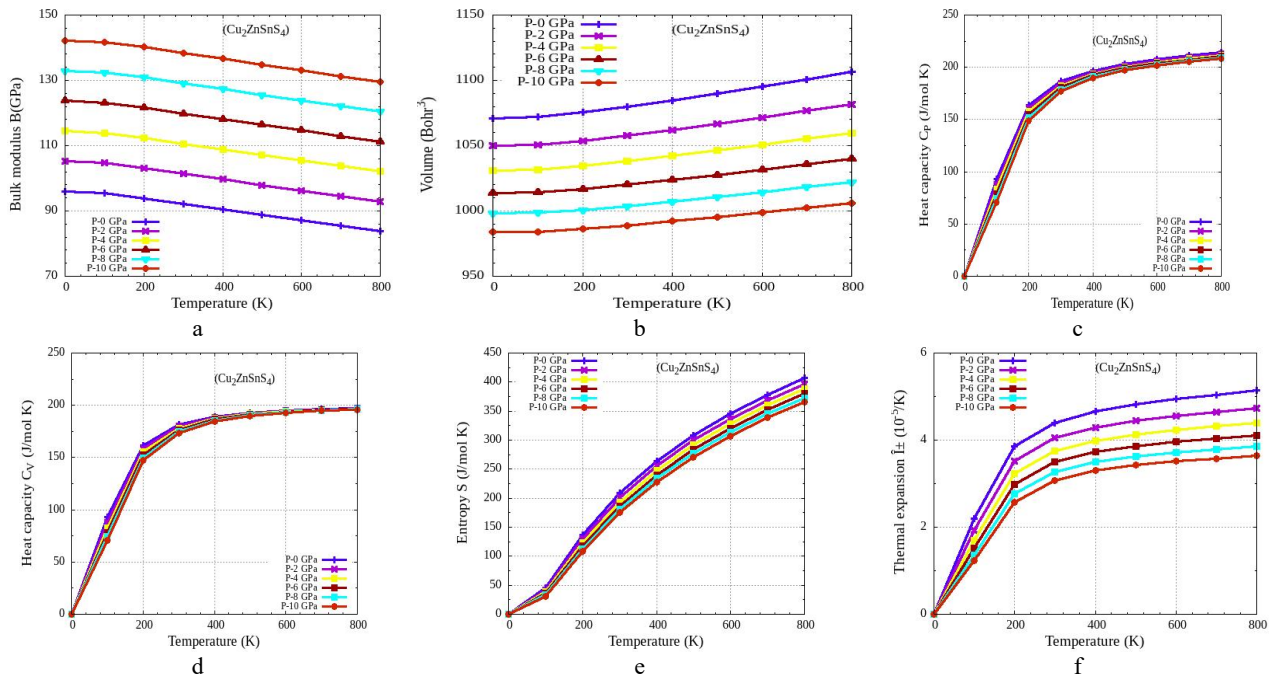


**Figure 7.** The Variations of a) Bulk modulus, b) Volume, c) Heat capacity ( $C_p$ ), d) Heat capacity ( $C_v$ ), e) Entropy, f) Thermal expansion of Cu<sub>2</sub>ZnSnS<sub>4</sub>

Also, with rising temperatures, it is easy to observe that V rises while B decreases. For a variety of purposes, a compound's heat capacity is important because it gives a basic understanding of the vibrational characteristics of substances. The following figures 7 (c, d) and 8 (c, d) depicts variations in heat capacity ( $C_V$ ) and ( $C_P$ ) at different temperatures and pressure ranges up to 10 GPa, respectively. We can infer from the figures that, at low temperatures,  $C_V$  and  $C_P$  follow the ( $T^3$ ) law while at high temperatures (Dulong-Petit limit), the temperature causes the value of  $C_P$  to increase, while the suppression of anharmonic results keeps the value of  $C_V$  nearly constant. The variation in entropy (S) with temperature is shown in Figures 7(e) and 8(e), confirming that for constant pressure, entropy increases as temperature rises. The value of the coefficient of thermal expansion changes with P and T, as shown in Figures 7(f) and 8(f). We can

easily observe that they increase rapidly up to 100 K then gradually increases. Above 200K, at high-pressure zones, it hikes approximately linearly, with a mild slope.

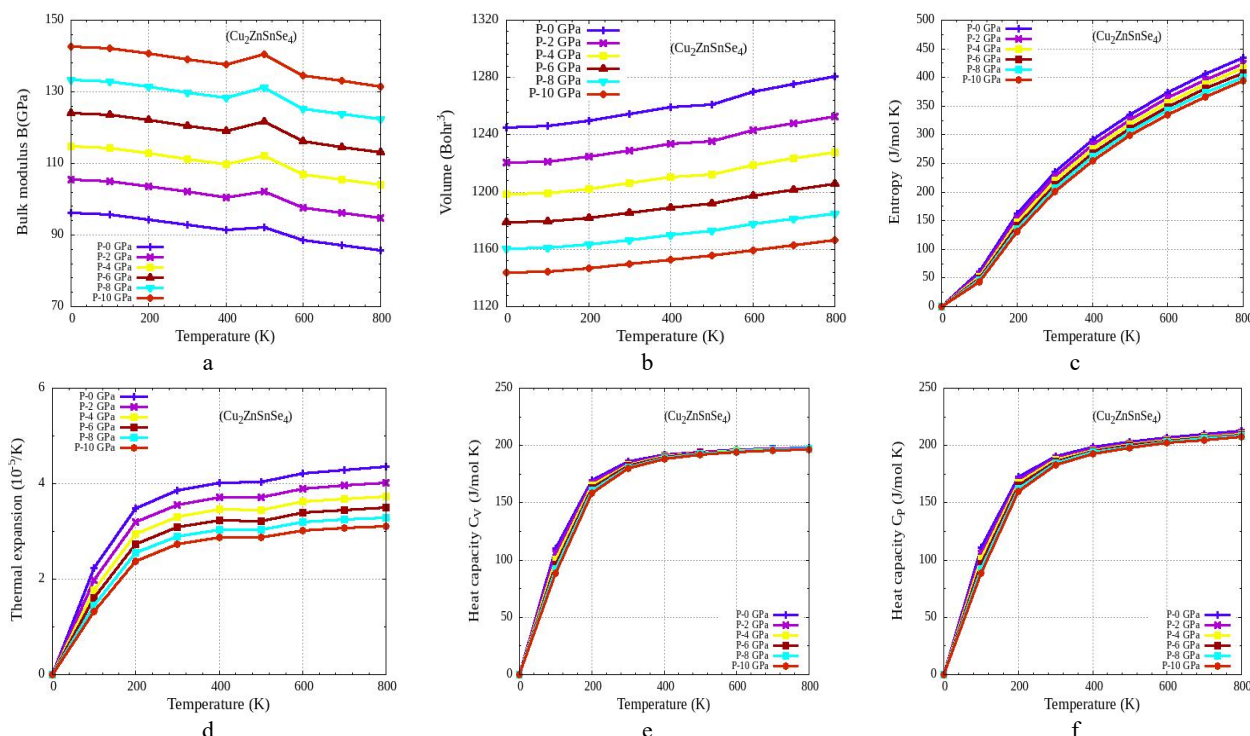


**Figure 8.** The Variations of a) Bulk modulus, b) Volume, c) Heat capacity ( $C_p$ ), d) Heat capacity ( $C_v$ ), e) Entropy, f) Thermal expansion of  $\text{Cu}_2\text{ZnSnS}_4$

### 3.6. Thermoelectric properties

Electrical conductivity ( $\sigma$ ), thermal conductivity ( $\kappa$ ), and Seebeck coefficients ( $S$ ) are some of the properties that determine the capacity of a material to convert heat into electricity during temperature gradients. The material having a higher Seebeck coefficient along with a high electrical conductivity is considered an effective thermoelectric material. Temperature and chemical potential were utilized to determine the TE parameters of kesterite  $\text{Cu}_2\text{ZnSnS}_4$  ( $\text{Cu}_2\text{ZnSnSe}_4$ ) materials using a semi-classical Boltzmann theory, which was executed in the BoltzTrap package [48]. However, Fig. 9 clearly shows how the TE characteristics depend on chemical potential throughout an ambient temperature range of 300-500K.

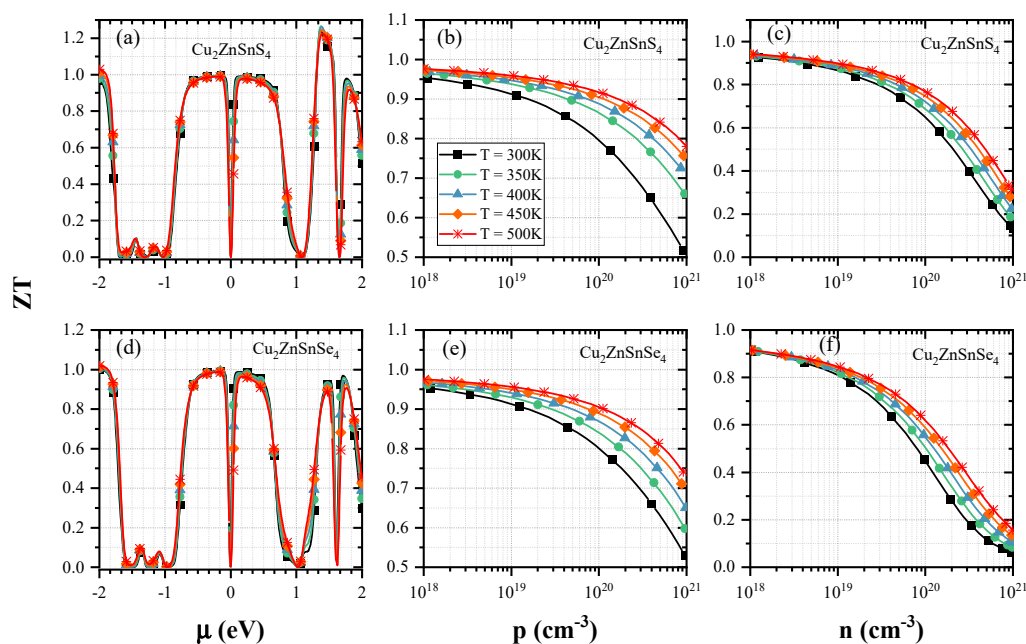


**Figure 9.** The Figure of merit  $ZT$  as a function of i) chemical potential ( $\mu$ ), ii) hole concentration ( $p$ ), iii) electron concentration ( $n$ ), (a-c) and (d-f) of  $\text{Cu}_2\text{ZnSnX}_4$  ( $X = \text{S}, \text{Se}$ )

The ZT is a unitless quantity that refers to the figure of merit, which is determined through the equation  $ZT = S^2\sigma T/\kappa$ , and is a significant factor in determining the effectiveness of a Thermoelectric material. In conceptual terms, a material must concurrently satisfy the competing demands of high Electrical Conductivity (EC) and low Thermal Conductivity (TC) for the ZT parameter to be near to one which is necessary for an efficient Thermoelectric material. While larger carriers have a greater S value, which raises the ZT, lighter carriers have more mobility (and hence EC). When residing in the forbidden energy gap for carrier concentration order of  $10^{18}$  and  $10^{19}$   $\text{cm}^{-3}$  (as seen in Fig. 9,10), here, ZT has a noticeably higher value that is greater than 0.95. The correlation between ZT and electron and hole concentrations has been depicted in the appropriate Figures 9 (b, c) and 10 (b, c). These figures also shows that the ZT values in  $\text{Cu}_2\text{ZnSnS}_4$ ( $\text{Cu}_2\text{ZnSnSe}_4$ ) materials are greater regardless of both (n or p) doping and gradually decrease as the dopant concentration is raised. Furthermore, the ZT of n-type  $\text{Cu}_2\text{ZnSnS}_4$  ( $\text{Cu}_2\text{ZnSnSe}_4$ ) is insensitive to variations in temperature and doping quantity. Hence result, n-type  $\text{Cu}_2\text{ZnSnS}_4$ ( $\text{Cu}_2\text{ZnSnSe}_4$ ) is anticipated to perform better than p-type  $\text{Cu}_2\text{ZnSnS}_4$ ( $\text{Cu}_2\text{ZnSnSe}_4$ ) for thermoelectric applications. Even,  $\text{Cu}_2\text{ZnSnS}_4$  exhibits a higher ZT value and is less dependent on T than  $\text{Cu}_2\text{ZnSnSe}_4$ . Consequently, n-type  $\text{Cu}_2\text{ZnSnS}_4$  is more suitable for thermoelectric applications. A material must have a high Seebeck coefficient (S) to be used in the manufacturing of effective thermoelectric devices. The temperature significantly influences this coefficient, which is set by the DOS profile along the energy band boundaries.

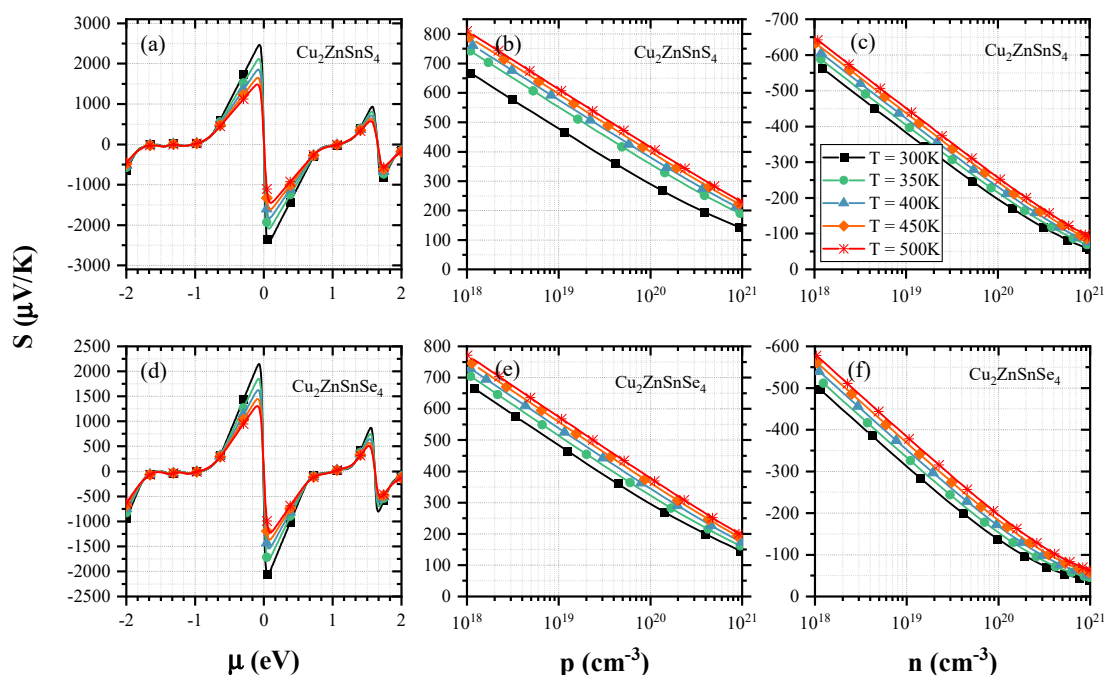


**Figure 10.** The Seebeck coefficient as a function of i) chemical potential ( $\mu$ ), ii) hole concentration (p), iii) electron concentration (n), (a-c) and (d-f) of  $\text{Cu}_2\text{ZnSnX}_4$  (X= S, Se)

Figures 9 and 10 (a, d) clearly shows that only when it is in the forbidden energy gap significant values of S can be observed. When electrons are charge carriers, the Seebeck coefficient is negative; when holes do so, it is positive. Regardless of doping level or carrier type, the quantity of S reduces with rising temperatures. Figures 9 (b, e) and 10 (c, f) depicts the parameter S in relationship with electron (n) and hole (p) concentrations, correspondingly. When the carrier concentration rises, the (S) parameter values steadily decrease from their high values in weakly doped n- and p-type materials. Nonetheless, the material of p-type is somewhat more vulnerable to temperature alterations. In comparison to  $\text{Cu}_2\text{ZnSnS}_4$  and  $\text{Cu}_2\text{ZnSnSe}_4$ ,  $\text{Cu}_2\text{ZnSnS}_4$  has a higher S parameter value. This verifies  $\text{Cu}_2\text{ZnSnS}_4$ 's suitability for TE applications over  $\text{Cu}_2\text{ZnSnSe}_4$ .

In Fig. 11a, 11b, and c, the ratio of calculated electrical conductivity to relaxation time ( $\sigma/\tau$ ) is plotted as a function of hole and electron concentrations within the range of  $10^{18}$  to  $10^{21}$   $\text{cm}^{-3}$ , demonstrating a cumulative trend. It is also displayed as a function of chemical potential. The parameter  $\sigma/\tau$  in n-type materials remains unchanged as the ambient temperature rises, whereas it does in p-type materials. This suggests that in  $\text{Cu}_2\text{ZnSnS}_4$ ( $\text{Cu}_2\text{ZnSnSe}_4$ ) materials, the scattering and mobility of electrons are less temperature-dependent than those of holes. Figure 12 displays the computed TC to relaxation time ratio as a function of time at any selected parameters such as doping level and temperature, the p-type material has a maximum ratio in comparison with the material of n-type, showing that p-type  $\text{Cu}_2\text{ZnSnX}_4$  (X= S, Se) has higher phonon scattering than n-type  $\text{Cu}_2\text{ZnSnX}_4$ . However, high thermal conductivity is needed for an effective PVA material to prevent heating, whereas low thermal conductivity is preferred for a prospective thermoelectric material to prevent thermal sorting. As a result, heavily doped p-type  $\text{Cu}_2\text{ZnSnSe}_4$  is better suited for Photovoltaic, while weakly doped n-type  $\text{Cu}_2\text{ZnSnS}_4$  is preferable for thermoelectric devices.

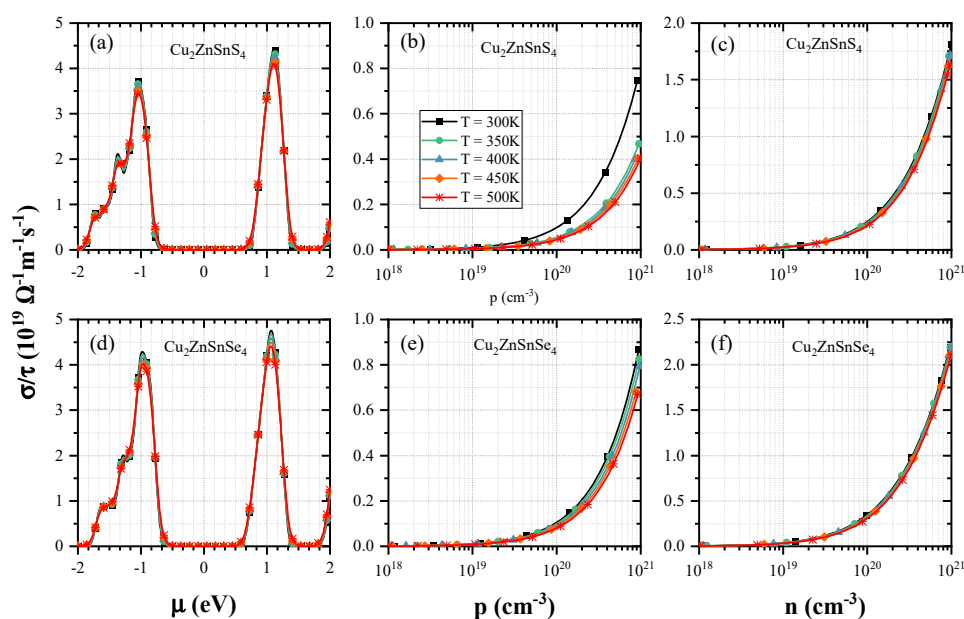


**Figure 11.** The  $\sigma/\tau$  as a function of i) chemical potential ( $\mu$ ), ii) hole concentration ( $p$ ), iii) electron concentration ( $n$ ), (a-c) and (d-f) of  $\text{Cu}_2\text{ZnSnX}_4$  ( $X = \text{S, Se}$ )

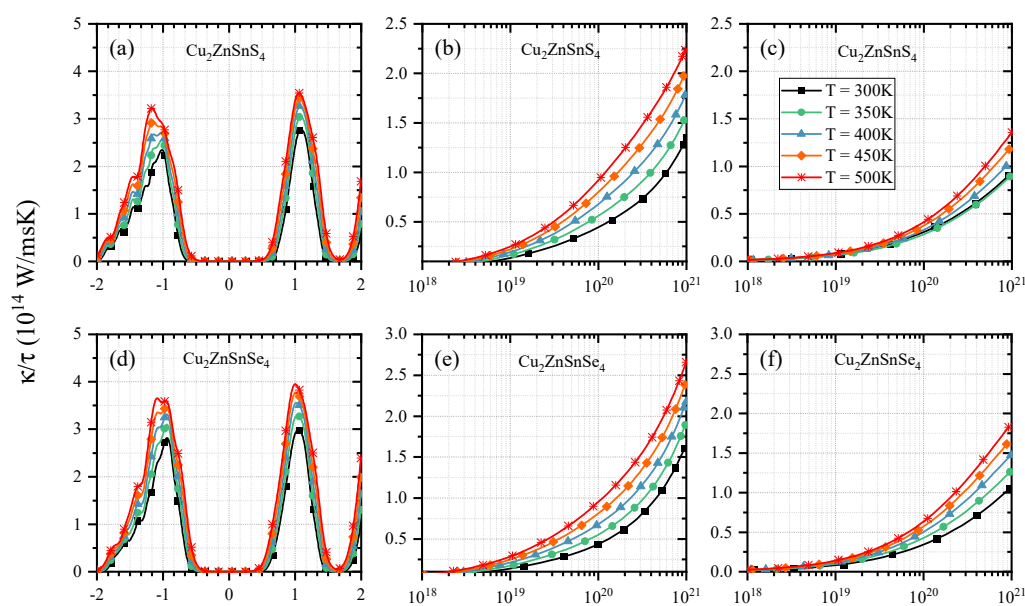


**Figure 12.** The  $\kappa/\tau$  as a function of i) chemical potential ( $\mu$ ), ii) hole concentration ( $p$ ), iii) electron concentration ( $n$ ), (a-c) and (d-f) of  $\text{Cu}_2\text{ZnSnX}_4$  ( $X = \text{S, Se}$ )

### 3.7 Theoretical power conversion efficiency

It is necessary to estimate a material's Theoretical Power Conversion efficiency (TPCE) or (PCE) before screening it for Photovoltaic applications. A photovoltaic (PV) device's power conversion efficiency is dependent on several parameters, such as the method used during device fabrication, material defects, and the material's optical and thermodynamic properties. [49] A practical technique for identifying materials appropriate for the PVA layer is the Spectroscopic limited maximum efficiency (SLME), which has been suggested by Yu et al. [50]. It is illustrated as the maximum possible theoretical efficiency achievable with a single junction-based solar cell composed of a specific photovoltaic material. [51] In this study, the SLME has been displayed in Figure 13 as a function of the  $\text{Cu}_2\text{ZnSnX}_4$  ( $X = \text{S, Se}$ ) thin film absorber layer thickness between 300 and 500 K temperature. The plot makes it obvious that as the film thickness is increased from 200 nm to 1 μm at 300K, the SLME of the  $\text{Cu}_2\text{ZnSnS}_4$  ( $\text{Cu}_2\text{ZnSnSe}_4$ ) material increases from 23.5% to 31.2% (22.5% to 31.9%), and then it stabilizes. Further supports the idea that temperature  $T$  has a significant influence on the parameter. The plot clearly shows that only a 1 μm thick photovoltaic application material film deposition is necessary to produce the greatest PCE. Even though the estimated SLME of  $\text{Cu}_2\text{ZnSnS}_4$  is marginally lower than that of  $\text{Cu}_2\text{ZnSnSe}_4$  the material. For PV, best-suited material is  $\text{Cu}_2\text{ZnSnSe}_4$ . However,  $\text{Cu}_2\text{ZnSnS}_4$  may be more suited for environmentally friendly PV systems due to its greater stability.



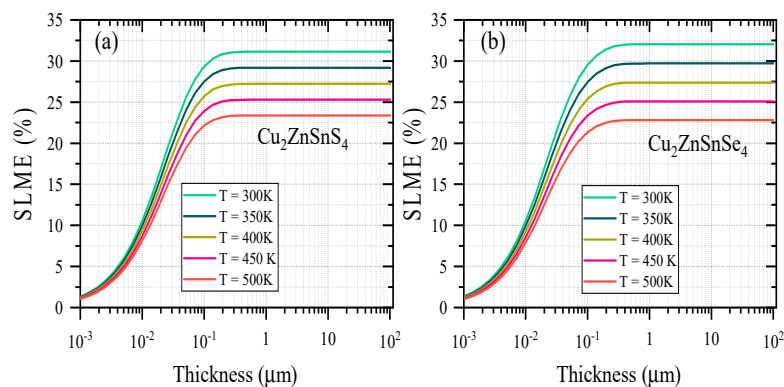


**Figure 13.** SLME as a function of the thickness of PVA material layer of a)  $\text{Cu}_2\text{ZnSnS}_4$  and b)  $\text{Cu}_2\text{ZnSnSe}_4$

#### 4. SUMMARY AND CONCLUSION

The fundamental structural, optical properties, elastic, thermoelectric, and thermal properties of potential semiconducting  $\text{Cu}_2\text{ZnSnS}_4$  (CZTS) and  $\text{Cu}_2\text{ZnSnSe}_4$  (CZTSe) materials have been carried out in this first-principles exploration. In which, the computed lattice constant of CZTS ( $a = 5.42 \text{ \AA}$ ,  $b = 5.42 \text{ \AA}$ ,  $c = 10.81 \text{ \AA}$  and CZTSe ( $a = 5.69 \text{ \AA}$ ,  $b = 5.69 \text{ \AA}$ ,  $c = 11.33 \text{ \AA}$  values are respectively. In terms of optical and electronic properties, the CZTS and CZTSe materials have absolute band gaps of 1.51 eV and 1.29 eV in the visible range separately with remarkable performance. The static dielectric constants of the selected materials were 4.91 (5.65). The Bulk modulus, Young's modulus, Elastic constants, and Shear modulus were then all evaluated. Similarly, Pugh's and Poisson's Ratio demonstrated their ductile nature. The thermodynamic stability enables it to obtain a ZT of unity at 300K to 500K temperatures. As a result, in both types of semiconductors (n or p), electron or hole mobility and scattering are independent of temperature. This indicates that it might be employed in thermoelectric applications. Undoubtedly, the n-type  $\text{Cu}_2\text{ZnSnS}_4$ , doped to a level of order  $10^{18} \text{ cm}^{-3}$ , is a promising material for thermoelectric products due to its appropriate values of key parameters, including ZT larger than 0.95 and S higher than  $200 \mu\text{V/K}$ . The high compressibility and temperature dependence of  $\text{Cu}_2\text{ZnSnSe}_4$  material might increase the stability of photovoltaic devices. The ability of  $\text{Cu}_2\text{ZnSnSe}_4$  film to offer SLME of up to 31.9% at room temperature demonstrates its viability as an inexpensive instead of effective Photovoltaic application material. Overall, the findings of the study indicates that these compounds are suggesting candidates for industrial use and open the way for further experimental research.

#### ORCID

© Bhanu Prakash, <https://orcid.org/0009-0000-4936-4874>; © Banwari Lal Choudhary, <https://orcid.org/0000-0002-9785-6547>  
© Ajay Singh Verma, <https://orcid.org/0000-0001-8223-7658>

#### REFERENCES

- [1] A. Polman, M. Knight, E.C. Garnett, B. Ehrler, and W. C. Sinke, "Photovoltaic materials: Present efficiencies and future challenges," *Science*, **352**, 4424 (2016). <https://doi.org/10.1126/science.aad4424>
- [2] D.M. Chapin, C.S. Fuller, and G.L. Pearson, "A new silicon p-n junction photocell for converting solar radiation into electrical power," *Journal of Applied Physics*, **25**, 676 (1954). <https://doi.org/10.1063/1.1721711>
- [3] G. Li, R. Zhu, and Y. Yang, "Polymer solar cells," *Nature Photonics*, **6**, 153 (2012). <https://doi.org/10.1038/nphoton.2012.11>
- [4] R.W. Miles, G. Zoppi, and I. Forbes, "Inorganic photovoltaic cells," *Materials Today*, **10**, 20-27 (2007). [https://doi.org/10.1016/S1369-7021\(07\)70275-4](https://doi.org/10.1016/S1369-7021(07)70275-4)
- [5] A. Bosio, G. Rosa and N. Romeo, "Past, present and future of the thin film CdTe/CdS solar cells," *Solar Energy*, **175**, 31-43 (2018). <https://doi.org/10.1016/j.solener.2018.01.018>
- [6] H.W. Schock, and R. Noufi, "CIGS-based solar cells for the next millennium," *Progress in Photovoltaics: Research and Applications*, **8**, 151-160 (2000). [https://doi.org/10.1002/\(SICI\)1099-159X\(200001/02\)8:1%3C151::AID-PIP302%3E3.0.CO;2-Q](https://doi.org/10.1002/(SICI)1099-159X(200001/02)8:1%3C151::AID-PIP302%3E3.0.CO;2-Q)
- [7] D.P. Pham, S. Lee, and J. Yi, "Potential high efficiency of GaAs solar cell with heterojunction carrier selective contact layers," *Physica B: Condensed Matter*, **611**, 412856 (2021). <https://doi.org/10.1016/j.physb.2021.412856>
- [8] M.A. Green, A.H. Baillie, and H.J. Snaith, "The emergence of perovskite solar cells," *Nature Photonics*, **8**, 506-514 (2014). <https://doi.org/10.1038/nphoton.2014.134>
- [9] S.C. Riha, B.A. Parkinson, and A.L. Prieto, "Solution-based synthesis and characterization of  $\text{Cu}_2\text{ZnSnS}_4$  nanocrystals," *Journal of the American Chemical Society*, **131**, 12054-12055 (2009). <https://doi.org/10.1021/ja9044168>
- [10] H. Katagiri, K. Jimbo, W.S. Maw, K. Oishi, M. Yamazaki, H. Araki, and A. Takeuchi, "Development of CZTS-based thin film solar cells," *Thin Solid Films*, **517**, 2455-2460 (2009). <https://doi.org/10.1016/j.tsf.2008.11.002>
- [11] K. Woo, Y. Kim, and J. Moon, "A non-toxic, solution-processed, earth-abundant absorbing layer for thin-film solar cells," *Energy & Environmental Science*, **5**, 5340-5345 (2012). <https://doi.org/10.1039/C1EE02314D>
- [12] B. Prakash, A. Meena, Y. K. Saini, S. Mahich, A. Singh, S. Kumari, C.S.P. Tripathi, and B.L. Choudhary, "Solution-processed CZTS thin films and its simulation study for solar cell applications with ZnTe as the buffer layer," *Environmental Science and Pollution Research*, **30**, 98671-98681 (2023). <https://doi.org/10.1007/s11356-022-23664-8>

- [13] J. Kim, H. Hiroi, T.K. Todorov, O. Gunawan, M. Kuwahara, T. Gokmen, D. Nair, M. Hopstaken, B. Shin, Y.S. Lee, W. Wang, H. Sugimoto, and D.B. Mitzi, "High efficiency  $\text{Cu}_2\text{ZnSn}$  (S, Se) 4 solar cells by applying a double  $\text{In}_2\text{S}_3/\text{CdS}$  emitter," *Advanced Materials*, **26**, 7427-7431 (2014). <https://doi.org/10.1002/adma.201402373>
- [14] Q. Guo, H.W. Hillhouse, and R. Agrawal, "Synthesis of  $\text{Cu}_2\text{ZnSnS}_4$  nanocrystal ink and its use for solar cells," *Journal of the American Chemical Society*, **131**, 11672-11673 (2009). <https://doi.org/10.1021/ja904981r>
- [15] M.C. Benachour, R. Bensaha, and R. Moreno, "Annealing duration influence on dip-coated CZTS thin films properties obtained by sol-gel method," *Optik*, **187**, 1-8 (2019). <https://doi.org/10.1016/j.ijleo.2019.05.015>
- [16] C. Xiong, M. Gao, and W. Gao, " $\text{Cu}_2\text{ZnSnS}_4$  (CZTS) thin films prepared by sol-gel spin-coating technique," *International Journal of Modern Physics B*, **34**, 2040019 (2020). <https://doi.org/10.1142/S0217979220400196>
- [17] F. Luckert, D.I. Hamilton, M.V. Yakushev, N.S. Beattie, G. Zoppi, M. Moynihan, I. Forbes, *et al.*, "Optical properties of high quality  $\text{Cu}_2\text{ZnSnSe}_4$  thin films," *Applied Physics Letters*, **99**, 062104 (2011). <https://doi.org/10.1063/1.3624827>
- [18] R.A. Wibowo, E.S. Lee, B. Munir, and K.H. Kim, "Pulsed laser deposition of quaternary  $\text{Cu}_2\text{ZnSnSe}_4$  thin films," *Physica status solidi (a)*, **204**, 3373-3379 (2007). <https://doi.org/10.1002/pssa.200723144>
- [19] M.V. Jyothirmai, H. Saini, N. Park, and R. Thapa, "Screening of suitable cationic dopants for solar absorber material CZTS/Se: A first principles study," *Scientific Reports*, **9**, 15983 (2019). <https://doi.org/10.1038/s41598-019-52410-3>
- [20] X. He, J. Pi, Y. Dai, and X. Li, "Elastic and thermo-physical properties of stannite-type  $\text{Cu}_2\text{ZnSnS}_4$  and  $\text{Cu}_2\text{ZnSnSe}_4$  from first-principles calculations," *Acta Metallurgica Sinica (English Letters)*, **26**, 285-292 (2013). <https://doi.org/10.1007/s40195-012-0248-4>
- [21] Y. Nouri, B. Hartiti, A. Batan, H. Labrim, S. Fadili, and P. Thévenin, " $\text{Cu}_2\text{XSnS}_4$  ( $X = \text{Mn}, \text{Fe}, \text{Co}$ ) semiconductors: Boltzmann theory and DFT investigations," *Solid State Communications*, **339**, 114491 (2021). <https://doi.org/10.1016/j.ssc.2021.114491>
- [22] H.M. Mohammedi, F. Chiker, H. Khachai, N. Benosman, R. Khenata, R. Ahmed, S.B. Omran, *et al.*, "Structural, optoelectronic, optical coating and thermoelectric properties of the chalcogenides type Kesterite  $\text{Ag}_2\text{CdSnX}_4$  (with  $X = \text{S}, \text{Se}$ ): A computational insight," *Materials Science in Semiconductor Processing*, **134**, 106031 (2021). <https://doi.org/10.1016/j.mssp.2021.106031>
- [23] M. Mesbahi, F. Serdouk, and M. Benkhedir, "A DFT Study of the Electronic and Optical Properties of Kesterite Phase of  $\text{Cu}_2\text{ZnGeS}_4$  Using GGA, TB-MBJ, and U Exchange Correlation Potentials," *Acta Physica Polonica A*, **134**, 358-361 (2018). <https://doi.org/10.12693/APhysPolA.134.358>
- [24] K. Schwarz, and P. Blaha, "Solid state calculations using WIEN2k," *Computational Materials Science*, **28**, 259-273 (2003). [https://doi.org/10.1016/S0927-0256\(03\)00112-5](https://doi.org/10.1016/S0927-0256(03)00112-5)
- [25] F. Z. Nainaa, N. Bekkioui, A. Abbassi, and H. Ez-Zahraouy, "First-principle study of structural, electronic, optical and electric properties of  $\text{Ag}_2\text{ZnGeX}_4$  (S, Se)," *Computational Condensed Matter*, **19**, e00364 (2019). <https://doi.org/10.1016/j.cocom.2019.e00364>
- [26] H.J. Monkhorst, and J.D. Pack, "Special points for Brillouin-zone integrations," *Physical review B*, **13**, 5188 (1976). <https://doi.org/10.1103/PhysRevB.13.5188>
- [27] Morteza Jamal, and Ghods City-Tehran-Iran, "IR ELAST," (2019).
- [28] G.K.H. Madsen, and D.J. Singh, "BoltzTraP. A code for calculating band-structure dependent quantities," *Computer Physics Communications*, **175**, 67-71 (2006). <https://doi.org/10.1016/j.cpc.2006.03.007>
- [29] F.D. Murnaghan, "On the theory of the tension of an elastic cylinder," *Proceedings of the National Academy of Sciences*, **30**, 382-384 (1944). <https://doi.org/10.1073/pnas.30.12.382>
- [30] J.P. Perdew, K. Burke, and M. Ernzerhof, "Generalized gradient approximation made simple," *Physical Review Letters*, **77**, 3865 (1996). <https://doi.org/10.1103/PhysRevLett.77.3865>
- [31] K. Lau, and A.K. McCurdy, "Elastic anisotropy factors for orthorhombic, tetragonal, and hexagonal crystals," *Physical Review B*, **58**, 8980 (1998). <https://doi.org/10.1103/PhysRevB.58.8980>
- [32] T. Maeda, S. Nakamura, and T. Wada, "First principles calculations of defect formation in in-free photovoltaic semiconductors  $\text{Cu}_2\text{ZnSnS}_4$  and  $\text{Cu}_2\text{ZnSnSe}_4$ ," *Japanese Journal of Applied Physics*, **50**, 04DP07 (2011). <https://doi.org/10.1143/JJAP.50.04DP07>
- [33] N.M. Shinde, D.P. Dubal, D.S. Dhawale, C.D. Lokhande, J.H. Kim, and J.H. Moon, "Room temperature novel chemical synthesis of  $\text{Cu}_2\text{ZnSnS}_4$  (CZTS) absorbing layer for photovoltaic application," *Materials Research Bulletin*, **47**, 302-307 (2012). <https://doi.org/10.1016/j.materresbull.2011.11.020>
- [34] M. Grossberg, J. Krustok, K. Timmo, and M. Altsaar, "Radiative recombination in  $\text{Cu}_2\text{ZnSnSe}_4$  monograins studied by photoluminescence spectroscopy," *Thin Solid Films*, **517**, 2489-2492 (2009). <https://doi.org/10.1016/j.tsf.2008.11.024>
- [35] S. Sharma, A.S. Verma, and V.K. Jindal, "Ab initio studies of structural, electronic, optical, elastic and thermal properties of silver gallium dichalcogenides ( $\text{AgGaX}_2$ :  $X = \text{S}, \text{Se}, \text{Te}$ )," *Materials Research Bulletin*, **53**, 218-233 (2014). <https://doi.org/10.1016/j.materresbull.2014.02.021>
- [36] M. Jamal, M. Bilal, I. Ahmad, and S.J. Asadabadi, "IRelast package," *Journal of Alloys and Compounds*, **735**, 569-579 (2018). <https://doi.org/10.1016/j.jallcom.2017.10.139>
- [37] S.K.R. Patil, S.V. Khare, Blair Richard Tuttle, J. K. Bording, and S. Kodambaka, "Mechanical stability of possible structures of PtN investigated using first-principles calculations," *Physical Review B*, **73**, 104118 (2006). <https://doi.org/10.1103/PhysRevB.73.104118>
- [38] Z.I. Wu, Er.J. Zhao, H.P. Xiang, X.F. Hao, X.J. Liu, and J. Meng, "Crystal structures and elastic properties of superhard  $\text{IrN}_2$  and  $\text{IrN}_3$  from first principles," *Physical Review B*, **76**, 054115 (2007). <https://doi.org/10.1103/PhysRevB.76.054115>
- [39] E. Haque, and M.A. Hossain, "First-principles study of elastic, electronic, thermodynamic, and thermoelectric transport properties of  $\text{TaCoSn}$ ," *Results in Physics*, **10**, 458-465 (2018). <https://doi.org/10.1016/j.rinp.2018.06.053>
- [40] J. Feng, "Mechanical properties of hybrid organic-inorganic  $\text{CH}_3\text{NH}_3\text{BX}_3$  ( $B = \text{Sn}, \text{Pb}$ ;  $X = \text{Br}, \text{I}$ ) perovskites for solar cell absorbers," *Apl Materials*, **2**, 081801 (2014). <https://doi.org/10.1063/1.4885256>
- [41] W. Voigt, *Lehrbuch der kristallphysik*, Macmillan New York (Teubner, Leipzig, 1928), p. 962.
- [42] K. Moradi, and A.A.S. Alvani, "First-principles study on Sr-doped hydroxyapatite as a biocompatible filler for photo-cured dental composites," *Journal of the Australian Ceramic Society*, **56**, 591-598 (2020). <https://doi.org/10.1007/s41779-019-00369-9>
- [43] O.L. Anderson, "A simplified method for calculating the Debye temperature from elastic constants," *Journal of Physics and Chemistry of Solids*, **24**, 909-917 (1963). [https://doi.org/10.1016/0022-3697\(63\)90067-2](https://doi.org/10.1016/0022-3697(63)90067-2)



- [44] P. Wachter, M. Filzmoser, and J. Rebizant, "Electronic and elastic properties of the light actinide tellurides," *Physica B: Condensed Matter*, **293**, 199-223 (2001). [https://doi.org/10.1016/S0921-4526\(00\)00575-5](https://doi.org/10.1016/S0921-4526(00)00575-5)
- [45] S.F. Pugh, "XCII. Relations between the elastic moduli and the plastic properties of polycrystalline pure metals," *The London, Edinburgh, and Dublin Philosophical Magazine and Journal of Science*, **45**, 823-843 (1954). <https://doi.org/10.1080/14786440808520496>
- [46] A.O. Roza, D.A. Pérez, and V. Luaña, "Gibbs2: A new version of the quasiharmonic model code. II. Models for solid-state thermodynamics, features and implementation," *Computer Physics Communications*, **182**, 2232-2248 (2011). <https://doi.org/10.1016/j.cpc.2011.05.009>
- [47] M.I. Ziane, D. Ouadjaout, M. Tablaoui, R. Nouri, W. Zermane, A. Djelloul, H. Bennacer, et al., "First-Principle Computed Structural and Thermodynamic Properties of  $\text{Cu}_2\text{ZnSn}(\text{S}_x\text{Se}_{1-x})_4$  Pentanary Solid Solution," *Journal of Electronic Materials*, **48**, 6991-7002 (2019). <https://doi.org/10.1007/s11664-019-07496-w>
- [48] G.K.H. Madsen, and D.J. Singh, "BoltzTraP. A code for calculating band-structure dependent quantities," *Computer Physics Communications*, **175**, 67-71 (2006). <https://doi.org/10.1016/j.cpc.2006.03.007>
- [49] M. Bercx, N. Sarmadian, R. Saniz, B. Partoens, and D. Lamoen, "First-principles analysis of the spectroscopic limited maximum efficiency of photovoltaic absorber layers for CuAu-like chalcogenides and silicon," *Physical Chemistry Chemical Physics*, **18**, 20542-20549 (2016). <https://doi.org/10.1039/C6CP03468C>
- [50] L. Yu, and A. Zunger, "Identification of potential photovoltaic absorbers based on first-principles spectroscopic screening of materials," *Physical Review Letters*, **108**, 068701 (2012). <https://doi.org/10.1103/PhysRevLett.108.068701>
- [51] M. Bercx, R. Saniz, B. Partoens, and D. Lamoen, "Exceeding the Shockley–Queisser limit within the detailed balance framework," in: *Many-body Approaches at Different Scales*, edited by G. Angilella and C. Amovilli, (Springer, Cham. 2018), pp. 177-184. [https://doi.org/10.1007/978-3-319-72374-7\\_15](https://doi.org/10.1007/978-3-319-72374-7_15)

**ДОСЛІДЖЕННЯ НА ОСНОВІ ПЕРОПРИНЦИПІВ НАПІВПРОВІДНИКОВИХ ЕКОЛОГІЧНО ЧИСТИХ МАТЕРІАЛІВ  $\text{Cu}_2\text{ZnSnX}_4$  ( $X = \text{S}, \text{Se}$ ) ДЛЯ НАСТУПНОГО ПОКОЛІННЯ ФОТОЕЛЕКТРИЧНИХ ЗАСТОСУВАНЬ**  
**Бхану Пракаш<sup>a</sup>, Аджит Сінгх<sup>b</sup>, Тарун Кумар Джоші<sup>c</sup>, Банварі Лал Чоудхарі<sup>a</sup>, Нейнсі Пандіт<sup>d</sup>, Аджай Сінгх Верма<sup>e,f</sup>**

<sup>a</sup>Кафедра фізичних наук, Банастанхалі Відьяпіт, Банастанхалі, Раджастан 304022, Індія

<sup>b</sup>Кафедра фізики, Коледж Дева Нагрі, Мірут, Уттар-Прадеш, 250002, Індія

<sup>c</sup>Кафедра фізики, Урядовий інститут Свами Вівекананда P. G. College, Neetich, Madhya Pradesh, 458441, Індія

<sup>d</sup>Кафедра фізики, Школа суміжних наук, Університет Дев Бхумі Уттаракханд, Дехрадун 248007, Індія


<sup>e</sup>Кафедра фізики, Інженерно-технологічна школа Ананда, Університет Шарда, Агра, 282007, Індія

<sup>f</sup>Університетський центр досліджень і розвитку, факультет фізики, Університет Чандігарха, Мохалі, Пенджаб, 140413, Індія

Напівпровідникові матеріали на основі четвертинної загальної форми  $\text{A}_2\text{BCX}_4$  зі структурами кестеритового типу є перспективними кандидатами для виготовлення тонкоплівкових сонячних елементів. Ми дослідили структурні, електричні, оптичні, пружні, термодинамічні та термоелектричні характеристики  $\text{Cu}_2\text{ZnSnX}_4$  ( $X = \text{S}, \text{Se}$ ) за допомогою методу FP-LAPW з імплантованим кодом Wien2k. Для управління обмінними та кореляційними потенціалами використовуються узагальнений градієнтний підхід Берка-Ернцгергофа (PBE-GGA) та модифікований метод Бекке-Джонсона за методом Транс-Блахи (TB-mBJ). Результати показують, що сполуки  $\text{Cu}_2\text{ZnSnS}_4$  та  $\text{Cu}_2\text{ZnSnSe}_4$  мають стабільні структури з прямими зонами при 1,51 eV та 1,29 eV відповідно. Оптичні характеристики цих сполук були оцінені за допомогою діелектричної функції, що дозволяє проаналізувати їхню відбивну здатність, показник заломлення та поглинання. Такі параметри пружності, як коефіцієнти об'єму, Юнга, П'ю та Пуассона, демонструють, що вони є пластичними та можуть формуватися у вигляді тонких плівок, що є важливою характеристикою фотоелектричних застосувань. Крім того, ми розрахували різні термодинамічні параметри: ентропію та постійний об'єм під тиском і температурою. Ми також визначили, що  $\text{Cu}_2\text{ZnSnX}_4$  ( $X = \text{S}, \text{Se}$ ) демонструє хороші термоелектричні характеристики щодо коефіцієнта якості при 300K, який майже дорівнює одиниці. Згідно з нашими висновками, ці матеріали є життєздатними кандидатами для майбутніх застосувань у чистій зеленій сонячній енергетиці.

**Ключові слова:** *Wien2k-DFT; сонячний елемент  $\text{Cu}_2\text{ZnSnX}_4$ ; структурний, пружність; термоелектричні властивості*

## COMPUTER SIMULATION STUDY OF ADSORPTION PROCESSES OF $C_{20}@C_n$ AND $C_{60}@C_n$ ( $n=1-5$ ) CARBON CLUSTERS ON RECONSTRUCTED SILICON Si(001) SURFACE

**Ikrom Z. Urolov<sup>a,b</sup>, Farid F. Umarov<sup>c</sup>,  Ishmumin D. Yadgarov<sup>a\*</sup>, Ganiboy T. Rakhmanov<sup>b</sup>,  
Khayitmurod I. Jabborov<sup>d,e</sup>**

<sup>a</sup>*U.A. Arifov Institute of Ion-Plasma and Laser Technologies, Academy of Sciences of the Republic of Uzbekistan, 100125, Tashkent, str. Durmon Yuli, 33*

<sup>b</sup>*Mirzo Ulugbek National University of Uzbekistan, Republic of Uzbekistan, 100174, Tashkent, Universitetskaya str., 4*

<sup>c</sup>*Kazakhstan-British Technical University, Almaty, str. Tole bi 59, Kazakhstan*

<sup>d</sup>*Tashkent state technical university named after Islam Karimov, Tashkent, Uzbekistan*

<sup>e</sup>*Tashkent University of information technologies named after Muhammad al-Khwarizmi, Tashkent, Uzbekistan*

\*Corresponding Author E-mail: [ishmuminyadgarov@gmail.com](mailto:ishmuminyadgarov@gmail.com)

Received March 27, 2025; revised June 17, 2025; accepted June 23, 2025

In today's nanotechnology field, one of the requirements of the current direction is the ability of carbon nanostructures to have a strong bond with the substrate surface among the materials formed by the interaction of different substrates with the surface of various substrates. The study and identification of new structures with similar properties is one of the problems facing modern theoretical research. The current research work was carried out as one of the solutions to the above-mentioned problems, in which the adsorption of fullerene molecules on silicon substrates using the molecular dynamics (MD) method is a continuation of our work on the adsorption of fullerene  $C_{20}$  and  $C_{60}$  molecules on the surface of silicon Si(001) reconstructed by  $C_n$  ( $n=1-5$ ) carbon clusters was simulated using the open source LAMMPS package based on the molecular dynamics method. Using the Tersoff interatomic potential, the interactions between the atoms of the substrate,  $C_n$  cluster, and fullerene molecules were expressed, and the adsorption energies of  $C_{20}@C_n$  and  $C_{60}@C_n$  carbon clusters, the length and nature of Si-C bonds, as well as stable adsorption states in trench and dimer rows were determined.

**Keywords:** Fullerene molecule; Base; Cluster; Trench; Dimer array; Modeling; Potential; Bond; Simulation; Adsorption

**PACS:** 61.48.-c, 02.70.Ns

### INTRODUCTION

Carbon-based nanostructures have remained relevant for decades. Fullerenes, nanotubes, graphene and graphene-based derivatives, carbon-based quantum dots, and the like are being widely studied and are gaining popularity. It is worth noting that among these nanostructures, fullerenes stand out sharply with their unique physical and chemical properties, promising practical applications. In particular,  $C_{20}$  [1], which has the highest adsorption capacity on the surface of the substrate due to the largest number of bends among fullerenes, and  $C_{60}$  [2], which has the highest symmetry among fullerenes, are making a fundamental difference in the latest generation of computers - quantum computers [3-6]. Despite the fact that many experimental studies on the adsorption of  $C_{60}$  and  $C_{20}$  fullerene molecules on the surfaces of metal and semiconductor substrates have been carried out using STM, XPS and STS [7-14] and theoretical studies using DFT, ab-initio, MD [15-19] methods, the adsorption of fullerene molecules with  $C_n$  carbon clusters on the surfaces of semiconductors, especially the interaction processes on the surfaces of silicon substrates, have been studied very little both theoretically and experimentally. It is known that the structures arising from the adsorption of fullerene molecules on the surfaces of various substrates are one of the current directions of scientific research due to their promising practical importance [20-29]. Also, in today's nanotechnology field, strong and stable binding of fullerene molecules to the surface is of great practical importance [30]. In particular, the binding of fullerene molecules on the surface of graphene substrates via  $C_n$  ( $n=1-5$ ) clusters are distinguished by its stability from the cluster-free adsorption of these molecules [31]. As a result of the high importance of stable adsorption states of fullerene molecules on silicon substrates in the production of molecular devices that replace semiconductor devices [32], it is important to study the adsorption of  $C_{60}$  and  $C_{20}$  molecules on the surface of reconstructed silicon Si(001) substrates via  $C_n$  clusters.

In this work, the adsorption processes of fullerene  $C_{20}$  and  $C_{60}$  molecules on the reconstructed silicon Si(001) surface through  $C_n$  ( $n=1-5$ ) carbon clusters exodrilled to fullerenes were studied based on the molecular dynamics (MD) method. In these processes, the adsorption energies of the  $C_n@C_{20}$  and  $C_n@C_{60}$  structures were determined to a first approximation, and the lengths of the Si-C bonds representing the interaction of the  $C_n$  carbon clusters with the substrate were found, conclusions were drawn about the nature (physical or chemical bond), and stable adsorption states and locations were determined by analyzing the results obtained.

### DESCRIPTION OF RESEARCH METHODOLOGY AND OBJECTS

One of the most important aspects of fullerenes is their 0D materiality, and this property has attracted attention in various fields since their discovery. The first representative of fullerenes,  $C_{60}$ , consisting of 60 carbon atoms, the

buckminster fullerene [33], discovered by Croto and his team, has gained a sharp recognition compared to other fullerene representatives. In this regard, the  $C_{60}$  fullerene molecule, together with  $C_{70}$ , is distinguished from fullerenes with a small atomic number by its strength and stability [34]. When talking about the fullerene  $C_{60}$ , it is certainly important to emphasize its symmetry. The  $C_{60}$  molecule has 120 different symmetries with self-return properties with respect to different axes and planes [35]. This feature makes it the most symmetrical molecule among molecules and fullerenes found in nature. Each carbon atom in it forms hybrid  $sp^2$  bonds with three side atoms,  $C_5-C_5$  with a length of 1.45 Å and  $C_6-C_6$  with a length of 1.40 Å [2, 16, 17].

The  $C_{20}$  fullerene molecule is the smallest or least carbon-containing member of the fullerene family [36], consisting of 12 pentagons and 30  $C_5-C_5$  bonds, according to Euler's theorem.  $C_{20}$  also has 120 different symmetries, making it the only fullerene with less than full icosahedral symmetry than  $C_{60}$ . [40].  $C_{20}$  has a number of practical applications in many fields, including high-temperature superconductivity, as has been theorized by Y. Miyamoto and M. Saito, I. Spagnolatti, and others [37-39].

Silicon has an atomic mass of 28, a valence of 4, and is the second most abundant chemical element on Earth (25.7%) after oxygen. It does not occur in free form, i.e., pure silicon, in nature [41]. Silicon monocrystal has diamond structure (fcc-face centered cubic), with a lattice constant of 5.43 Å and a shortest distance between atoms at lattice sites of 2.35 Å [42].

All simulations in the study were performed in the open source LAMMPS package based on the MD method [43]. The potential energies resulting from the interactions between the  $C_{20}@C_n$  and  $C_{60}@C_n$  carbon clusters and the atoms forming the substrate were expressed using the Tersoff interatomic potential [44]. The coordinates of the atoms of the silicon substrate, which were one of the objects of the study, were generated using the LAMMPS package and reconstructed by energy minimization. The reconstructed silicon monocrystal used as the substrate consists of 1083 atoms and has a size of  $34 \times 34 \times 15.2$  Å (Fig. 1, a). Also, in order to check whether the size effects can be observed in the results determined in the study, the interaction of randomly selected  $C_{20}@C_n$  and  $C_{60}@C_n$  cluster samples with reconstructed silicon monocrystalline substrates consisting of 1927, 5692 and 18630 atoms was studied. As a result, it was confirmed that size effects are not observed. The coordinates of  $C_{20}$  and  $C_{60}$  fullerene molecules were obtained using the nanotube modeler computer program (Fig. 1, b, c) and  $C_n$  carbon clusters were created in the JMOL computer visualization program [45]. The coordinates of the structures formed by these clusters with  $C_{20}$  and  $C_{60}$  fullerene molecules with a given configuration were also performed using the same program. The Si-C bond lengths were also measured in the JMOL program, visualizing the adsorption of  $C_{20}@C_n$  and  $C_{60}@C_n$  clusters with the substrate, and precisely when the interaction reached an equilibrium state. A Noze-Hoover thermostat [46] was used to maintain the selected temperature for the NVT ensemble. The selected temperature for all simulations was 0 K. The Verlet-velocity time scheme was integrated with a time step of 1.0 fs. The center of mass of the system was kept fixed during the simulation to avoid any translational motion. Each simulation was continued for a time period of 10 ns to 50 ns until an equilibrium state was reached. All results were determined based on the energy minimization method. Figure 1d) shows examples of different shapes of  $C_n$  carbon clusters for the case of  $n=2-5$ , and bonds of this shape are found in all adsorptions of  $C_{20}@C_n$  and  $C_{60}@C_n$  clusters and are distinguished by their stability compared to other shapes.

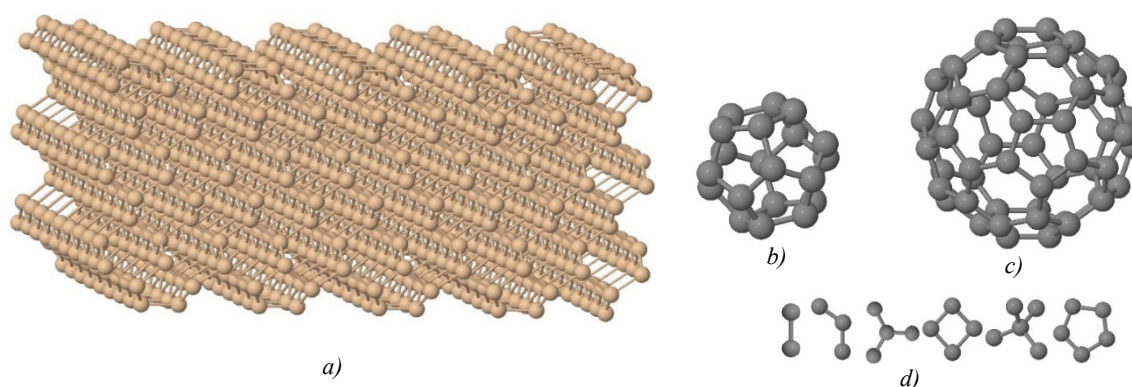


**Figure 1.** a) A silicon substrate with dimensions of  $34 \times 34 \times 34 \times 15.2$  (Å); a) and b) fullerene  $C_{20}$  and  $C_{60}$  molecules, respectively; d)  $C_n$  carbon cluster samples

### CALCULATION OF ADSORPTION ENERGY

As mentioned above, the potential energies of the atoms constituting the objects, i.e. the total potential energies of the substrate and the  $C_{20}@C_n$  and  $C_{60}@C_n$  carbon clusters at the time of their unexposed and observed adsorption, were determined by energy minimization. After that, the adsorption energies of the  $C_{20}@C_n$  and  $C_{60}@C_n$  clusters were determined by the following traditional method [47-50]:

$$E_{\text{ads}} = E_{\text{ads/sub}}^{\text{tot}} - (E_{\text{sub}}^{\text{tot}} + E_{\text{ads}}^{\text{tot}}). \quad (1)$$

Here,  $E_{\text{ads}}$  is the adsorption energy of C<sub>20</sub>@C<sub>n</sub> and C<sub>60</sub>@C<sub>n</sub> carbon clusters on the substrate surface at the selected temperature,  $E_{\text{ads/sub}}^{\text{tot}}$  is the total potential energy of the entire system at the time of interaction between the substrate and the C<sub>20</sub>@C<sub>n</sub> or C<sub>60</sub>@C<sub>n</sub> carbon clusters, i.e., the carbon clusters are adsorbed on the substrate, and  $E_{\text{sub}}^{\text{tot}}$  and  $E_{\text{ads}}^{\text{tot}}$  are the potential energies of the substrate and the C<sub>20</sub>@C<sub>n</sub> or C<sub>60</sub>@C<sub>n</sub> carbon clusters, respectively, determined by separately simulating and minimizing the energy. All energy values are determined at a temperature of 0 K.

### DESCRIPTION AND ANALYSIS OF RESEARCH RESULTS

In the research work, the adsorption of C<sub>20</sub> and C<sub>60</sub> fullerene molecules by C<sub>n</sub> clusters on the reconstructed silicon Si(001) surface through the dimer array and trench by C<sub>n</sub> carbon clusters was observed according to the structures and configurations that can occur depending on the number of atoms in the carbon cluster. For example, in the symbolism of the compound formed by the fullerene C<sub>20</sub> molecule with the carbon C<sub>3</sub> cluster as C<sub>20</sub>@C<sub>3</sub>(1+2), the carbon atoms in the cluster are attached to the fullerene molecule with a single carbon atom, which can be seen in Figure 2 below. Therefore, in the designations in the configuration column of the Table, the first of the numbers in parentheses indicates how many atoms the carbon cluster is attached to the fullerene molecule, and the last number indicates how many carbon atoms are present at the other end of the carbon C<sub>n</sub> cluster. The symbols representing the configurations in the form tC<sub>20</sub>@C<sub>n</sub> or tC<sub>60</sub>@C<sub>n</sub> indicate that the adsorption of C<sub>20</sub>@C<sub>n</sub> and C<sub>60</sub>@C<sub>n</sub> carbon clusters, respectively, was observed in the trench.

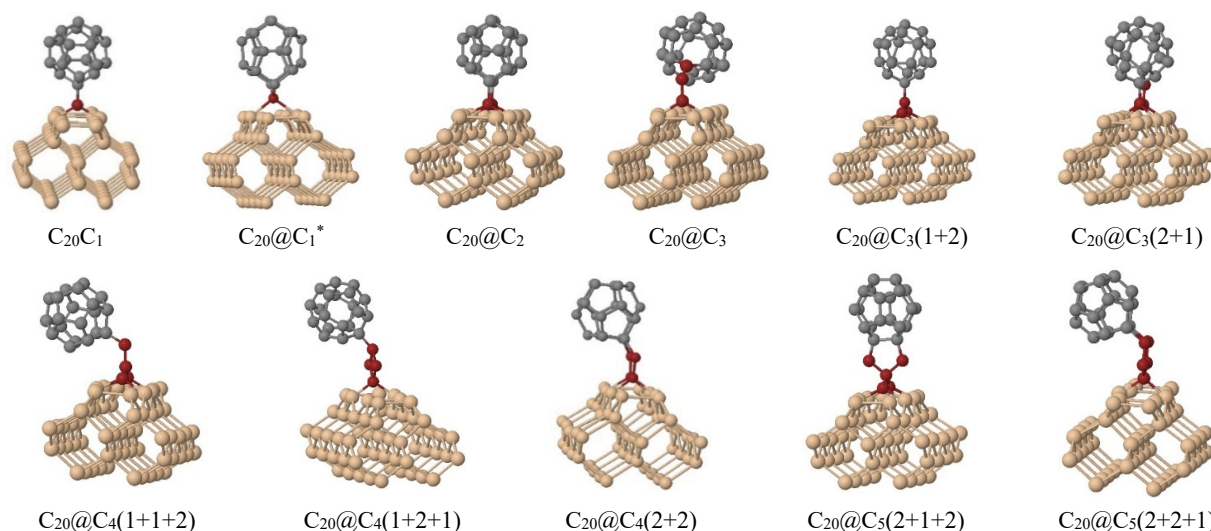


**Figure 2.** Adsorption states of C<sub>20</sub>@C<sub>n</sub> (n=1-5) clusters in a dimer array on a silicon substrate surface: carbon atoms in C<sub>n</sub> carbon clusters are shown in dark brown

By comparing the results obtained, it can be concluded that all the adsorptions of the C<sub>20</sub>@C<sub>n</sub> cluster in the dimer row and trench are of a chemical adsorption nature, which indicates the stability of these bonds. According to the conclusion made in the research work of T. Sergeiva et al. [51], when the Si-C bond length is 1.93-1.94 Å or less, silicon-carbon bonds are considered covalent bonds. Also, when comparing the number of Si-C bonds formed during adsorption, it can be concluded that the adsorption energy is not strongly related to the number of bonds, which can be attributed to the presence of weak physical bonds in the bonds. When the adsorption energies and Si-C bond lengths of the C<sub>20</sub>@C<sub>n</sub> carbon cluster in the dimer row and trench are compared in general, it can be seen from Table 1 that the adsorptions in the dimer row are relatively stable. This is because the double bonds in the reconstructed silicon atoms in the dimer series have the potential to become single bonds. Another reason for this is that the double-bonded Si-Si bonds in the dimer series have been completely broken.

The adsorption energies and lengths of Si-C bonds formed by the C<sub>60</sub>@C<sub>n</sub> cluster on the silicon substrate surface in combination with the stable forms of the C<sub>n</sub> carbon cluster are presented in Table 2. Comparing these results, we can also come to the same conclusions as above, namely, the adsorption energies of the C<sub>60</sub>@C<sub>n</sub> cluster are relatively larger in the dimer series and, accordingly, the adsorptions in these cases are stable, and also the bonds observed in the dimer series consist mainly of pure chemical bonds or covalent bonds. Since the bonds with the tC<sub>60</sub>@C<sub>2</sub>, tC<sub>60</sub>@C<sub>2</sub>(1+1) and tC<sub>60</sub>@C<sub>3</sub> configurations occur with saturated, that is, silicon atoms forming four covalent bonds, their lengths also correspond to physical bonds and therefore the adsorption energies in them differ sharply from the adsorption energies in the trench. It can be seen from the tables that the adsorption energies observed in the dimer series with carbon clusters of the form C<sub>20</sub>@C<sub>3</sub>(1+2), C<sub>20</sub>@C<sub>4</sub>(1+1+2), C<sub>20</sub>@C<sub>5</sub>(2+1+2) and C<sub>60</sub>@C<sub>4</sub>(1+1+2) differ sharply from the binding energies observed in other states and forms. The reason for the observation of such states can be shown that two pairs of Si-Si bonds, which are the result of the reconstruction of these bonds in the dimer series, are broken and form double bonds with carbon atoms in the C<sub>n</sub> cluster, and all of these bonds, except for the C<sub>60</sub>@C<sub>4</sub>(1+1+2) cluster, are chemical bonds.



**Table 1.** Adsorption configurations, adsorption energies (eV) and Si-C bond length intervals (Å) of C<sub>20</sub>@C<sub>n</sub> carbon clusters

No.	configurations	$E_{\text{ads}}$ (eV)	$\lambda$ (Å)
1	C <sub>20</sub> @C <sub>1</sub>	-6.4493	1.86
2	C <sub>20</sub> @C <sub>1</sub> *	-4.9343	1.91 – 1.92
3	C <sub>20</sub> @C <sub>2</sub>	-8.8248	1.94
4	C <sub>20</sub> @C <sub>3</sub>	-6.4395	1.86
5	C <sub>20</sub> @C <sub>3</sub> (1+2)	-11.6994	1.87
6	C <sub>20</sub> @C <sub>3</sub> (2+1)	-5.6031	1.95 – 2.06
7	C <sub>20</sub> @C <sub>4</sub> (1+1+2)	-11.6913	1.87
8	C <sub>20</sub> @C <sub>4</sub> (1+2+1)	-5.7340	1.89 – 1.90
9	C <sub>20</sub> @C <sub>4</sub> (2+2)	-6.4409	1.99
10	C <sub>20</sub> @C <sub>5</sub> (2+1+2)	-11.7498	1.87
11	C <sub>20</sub> @C <sub>5</sub> (2+2+1)	-5.0312	1.91
12	tC <sub>20</sub> @C <sub>1</sub>	-6.6687	1.93 – 2.01
13	tC <sub>20</sub> @C <sub>2</sub>	-4.8900	1.95
14	tC <sub>20</sub> @C <sub>3</sub>	-4.6791	1.94 – 1.95
15	tC <sub>20</sub> @C <sub>3</sub> (1+2)	-7.9494	1.95
16	tC <sub>20</sub> @C <sub>3</sub> (2+1)	-6.4421	1.84 – 1.90
17	tC <sub>20</sub> @C <sub>4</sub> (1+1+2)	-5.6722	1.84 – 2.16
18	tC <sub>20</sub> @C <sub>4</sub> (1+2+1)	-4.2451	1.91 – 2.20
19	tC <sub>20</sub> @C <sub>4</sub> (2+2)	-4.3251	1.85 – 1.97
20	tC <sub>20</sub> @C <sub>5</sub> (2+1+2)	-7.6368	1.84 – 1.94
21	tC <sub>20</sub> @C <sub>5</sub> (2+2+1)	-4.5384	1.89 – 2.14

**Table 2.** Adsorption configurations, adsorption energies (eV) and Si-C bond length intervals (Å) of the C<sub>60</sub>@C<sub>n</sub> carbon clusters

No.	configurations	$E_{\text{ads}}$ (eV)	$\lambda$ (Å)
1	C <sub>60</sub> @C <sub>1</sub>	-4.8154	1.86
2	C <sub>60</sub> @C <sub>1</sub> *	-4.4635	1.88
3	C <sub>60</sub> @C <sub>2</sub>	-2.5317	1.86
4	C <sub>60</sub> C <sub>2</sub> @(1+1)	-5.638	1.94
5	C <sub>60</sub> @C <sub>3</sub>	-4.8035	1.86
6	C <sub>60</sub> @C <sub>3</sub> (1+2)	-8.5342	1.87
7	C <sub>60</sub> @C <sub>3</sub> (2+1)	-3.4031	1.91
8	C <sub>60</sub> @C <sub>4</sub>	-4.0955	1.89 – 1.90
9	C <sub>60</sub> @C <sub>4</sub> (1+1+2)	-10.8257	1.94 – 2.00
10	C <sub>60</sub> @C <sub>4</sub> (2+1+1)	-4.8039	1.86
11	C <sub>60</sub> @C <sub>4</sub> (2+2)	-3.1636	1.93 – 1.94
12	C <sub>60</sub> @C <sub>5</sub> (2+1+2)	-8.5874	1.87
13	C <sub>60</sub> @C <sub>5</sub> (2+2+1)	-2.9324	1.88
14	tC <sub>60</sub> @C <sub>1</sub>	-6.3041	1.95 – 2.14
15	tC <sub>60</sub> @C <sub>2</sub>	-1.5059	2.07
16	tC <sub>60</sub> @C <sub>2</sub> (1+1)	-1.1878	1.96
17	tC <sub>60</sub> @C <sub>2</sub> *	-4.8662	1.95
18	tC <sub>60</sub> @C <sub>3</sub>	-1.1962	1.95
19	tC <sub>60</sub> @C <sub>3</sub> (1+2)	-7.9511	1.85 – 1.86
20	tC <sub>60</sub> @C <sub>3</sub> (2+1)	-4.9097	1.90
21	tC <sub>60</sub> @C <sub>4</sub>	-5.0921	1.90 – 2.09
22	tC <sub>60</sub> @C <sub>4</sub> (1+1+2)	-6.9512	1.83 – 1.90
23	tC <sub>60</sub> @C <sub>4</sub> (2+1+1)	-5.9131	1.87 – 2.02
24	tC <sub>60</sub> @C <sub>4</sub> (2+2)	-6.1636	1.86 – 1.90
25	tC <sub>60</sub> @C <sub>5</sub> (2+1+2)	-7.6248	1.90 – 2.10
26	tC <sub>60</sub> @C <sub>5</sub> (2+2+1)	-4.5442	1.89 – 2.14

\*- These are cases where the C<sub>1</sub> and C<sub>2</sub> carbon atoms form double bonds with the C<sub>20</sub> and C<sub>60</sub> fullerene molecules, and such cases were observed with the C<sub>20</sub>@C<sub>1</sub>\*, C<sub>60</sub>@C<sub>1</sub>\*, and tC<sub>60</sub>@C<sub>2</sub>\* clusters.

Side views of the adsorption of C<sub>20</sub>@C<sub>n</sub> and C<sub>60</sub>@C<sub>n</sub> carbon clusters on the silicon substrate in the dimer row and trench are shown in Figures 2, 4 and 3, 5, respectively. It can be seen from these figures that in the adsorption configurations of C<sub>20</sub>@C<sub>n</sub> and C<sub>60</sub>@C<sub>n</sub> carbon clusters in the dimer row, the cleavage of these bonds was observed in the dimer (Si-Si) bonds involved in the Si-C bond. This indicates that the interaction of C<sub>n</sub> clusters with silicon atoms

is stronger than the interaction between silicon atoms in the dimers. The opposite situation of the same aspect can be observed in the adsorption of  $C_{20}@C_n$  and  $C_{60}@C_n$  carbon clusters in the trench, i.e., the dimer bonds were not broken by the interaction of Si-C bonds formed with silicon atoms at the ends of the dimer bonds in the two dimer arrays. Also, under the influence of Si-C bonds formed between the silicon atoms in the second layer of the trench and the  $C_{20}@C_n$  carbon clusters, the Si-Si bonds formed with the silicon atoms in this layer and the first layer (in dimer bonds) were broken.

Such new stable structures could enable high-temperature operation without the need for high-temperature cooling, for example when used as solid-state qubits in quantum computers. It is also known that replacing the carbon-coated silicon structures used in lithium-ion batteries with fullerene-coated silicon structures would increase the life cycle and performance of these devices [52].

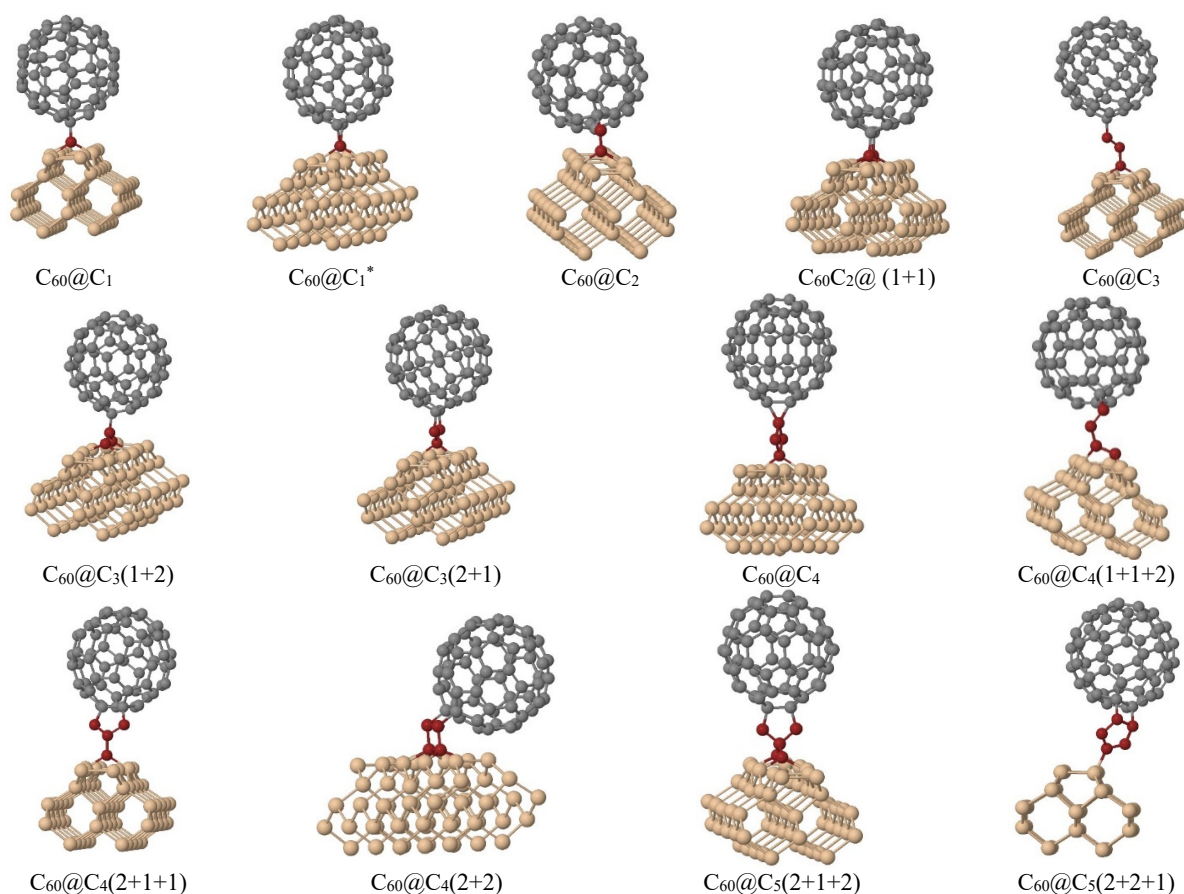


**Figure 3.** Adsorption states of  $C_{60}@C_n$  carbon clusters in dimer arrays on the surface of a silicon substrate

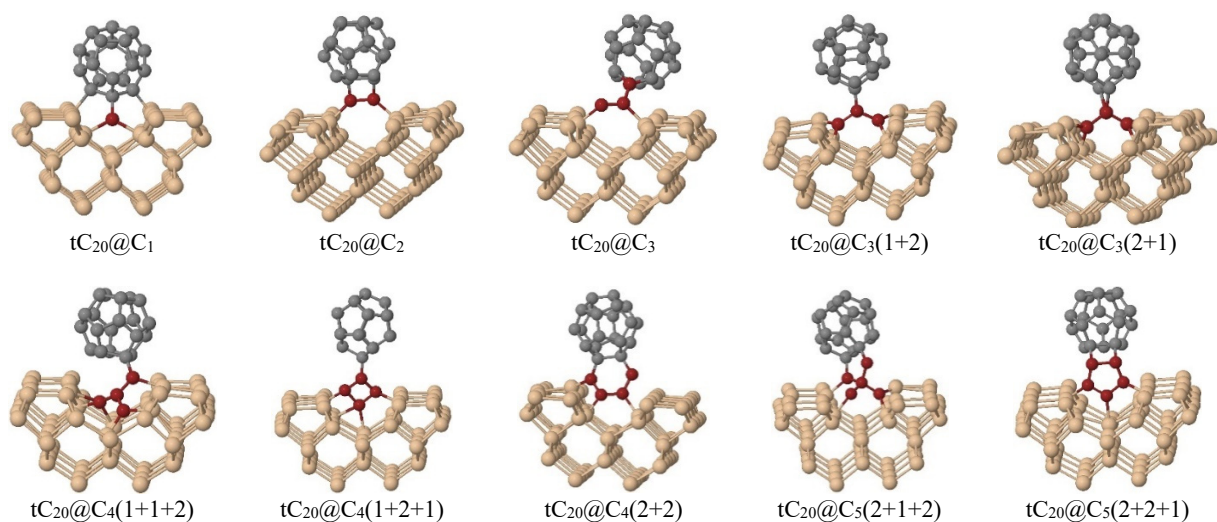


**Figure 4.** Adsorption states of  $C_{20}@C_n$  carbon clusters along the trench (dimer row spacing).



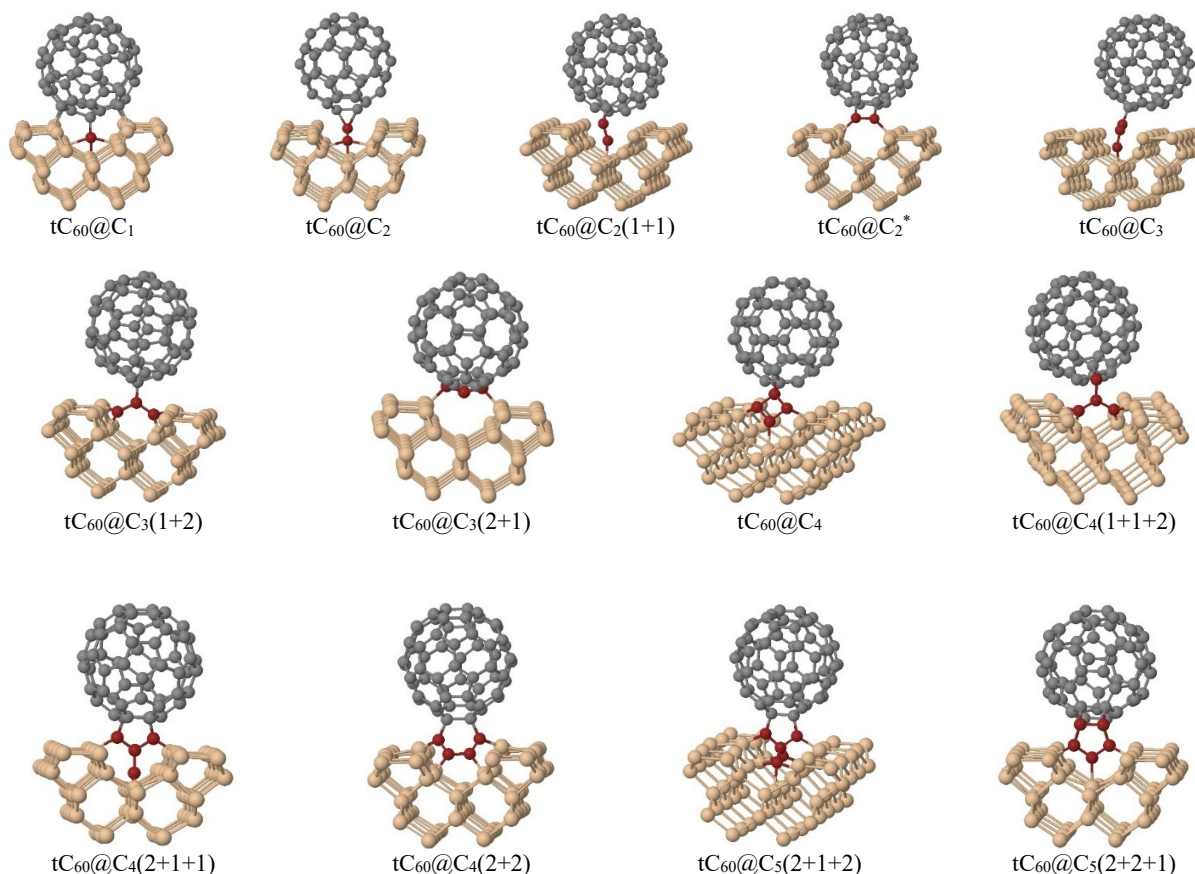


**Figure 5.** Adsorption states of  $C_{60}@C_n$  carbon clusters along the trench

### CONCLUSIONS

According to the results obtained, the following conclusions were drawn: a) the adsorption of  $C_n$  ( $n=1-5$ ) carbon clusters exodrilled fullerene  $C_{20}$  and  $C_{60}$  molecules on the reconstructed silicon Si(001) surface differs from the adsorption of pure  $C_{20}$  and  $C_{60}$  fullerene molecules on this substrate surface by a sharp stability [19]; b) the adsorption of  $C_{20}@C_n$  and  $C_{60}@C_n$  carbon clusters in the dimer series is more stable than the adsorption in the trench and, depending on the length of the Si-C bonds, they consist of covalent bonds; c) the adsorption energy does not depend on the number of bonds formed during the interaction, since physical bonds also exist within these bonds. The highly stable adsorption of  $C_{20}@C_n$  and  $C_{60}@C_n$  carbon clusters on the reconstructed silicon Si(001) surface leads to potential applications in electronics, optoelectronics, catalysis, and materials science. This is because the strength and stability of the fullerene-silicon bonds enable long-term operation, increased reliability, and reduced temperature sensitivity.

### Acknowledgements

The authors are grateful for fruitful collaborations with Dr. Farid Umarov. This work was assisted by the fundamental research program of the Academy Science of Uzbekistan.

### ORCID

©Ishmumin D Yadgarov, <https://orcid.org/0000-0002-4808-2258>

### REFERENCES

- [1] A.J. Du, Z. Y. Pan, Y. K. Ho, Z. Huang, and Z. X. Zhang, "Memory effect in the deposition of  $C_{20}$  fullerenes on a diamond surface," *Physical Review B*, **66**, 035405 (2002). <https://doi.org/10.1103/PhysRevB.66.035405>
- [2] S. Thakral, and R.M. Mehta, "Fullerenes: An introduction and overview of their biological properties," *Indian journal of pharmaceutical science*, **68**(1), 13-19 (2006). <https://doi.org/10.4103/0250-474X.22957>
- [3] S. Park, D. Srivastava, and K. Cho, "Endo-fullerenes and doped bucky onions as seed materials for solid state quantum bits," in: *Materials Research Society Symposium Proceedings. Volume 675. Nanotubes, Fullerenes, Nanostructured and Disordered Carbon*, (San Francisco, California, USA, 2001). <https://apps.dtic.mil/sti/tr/pdf/ADP012136.pdf>
- [4] QIPD-DF, an EU funded project. <http://planck.thphys.may.ie/QIPDDF>
- [5] W. Harneit, "Fullerene-based electron-spin quantum computer," *Phys. Rev. A*, **65**, 184 (2002). <https://doi.org/10.1103/PhysRevA.65.032322>
- [6] C. Meyer, W. Harneit, B. Naydenov, K. Lips, and A. Weidinger, " $N@C_{60}$  and  $P@C_{60}$  as quantum bits," *Appl. Magn. Reson.* **27**, 123–132 (2004). <https://doi.org/10.1007/BF03166307>

- [7] J. Lee, and M. Kang, "Structure and bonding nature of C<sub>60</sub>/Si(100)-c(4×4): density-functional theory calculations," *Phys. Rev. B*, **7**, 25305.1–25305.5 (2007). <https://doi.org/10.1103/PhysRevB.75.125305>
- [8] O. Senftleben, T. Stimpel-Lindner, I. Eisele, and H. Baumgaertner, "Epitaxial silicon overgrowth of C<sub>60</sub> on the Si(100)-2×1 surface," *Surf. Sci.* **602**, 493–498 (2008). <https://doi.org/10.1016/j.susc.2007.10.043>
- [9] F. Yasunori, S. Koichiro, and K. Atsushi, "Transition of an adsorption state of C<sub>60</sub> on a Si(111)7×7 surface revealed by high-resolution electron-energy-loss spectroscopy," *Physical Review B*, **56**, 12124 (1997). <https://doi.org/10.1103/PhysRevB.56.12124>
- [10] D.A. Olyanich, V.V. Mararov, T.V. Utas, A.V. Zotov, and A.A. Saranin, "Adsorption and self-assembly of fullerenes on Si(111)√3+√3 Ag: C<sub>60</sub> versus C<sub>70</sub>," *Surface Science*, **653**, 138-142 (2016). <https://doi.org/10.1016/j.susc.2016.06.016>
- [11] S. Suto, K. Sakamoto, D. Kondo, T. Wakita, A. Kimura, A. Kakizaki, C.-W. Hu, *et al.*, "Interaction of C<sub>60</sub> with Si(111)7×7 and Si(100)2×1 surfaces studied by STM, PES and HREELS: annealing effect," *Surface Science*, **438**, 242-247 (1999). [https://doi.org/10.1016/S0039-6028\(99\)00576-2](https://doi.org/10.1016/S0039-6028(99)00576-2)
- [12] W. Haiqian, Z. Changgan, L. Qunxiang, W. Bing, Ya. Jinlong, J.G. Hou, and Q. Zhu, "Scanning tunneling spectroscopy of individual C<sub>60</sub> molecules adsorbed on Si(111)-7×7 surface," *Surface Science*, **442**, 1024-1028 (1999). [https://doi.org/10.1016/S0039-6028\(99\)00977-2](https://doi.org/10.1016/S0039-6028(99)00977-2)
- [13] O. Kazuhiro, N. Masashi, U. Hirobumi, K. Tetsuo, Ya. Yoshiyuki, M. Kozo, J. Yoshinobu, *et al.*, "Regioselective cycloaddition reaction of alkene molecules to the asymmetric dimer on Si(100)c(4x2)," *J. Am. Chem. Soc.* **129**, 1242-1245 (2007). <https://doi.org/10.1021/ja066285i>
- [14] Ch. Dong, and S. Dror, "Temperature effects of adsorption of C<sub>60</sub> molecules on Si(111)-(7×7) surfaces," *Physical Review B*, **49**, 7612 (1994). <https://doi.org/10.1103/PhysRevB.49.7612>
- [15] L.J. Yo, and H.K. Myung, "Adsorption structure of a single C<sub>60</sub> molecule on Si(111)-(7×7): density-functional calculations," *Surface Science*, **602**, 1408-1412 (2008). <https://doi.org/10.1016/j.susc.2008.02.014>
- [16] P.D. Godwin, S.D. Kenny, R. Smith, and J. Belbruno, "The structure of C<sub>60</sub> and endohedral C<sub>60</sub> on the Si(100) surface," *Surface Science*, **490**, 409–414 (2001). [https://doi.org/10.1016/S0039-6028\(01\)01365-6](https://doi.org/10.1016/S0039-6028(01)01365-6)
- [17] P.D. Godwin, S.D. Kenny, and R. Smith, "The bonding sites and structure of C<sub>60</sub> on the Si(100) surface," *Surf. Sci.* **529**, 237-246 (2003). [https://doi.org/10.1016/S0039-6028\(03\)00074-8](https://doi.org/10.1016/S0039-6028(03)00074-8)
- [18] B. Khaoula, D. Eric, S. Regis, H. Marie-Christine, and S. Philippe, "C<sub>60</sub> molecules grown on a Si-supported Nanoporous Supramolecular Network: a DFT study," *Physical Chemistry Chemical Physics*, **16**(28), 14722–14729 (2014). <https://doi.org/10.1039/C4CP01677G>
- [19] I.Z. Urolov, I.D. Yadgarov, F.F. Umarov, G.T. Rakhmanov, and Kh.I. Jabbarov, "Computer Simulation of Adsorption of C<sub>60</sub> Fullerene Molecule on Reconstructed Si(100) Surface," *East Eur. J. Phys. (2)*, 256-262 (2024). <https://doi.org/10.26565/2312-4334-2024-2-25>
- [20] J. Coro, M. Suarez, L.S.R. Silva, K.I.B. Eguiluz, and G.R. Salazar-Banda, "Fullerene applications in fuel cell: a review," *International journal of hydrogen energy*, **41**(40), 17944-17959 (2016). <https://doi.org/10.1016/j.ijhydene.2016.08.043>
- [21] M. Yoon, S. Yang, E. Wang and Z. Zhang, "Charged Fullerenes as High-Capacity Hydrogen Storage Media," *Nano letters*, **7**, 2578-2583 (2007). <https://doi.org/10.1021/nl070809a>
- [22] H.J. Ren, C.X. Cui, X.J. Li, and Y.J. Liu, "A DFT study of the hydrogen storage potentials and properties of Na- and Li-doped fullerenes," **42**(1), 312-321 (2017). <https://doi.org/10.1016/j.ijhydene.2016.10.151>
- [23] M.H. Yun, J.W. Kim, S.Y. Park, D.S. Kim, B. Walker, and J.Y. Kim, "High-efficiency, hybrid Si/C<sub>60</sub> heterojunction solar cells," *Journal of materials chemistry A*, **4**, 16410-16417 (2016). <https://doi.org/10.1039/c6ta02248k>
- [24] T. Gattia, E. Menna, M. Meneghetti, M. Maggini, A. Petrozzab, and F. Lamberti, "The Renaissance of fullerenes with perovskite solar cells," *Nano energy*, **41**, 84 (2017). <https://doi.org/10.1016/j.nanoen.2017.09.016>
- [25] F. Moussa, "5-[60] Fullerene and derivatives for biomedical applications," *Nanobiomaterials*, 113-136 (2018). <https://doi.org/10.1016/B978-0-08-100716-7.00005-2>
- [26] S. Thakral, and R.M. Mehta, "Fullerenes: An Introduction and Overview of Their Biological Properties Biological Properties," *Indian Journal of Pharmaceutical Sciences*, **68**, 13-19 (2006). <https://doi.org/10.4103/0250-474X.22957>
- [27] M.E. Turan, Y. Sun, and Y. Akgul, "Mechanical, tribological and corrosion properties of fullerene reinforced magnesium matrix composites fabricated by semi powder metallurgy," *Journal of alloys and compounds*, **740**, 1149-1158 (2018). <https://doi.org/10.1016/j.jallcom.2018.01.103>
- [28] S. Bronnikov, A. Podshivalov, S. Kostromin, M. Asandulesa, and V. Cozan, "Electrical conductivity of polyazomethine/fullerene C<sub>60</sub> nanocomposites," *Physics letters A*, **381**, 796-800 (2017). <http://dx.doi.org/10.1016/j.physleta.2016.12.045>
- [29] P.A. Kumar, V.V. Namboodiri, G. Joshi, and K.P. Mehta, "Fabrication and applications of fullerene-based metal nanocomposites: A review," *Journal of materials research*, **36**, 114-128 (2021). <http://dx.doi.org/10.1557/s43578-020-00094-1>
- [30] S. Yao, X. Yuan, L. Jiang, T. Xiong, and J. Zhang, "Recent progress on fullerene-based materials: synthesis, properties, modifications, and photocatalytic applications," *Materials*, **13**, 1-39 (2020). <https://doi.org/10.3390/ma13132924>
- [31] I.D. Yadgarov, F.F. Umarov, A.S. Kosimov, Kh.I. Jabbarov, and Sh.Y. Aminov, "Simulation of interaction processes of C<sub>20</sub> fullerene with graphene," *East Eur. J. Physics*, (4), 226-230 (2023). <https://doi.org/10.26565/2312-4334-2023-4-28>
- [32] J. Li, Y. Cui, and L. Zhang, "C<sub>60</sub> adsorption on defective Si(100) surface having one missed dimer from atomic simulations at electrical level," *Arabian journal of chemistry*, **16**, 104816 (2023). <https://doi.org/10.1016/j.arabjc.2023.104816>
- [33] H.W. Kroto, J.R. Heath, S.C. O'Brein, R.F. Curl and R.E. Smalley, "C<sub>60</sub>: Buckminsterfullerene," *Nature*, **318**, 162–163 (1985). <https://doi.org/10.1038/318162a0>
- [34] M. Paukov, Ch. Kramberger, I. Begichev, M. Kharlamova, and M. Burdanova, "Functionalized fullerenes and their applications in electrochemistry, solar cells, and nanoelectronics," *Materials*, **16**, 1276 (2023). <https://doi.org/10.3390/ma16031276>
- [35] M. Huijing, F. Xuyang, K. Shuangyu, and C. Yingxiang, "Adsorption geometries and interface electronic structure of C<sub>60</sub> on Si(100)2×1 reconstruction surface," *Surface Science*, **690**, 121484 (2019). <https://doi.org/10.1016/j.susc.2019.121484>
- [36] M. Juris, "Goldberg variations challenge," *Analytical and Bioanalytical Chemistry*, **385**(1), 6–7 (2006). <https://doi.org/10.1007/s00216-006-0358>

- [37] Y. Miyamoto, and M. Saito, "Condensed phases of all-pentagon C<sub>20</sub> cages as possible superconductors," *Phys. Rev. B*, **63**, 161401 (2001). <https://doi.org/10.1103/PhysRevB.63.161401>
- [38] M. Saito and Y. Miyamoto, "Theoretical Identification of the Smallest Fullerene, C<sub>20</sub>," *Physical review letters*, **87**(3), 035503 (2001). <https://doi.org/10.1103/PhysRevLett.87.035503>
- [39] I. Spagnolatti, M. Bernasconi, and G. Benedek, "Electron-phonon interaction in the solid form of the smallest fullerene C<sub>20</sub>," *Europhys. Lett.* **59**(4), 572–578 (2002). <https://doi.org/10.1209/epl/i2002-00384-1>
- [40] F. Lin, E.S. Sorenson, C. Kallin, and A.J. Berlinsky, "C<sub>20</sub>, the smallest fullerene," in: *Handbook of Nanophysics: Clusters and Fullerenes*, edited by K.D. Sattler, (CRC Press, 2009).
- [41] W.M. Haynes, *Handbook of chemistry and physics*, 97<sup>th</sup> edition, (CRC press, 2017), pp. 4-33.
- [42] R. Taylor, J.P. Hare, A.K. Abdul-Sada, and H.W. Kroto, "Isolation, separation and characterisation of the fullerenes C<sub>60</sub> and C<sub>70</sub>: the third form of carbon," *J. Chem. Soc. Chem. Commun.* **1423**, (1990). <https://doi.org/10.1039/c39900001423>
- [43] Sandia National Laboratories, Large-scale Atomic/Molecular Massively Parallel Simulator (LAMMPS), 2023, <https://www.lammps.org/>
- [44] P. Erhart, and K. Albe, "Analytical potential for atomistic simulations of silicon, carbon, and silicon carbide," *Physical Review B*, **71**, 035211 (2005). <https://doi.org/10.1103/PhysRevB.71.035211>
- [45] Java, Jmol, 2023, <http://www.jmol.org/>
- [46] W.G. Hoover, "Canonical dynamics: Equilibrium phase-space distributions", *Physical Review A*, **31**, 1695 (1985). <https://doi.org/10.1103/PhysRevA.31.1695>
- [47] Y.S. Al-Hamdani, *et al.*, "Properties of the water to boron nitride interaction: From zero to two dimensions with benchmark accuracy," *Journal of Chemical Physics*, **144**, 154706 (2016). <https://doi.org/10.1063/1.4985878>
- [48] D.C. Sorescu, *et al.*, "First-principles calculations of the adsorption, diffusion, and dissociation of a CO molecule on the Fe (100) surface," *Physical Review B*, **66**, 035416 (2002). <https://doi.org/10.1103/PhysRevB.66.035416>
- [49] C. Zhou, J. Wu, B. Han, S. Yao, and H. Cheng, "Adsorption of fullerenes C<sub>n</sub> (n=32,36,40,44,48,60) on the GaAs(001)-c(4×4) reconstructed surface," *Physical review B*, **73**, 195234 (2006).
- [50] F. Demiray, I. Sidir, and Y.G. Sidir, "Structural and electronic properties of cyanide-coated fullerene C<sub>20</sub>@(CN)<sub>n</sub> (n = 0–20): An ab initio approach," *The European physical journal plus*, **131**, 250 (2016). <https://doi.org/10.1140/epjp/i2016-16250-0>
- [51] T. Sergeieva, D. Mandal, and D.M. Andrada, "Chemical Bonding in Silicon Carbonyl Complexes," *Chemistry – A European journal*, **27**, 1-10 (2021). <http://dx.doi.org/doi.org/10.1002/chem.2021>
- [52] W. Tan, *et al.*, "Fullerene-like elastic carbon coatings on silicon nanoparticles by solvent controlled association of natural polyaromatic molecules as high-performance lithium-ion battery anodes," *Energy storage materials*, **45**, 412-421 (2022). <https://doi.org/10.1016/j.ensm.2021.11.040>

### КОМП'ЮТЕРНЕ МОДЕЛЮВАННЯ ДОСЛІДЖЕННЯ ПРОЦЕСІВ АДСОРБЦІЇ ВУГЛЕЦЕВИХ КЛАСТЕРІВ C<sub>20</sub>@C<sub>n</sub> ТА C<sub>60</sub>@C<sub>n</sub> (n=1-5) НА РЕКОНСТРУЙОВАНІЙ ПОВЕРХНІ КРЕМНІЮ Si(001)

Ікром З. Уролов<sup>a,b</sup>, Фарід Ф. Умаров<sup>c</sup>, Ішмумін Д. Ядгаров<sup>a</sup>, Ганібой Т. Рахманов<sup>b</sup>, Хайтмурод І. Джабборов<sup>d,e</sup>

<sup>a</sup>Інститут іонно-плазмових та лазерних технологій ім. У.А. Аріфова Академії наук Республіки Узбекистан, 100125, Ташкент, вул. Дурмон Юлі, 33

<sup>b</sup>Національний університет Узбекистану імені Мірзо Улугбека, Республіка Узбекистан, 100174, Ташкент, вул. Університетська, 4

<sup>c</sup>Казахстансько-британський технічний університет, Алмати, вул. Толе бі 59, Казахстан



<sup>d</sup>Ташкентський державний технічний університет імені Іслама Карімова, Ташкент, Узбекистан

<sup>e</sup>Ташкентський університет інформаційних технологій імені Мухаммада аль-Хорезмі, Ташкент, Узбекистан

У сучасній галузі нанотехнологій однією з вимог сучасного напрямку є здатність вуглецевих наноструктур мати міцний зв'язок з поверхнею підкладки серед матеріалів, утворених внаслідок взаємодії різних підкладок з поверхнею різних підкладок. Вивчення та ідентифікація нових структур з подібними властивостями є однією з проблем, що стоять перед сучасними теоретичними дослідженнями. Поточна дослідницька робота була проведена як одне з рішень вищезазначених проблем, в якій адсорбція молекул фулерену на кремнієвих підкладках за допомогою методу молекулярної динаміки (МД) є продовженням нашої роботи з адсорбції молекул фулерену C<sub>20</sub> та C<sub>60</sub> на поверхні кремнію Si(001), реконструйованого вуглецевими кластерами C<sub>n</sub> (n=1-5), була змодельована за допомогою пакета з відкритим кодом LAMMPS на основі методу молекулярної динаміки. Використовуючи міжатомний потенціал Терсоффа, було виражено взаємодії між атомами субстрату, кластером C<sub>n</sub> та молекулами фулерену, а також визначено енергії адсорбції вуглецевих кластерів C<sub>20</sub>@C<sub>n</sub> та C<sub>60</sub>@C<sub>n</sub>, довжину та природу зв'язків Si-C, а також стабільні стани адсорбції в траншеях та рядах димерів.

**Ключові слова:** молекула фулерену; основа; кластер; траншея; масив димерів; моделювання; потенціал; зв'язок; симуляція; адсорбція

## ENERGY AND ANGULAR DISTRIBUTIONS OF SCATTERED $\text{Ar}^+$ IONS WITH A BLUE PHOSPHORUS SURFACE AT SLIDING ANGLES

 **U.O. Kutliev**<sup>a</sup>,  **O.A. Sattarova**<sup>b\*</sup>, **N.U. Setmetov**<sup>c</sup>, **J.U. Ismoilov**<sup>a</sup>

<sup>a</sup>*Urgench State University named after Abu Raykhan Beruni, Department of Physics, Khamid Olimjan street.14, Urgench 220100, Uzbekistan*

<sup>b</sup>*Urgench branch of Tashkent Medical Academy, Biomedical, physical culture and sports, Al-Khwarizmi Street, 28, Urgench 220100, Uzbekistan*

<sup>c</sup>*Tashkent University of Information Technologies named after Muhammad al-Khorazmi, Urganch branch, department Telecommunication engineering, Al-Khorazmi Street.110, Urgench 220100, Uzbekistan*

\*Corresponding Author E-mail: [sattarovaanaxon@gmail.com](mailto:sattarovaanaxon@gmail.com)

Received April 24, 2025; revised June 19, 2025; accepted June 25, 2025

This article presents the theoretical results of energy and angular distributions of  $\text{Ar}^+$  ions from the surface of blue phosphorus at a small value of the angle of incidence and initial energy receiving by computer simulation method. It is shown that at a small value of the initial energy of ions from the trajectory of scattered ions it is possible to obtain the general shape of the surface semichannel. Moreover, increasing the value of the initial energy makes it possible to obtain the full shape of the semichannel, as well as the shadow behind the semichannel, which provides information on the location of the atom of the second layer. It is established that in the energy distribution due to an increase in the value of the initial energy a multi-peak structure is formed. This makes it possible to determine the surface structure. The obtained angular distribution shows that there is a specular and multiple scattering of ions from the target.

**Keywords:** *Ion scattering; Semichannel; Computer simulation; Ion bombardment; Energy and angular distributions*

**PACS:** 34.35.+a, 68.49.Sf, 79.20.Rf

### INTRODUCTIONS

Low-energy small-angle ion scattering (Low Energy Ion Scattering (LEIS) is one of the most sensitive and accurate methods of material surface analysis [1-5]. This method allows obtaining information about the composition, structure and properties of the upper atomic layer of a solid. LEIS is based on the detection of ions scattered from the sample surface at small angles. The ions used typically have energies of several hundred to several thousand electron volts. Due to the small penetration depth of the ions (less than one nanometer), the method provides exceptionally high sensitivity to atoms located on the surface itself [6-8]. One of the main advantages of LEIS is its ability to selectively analyze only the upper atomic layer, unlike other spectroscopic methods that penetrate deeper into the material. This makes it an indispensable tool for studying surface modification processes, adsorption, catalysts, and for monitoring surface cleanliness.

Blue phosphorus is an allotropic form of phosphorus with unique electronic and structural properties, making it a promising material for micro- and nanoelectronics. Unlike black phosphorus, blue phosphorus has a stable two-dimensional hexagonal lattice similar to graphene, but with semiconductor properties. One of the key parameters determining the suitability of a material for microelectronics is the band gap. For blue phosphorus, it is in the range from ~1.9 to 2.0 eV (depending on the number of layers and the substrate), making it suitable for creating field-effect transistors, photodetectors and other components of nanoscale electronics [9-13]. Therefore, due to the great interest in the structure of blue phosphorus, we studied the energy and angular distributions of scattered  $\text{Ar}^+$  ions from the surface of blue phosphorus at low values of the initial energy and incidence angle.

### METHOD OF RESEARCH AND DISCUSSION OF RESULTS

Binary Collision Approximation Method (BCA) is widely used to model the interaction of ions with a solid surface, especially in problems related to ion scattering, ion implantation and surface structure analysis [14]. The BCA method is based on the assumption that the motion of ions during interaction with target atoms can be described as a sequence of independent two-particle collisions – between the probe ion and an individual atom of the material. In this case, many-body interactions and collective effects are ignored, which significantly simplifies the calculations. There are many advantages of this method [15]. BCA allows modeling the processes of ion interaction with a surface without significant resource costs, especially in comparison with more complex methods such as molecular dynamics. Despite its approximate nature, the method gives good quantitative estimates for a wide range of energies (from tens of eV to several MeV) [16]. It is especially effective in modeling processes in low-energy ion scattering methods, where interactions are limited to the upper layers.

In our calculations, we considered a semichannel formed on the surface of blue phosphorus (Fig. 1). It has a zigzag form. And this semichannel was divided into two parts from the middle. And the first part of the semichannel was divided



into 1000 aiming points (in the direction of  $I$ ).  $Ar^+$  ions with small values of initial energy at sliding angles were directed to each aiming point.

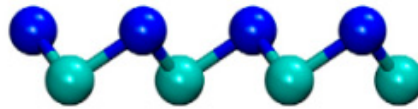


**Figure 1.** The semichannel, formed on the surface of blue phosphorus

One of the main objectives of this work was to study the trajectory of scattered ions, since the trajectory of scattered ions mainly determines the formation of peaks in energy and angular distributions. We analyzed the trajectories of scattered  $Ar^+$  ions with an initial energy of  $E_0 = 1$  and 3 keV and at angles of incidence  $\psi = 9-15^\circ$ . The choice of such a value of the incidence angle is due to the fact that the width of the semichannel formed on the surface of blue phosphorus is quite wide and is 4.2 Å. To study the trajectory of scattered ions from this semichannel, it was sufficient to study the trajectory of ions scattered from half of the semichannel, since the remaining ion trajectories are symmetrical.

### RESEARCH METHOD AND RESULTS

Fig. 2 shows the trajectories of scattered  $Ar^+$  ions with an initial energy of  $E_0 = 1$  keV and at angles of incidence  $\psi = 9, 11, 13$  and  $15^\circ$ . At  $\psi = 9^\circ$  (Fig. 2.1 a), the incident ions began to penetrate into the surface semichannel. And it is noticeably visible that the set of trajectories of scattered ions began to form the shape of a semichannel, as well as the location of the atom located at the bottom of the semichannel. It can also be seen that a small part of the ions penetrated into the crystal (were implanted). The number of trajectories of refocused ions is also large. And Fig. 2.1b shows the trajectories of scattered ions at  $\psi = 11^\circ$ . It is seen that the shape of the semi-channel was completely formed. And the ions were focused more clearly. The number of trajectories of overfocused ions decreased. Fig. 2.1c shows the trajectories of scattered ions at  $\psi = 13^\circ$ . In this case, the location of the atom, which is at the bottom of the semi-channel and it focuses many ions, is clearly visible. The number of trajectories of overfocused ions also became even smaller. Most of the ions were implanted inside the crystal. At  $\psi = 15^\circ$  (Fig.2.1d), the number of implanted and focused ions increased significantly.

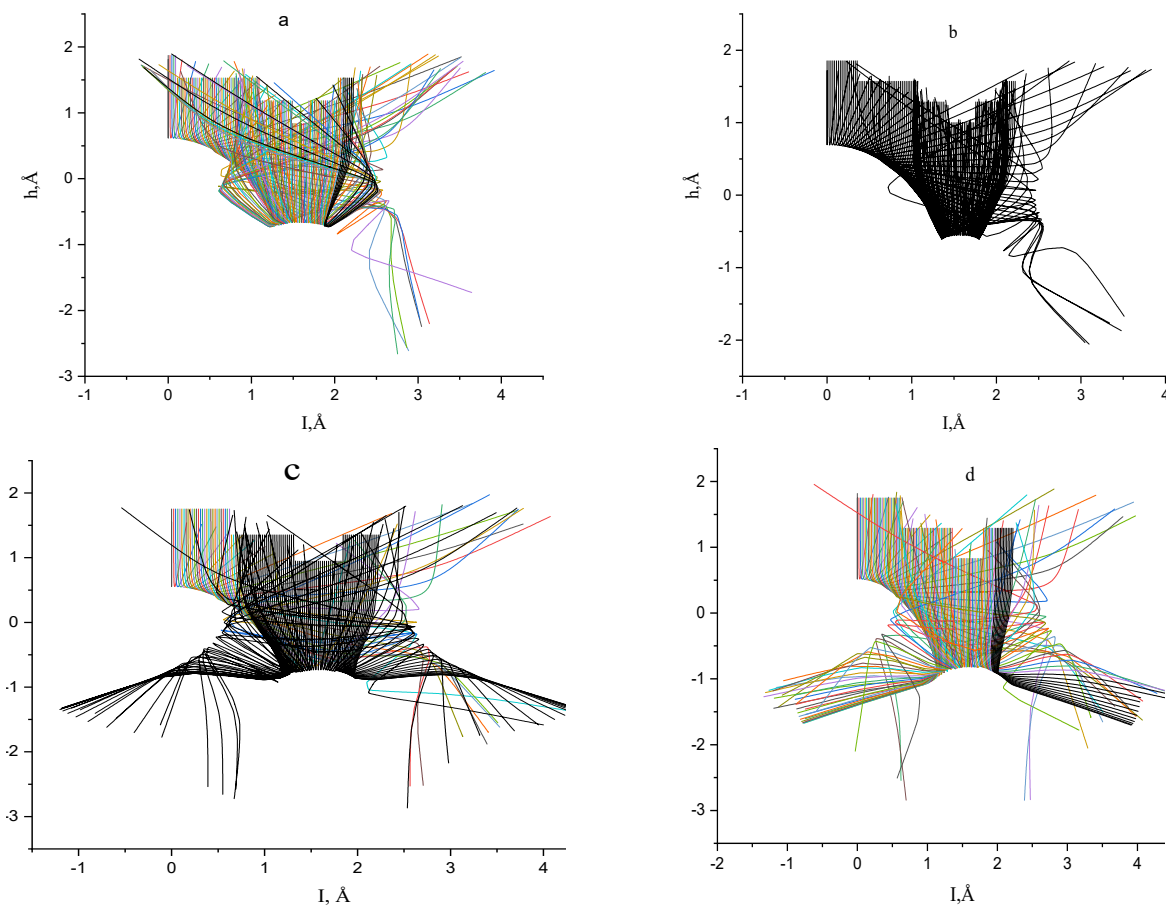


**Figure 2.** Trajectories of scattered  $Ar^+$  ions from a surface semichannel that formed on the surface of blue phosphorus with an initial energy of  $E_0 = 1$  keV and at angles of incidence  $\psi = 9, 11, 13$  and  $15^\circ$

Fig. 3 shows the energy and angular distributions of scattered Ar<sup>+</sup> ions from the surface semichannel, which was formed on the surface of blue phosphorus with the initial energy  $E_0 = 1$  keV and at angles of incidence  $\psi = 9, 11, 13$  and  $15^\circ$ . From the energy distribution (Fig.3a) it is evident that at the incidence angle values ( $\psi = 9, 11$  and  $13^\circ$ ) the spectrum contains a single peak shape. This is due to the fact that the energy values of scattered ions from the bottom and the surface atomic row are close to each other.

And at  $\psi = 15^\circ$  penetration of ions inside increased, which formed a complex trajectory and therefore an energy spectrum is observed, which has a two-peak shape. In the angular spectrum of scattered ions, two peaks are observed (Fig. 3b). The first peak refers to ions scattered from the plane of incidence and the second peak refers to mirror scattered ions.

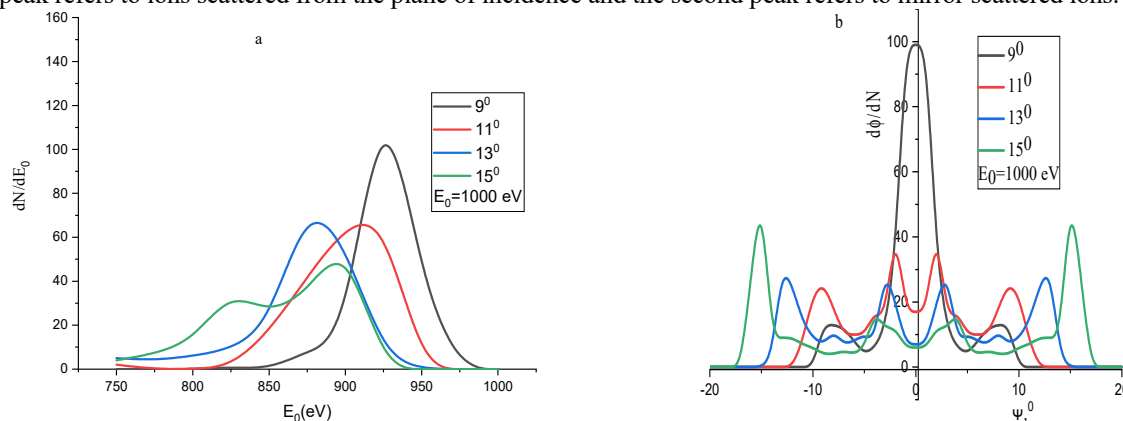


**Figure 3.** Energy (a) and angular (b) distributions of scattered ions Ar<sup>+</sup> from a semichannel formed on the surface of blue phosphorus with an initial energy of  $E_0 = 1$  keV and at angles of incidence  $\psi = 9, 11, 13$  and  $15^\circ$

Fig. 4 shows the characteristic trajectories of scattered Ar<sup>+</sup> ions from the semichannel formed on the surface of blue phosphorus with the initial energy  $E_0 = 3$  keV at incidence angles  $\psi$  of  $= 9, 11, 13$  and  $15^\circ$ . At the  $\psi = 9^\circ$  the Ar<sup>+</sup> ions penetrated the surface semichannel, and implantation of ions in small quantities is also observed (Fig. 4a). The ion trajectories consist of specularly scattered, focused and overfocused ion trajectories. In general, the shape of the surface semichannel can be determined. Fig. 4b shows the trajectory at  $\psi = 11^\circ$ . At this value of the ion incidence angle, the full shape of the semichannel can be seen. It can also be seen that the number of implanted ions has increased than at  $\psi = 9^\circ$ .

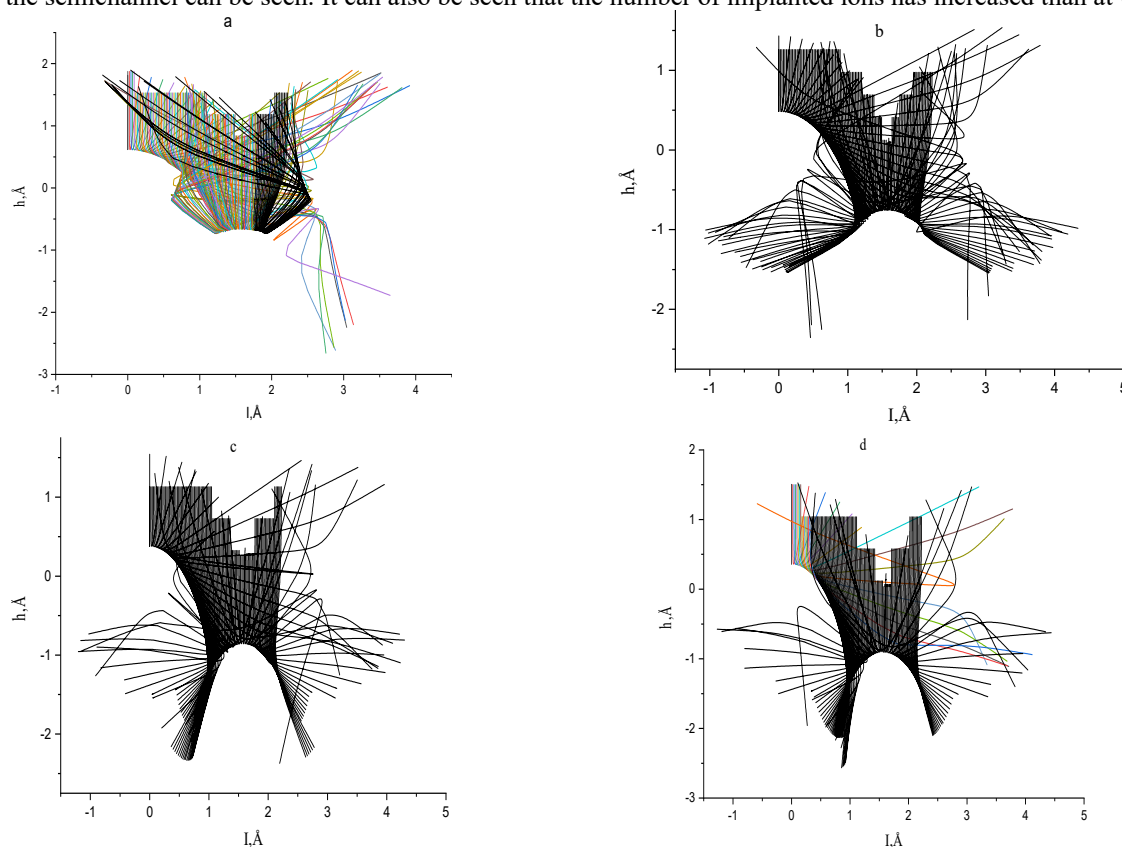


**Figure 4.** Energy (a) and angular (b) distributions of scattered ions Ar<sup>+</sup> from a semichannel formed on the surface of blue phosphorus with an initial energy of  $E_0 = 3$  keV and at angles of incidence  $\psi = 9, 11, 13$  and  $15^\circ$



It should be noted that from the trajectory of scattered ions, the location of the atom of the semichannel, located at the bottom of the semichannel, could also be more clearly seen. This can be observed by the formation of a shadow on the back side of the atom. Fig. 4c shows the ion trajectory at  $\psi=13^\circ$ . From the figure one can see that the implantation of ions into the crystal occurs around the atom located at the bottom of the semi-channel. It should be noted that at this value of the angle of incidence of ions, trajectories are observed, scattered from the surface atomic row, from the semi-channel and implanted ions (crossing the walls of the semi-channel). And at  $\psi=15^\circ$  the shadow formed behind the atom of the semichannel, located at the bottom of the semi-channel, narrowed even more compared to  $\psi=13^\circ$  due to the increase in the angle of incidence. It should be noted that at this value of the angle of incidence the number of ions that crossed the walls of the semichannel decreased.

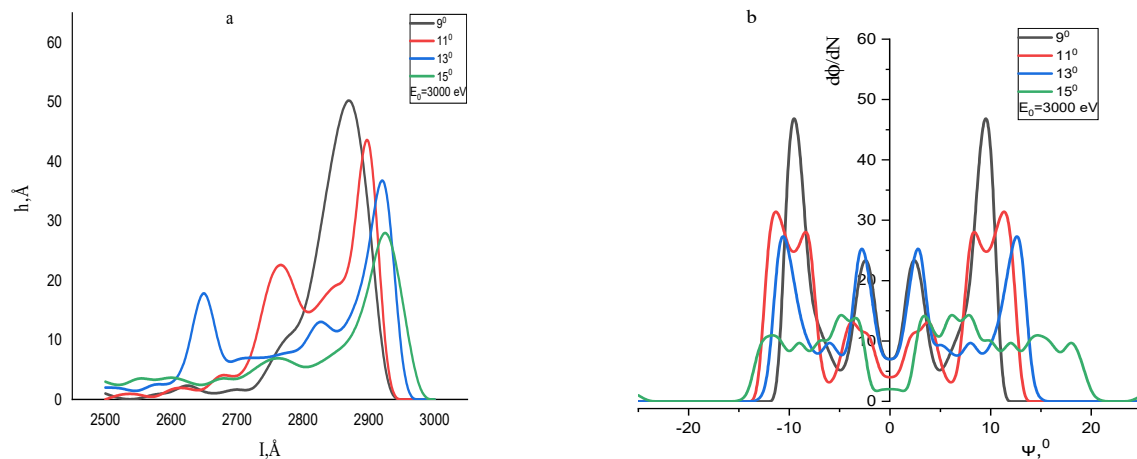


**Figure 5.** Energy and angular distributions of scattered  $\text{Ar}^+$  ions from a surface semichannel that formed on the surface of blue phosphorus with an initial energy of  $E_0 = 3$  keV and at angles of incidence  $\psi = 9, 11, 13$  and  $15^\circ$

Fig.5 shows the energy and angular distributions of scattered  $\text{Ar}^+$  ions from the surface semichannel, which was formed on the surface of blue phosphorus with an initial energy of  $E_0 = 3$  keV at the angles of incidence  $\psi = 9, 11, 13$  and  $15^\circ$ .

The energy distribution (Fig. 5a) contains two peaks in all values of the incidence angle. The peak formed by the high-energy part of the distribution refers to ions scattered from the surface atomic row, and the peak located in the low-energy part of the distribution refers to ions scattered from the bottom of the semichannel. A low-intensity peaks formed by the low-energy part of the distribution refers to ions multiple scattered from the wall of the semichannel. Fig. 5b shows the angular distribution of scattered  $\text{Ar}^+$  ions from the surface semichannel, which was formed on the surface of blue phosphorus with an initial energy of  $E_0 = 3$  keV at the angles of incidence  $\psi = 9, 11, 13$  and  $15^\circ$ . It is seen that the angular distribution also contains two peaks. The first peak refers to specularly scattered ions, and the second peak is formed at  $\psi/2$  and it refers to ions multiple scattered ions inside the semichannel.

## CONCLUSIONS

We have studied the energy and angular distributions of scattered  $\text{Ar}^+$  ions from the surface semichannel, which was formed on the surface of blue phosphorus with the initial energy  $E_0 = 1$  and  $3$  keV at the angles of incidence  $\psi = 9, 11, 13$  and  $15^\circ$ . It is shown that an increase in the initial energy leads to a splitting of the peak into at least two parts, which corresponds to ions scattered from the surface atomic row, from the semichannel. Low-intensity peaks of ions, repeatedly scattered from the wall of the semichannel are also observed. Thus, the trajectories of scattered ions are analyzed and it is shown that due to an increase in the initial energy, cones (shadow) are formed on the back side of the atom of the semichannel, located on the bottom of the semichannel.

## ORCID

Uchkun O. Kutliev, <https://orcid.org/0000-0003-2241-2025>; Onaxon A. Sattarova, <https://orcid.org/0009-0006-3263-4640>

## REFERENCES

- [1] M. Werner, J.W. Roberts, R.J. Potter, K. Dawson, and P.R. Chalker, "Elucidation of ALD MgZnO deposition processes using low energy ion scattering," *J. Vac. Sci. Technol. A*, **36**, 02D406 (2018). <https://doi.org/10.1116/1.5015958>
- [2] A.A. Zameshin, A.E. Yakshin, J.M. Sturm, H.H. Brongersma, and F. Bijkerk, "Double matrix effect in Low Energy Ion Scattering from La surfaces," *Appl. Surf. Sci.* **440**, 570–579 (2018). <https://doi.org/10.1016/j.apsusc.2018.01.174>
- [3] U.O. Kutliev, M.U. Otabaev, M.K. Karimov, F.K. Masharipov, and I. Woiciechowski, "Scattering of low-energy  $\text{Ne}^+$  ions from the stepped surface of  $\text{InGaP}(001)\langle 110 \rangle$  at the small angles of incidence," *Physics and Chemistry of Solid State*, **24**(3), 542–548 (2023). <https://doi.org/10.15330/PCSS.24.3.542-548>
- [4] K.S. Daliev, Sh.B. Utamuradova, J.J. Khamdamov, M.B. Bekmuratov, O.N. Yusupov, Sh.B. Norkulov, and Kh.J. Matchonov, "Defect Formation in MIS Structures Based on Silicon with an Impurity of Ytterbium," *East Eur. J. Phys.* (4), 301-304 (2024). <https://doi.org/10.26565/2312-4334-2024-4-33>

- [5] U.O. Kutliev, Sh. Sadullaev, A. Saidova, and I. Tangribergenov, "Studying the Trajectory of Small-Angle Scattered Ar<sup>+</sup> Ions from CdTe(001) <110> Surface Semichannel," *International Journal of Thin Film Science and Technology*, **14**(1), 11-14 (2025). <https://dx.doi.org/10.18576/ijtfst/140102>
- [6] Sh.R. Sadullaev, U.O. Kutliev, A.Yu. Saidova, G.O. Jumanazarov, and R.R. Ruzmetov, "Investigation of Ar<sup>+</sup> ions scattering from the surface CdTe(001) <110> at the glancing incidence," *East Eur. J. Phys.* (2), 206-210 (2025). <https://doi.org/10.26565/2312-4334-2025-2-21>
- [7] D.A. Tashmukhamedova, M.B. Yusupjanova, G.K. Allayarova, and B.E. Umirzakov, "Crystal structure and band gap of nanoscale phases of Si formed at various depths of the near-surface region of SiO<sub>2</sub>," *Technical Physics Letters*, **46**(10), 972–975 (2020). <https://doi.org/10.1134/S1063785020100144>
- [8] M. Draxler, R. Gruber, H.H. Brongersma, and P. Bauer, "Velocity scaling of Ion neutralization in low energy ion scattering," *Phys. Rev. Lett.* **89**, 263201 (2002). <https://doi.org/10.1103/PhysRevLett.89.263201>
- [9] M.K. Karimov, U.O. Kutliev, M.U. Otabaev, and I.A. Khajieva, "Investigation of stepped InP(001)<110> surface by the method of low energy ion scattering," *Journal of Physics Conference Series*, **2373**(3), 032003 (2022). <https://doi.org/10.1088/1742-6596/2373/3/032003>
- [10] R. Souda, M. Aono, C. Oshima, S. Otani, and Y. Ishizawa, "Shadowing and focusing effects in the angular distributions of low-energy rare-gas ions scattered from solid surfaces," *Surf. Sci.* **179**, 199–208 (1987). [https://doi.org/10.1016/0039-6028\(87\)90130-0](https://doi.org/10.1016/0039-6028(87)90130-0)
- [11] K.S. Kim, Y. Zhao, H. Jang, S.Y. Lee, J.M. Kim, K.S. Kim, J.H. Ahn, *et al.*, "Large-scale pattern growth of graphene films for stretchable transparent electrodes," *Nano Lett.* **457**, 706-710 (2009). <https://doi.org/10.1038/nature07719>
- [12] Ch.T. Cho, G. Bosco, and E. Van Der Kolk, "The potential of SiO<sub>2</sub>:Al<sup>3+</sup>, Eu<sup>2+</sup> blue phosphor coatings in greenhouse application," *Optical Materials*, **157**, 116047 (2024). <https://doi.org/10.1016/j.optmat.2024.116047>
- [13] D.A. Sherman, W. Kamal, S.J. Elston, A.A. Castrejon-Pita, S.M. Morris, and J.Ch. Tan, "Stable photoinduced metal-organic nanosheet blue phosphor for white light emission," *Materials Today Chemistry*, **38**, 102089 (2024). <https://doi.org/10.1016/j.mtchem.2024.102089>
- [14] H. Tian, W. Xie, M. Xie, Ch. Zhu, H. Xu, and Sh.Y. Tong, "Prediction of topotactic transition from black to blue phosphorus induced by surface Br adsorption," *Materials Science*, arXiv:2404.05575. <https://doi.org/10.48550/arXiv.2404.05575>
- [15] Y. Li and X. Chen, "Dirac Fermions in Blue-Phosphorus," *D. Mater.* **1**, 031002 (2014). <https://doi.org/10.1088/2053-1583/1/3/031002>
- [16] J.T. Drobny, and D. Curreli, "RustBCA: A High-Performance Binary-Collision-Approximation Code for Ion-Material Interactions," *Journal of open source softway*, **6**(64), 3298 (2021). <https://doi.org/10.21105/joss.03298>
- [17] S.R. Alavi, and F. Snider, "Complete binary collision approximation for the gas transport coefficients via the time correlation formulation," *The Journal of Chemical Physics*, **109**, 3452 (1998). <https://doi.org/10.1063/1.476940>
- [18] J. Drobny, A. Hayes, D. Curreli, and D.N. Ruzic, "F-TRIDYN: A Binary Collision Approximation code for simulating ion interactions with rough surfaces," *Journal of Nuclear Materials*, **494**, 278-283 (2017). <https://doi.org/10.1016/j.jnucmat.2017.07.037>

### ЕНЕРГЕТИЧНИЙ ТА КУТОВИЙ РОЗПОДІЛ РОЗСІЯНИХ ІОНІВ Ar<sup>+</sup> З ПОВЕРХНІ БЛАКИТНОГО ФОСФОРУ ПІД КОВЗАЮЧИМИ КУТАМИ

У.О. Кутлієв<sup>а</sup>, О.А. Саттарова<sup>б</sup>, Н.У. Сетметов<sup>с</sup>, Дж.У. Ісмойлов<sup>а</sup>

<sup>а</sup>Ургенський державний університет імені Абу Райхана Беруні, кафедра фізики,  
вул. Хаміда Олімджана, 14, Ургенч 220100, Узбекистан

<sup>б</sup>Ургенська філія Ташкентської медичної академії, кафедра біомедицини, фізичної культури та спорту,  
вул. Аль-Хорезмі, 28, Ургенч 220100, Узбекистан

<sup>с</sup>Ташкентський університет інформаційних технологій імені Мухаммада аль-Хорезмі, Ургенська філія, кафедра  
телекомунікаційної інженерії, вул. Аль-Хорезмі, 110, Ургенч 220100, Узбекистан

У цій статті представлені теоретичні результати розподілу енергії та кутових розподілів іонів Ar<sup>+</sup> з поверхні блакитного фосфору при малому значенні кута падіння та початкового отримання енергії методом комп'ютерного моделювання. Показано, що при малому значенні початкової енергії іонів з траєкторії розсіяних іонів можна отримати загальну форму поверхневого півканалу. Більше того, збільшення значення початкової енергії дозволяє отримати повну форму півканалу, а також тінь за півканалом, що надає інформацію про розташування атома другого шару. Встановлено, що в розподілі енергії внаслідок збільшення значення початкової енергії формується структура з багатьма піками. Це дає змогу визначити структуру поверхні. Отриманий кутовий розподіл показує, що існує дзеркальне та багаторазове розсіювання іонів від мішені.

**Ключові слова:** розсіювання іонів; півканал; комп'ютерне моделювання; бомбардування іонами; енергетичний та кутовий розподіл

## EFFECT OF COBALT DOPING ON THE STRUCTURAL, MORPHOLOGICAL, OPTICAL, AND MAGNETIC PROPERTIES OF ZnO THIN FILMS PREPARED BY ULTRASONIC SPRAY TECHNIQUE

Z. Daas<sup>a</sup>, A. Bouabellou<sup>a</sup>, K. Daas<sup>b</sup>, D. Belfennache<sup>c\*</sup>, K. Benzouai<sup>a</sup>, M. Mahtali<sup>a</sup>, R. Yekhlief<sup>c</sup>

<sup>a</sup>Thin Films and Interfaces Laboratory, Constantine 1- Frères Mentouri University, 25017 Constantine, Algeria

<sup>b</sup>Laboratory of Mathematics and Their Interactions, Boussouf Abdelhafid University Center, Mila, Algeria

<sup>c</sup>Research Center in Industrial Technologies CRTI, P.O. Box 64, Cheraga, 16014 Algiers, Algeria

\*Corresponding Author E-mail: [belfennachedjamel@gmail.com](mailto:belfennachedjamel@gmail.com)

Received June 1, 2025; revised July 29, 2025; accepted August 5, 2025

Zinc-cobalt oxide ( $Zn_{1-x}Co_xO$ ) thin films refer to a semiconductor material based on zinc oxide (ZnO) doped with cobalt (Co). This material is studied mainly for its modified magnetic, electronic and optical properties, particularly in the context of diluted magnetic semiconductors (DMS). This study analyzes the effect of cobalt doping on the structural optical, and magnetic properties of ZnO thin films, fabricated using a low-cost, scalable ultrasonic spray technique. Zinc-cobalt oxide ( $Zn_{1-x}Co_xO$ ) thin films were successfully deposited on glass substrates using the ultrasonic spray pyrolysis technique at a substrate temperature of 450 °C, with cobalt doping concentrations of  $x = 0\%$ , 1%, 3%, and 5%. X-ray diffraction (XRD) analysis revealed a hexagonal wurtzite structure for all samples, with no secondary phases, indicating effective incorporation of  $Co^{2+}$  ions into the ZnO lattice. Raman spectroscopy indicated the emergence of structural disorder and defect-related modes, consistent with the increase in Urbach energy. Scanning electron microscopy (SEM) showed granular surface morphologies, and a non-homogeneous surface pattern is visible on all samples. Atomic Force Microscopy (AFM) showed an increase in surface roughness and grain size with increasing doping concentration. Optical measurements confirmed high transmittance in the visible range and a gradual decrease in optical band gap from 3.21 eV to 2.95 eV with increasing Co content. The spectroscopy, and vibrating sample magnetometer (VSM) revealed that all films are intrinsically ferromagnetic. The origin of the ferromagnetism was found to be an intrinsic property of the Co-doped ZnO thin films.

**Keywords:** Spray Technique, ZnO Thin Films, Cobalt doping, RAMAN, Diluted Magnetic Semiconductors (DMS)

**PACS:** 73.50.-h, 73.50.Pz

### 1. INTRODUCTION

Semiconductors play a fundamental role in modern technology due to their ability to control the flow of electricity, thus enabling the manufacture of components such as transistors and integrated circuits that are the basis of computers, smartphones and other electronic devices [1,2]. They are also used in solar panels for the conversion of solar energy into electricity [3-5]. Zinc oxide (ZnO) is one of the most competitive transparent semiconductors. It can crystallize under normal conditions of temperature and pressure in the wurtzite structure which is the most stable and preferred [6,7]. This structure formed by the stacking of planes of atoms ( $O^{2-}$ ) and ( $Zn^{2+}$ ) in tetrahedral coordinates does not have a center of symmetry, which generates a spontaneous polarization field along the  $c$  axis [8]. This polarity as well as the piezoelectric polarity thermodynamically favor the preferential growth of ZnO along the (002) direction and improve their mechanical and optoelectronic properties [9]. In recent years, many researchers have discovered some extraordinary elements with better chemical, electronic, optical and especially magnetic qualities [10,11]. Doping is the most commonly used strategy to improve the quality of semiconductors [12,13]. Due to the excellent characteristics (optical, electrical and magnetic) of transition metals, especially cobalt, Co-doped ZnO ( $Zn_{1-x}Co_xO$ ) thin films are widely used in industry for applications such as optoelectronics, spintronics, sensors, ... etc. [14,15].

Several methods have been used to synthesize thin films, including: Sol-gel processes [16], metal-organic chemical vapor deposition (MOCVD) [17], Micro-ondes-Cyclotron Résonance Électronique (MW-ECR) [18], Plasma-Enhanced Chemical Vapor Deposition (PECVD) [19] chemical bath deposition (CBD) [20], sputtering [21], and spray technique [22]. The latter is one of the most used techniques among them, because of the potent technique for creating a variety of powdered materials, including metals, metal oxides, superconducting materials, and nanophase materials, is spray pyrolysis. It also offers several advantages over alternative powder synthesis methods, including superior control over chemical uniformity, stoichiometry in multi-component systems, and high powder purity.

It should be remembered that cobalt is clearly capable of modifying the various properties of ZnO. Indeed, much research has been done to study the effect of cobalt doping on the optical, structural, and morphological properties of ZnO thin films. However, little effort has been devoted to explaining the effect of cobalt doping on the ferromagnetic properties of the ZnO thin films. Our work consists in developing thin films of  $Zn_{1-x}Co_xO$ , deposited on glass substrates by spray technique. Our objective is to consider a correlation between the Co doping effect and the structural, morphological, optical and magnetic properties of the thin films obtained. To achieve this objective, the structure, morphology as well as the optical and magnetic properties of the layers produced were studied using different techniques: X-ray diffraction

(XRD) and Raman spectroscopy, scanning electron microscopy and atomic force microscopy (SEM and AFM), UV-Visible, the spectrophotometry, spectroscopy, and vibrating sample magnetometer (VSM).

## 2. EXPERIMENTAL PROCEDURE

Spray ultrasonics was used to deposit the  $Zn_{1-x}Co_xO$  thin films (where  $x = 0, 0.01, 0.03, \text{ and } 0.05$ ) on glass substrates. Precursors included cobalt acetate tetrahydrate  $[Co(CH_3COO)_2 \cdot 4H_2O]$  and zinc acetate dihydrate  $[Zn(CH_3COO)_2 \cdot 2H_2O]$ . The spray solution was made by dissolving the powders in methanol at the appropriate molar ratios, keeping the molarity at  $0.1 \text{ mol L}^{-1}$ . An ultrasonic nebuliser, which transforms liquid into a consistent stream of small droplets with an average diameter of  $40 \mu\text{m}$  (as defined by the manufacturer), was then used to spray the solution onto heated glass substrates. The thin films were deposited for 2 min at a temperature of  $450 \text{ }^\circ\text{C}$ .

## 3. RESULTS AND DISCUSSION

### 3.1 The XRD Analysis of Co-doped ZnO Thin Films

The X-ray diffraction (XRD) patterns of Co-doped ZnO thin films at different doping concentrations (0%, 1%, 3%, and 5%) are presented in Fig. (1.a).

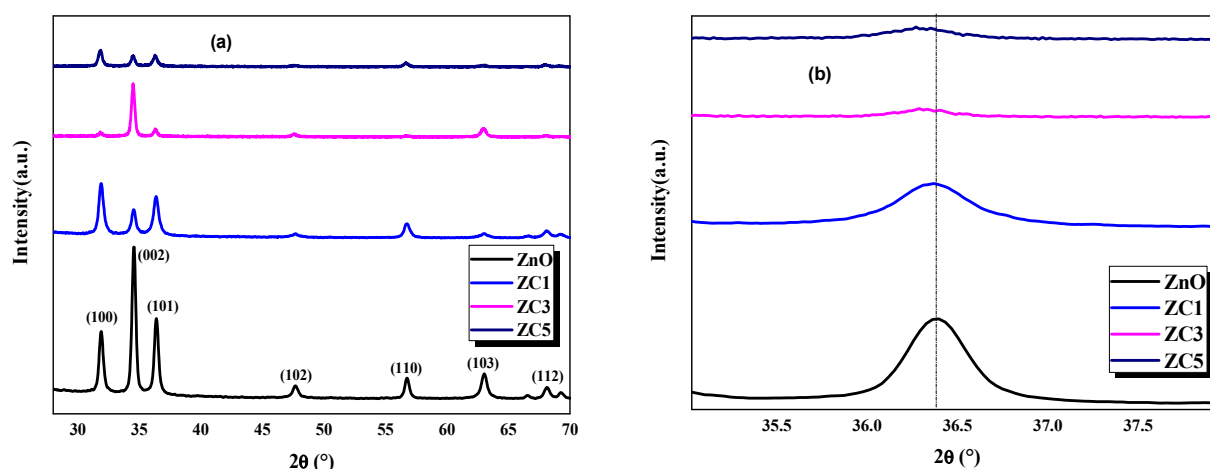


**Figure 1.** X-ray diffraction spectra of ZnO thin films doped with cobalt at different concentrations, (a) XRD pattern, (b) Zoomed-in view of the (101) diffraction peak

The diffraction peaks appear at  $2\theta = 31.92^\circ, 34.56^\circ, 36.39^\circ, 47.62^\circ, 56.72^\circ, 62.95^\circ, 67.97^\circ, \text{ and } 69.19^\circ$  corresponding to the (100), (002), (101), (102), (110), (103), (112), and (201) crystallographic planes, respectively, in the undoped ZnO sample. This confirms that the samples possess a hexagonal wurtzite structure and belong to the space group  $P63mc$ , as reported in JCPDS card No. 36-1451 [23]. Fig. (1.b) shows an enlarged view of the (101) peak, where a slight shift in the peak position is observed compared to pure ZnO, indicating the successful incorporation of  $Co^{2+}$  ions into the ZnO crystal lattice [24]. Furthermore, no secondary phases or structural changes are detected due to Co doping, which confirms the high phase purity of the samples and suggests that  $Co^{2+}$  ions substitute  $Zn^{2+}$  ions at the lattice sites rather than occupying interstitial positions [25]. The sharp and narrow diffraction peaks reflect the crystalline nature of the synthesized nanoparticles. The substitution of  $Zn^{2+}$  ions (ionic radius =  $0.60 \text{ }^\circ\text{A}$ ) by  $Co^{2+}$  ions (ionic radius =  $0.58 \text{ }^\circ\text{A}$ ) induces crystal defects due to the difference in ionic radii, leading to a reduction in crystallinity, an increase in lattice parameters, and an increase in unit cell volume. The changes observed in peak intensity and full width at half maximum (FWHM) can be attributed to increases in crystallite size and the presence of micro-strain within the crystal structure.

The relation

$$\frac{1}{d_{hkl}^2} = \frac{4}{3} \frac{h^2 + hk + k^2}{a^2} + \frac{l^2}{c^2} \quad (1)$$

can be used to determine the spacing between planes  $d$  in a hexagonal construction. Here,  $a$  and  $c$  are lattice constants, and  $d_{hkl}$  is the interplanar distance that corresponds to its Miller indices of the  $h$ ,  $k$ , and  $l$  planes.

This formula is used to get the lattice constant  $a$  for the (100) plane:

$$a = \frac{\lambda}{\sqrt{3} \sin \theta_{100}} \quad (2)$$

For the (002) plane, the lattice constant  $c$  is computed using the formula: The lattice constant  $c$  for the (002) plane is calculated by,

$$c = \frac{\lambda}{\sin \theta_{002}} \quad (3)$$

Strain, ionic radii, crystal structure flaws, and dopant concentration all affect the lattice parameters. Additionally, the substitution of Co in the ZnO lattice is confirmed by the changes in the d-value, cell characteristics, volume, bond length, average crystallite size, shift in peak position, and peak intensity. Co doping has no effect on ZnO’s hexagonal wurtzite structure.

The relationship that determines a unit cell’s volume is:

$$V = \frac{\sqrt{3}}{2} a^2 c \tag{4}$$

Lattice parameters are a and c. As the amount of Co doping grows, as seen in Table 1, the unit cell’s volume (v) also increases. Vegard’s law states that changes in the lattice constant, a rise in the unit cell’s volume, and the reduced ionic radius of the Co ion relative to Zn ions [26] are indicators of the incorporation of Co<sup>2+</sup> ions into the ZnO lattice. According to [27], the tetrahedral coordination of Zn<sup>2+</sup> is not entirely filled by Co<sup>2+</sup>. Co<sup>2+</sup> in octahedral coordination with low spin r = 0.065 nm and high spin 0.075 nm [28].

The Debye-Scherrer equation:

$$D = \frac{\kappa\lambda}{\beta \cos \theta} \tag{5}$$

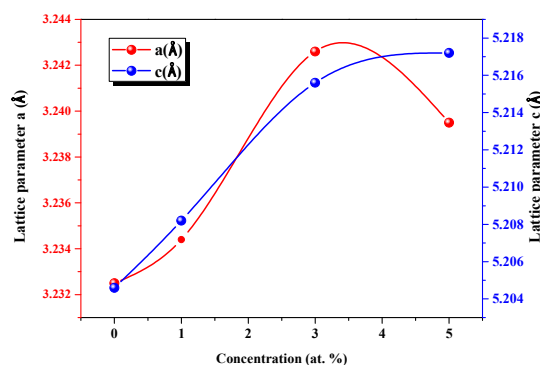
was used to determine the crystalline size, where λ is the X-ray wavelength (1.5406 Å), β is the full width at half maximum (FWHM) in radians of the X-ray diffraction peak, θ is the Bragg’s angle, and D is the mean size of crystallites (nm).

Table 1 lists all of the estimated lattice parameters (a and c), interplanar spacing (d), crystallite size (D) including the average crystallite size (D<sub>moy</sub>), unit cell volume, as well as the peak positions given by 2θ, Miller indices (hkl), peak intensities, full width at half maximum (FWHM), and the calculated strain (ε) and stress (σ) values for each individual peak of ZnO samples with different doping percentages.

**Table 1.** Structural properties of ZnO samples with different doping percentages, listed by individual peaks

Sample	2θ (deg)	(hkl)	Intensity (u.a.)	FWHM (deg)	D (nm)	D <sub>moy</sub> (nm)	d(°Å)	a(°Å)	c(°Å)	Strain ε (%)	Stress σ (GPa)	Volume (°Å <sup>3</sup> )
ZnO	31.92	(100)	1442.35	0.3988	20.7191	21.4631	2.7995	3.2325	— 5.2046	-0.0077	0.0179	47.089
	34.56	(002)	3486.06	0.3676	22.6327		2.6023	—	—			
	36.39	(101)	1810.56	0.3975	21.0375		—	—	—			
ZC1	31.91	(100)	1171.25	0.4108	20.1133	21.8926	2.8013	3.2344	— 5.2082	0.0615	-0.1432	47.225
	34.54	(002)	535.81	0.3666	22.6932		2.6041	—	—			
	36.36	(101)	860.9	0.3656	22.8711		—	—	—			
ZC3	31.80	(100)	109.05	0.4199	19.6721	25.1173	2.8093	3.2426	5.2156	0.2037	-0.4748	47.522
	34.50	(002)	1299.408	0.3063	27.1578		2.6078	—	—			
	36.28	(101)	170.29	0.2931	28.52		—	—	—			
ZC5	31.87	(100)	361.78	0.3752	22.0196	24.9678	2.8061	3.2395	— 5.2172	0.2345	-0.5482	47.476
	34.49	(002)	228.05	0.3068	27.1128		2.6086	—	—			
	36.26	(101)	246.57	0.3628	23.0410		—	—	—			

Fig. 2 displays the graphical representation of the lattice parameters a and c for the ZnO, ZC1, ZC3, and ZC5 thin films.



**Figure 2.** Variation of lattice parameters and of ZnO thin films with Co concentration



### 3.2. Raman Characterization

The micro-Raman spectroscopy analysis of our samples will allow us to better visualize the doping effect and also confirm the results of the X-ray diffraction study. The Raman scattering spectra of  $Zn_{1-x}Co_xO$  thin films with different Cobalt contents ( $x = 0; 1; 3; \text{ and } 5\%$ ) recorded between  $50\text{-}1500\text{ cm}^{-1}$  are shown in Fig. 3. As shown in this figure, the Raman spectra only present:

Two predominant peaks: one at  $560\text{-}570\text{ cm}^{-1}$  and the other peak at about  $1100\text{ cm}^{-1}$  corresponding to the two longitudinal optical modes  $A_1(LO)$  and  $A_1(2LO)$  in all samples (pure and doped). The presence of a Raman  $E_2$  High peak near  $431\text{ cm}^{-1}$  (infinitely small, whose intensity decreases with doping) reveals the generation of new defects during doping following the substitution of zinc sites by cobalt ions (The ionic radius of  $Co^{2+}$  is slightly smaller than that of  $Zn^{2+}$ ). In other words, the ionic radius of  $Co^{2+}$  is about  $0.58\text{ \AA}$  ( $0.058\text{ nm}$ ) while that of  $Zn^{2+}$  is about  $0.60\text{ \AA}$  ( $0.060\text{ nm}$ .) [29], which confirms the DRX results that have been discussed previously. A peak at  $800\text{ cm}^{-1}$  emitted by the glass substrate, due to good transmittance in the visible [30].

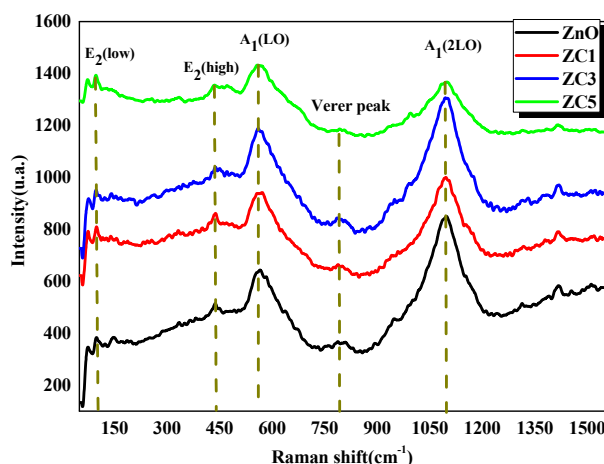


**Figure 3.** Micro Raman spectra for undoped and Co doped ZnO thin films

A significant perturbation of the intensities of the two predominant peaks is also observed depending on the doping element content. Electron-phonon coupling is very important to explain the optoelectronic properties of crystalline semiconductors and to translate the appearance of these two longitudinal modes  $A_1(LO)$  and  $A_1(2LO)$  as well as their intensities. This coupling strength between electrons and longitudinal phonons (LO) in polar semiconductors is determined by the intensity ratio ( $A_1(2LO)/A_1(LO)$ ), between the second and first order Raman vibration of the longitudinal  $A_1$  mode [31].

Two contributing mechanisms can explain this phenomenon:

1. The long-range interaction present inside the nanocrystal, mainly due to the macroscopic electric field linked to longitudinal phonons (LO) and called the “Fröhlich mechanism”. It strongly expresses the polarity of the semiconductor which serves to increase the electron-phonon coupling and implicitly the size of the crystallites [32].

2. The deformation potential which is a mechanism that relates the change in the energy of the electronic distribution to the stress in the solid, it is then sensitive to external surface defects (lattice deformation) [33] which serves to compensate for the large drop in the Fröhlich mechanism in the deformed solid, by increasing the electron-phonon coupling for infinitely small crystallite sizes. The characteristics of the  $A_1(LO)$  and  $A_1(2LO)$  modes are calculated and grouped in Table.2.

**Table 2.** Frequencies of different vibration modes of pure and doped ZnO films

Doping (% Co)	$A_1(LO)$		$A_1(2LO)$		$I_{A_1(2LO)}/I_{A_1(LO)}$
	Center ( $cm^{-1}$ )	Intensity (u.a)	Center ( $cm^{-1}$ )	Intensity (u.a)	
0	567.76	637.18	1099.93	851.47	1.33
1	569.64	936.42	1096.17	998.06	1.06
3	566.19	1186.23	1098.056	1300.50	1.09
5	560.55	1433.81	1094.29	1371.27	0.95

It is observed that the deformation of pure ZnO ( $\sigma = 0.0179\text{ GPa}$ , see Table. 1) results in a ratio of the  $I_{A_1(2LO)}/I_{A_1(LO)}$  intensities of 1.33. This is an important value to express the electron-phonon coupling and then shows a large polarity of the produced layers, which was translated by a large preferential orientation of the crystallites along the (002) direction as already shown in the DRX diffractograms. As the doping level increases (at 5% Co), the lattice deformation, accompanied by a slight increase in crystallite size, is the origin of the decrease in the electron-phonon coupling (from 1.33 to 0.95), while the small perturbation of the electron-phonon coupling value (from 1.06 to 1.09) is the cause of a slight improvement of the Fröhlich mechanism for the 3% Co doped ZnO layers. Beyond this dopant amount, the electron-phonon coupling value will decrease rapidly to reach 0.95. This can be explained by the quantum



confinement effect governed by the strain potential and caused by the migration of cobalt ( $\text{Co}^{2+}$ ) ions towards the grain boundaries. This has the effect of limiting the substitution of  $\text{Zn}^{2+}$  sites by  $\text{Co}^{2+}$  ions in the ZnO lattice as previously suggested.

### 3.3. Morphological Characterization

The surface condition of a sample is a very important factor in understanding certain properties such as morphology, roughness, and grain size. It is in this context that we used scanning electron microscopy (SEM) and atomic force microscopy (AFM).

#### 3.3.1. Scanning Electron Microscopy

Fig. 4 shows SEM images taken on pure and Co-doped ZnO samples (1%, 3%, and 5%). These images show granular surface morphologies, and a non-homogeneous surface pattern is visible on all samples.

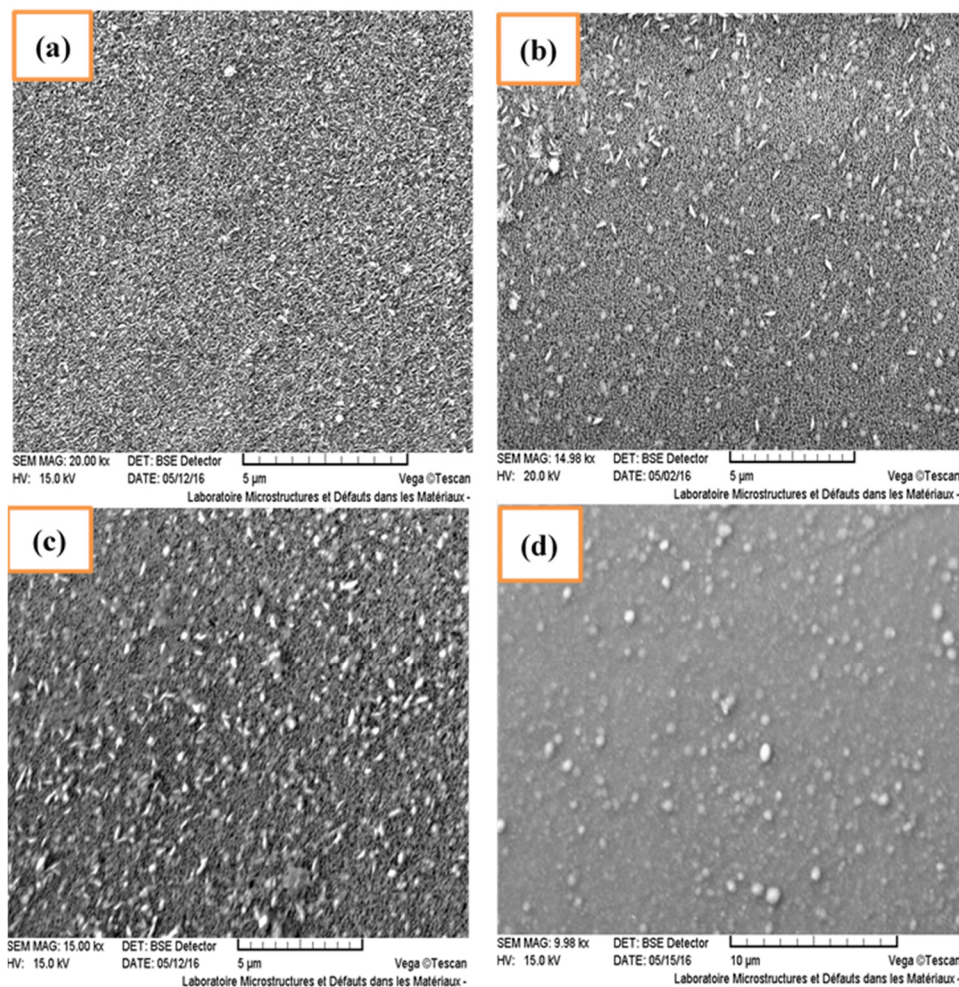


**Figure 4.** SEM images of the ZnO thin films at different Co doping concentrations (a): 0%, (b): 1%, (c): 3%, and (d): 5% Co

It is plausible that the smooth nature of the glass substrate hinders the perfect development of ZnO thin films. In addition, some holes, due to hydrogen bubbles released on the surface of the deposits, are observed; thus inhibiting the rate of deposition of the alloy in certain surface sites, which leads to the appearance of holes observed in the images. It is clear that they are distributed over the entire substrate for the pure ZnO sample. But for the 1% Co (Fig.4.a) doped layer, these microstructures are developed, their average diameter has increased and their density has decreased and we also notice the presence of very small particles, of clear contrast, on the surface of the grains. For the 3% Co doped layer, these bright spherical particles, more numerous than in the 1% Co doped layer. These particles are less adherent to the substrate, but have an average diameter which tends to increase. The last sample in Fig.4.c (5% Co doped layer) prepared shows good adhesion to the substrate and good coalescence of bright spherical particles. The formation of such structures in thin films obtained by spray pyrolysis is due to the relaxation of stresses resulting from the conditions of elaboration, namely: the nature of the substrate [34], the concentration of the solution [35], the nature of the solvent [36], the temperature as well as the heating rate, the drying process [37, 38] and the thickness of the layers [39, 40]. Two contributing causes are at the origin of these instabilities:

1. The desorption of the hydroxyl group containing in the solvent during annealing of the ZnO layer causes a deformation of the sample involved [41]. Consequently, a network consisting of mixed phases of liquid and solid has been constructed. Doping effect (Co) on the properties of ZnO thin films As the thermal expansion coefficients of the glass and the deposited layer are approximately equal, the annealing process does not generate any compressive stress so the grain size does not change. This explanation remains useless in our case, as our samples are produced under the same conditions and using the same protocol.

2. The second explanation is related to the internal deposition stress. When this stress exceeds a certain limit value, the flat surface becomes unstable and the average grain diameter changes. This assumption is more favorable in our case, given that our samples are produced in the same way, except for the dopant percentage that changes. As a result, spherical grains form on the surface of the thin films during production due to the cobalt doping effect.

### 3.3.2. Atomic force microscopy (AFM) characterization

To clearly visualize the doping effect on the topology of the obtained layers, a series of AFM images is presented in Fig.5.

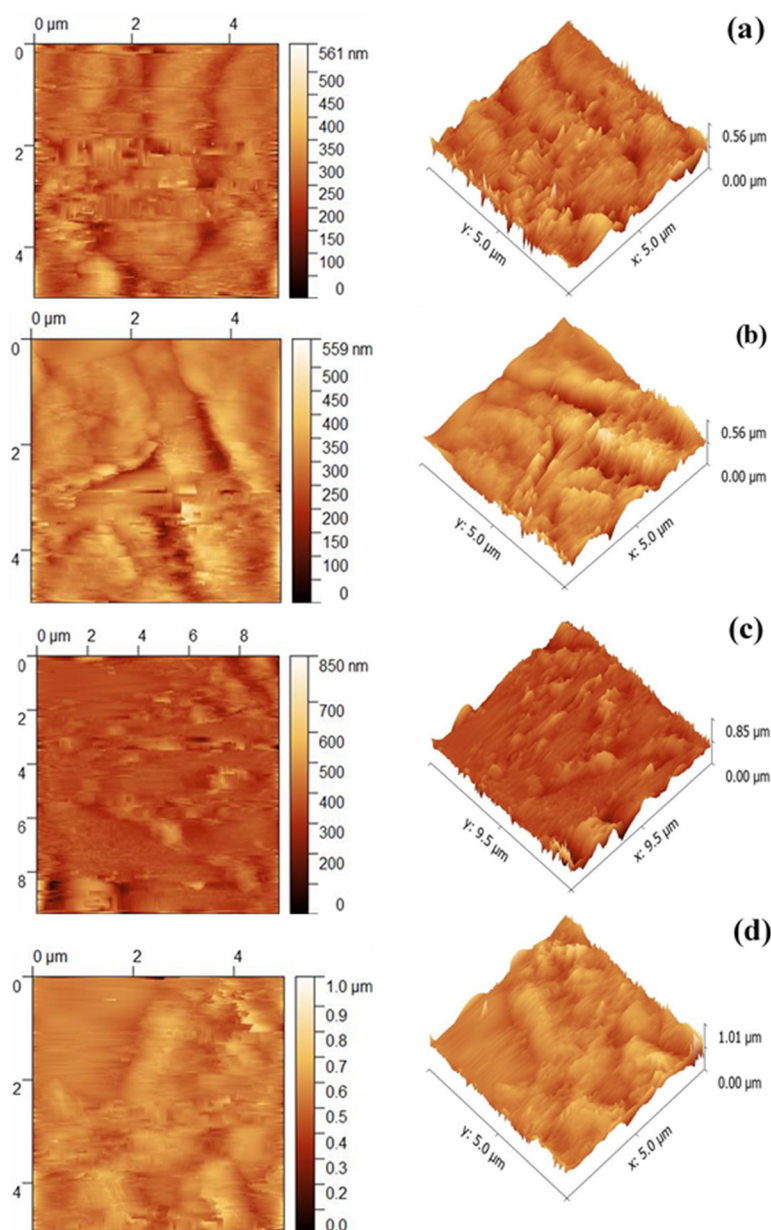


**Figure 5.** AFM images of the ZnO thin films at different Co doping concentrations (a) : 0%, (b): 1%, (c): 3%, and (d): 5% Co

The roughness values of the produced surfaces were estimated from the RMS (Root-Mean-Square) values. The images show the particular wrinkling structure. As these images represent the topology of the pure and doped (1% to 5% Co) ZnO layers, we note that our layers are very preferentially oriented. As observed in Fig. 5 (a, 2D and 3D), the surface of the pure ZnO layers consists of grains distributed in a mixed wavy structure, containing valleys and ridges, with an

RMS value of 37.26 nm. When the cobalt (Co) doping rate increases and reaches 1% Co, the morphology of the formed surface changes abruptly into a coalescent structure of folds (wrinkles) (Fig.5 b, 2D and 3D), probably due to the effects of internal stresses. This phenomenon can be explained by the substitution of  $Zn^{2+}$  ions by  $Co^{2+}$  ions at the deposition surface. This substitution is the origin of a compressive stress caused by the difference in the ionic radii of the two ions ( $Co^{2+}$  and  $Zn^{2+}$ ). For a concentration of 3% (Fig. 5.c, 2D and 3D), the peaks become free of all types of constraints and this transformation can be due to the decrease in internal stress as previously shown in the XRD section. A good, homogeneous, and highly adherent wavy layer forms. The grains were forced to orient themselves along the (002) axis by the effect of large dipolar interactions, but when the doping value 5% Co (Fig.5 d, 2D and 3D) corresponding to the cobalt substitution limit in the ZnO matrix, the ( $Co^{2+}$ ) ions tend to move towards the grain boundaries, which results in a retardation of grain growth along the c axis. Under these conditions, stress relaxation has been induced and valleys and peaks begin to disappear [42]. In addition, some holes, due to hydrogen bubbles released on the surface of the deposits, are observed; thereby inhibiting the deposition rate of the alloy in some surface sites, which leads to the appearance of holes observed on the images. To clarify this explanation more, we drew the graph that represents the crystallite size and RMN roughness deduced from AFM as a function of the % cobalt concentration in Fig. 6.

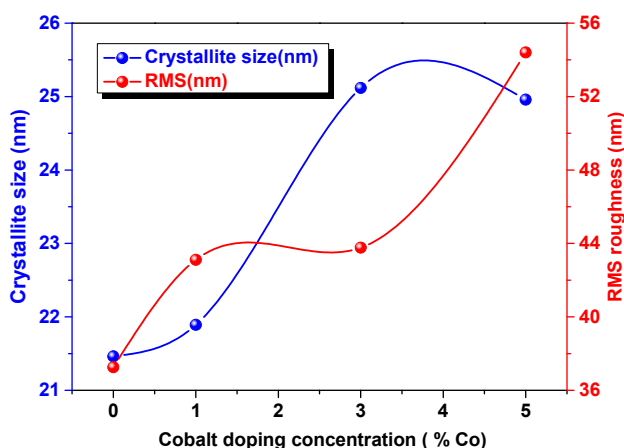


Figure 6. Crystallite size and RMN roughness deduced from AFM as a function of the % cobalt doping concentrations

### 3.4. Optical properties 3.4.1. UV-Visible Spectroscopy

Fig. 7 shows the optical transmission spectra of thin films of ZnO, ZC1, ZC3 and ZC5, deposited on glass substrates at 450 °C. The measurements were carried out over a wavelength range of 300–800 nm. The results indicate oscillations in all the doped films (ZC1, ZC2 and ZC3). These oscillations result from the interference between the light reflected from the film surface and the interface between the film and the substrate [43]. These oscillations were recorded by Shakit et al [44] and Aboud et al. [45]. After doping, the pure, transparent film turns green. It is evident that the transmission decreases with increasing Co concentration in the deposited films. This decrease could be attributed to the increase in the absorption of the film after doping, resulting from the contribution of  $Co^{2+}$  to the absorption process. Three absorption bands are represented in the transmission spectra at 546 nm, 598 nm and 636 nm, related to the d-d transitions of  $Co^{2+}$  ions. According to the literatures [46,47] these absorptions result from d-d transitions of high-spin  $Co^{2+}$  ions, which could be attributed to the  ${}^4A_2 \rightarrow {}^2E(G)$ ,  ${}^4A_2 \rightarrow {}^4T_1(P)$  and  ${}^4A_2 \rightarrow {}^2A_1(G)$  transitions, respectively [47–50]. This result indicates the successful substitution of  $Co^{2+}$  into  $Zn^{2+}$  sites, where no  $CoO$  or  $Co_3O_4$  phase was indicated by XRD results.

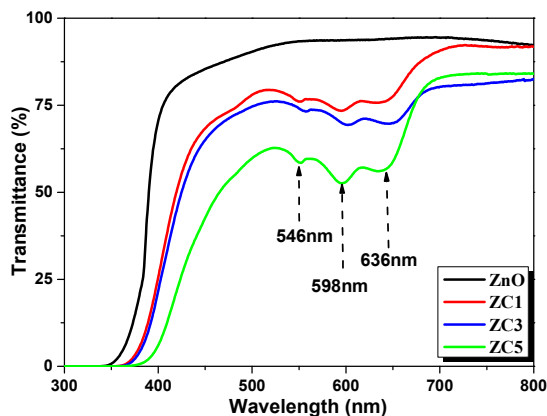
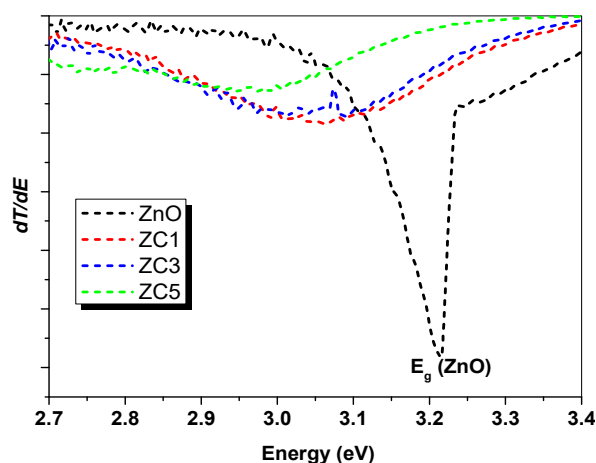


Figure 7. Optical Transmittance spectra of pure ZnO and Co doped ZnO thin films

### 3.4.2. Calculation of the optical gap

According to the Ridley model [51], based on the absorption band threshold, the gap energy values are estimated from the position of the predominant peak. Fig. 8 shows the first derivatives of the optical transmission as a function of the photon energy ( $h\nu$ ): ( $dT/dE$ ). It can be seen that the band gap values decreased progressively with increasing cobalt doping concentration, with values of 3.21 eV for ZnO, 3.06 eV for ZC1, 3.01 eV for ZC3 and 2.95 eV for ZC5. However, these values are lower than those of bulk ZnO (3.27 eV). In our case, the deformation of the crystal lattice, the modification of the electronic structure, slight increase in the average grain size are mainly the origins of a decrease in the optical gap value [52]. This broadening is a direct consequence of quantum mechanics: electronic levels are confined in a potential well whose size is close to the typical wavelengths of electrons. By sufficiently increasing the size of semiconductor particles, the absorption threshold is shifted towards lower energies, the gap becomes wider and the electronic structure is affected [53].



**Figure 8.** The first derivative of transmittance ( $dT/dE$ ) as a function of energy ( $h\nu$ ) for ZnO, ZC1, ZC3, and ZC5 thin films

The Urbach energy is a characteristic parameter of energetic disorder in the band edges. It was calculated based on the following equation:

$$\ln(\alpha) = \ln(\alpha_0) + \frac{h\nu}{E_U} \quad (6)$$

where  $\alpha_0$  is a constant,  $h\nu$  is the photon energy, and  $E_U$  is the Urbach energy.

The results of the band gap and Urbach energy calculations are represented in Fig. 9. The Urbach energy was found to increase with increasing Co content, indicating a rise in the energetic disorder within the films, which is directly related to structural defects. This result correlates well with the increase in the intensity of the A1(low)/E1(low) peaks as a function of Co doping, as observed in the Raman spectra.

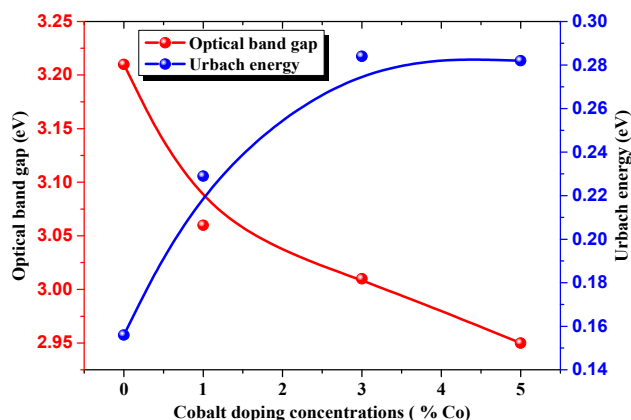


**Figure 9.** The evolution of both the optical gap energy ( $E_g$ ), the Urbach energy ( $E_u$ ) as a function of Co doping

### 3.5. Magnetic properties

Cobalt-doped ZnO ( $Zn_{1-x}Co_xO$ ) thin films exhibit interesting magnetic properties, particularly in the context of diluted magnetic semiconductors (DMS). These materials are attracting attention for potential applications in spintronics, which exploits both charge and spin of electrons [54,55]. In this section, we will study the magnetic properties of (1, 3,



and 5 Co) doped ZnO thin films. Fig. 10 (a,b) shows the hysteresis loops taken from the Co-doped ZnO samples (1%, 3%, and 5%) in room temperature. The magnetic parameters, namely saturation field ( $H_s$ ), coercivity ( $H_c$ ), saturation magnetization and remanent magnetization (MR), estimated from the M-H curves at room temperature, are presented in Table 3.

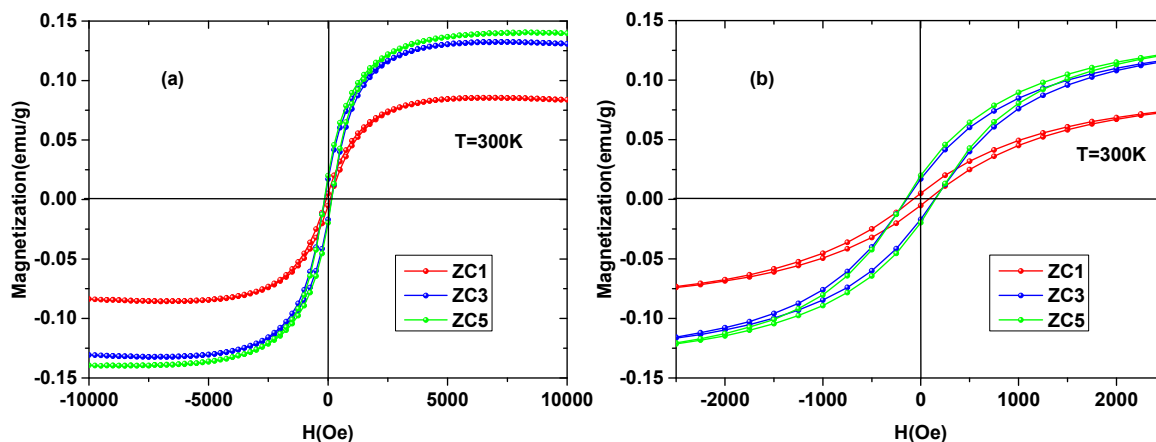


Figure 10. hysteresis loops taken from the Co-doped ZnO samples (1%, 3%, and 5%) in room temperature

Table 3. Values of different magnetic properties

Doping (% Co)	Saturation field ( $H_s$ )	Coercive field ( $H_c$ )	Saturation magnetization $M_s$	Remanence $M_r$
1	7000	78.92	0.08543	0.00511
3	7500	143.82	0.13242	0.01702
5	8250	151.45	0.14033	0.01983

The curves show a hysteresis or remanence indicating the presence of ferromagnetism but at a concentration of 1% Cobalt and present a weak ferromagnetism. Moreover, the saturation field  $H_s$  is increased with increasing cobalt concentration (Fig.8, a)) and the low field region of hysteresis loops (Fig. 8(b)) shows that the coercive field  $H_c$  values are in the range of 78.92 to 151.45 Oe. Studies [56-58] show that cobalt-doped ZnO can exhibit ferromagnetism at room temperature, which is of interest for spintronics, but the origin of this ferromagnetism is still controversial this behavior depends on several experimental factors are:

- Co concentration: Low doping (<5%) sometimes promotes ferromagnetism, but at higher concentrations, the behavior often becomes paramagnetic or antiferromagnetic.
- Presence of free carriers (electrons): Ferromagnetism can be induced by the presence of free carriers (Zener model), and the presence of oxygen vacancies can promote it.
- The Synthesis method strongly influences magnetic properties. Ferromagnetism is sometimes observed in inhomogeneous thin films. This ferromagnetic signal was observed by Mamani et al. [59] on thin films of cobalt-doped ZnO prepared by EB-PVD at room temperature and on thin films of Co and N doped ZnO prepared by two distinct methods Sol-gel and PLD by Ramasubramanian et al. [60] and by Dhruvashi et al [61].

These results, however, seem to contradict the ferromagnetic character of thin films produced by magnetron sputtering [62,63] and by other production methods [64-68]. The origin of this inconsistency is still not clear, but there are hypotheses according to which ferromagnetism would be sensitive to the methods and conditions of production of Co doped ZnO [69].

## 5. CONCLUSION

In this work, we conducted a study focused on zinc oxide in the form of cobalt-doped thin films, with the objective of developing and then investigating the doping effect on the structural, morphological, optical, and magnetic properties of ZnO thin films developed by spray technique. This configuration is the ultimate key to the potential applications of  $Zn_xCo_{1-x}O$  thin films. This is why we fabricated a series of samples by varying the doping level. To fully understand the impact of this factor on the properties of ZnO, we used a range of characterization techniques, including X-ray diffraction, Raman spectrophotometry, scanning electron microscopy (SEM), atomic force microscopy (AFM), UV-visible spectrophotometry, and spectroscopy, and vibrating sample magnetometer (VSM).

Structural XRD studies of the films reveal that our films are polycrystalline with a hexagonal wurtzite structure and a preferential unidirectional orientation, along the [002] direction. XRD analysis clearly indicates that the dopant is incorporated into the ZnO lattice without any phase segregation occurring in these films. Raman spectroscopic analyses demonstrated the very good texturization of the films, by the presence of two intense, dominant peaks corresponding to the longitudinal  $A_1(LO)$  and its 2nd order  $A_1(2LO)$  vibration modes. SEM images reveal granular surface morphologies, their densities and diameters increasing with increasing doping levels, and a non-homogeneous surface pattern is visible on all samples. However, the AFM images confirmed the XRD results, showing a vertical and preferential growth of the

grains along the (002) direction, and also that the layers consist of grains distributed in a mixed wavy structure, containing valleys and ridges, with an RMS value between 37.25 nm and 54.4 nm. The optical characterization of the developed layers revealed oscillations in all the doped films. These oscillations result from the interference between the light reflected by the film surface and the interface between the film and the substrate. It is evident that the transmission decreases with the increase in Co concentration in the deposited films. This decrease is attributed to the increase in the absorption of the film after doping, resulting from the contribution of  $\text{Co}^{2+}$  to the absorption process. This result indicates the successful substitution of  $\text{Co}^{2+}$  in the  $\text{Zn}^{2+}$  sites. The doping effect on the gap energy of ZnO films is manifested by a decrease (from 3.212 eV to 2.95 eV) as a function of the dopant concentration, which may be due to quantum confinement in the ZnO matrix. The VSM revealed that all films are intrinsically ferromagnetic. The substantial enhancement of ferromagnetism has been observed upon increase Co doping. Hence the effect of Co doping on ZnO thin films is highly enhanced ferromagnetism and proper Co substituted ZnO films. Overall, these results demonstrate that cobalt doping significantly affects the physical properties of ZnO, offering the potential to tailor them for future electronic or optoelectronic applications.

Finally, due to the vast complexity of the effect of cobalt doping on the ferromagnetic properties of the ZnO thin films, several issues are still open for future investigation in order to fully understand the abilities and limitations of influence cobalt doping on the ferromagnetic properties of the ZnO thin films. Hopefully, the results presented in this work gives a contribution to this understanding

#### ORCID

Abderrahmane Bouabellou, <https://orcid.org/0009-0009-0854-9616>

Djamel Belfennache, <https://orcid.org/0000-0002-4908-6058>

#### REFERENCE

- [1] M. Vali, and A. Bayani, *Mat Sci Semicon Proc.* **195**, 109599 (2025). <https://doi.org/10.1016/j.mssp.2025.109599>
- [2] Y. Sun, T. Wang, J. Luo, J. Chen, W. Huang, and J. Ding, *Mater. Today Electron.* **12**, 100151 (2025). <https://doi.org/10.1016/j.mtelec.2025.100151>
- [3] D. Belfennache, D. Madi, N. Brihi, M.S. Aida, and M.A. Saeed, *Appl. Phys. A*, **124**, 697 (2018). <https://doi.org/10.1007/s00339-018-2118-z>
- [4] I. Hanif, and I. Iatsunskyi, *Int. J. Hydrog. Energy*, **109**, 174 (2025). <https://doi.org/10.1016/j.ijhydene.2025.01.491>
- [5] R. Ouldamer, D. Belfennache, D. Madi, R. Yekhlef, S. Zaiou, and M.A. Ali, *J. Ovonic. Res.* **20**(1), 45 (2024). <https://doi.org/10.15251/JOR.2024.201.45>
- [6] Y. Benkrima, S. Benhamida, and D. Belfennache, *Dig. J. Nanomater. Bios.* **18**(1), 11 (2023) <https://doi.org/10.15251/DJNB.2023.181.11>
- [7] Y. Benkrima, M.E. Soudani, D. Belfennache, H. Bouguettaia, and A. Souigat, *J. Ovonic. Res.* **18**(6), 797 (2022). <https://doi.org/10.15251/JOR.2022.186.797>
- [8] Ü. Özgür, Ya. I. Alivov, C. Liu, A. Teke, M.A. Reshchikov, S. Doğan, V. Avrutin, *et al.*, *J. Appl. Phys.* **98**(4), 041301 <https://doi.org/10.1063/1.1992666>
- [9] R. Kurniawan, I.M. Sutjahja, T. Winata, T. S. Herg, J. Ding, A. Rusydi, and Y. Darma, *Opt. Mater. Express*, **7**(11), 3902 (2017). <https://doi.org/10.1364/OME.7.003902>
- [10] L. Wang, *Comput. Methods Appl. Mech. Eng.* **445**, 118205 (2025). <https://doi.org/10.1016/j.cma.2025.118205>
- [11] Z. Wang, Q. Chen, Z. Qi, Z. Song, Z. Wang, B. Cao, S. Pan, J. Pang, and W. Wang, *Intermetallics*, **185**, 108886 (2025). <https://doi.org/10.1016/j.intermet.2025.108886>
- [12] D. Belfennache, N. Brihi, and D. Madi, *Proceeding of the IEEE xplore, 8<sup>th</sup> (ICMIC) (2016)*. 7804164, 497–502 (2017). <https://doi.org/10.1109/ICMIC.2016.7804164>
- [13] Y. Benkrima, D. Belfennache, R. Yekhlef, and A. M. Ghaleb, *Chalcogenide Lett.* **20**(8), 609-618 (2023). <https://doi.org/10.15251/CL.2023.208.609>
- [14] M. Shkir, *Mater. Sci. Eng. B*, **284**, 115861 (2022). <https://doi.org/10.1016/j.mseb.2022.115861>
- [15] S.D. Lokhande, H.A. Varudkar, M.B. Awale, L.H. Kathwate, J.S. Dargad, and V.D. Mote, *Materials Letters*, **337**, 133919 (2023). <https://doi.org/10.1016/j.matlet.2023.133919>
- [16] F. Hadji, Y. Rassim, D. Belfennache, R. Yekhlef, N. Bounar, M.A. Bradai, M. Hemdan, and M.A. Ali, *Egypt. J. Chem.* **68**, 63 (2025). <https://doi.org/10.21608/ejchem.2024.283147.9600>
- [17] O.A. Akinwumi, K.O. Olumurewa, A.T. Famojuro, and O.O. Akinwunmi, *Next Materials*, **8**, 100883 (2025). <https://doi.org/10.1016/j.nxmate.2025.100883>
- [18] S. Mahdid, D. Belfennache, D. Madi, M. Samah, R. Yekhlef, and Y. Benkrima, *J. Ovonic. Res.* **19**(5), 535-545 (2023). <https://doi.org/10.15251/JOR.2023.195.535>
- [19] R. Ouldamer, D. Madi, and D. Belfennache, in: *Advanced Computational Techniques for Renewable Energy Systems, IC-AIRES, 2022*, Lecture Notes in Networks and Systems, **591**, edited by M. Hatti, (Springer, Cham, 2023). pp. 700-705. [https://doi.org/10.1007/978-3-031-21216-1\\_71](https://doi.org/10.1007/978-3-031-21216-1_71)
- [20] F. Saker, L. Remache, D. Belfennache, K.R. Chebouki, and R. Yekhlef, *Chalcogenide Letters*, **22**(2), 151 (2025). <https://doi.org/10.15251/CL.2025.222.151>
- [21] R.C. Greenhalgh, A. Abbas, V. Kornienko, and J.M. Walls, *Sol. Energy Mater. Sol. Cells*, **292**, 113742 (2025). <https://doi.org/10.1016/j.solmat.2025.113742>
- [22] Y. Bellal, A. Bouhank, D. Belfennache, R. Yekhlef, *East Eur. J. Phys.*, **(1)**, 170-176 (2025). <https://doi.org/10.26565/2312-4334-2025-1-16>
- [23] N.K. Singh, V. Koutu, and M.M. Malik, *J. Sol-Gel Sci. Technol.* **91**, 324 (2019). <https://doi.org/10.1007/s10971-019-05004-4>



- [24] I. Djerdj, Z. Jagli'ci'c, D. Ar'con, and M. Niederberger, *Nano scale*, **2**(7), 1096 (2010). <https://doi.org/10.1039/c0nr00148a>
- [25] U. Godavarti, V.D. Mote, and M. Dasari, *J. Asian Ceram. Soc.* **5**, 391 (2017). <https://doi.org/10.1016/j.jascer.2017.08.002>
- [26] L. Vegard, *Zeitschrift für Physik*, **5**(1), 17 (1921). <http://dx.doi.org/10.1007/BF01349680>
- [27] S. Roguai, and A. Djelloul, *Appl. Phys. A: Mater. Sci. Process.* **125**(12), 1 (2019). <https://doi.org/10.1007/s00339-019-3118-3>
- [28] M. Bouloudenine, N. Viart, S. Colis, J. Kortus, and A. Dinia, *Appl. Phys. Lett.* **87**, 05250 (2005). <https://doi.org/10.1063/1.2001739>
- [29] A. Manikandan, E. Manikandan, B. Meenatchi, S. Vadivel, S.K. Jaganathan, R. Ladchumananandasivam, M. Henini, *et al.*, *J. Alloys Compd.* **723**, 1155 (2017). <https://doi.org/10.1016/j.jallcom.2017.06.336>
- [30] I.S. Yahia, A.A.M. Farag, M. Cavas, and M.F. Yakuphanoglu, *Superlattices Microstruct.* **53**, 63 (2013). <https://doi.org/10.1016/j.spmi.2012.09.008>
- [31] A.C. Gandhi, W.S. Yeoh, M.A. Wu, C.H. Liao, D.Y. Chiu, W.L. Yeh, and Y.L., *Huang, Nanomaterials*, **8**(8), 632 (2018). <https://doi.org/10.3390/nano8080632>
- [32] G. Scamarcio, V. Spagnolo, G. Ventruti, M. Lugara, and M.G.C. Righini, *Phys. Rev. B*, **53**, R10489 (1996). <https://doi.org/10.1103/PhysRevB.53.R10489>
- [33] A.K. Ojha, M. Srivastava, S. Kumar, R. Hassanein, J. Singh, M.K. Singh, and A. Materny, *Vib. Spectrosc.* **72**, 90 (2014). <https://doi.org/10.1016/j.vibspec.2014.02.013>
- [34] W. Chebil, *Indian Journal of Pure & Applied Physics, (IJPAP)*, **53**(8), 521-529 (2015).
- [35] M. Soyulu, and M. Coskun, *J. Alloys. Compd.* **741**, 957 (2018). <https://doi.org/10.1016/j.jallcom.2018.01.079>
- [36] C.Y. Tsay, K.S. Fan, Y.W. Wang, C.J. Chang, Y.K. Tseng, and C.K. Lin, *Ceramics International*, **36**(6), 1791 (2010). <https://doi.org/10.1016/j.ceramint.2010.03.005>
- [37] J. Li, D. Yang, and X. Zhu, *Materials technology*, **33**(3), 198 (2018). <https://doi.org/10.1080/10667857.2017.1396775>
- [38] C.Y. Tsay, K.S. Fan, S.H. Chen, and C.H. Tsai, *J. Alloys. Compds.* **495**(1), 126 (2010). <https://doi.org/10.1016/j.jallcom.2010.01.100>
- [39] J. Li, X. Zhu, P. Gu, X. Zhang, X. Li, Y. Chen, and D. Yang, *Materials Technology*, **34**(2), 80 (2018). <https://doi.org/10.1080/10667857.2018.1523086>
- [40] N. Kaneva, A. Bojinova, K. Papazova, D. Dimitrov, I. Svinjarov, and M. Bogdanov, *Bulg. Chem. Commun.* **47**, 395 (2015).
- [41] M. Yilmaz, and A. Şakir, *Mater. Sci. Semicond. Process.* **40**, 162 (2015). <https://doi.org/10.1016/j.mssp.2015.06.064>
- [42] A. Maache, A.Chergui, D. Djouadi, B. Benhaoua, A. Chelouche, and M. Boudissa, *Optik*, **180**, 1018 (2019). <https://doi.org/10.1016/j.ijleo.2018.11.002>
- [43] J. Singh, *Optical Properties of Condensed Matter and Applications*, vol. 6, (John Wiley & Sons, 2006). <https://doi.org/10.1002/0470021942>
- [44] N. Shakti, and P.S. Gupta, *Appl. Phys. Res.* **2**(1), 19 (2010) <https://doi.org/10.5539/apr.v2n1p19>
- [45] A.A. Aboud, M. Shaban, and N. Revaprasadu, *RSC Adv.* **9**(14), 7729 (2019). <https://doi.org/10.1039/c8ra10599e>
- [46] S. Yang, B.Y. Man, M. Liu, C.S. Chen, X.G. Gao, C.C. Wang, and B. Hu, *Phys. B: Condens. Matter*, **405**(18), 4027 (2010). <https://doi.org/10.1016/j.physb.2010.06.050>
- [47] C. Song, F. Zeng, K.W. Geng, X.B. Wang, Y.X. Shen, and F. Pan, *J. Magn. Magn Mater.* **309**(1), 25 (2007). <https://doi.org/10.1016/j.jmmm.2006.06.012>
- [48] E. Gungor, T. Gungor, D. Caliskan, A. Ceylan, and E. Ozbay, *Appl. Surf. Sci.* **318**, 309 (2014). <https://doi.org/10.1016/j.apsusc.2014.06.132>
- [49] M. Ivill, S.J. Pearton, S. Rawal, L. Leu, P. Sadik, R. Das, A.F. Hebard, *et al.*, *New J. Phys.* **10**(6), 065002 (2008). <https://doi.org/10.1088/1367-2630/10/6/065002>
- [50] A.C. Tuan, *et al.*, *Phys. Rev. B*, **70**, 054424 (2004). <https://doi.org/10.1103/PhysRevB.70.054424>
- [51] B.K. Ridley, *Quantum Processes in Semiconductors*, 5<sup>th</sup> edn. (Oxford, 2013). <https://doi.org/10.1093/acprof:oso/9780199677214.001.0001>
- [52] S.H. Deng, M.Y. Duan, M. Xu, and L. He, *Physica B: Condensed Matter*, **406**(11), 2314 (2011). <https://doi.org/10.1016/j.physb.2011.03.067>
- [53] A. Salah, A.M. Saad, and A.A. Aboud, *Optical Materials*, **113**, 110812 (2021). <https://doi.org/10.1016/j.optmat.2021.110812>
- [54] A.T. Naziba, M.T. Nafisa, R. Sultana, Md.F. Ehsan, A.R.M. Tareq, R. Rashid, H. Das, *et al.*, *J. Magn. Magn. Mater.* **593**, 171836 (2024). <https://doi.org/10.1016/j.jmmm.2024.171836>
- [55] R.A. Torquato, S.E. Shirsath, R.H.G.A. Kiminami, and A.C.F.M. Costa, *Ceramics International*, **44**(4), 4126 (2018). <https://doi.org/10.1016/j.ceramint.2017.11.213>
- [56] M. Zhong, W. Wu, H. Wu, and S. Guo, *J. Alloys. Compds.* **765**, 69 (2018). <https://doi.org/10.1016/j.jallcom.2018.06.228>
- [57] J.K. Park, K.W. Lee, S.J. Noh, H.S. Kim, and C.E. Lee, *Curr. Appl. Phys.* **14**(2), 206 (2014). <https://doi.org/10.1016/j.cap.2013.11.004>
- [58] B. Salameh, A.M. Alsmadi, and M. Shatnawi, *J. Alloys. Compds.* **835**, 155287 (2020). <https://doi.org/10.1016/j.jallcom.2020.155287>
- [59] N.C. Mamani, *J. Alloys. Compds.* **695**, 2682 (2017). <https://doi.org/10.1016/j.jallcom.2016.11.183>
- [60] S. Ramasubramanian, R. Thangavel, M. Rajagopalan, A. Thamizhavel, K. Asokan, D. Kanjilal, and J. Kumar, *Curr. Appl. Phys.* **13**, 1547 (2013). <https://doi.org/10.1016/j.cap.2013.05.010>
- [61] Dhruvashi, and P.K. Shishodia, *Thin Solid Films*, **612**, 55 (2016). <https://doi.org/10.1016/j.tsf.2016.05.028>
- [62] X.J. Liu, C. Song, P.Y. Yang, F. Zeng, and F. Pan, *Appl. Surf. Sci.* **254**, 3167 (2008). <https://doi.org/10.1016/j.apsusc.2007.10.078>
- [63] W. Zhuliang, L. Xiaoli, J. Fengxian, T. Baoqiang, L. Baohua, and X. Xiaohong, *Rare. Metal. Mat. Eng.* **37**(5), 0831 (2008). [https://doi.org/10.1016/S1875-5372\(09\)60021-7](https://doi.org/10.1016/S1875-5372(09)60021-7)
- [64] H.-J. Lee, S.-Y. Jeong, C. Cho, and C. Park, *Appl. Phys. Lett.* **81**, 4020 (2002). <https://doi.org/10.1063/1.1517405>
- [65] C.B. Fitzgerald, M. Venkatesan, J.G. Lunney, L.S. Dorneles, and J.M.D. Coey, *Appl. Surf. Sci.* **247**, 493 (2005). <https://doi.org/10.1016/j.apsusc.2005.01.043>

- [66] L.S. Dorneles, M. Venkatesan, R. Gunning, P. Stamenov, J. Alaria, M. Rooney, J.G. Lunney, and J.M.D. Coey, *J. Magn. Magn. Mater.* **310**, 2087 (2007). <https://doi.org/10.1016/j.jmmm.2006.10.1017>
- [67] A. Zukova, A. Teiserskis, V. Kazlauskienė, Y.K. Gun'ko, and S. Dijken, *J. Magn. Magn. Mater.* **316**, e203 (2007). <https://doi.org/10.1016/j.jmmm.2007.02.090>
- [68] J.H. Kim, H. Kim, D. Kim, Y.E. Ihm, and W.K. Choo, *J. App. Phys.* **92**, 6066 (2002). <https://doi.org/10.1063/1.1513890>
- [69] R.K. Singhal, A. Samariya, Y.T. Xing, S. Kumar, S.N. Dolia, U.P. Deshpande, T. Shripathi, and E.B. Saitovitch, *J. Alloys. Compd.* **496**, 324 (2010). <https://doi.org/10.1016/j.jallcom.2010.02.005>

**ВПЛИВ ЛЕГУВАННЯ КОБАЛЬТОМ НА СТРУКТУРНІ, МОРФОЛОГІЧНІ, ОПТИЧНІ ТА МАГНІТНІ  
ВЛАСТИВОСТІ ТОНКИХ ПЛІВОК ZnO, ВИГОТОВЛЕНИХ ТЕХНІКОЮ УЛЬТРАЗВУКОВОГО НАПИЛЕННЯ**

**З. Даас<sup>а</sup>, А. Буабеллу<sup>а</sup>, К. Даас<sup>б</sup>, Д. Бельфеннаше<sup>с</sup>, К. Бензуаї<sup>а</sup>, М. Махталі<sup>а</sup>, Р. Єхлеф<sup>с</sup>**

<sup>а</sup>Лабораторія тонких плівок та інтерфейсів, Університет Костянтина I-Фрер Ментурі, 25017 Костянтин, Алжир

<sup>б</sup>Лабораторія математики та їх взаємодій, Університетський центр Буссуфа Абдельхафіда, Міла, Алжир

<sup>с</sup>Науково-дослідний центр промислових технологій CRTI, P.O. Box 64, Черага, 16014 Алжир, Алжир

Тонкі плівки оксиду цинку-кобальту ( $Zn_{1-x}Co_xO$ ) відносяться до напівпровідникового матеріалу на основі оксиду цинку (ZnO), легovanого кобальтом (Co). Цей матеріал вивчається головним чином через його модифіковані магнітні, електронні та оптичні властивості, зокрема в контексті розбавлених магнітних напівпровідників (РМП). У цьому дослідженні аналізується вплив легування кобальтом на структурні оптичні та магнітні властивості тонких плівок ZnO, виготовлених за допомогою недорогого, масштабованого методу ультразвукового напилення. Тонкі плівки оксиду цинку-кобальту ( $Zn_{1-x}Co_xO$ ) були успішно нанесені на скляні підкладки за допомогою методу ультразвукового напилення при температурі підкладки 450 °C, з концентраціями легування кобальтом  $x = 0\%$ , 1%, 3% та 5%. Рентгенівський дифракційний (XRD) аналіз виявив гексагональну структуру вюрциту для всіх зразків без вторинних фаз, що свідчить про ефективне включення іонів  $Co^{2+}$  у решітку ZnO. Раманівська спектроскопія вказала на появу структурного безладу та дефектних мод, що узгоджується зі збільшенням енергії Урбаха. Скануюча електронна мікроскопія (SEM) показала зернисту морфологію поверхні, а на всіх зразках видно неоднорідний малюнок поверхні. Атомно-силова мікроскопія (АСМ) показала збільшення шорсткості поверхні та розміру зерен зі збільшенням концентрації легування. Оптичні вимірювання підтвердили високий коефіцієнт пропускання у видимому діапазоні та поступове зменшення ширини оптичної забороненої зони від 3,21 eV до 2,95 eV зі збільшенням вмісту Co. Спектроскопія та вібраційний магнітометр (VSM) показали, що всі плівки є внутрішньо феромагнітними. Було виявлено, що походження феромагнетизму є внутрішньою властивістю тонких плівок ZnO, легованих кобальтом.

**Ключові слова:** *техніка напилення; тонкі плівки ZnO; легування кобальтом; раманівська спектроскопія; розбавлені магнітні напівпровідники (РМН)*

## STRUCTURAL, ELECTRONIC AND ELASTIC PROPERTIES OF POTASSIUM IODIDE, UNDER PRESSURE: AN AB-INITIO ANALYSIS STUDY

 Hamza Rekab-Djabri<sup>a,b,\*</sup>, S. Zaiou<sup>c,d</sup>,  Ahmed Azzouz-Rached<sup>e</sup>,  Ammar Benamrani<sup>f</sup>, Salah Daoud<sup>g</sup>,  D. Belfennache<sup>h</sup>, R. Yekhle<sup>f</sup>, Nabil Beloufa<sup>i</sup>

<sup>a</sup>Laboratory of Micro and Nanophysics (LaMiN), National Polytechnic School Oran, ENPO-MA, BP 1523 El M'Naouer 31000, Oran, Algeria

<sup>b</sup>Faculty of Nature and Life Sciences and Earth Sciences AMO University, Bouira 10.000, Algeria

<sup>c</sup>Laboratory for Studies of Surfaces and Interfaces of Solid Materials (LESIMS), University Setif 1, 19000 Setif, Algeria

<sup>d</sup>Faculty of Natural Sciences and Life, Setif-1 University, 19000 Setif, Algeria

<sup>e</sup>Faculty of Sciences, Saad Dahleb University of Blida 1, Route de Soumaa, B. P. 270, Blida, Algeria

<sup>f</sup>Laboratory of Materials Physics, Radiation and Nanostructures (LPMRN), Faculty of Sciences and Technology, University of Mohamed El Bachir El Ibrahimi-BBA, 34000, Bordj Bou Arreridj, Algeria

<sup>g</sup>Laboratory of Materials and Electronic Systems, Faculty of Sciences and Technology, University Mohamed El Bachir El Ibrahimi of BBA, 34000 Bordj Bou Arreridj, Algeria

<sup>h</sup>Research Center in Industrial Technologies CRTI, P.O. Box 64, Cheraga, 16014 Algiers, Algeria

<sup>i</sup>Hydrometeorological Institut for Formation and Research IHFR, Oran, Algeria

\*Correspondence Author E-mail: [belfennachedjamel@gmail.com](mailto:belfennachedjamel@gmail.com)

Received May 14, 2025; revised July 16, 2025; accepted July 28, 2025

In this work, a recent version of the full potential linear muffin-tin orbitals (FP-LMTO) method was employed, using the local density approximation (LDA) within the framework of density functional theory (DFT). This approach was applied to study the structural, electronic and elastic behavior of the potassium iodide (KI) compound under pressure. The calculated structural parameters exhibit strong agreement with available theoretical and experimental data. The RS phase was identified as the most stable structure for KI material. The phase transition from NaCl-type (B1) to CsCl-type (B2) phase occurs at pressure of 1.633 GPa, which is quite consistent with the experimental values. Furthermore, the band structure of KI revealed a wide-band gap semiconductor behavior across all examined phases. The obtained bulk modulus values were relatively low, suggesting weak resistance to fracture. The elastic constants for KI in RS, CsCl, ZnS, HCP, and WZ structures were determined and found to meet Born's stability conditions. We esteem, there is no values available in the literature on the elastic constants for KI in CsCl, ZnS and WZ phases. All analyzed structures displayed ductile characteristics and ionic bonding features. Additionally, anisotropic properties were observed in all phases. The compound's stiffness was evaluated using Poisson's ratio and Cauchy's pressure. Results indicated that the CsCl phase is the most rigid among the studied configurations.

**Keywords:** Potassium iodide (KI); FP-LMTO; Electronic properties; Elastic properties; Phase transition

**PACS:** 73.50.-h, 73.50.Pz

### 1. INTRODUCTION

Alkali halides, such as potassium iodide (KI), are known as insulating salts composed of alkali metal cations and halide anions, with ions derived from group IA and VIIA elements in the periodic table. Under standard conditions, these materials typically crystallize in the Rocksalt (RS) structure [1]. Alkali iodides have played a crucial role in solid-state physics research since the 20<sup>th</sup> century [2-6], and continue to do so in more recent studies [7-9]. They have attracted considerable interest due to their unique features, such as crystal structure transitions under elevated pressures. Within the alkali halide family, potassium iodide (KI) has been specifically selected for this investigation. These compounds are widely recognized in the scientific community. KI, for instance, is frequently cited in nanoscience research, including studies involving single-walled carbon nanotubes [10,11].

Additionally, KI and similar materials are utilized in chemical processes and have notable medical applications, particularly in thyroid-related treatments. While KI has been examined both experimentally and theoretically in its RS phase across various studies, its other structural forms have received less attention. As an example, for the RS phase, the experimental lattice constant was reported as 7.094 Å [7], while in the CsCl structure it measured 7.342 Å [12]. The bulk modulus (B) for KI was experimentally found by Weir *et al.* [13] to be 11.6 GPa, whereas theoretical results from Cortona *et al.* [14] suggest a value of 13.8 GPa. A particularly interesting aspect of alkali halides is their capacity to undergo phase changes under low pressure. The pressure at which such structural phase transitions occur is referred to as the transition pressure (Pt).

According to experiments, at comparatively low pressures, a phase change from the RS structure (B1) to the CsCl structure (B2) takes place. For KI, transition pressure values were determined by Asaumi *et al.* [5] to be 1.9 GPa and Barsch *et al.* [17] to be 1.73 GPa. In the RS structure, the electrical characteristics of KI have been examined. Teegarden *et al.* [20] determined the energy band gap (Eg) values from absorption spectra graphs, and the values for KI

in the RS structure were 6.1 eV and 6 eV. Hopfield *et al.* [21] conducted additional experimental work that yielded an energy band gap of 6.34 eV for KI in the RS structure. The energy band gap for both KI in RS was also calculated. Using the full potential linearized muffin-tin orbital (FP-LMTO) method, the results showed that the KI was 5.984 eV [7], 4.26 eV [22], and 5.951 eV [23]. The first-principles linearized augmented-plane-wave band method yielded the same results. These energy band gap data show that the compound KI in the RS structure exhibits wide-band gap semiconducting properties. Numerous elastic constants and moduli, including the bulk and young moduli, can be used to depict the elastic properties of any compound. But for cubic structures, the most fundamental elastic constants are  $C_{11}$ ,  $C_{12}$ , and  $C_{44}$ ; for hexagonal structures, there are two more:  $C_{13}$  and  $C_{33}$ . Numerous theoretical and experimental approaches have been used to examine the elastic constants for KI. Using the ultrasonic pulse technique, Norwood and Briscoe determined the elastic constants for KI and discovered that  $C_{11}$ ,  $C_{12}$ , and  $C_{44}$  have values of 27.1, 4.5, and 3.64 GPa, respectively [24]. Bridgman reported  $C_{11}$ ,  $C_{12}$ , and  $C_{44}$  values of 33.2, 5.78, and 6.2 GPa [25]. The homogenous deformation method, on the other hand, served as the foundation for Sarkar and Sengupta's theoretical computation of the elastic constants, which yielded values of 31.7, 3.2, and 4.2 GPa for  $C_{11}$ ,  $C_{12}$ , and  $C_{44}$ , respectively [19]. Lastly, Gahn *et al.* [26] determined the Young modulus to be 15.3 GPa.

This study attempts to increase our understanding of the structural, elastic, and electrical characteristics of the compound KI in the following structures: wurzite (WZ), hexagonal close packed (A3), zincblende (ZB), nickel arsenide (NiAs), rock salt (RS), and cesium chloride (CsCl).

## 2. COMPUTATIONAL DETAILS

Within the functional of density functional theory (DFT) [27-29], the FP-LMTO method, as implemented in the LMTART code [30], was used to accomplish the computations given in this work. We employed the local density approximation (LDA) for exchange correlation potential, as specified by *Benkrama et al.* [31-33], for the electron-electron interaction in the total energy calculations. Using spherical harmonics, the electron charge density and crystal potential inside muffin-tin (MT) spheres were increased up to  $l_{max} = 6$ . The parameters utilized in the current computations are listed in Table 1 and include the radius of the muffin-tin (RMT) spheres, the number of plane waves (NPLW) employed, and the kinetic energy required to guarantee convergence (Ecutoff) for each of the eight crystal structures that were examined.

**Table 1.** The plane wavenumber NPLW, energycut-off (in Ry) and the muffin-tin radius (RMT) (in a.u) used in calculation for binary KI.

Structure	NPLW	$E_{cuttot}(Ry)$	RMT(u.a)	
	KI	KI	K	I
NaCl(B1)	223	12.6	3.26	3.393
CsCl(B2)	215	11.1	3.496	3.496
ZnS(B3)	228	11	3.058	3.313
Wz(B4)	390	9.1	3.046	3.224
NiAs(B8-1)	136	21.7	3.236	3.368
HCP (A3)	136	21.7	3.807	3.807

In the cubic symmetry of the NaCl (B1), CsCl (B2), and ZnS (B3) structures shown in Fig. 1(a, b, and c), the unit cell volume is solely dependent on the lattice constant a.

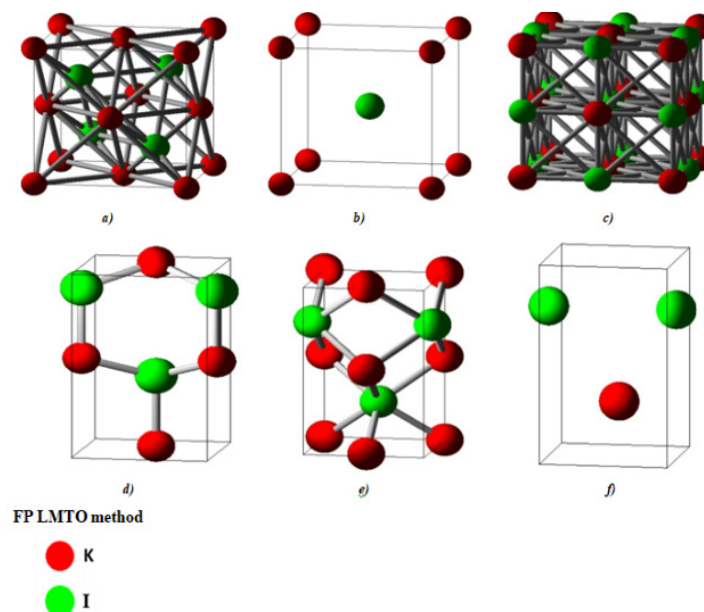


**Figure 1.** Crystal structure of KI in a-NaCl(B1), b-CsCl(B2), c-ZnS(B3), d- Wurtzite (B4), e-HCP(A3), and h-NiAs(B8\_1)

The unit cell volume in other structures, such as wurtzite (B4), NiAs (B81), and HCP (A3), as shown in Fig. 1(d, e, and f), relies on several lattice constants ( $z$ ,  $a$ ,  $c/a$  ratio, and internal parameter  $u$ ); hence, each of these structures needs to be optimized. Table 2 lists the locations of the potassium (K) and iodide (I) atoms in each of the KI compound's aforementioned structures.

These structures have the following space groups: B1:  $Fm\bar{3}m$ , B2:  $Pm\bar{3}m$ , B3:  $F43m$ , B4:  $P63mc$ , A3:  $P63/mmc$ , and B81:  $P63/mmc$ .

**Table 2.** Location of atoms for the six phases

	Potassium (K)		Iodide (I)	
	1 <sup>st</sup> atom	2 <sup>nd</sup> atom	1 <sup>st</sup> atom	2 <sup>nd</sup> atom
NaCl(B1)	0.0 ;0.0 ;0.0		1/2; 1/2; 1/2	
CsCl(B2)	0.0 ;0.0 ;0.0		1/2; 1/2; 1/2	
ZnS(B3)	0.0 ;0.0 ;0.0		1/4; 1/4; 1/4	
Wz(B4)	0.0 ;0.0 ;0.0	1.2; -1/2√3; 1/2	0.0; 0.0; u	1.2; -1/2√3; (0.5+u)
NiAs(B8-1)	0.0 ;0.0 ;0.0	0.0; 0.0; 1/2	1.2; 1/√12; 1/4	1.2; -1/√12; 3/4
HCP (A3)	1.2; 1/2√3; 1/4		1.2; 1/2√3; 3/4	

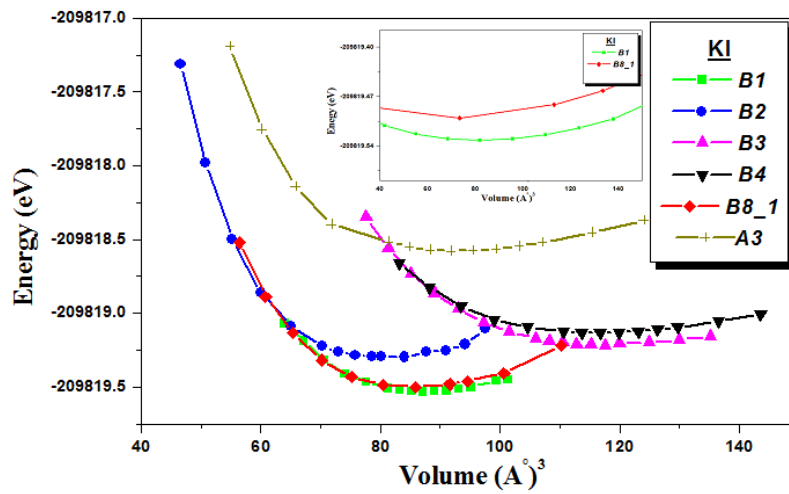


**Figure 2.** Total energy versus volume for six phases of KI in the LDA approximation

### 3. RESULTS AND DISCUSSION

#### 3.1. Structural phase stability

We plotted the  $E(V)$  curves in this work to determine the structural properties of the semiconductor compound KI for each of the six structures considered: NaCl (B1), CsCl (B2), ZnS (B3), Wurtzite (B4), NiAs (B8\_1) and HCP (A3). Using the Murnaghan equation of state (EOS), which can be written as follows [27], the equilibrium lattice constant  $a_0$ , the bulk modulus  $B_0$  and the pressure derivative of the bulk modulus  $B_0'$  were calculated by minimizing the total energy.

$$E(V) = E_0 + \frac{B_0}{B_0(B_0-1)} \left[ V \left( \frac{V_0}{V} \right)^{B_0} - V_0 \right] + \frac{B_0}{B_0} (V - V_0), \quad (1)$$

with  $V_0$  is the volume of the equilibrium and  $E_0$  is the energy of the ground state that corresponds to that volume. The minimum of the curve  $E_{tot}(V)$  provides the constant of the equilibrium lattice.

$B_0$ : the compressibility modulus is determined by the following equation:

$$B_0 = \left( V \frac{\partial^2 E}{\partial V^2} \right). \quad (2)$$

$B_0'$ : the derivative of the compressibility module:

$$B_0' = \frac{\partial B}{\partial P}. \quad (3)$$

Table 3 lists the results obtained for the structural parameters, together with the available experimental [13] and theoretical results [14], [18], [7], and [23]. Table 3 makes it evident that our results match well with those derived from previous experimental and ab-initio computations. According to Table 3's data, LDA understates the lattice parameter,  $a$ , for the B1 structure by roughly 0.39% when compared to the experimental value of 7.067 [13]. However, Table 3 shows that the first derivative of the bulk modulus is underestimated in comparison to the experimental data, and the computed bulk modulus is inflated in LDA, accessible experimental results. In actuality, the bulk modulus and its first derivative values are more susceptible to variations in the parameters employed in ab initio computations.



**Table 3.** Calculated structural parameters: bulk modulus  $B_0$  and its first derivatives  $B'_0$ , equilibrium lattice constants  $a$ , and structural parameter  $c/a$  for several phases examined for KI

Parameters		NaCl (B1)	CsCl (B2)	ZnS (B3)	WZ (B4)	NiAs (B8_1)	HCP (A3)
KI	This Work	87.21	77.933	117.95	116.25	85.13	92.41
	Other work						
$V_0(\text{\AA}^3)$	Theo						
	Exp						
$a_0(\text{\AA})$	This Work	7.039	4.271	7.784	5.916	4.853	4.027
	Other work						
	Theo	7.03 <sup>c</sup> , 7.213 <sup>d</sup> , 7.094 <sup>e</sup>					
	Exp	7.067 <sup>a</sup>					
$B_0(\text{GPa})$	This Work	15.299	18.535	9.856	8.826	17.35	10.885
	Other work						
	Theo	11.6 <sup>a</sup> , 13.8 <sup>c</sup>					
	Exp						
$B'_0$	This Work	3.795	4.226	3.807	4.028	3.335	4.101
	Other work						
	Theo						
	Exp						
$c/a$	This Work					1.719	1.633
$E_{\text{min}}(\text{Ryd})$		-15427.90	-15427.886	-15427.88	-15427.8		-15427.3

a-Ref [13], c-Ref [14], d-Ref [18], e-Ref [23], g-Ref [7],

Five other phases are examined in order to examine how atom positions affect the structural characteristics of KI: CsCl (B2), ZnS (B3), WZ (B4), NiAs (B8\_1), and HCP (A3). Our results for the B2, B3, B4, B8\_1, and A3 phases are predictions and could be used as a guide for future research because, as far as we are aware, no additional ab-initio calculations or experimental data regarding the structural parameters for KI in these phases are available in the literature.

### 3.2. Phase transition pressure

A change in the lattice structure, or phase transformation, results in a change in the properties. According to experiments, exposing a material to high pressures might result in a noticeable change in its characteristics that indicates modifications to the structures [5, 18, 12, 34]. For instance, numerous tests have demonstrated that the lattice structure changes from RS to CsCl when high pressure is applied to KI.

Using the enthalpy  $H$ , which contains the following formula, is a more straightforward and precise way to determine the transition pressure [4, 30].

$$H = E + P.V, \quad (4)$$

At the transformation point, the enthalpy of two structures will be the same. Equation (4) can be used to demonstrate this in the following way:

$$P_t = -\frac{dE}{dV}. \quad (5)$$

$$P_t \cdot dV = -dE. \quad (6)$$

By integrating both sides:

$$P_t (V_2 - V_1) = -(E_2 - E_1). \quad (7)$$

Rearranging the variables:

$$E_1 + P_t V_1 = E_2 + P_t V_2. \quad (8)$$

Using equation (5):

$$H_1 = H_2. \quad (9)$$

Since both coordinates (enthalpy and pressure) are the same during the phase transformation, a graph of enthalpy vs. pressure for two structures that undergo transition will, in practice, have a crossing point. The transition pressure is the pressure present at this moment. In our earlier study, this approach produced very positive results [35-38, 84, 81, 80, 79]. Fig. 3 displays the enthalpy versus pressure plots that were utilized to determine the transition pressures. Table 4 lists the transition pressure values along with some of the available computed and experimental results. The  $P_t$  levels found in this study agree with those found in the previous studies listed in Table 4.

**Table 4.** Calculated values of the transition pressure  $P_t$  and transition volumes for KI using the GGA approximation

Phases	Volume		Transition pressure (GPa)		
	$V(\text{\AA}^3)$	Reduct (%)	Presentwork	Other works	
				Theo	Exp
B1→B2	$V_{B1}$ 87.217	10.64	1.633	2 <sup>a</sup>	1.73 <sup>b</sup> 1.9 <sup>c</sup>
	$V_{B2}$ 77.933				

a-Ref. [7], b-Ref. [17], c-Ref. [5]



One transition is predicted by Fig. 3 at the curves' junction sites (equal enthalpies). At roughly 01.633 GPa, the B1 structure gives way to the B2 structure above the crossover from B1 to B2. Our estimated pressure of 1.633 GPa for the B1→B2 transition is quite consistent with the experimental values of Barsch et al. [17] and Assaumi [17], which differ by 18.35%, 5.60 %, and 14.05 %, respectively, and with the earlier theoretical values of 2 GPa found by Ramola *et al.* [7].

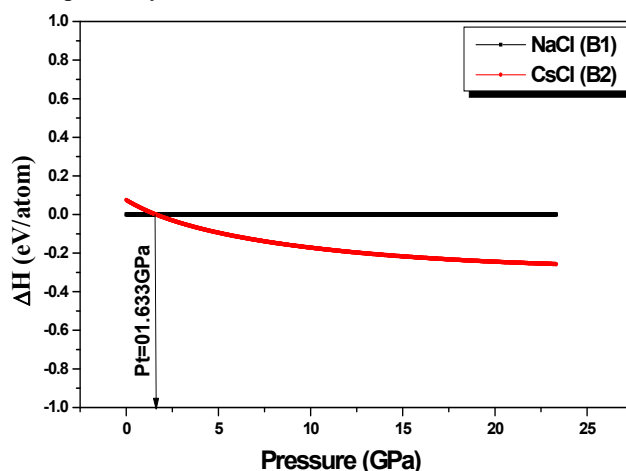


**Figure 3.** Variation of  $\Delta H$  (eV/atom) versus  $P_t$  (GPa) for CsCl-B2. The reference Gibbs free energy is set for the rocksalt phase NaCl-B1

### 3.3. Electronic properties

#### 3.2.1. Bande structure

The energy is computed along high symmetry lines, and the band structure (BS) was obtained with the LDA approximation. The optimized lattice constants were used in the calculations. Figure 4 displays the BS graphs for KI in each of the structures that were studied.

The BS graphs show the band gap between the valence and conduction bands. Together with the findings of earlier research on the RS structure, Table 5 lists the values of  $e_g$ , which is computed as the difference between MVB and MCC. With the other known experimental and theoretical findings, the energy band gap value is underestimated by the LDA approximation. Direct energy band gaps along the  $\Gamma$  symmetry point are observed for the following structures: RS, ZB, NiAs, HCP, and WZ, with values listed in Table (5). In contrast, the CsCl structure exhibits an indirect band gap between the high symmetry points of M and  $\Gamma$ .

In every structure examined in this work (RS, CsCl, ZB, HCP, NiAs, and WZ) the energy band gap values show that KI is a semiconductor.

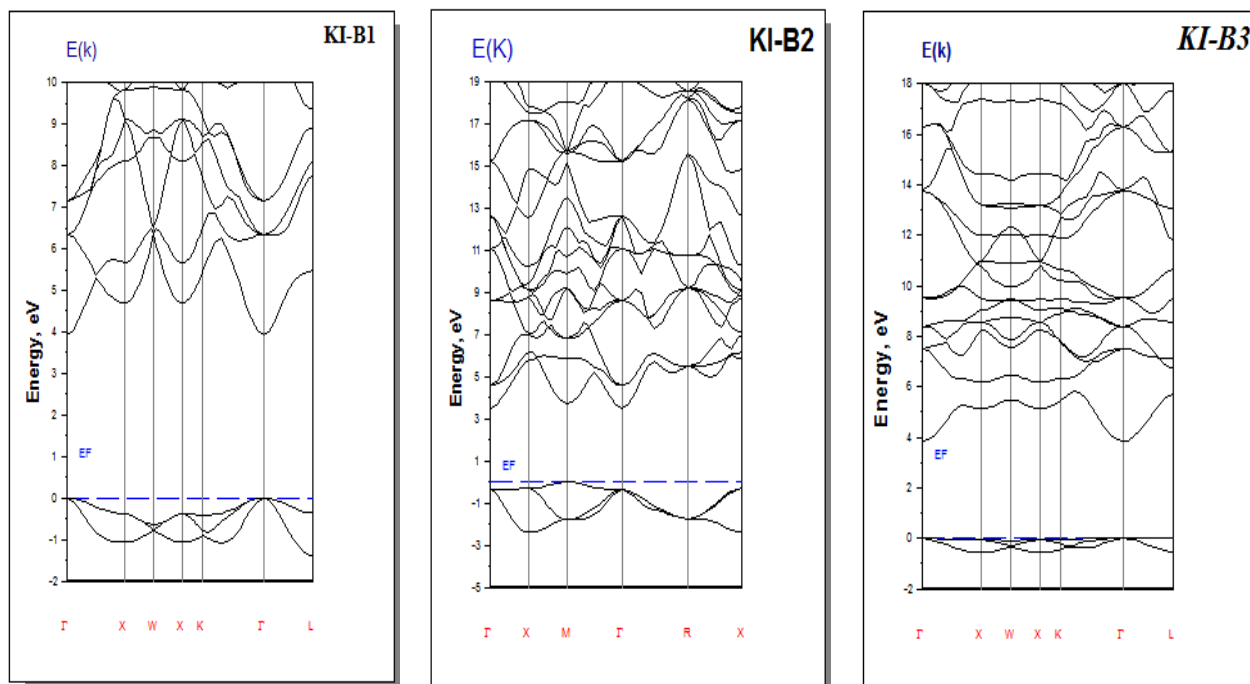


**Figure 4.** Band structure of KI, in different structures studied

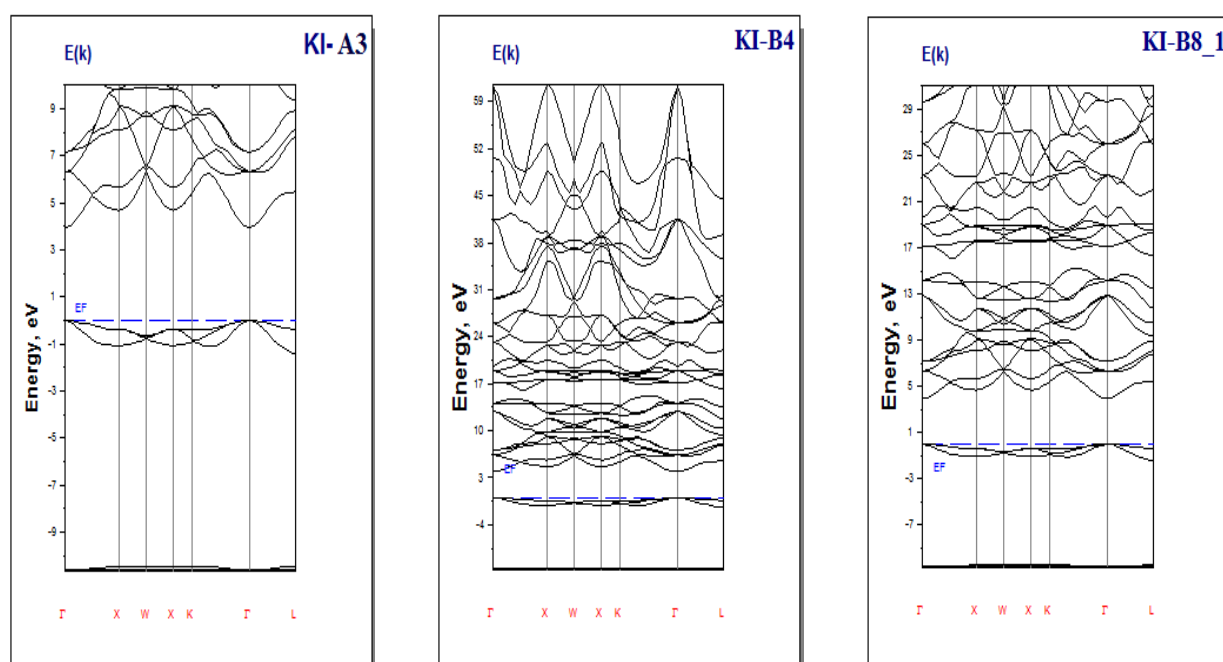


Figure 4. Band structure of KI, in different structures studied  
(continued)

Table 5. The gap calculated for KI in different structures studied.

	Phase	Nature of gap	Present work	Type	Other works
KI	B1	$\Gamma \rightarrow \Gamma$	3.936	direct	5.984 <sup>b</sup> , 6.2 <sup>c</sup> , 4.26 <sup>d</sup> , 5.951 <sup>e</sup> <sub>mBJ</sub> 6.34 <sup>a</sup> <sub>exp</sub>
	B2	$M \rightarrow \Gamma$	3.512	Indirect	
	B3	$\Gamma \rightarrow \Gamma$	3.836	direct	
	B8_1	$\Gamma \rightarrow \Gamma$		direct	
	A3	$\Gamma \rightarrow \Gamma$		direct	

a-Ref. [21], b-Ref. [7], c-Ref. [62], d-Ref. [22], e-Ref. [23]

### 3.2.2. Density of state

As a function of energy, the DOS displays the number of states that electrons can occupy. Figure 5 displays the DOS graphs for KI.

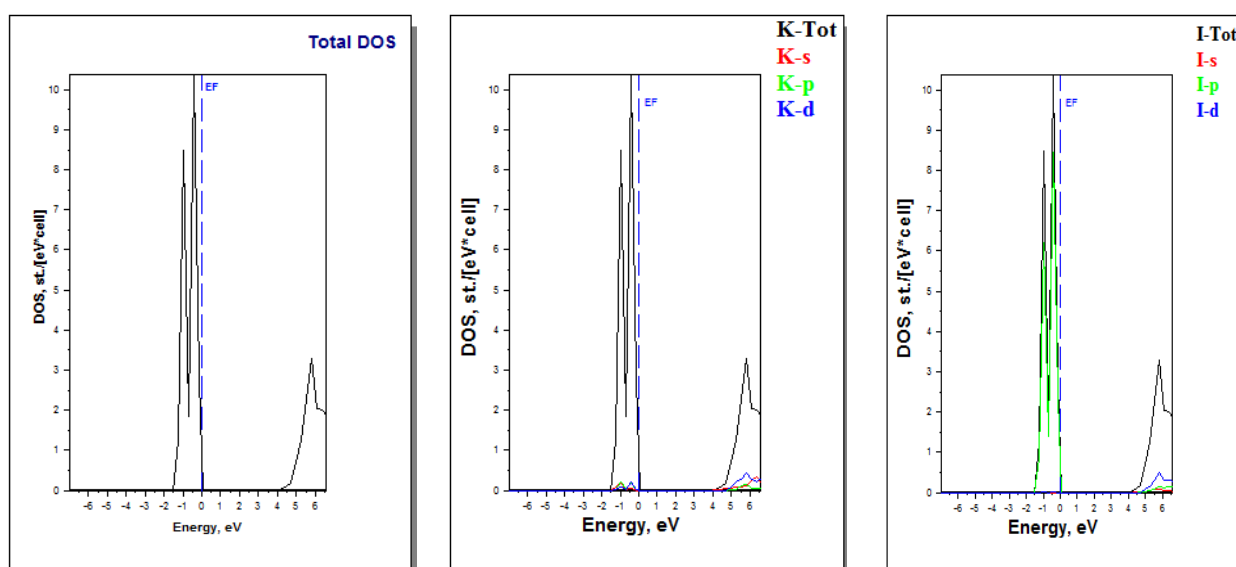
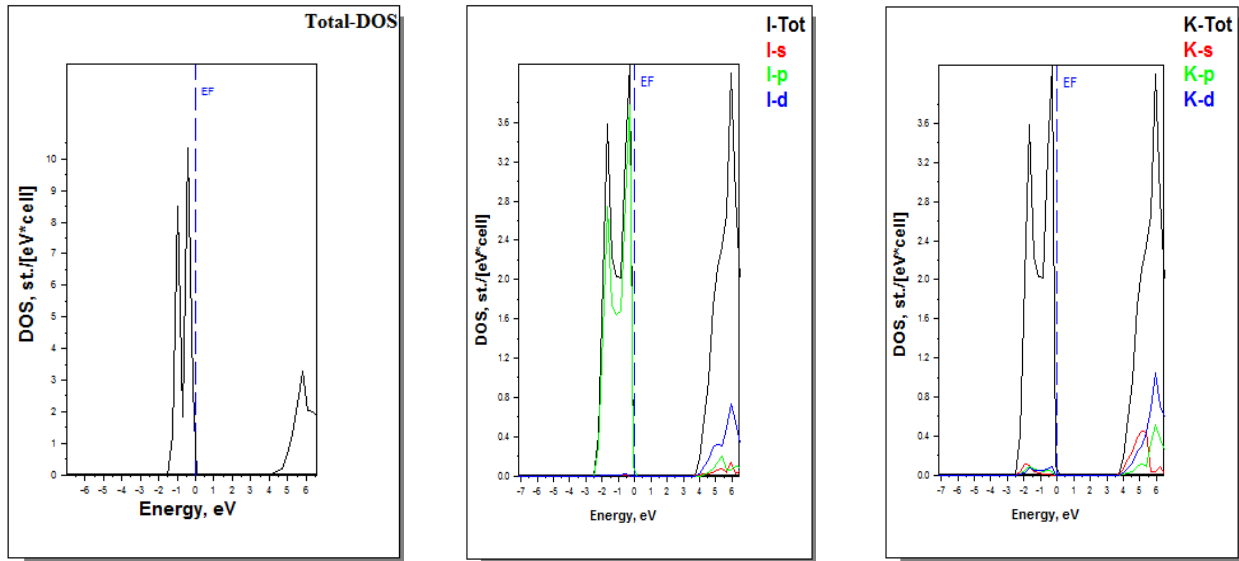


Figure 5. Density of states (DOS) of KI in the different structures studied



**Figure 5.** Density of states (DOS) of KI in the different structures studied  
(continued)

Since peaks B3, B4, B8\_1, and A3 are very identical to peak B1, we did not include them. The Fermi energy (EF) is shown by the dotted line in the DOS graphics. There is only one peak for the energies below the Fermi energy in the structures RS, CsCl, ZB, A3, and NiAs. The p-state in the iodide contributes the most to the DOS, while the p-state in the potassium contributes only a little. In contrast, three peaks are visible in the WZ structure: the first peak is contributed by the potassium's s-state, the second peak combines the contributions of the potassium's p-state and the iodide's s-state, and the third peak is created by the iodide's p-state with a minor contribution from the potassium's p-state.

### 3.4. Elastic properties

Knowing a material's elastic properties, such as its elastic constants and moduli, allows one to predict how the material will react to external stress. Because of the cubic structures' symmetry, only three elastic constants « $C_{11}$ ,  $C_{12}$ , and  $C_{33}$ » are needed [39], while five elastic coefficients « $C_{11}$ ,  $C_{12}$ ,  $C_{13}$ ,  $C_{33}$ , and  $C_{55}$ » were needed for the hexagonal systems [40]. One crucial instrument for assessing a material's stability is its elastic constants. The generalized requirements of stability must be met for a material to be deemed mechanically stable, and they are [41].

$$C_{11} > 0, C_{11} - C_{12} > 0, C_{44} > 0 \text{ and } C_{11} + 2C_{12} > 0, \quad (9)$$

for the cubic structures. Additional criteria are required for the hexagonal structures as follows [41]:

$$C_{11} > |C_{12}| \text{ and } C_{55} > 0, \quad (10)$$

where:  $C_{44} = C_{55}$  for the hexagonal structures.

When anticipating a material's mechanical characteristics, including its stiffness, hardness, brittleness, and ductility, elastic moduli are crucial. The bulk modulus (B), shear modulus (S), Young's modulus (Y), compressibility ( $\beta$ ), anisotropic factor (A), Poisson's ratio ( $\nu$ ), and so on are examples of these elastic moduli.

The elastic properties KI in RS, CsCl, ZB, NiAs and WZ structures at ambient pressure were investigated in this work using the optimized lattice constants. This was accomplished by calculating the stress produced by a tiny strain applied to the optimized unit cell, which in turn led to the computation of the elastic constants. Numerous models have been proposed to determine the elastic moduli in terms of the elastic constants; the most widely used models are the Voigt, [42], Reuss, [43], and Hill [44] models. The Hill model is taken into consideration in this work. The Hill model's bulk modulus is determined by averaging the Voigt and Reuss models' bulk moduli, as follows:

$$B_H = \frac{B_V + B_R}{2}, \quad (11)$$

where  $B_H = B_V = B_R = \frac{1}{3}(C_{11} + 2C_{12})$  for the cubic structures<sup>45</sup>. While for the hexagonal structures, the formulas are as follows [45-48]:

$$B_V^{Hex} = \frac{1}{9}(2C_{11} + C_{33} + 2C_{12} + 4C_{13}), \quad (12)$$

$$B_R^{Hex} = \frac{(C_{11} + C_{12})C_{33} - 2C_{13}^2}{C_{11} + C_{12} + 2C_{33} - 4C_{13}}, \quad (13)$$

$$B_H^{Hex} = \frac{B_V + B_R}{2}. \quad (14)$$

The shear modulus is also calculated using the following formulas [67, 68, 71, 72]

$$S_V^{Cubic} = \frac{C_{11} - C_{12} + 3C_{44}}{5}, \quad (15)$$

$$S_R^{Cubic} = \frac{5(C_{11} - C_{12})C_{44}}{3(C_{11} - C_{12}) + 4C_{44}}, \quad (16)$$

$$S_H^{Cubic} = \frac{S_V^{Cubic} + S_R^{Cubic}}{2}, \quad (17)$$

$$S_V^{Hex} = \frac{1}{30} [7C_{11} - 5C_{12} + 12C_{44} + 2C_{33} - 4C_{13}], \quad (18)$$

$$S_R^{Hex} = \frac{5}{2} \left[ \frac{((C_{11} + C_{12})C_{33} - 2C_{12}^2)C_{44}C_{66}}{3B_V^{Hex}C_{44}C_{66} + ((C_{11} + C_{12})C_{33} - 2C_{12}^2)(C_{44} + C_{66})} \right], \quad (19)$$

with  $C_{66}$  being given as [48-50].

$$C_{66} = \frac{1}{2}(C_{11} - C_{12}), \quad (20)$$

$$S_H^{Hex} = \frac{S_V^{Hex} + S_R^{Hex}}{2}. \quad (21)$$

The following formulas [51, 52] are used to compute the Young's modulus (Y) and Poisson's ratio using the Hill model results of the bulk and shear moduli.

$$Y = \frac{9SB}{S + 3B}, \quad (22)$$

$$\nu = \frac{3B - 2S}{2(3B + S)}. \quad (23)$$

The anisotropy factor and the material's hardness were among the other variables that were computed. The relations [53,54] were used to compute the anisotropic factor.

$$A_{Cubic} = \frac{2C_{44}}{C_{11} - C_{12}}, \quad (24)$$

$$A_{Hex} = \frac{4C_{44}}{C_{11} + C_{33} - 2C_{13}}. \quad (25)$$

Chen's Vickers hardness formula, which is as follows [55], was applied to determine the hardness.

$$H_v = 2 \left( \frac{S}{B^2} \right)^{0.585} - 3. \quad (26)$$

Moreover, Cauchy pressure (Cs) was calculated using the forms as [56]:

$$C_S^{Cubic} = C_{12} - C_{44}, \quad (27)$$

$$C_S^{Hex} = C_{12} - C_{55}. \quad (28)$$

The Born's conditions are satisfied by the elastic constants for KI in the RS, CsCl, Wz, HCP, and ZB structures displayed in Table 6 [57]. Using Murnaghan's equation of state [30], the values for the bulk modulus are in excellent agreement with the findings shown in tables 3. The structures RS, CsCl, ZB, and WZ have low bulk modulus values, which suggest that they have poor resistance to breaking under pressure. On the other hand, because of its largest bulk modulus value, CsCl is thought to be the hardest structure for KI and the least compressible ( $\beta = 1/B$ ).

Out of all the structures, the ZB structure has the maximum compressibility and the lowest bulk modulus.

**Table 6.** The elastic constants, the bulk modulus calculated by Hill's approximation for KI in RS, CsCl and ZB and Wz structures in (GPa)

Phase		C <sub>11</sub>	C <sub>12</sub>	C <sub>44</sub>	B	C <sub>13</sub>	C <sub>33</sub>	C <sub>55</sub>
NaCl (B1)	<i>This Work</i>	24.1738	3.890	3.8400	10.651			
	<i>Exp Reslt</i>	27.1 <sup>a</sup>	4.5 <sup>a</sup>	3.64 <sup>a</sup>	6.2			
		33.2 <sup>b</sup>	5.78 <sup>b</sup>	<sup>b</sup>				
	<i>Othr Theor</i>	31.7 <sup>c</sup>	3.2 <sup>c</sup>	4.2 <sup>c</sup>				
CsCl (B2)	<i>This Work</i>	33.9234	3.195	2.3456	13.437			
ZnS (B3)	<i>This Work</i>	7.5379	6.916	5.0597	7.123			
WZ (B4)	<i>This Work</i>	14.7989	5.610		9.543	7.9129	13.485	3.222

a-Ref. [24], b-Ref. [25], c-Ref. [19].

Table 7 shows the factors and elastic moduli. If the anisotropic component  $A=1$ , the material is said to be totally isotropic; any departure indicates the degree of anisotropy. Since none of the structures « RS, CsCl, and ZB » have an isotropy of one, they all exhibit anisotropic behavior. Conversely, the WZ structure exhibits isotropic behavior with an isotropy of nearly 1.

**Table 7.** For KI compound in RS, CsCl, ZB, and WZ structures, the computed Hill's Shear modulus ( $S_H$ ), Young's modulus ( $Y_H$ ) in (GPa), Poisson's ratio ( $\nu_H$ ), the anisotropic ratio ( $A$ ), the B/S ratio, the Cauchy pressure (PC) in (GPa), the compressibility ( $\beta$ ) in (1/GPa), and the Hardness ( $H_v$ )

Symbol	NaCl (B1)	CsCl (B2)	ZnS (B3)	WZ (B4)
$S_H$	5.735	5.55	1.935	3.565
$Y_H$	14.586	14.635	5.322	9.51
$\nu_H$	0.271	0.318	0.375	0.333
$A$	0.3786	0.1527	16.2875	1.0358
$B_H/S_H$	1.8572	2.4211	3.6811	2.6768
$C_s$	0.0504	0.8496	1.8569	2.3838
$\beta_H$	0.0938	0.7442	0.1404	0.1048
$H_v$	-0.3071	-0.0629	-2.35947	-1.6705

The (B/S) ratio can be used to assess a material's brittleness or ductility. Every structure in Table 7 has B/S ratios greater than 1.75, indicating that the KI in those structures is ductile. In contrast, the RS has the highest shear modulus, which is extremely near to that of the CsCl structure. A material's stiffness can be studied using Young's modulus ( $Y$ ); the greater the value of  $Y$ , the stiffer the material. With the largest value of  $Y$ , the CsCl structure of KI appears to be the stiffest structure. This is supported by the fact that the CsCl structure has the highest hardness ( $H$ ). In contrast, the ZB structure has the lowest  $Y$  and  $H$ , making it the least stiff. The inferences drawn from the bulk modulus values are supported by these findings.

All of the structures in Table 7 exhibit positive Cauchy's pressure ( $C_s$ ) values, indicating that ionic bonding is the predominant bonding type. Although ionic bonds remain the predominant form of bonding, it is reasonable to state that the RS structure has the "highest covalent bonding" of all because its  $C_s$  has the lowest value, which is quite near to zero. Since all of the  $\nu$  values are greater than 0.25, which indicates ionic bonding inside the material, this is consistent with the Poisson's ratio results.

## 5. CONCLUSION

Potassium iodide was investigated using the FP-LMTO technique within the density functional theory (DFT) and the LDA Approximation in a number of distinct structures, including RS, CsCl, ZB, NiAs, HCP, and WZ. The adjusted lattice parameters and bulk modulus matched previous theoretical and experimental results. Using the LDA approximation, band gaps were determined and compared to the findings of existing theoretical and experimental research. The resulting values are lower than the reference values, which should be noted. It is well known that LDA lowers band gaps. The improved lattice constants were also used to analyze the elastic properties. The elastic constants for the RS, CsCl, ZB and WZ structures satisfied Born's stability requirements. The CsCl structure had the highest bulk modulus when compared to other structures, suggesting that it was more resistant to breaking. In contrast, the ZB structure exhibited the lowest bulk modulus. Poisson's ratio values varied from 0.271 to 0.375, despite the fact that all structures had positive Cauchy pressure values, which suggested ionic bonding inside the lattice. It was found that the ZB structure had the lowest hardness and the RS structure the highest. The rigidity of the materials was assessed using Young's modulus, where the ZB structure had the lowest value and the RS structure the highest. For all stable structures, the anisotropic component ( $A$ ) was found to be anisotropic, with values that were far from unity.

## ORCID

©Hamza Rekab Djabri, <https://orcid.org/0000-0002-2458-1335>; ©Ahmed Azzouz Rached, <https://orcid.org/0000-0003-4852-1000>  
 ©Ammar Benamrani, <https://orcid.org/0000-0002-6886-656X>; ©Djamel Belfennache, <https://orcid.org/0000-0002-4908-6058>

## REFERENCE

- [1] B.P. Mamula, B. Kuzmanović, M.M. Ilić, N. Ivanović, and N. Novaković, *Physica B: Condensed Matter*, **545**(36), 146 (2018). <https://doi.org/10.1016/j.physb.2018.06.008>
- [2] R.G. Bessent, and A.W. Runciman, *Br. J. Appl. Phys.* **17**(8), 991 (1966). <https://doi.org/10.1088/0508-3443/17/8/302>
- [3] L.S. Combes, S.S. Ballard, and K.A. McCarthy, *JOSA*, **41**(4), 215 (1951). <https://doi.org/10.1364/JOSA.41.000215>
- [4] J.T. Lewis, A. Lehoczky, and C.V. Briscoe, *Phys. Rev.* **161**(3), 877 (1967) <https://doi.org/10.1103/PhysRev.161.877>
- [5] K. Asaumi, and Mori, *T. Phys. Rev. B*, **28**(6), 3529 (1983). <https://doi.org/10.1103/PhysRevB.28.3529>
- [6] K.J. Teegarden, *Phys. Rev.* **105**(4), 1222 (1957). <https://doi.org/10.1103/PhysRev.105.1222>
- [7] Y. Ramola, C.N. Louis, and A. Amalraj, *Chem. Mater. Eng.* **5**(3), 65 (2017). <https://doi.org/10.13189/cme.2017.050302>
- [8] Y. Ramola, J. Merlinebetsy, C.N. Louis, and A. Amalraj, *Chemical and Materials Engineering*, **7**(2), 9 (2019). <https://doi.org/10.13189/cme.2019.070201>
- [9] The COSINE-100 Collaboration, **564**, 83 (2018). <https://doi.org/10.1038/s41586-018-0739-1>
- [10] C. Yam, C. Ma, X. Wang, and G. Chen, *Appl. Phys. Lett.* **85**(19), 4484 (2004). <https://doi.org/10.1063/1.1819510>

- [11] I. Ohlídal, and D. Franta, Handbook of Optical Constants of Solids, **3**, 857 (1997). <https://doi.org/10.1016/B978-012544415-6.50136-9>
- [12] R.B. Jacobs, Phys. Rev. **54**(6), 468 (1938). <https://doi.org/10.1103/PhysRev.54.468>
- [13] S.T. Weir, J. Akella, C. Aracne-Ruddle, Y.K. Vohra, and S.A. Catledge, Appl. Phys. Lett. **77**(21), 3400 (2000). <https://doi.org/10.1063/1.1326838>
- [14] P. Cortona, Phys. Rev. B, **46**, 2008 (1992). <https://doi.org/10.1103/PhysRevB.46.2008>
- [15] Z.P. Chang, and G.R. Barsch, J. Phys. Chem. Solids, **32**(1), 27 (1971). [https://doi.org/10.1016/S0022-3697\(71\)80005-7](https://doi.org/10.1016/S0022-3697(71)80005-7)
- [16] M. Ghafelehbashi, D.P. Dandekar, and A.L. Ruoff, J. Appl. Phys. **41**(2), 652 (1970). <https://doi.org/10.1063/1.1658728>
- [17] G.R. Barsch, and H.E. Shull, Physica status solidi (b), **43**(2), 637 (1971). <https://doi.org/10.1002/pssb.2220430224>
- [18] A. Asenbaum, O. Blaschko, and H.D. Hochheimer, Phys. Rev. B, **34**(3), 1968 (1986). <https://doi.org/10.1103/PhysRevB.34.1968>
- [19] A.K. Sarkar, and S. Sengupta, Physica status solidi (b), **36**(1), 359 (1969). <https://doi.org/10.1002/pssb.19690360137>
- [20] K. Teegarden, and G. Baldini, Phys. Rev. **155**(3), 896 (1967). <https://doi.org/10.1103/PhysRev.155.896>
- [21] J.J. Hopfield, and J.M. Worlock, Phys. Rev. **137**, A1455 (1965). <https://doi.org/10.1103/PhysRev.137.A1455>
- [22] J. Li, C.G. Duan, Z.Q. Gu, and D.S. Wang, Phys. Rev. B, **57**(4), 2222 (1998). <https://doi.org/10.1103/PhysRevB.57.2222>
- [23] M. Bashi, H.R. Aliabad, A.A. Mowlavi, I. Ahmad, Solid State Nucl. Magn. Reson. **82**, 10 (2017). <https://doi.org/10.1016/j.ssnmr.2016.12.009>
- [24] M.H. Norwood, and C.V. Briscoe, Physical Review, **112**(1), 45 (1958). <https://doi.org/10.1103/PhysRev.112.45>
- [25] P.W. Bridgman, Proc. Am. Acad. Arts Sci. **64**, 305 (1929). [http://nobelprize.org/nobel\\_prizes/physics/laureates/1946/bridgman-bio.html](http://nobelprize.org/nobel_prizes/physics/laureates/1946/bridgman-bio.html)
- [26] C. Gahn, and A. Mersmann, Chem. Eng. Sci. **54**(9), 1273 (1999). [https://doi.org/10.1016/S0009-2509\(98\)00450-3](https://doi.org/10.1016/S0009-2509(98)00450-3)
- [27] Y. Benkrima, D. Belfennache, R. Yekhlef, and A.M. Ghaleb, Chalcogenide Lett. **20**, 609 (2023). <https://doi.org/10.15251/CL.2023.208.609>
- [28] Y. Achour, Y. Benkrima, I. Lefkaier, and D. Belfennache, J. Nano- Electron. Phys. **15**(1), 01018 (2023) [https://doi.org/10.21272/jnep.15\(1\).01018](https://doi.org/10.21272/jnep.15(1).01018)
- [29] Y. Benkrima, D. Belfennache, R. Yekhlef, M.E. Soudani, A. Souiga, and Y. Achour, East Eur. J. Phys. (2), 150 (2023). DOI:10.26565/2312-4334-2023-2-14
- [30] H.R. Djabri, R. Khatir, S. Louhibi-Fasla, I. Messaoudi, and H. Achour, Comput. Condens. Matter, **10**, 15 (2017). <https://doi.org/10.1016/j.cocom.2016.04.003>
- [31] Y. Benkrima, A. Achouri, D. Belfennache, R. Yekhlef, and N. Hocine, East Eur. J. Phys. (2), 215 (2023). DOI:10.26565/2312-4334-2023-2-23
- [32] Y. Benkrima, S. Benhamida, and D. Belfennache, Dig. J. Nanomater. Bios. **18**(1), 11 (2023) <https://doi.org/10.15251/DJNB.2023.181.11>
- [33] Y. Benkrima, M.E. Soudani, D. Belfennache, H. Bouguettaia, and A. Souigat, J. Ovonic. Res. **18**(6), 797 (2022). <https://doi.org/10.15251/JOR.2022.186.797>
- [34] H.G. Drickamer, R.W. Lynch, R.L. Clendenen, and E.A. Perez-Albueene, Solid State Phys. **19**, 135 (1967). [https://doi.org/10.1016/S0081-1947\(08\)60529-9](https://doi.org/10.1016/S0081-1947(08)60529-9)
- [35] N. Beloufa, Y. Cherchab, S. Louhibi-Fasla, S. Daoud, H. Rekab-Djabri, and A. Chahed, Comput. Condens. Matter. **30**, e00642 (2022). <https://doi.org/10.1016/j.cocom.2022.e00642>
- [36] N. Rahman, M. Husain, W. Ullah, A. Azzouz-Rached, Y.M. Alawaideh, H. Albalawi, Z. Bayhan, *et al.*, Inorg. Chem. Commun. **166**, 112625 (2024). <https://doi.org/10.1016/j.inoche.2024.112625>
- [37] S. Daoud, P.K. Saini, and H. Rekab-Djabri, J. Nano- Electron. Phys. **12**(6), 06008 (2020). [https://doi.org/10.21272/jnep.12\(6\).06008](https://doi.org/10.21272/jnep.12(6).06008)
- [38] R. Yagoub, H.R. Djabri, S. Daoud, N. Beloufa, M. Belarbi, A. Haichour, C. Zegadi, and S.L. Fasla, Ukr. J. Phys. **66**, 699 (2021). DOI: 10.15407/ujpe66.8.699
- [39] J. Yan, J. Zhao, J. Sheng, B. Wang, and J. Zhao, Mater. Today Commun. **41**, 110966 (2024). <https://doi.org/10.1016/j.mtcomm.2024.110966>
- [40] K. Burke, Friends, *The ABC of DFT*, (Department of Chemistry, University of California, Irvine, CA 2007).
- [41] J.P. Perdew, Phys. Rev. B, **33**(12), 8822 (1986). <https://doi.org/10.1103/PhysRevB.33.8822>
- [42] J.P. Perdew, K. Burke, and M. Ernzerhof, Phys. Rev. Lett. **77**(18), 3865 (1996). <https://doi.org/10.1103/PhysRevLett.77.3865>
- [43] A.D. Becke, and E.R. Johnson, J. Chem. Phys. **124**(22), 221101 (2006). <https://doi.org/10.1063/1.2213970>
- [44] R. Hill, Proc. Phys. Soc. A, **65**, 349 (1952). <https://doi.org/10.1088/0370-1298/65/5/307>
- [45] J.P. Perdew, J. Tao, V.N. Staroverov, and G.E. Scuseria, J. Chem. Phys. **120**(15), 6898 (2004). <https://doi.org/10.1063/1.1665298>
- [46] A.D. Becke, and E.R. Johnson, J. Chem. Phys. **124**(22), 221101 (2006). <https://doi.org/10.1063/1.2213970>
- [47] A.D. Becke, and M.R. Roussel, Phys. Rev. A, **39**(8), 3761 (1989). <https://doi.org/10.1103/PhysRevA.39.3761>
- [48] F. Tran, and P. Blaha, Phys. Rev. Lett. **102**(22), 226401 (2009). <https://doi.org/10.1103/PhysRevLett.102.226401>
- [49] Y. Guermi, K. Hocine, M. Drief, T. Lantri, H. Rekab-Djabri, A. Maizia, and N.E. Benkhetou, Opt. Quant. Electron. **56**(4), 537 (2024). <https://doi.org/10.1007/s11082-023-06056-1>
- [50] F. Benguesmia, A. Benamrani, L. Boutahar, H. Rekab-Djabri, and S. Daoud, J. Phys. Chem. Res. **1**(2), 25 (2022). <https://doi.org/10.58452/jpcr.v1i2.24>
- [51] J. Jiang, J. Chem. Phys. **138**(13), 134115 (2013). <https://doi.org/10.1063/1.4798706>
- [52] O.K. Andersen, Phys. Rev. B, **12**(8), 3060 (1975). <https://doi.org/10.1103/PhysRevB.12.3060>
- [53] R. Jaradat, M. Abu-Jafar, I. Abdelraziq, S.B. Omran, D. Dahliah, and R. Khenata, Mater. Chem. Phys. **208**, 132 (2018). <https://doi.org/10.1016/j.matchemphys.2018.01.037>
- [54] P. Blaha, K. Schwarz, P. Sorantin, and S.B. Trickey, Comput. Phys. Commun. **59**(2), 399 (1990). [https://doi.org/10.1016/0010-4655\(90\)90187-6](https://doi.org/10.1016/0010-4655(90)90187-6)
- [55] H. Ibach, and H. Lueth, Solid-state physics. An introduction to principles of materials science, (Springer, Berlin, 2009). <https://doi.org/10.1007/978-3-540-93804-04>



- [56] S.H. Simon, *Problems for Solid State Physics*, (3rd Year Course 6) Hilary Term, (Oxford University, 2011).  
[57] M. Born, K. Huang, and M. Lax, *Journal of Physics*, **23**(7), 474 (1955). <https://doi.org/10.1119/1.1934059>

**СТРУКТУРНІ, ЕЛЕКТРОННІ ТА ПРУЖНІ ВЛАСТИВОСТІ ЙОДИДУ КАЛІЮ ПІД ТИСКОМ:  
ДОСЛІДЖЕННЯ АВ-INITIO**

**Хамза Рекаб-Джабрі<sup>a,b</sup>, С. Зайоу<sup>c,d</sup>, Ахмед Аззуз-Рашед<sup>e</sup>, Аммар Бенамрані<sup>f</sup>, Салах Дауд<sup>g</sup>, Д. Белфеннаше<sup>h</sup>, Р. Єхлеф<sup>h</sup>,  
Набіль Белуфа<sup>i</sup>**

<sup>a</sup>Лабораторія мікро- та нанофізики (LaMiN), Національна політехнічна школа Орана, ENPO-MA, BP 1523  
Ель-М'Науер 31000, Оран, Алжир

<sup>b</sup>Факультет природничих наук та наук про Землю, Університет АМО, Буйра 10.000, Алжир

<sup>c</sup>Лабораторія досліджень поверхонь та меж розділу твердих матеріалів (LESIMS), Університет Сетіф 1, 19000 Сетіф, Алжир

<sup>d</sup>Факультет природничих наук та наук про життя, Сетіф-1 Університет, 19000 Сетіф, Алжир

<sup>e</sup>Факультет наук, Університет Саада Дахлаба в Бліді 1, вул. Соумаа, В. Р. 270, Бліда, Алжир

<sup>f</sup>Лабораторія фізики матеріалів, радіації та наноструктур (LPMRN), Факультет наук і технологій, Університет Мохамеда Ель  
Бачіра Ель Ібрагімі-ВВА, 34000, Бордж Бу Аррерідж, Алжир

<sup>g</sup>Лабораторія матеріалів та електронних систем, Факультет наук і технологій, Університет Мохамеда Ель Бачіра Ель Ібрагімі,  
ВВА, 34000 Бордж Бу Аррерідж, Алжир

<sup>h</sup>Науково-дослідний центр промислових технологій CRTI, P.O. A/c 64, Черага, 16014 Алжир, Алжир

<sup>i</sup>Гідрометеорологічний інститут формування та досліджень IHFR, Оран, Алжир

У цій роботі було використано нещодавню версію методу повного потенціалу лінійних мафін-тинових орбіталей (FP-LMTO) з використанням наближення локальної густини (LDA) в рамках теорії функціоналу густини (DFT). Цей підхід було застосовано для вивчення структурної, електронної та пружної поведінки сполуки йодиду калію (KI) під тиском. Розраховані структурні параметри демонструють сильну відповідність з наявними теоретичними та експериментальними даними. Фаза RS була визначена як найстабільніша структура для матеріалу KI. Фазовий перехід від фази типу NaCl (B1) до фази типу CsCl (B2) відбувається при тиску 1,633 ГПа, що цілком узгоджується з експериментальними значеннями. Крім того, зонна структура KI виявила широкозонну напівпровідникову поведінку у всіх досліджених фазах. Отримані значення модуля об'ємної пружності були відносно низькими, що свідчить про слабку стійкість до руйнування. Було визначено константи пружності для KI в структурах RS, CsCl, ZnS, HCP та WZ, які відповідають умовам стійкості Борна. Ми вважаємо, що в літературі немає значень констант пружності для KI у фазах CsCl, ZnS та WZ. Усі аналізовані структури демонстрували пластичні характеристики та особливості іонних зв'язків. Крім того, анізотропні властивості спостерігалися у всіх фазах. Жорсткість сполуки оцінювали за допомогою коефіцієнта Пуассона та тиску Коші. Результати показали, що фаза CsCl є найжорсткішою серед досліджуваних конфігурацій.

**Ключові слова:** йодид калію (KI); FP-LMTO; електронні властивості; еластичні властивості; фазовий перехід